Transactions of the ASME®

Journal of Heat Transfer

Published Quarterly by The American Society of Mechanical Engineers

VOLUME 114 • NUMBER 2 • MAY 1992

HEAT TRANSFER DIVISION
Chairman, **J. R. WELTY**
Secretary, **O. A. PLUMB**
Technical Editor, **R. VISKANTA**
Associate Technical Editors,
R. O. BUCKIUS (1993)
W. A. FIVELAND (1992)
L. S. FLETCHER (1992)
F. P. INCROPERA (1993)
H. R. JACOBS (1992)
J. H. KIM (1993)
J. R. LLOYD (1992)
D. M. McELIGOT (1992)
R. J. SIMONEAU (1993)
W. A. SIRIGNANO (1992)
L. C. WITTE (1992)

BOARD ON COMMUNICATIONS
Chairman and Vice President
M. E. FRANKE

Members-at-Large
W. BEGELL
T. F. CONRY
T. DEAR
R. L. KASTOR
J. KITTO
R. MATES
W. MORGAN
E. M. PATTON
R. E. REDER
A. VAN DER SLUYS
F. M. WHITE
B. ZIELS

President, **N. H. HURT, JR.**
Executive Director,
D. L. BELDEN
Treasurer,
ROBERT A. BENNETT

PUBLISHING STAFF
Mng. Dir., Publ.,
CHARLES W. BEARDSLEY
Managing Editor,
CORNELIA MONAHAN
Sr. Production Editor,
VALERIE WINTERS
Production Assistant,
MARISOL ANDINO

Transactions of the ASME, Journal of Heat Transfer (ISSN 0022-1481) is published quarterly (Feb., May, Aug., Nov.) for $160.00 per year by The American Society of Mechanical Engineers, 345 East 47th Street, New York, NY 10017. Second class postage paid at New York, NY and additional mailing offices. POSTMASTER: Send address changes to Transactions of the ASME, Journal of Heat Transfer, c/o THE AMERICAN SOCIETY OF MECHANICAL ENGINEERS, 22 Law Drive, Box 2300, Fairfield, NJ 07007-2300.
CHANGES OF ADDRESS must be received at Society headquarters seven weeks before they are to be effective. Please send old label and new address.
PRICES: To members, $36.00, annually: to nonmembers, $160.00. Add $15.00 for postage to countries outside the United States and Canada.

STATEMENT from By-Laws. The Society shall not be responsible for statements or opinions advanced in papers or . . . printed in its publications (B7.1, para. 3).
COPYRIGHT © 1992 by The American Society of Mechanical Engineers. Reprints from this publication may be made on condition that full credit be given the TRANSACTIONS OF THE ASME, JOURNAL OF HEAT TRANSFER, and the author, and date of publication be stated.

INDEXED by Applied Mechanics Reviews and Engineering Information, Inc.
Canadian Goods & Services Tax Registration #126148048

ANNOUNCEMENTS

TECHNICAL PAPERS

Downloaded 04 Feb 2011 to 194.85.80.107. Redistribution subject to ASME license or copyright; see http://www.asme.org/terms/Terms_Use.cfm

(Contents continued)

TECHNICAL NOTES

1990 Max Jakob Memorial Award Lecture

Viscoelastic Fluids: A New Challenge in Heat Transfer

J. P. Hartnett
Energy Resources Center,
The University of Illinois at Chicago,
Chicago, IL 60680

A review of the current knowledge on the fluid mechanics and heat transfer behavior of viscoelastic aqueous polymer solutions in channel flow is presented. Both turbulent and laminar flow conditions are considered. Although the major emphasis is on fully established circular pipe flow, some results are also reported for flow in a 2:1 rectangular channel. For fully established turbulent channel flow, it was found that the friction factor, f, and the dimensionless heat transfer factor, j_H, were functions of the Reynolds number and a dimensionless elasticity value, the Weissenberg number. For Weissenberg values greater than approximately 10 (the critical value) the friction factor was found to be a function only of the Reynolds number; for values less than 10 the friction factor was a function of both Re and Ws. For the dimensionless heat transfer coefficient j_H the corresponding critical Weissenberg value was found to be about 100. The heat transfer reduction is always greater than the friction factor reduction; consequently, the heat transfer per unit pumping power decreases with increasing elasticity. For fully established laminar pipe flow of aqueous polymer solutions, the measured values of the friction factor and dimensionless heat transfer coefficient were in excellent agreement with the values predicted for a power law fluid. For laminar flow in a 2:1 rectangular channel the fully developed friction factor measurements were also in agreement with the power law prediction. In contrast, the measured local heat transfer coefficients for aqueous polymer solutions in laminar flow through the 2:1 rectangular duct were two to three times the values predicted for a purely viscous power law fluid. It is hypothesized that these high heat transfer coefficients are due to secondary motions, which come about as a result of the unequal normal stresses occurring in viscoelastic fluids. The anomalous behavior of one particular aqueous polymer solution—namely, polyacrylic acid (Carbopol)—is described in some detail, raising some interesting questions as to how viscoelastic fluids should be classified. In closing, a number of challenging research opportunities in the study of viscoelastic fluids are presented.

Introduction

Interest in viscoelastic fluids goes back almost a half century, triggered by the discovery of Mysels (1949) and Toms (1948), who found that the addition of small amounts of a high-molecular-weight polymer to a Newtonian fluid in turbulent pipe flows resulted in a dramatic decrease in pressrue drop. Evidence of this behavior is shown on Fig. 1 (Cho and Hartnett, 1982), which reveals that the presence of 10 parts per million by weight (wppm) of polyacrylamide in water results in a 40 percent reduction in pressure drop and a comparable decrease in pumping power. In the intervening years many studies of the fluid mechanical behavior of such fluids have been carried out (Cho and Hartnett, 1985). In contrast, relatively little attention has been paid to heat transfer processes associated with these fluids. As it turns out, such fluids are viscoelastic, a class of fluids of considerable interest in the chemical, pharmaceutical, and food industries. In the processing of these fluids they are often exposed to heat transfer, and consequently a knowledge of their heat transfer behavior is important in the design of such industrial equipment.

It is the goal of this review to introduce some of the characteristics that distinguish viscoelastic fluids from Newtonian fluids. In particular, those factors that influence the fluid mechanics and heat transfer behavior of viscoelastic fluids, especially aqueous polymer solutions, will be emphasized. Turbulent flow will be treated first, then laminar flow. Both circular and noncircular channels will be covered. The article concludes with a brief discussion dealing with future research opportunities.

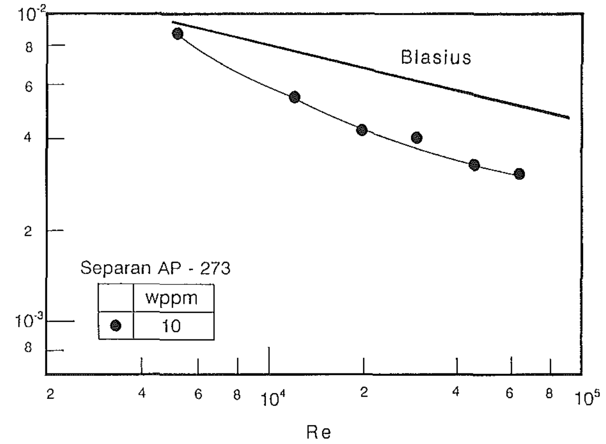

Fig. 1 Influence of addition of 10 wppm of polyacrylamide on pressure drop of water in fully established turbulent pipe flow

Viscoelastic Fluids

Viscoelastic fluids may be prepared by adding to water a high-molecular-weight polymer, such as one of those shown on Fig. 2. Such fluids are generally non-Newtonian and the apparent viscosity (defined as the ratio of the shear stress to the shear rate) of such viscoelastic fluids is dependent on the shear rate. Furthermore as shown on Fig. 3, the normal stresses on the three orthogonal faces (P_{xx}, P_{yy}, and P_{zz}), which are equal in Newtonian fluids, for incompressible isometric flow are not equal in viscoelastic fluids. Finally, under channel flow conditions, such as exemplified by the plane Couette flow

---

Contributed by the Heat Transfer Division and presented at the 3rd ASME/JSME Joint Thermal Engineering Conference, Reno, Nevada, March 18, 1991. Manuscript received by the Heat Transfer Division November 1991; revision received March 1992. Keywords: Forced Convection, Non-Newtonian Flows and Systems.

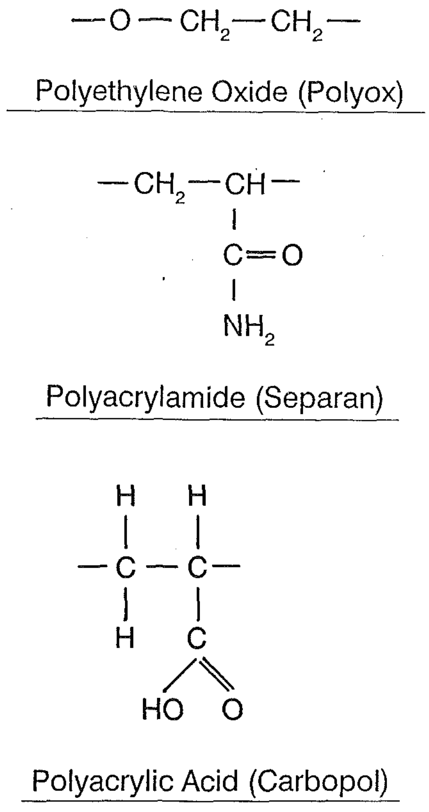

Fig. 2 Basic chemical structure of typical polymers used in experimental studies

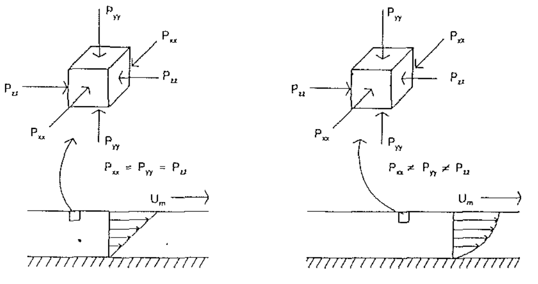

Newtonian Fluid (Viscosity not Function of Shear Rate) Viscoelastic Fluid (Viscosity is Function of Shear Rate)

Fig. 3 Couette flow of Newtonian fluid and viscoelastic fluid

shown on Fig. 3, if the external force driving the flow is suddenly removed, a Newtonian fluid ceases to flow. In contrast, a viscoelastic fluid actually continues to move, coming to rest after a time interval λ, called the relaxation time. In general, the more elastic the fluid, the greater the magnitude of the relaxation time.

In the study of the pressure drop and heat transfer behavior of Newtonian fluids, it is customary to introduce dimensionless quantities such as the friction factor, the Nusselt number, the Reynolds number, and the Prandtl number. A new dimensionless number, the Weissenberg number, appears in the case of viscoelastic fluids, and is defined as:

$$\mathrm{Ws} = \lambda U/d \tag{1}$$

The Weissenberg number is the ratio of the relaxation time of the fluid, λ, to the characteristic time of the flow, d/U; the larger the Weissenberg number, the more elastic the flow.

The evaluation of the relaxation time, λ, is in general a

Nomenclature

A = cross-sectional area, m^2
C_p = specific heat of fluid, J/kg•K
d = diameter of circular pipe, m
d_h = hydraulic diameter of the duct, $= 4A/P$, equal to d for circular pipe, m
f = fanning friction factor $= \tau_w/(\rho U^2/2)$
Gz = Graetz number $= \dot{m}C_p/kz$
h = local convective heat transfer coefficient $= q''/(T_w - T_b)$, W/m^2•K
$H1(1L)$ = thermal boundary conditions representing constant wall heat flux axially and constant temperature peripherally on one longer wall of the rectangular duct
$H1(2L)$ = thermal boundary conditions representing constant wall heat flux axially and constant temperature peripherally on two longer walls of the rectangular duct
$H1(4)$ = thermal boundary conditions representing constant wall heat flux axially and constant temperature peripherally on all four walls of the rectangular duct
j_H = Colburn heat transfer factor $= \mathrm{Nu}/\mathrm{RePr}^{1/3}$
k = thermal conductivity, W/m•K
K = consistency index in power law model, $N•s^n/m^2$
$\dot{m}$ = mass flow rate, kg/s
n = power law index in power law model
Nu = local Nusselt number $= hd_h/k$
Nu_{L1} = local Nusselt number for lower wall in the case of $H1(1L)$ boundary condition
Nu_{u1} = local Nusselt number for upper wall in the case of $H1(1L)$ boundary condition
P = wetted perimeter, m
Pr = Prandtl number $= \eta C_p/k$
P_{xx} = normal stress in the x direction
P_{yy} = normal stress in the y direction
P_{zz} = normal stress in the z direction
q'' = heat flux per unit heating area, W/m^2
R = pipe radius, m
r = local radius, m
Ra_q = Rayleigh number $= C_p\rho^2 g\beta q'' d_h^4/k^2\eta$
Re = Reynolds number $= \rho U d_h/\eta$
Re′ = Metzner-Reed generalized Reynolds number, defined in Eq. (7)
Re* = Kozicki generalized Reynolds number, defined in Eq. (10)
T_b = local fluid bulk temperature, °C
T_w = local wall temperature of the duct, °C
u = velocity component in axial direction, m/s
U = mean velocity in axial direction, m/s
Ws = Weissenberg number $= \lambda U/d_h$
z = axial rectilinear coordinate, or axial location from the duct entrance, m
β = volumetric coefficient of thermal expansion, $°C^{-1}$
$\dot{\gamma}$ = shear rate, 1/s
η = fluid apparent viscosity $= \tau_w/\dot{\gamma}$, $N•s/m^2$
η_o = zero shear rate apparent viscosity, $N•s/m^2$
η_∞ = shear rate apparent viscosity evaluated at $\dot{\gamma}$ approaching infinity, $N•s/m^2$
λ = relaxation time, s
λ^* = characteristic time constant, s
ρ = density of fluid, kg/m^3
τ_w = shear stress at wall, N/m^2
τ = shear stress, N/m^2

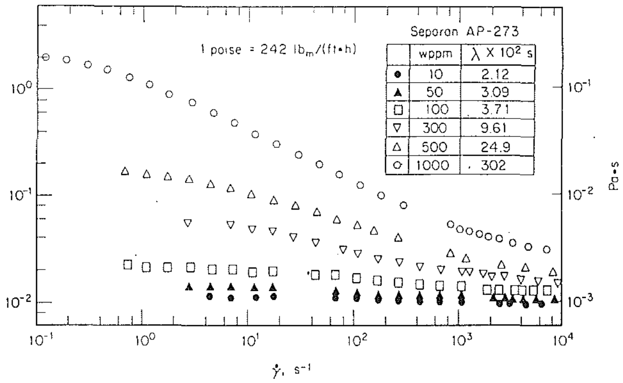

Fig. 4 Apparent viscosity as a function of shear rate of aqueous polyacrylamide solution, with polymer concentration as a parameter

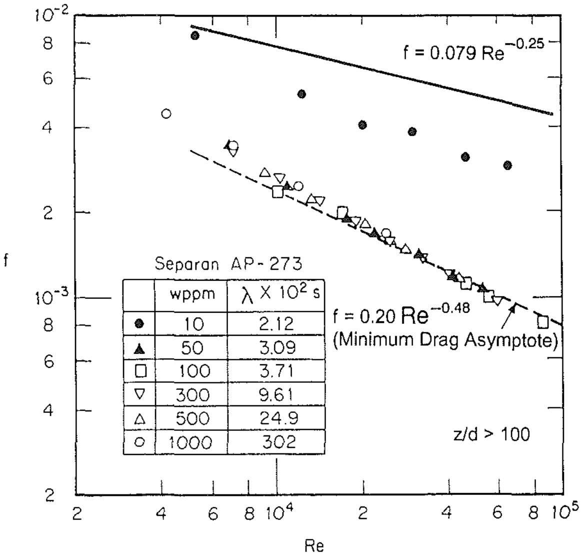

Fig. 5 Friction factor as a function of Reynolds number for aqueous polyacrylamide solutions, with polymer concentration as a parameter

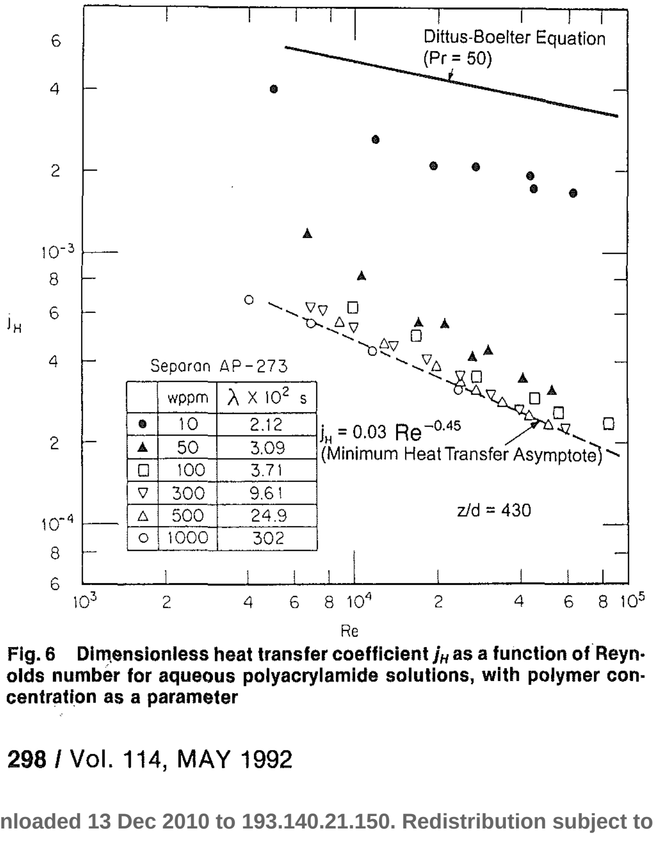

Fig. 6 Dimensionless heat transfer coefficient j_H as a function of Reynolds number for aqueous polyacrylamide solutions, with polymer concentration as a parameter

difficult task. However, Bird (1965) and other investigators have proposed the use of relatively simple Newtonian models for this purpose. As an example of this approach, consider the Powell-Eyring model:

$$\eta = \eta_\infty + (\eta_0 - \eta_\infty)\,\frac{\sinh^{-1}\lambda^*\dot{\gamma}}{\lambda^*\dot{\gamma}} \tag{2}$$

Here $\dot{\gamma}$ is the shear rate, η_∞ and η_0 are the apparent viscosities evaluated at large values of $\dot{\gamma}$ (i.e., $\dot{\gamma} \to \infty$) and at very low values of $\dot{\gamma}$ (i.e., $\dot{\gamma} \to 0$), respectively. If η is measured as a function of $\dot{\gamma}$, then it is possible to determine the value of λ^*, the characteristic time constant, which provides the best fit to the experimentally determined relationship between η and $\dot{\gamma}$. It is generally assumed that the relaxation time, λ, and the characteristic time constant λ^* are related; for convenience they are often taken as equal.

In summary the following statements may be made about viscoelastic fluids:

- The apparent viscosity is dependent on shear rate.
- The stresses on orthogonal faces are not equal.
- A finite time is required for a strain response in the fluid when the stress imposed on the fluid boundaries is changed.
- A new dimensionless quantity, the Weissenberg number, characterizes the elastic nature of the fluid.

Turbulent Flow of Aqueous Polymer Solutions

Turbulent Flow in Circular Tubes. Factors influencing the pressure drop and heat transfer behavior of viscoelastic aqueous polymer fluids involve all of the conventional dimensionless quantities plus the Weissenberg number. The Weissenberg number, in turn, is influenced by the concentration and the chemistry of the polymer, the chemistry of the solvent, and last, but not least, the degradation of the polymer. This last factor, polymer degradation, results from the rupture of the polymer bonds due to the shearing stresses encountered during the circulation of an aqueous polymer solution through a flow system.

The influence of polymer concentration is brought out on Figs. 4–6. Figure 4 presents the apparent viscosity as a function of shear rate for various concentrations of polyacrylamide (Separan AP 273 from Dow Chemical Company) in Chicago tap water (Cho and Hartnett, 1982). Figures 5 and 6 present fully established friction factors and dimensionless heat transfer coefficients for these fluids.

At the lowest concentration, 10 wppm, the measured apparent viscosity is not observably different from that of water alone, but the experimental friction factors and the dimensionless heat transfer factors, j_H, are significantly reduced from the Newtonian values. It should also be noted that the measured reduction in heat transfer is greater than the reduction in pressure drop.

An increase in the polymer concentration results in an increase of the apparent viscosity (especially at lower shear rates) and an increase in the characteristic time λ. The corresponding friction factor, shown on Fig. 5, decreases with an increase in polymer concentration, reaching an asymptotic value at approximately 50 wppm. Further increases in the polymer concentration have no effect on the friction factor. Such asymptotic friction factor behavior was first reported by Virk et al. (1970).

In the case of heat transfer, the experimental j_H factor evaluated at z/d equal to 430 decreases with increasing polymer concentration until a concentration of 300-500 wppm is reached, as shown on Fig. 6. Further increases of the polymer concentration do not lead to further reduction in the heat transfer, and an asymptotic value of the dimensionless heat transfer is reached. In general, as noted above for the 10 wppm solution, the heat transfer reduction for a fixed polymer concentration is always greater than the pressure drop reduction.

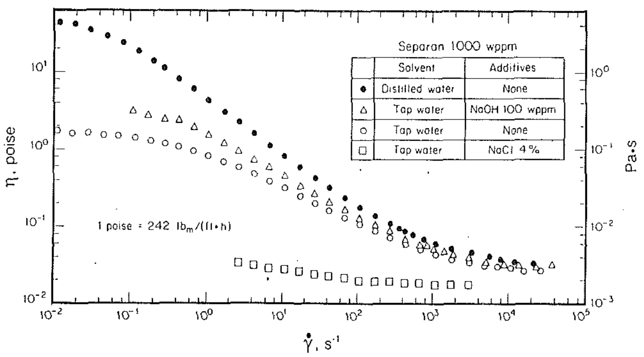

Fig. 7 Apparent viscosity as a function of shear rate for various solvent-additive combinations

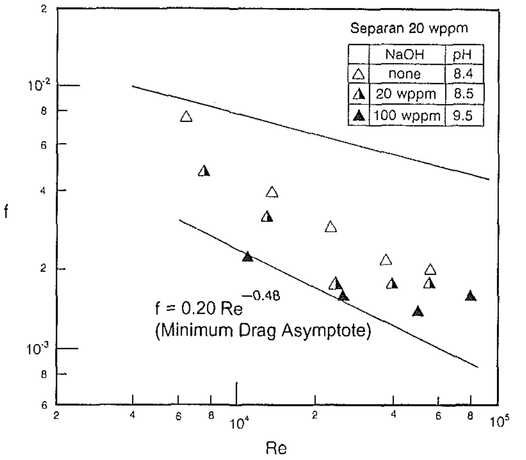

Fig. 8 Friction factor as a function of Reynolds number for various solvent-additive combinations

Thus the heat transfer per unit of pumping power decreases with increasing polymer concentration when compared at a constant Reynolds number.

The hydrodynamic and thermal entrance lengths are also influenced by the polymer concentration (i.e., by the fluid elasticity). The entrance lengths increase from values of 10 to 20 pipe diameters for water to 100 pipe diameters for the hydrodynamic entrance length and 500 pipe diameters for the thermal entrance length for high polymer concentrations. Toh and Ghajar (1988) report thermal entrance region Nusselt values for the turbulent flow of two different polyacrylamides in circular test sections of 1.11 and 1.88 cm i.d. under constant wall heat flux conditions.

Turning next to the influence of solvent chemistry on the behavior of an aqueous polymer solution, Fig. 7 shows the measured apparent viscosity as a function of shear rate for 1000 wppm of polyacrylamide in Chicago tap water; in Chicago tap water with 100 wppm of sodium hydroxide; in Chicago tap water with 4 percent sodium chloride to simulate sea water; and in distilled water. The solution with distilled water has a value of the zero shear rate viscosity η_0, which is an order of magnitude greater than the other solutions. Generally, for a given polymer an increase in the zero shear rate viscosity is associated with an increase in the elasticity and as a result it can be concluded that the elasticity of the distilled water solution is the highest of the four solutions.

Evidence of the solvent chemistry effect is also seen on Fig. 8, which reveals the friction factor for 20 wppm of polyacrylamide with Chicago tap water as the solvent. The addition of 20 wppm of sodium hydroxide to the solution results in a decrease in the friction factor at a fixed Reynolds number. If the concentration of sodium hydroxide is increased to 100 wppm an even greater reduction in the friction factor results.

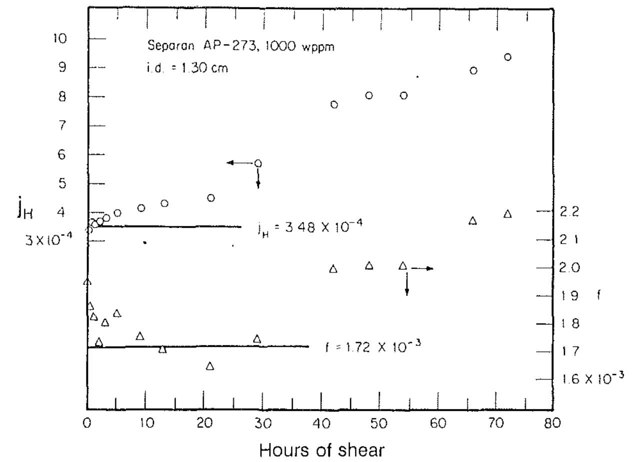

Fig. 9 Friction factor and dimensionless heat transfer coefficient of 1000 wppm aqueous polyacrylamide solutions as a function of hours of circulation in the flow loop

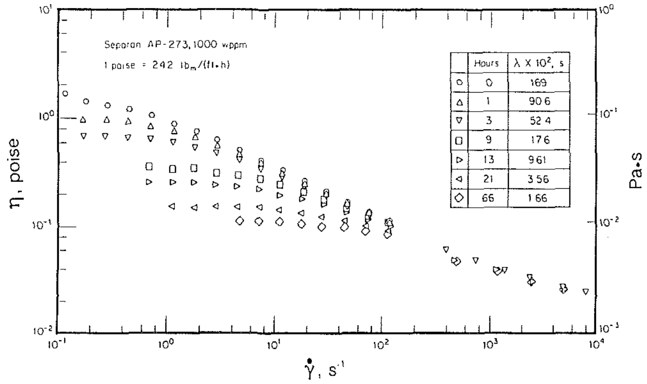

Fig. 10 Apparent viscosity versus shear rate of 1000 wppm aqueous polyacrylamide solution as a function of hours of circulation in the flow loops

Heat transfer results are similarly influenced by solvent chemistry.

The influence of polymer degradation is brought out clearly in Figs. 9 and 10. In these experiments a 1000 wppm solution of polyacrylamide in Chicago tap water is circulated at a constant flow rate for over 70 hours and the friction factor, f, and the heat transfer factor, j_H, are measured as a function of time. From Fig. 9 it can be seen that the friction factor decreases slightly at the start (probably reflecting improved mixing of the polymer and the solvent), remaining approximately constant for some hours and then begins to increase. In contrast, the heat transfer factor begins to increase almost immediately. The corresponding values of the viscosity and the characteristic time as a function of the hours of circulation are presented on Fig. 10. At the initial state the zero shear rate viscosity was approximately 2 poise while the characteristic time was of the order of 1.69 seconds. After circulating for some 21 hours, the value of the low shear rate apparent viscosity was an order of magnitude lower and the characteristic time had decreased to 0.036 seconds. Thus as the fluid circulates, the long molecular chains are constantly being broken by the shearing stresses and the fluid become less and less elastic as reflected in the ever-decreasing values of η and λ.

All of the above described results can be generalized if the rheology of the flow is constantly monitored so that the values of the apparent viscosity versus shear rate and the corresponding values of the characteristic time, λ, are known as a function of circulation time of the fluid. Then the fully established friction factor and the fully established dimensionless heat

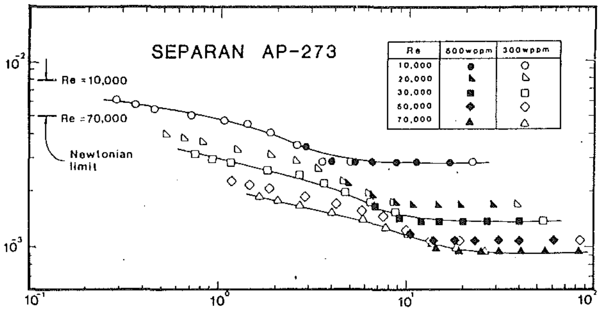

Fig. 11 Friction factor of aqueous polyacrylamide solutions as a function of Weissenberg number with Reynolds number as parameter

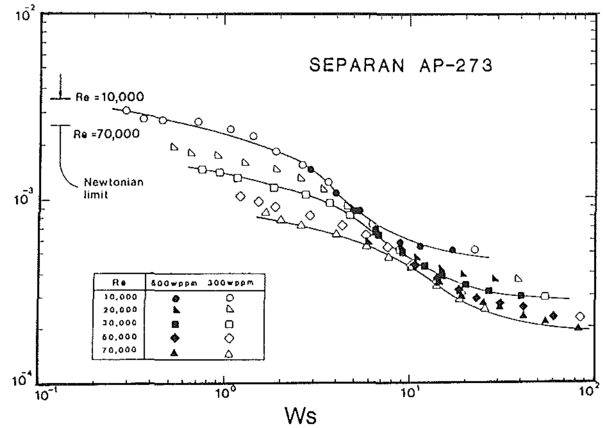

Fig. 12 Dimensionless heat transfer of aqueous polyacrylamide solutions as a function of Weissenberg number with Reynolds number as a parameter

transfer can be presented as a function of the Weissenberg and Reynolds numbers that prevail at the time of interest. The generalized behavior of the friction factor is shown on Fig. 11, where it may be seen that for a fixed Reynolds number the friction factor decreases with increasing Weissenberg number, reaching an asymptotic value at a Weissenberg number of approximately 10 (Hartnett and Kwack, 1985). Beyond this asymptotic value the fully established friction factor is a function only of the Reynolds number.

Figure 12 shows the corresponding heat transfer behavior of the aqueous polymer solution (Hartnett and Kwack, 1985). Here the asymptotic behavior occurs at a much higher value of the Weissenberg number, approximately 100. Below this value, the fully established j_H factor is a function of both the Reynolds and the Weissenberg numbers, while at values of the Weissenberg number greater than approximately 100, j_H is a function only of the Reynolds number.

The same behavior has been reported for other aqueous polymer solutions (Ghajar and Azar, 1988) and the approach reported here should be useful in generalizing experimental results for other aqueous polymer solutions.

Turbulent Flow in Noncircular Channels. Heat transfer and pressure drop results for drag-reducing fluids in turbulent flow through noncircular geometries are relatively rare. However, on the basis of available results for rectangular channels (Kostic and Hartnett, 1985; Bhamidipaty, 1988) the following approach appears reasonable. If experimental pipe flow data are available for a given aqueous polymer solution (such as Separan AP273 on Figs. 5 and 6), then these results may be used with the hydraulic diameter replacing the pipe diameter to estimate the friction factor and the heat transfer coefficient of the same polymer solution in turbulent flow through a noncircular channel. The thermal boundary condition (i.e., constant wall temperature, constant heat flux, one wall heated, two walls heated, etc.) will undoubtedly have some influence, but the recommended approach should yield engineering predictions with an accuracy of 10 to 20 percent. However, this approach will probably fail in geometries such as triangular channels with very sharp corners, where the confining walls will result in an extended laminar region (Eckert and Irvine, 1960).

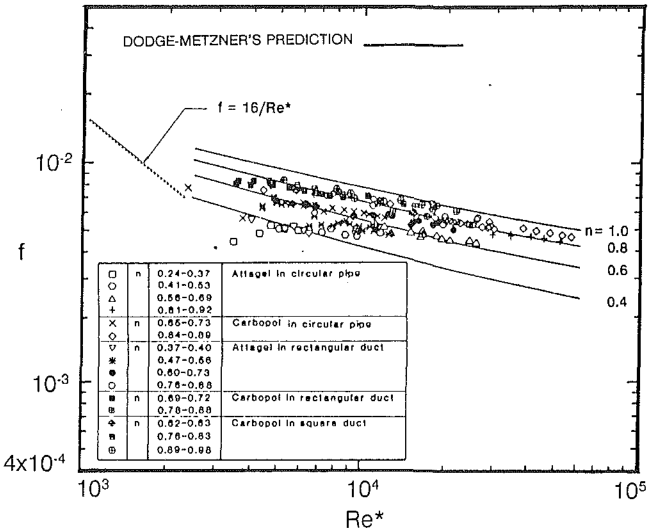

Fig. 13 Friction factor as a function of the Kozicki generalized Reynolds number for aqueous Carbopol solutions and clay slurries in fully established turbulent channel flow

Anomalous Behavior of Aqueous Polyacrylic Acid Solutions. An exception to the generally observed drag-reducing behavior of aqueous polymer solutions described above occurs in the case of aqueous solutions of polyacrylic acid (Carbopol from B. F. Goodrich Co.). Aqueous solutions of Carbopol when neutralized with sodium hydroxide to a pH value of approximately 7 become highly non-Newtonian, exhibiting a viscosity that is highly dependent on shear rate. Furthermore, rheological measurements taken on an oscillatory viscometer (Xie and Hartnett, 1992) clearly demonstrate that such solutions are viscoelastic. Nevertheless, the pressure drop and heat transfer behavior of neutralized aqueous Carbopol solutions in turbulent pipe flow reveals little reduction in either of these quantities. Rather, they behave like clay slurries (e.g., Attagel 40 from Engelhard Minerals and Chemicals Corporation) and they have been generally identified as purely viscous non-Newtonian fluids. Their dimensionless pressure drop and heat transfer performance are related to the Kozicki generalized Reynolds number Re* and the power low exponent n. Figure 13 shows experimental results for the friction factor behavior of clay slurries and of aqueous Carbopol solutions in turbulent flow for both circular tubes and rectangular ducts. A semi-empirical prediction of this behavior has been advanced by Dodge and Metzner (1959) for purely viscous non-Newtonian flow in a circular tube and extended by Kostic and Hartnett (1984) to noncircular geometries:

$$1/\sqrt{f} = (4.0/n^{0.75}\log_{10}[\mathrm{Re}^*(f)^{1-n/2}] - 0.4/n^{1.2} \qquad (3)$$

The prediction is seen to be in good agreement with the experimental data for both circular and rectangular channels.

The heat transfer behavior of Carbopol solutions is also found to be in good agreement with the results found for clay slurries. Simplified purely viscous formulations are available that are in good agreement with experimental data (Hartnett and Kostic, 1989).

The major point to be made here is that viscoelastic solutions of Carbopol act as purely viscous non-Newtonian fluids, such

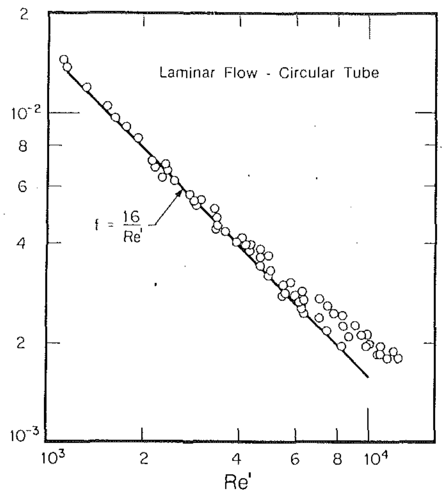

Fig. 14 Friction factor as a function of the Metzner generalized Reynolds number, Re′, for aqueous polymer solutions in fully established laminar pipe flow; polymer concentrations range from 1500 wppm to 5000 wppm

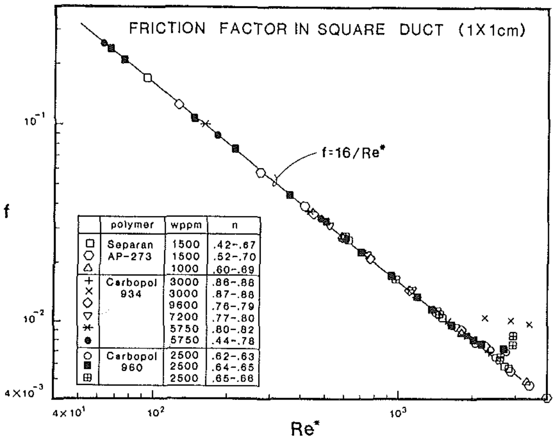

Fig. 15 Friction factor as a function of the Kozicki generalized Reynolds number, Re*, for aqueous polymer solution in fully established laminar flow through a square duct

as clay slurries, when flowing turbulently through circular and noncircular channels.

Laminar Flow of Aqueous Polymer Solutions

Laminar Flow in Circular Tubes. Viscoelastic fluids in fully established steady state flow through circular tubes behave as purely viscous fluids, since there is no mechanism for the elastic nature of the fluid to be manifested. Thus, the simple power law model gives excellent predictions of the fluid behavior. Here it is assumed that the shear stress is related to the shear rate by the power law

$$\tau = K\dot{\gamma}^n \tag{4}$$

Then a solution of the momentum equation for the fully established velocity profile yields

$$\frac{u}{U} = \frac{3n+1}{n+1}\left[1 - (r/R)^{\frac{n+1}{n}}\right] \tag{5}$$

This leads to the following prediction for the fully developed friction factor:

$$f = 16 / \frac{\rho U^{2-n} d^n}{K\left(\frac{3n+1}{4n}\right)^n 8^{n-1}} \tag{6}$$

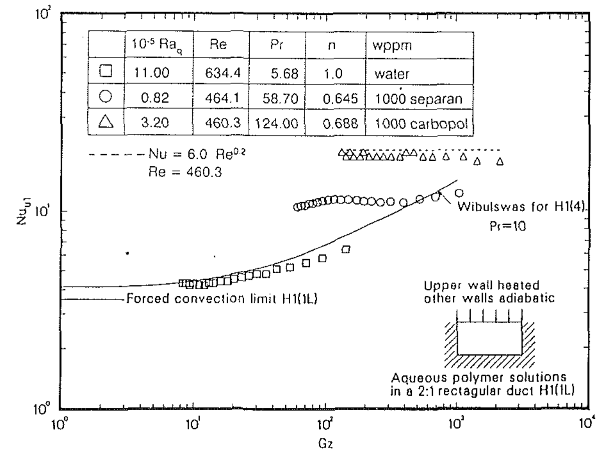

Fig. 16 Local Nusselt number for water, aqueous polyacrylamide, and aqueous polyacrylic acid solutions as a function of Graetz number for upper wall heated, other walls adiabatic

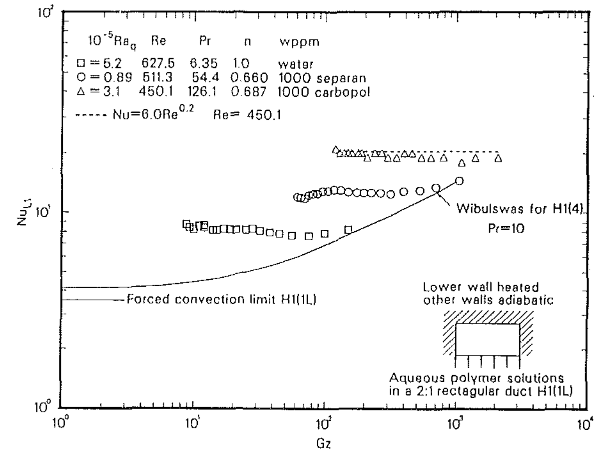

Fig. 17 Local Nusselt number for water, aqueous polyacrylamide, and aqueous polyacrylic acid solutions as a function of Graetz number for lower wall heated, other walls adiabatic

Metzner and Reed (1955) identified the denominator as a generalized Reynolds number

$$\mathrm{Re}' = \rho U^{2-n} d^n / \left(\frac{3n+1}{4n}\right)^n K\, 8^{n-1} \tag{7}$$

and noted that

$$f = 16/\mathrm{Re}' \tag{8}$$

The formulation reduces to the conventional relationship for Newtonian fluids. Figure 14 presents pressure drop measurements for both aqueous polyacrylamides and aqueous polyethylene oxide solutions taken in three different diameter tubes (Ng et al., 1980). The experimental data are in good agreement with the power law predictions.

The fully established velocity distribution resulting from the solution of the momentum equation can be substituted into the energy equation and the equation can be solved for either the constant heat flux or the constant wall temperature boundary condition. Detailed experimental heat transfer results covering a wide range of power law exponents and thermal boundary conditions are available and are in agreement with the power law predictions (Cho and Hartnett, 1982).

On the basis of the available measurements of friction factors and Nusselt numbers, it can be concluded that viscoelastic fluids in steady laminar pipe flow behave as purely viscous non-Newtonian fluids. However, under unsteady flow conditions (e.g., pulsating flows, entrance region flows, etc.) the behavior of viscoelastic fluids is expected to deviate from that of purely viscous fluids since the fluid elasticity can now come into play.

Laminar Flow in Rectangular Channels. The purely viscous power law model was shown to predict the pressure drop and heat transfer behavior of viscoelastic aqueous polymer solutions in fully established laminar pipe flow. It seems reasonable, as a first approximation, to try the same approach when dealing with aqueous polymer solutions in fully established laminar flow through rectangular channels.

Kozicki et al. (1966) showed that the friction factor for fully established laminar flow of a power law fluid in a rectangular channel can be given with good accuracy by the following relationship:

$$f = 16/\text{Re}^* \tag{9}$$

where Re^* is the Kozicki generalized Reynolds number

$$\text{Re}^* = \rho U^{2-n} d_h^n \Big/ \left[8^{n-1} K \left(b + \frac{a}{n} \right)^n \right] \tag{10}$$

Here a and b are functions of the aspect ratio (Kozicki et al., 1966). Equations (9) and (10) are valid for other geometries as well. In the case of the circular tube the values of a and b are 0.25 and 0.75, respectively, and Re^* becomes identical with Re', and Eq. (6) becomes a special case of the generalized Kozicki formulation.

Experimental pressure drop measurements have been reported for viscoelastic aqueous polymer solutions in laminar flow through a square duct (Hartnett et al., 1986), a 2:1 rectangular duct (Hartnett and Kostic, 1985) and a 5:1 rectangular duct (Bhamidipaty, 1988). Figure 15 presents the square duct measurements taken under isothermal conditions, and they are seen to be in excellent agreement with the power law prediction. Measured friction factors for the 2:1 duct and the 5:1 duct taken under nonadiabatic conditions show some scatter, but overall the agreement with the power law prediction is within ±10 percent. On the basis of these experimental results it can be concluded that the fully developed friction factors for the laminar flow of aqueous polymer solutions in rectangular channels may be predicted with good accuracy by the power law model. Furthermore, it is tentatively recommended that the power law prediction be used to estimate the fully established friction factor for the laminar flow of aqueous polymer solutions through any noncircular geometry, whose cross section does not vary in the flow direction.

Turning to the heat transfer behavior of aqueous polymer solutions flowing through rectangular geometries, the power law model might appear to offer a reasonable estimate. This model has been shown to yield acceptable predictions of the pressure drop and heat transfer for established laminar pipe flow, as well as reasonable estimates of the pressure drop for established laminar flow in rectangular channels. The analytical approach is straightforward and local Nusselt values have been reported over a range of aspect ratios and power law exponents for a number of thermal boundary conditions (Hartnett and Kostic, 1989). For a fixed aspect ratio and a given set of thermal boundary conditions, the local Nusselt number increases by approximately 10 percent from the Newtonian value as the power law index decreases to 0.5.

Against this background, laminar flow experimental heat transfer studies have been carried out in a 2:1 rectangular duct with aqueous solutions of polyacrylamide (Separan AP273) by Kostic (1984) and Xie (1991) and with aqueous polyacrylic acid (Carbopol 934) solutions by Xie (1991). The experimental procedure was validated by measurements with water as the test fluid with the upper wall being heated and the other three walls adiabatic. The thermal boundary condition approximated constant heat flux axially and constant temperature peripherally. Free convection effects should be negligible for this case.

Figure 16 presents the measured local Nusselt values for water and several aqueous polymer solutions. Also shown is the Newtonian prediction of Wibulswas (1966) for the case where all four walls are heated, the $H1(4)$ boundary condition, with simultaneous development of velocity and temperature distribution and a Prandtl number of 10. Also, shown for reference is the limiting Nusselt value when only one of the longer walls is heated,the $H1(1L)$ boundary condition (Shah and London, 1978), which is seen to result in lower values of the heat transfer coefficient as compared to the $H1(4)$ condition. Taking this into account, the measured heat transfer performance of water is in general agreement with the predicted values.

If the aqueous polymer solutions behaved as purely viscous fluids, their local Nusselt values should be approximately 10 percent higher than the values measured for water. In actuality the measured Nusselt values for both aqueous polymer solutions were three to four times greater than found for water. The fact that the Carbopol solution, which behaved like a clay slurry under turbulent flow condition, actually shows higher Nusselt values than the Separan solution is of special interest.

Experimental results were also obtained for the case where the lower wall was heated and the other three walls adiabatic (Fig. 17). As expected, the water results were higher for this case, as compared to the upper wall heating condition, revealing the effects of free convection. In contrast, the two aqueous polymer solutions demonstrated about the same behavior for the upward heating case as found in the downward heating configuration.

These experimental results are consistent with earlier predictions of Green and Rivlin (1956) and Wheeler and Wissler (1966) that normal stress differences acting on the fluid boundary of viscoelastic fluids in laminar flow through noncircular geometries give rise to secondary flows. It is hypothesized that these secondary motions completely overwhelm any free convection effects in the aqueous polymer experiments reported here. Furthermore, since it is predicted that the secondary flows increase with fluid elasticity, it appears that the aqueous Carbopol solution is more elastic than the Separan solution. Other investigators (for example, Kostic, 1991) suggest that the increased heat transfer may be associated with the combination of a weakly elastic fluid and flow-induced anisotropic behavior. Finally, it should be noted that in spite of the presence of secondary flows, the fully established friction factor for laminar flow through noncircular channels can be predicted with good accuracy by the purely viscous power law relationship.

Concluding Remarks

Although a reasonable estimate of the pressure drop and heat transfer may be made for some aqueous polymer solutions under certain conditions, the behavior of these fluids is in general not well understood. For example, we cannot explain why viscoelastic aqueous Carbopol solutions under turbulent flow conditions behave like purely viscous clay slurries and not like other aqueous polymer solutions. In contrast, under laminar flow conditions such Carbopol solutions show viscoelastic behavior. This observation brings out the following experimental and analytical research challenges:

- Characterization of viscoelastic fluids: What basic rheological properties need to be measured in order to be able to predict pressure drop and heat transfer?
- Development of new instrumentation and new techniques to measure basic rheological properties (e.g., the first and second normal stress differences and the extensional viscosity for low and moderate polymer concentrations).
- Formulation of analytical models that are simple enough to predict laminar flow heat transfer performance but sufficiently complex to capture the physics.

- Measurements of the velocity distribution for laminar flow in noncircular channels.

One interesting question that remains unanswered is whether a purely viscous non-Newtonian fluid exists. It has been demonstrated that a viscoelastic fluid behaves like a purely viscous fluid under fully established laminar pipe flow conditions and accordingly the purely viscous fluid model is useful as a predictive tool. Nevertheless, to the author's knowledge, rheological measurements of the phase shift between the shear strain input and the shear stress output show all of the non-Newtonian fluids studied to date to be viscoelastic. If a purely viscous non-Newtonian fluid can be identified, it would be interesting to show that there are no secondary flows associated with the fully established laminar flow of such fluids through noncircular channels.

Clearly, there are many interesting and important research opportunities associated with this important class of viscoelastic fluids.

Acknowledgments

The author is indebted to many of his colleagues who supported his nomination for the Max Jakob Award. Special mention is made of this sponsorship of E. M. Sparrow and the support of the Max Jakob Award Committee. The lifelong advice and counsel of W. M. Rohsenow, R. A. Seban, and E. R. G. Eckert played a major role in the professional life of the author. Last, but certainly not least, there would have been no award if it were not for the major research contributions of the professional colleagues and graduate students who have worked with the author over the past three decades. Financial support of the Engineering Division of the Office of Basic Energy Sciences of the U. S. Department of Energy under its grant No. ER13311 is also appreciated.

References

Bhamidipaty, K. R., 1988, "Heat Transfer to Viscoelastic Fluids in a 5:1 Rectangular Duct," Ph.D. Thesis, Department of Mechanical Engineering, University of Illinois at Chicago.

Bird, R. B., 1965, "Experimental Tests of Generalized Newtonian Models Containing Zero Shear Rate Viscosity and a Characteristic Time," *Canadian J. Chemical Engineering*, Vol. 43, pp. 161-168.

Cho, Y. I., and Hartnett, J. P., 1982, "Non-Newtonian Fluids in Circular Pipe Flow," *Advances in Heat Transfer*, Vol. 15, Academic Press, New York, pp. 59-141.

Cho, Y. I., and Hartnett, J. P., 1985, "Non-Newtonian Fluids," *Handbook of Heat Transfer Applications*, McGraw-Hill, New York, pp. 2-1 to 2-50.

Dodge, D. W., and Metzner, A. B., 1959, "Turbulent Flow of Non-Newtonian Fluids," *AIChE J.*, Vol. 5, pp. 189-204.

Eckert, E. R. G., and Irvine, T. F., Jr., 1960, "Pressure Drop and Heat Transfer in a Duct With Triangular Cross-Section," ASME JOURNAL OF HEAT TRANSFER, Vol. 82, pp. 125-138.

Green, A. E., and Rivlin, R. S., 1956, "Steady Flow of Non-Newtonian Fluids Through Tubes," *Q. Appl. Math.*, Vol. XIV, pp. 299-308.

Ghajar, A. J., and Azar, M. Y, 1988, "Empirical Correlations for Friction Factor in Drag-Reducing Turbulent Pipe Flow," *International Communication on Heat and Mass Transfer*, Vol. 15, pp. 705-718.

Hartnett, J. P., and Kostic, M., 1985, "Heat Transfer to a Viscoelastic Fluid in Laminar Flow Through a Rectangular Channel," *International Journal of Heat and Mass Transfer*, Vol. 28, pp. 1147-1155.

Hartnett, J. P., Kwack, E. Y., 1985, "Empirical Correlations of Turbulent Friction Factors and Heat Transfer Coefficients of Aqueous Polyacrylamide Solutions," *Proceedings of International Symposium on Heat Transfer*, Beijing.

Hartnett, J. P., Kwack, E. Y., and Rao, B. K., 1986, "Hydrodynamic Behavior of Non-Newtonian Fluids in a Square Duct," *J. Rheology*, Vol. 30(S), pp. 545-559.

Hartnett, J. P., and Kostic, M., 1989, "Heat Transfer in Rectangular Ducts," *Advances in Heat Transfer*, Vol. 19, Academic Press, pp. 247-356.

Kostic, M., 1984, "Heat Transfer and Hydrodynamics of Water and Viscoelastic Fluid Flow in a Rectangular Duct," Ph.D. Thesis, Department of Mechanical Engineering, University of Illinois at Chicago.

Kostic, M., and Hartnett, J. P., 1984, "Predicting Turbulent Friction Factors of Non-Newtonian Fluids in Non-Circular Ducts," *International Communication on Heat Mass Transfer*, Vol. 11, pp. 345-352.

Kostic, M., and Hartnett, J. P., 1985, "Heat Transfer Performance of Aqueous Polyacrylic Solutions in Turbulent Flow Through Rectangular Channels," *International Communication on Heat Mass Transfer*, Vol. 12, pp. 483-490.

Kostic, M., 1991, Personal Communication.

Kozicki, W., Chou, C. H., and Tiu, C., 1966, "Non-Newtonian Flow in Ducts of Arbitrary Cross-Section," *Chemical Engineering Science*, Vol. 21, pp. 665-679.

Metzner, A. B., and Reed, J. C., 1955, "Flow of Non-Newtonian Fluids—Correlation of the Laminar, Transition and Turbulent Flow Regions," *AIChE J.*, Vol. 1, pp. 434-440.

Mysels, K. J., 1949, "Flow of Thickened Fluids," U.S. Patent No. 2,492,173.

Ng, K. S., Cho, Y. I., and Hartnett, J. P., 1980, "Heat Transfer Performance of Concentrated Polyethylene Oxide and Polyacrylamide Solutions," *AIChE J. Symposium Series No. 199*, Vol. 76, pp. 250-256.

Shah, R. K., and London, A. L., 1978, "Laminar Flow Forced Convection in Ducts," *Advances in Heat Transfer*, Suppl. 1, Academic Press.

Toh, K. H., and Ghajar, A. J., 1988, "Heat Transfer in the Thermal Entrance Region for Viscoelastic Fluids in Turbulent Pipe Flows," *Int. J. Heat and Mass Transfer*, Vol. 31, pp. 1261-1268.

Toms, B. A., 1948, "Some Observations on the Flow of Linear Polymer Solutions Through Straight Tubes at Large Reynolds Numbers," *Proceedings of 1st International Congress on Rheology*, North Holland, Amsterdam, Vol. 2, pp. 135-141.

Virk, P. S., Mickley, H. S., and Smith, K. A., 1970, "The Ultimate Asymptote and Mean Flow Structure in Toms' Phenomena," *J. Appl. Mech.*, Vol. 37, pp. 488-493.

Wheeler, J. A., and Wissler, E. H., 1966, "Steady Flow of Non-Newtonian Fluids in a Square Duct," *Trans. Soc. Rheology*, Vol. 10, pp. 353-367.

Wibulswas, P., 1966, "Laminar Heat Transfer in Non-circular Ducts," Ph.D. Dissertation, Department of Mechanical Engineering, University of London.

Xie, C. B., 1991, "Laminar Heat Transfer of Newtonian and Non-Newtonian Fluids in a 2:1 Rectangular Duct," Ph.D. Thesis, Department of Mechanical Engineering, University of Illinois at Chicago.

Xie, C. B., and Hartnett, J. P., 1992, "Influence of Rheology on Laminar Heat Transfer to Viscoelastic Fluids in a Rectangular Channel," to be published in *Industrial and Engineering Chemistry Research*, Vol. 31.

Transient Heat Transfer in a Conducting Particle With Internal Radiant Absorption

A. Tuntomo
Post-doctoral Fellow.

C. L. Tien
A. Martin Berlin Professor.

Department of Mechanical Engineering,
University of California,
Berkeley, CA 94720

The objective of the present work is to analyze rigorously the transient heat transfer of an irradiated particle by treating the radiant absorption on a local basis. A new conduction-to-radiation parameter is introduced to characterize the relative importance of heat transfer by conduction as compared with that by radiation. The study on the transient temperature field as a function of conduction-to-radiation parameter establishes a criterion identifying the circumstances where heat transfer by radiation is so predominant that conduction is negligible. The current effort is also directed at developing a convenient method for predicting the transient local maximum temperature and explosion time delay of an intensely irradiated liquid droplet.

Introduction

Since the spatial distribution of radiant absorption within an irradiated particle can be highly nonuniform, the temperature may rise unevenly, generating a thermal gradient and, thereby, heat transport phenomena. The assumption of uniform volume absorption or boundary absorption is no longer an appropriate method to account for radiation interaction with small particles. Homogeneous volume absorption exists only when the size-to-wavelength parameter is smaller than one, while boundary absorption occurs only when the parameter is large. It is the objective of the present work to analyze rigorously the heat transfer in a conducting particle with internal radiant absorption. Unlike the conventional method, the current one treats radiative absorption on a local basis, rather than global interaction. The central theory applied here is the classical electrodynamics of Maxwell's equations from which the local distribution of radiant absorption within a particle is obtained.

Previous work concerning heat transfer in an irradiated particle often neglected the thermal diffusion term in its analysis (Pendleton, 1985; Chitanvis, 1987). Park and Armstrong (1989) present slow and fast heating regimes for the heating of an irradiated droplet by carrying out a one-dimensional analysis. In their slow heating regime, the quasi-steady-state approximation was adopted; in the fast heating regime, the energy loss through conduction to the ambient gas was neglected. There was, however, neither any criterion nor justification provided as to when the conduction term in the energy equation was negligible. A new conduction-to-radiation parameter is introduced in the present study, and its effect on the heat transfer behavior of an irradiated particle is investigated. This nondimensional radiation parameter is useful to characterize the relative importance of energy transfer by conduction as compared with that by radiation. The transient temperature field as a function of conduction-to-radiation parameter is studied, particularly, to establish a criterion that identifies the circumstances where heat transfer by thermal radiation is so predominant that thermal diffusion is negligible. The current effort is also directed at predicting the local maximum temperature and explosion time delay of an intensely irradiated liquid droplet by the approximate relations presented here. The local maximum temperature and explosion time of a water droplet obtained from the approximate relations are compared with previous analytical results (Prishivalko and Leiko, 1980; Prishivalko, 1983). The transient temperature distribution in a 20-μm-radius water droplet irradiated by a CO_2 laser is calculated, and is qualitatively compared with the experimental observations of Kafalas and Ferdinand (1973).

Analysis

The present analysis focuses on the transient temperature distribution induced by electromagnetic heating. When an infrared electromagnetic wave penetrates a particle, its energy is locally absorbed and dissipated as heat within the medium. As a result, the temperature of the irradiated particle rises. The current work numerically solves the transient energy equation with electromagnetic heating as the source term to determine the temperature distribution of an irradiated particle. Both the thermal diffusion and volumetric radiation heat source terms are considered in the energy equation to account for the heat transport for such a system. The internal distribution of absorbed radiant energy is obtained from the solution of Maxwell's equations (Bohren and Huffman, 1983; Tuntomo et al., 1991). A homogeneous spherical particle irradiated by an unpolarized, uniform, monochromatic plane wave is assumed to simplify the analysis.

Assumptions. The following assumptions are made for the theoretical study of the heat transfer phenomena in a small particle, irradiated by an unpolarized monochromatic plane wave:

1 The temperature field is axisymmetric, only radial and azimuthal dependent.

2 Thermophysical properties and complex refractive index of the particle are constant with respect to temperature variation.

3 Evaporation is neglected in the case of a liquid droplet.

4 Heat transfer inside the droplet is considered to be purely conductive.

Assumption (1) is valid only when an unpolarized electromagnetic wave is considered. The reason is that the spatial distribution of absorbed radiant energy in a sphere, engendered by unpolarized electromagnetic wave, is axisymmetric. The validity of assumption (2) has been verified in previous work (Prishivalko and Leiko, 1980). It is reported that, for an irradiated water droplet, the explosion times obtained with constant properties agree within 3 percent of tolerance with those determined with temperature-dependent properties. Thus, a constant properties assumption is considered to be accurate enough for describing the heat transport process. Assumption

---

Contributed by the Heat Transfer Division and presented at the 3rd ASME/JSME Thermal Engineering Joint Conference, Reno, Nevada, March 17-22, 1991. Manuscript received by the Heat Transfer Division August 13, 1990; revision received April 1, 1991. Keywords: Radiation, Radiation Interactions, Transient and Unsteady Heat Transfer.

(3) is appropriate because the nonstationary thermal process in this problem is too fast to allow a substantial amount of liquid to be evaporated from the droplet before micro-explosion occurs. As observed in a previous study (Prishivalko and Leiko, 1980), the time needed for an intensely irradiated droplet to reach explosive boiling condition is so short that the radius of the droplet alters by not more than 8 percent before the onset of explosion. Since the droplet is extremely tiny, the Rayleigh number, which is a function of the cube of the characteristic length, is very small in this problem. As stated in assumption (4), free internal convection caused by buoyancy effect is, therefore, neglected.

Formulation. The governing equation for the temperature field in a particle with internal radiant absorption is obtained from the conservation of energy. Subject to the stated assumptions, the transient energy equation in two-dimensional spherical coordinates with thermal diffusion and volumetric radiation heat source term can be written as

$$\rho c_p \frac{\partial T}{\partial t} = K\left[\frac{1}{r^2}\frac{\partial}{\partial r}\left(r^2\frac{\partial T}{\partial r}\right) + \frac{1}{r^2 \sin\theta}\frac{\partial}{\partial \theta}\left(\sin\theta\frac{\partial T}{\partial \theta}\right)\right] + Q(r, \theta) \quad (1)$$

where T is temperature, t time, ρ mass density, c_p specific heat, and K thermal conductivity. The internal distribution of absorbed radiant energy, Q, is expressed as

$$Q(r, \theta) = \frac{4\pi n k I_o}{\lambda} S(r, \theta) \quad (2)$$

where I_o is the intensity of incident radiation, λ is the wavelength, n and k are respectively the real and imaginary parts of the complex refractive index. The spatial function, S, denotes the normalized source function and is defined as

$$S(r, \theta) = \left|\frac{\mathbf{E}}{E_o}\right|^2 \quad (3)$$

where **E** is internal electric field and E_o is the amplitude of incident wave. The absorbed energy distribution, Q, is determined from the solution of Maxwell's equations. The detail of computing Q has been discussed in previous work (Tuntomo et al., 1990). By substituting Eq. (2) into Eq. (1), the governing equation for the temperature field of an irradiated sphere becomes

$$\rho c_p \frac{\partial T}{\partial t} = K\left[\frac{1}{r^2}\frac{\partial}{\partial r}\left(r^2\frac{\partial T}{\partial r}\right) + \frac{1}{r^2 \sin\theta}\frac{\partial}{\partial \theta}\left(\sin\theta\frac{\partial T}{\partial \theta}\right)\right] + \frac{4\pi n k I_o}{\lambda} S(r, \theta) \quad (4)$$

The resulting governing equation has to satisfy the following initial and boundary conditions:

Initial Condition

$$T(r, \theta, t=0) = T_o \quad (5a)$$

Boundary Conditions at $t>0$

$$|T(r=0, \theta, t)| < \infty \quad (5b)$$

$$\frac{\partial T}{\partial r}(r=a, \theta, t) = 0 \quad (5c)$$

$$\frac{\partial T}{\partial \theta}(r, \theta=0, t) = \frac{\partial T}{\partial \theta}(r, \theta=\pi, t) = 0 \quad (5d)$$

Note that in Eq. (5*c*), an adiabatic boundary condition is imposed at the surface of the particle. In reality, the particle does lose heat at its surface via convection and radiation. The maximum possible flux of both convection, given by $h(T - T_\infty)$, and emitted radiation, given by σT^4, is, however, much smaller than the incident radiative flux, where h denotes heat transfer coefficient, T_∞ ambient temperature, and σ Stefan-Boltzmann constant. Thus, an adiabatic boundary condition is appropriate.

Nondimensionalization. A set of appropriate nondimensional variables defined for simplifying the analysis is listed below:

$$T^* = \frac{T - T_o}{T_c - T_o}; \quad r^* = \frac{r}{a}; \quad t^* = \frac{t}{t_c} \quad (6)$$

where T^* is nondimensional temperature, r^* radius, and t^* time. The characteristic temperature, T_c, is assigned to be the maximum possible temperature of a material before the onset of phase transition. For a solid, the characteristic temperature is the one at the melting point. For liquid, it is the spinodal temperature. In the case of a water droplet, the characteristic temperature is set to 578 K, which is the maximum superheat temperature of water at 1 atm. The attainment of a temperature of 578 K is commonly adopted by previous investigators (Prishivalko, 1980; Pendleton, 1985) as a criterion to characterize the onset of micro-explosion in water droplet. It has also been shown that observed delays in laser-induced explosion of water droplets could be explained by homogeneous nucleation of vapor caused by superheating (Park et al., 1990). The physical radius is chosen as the reference length scale in the nondimensionalization of independent variable. The time, t_c, is the characteristic time scale of radiation absorption and is defined as

$$t_c = \frac{\rho c_p a \Delta T}{2 n k x I_o} \quad (7)$$

where x is the size-to-wavelength parameter, and ΔT is given by

$$\Delta T = T_c - T_o \quad (8)$$

Substituting the nondimensional variables listed in Eq. (6) into the energy Eq. (4) and the initial and boundary conditions (5*a*–*d*) gives

Nomenclature

a = sphere radius
c_p = specific heat
E = internal electric field vector
E_o = incident electric field amplitude
I_o = intensity of incidence radiation
k = extinction coefficient
K = thermal conductivity
n = real refractive index
N = conduction-to-radiation parameter
Q = internal distribution of radiant absorption
r = radial coordinate
S = normalized source function
$S_{\max}$ = local maximum radiant absorption
t = time
t_c = characteristic time scale
t_{expl} = explosion time delay
T = temperature
T_c = characteristic temperature
$T_{\max}$ = local maximum temperature
T_o = initial temperature
x = size parameter = $2\pi a/\lambda$
α = thermal diffusivity
λ = wavelength
θ = polar coordinate
ρ = mass density

Superscripts

$*$ = nondimensional variables

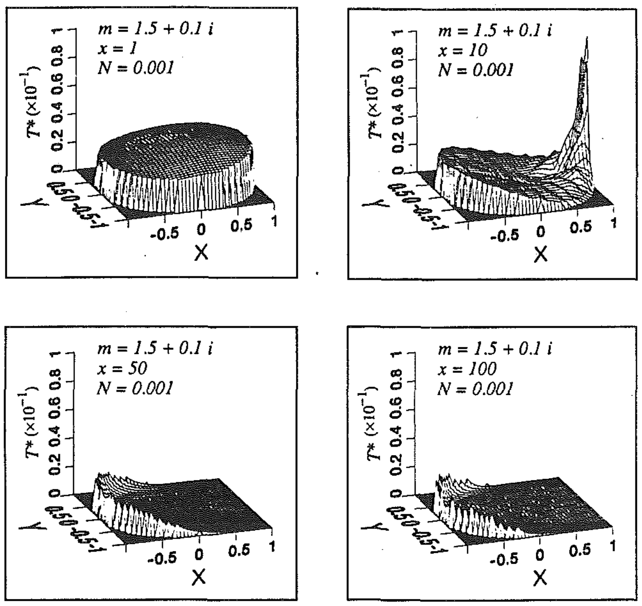

Fig. 1 Temperature distribution for various size parameters and constant N at $t^*=0.04$

$$\frac{\partial T^*}{\partial t^*}=N\left[\frac{1}{r^{*2}}\frac{\partial}{\partial r^*}\left(r^{*2}\frac{\partial T^*}{\partial r^*}\right)+\frac{1}{r^{*2}\sin\theta}\frac{\partial}{\partial \theta}\left(\sin\theta\,\frac{\partial T}{\partial \theta}\right)\right]+S(r^*,\theta) \qquad (9)$$

$$T^*(r^*,\theta,t^*)=0 \qquad (10a)$$

$$|T^*(r^*=0,\theta,t^*)|<\infty \qquad (10b)$$

$$\frac{\partial T^*}{\partial r^*}(r^*=1,\theta,t^*)=0 \qquad (10c)$$

$$\frac{\partial T^*}{\partial \theta}(r^*,\theta=0,t^*)=\frac{\partial T^*}{\partial \theta}(r^*,\theta=\pi,t^*)=0 \qquad (10d)$$

where N is the conduction-to-radiation parameter defined as

$$N=\frac{K\Delta T}{2nkaxI_o} \qquad (11)$$

This dimensionless parameter is a qualitative ratio of the conductive-to-radiative heat fluxes.

Numerical Scheme. The analytical solution to the above equations is not feasible due to the highly complicated radiation heat source term. A fully implicit numerical method is, therefore, employed to determine the transient temperature distribution of an irradiated particle. The system of Eqs. (9), (10*a*–*d*) is discretized by the implicit finite-difference scheme. The second-order centered difference is utilized for the discretization of the spatial derivatives in the diffusion terms, while the first-order finite difference is used for that of the time derivative. Since the temperature gradients in some of the conditions are expected to be large near the surface of the particle, a very fine grid spacing near the surface is required for the accuracy of the results. Therefore, a variable spacing grid system is adopted in radial direction. The grid spacing in angular direction remains uniform. The alternate direction predictor corrector method, which provides unconditional stability (Patnaik, 1986; Chiang et al., 1989), is applied for solving the resulting discretized equations.

Results and Discussion

The temperature fields determined from Eq. (9) are presented here in a three-dimensional form to demonstrate clearly their spatial variation. The effect of the size parameter on the spatial variation of temperature distribution is illustrated in Fig. 1. Lying on the x-y plane is the cross section of a spherical particle, where the irradiation traverses from left to right in the positive x direction. The magnitude of the dimensionless temperature, T^*, is shown by the scale along the vertical axis. The temperature fields of four irradiated particles, which have the same complex refractive index, $1.5+0.1i$, but different diameters, are plotted. The size parameters, x, of the particles range from 1 to 100; while the conduction-to-radiation parameter is fixed at 0.001. It can be discerned from Fig. 1 that the temperature distribution for $x=1$ is fairly uniform. However, as the size parameter increases, the temperature field becomes highly uneven. The distribution has a very sharp peak at the back side of the particle, as shown for the case of $x=10$. This precipitous increase of temperature gradient at the back side is due to the focusing effect, where the curved surface of the particle acts like a convex lens and concentrates the electromagnetic waves at the focal point. As the size parameter increases further, the skin absorption becomes predominant; and hence, the temperature distribution shows a maximum at the illuminated surface, as depicted for the cases of $x=50$ and 100. It should be noted that the temperature fields plotted in this figure for various size parameters are coherent with the internal distributions of radiant absorption presented in the previous work (Tuntomo et al, 1991).

The conduction-to-radiation parameter, N, introduced in this study characterizes the importance of heat transfer by thermal conduction in relation to that by radiation. The physical significance of this number is better envisioned if it is rearranged in the form

$$N=\frac{K\Delta T/a}{2nkxI_o}=\frac{\text{Conductive flux}}{\text{Radiative flux}} \qquad (12)$$

The large value of N corresponds to the conduction-dominating case, and the small value to the radiation-dominating case. This number is generally more fundamental than the conventional one (Ozisik, 1973). This new dimensionless number involves both n and k, the fundamental optical properties of a material, in the denominator, which corresponds to the radiative flux; whereas the conventional one has only n in the denominator. The conventional conduction-to-radiation parameter has the temperature in the numerator and the one in the denominator canceling each other out. Strictly speaking, the characteristic temperature in the numerator, which corresponds to the conductive flux, should not be canceled out with the one in the denominator, since they are not comparable. The characteristic temperature in the numerator is a value to indicate the temperature gradient, which induces thermal diffusion, while the one in the denominator is a number to quantify the radiative flux. The current one, however, considers the maximum possible temperature between two points in the medium as the characteristic temperature in the numerator. This practice is more appropriate since heat transfer by conduction is governed by temperature gradient.

The effect of the conduction-to-radiation parameter on the heat transfer phenomena of an irradiated microscale particle is presented in Fig. 2. The volumetric radiation heat source terms for all the cases in the plots are identical, since both the complex refractive indices and size parameters of all the cases are fixed at $1.5+0.01i$ and 10, respectively. These specific values of m and x are chosen for the computation because they provide a very typical distribution of internal radiant absorption. This typical distribution has a very strong, sharp peak at the back side of the particle, and thus creates an extremely large energy gradient. In the figure, the temperature distributions at the same nondimensional time, $t^*=0.03$, are plotted for various N. The plot with $N=0.0$ illustrates the temperature

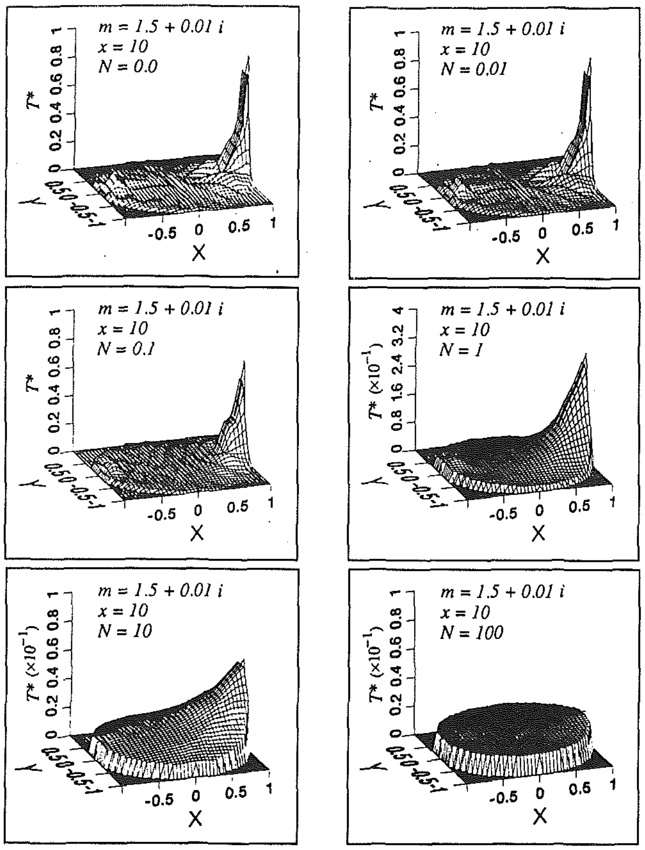

Fig. 2 Temperature distribution for various conduction-to-radiation parameters and constant x at $t^* = 0.03$

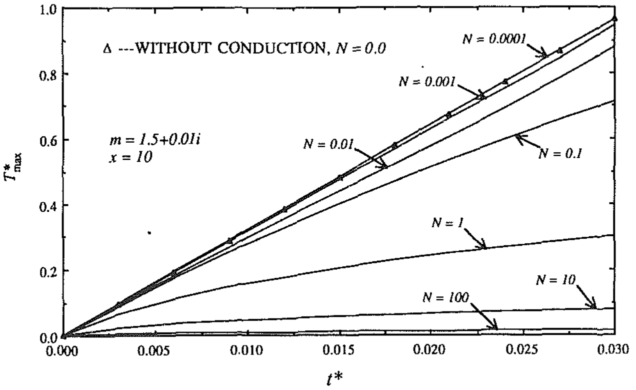

Fig. 3 Dimensionless local maximum temperature as a function of time, t^*, for different conduction-to-radiation parameters, N

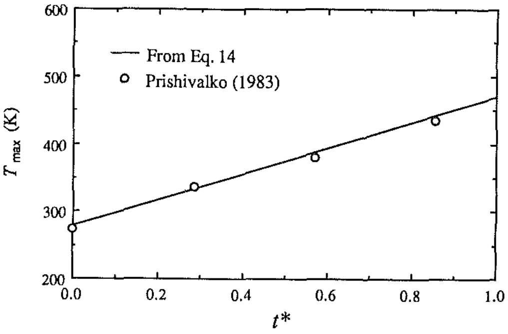

Fig. 4 Transient local maximum temperature of a 15-μm-radius water droplet irradiated by a CO_2 laser with an intensity of 10^5 W/cm^2

field obtained with the conduction term neglected. It can be seen that the temperature distribution for $N = 0.01$ is almost identical to that for $N = 0.0$. The reason is that, at such a low value of N, the rate of heat transfer by thermal radiation is so large that thermal diffusion becomes negligible. The importance of thermal diffusion, however, becomes comparable to that of radiation as N increases. The energy at the local maximum diffuses out and the peak turns smoother, as shown in the cases for $N = 0.1$ and $N = 1$. As N increases further, heat transfer by conduction becomes predominant. The uniform temperature field observed in the case for $N = 100$ is due to the fact that the energy absorbed unevenly within the particle can be rapidly and evenly distributed throughout the medium by thermal diffusion. The transient temperature field at $N \geq 100$ can be evaluated by the lump capacitance approximation if t is larger than the thermal diffusion characteristic time, given by a^2/α, where α is thermal diffusivity, since heat transfer by conduction is so efficient at such values of N, as compared with that by radiation.

The local maximum temperatures, $T^*_{\max}$, of an irradiated particle with various conduction-to-radiation parameters, are presented in Fig. 3 as a function of time. The local maximum temperatures for N ranging from 0.0001 to 100 are compared with the one for $N = 0$ in the figure. It is demonstrated that the agreement between the local maximum temperatures for $N \leq 0.01$, and that for $N = 0$ is within 10 percent of tolerance. The discrepancy between them, however, increases dramatically as N is increased. Based on the results shown in Figs. 2 and 3, it can be concluded that heat transfer by thermal diffusion can be neglected when the conduction-to-radiation parameter is smaller than 0.01.

The energy equation for the case of $N < 0.01$ can, therefore, be simplified as follows:

$$\frac{\partial T^*}{\partial t^*} = S(r^*, \theta) \tag{13}$$

Since the volumetric radiation heat source term is not a function of time, the transient temperature distribution can easily be determined by integrating Eq. (13) with respect to time. The resulting equation is written as

$$T^*(r^*, \theta, t^*) = S(r^*, \theta)\Delta t^* \tag{14}$$

The local maximum temperature as a function of time can also be obtained from Eq. (14) by substituting $S(r^*, \theta)$ for the local maximum radiant absorption, $S_{\max}$. The solution of Maxwell's equation has to be utilized for computing the value of $S_{\max}$.

The local maximum temperature of a water droplet irradiated by a CO_2 laser with an intensity of 10^5 W/cm^2 has been determined from Eq. (14). The result is given in Fig. 4, and is compared with that of Prishivalko (1983), which is obtained by numerically solving the energy equation with conduction and volumetric radiation heat source terms included. The agreement between the two results is excellent. The radius of the droplet is 15 μm, and the complex refractive index of water at 10.6 μm is $1.18 + 0.07i$. Hence, the conduction-to-radiation parameter in this case is 0.009. The local maximum temperature obtained from Eq. (14) for such a small value of N is, therefore, expected to be accurate, as confirmed by the figure.

In addition, if the intensity of an incidence beam is large, the time needed for micro-explosion to occur can be approximated by

$$t^*_{\text{expl}} = \frac{1}{S_{\max}} \tag{15}$$

where t^*_{expl} denotes dimensionless explosion time delay. This formula is obtained by rearranging Eq. (14) and substituting $S_{\max}$ for $S(r^*, \theta)$. The dimensionless temperature, T^*, is set to 1, since the onset of micro-explosion is assumed to happen when the temperature of the hottest spot within the droplet reaches the maximum superheat temperature of the liquid.

Table 1 Water droplet explosion time delay obtained from (*a*) the approximate relation, Eq. (15), and (*b*) Prishivalko and Leiko (1980)

Radius (μm)	I_0 (W/cm^2)	$t_{\text{expl.}}$	(μs)
		a	b
10	5×10^4	18.68	37.74
15		26.02	38.25
25		26.52	37.76
10	5×10^5	1.86	2.31
15		2.60	2.91
25		2.66	2.73
10	1×10^6	0.93	0.97
15		1.30	1.39
25		1.33	1.32

Equation (15) has been applied to determine the explosion time delay of a water droplet irradiated by a CO_2 laser. The explosion times computed from the approximate equation and those determined by Prishivalko and Leiko (1980) are presented in Table 1 for various droplet radii and incident radiant intensities. One can see that the results from the approximate method agree well with those from Prishivalko and Leiko (1980) at high intensity. The agreement becomes worse as the radiant intensity is decreased. The explosion times predicted by Eq. (15) for the cases of $I_o = 5\times10^4$ W/cm^2 are much shorter than those from the previous investigators. The conduction-to-radiation parameters in these cases are not less than 0.01, and hence, heat transfer by conduction should not be neglected. The large discrepancies at low intensity are, thus, attributed to the omission of thermal diffusion in the approximate formula. A large value of N, as in the case of $I_o = 5\times10^4$ W/cm^2, results in a more rapid diffusion of the energy at the maximum temperature within the droplet and, thereby, in an increase in the time needed to attain the superheat temperature.

The temperature fields of two identical water droplets irradiated with different radiant intensities are plotted in Figs. 5 and 6 at various times. The intensities applied on the droplets in Figs. 5 and 6 are 10^{11} W/m^2 and 10^7 W/m^2, respectively. The magnitude of the temperature fields in both figures increases as time proceeds. The shapes of the distributions in the case of $I_o = 10^{11}$ W/m^2 remains unchanged with time, whereas those in the case of $I_o = 10^7$ W/m^2 keeps varying with time and eventually becomes flat at $t^* = 1$. This phenomenon can be explained by the use of the conduction-to-radiation parameter. For high radiant intensity, the value of N is small, and thus, the heat transfer mechanism is dominated by radiation. The transient temperature field due to strong irradiation responds in a manner according to Eq. (14). For low radiant intensity, the value of N is large, and thus, thermal diffusion is the dominating heat transfer mechanism. Under this condition, the diffusion mechanism is able uniformly and efficiently to distribute the energy within the medium, whenever there is absorbed radiant energy locally concentrated at a spot in the droplet.

The three-dimensional temperature fields plotted in Fig. 5 are also compared to the pattern of explosive vaporization of a water droplet shown in the photographs taken experimentally by Kafalas and Ferdinand (1973). The photographs illustrate the onset of the explosion of a 20-μm-radius droplet being radiated by a 10.6-μm laser pulse. By observing the explosion pattern, it can be inferred that the illuminated surface of the droplet has higher temperature than the rest of the volume (Kafalas and Ferdinand, 1975; Pendleton, 1985). This experimentally observed energy distribution agrees well with the theoretical results presented in Fig. 5.

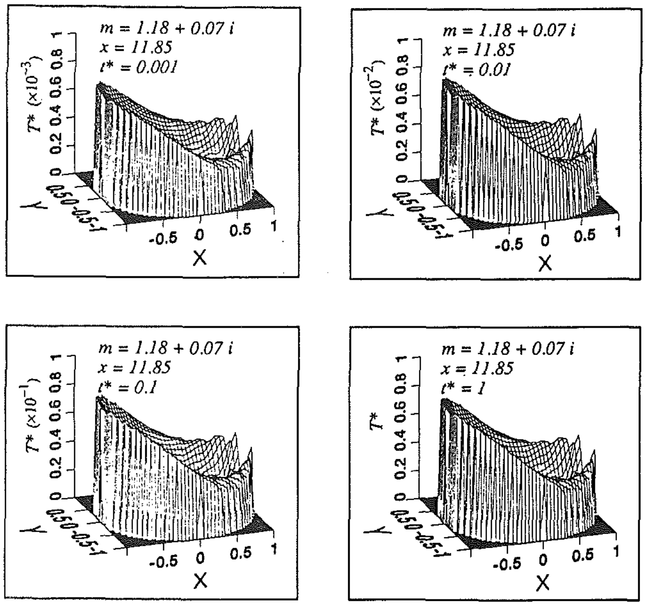

Fig. 5 Transient temperature distribution of a 20-μm-radius water droplet irradiated by a CO_2 laser with an intensity of 10^{11} W/m^2

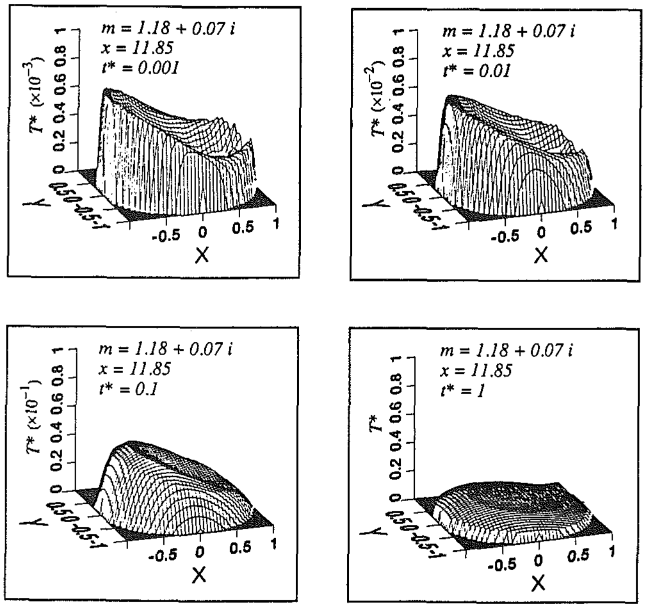

Fig. 6 Transient temperature distribution of a 20-μm-radius water droplet irradiated by a CO_2 laser with an intensity of 10^7 W/m^2

Conclusions

The transient energy equation, which includes conduction and volumetric radiation heat source terms, is solved numerically to obtain the temperature distribution of an irradiated particle. The solution from electromagnetic theory is applied to determine the internal distribution of absorbed radiant energy. The effect of size parameter on temperature distribution is examined. The shapes of the distributions for various size parameters and at a low value of conduction-to-radiation parameter are found coinciding with the patterns of the internal radiant absorption distributions presented in the previous work (Tuntomo et al., 1991).

The conduction-to-radiation parameter, N, introduced here characterizes the relative importance of conduction with respect to radiation. A criterion that identifies the circumstances where conduction is negligible as compared with radiation is established by studying the transient thermal behavior of the particle as a function of conduction-to-radiation parameter. It is observed from the results that the thermal diffusion term can be neglected from the energy equation without incurring too much error only when the value of the parameter is less than 0.01. The error in computing the temperature distribution, induced by omitting the conduction term, is less than 10 percent in the cases considered here for $N<0.01$. It is also observed that when $N\geq 100$ and $t>a^2/\alpha$, the lump capacitance approximation can be applied to calculate the transient temperature of an irradiated particle.

Simple approximate methods, Eqs. (14) and (15), for predicting the local maximum temperature and explosion time delay of an *intensely* illuminated droplet are presented. Special emphasis is laid on a water droplet irradiated by a CO_2 laser. The local maximum temperature and explosion time determined from the approximate relations for such a system are compared with the numerical results reported in previous work (Prishivalko and Leiko, 1980; Prishivalko, 1983). The comparisons show that these approximate relations can accurately predict the local maximum temperature and explosion time of an irradiated droplet, if the conduction-to-radiation parameter of the system is less than 0.01.

References

Bohren, C. F., and Huffman, D. R., 1983, *Absorption and Scattering of Light by Small Particles*, Wiley, New York, pp. 82–100.

Chiang, C. H., Raju, M. S., and Sirignano, W. A., 1989, "Numerical Analysis of Convecting, Vaporizing Fuel Droplet With Variable Properties," *International Journal of Heat and Mass Transfer*, in press.

Chitanvis, S. M., 1987, "Explosive Vaporization of Small Droplets by a High-Energy Laser Beam," *Journal of Applied Physics*, Vol. 62, pp. 4387–4393.

Kafalas, P., and Ferdinand, A. P., Jr., 1973, "Fog Droplet Vaporization and Fragmentation by a 10.6-μm Laser Pulse," *Applied Optics*, Vol. 12, pp. 29–33.

Ozisik, M. N., 1973, *Radiative Transfer and Interaction With Conduction and Convection*, Wiley, New York, pp. 454–494.

Park, B. S., and Armstrong, R. L., 1989, "Laser Droplet Heating: Fast and Slow Heating Regimes," *Applied Optics*, Vol. 28, pp. 3671–3680.

Park, B. S., Biswas, A., Armstrong, R. L., and Pinnick, R. G., 1990, "Delay of Explosive Vaporization in Pulsed Laser-Heated Droplets," *Optics Letters*, Vol. 15, pp. 206–208.

Patnaik, G., 1986, "A Numerical Solution of Droplet Vaporization With Convection," Ph.D. Dissertation, Carnegie-Mellon University, Pittsburgh, PA.

Pendleton, J. D., 1985, "Water Droplets Irradiated by a Pulsed CO_2 Laser: Comparison of Computed Temperature Contours With Explosive Vaporization Patterns," *Applied Optics*, Vol. 24, pp. 1631–1637.

Prishivalko, A. P., 1980, "Influence of Variation of Optical Constants of Drop Material on Its Heating, Evaporation, and Rupture Under the Action of Radiation," *Journal of Applied Spectroscopy*, Vol. 33, pp. 892–896.

Prishivalko, A. P., and Leiko, S. T., 1980, "Radiative Heating and Evaporation of Droplets," *Journal of Applied Spectroscopy*, Vol. 33, pp. 1137–1143.

Prishivalko, A. P., 1983, "Heating and Destruction of Water Drops on Exposure to Radiation With Inhomogeneous Internal Heat Evolution," *Soviet Physics Journal*, Vol. 26, pp. 142–148.

Tuntomo, A., Tien, C. L., and Park, S. H., 1991, "Internal Distribution of Radiant Absorption in a Spherical Particle," ASME JOURNAL OF HEAT TRANSFER, Vol. 113, pp. 407–412.

Thermal Resonance Under Frequency Excitations

D. Y. Tzou
Department of Mechanical Engineering,
University of New Mexico,
Albuquerque, NM 87131
Mem. ASME

The resonance phenomenon of thermal waves is studied in this work. Under the excitation of a body heat source oscillating at a certain frequency, both the temperature and the heat flux waves are found excitable to resonance. The physical conditions necessary for this unusual behavior to occur are obtained in terms of the resonance amplitude and the modal frequency. It has been shown that thermal resonance is a high-mode phenomenon. Only the wave modes with a modal frequency exceeding a critical value of 0.6436f, with f being the critical frequency of the solid medium, may present resonance. This unique behavior is attributed to the partition of the over- and underdamped waves oscillating in time. The critical mode numbers governing (i) the transition from an over- to an underdamped mode, and (ii) the occurrence of thermal resonance phenomenon, are derived analytically. A length parameter, the relaxation distance extended from the concept of relaxation time, is found to dominate these critical mode numbers. Last, the thermal wave speed is related to the resonance frequency, which provides an alternative approach to determining the thermal wave speed in solids.

Introduction

The merit of the wave model, in contrast to the classical diffusion theory, lies in its unique way of describing a thermal signal propagating in solids with a finite wave speed. The finite wave speed has intrinsic influences on the mechanisms of heat transfer. Mathematically, it renders an energy equation hyperbolic in nature. While the thermal wave speed resides in the wave term, the thermal diffusivity plays a role of damping in the thermal wave propagation. The weighted effect between the two is defined as the relaxation time (Chester, 1963) in the wave theory. Under this frame, the classical diffusion theory is a special case of immediate response and the relaxation time is zero. The so-called hyperbolic theory of heat conduction (Baumeister and Hamill, 1969; Taitel, 1972; Wiggert, 1977; Vick and Özişik, 1983, Özişik and Vick, 1984; Frankel et al., 1987) studies the relaxation behavior in the history of thermal wave propagation. For both temperature and flux waves, a general feature is that a sharp wavefront exists when penetrating through a solid medium. In addition, for problems involving a fast-moving heat source (Tzou, 1989a, 1989b) or a rapidly propagating crack tip (Tzou, 1990a, 1990b), the thermal shock formation is a physical phenomenon pertinent to the wave theory. The mechanisms involved are much more than a simple switch from a parabolic to a hyperbolic equation. A detailed survey categorizing past research according to their different emphases is provided in a recent annual review article by Tzou (1991a).

From a physical point of view, the thermal wave model possesses a *path-dependency* behavior, which cannot be depicted by the diffusion theory. This important characteristic can be illustrated as follows. According to the constitutive relation in the thermal wave model,

$$\mathbf{q}(\mathbf{r}, t+\tau) = -k\nabla T(\mathbf{r}, t), \tag{1}$$

a phase lag τ (or called the relaxation time) exists between the heat flux and the temperature gradient in the time history. The temperature gradient established in a material volume at time t results in a heat flux that occurred at a *later* time $t+\tau$ due to the insufficient time of response. For combining with the energy equation, however, all the physical quantities involved must be at the same instant of time. The Taylor's series expansion is thus applied to the heat flux $\mathbf{q}$ in Eq. (1) to give

$$\mathbf{q}(\mathbf{r}, t) + \mathbf{q}_t(\mathbf{r}, t)\tau + \mathbf{q}_{tt}(\mathbf{r}, t)\tau^2/2! + \cdots = -k\nabla T(\mathbf{r}, t). \tag{2}$$

In the *linearized* thermal wave theory, the phase lag τ is assumed small and the higher order terms in Eq. (2) are neglected. By retaining only the first-order term in τ, the constitutive Eq. (2) becomes

$$\mathbf{q}(\mathbf{r}, t) + \tau\mathbf{q}_t(\mathbf{r}, t) = -k\nabla T(\mathbf{r}, t). \tag{3}$$

An explicit expression for $\mathbf{q}$ in relation to ∇T results from a direct integration:

$$\mathbf{q}(\mathbf{r}, t) = -\frac{k}{\tau}\exp(-t/\tau)\int_0^t \exp(\zeta/\tau)\nabla T(\mathbf{r}, \zeta)d\zeta, \tag{4}$$

which yields the following algebraic form by the mean value theorem:

$$\mathbf{q}(\mathbf{r}, t) = -\frac{k}{\tau}\exp(-t/\tau)\,[\exp(\Gamma/\tau)\nabla T(\mathbf{r}, \Gamma)] \quad \text{for } \Gamma\in[0, t]. \tag{5}$$

The value of Γ depends on the entire history of the function $[\exp(\Gamma/\tau)\nabla T(\mathbf{r}, \Gamma)]$ from 0 to t. Equation (5), consequently, indicates that the heat flux at time t depends on the *entire history* of the temperature gradient established from 0 to t. This observation, in essence, is parallel to the model of fading memory proposed by Gurtin and Pipkin (1968). Such a path dependency in heat conduction, obviously, cannot be described by a diffusion behavior assuming an immediate response between the heat flux and the temperature gradient. Note that the response becomes immediate only if the speed of heat propagation (C) approaches infinity. This is an implicit assumption made in the classical diffusion model.

In practice, there exist some situations where the wave nature in heat conduction dominates over the diffusion behavior. In the early stage of an abrupt boundary heating (Vick and Özişik, 1983; Özişik and Vick, 1984), for example, discontinuities in both temperature and flux have been demonstrated for temperature ripples propagating in one-dimensional solids. In multidimensional media, accumulation of thermal energy in a preferential direction around a fast-moving heat source (Tzou, 1989a, 1989b) and a rapidly propagating crack tip (Tzou, 1990a,

---

Contributed by the Heat Transfer Division for publication in the JOURNAL OF HEAT TRANSFER. Manuscript received by the Heat Transfer Division November 5, 1990; revision received September 15, 1991. Keywords: Conduction.

1990b) results in the formation of thermal shock waves. The shock structure evolves from a flat to a quasi-hyperboloidal surface when additional constraints are imposed in the direction perpendicular to the plane containing the moving origin (Tzou, 1990c). Especially in a process involving material damage, moreover, the thermal cracks can be initiated in a time interval much shorter than that required for the diffusion behavior to be retrieved. Consequently, the wave nature in heat conduction must be considered in the analysis. Significant deviations in the orientations of crack initiations from the diffusion theory, for example, have been demonstrated by Tzou (1989c), who presents a completely different fracture pattern from that predicted by a diffusion behavior. The other characteristics of thermal waves, such as the restrictions from the causality condition in the special theory of relativity (Kelley, 1968; Van Kampen, 1970) and the kinetic theory of molecular collisions (Bubnov, 1976; Berkovsky and Bashtovoi, 1977; Cheng, 1989), have been included as an entirety in the annual review article by Tzou (1991a) and will not be repeated here.

The success of the thermal wave model lies in the determination of the thermal wave speed in solids. It is an intrinsic thermodynamic property of the solid medium but, unfortunately, it has not been well established for engineering materials yet. In addition to the early work involving liquid helium by Peshkov (1944), a recent work by Kaminski (1990) reported the thermal wave speed and the relaxation time for media with nonhomogeneous inner structures. The thermocouples were used to detect the arrival of thermal signals. This is possible because the thermal wave speeds are in the range of millimeters per second (mm/s) for the media under considerations. In promoting the thermal wave theory to the level of engineering applications, however, a method capable of detecting the thermal wave speed in general is necessary. Especially for metals under normal conditions, the thermal wave speed is approximately on the order of 10^2 to 10^3 m/s. The thermocouples may not be applicable for these media with multicrystalline structures because the thermal signal may arrive much faster than that required for an effective response.

Various ways for detecting the thermal wave speed in metals have been sought during the development of the thermal shock phenomena. For crack trajectory emanating from the heat source, for example, Tzou (1989b) made an attempt to correlate the crack initiation angle to the thermal wave speed. The complication of this approach, however, lies in the further dependence on the fracture criteria predicting the orientations of crack extension. Alternatively, the present work proposes a frequency approach emphasizing the response of thermal waves to external excitations. Through the flux formulation, first, the thermal *resonance* phenomena will be demonstrated analytically. The overdamped and the underdamped modes will then be separated to determine the excitable modes. At this stage, the thermal resonance will be shown to be a *high-mode* phenomenon. Second, the resonance frequency of the thermal wave will be related to the thermal wave speed. Based on the resonance frequency measured in the future experiment, the thermal wave speed can then be computed analytically.

The Flux Formulation

When combining Eq. (3) with the energy equation

$$-\nabla\cdot\mathbf{q}+S=\rho C_p T_t, \tag{6}$$

the result may either have a temperature (T) or heat flux ($\mathbf{q}$) representation. The T representation is obtained by eliminating $\mathbf{q}$ from the two equations:

$$\alpha\nabla^2 T+(1/\rho C_p)[S+(\alpha/C^2)S_t]=(\alpha/C^2)T_{tt}+T_t, \tag{7}$$

with τ being replaced by α/C^2 (Chester, 1963). The $\mathbf{q}$ representation, on the other hand, is obtained by eliminating T:

$$\alpha\{\nabla[\nabla\cdot\mathbf{q}]-\nabla S\}=(\alpha/C^2)\mathbf{q}_{tt}+\mathbf{q}_t \tag{8}$$

which has the same mathematical structure in time as Eq. (7). The use of the T or $\mathbf{q}$ representation depends on the boundary conditions. For problems involving temperature-specified boundary conditions, obviously, the T representation is more preferable. For problems involving flux-specified boundary conditions, on the other hand, the $\mathbf{q}$ representation is more convenient to use for avoiding the complex inversion from Eq. (4). This feature was first indicated by Frankel et al. (1985) and further demonstrated by Tzou (1989a, 1990a). In both formulations, note that an *apparent* heat source term, $(\alpha/C^2)S_t$ in Eq. (7) and ∇S in Eq. (8), exists due to the effect of finite wave speed.

Because thermal resonance is an aggravated response in time, consideration of a one-dimensional problem is sufficient. As an example, the boundary conditions at the two ends of the solid ($x = 0$ and L) will be assumed insulated to simulate a situation in the laboratory. It will be seen, however, that the approach adopted here is sufficiently general to cover other situations with different boundary conditions. The insulated boundary conditions involve heat fluxes, which necessitate consideration of the $\mathbf{q}$ representation. In a one-dimensional situation, Eq. (8) degenerates into the following form:

$$q_{xx}=(1/C^2)q_{tt}+(1/\alpha)q_t+\nabla S(x,\,t), \tag{9}$$

which is to be solved under the boundary conditions:

$$q(0,\,t)=q(L,\,t)=0. \tag{10}$$

The Resonance Phenomenon

For a body heat source oscillating at a frequency Ω in time, the heat source function $S(x, t)$ can be expressed as

$$S(x,\,t)=Q\,\exp(i\Omega t)g(x) \tag{11}$$

with Q being the strength of the applied heat source and $g(x)$ describing the nonhomogeneous distribution along the x direction. Combining Eqs. (9) and (11), the energy equation becomes

Nomenclature

C = thermal wave speed, m s^{-1}
C_p = heat capacity, kJ kg^{-1} K^{-1}
f = critical frequency, s^{-1}
k = thermal conductivity, W m^{-1} K^{-1}
L = length of the one-dimensional solid, m
n = mode number of temperature waves
q = heat flux vector, W m^{-2}
Q = intensity of the specific heat source, W m^{-3}
S = heat source per unit volume, W m^{-3}
t = physical time, s
x = physical dimension, m
α = thermal diffusivity, m^{2}s^{-1}
ζ_n = damping rate defined as $i\eta_n$ for overdamped modes, s^{-1}
η_n = damping rate for underdamped waves, s^{-1}
ρ = mass density, kg m^{-3}
τ = relaxation time, s
ω_n = modal frequency of the temperature wave, s^{-1}

Superscripts and Subscripts

X_n = the physical quantity X of the nth mode in oscillation
$X_{,x}$ = differentiations to X with respect to x
X^* = dimensionless quantity of X

$$q_{xx}=(1/C^2)q_{tt}+(1/\alpha)q_t+Q\exp(i\Omega t)G(x), \qquad (12)$$

where the derivative of $g(x)$, $dg(x)/dx$, is represented by another function of $G(x)$. The purpose, then, is to find specific values of Ω (the excitation frequency) at which the amplitude of the heat flux wave is amplified.

Bearing the time response in mind, the heat flux wave is expressed in terms of its modal representation:

$$q(x,\ t)=\sum_{n=1}^{\infty}\Lambda_n(t)\phi_n(x) \qquad (13)$$

with $\Lambda_n(t)$ being the time-dependent amplitude of the thermal wave. In principle, any orthogonal set of eigenfunctions $\phi_n(x)$ in the physical domain from $x = 0$ to L can be used for the purpose of expansion. In relation to the *undamped* thermal waves, however, the ϕ_n functions satisfying the wave equation:

$$q_{xx}=(1/C^2)q_{tt} \qquad (14)$$

will be selected. In other words, the damping effect from the thermal diffusivity, refer to Eq. (12), is omitted in constructing the eigenfunctions. Equation (14) allows a harmonic solution in time

$$q(x,\ t)=\sum_{n=1}^{\infty}\phi_n(x)\ \exp(i\omega_n t). \qquad (15)$$

Substituting Eq. (15) into Eq. (14) then yields

$$\phi_{n,\ xx}=-(\omega_n/C)^2\phi_n \qquad (16)$$

which, along with the boundary condition (10), determines the eigenfunctions of $\phi_n(x)$:

$$\phi_n(x)=\sin(\omega_n x/C)\ \text{with}\ \omega_n=n\pi C/L \quad \text{and}\ n=1,\ 2,\ 3,\ \ldots,\ \text{etc.} \qquad (17)$$

The time-varying amplitude $\Lambda_n(t)$ of the heat-flux wave can be determined by combining Eqs. (12) and (13). This results in

$$(1/C^2)\Lambda_{n,\ tt}+(1/\alpha)\Lambda_{n,\ t}+(\omega_n/C)^2\Lambda_n=-QD_n\exp(i\Omega t), \qquad (18)$$

where D_n are the Fourier coefficients of the function $G(x)$:

$$D_n=\int_0^L G(x)\phi_n(x)dx\Big/\int_0^L\phi_n^2(x)dx \qquad (19)$$

With the eigenfunctions shown by Eq. (17), for instance,

$$D_n=(2/L)\int_0^L G(x)\ \sin(n\pi x/L)dx \quad \text{for}\ n=1,\ 2,\ 3,\ldots,\text{etc.} \qquad (20)$$

In response to the harmonic excitation $\exp(i\Omega t)$ of the heat source, an admissible form for the amplitude function $\Lambda_n(t)$ is

$$\Lambda_n(t)=A_n\ \exp(i\Omega t). \qquad (21)$$

By substituting Eq. (21) into Eq. (18), the complex amplitude A_n is thus obtained:

$$A_n=-QD_n\frac{1}{(\omega_n^2-\Omega^2)/C^2+i(\Omega/\alpha)}. \qquad (22)$$

The heat flux wave under the frequency excitation is then completely determined by combining Eqs. (13), (21), and (22).

In reality, however, measurement on the temperature response is much easier than that on the heat flux. For this purpose, the temperature response can be obtained directly from Eq. (3). Under the same frequency excitation, assume the following form for temperature:

$$T(x,\ t)=\sum_{n=1}^{\infty}B_n\ \exp(i\Omega t)\phi_{n,\ x}\ \text{and consequently}$$

$$T_x(x,\ t)=\sum_{n=1}^{\infty}B_n\ \exp(i\Omega t)\phi_{n,\ xx}. \qquad (23)$$

Substitution of Eqs. (13), (21), and (23) into Eq. (3) then gives

$$B_n=-(Q/k)(C/f)^2D_nA_\Omega, \qquad (24)$$

with

$$A_\Omega(n)=\frac{1+i\Omega^*}{\omega_n^{*2}[\omega_n^{*2}-\Omega^{*2})+i\Omega^*]},\quad \Omega^*=\Omega/f,\ \text{and}\ \omega_n^*=\omega_n/f. \qquad (25)$$

The critical frequency f, reciprocal of the relaxation time τ, is introduced here for the purpose of nondimensionalizations. Note that B_n in Eq. (24) is the amplitude of the temperature wave excited by the oscillating heat source. While the other parameters in Eq. (24) are independent of the excitation frequency Ω, the amplitude B_n is dominated by the norm of

$$|A_\Omega|=\sqrt{A_\Omega\overline{A}_\Omega}. \qquad (26)$$

It depends on both the modal frequency ω_n (defined in Eq. (17)) and the oscillating frequency Ω of the heat source. Should a resonance phenomenon be possible, the norm of $|A_\Omega|$ shown by Eq. (26) possesses exaggerated values at specific values of Ω.

By substituting Eq. (25) into Eq. (26), a careful manipulation yields the following expression:

$$|A_\Omega|=[\omega_n^{*2}(\Omega^{*2}+1)(\omega_n^{*2}-2\Omega^{*2})+\Omega^{*6}+2\Omega^{*4}+\Omega^{*2}]^{1/2}/\{\omega_n^{*2}[\omega_n^{*4}+\Omega^{*2}(1-2\omega_n^{*2})+\Omega^{*4}]\}. \qquad (27)$$

In thermal resonance, the maximum amplitude of the temperature wave is then depicted by the following condition:

$$\frac{d|A_\Omega|}{d\Omega^*}=0, \qquad (28)$$

which gives a complicated equation to be solved for the specific values of Ω^*:

$$[2\Omega^*\omega_n^{*4}-4\Omega^*(2\Omega^{*2}+1)\omega_n^{*2}+6\Omega^{*5}+8\Omega^{*3}+2\Omega^*]/\{2(\omega_n^{*4}-2\omega_n^{*2}\Omega^{*2}+\Omega^{*4}+\Omega^{*2})\cdot[(\Omega^{*2}+1)\omega_n^{*4}-2\Omega^{*2}\omega_n^{*2}(\Omega^{*2}+1)+\Omega^{*6}+2\Omega^{*4}+\Omega^{*2}]^{1/2}\}+2\Omega^*(2\omega_n^{*2}-2\Omega^{*2}-1)\cdot[(\Omega^*+1)\omega_n^{*4}-2\omega_n^{*2}\Omega^{*2}(\Omega^{*2}+1)+\Omega^{*6}+2\Omega^{*4}+\Omega^{*2}]^{1/2}/(\omega_n^{*4}-2\omega_n^{*2}\Omega^{*2}+\Omega^{*4}+\Omega^{*2})^2=0. \qquad (29)$$

For a specified value of modal frequency ω_n^*, Eq. (29) presents a special type of eighth-order polynomial for Ω^*. It can be elegantly arranged into the following form:

$$[\Omega^{*2}-\omega_n^*\sqrt{\omega_n^{*2}+2}+1]\cdot[\Omega^{*2}+\omega_n^*\sqrt{\omega_n^{*2}+2}+1]\cdot\left[\Omega^{*2}-\frac{\sqrt{1-4\omega_n^{*2}}+2\omega_n^{*2}-1}{2}\right]\cdot\left[\Omega^{*2}-\frac{-\sqrt{1-4\omega_n^{*2}}+2\omega_n^{*2}-1}{2}\right]=0 \qquad (30)$$

which renders eight possible roots for Ω^*:

$$\Omega^*=\pm\sqrt{\omega_n^*\sqrt{\omega_n^{*2}+2}-1},\quad \Omega^*=\pm i\sqrt{\omega_n^*\sqrt{\omega_n^{*2}+2}-1} \qquad (31)$$

$$\Omega^*=\pm\sqrt{\{\sqrt{1-4\omega_n^{*2}}+2\omega_n^{*2}-1\}/2},\quad \text{and}\ \Omega^*=\pm\sqrt{\{-\sqrt{1-4\omega_n^{*2}}+2\omega_n^{*2}-1\}/2}. \qquad (32)$$

They are the specific values of Ω^*, the dimensionless frequency of the applied heat source, at which amplitudes of temperature waves reach maxima. Due to rationalization in the process, however, some auxiliary roots exist and a careful examination is needed to determine the acceptable solution on a physical basis:

(*i*) The oscillating frequency Ω^* of the applied heat source must be real. Referring to the first root in Eq. (32), this condition requires

$$1-4\omega_n^{*2}>0 \text{ or equivalently } \omega_n^*<1/2 \quad \text{(for the inner square root)} \tag{33}$$

and

$$\sqrt{1-4\omega_n^{*2}}+2\omega_n^{*2}-1>0 \quad \text{(for the outer square root).} \tag{34}$$

Combination of Eqs. (33) and (34) then gives the following condition:

$$4\omega_n^{*4}<0, \tag{35}$$

which is not allowable for modal frequencies ω_n^* being real. The first root in Eq. (32) is therefore not acceptable.

(*ii*) Similar consideration can be given to the second root in Eq. (32). The corresponding condition to Eq. (34) reads

$$2\omega_n^{*2}-1>\sqrt{1-4\omega_n^{*2}}. \tag{36}$$

For $\omega_n^* < 1/2$, as constrained by Eq. (33), the quantity of $(2\omega_n^{*2}-1)$ on the left-hand side of the equation is negative. The condition of Eq. (36), therefore, cannot be satisfied by any real value of ω_n^*.

(*iii*) Turning to the first root in Eq. (31), similarly, a real value of Ω^* requires that

$$\omega_n^{*2}+2>0 \quad \text{(for the inner square root)} \tag{37}$$

and

$$\omega_n^* \sqrt{\omega_n^{*2}+2}-1>0 \quad \text{(for the outer square root).} \tag{38}$$

Equation (37) is satisfied for all the real values of ω_n^*. Equation (38), however, imposes a constraint on ω_n^*:

$$\omega_n^*>\sqrt{\sqrt{2}-1}\simeq 0.6436. \tag{39}$$

For the first root in Eq. (31) being physically acceptable, Eq. (39) specifies the physical domain for ω_n^*. Finally, under the same constraint of Eq. (38), the second root in Eq. (31) is dropped because it simply yields complex conjugates of the first roots in Eq. (31).

Based on these observations, in summary, there exists only one root for Eq. (29) or (30)

$$\Omega_{\max}^*=\sqrt{\omega_n^* \sqrt{\omega_n^{*2}+2}-1} \text{ subject to } \omega_n^*>0.6436 \tag{40}$$

which is physically acceptable. The subscript "max" is added to Ω^* for insuring that $\Omega_{\max}^*$ is the externally applied frequency, rendering a maximum amplitude of $|A_\Omega|$. Equation (40) relates the applied frequency $(\Omega_{\max}^*)$ to the modal frequency (ω_n^*) of the temperature wave. This indicates that only the temperature wave with a modal frequency (ω_n) greater than 0.6436*f* may present a resonance pattern in the frequency response. In comparison with the resonance phenomena in beams or plates (Meirovitch, 1967), where *all* the displacement modes are basically excitable to resonate, this is another unusual behavior of thermal waves.

For the thermal resonance to occur, an explicit expression in terms of the critical mode number n can be obtained by substituting Eq. (17) (for the modal frequency ω_n^*) into Eq. (39):

$$n \geq 0.6436 \frac{1}{\pi} \frac{L}{C\tau} \simeq 0.2049 \frac{L}{C\tau}. \tag{41}$$

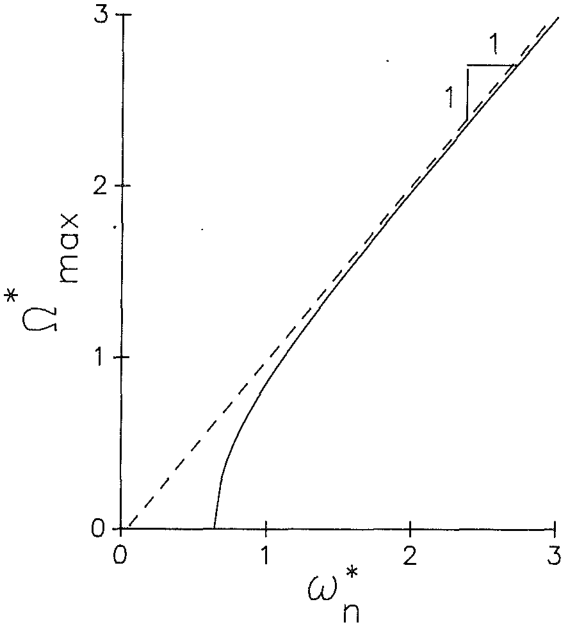

Fig. 1 The applied frequency driving temperature resonance in relation to the modal frequency, Eq. (31) subject to the constraint of $\omega_n^* > 0.6436$; also, the asymptotic behavior of $\Omega_{\max}^* \simeq \omega_n^*$ when $\omega_n^* \geq 2$

This shows that the critical mode number for the thermal resonance to occur is predominant by the ratio of L (the length of the one-dimensional solid) to a length-like quantity $C\tau$. In parallel to the definition of the relaxation time, the quantity $C\tau$ can be defined as the *relaxation distance*, which is another intrinsic property of the solid medium. It is related to the thermal diffusivity (α) and the thermal wave speed (C) by $C\tau = \alpha/C$. For the sand specimen examined by Kaminski (1990) with the values of C and τ, respectively, being 0.143 mm/s and 20 s, the value of $C\tau \simeq 2.86$ mm and a value of $n \gtrsim 71.6$ results from Eq. (41). This implies that only the 72nd mode and thereafter may present a thermal resonance pattern under frequency excitations.

The corresponding maximum amplitude of the temperature wave, denoted by $|A_\Omega|^{\max}$, can be obtained by substituting Eq. (40) into Eq. (27). The result is

$$|A_\Omega|^{\max}=[2\omega_n^*(\omega_n^{*2}+2)(\omega_n^{*2}+2)^{1/2} - (2\omega_n^{*4}+5\omega_n^{*2}+2)]^{1/2}/\omega_n^{*2}[2\omega_n^*(\omega_n^{*2}+2) - (2\omega_n^{*2}+1)(\omega_n^{*2}+2)^{1/2}], \text{ for } \omega_n^*>0.6436. \tag{42}$$

In relation to the modal frequencies ω_n^*, according to Eq. (40), the required frequencies $\Omega_{\max}^*$ for the thermal resonance to occur are displayed in Fig. 1. The curve starts with $\omega_n^* = 0.6436$ as constrained by Eq. (39). For smaller values of ω_n^*, the resonance frequency $\Omega_{\max}^*$ is slightly smaller than the modal frequency ω_n^*. For larger values of ω_n^* ($\omega_n^* \geq 2$ approximately), the value of $\Omega_{\max}^*$ approaches the modal frequency ω_n^*. This result can be shown analytically. By arranging Eq. (40) in the following form:

$$(\omega_n^*+\Omega_{\max}^*)(\omega_n^*-\Omega_{\max}^*)(\omega_n^{*2}+\Omega_{\max}^{*2}+2)=1, \tag{43}$$

it is readily seen that $\omega_n^* = \Omega_{\max}^*$ is an asymptote of the frequency curve. The value of $\Omega_{\max}^*$, therefore, approaches that of ω_n^* when ω_n^* becomes large. Figure 2 shows the amplitude of the temperature wave, Eq. (27), in response to the frequency excitation. The peak value in each curve is $|A_\Omega|^{\max}$ obtained analytically in Eq. (42). When the modal frequency ω_n^* increases from 0.6436 to 1, the amplitude of $|A_\Omega|^{\max}$ decreases. The resonance frequency at which the amplitude possesses a maximum value, however, approaches the modal frequencies ω_n^* of the corresponding modes. This feature is further illustrated in Fig. 3 for higher modes with $\omega_n^* = 5$, 7, and 10. For these modes, the values of the maximum amplitudes are approximately two orders of magnitude lower than those of the lower modes shown in Fig. 2, but the resonance phenomena are more pronounced.

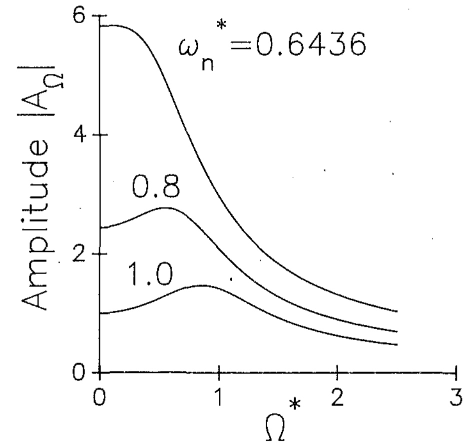

Fig. 2 Resonance of thermal waves with modal frequencies ω_n^* being 0.6436, 0.8, and 1 (lower modes) in the frequency domain under external excitations

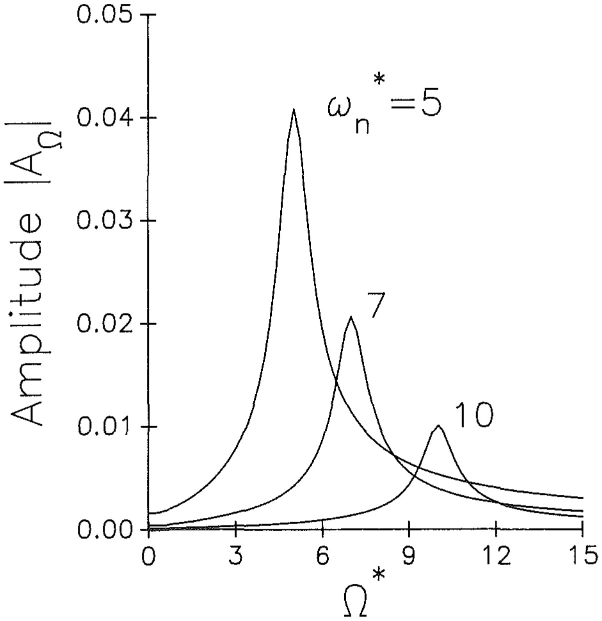

Fig. 3 Resonance of thermal waves with modal frequencies ω_n^* being 5, 7, and 10 (higher modes) in the frequency domain under external excitations

Over- and Underdamped Waves

For the thermal resonance to occur, as shown by Eq. (41), the mode number must exceed a critical value. This unusual behavior can be understood by studying the transition of the eigenmodes of the heat flux wave governed by

$$q_{xx}=(1/C^2)q_{tt}+(1/\alpha)q_t. \tag{44}$$

Subject to the same boundary conditions as in Eq. (10), it will be shown that the modes with a modal number $n < 0.6436 \frac{1}{\pi}\frac{L}{C\tau}$, refer to Eq. (41), are essentially *overdamped*. These modes consume all the thermal energy supplied by the heat source and no resonance could occur. To show this behavior, let us start with the modal representation of the heat flux wave:

$$q(x,t)=\sum_{n=1}^{\infty}\exp[-t/(2\tau)][E_n\cos(\eta_n t) + F_n\sin(\eta_n t)]\phi_n(x), \tag{45}$$

with η_n being the *damped* modal frequencies and $\phi_n(x)$ the same eigenfunctions as those shown by Eq. (17). Substitution of Eq. (45) into Eq. (44) yields

$$\eta_n^*=\frac{\sqrt{4(\omega_n^*)^2-1}}{2} \text{ where } \eta_n^*=\eta_n/f \text{ and } \omega_n^*=\omega_n/f. \tag{46}$$

In the case that

$$\omega_n^*>1/2 \text{ or } \omega_n>f/2, \tag{47}$$

the damped frequencies η_n^* in Eq. (46) are real. The heat flux wave oscillates sinusoidally but its amplitude decays exponentially in the time history. Equation (45) is defined as an *underdamped wave* in this case. For $\omega_n^*<1/2$ or $\omega_n<f/2$, on the other hand, the values of η_n^* become imaginary and the trigonometric functions in Eq. (45) degenerate into hyperbolic functions. In this case, the amplitude function does not oscillate in time and the flux wave defined by Eq. (45) becomes *overdamped*. In contrast to vibrations of beams or plates, however, the case of $\omega_n^* = 1/2$ does not provide the condition for *critical damping*. This is due to the presence of the additional exponential function, $\exp[-t/(2\tau)]$, in Eq. (45). By the same procedure as that used from Eqs. (22)–(25), the temperature wave in correspondence can be obtained as

$$T(x,t)=\sum_{n=1}^{\infty}\exp[-t/(2\tau)][(F_n\eta_n-E_n/2)\cos(\eta_n t) - (F_n/2+\eta_n E_n)\sin(\eta_n t)]\,\phi_{n,x} \tag{48}$$

This involves the same trigonometric functions as those in the heat flux wave. All the previous discussions, therefore, are equally applied. The Fourier coefficients E_n and F_n in these equations can be determined by the initial conditions imposed on the heat flux or the temperature (Tzou, 1991b). The procedure is fundamental and the results will be omitted here because they do not affect the frequency response of the thermal waves.

The critical condition represented by Eq. (47), similar to Eq. (41), can be expressed by the mode number:

$$n\geq 0.5\frac{1}{\pi}\frac{L}{C\tau}. \tag{49}$$

Equation (49) is the critical mode number beyond which the *underdamped modes activate*. Equation (41), on the other hand, is the critical mode number beyond which the *thermal resonance could occur*. The difference of the two reveals the eigenmodes in transition. These modes with $0.5\frac{1}{\pi}\frac{L}{C\tau} < n < 0.6436\frac{1}{\pi}\frac{L}{C\tau}$, though underdamped in nature, cannot be excited to resonate due to the strong effect of damping from the exponential function $\exp[-t/(2\tau)]$. It is not until the mode number exceeds the critical value of $0.6436\frac{1}{\pi}\frac{L}{C\tau}$ that the oscillatory behavior overcomes the damping and the thermal waves becomes effectively responsive to the frequency excitation. Note also that the rate of damping, $1/2\tau \equiv f/2$, is proportional to the critical frequency. A solid medium with a larger value of C (the thermal wave speed) or a smaller value of α (the thermal diffusivity), therefore, provides stronger damping to the oscillation of thermal waves.

Relation to the Thermal Wave Speed

The thermal resonance can be applied, at least in principle at this stage, to increase the energy efficiency in microwave heating. Under the same intensity of the heat source, for example, it is desirable to operate the heating frequency in the neighborhood of the resonance frequency so that a maximum response of temperature in the heated object results. Especially for the fine treatment in material processings, the knowledge of thermal resonance could have a great potential in future applications.

Another important application of the thermal resonance phenomenon, as mentioned before, is to provide an alternative approach to determine the thermal wave speed in general. For solid media transferring the thermal energy with a relatively low speed, traditional devices such as thermocouples may be sufficient to detect the arrival of thermal waves. The work by Kaminski (1990) is a typical example in this category. For energy transfer at a high speed, such as that in metals, however, the resonance frequency of the thermal wave could be used to avoid the insufficient time of response. The principle is illustrated as follows. For a solid medium subject to a frequency excitation, first, the resonance frequency of the temperature wave is determined from the *experiment*. The measured value should be close to the $\Omega_{\max}$ defined in Eq. (40). The desired mode of excitation, especially the mode number n, should be selected in this phase. In fact, it helps to determine the approximate range of the oscillating frequencies of the heat source in producing the resonance phenomenon. Equation (40) can then be used to relate the resonance frequency to the thermal wave speed. According to its reverse expression,

$$\omega_n^* = \sqrt{\sqrt{\Omega_{\max}^{*4} + 2\Omega_{\max}^{*2} + 2} - 1} \text{ with } \Omega_{\max}^* = \Omega_{\max}/f \qquad (50)$$

and the modal frequencies ω_n^* defined in Eq. (17), one has

$$[\alpha(n\pi/L)^2]\tau + 1 = \sqrt{\Omega_{\max}^4\tau^4 + 2\Omega_{\max}^2\tau^2 + 2}. \qquad (51)$$

Note that the critical frequency (f) has been replaced by the reciprocal of the relaxation time ($1/\tau$). Equivalently, Eq. (51) gives a fourth-order algebraic equation,

$$\Omega_{\max}^4\tau^4 + [2\Omega_{\max}^2 - (n\pi/L)^4\alpha^2]\tau^2 - [2\alpha(n\pi/L)^2]\tau + 1 = 0, \qquad (52)$$

to be solved for τ. Its value depends on the resonance frequency ($\Omega_{\max}$), the length of the one-dimensional solid (L), the mode number being excited (n), and the thermal diffusivity (α). In general, a numerical solution is needed for solving Eq. (52). Based on the calculated value of τ, then, the thermal wave speed C can be determined as

$$C = \sqrt{\alpha/\tau}. \qquad (53)$$

The advantage of this approach lies in that it does not depend on the short time response of the thermal devices for detecting the arrival of thermal signals. However, there would be another technical problem to overcome. The potential obstacle lies in the applied frequency, which is sufficiently high to drive the thermal wave to resonance. According to Figs. 2 and 3, the required frequency is close to the modal frequency of the temperature wave. According to the constraint in Eq. (39), moreover, an excitable mode must have a modal frequency being greater than $0.6436f$. For producing thermal resonance in metals under normal conditions, as an estimate, the *minimum* value of the applied frequency is $0.6436f$, which is in the order of giga- to terahertz. In such a high-frequency range, the use of infrared or even optical laser seems necessary.

Limiting Cases

In connection with future experimental support, one of the most important objectives of this analysis is to identify the dominant physical parameters governing the mechanisms of thermal resonance. In waiting for the experimental evidence to come, bridging the proposed phenomena to the ones we are familiar with is necessary to reveal the essence of thermal wave amplifications.

(a) The Diffusion Behavior. Fourier's law of heat conduction assumes an immediate response between the temperature gradient and the heat flux vector at a material point. As a result, the thermal wave speed (C) approaches infinity and the relaxation time (τ) and the relaxation distance ($C\tau$), respectively, approach zero. The energy Eq. (7) in this case reduces to the diffusion equation. The critical mode number separating the overdamped modes from the underdamped modes, Eq. (49), approaches infinity ($n \to \infty$), which implies that *all* the wave modes in Eq. (48) are overdamped. The critical mode number for thermal resonance to occur, Eq. (41), approaches infinity as well, which implies none of the modes is excitable to resonate. The resonance phenomenon, therefore, is a unique feature pertinent to the wave theory and cannot be depicted by the classical diffusion model. Note that amplifications of the amplitude of temperature induced by acoustic waves (Imber, 1991) in a Fourier solid should be distinguished from that being proposed in this study. When the thermal diffusion equation is coupled with the acoustic wave equation, resonance of acoustic waves may aggravate the source term in the diffusion equation, which renders an amplification of the temperature response. The resonance phenomenon proposed in this study, on the other hand, is a short-time response of the thermal field alone, which does not depend on the existence of another field.

(b) The Wave Behavior. Another limiting behavior is the case with thermal diffusivity (α) approaching infinity. The energy Eq. (7) in this case reduces to the standard wave equation without damping. The body heating, however, is dominated by the apparent heat source involving the time derivative of the real heat source (S_t). This is a unique feature distinguishing the thermal wave theory from the propagation of stress or acoustic waves. The relaxation time and the relaxation distance, respectively, approach infinity in this case. The critical mode numbers for activations of underdamped wave (Eq. (49)) and thermal resonance (Eq. (41)) are reduced to a value of zero, which implies that all the modes are oscillatory and excitable to resonate. With the relaxation time approaching infinity, moreover, Eq. (51) for the resonance frequency reduces to

$$\Omega_{\max} = \omega_n. \qquad (54)$$

This is a well-known behavior (Merovitch, 1967, for example) for an undamped mechanical system subjecting to frequency excitations. Also, Eq. (54) gives a clear physical interpretation for the asymptote of the frequency Eq. (43). For higher modes with larger values of modal frequencies, the wave behavior is more pronounced and the resonance frequency approaches the modal frequencies of waves without damping.

Conclusions

The resonance phenomenon of thermal waves in response to frequency excitations has been studied analytically in this work. The thermal resonance appears to be a high-mode phenomenon because it occurs only for modes with modal frequencies exceeding a critical value of $0.6436f$. The mode with a modal frequency being $0.5f$ separates the underdamped from the overdamped modes. In terms of the eigenmode number n, the conditions for modal transition and thermal resonance are summarized by

$$\begin{aligned} &0 < n < \frac{0.5}{\pi}\frac{L}{C\tau} \text{ for overdamped modes,} \\ &\frac{0.5}{\pi}\frac{L}{C\tau} < n \text{ for underdamped modes, and} \\ &\frac{0.6436}{\pi}\frac{L}{C\tau} < n \text{ for thermal resonance to occur.} \end{aligned} \qquad (55)$$

For eigenmodes between $\frac{0.5}{\pi}\frac{L}{C\tau}$ and $\frac{0.6436}{\pi}\frac{L}{C\tau}$, a restoration stage exists *prior to* the occurrence of thermal resonance. For these modes, the oscillatory energy is supplied to the energy consumed by the underdamped waves. The excessive amount then contributes to the resonance amplitude for wave modes beyond this range. The critical mode numbers (n) in Eq. (55) are governed by the ratio of the length of the one-dimensional solid (L) to a length-like quantity ($C\tau$). The quantity of $C\tau$, in parallel to the definition of relaxation time, is defined as the relaxation distance. In terms of the thermal diffusivity (α) and the thermal wave speed (C), $\tau = \alpha/C^2$ and $C\tau = \alpha/C$. Both are intrinsic thermal properties of the medium. For producing a resonance phenomenon, it is desirable to have the excitable modal frequencies as low as possible. A solid medium with a larger value of the relaxation distance ($C\tau$) and/or an experimental coupon with a smaller characteristic length (L) is preferable for the occurrence of the thermal resonance.

The resonance frequency of thermal waves leads to an alternative approach for determining the thermal wave speed; refer to Eqs. (52) and (53). From an analytical point of view, this approach has been illustrated in detail. The requirement of oscillations in the high-frequency range, however, is a tradeoff for the fast response of thermal devices in time. Feasibility of the frequency approach will be left to the support of future experiments.

Acknowledgments

This paper is accomplished in the course of research supported by the National Science Foundation under grant No. CTS-8922494 with the University of New Mexico.

References

Baumeister, K. J., and Hamill, T. D., 1969, "Hyperbolic Heat Conduction Equation—A Solution for the Semi-infinite Body Problem," ASME JOURNAL OF HEAT TRANSFER, Vol. 91, pp. 543-548.

Berkovsky, B. M., and Bashtovoi, V. G., 1977, "The Finite Velocity of Heat Propagation From the Viewpoint of Kinetic Theory," *International Journal of Heat and Mass Transfer*, Vol. 20, pp. 621-626.

Bubnov, V. A., 1976, "Wave Concepts in the Theory of Heat," *International Journal of Heat and Mass Transfer*, Vol. 19, pp. 175-184.

Cheng, K. J., 1989, "Wave Characteristics of Heat Conduction Using a Discrete Microscopic Model," ASME JOURNAL OF HEAT TRANSFER, Vol. 111, pp. 225-231.

Chester, M., 1963, "Second Sound in Solids," *Physical Review*, Vol. 131, pp. 2013-2015.

Frankel, J. I., Vick, B., and Özişik, M. N., 1985, "Flux Formulation of Hyperbolic Heat Conduction," *Journal of Applied Physics*, Vol. 58, pp. 3340-3345.

Frankel, J. I., Vick, B., and Özişik, M. N., 1987, "General Formulation and Analysis of Hyperbolic Heat Conduction in Composite Media," *International Journal of Heat and Mass Transfer*, Vol. 3, pp. 467-477.

Gurtin, M. E., and Pipkin, A. C., 1968, "A General Theory of Heat Conduction With Finite Wave Speeds," *Archive for Rational Mechanics and Analysis*, Vol. 31, pp. 113-126.

Imber, M., 1991, private communications.

Kaminski, W., 1990, "Hyperbolic Heat Conduction Equation for Materials With a Nonhomogeneous Inner Structure," ASME JOURNAL OF HEAT TRANSFER, Vol. 112, pp. 555-560.

Kelley, D. C., 1968, "Diffusion: A Relativistic Appraisal," *American Journal of Physics*, Vol. 36, pp. 585-591.

Meirovitch, L., 1967, *Analytical Methods in Vibrations*, Chap. 9, Macmillan, New York.

Özişki, M. N., and Vick, B., 1984, "Propagation and Reflection of Thermal Waves in a Finite Medium," *International Journal of Heat and Mass Transfer*, Vol. 27, pp. 1845-1854.

Peshkov, V., 1944, "Second Sound in Helium II," *USSR Journal of Physics*, Vol. VIII, pp. 381-394.

Taitel, Y., 1972, "On the Parabolic, Hyperbolic, and Discrete Formulation of the Heat Conduction Equation," *International Journal of Heat and Mass Transfer*, Vol. 15, pp. 369-371.

Tzou, D. Y., 1989a, "On the Thermal Shock Wave Induced by Moving Heat Source," ASME JOURNAL OF HEAT TRANSFER, Vol. 111, pp. 232-238.

Tzou, D. Y., 1989b, " Shock Wave Formation Around a Moving Heat Source in a Solid With Finite Speed of Heat Propagation," *International Journal of Heat and Mass Transfer*, Vol. 32, pp. 1979-1987.

Tzou, D. Y., 1989c, "The Effects of Thermal Shock Waves on the Crack Initiation Around a Moving Heat Source," *Journal of Engineering Fracture Mechanics*, Vol. 34, pp. 1109-1118.

Tzou, D. Y., 1990a, "Thermal Shock Waves Induced by a Moving Crack," ASME JOURNAL OF HEAT TRANSFER, Vol. 112, pp. 21-27.

Tzou, D. Y., 1990b, "Thermal Shock Waves Induced by a Moving Crack—A Heat Flux Formulation," *International Journal of Heat and Mass Transfer*, Vol. 33, pp. 877-885.

Tzou, D. Y., 1990c, "Three-Dimensional Structures of the Thermal Shock Waves Around a Rapidly Moving Heat Source," *International Journal of Engineering Sciences*, Vol. 28, pp. 1003-1017.

Tzou, D. Y., 1991a, "Thermal Shock Phenomena Under High Rate Response in Solids," *Annual Review of Heat Transfer*, Chang-Lin Tien, ed., Vol. IV, Chap. 3, Hemisphere Publishing Corp., Washington, DC.

Tzou, D. Y., 1991b, "Resonance of Thermal Waves Under Frequency Excitations," *Fundamentals of Conduction*, ASME HTD-Vol. 173, M. Imber and M. M. Yovanovich, eds., pp. 11-20.

Van Kampen, N. G., 1970, "A Model for Relativistic Heat Transfer," *Physica*, Vol. 46, pp. 315-332.

Vick, B., and Özişik, M. N., 1983, "Growth and Decay of a Thermal Pulse Predicted by the Hyperbolic Heat Conduction Equation," ASME JOURNAL OF HEAT TRANSFER, Vol. 105, pp. 902-907.

Weymann, H. D., 1967, "Finite Speed of Heat Propagation in Conduction, Diffusion, and Viscous Shear Motion," *American Journal of Physics*, Vol. 35, pp. 488-496.

Wiggert, D. C., 1977, "Analysis of Early-Time Heat Conduction by Method of Characteristics," ASME JOURNAL OF HEAT TRANSFER, Vol. 99, pp. 35-40.

J. Fransaer
Research Fellow.

J. R. Roos
Professor and Head of Chemical
Materials Engineering.

Department of Metallurgy and
Materials Engineering,
Katholieke Universiteit Leuven,
B-3001 Heverlee, Belgium

The Temperature Field Around a Spherical Ridge or Trough in a Plane

An analytical solution, which describes the temperature field around a single spherical particle partly embedded in a plane or around a trough making an arbitrary contact angle with a plane, is presented here. The temperature distributions for three cases are studied: the temperature distribution around a conducting bowl or trough, the temperature distribution around a non-conducting bowl or trough present in a conducting plane, and the temperature profile around a conducting bowl or trough conducting heat toward a sink at infinity. The normalized heat flux distribution on the plane and particle is presented. The various incremental resistances caused by a single and a dilute planar random array of truncated spherical particles are also derived.

1 Introduction

When a heat transfer operation results in the evolution of a vapor, the vapor forms bubbles at nucleation sites on the heated surfaces. These bubbles have various effects on the thermal resistance of the heat transfer process. In the bulk fluid, the bubbles decrease the effective conductivity of the fluid, with a concomitant increase in the thermal resistance. On the heat exchange surface, the bubbles resist thermal flux and reduce the effective heat exchange area by blocking part of it. The bubbles also relieve part of the added thermal resistance by the enhanced mass transfer caused by the convective stirring of the growing, coalescing, and disengaging bubbles. Despite the importance of the thermal effects of bubbles, the volume of work devoted to the study of these effects is limited, since the theoretical treatment of the thermal losses caused by the bubble layer, including thermodynamic and convective effects, requires the simultaneous solution of the full thermal and mass-transfer equation in the bubble layer. In fact, only the fluid flow about an expanding hemispherical bubble sitting on a plane (Witze et al., 1968) and the solution of the heat conduction equation for a single spherical bubble tangent to an infinite plane (Fransaer et al., 1990) were analytically solved. Experiments show that the bubbles in surface boiling rarely grow as perfect hemispheres or spheres but rather as a distribution of shapes between these two extremes. This paper is an extension of a previous analysis (Fransaer et al., 1990), which dealt with the thermal effect of particles tangent to a surface. The present work concerns the thermal effects of particles or bubbles making arbitrary contact angles with a surface. The truncated spheres studied in this work bear closer resemblance to a real bubble and offer the possibility of studying certain aspects not yet revealed by the (hemi)spherical geometry.

In actual practice, a heat exchange surface is never really flat but has irregularities that arise due to corrosion or fouling, or that are intentionally added to improve the heat transfer. The temperature distribution around a conducting truncated sphere in a linear temperature gradient models the influence of fouling or surface irregularities of a heated surface on the flow of heat. Moreover, in the case where the contact angle is negative, the model no longer concerns the influence of bulges, but deals with troughs in a surface, which can result from pitting corrosion.

2 The Governing Equations: Toroidal Coordinates

When applying the method of separation of variables on the Laplace equation describing the temperature field about a truncated sphere, the coordinate surfaces must coincide with the physical boundaries of the problem. This leads to the use of the toroidal coordinate system, which is defined as follows: If A and B are points on a straight line through the origin (Fig. 1), perpendicular to the z axis and making an angle ϕ with the x axis, we take as the coordinates of a point P in the plane $\phi=\text{const}$, the value of $\ln AB/BP$ that is denoted by η, the angle APB denoted θ, and the azimuthal angle ϕ. The distance $2a$ between A and B is taken to be constant. The orthogonal transformation between the cylindrical coordinate system (r, z), where the z axis coincides with the symmetry axis, and the toroidal system is:

$$z+ir=ia\coth\frac{1}{2}(\eta+i\theta). \tag{1}$$

Separating the real and imaginary parts, we find that r and z are given by the equations[1]:

$$r=\frac{a\sinh\eta}{\cosh\eta-\mu} \tag{2a}$$

$$z=\frac{a\sin\theta}{\cosh\eta-\mu} \tag{2b}$$

where μ is $\cos\theta$ and a is equal to the radius of the contour of intersection of the sphere and the $z=0$ plane. The coordinate surfaces $\eta=\text{const}$ $(0\le\eta<\infty)$ are a family of anchor rings or tores. Another group consists of spherical bowls orthogonal to the anchor rings and these occur at $\theta=\text{const}$ $(-\pi\le\theta<\pi)$. A third family is comprised of half-planes orthogonal to the rings and bowls (Fig. 1), and these occur at $\phi=\text{const}$ $(0\le\phi<2\pi)$. The normal separable solutions of the Laplace equation $\nabla^2T=0$ in toroidal coordinates contain toroidal or ring functions of the first and second kind: $P^m_{n-1/2}$ and $Q^m_{n-1/2}$. As pointed out by Miloh (1981), these harmonics are inappropriate for the description of the temperature field around a truncated sphere since η varies continuously on the sphere surface from 0 to ∞, where both functions become unbounded. Therefore recourse is made to the Legendre functions of imaginary order (conal functions) introduced by Hobson (1931). Using the conal functions, the general solution to the conduction equation is given by:

Contributed by the Heat Transfer Division for publication in the JOURNAL OF HEAT TRANSFER. Manuscript received by the Heat Transfer Division December 1990; revision received October 1991. Keywords: Conduction, Fouling, Mass Transfer.

[1] Note that our conventions differ from those of Sneddon (1972).

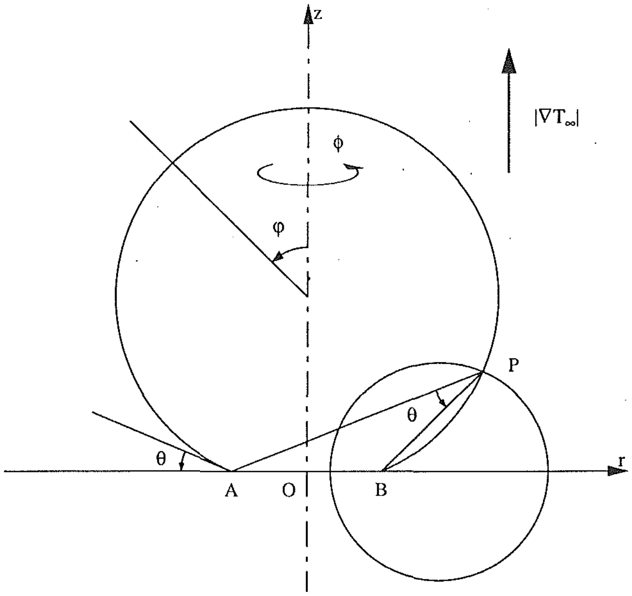

Fig. 1 Definition of the toroidal coordinate system: geometrical configuration of the boundaries; plane with spherical bump

$$T=(\cosh\eta-\mu)^{1/2}\begin{Bmatrix}P^{m}_{-\frac{1}{2}+ip}(\cosh\eta)\\ Q^{m}_{-\frac{1}{2}+ip}(\cosh\eta)\end{Bmatrix}\begin{Bmatrix}\sinh p\theta\\ \cosh p\theta\end{Bmatrix}\begin{Bmatrix}\sin m\phi\\ \cos m\phi\end{Bmatrix} \tag{3}$$

All variables in this paper are dimensionless. The distances are made dimensionless with respect to the radius of the projection of the truncated sphere or trough on the $z=0$ plane. The temperature is made dimensionless so that $T=z$ corresponds to the dimensionless temperature profile at infinity. In the case of the conducting bowl or trough on an isolating surface, the temperature field is cast in dimensionless form by dividing the temperature field by the constant surface temperature T_0 of the bowl or trough.

3 Applications

3.1 Temperature Field Around a Conducting Truncated Sphere or Trough. The dimensionless temperature distribution around a bowl or trough on a surface when the field at infinity is linear requires the solution of the conduction equation $\nabla^2 T=0$. Taking the temperature on the $z=0$ plane as a reference temperature, the expression for the dimensionless temperature far away from the bowl is $T=z$. The solution of the heat conduction equation for this particular geometry can be obtained from the superposition of the linear temperature field far from the origin and a disturbance temperature field T_d:

$$\nabla^2(z+T_d)=0. \tag{4}$$

The uniform gradient is a solution of the Laplace equation without any disturbance. The second term, which is a correction due to the presence of the sphere or trough, is a particular solution of the Laplace equation in toroidal coordinates. From the general solution, given in Section 2, an appropriate solution for T_d can be constructed:

$$T_d=(\cosh\eta-\mu)^{1/2}\int_0^\infty \{A(p)\sinh p\theta + B(p)\cosh p\theta\}K_p(\cosh\eta)dp \tag{5}$$

where $A(p)$ and $B(p)$ are unknown functions to be determined from the boundary conditions. Following Hobson, we use a shorthand notation for the conal functions:

$$K_p(\cosh\eta)=P_{-\frac{1}{2}+ip}(\cosh\eta). \tag{6}$$

Since there are no discrete eigenvalues for the p coordinate, solution of Eq. (5) requires integration of the general solutions rather than summation.[2] The boundary conditions for the disturbance temperature field can be expressed as:

$$T_d=-z \quad (\theta=\theta_0 \text{ and } \theta=-\theta_0) \tag{7a}$$

$$T_d=0 \quad (\theta=0) \tag{7b}$$

$$T_d\rightarrow 0 \quad (\eta,\ \theta\rightarrow 0) \tag{7c}$$

The disturbance must be an even function in θ (Eq. (7*b*)) and must vanish both on the $z=0$ plane and far from the sphere (7*c*). Equation (7*a*) matches the linear field to the disturbance on the sphere surface. Boundary condition Eq. (7*b*) implies that $B(p)=0$. Boundary condition Eq. (7*a*) can be satisfied by expanding the linear field in conal harmonics using the identity:

$$\frac{1}{(\cosh\eta-\mu)^{1/2}}=2^{1/2}\int_0^\infty \frac{\cosh p(\pi-\theta)}{\cosh(p\pi)}K_p(\cosh\eta)dp. \tag{8}$$

After deriving the former expression and comparing like terms with Eq. (5), the desired dimensionless temperature distribution is obtained:

$$T=z-2^{3/2}a(\cosh\eta-\mu)^{1/2}\times\int_0^\infty p\frac{\sinh p(\pi-\theta_0)\sinh p\theta}{\cosh p\pi\sinh p\theta_0}K_p(\cosh\eta)dp. \tag{9}$$

---

[2] Note that the integration is done with respect to the order of the conal functions.

Nomenclature

$A(p)$, $B(p)$ = separation functions
E^2 = Stokes stream function operator
K = complete elliptical integral of the first kind
K_p^m = conal functions
p = dummy integral argument
P_n, Q_n = Legendre functions of the first and second kind
r = dimensionless radial position in cylindrical coordinates
T = dimensionless temperature
T_d = dimensionless temperature disturbance
T_0 = temperature of the bowl (cap) or trough, K
z = dimensionless axial position in cylindrical coordinates
ϵ_n = Neumann's symbol; $\epsilon_n = 1$ for $n=0$ and $\epsilon_n = 2$ for $n = 1, 2, 3, \ldots$
η, θ, ϕ = toroidal coordinate system
μ = cos θ
ρ, ψ, ϕ = spherical coordinate system
Ψ = Stokes stream function
Ψ_d = disturbance stream function
∇^2 = Laplace operator

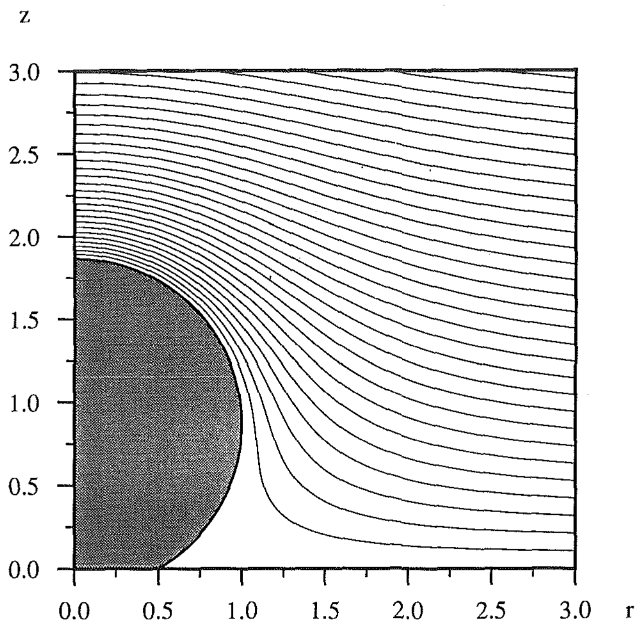

Fig. 2(*a*) Sectional view of the isotherms around a conductive spherical bowl on a conductive plane placed in a linear temperature gradient, when the bowl makes a contact angle of 30 deg

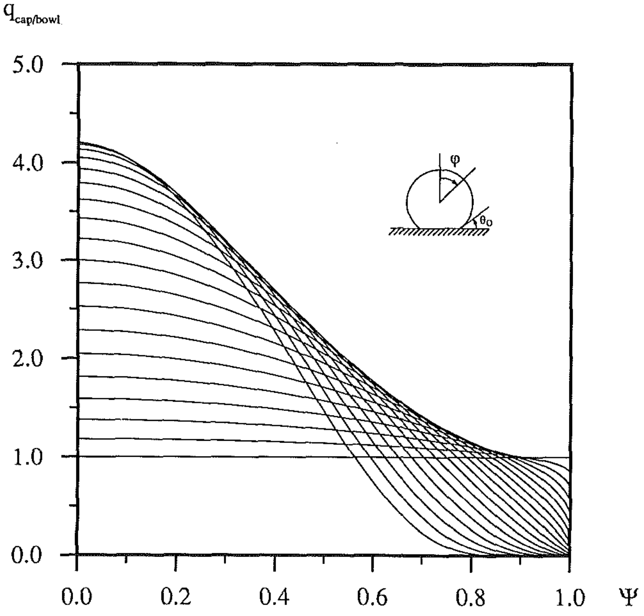

Fig. 2(*b*) Heat flux distribution versus scaled distance x on the $z=0$ plane around a conducting bowl (cap) for various values of the contact angle θ_0: 0(10)180

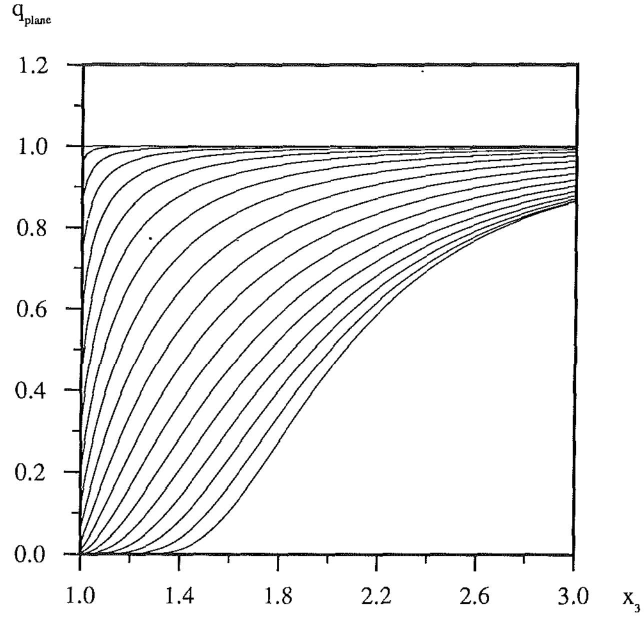

Fig. 2(*c*) Heat flux distribution on a conducting bowl (cap) placed on a conducting plane for various values of the contact angle θ_0: 0(10)180

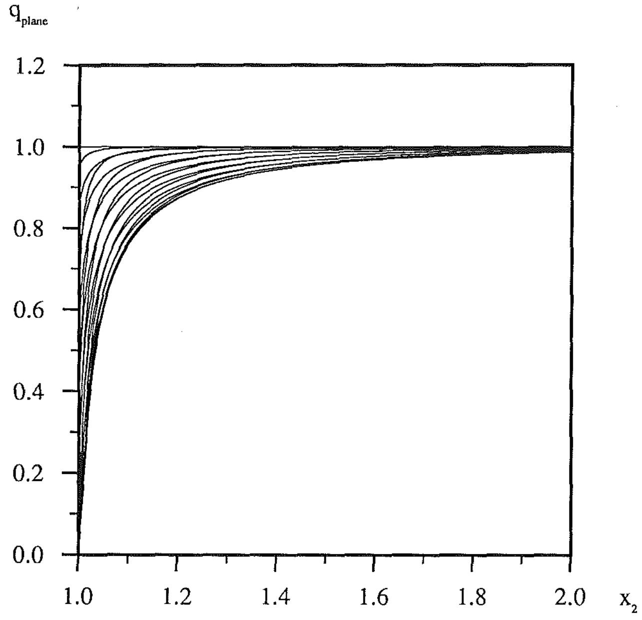

Fig. 2(*d*) Heat flux distribution on the $z=0$ plane around a conducting trough for various values of the contact angle θ_0: 0(−10)−180

The expression in Eq. (9) for the temperature field is not very convenient from a numerical point of view because no series approximation exists for the conal functions. To arrive at a useful expression for the temperature field, the properties of the Mehler-Fock transform of the zeroth order were invoked and Eq. (9) was rewritten as:

$$T=z-\frac{2^{3/2}}{\pi^{1/2}}a(\cosh\eta-\mu)^{1/2}\int_{\eta}^{\infty}\frac{G_s(t)}{(\cosh t-\cosh\eta)^{1/2}}dt \qquad (10)$$

where $G_s(t)$ is defined as a Fourier sinus transform:

$$G_s(t)=-\frac{2^{1/2}}{\pi^{1/2}}\int_0^{\infty}p\frac{\sinh p(\pi-\theta_0)\sinh p\theta}{\sinh p\pi\sinh p\theta_0}\sin tp\,dp. \qquad (11)$$

Using a series expansion for the quotient of two hyperbolic sine functions (Gradshteyn and Ryzhik, 1980) and applying the definition integral of the Legendre functions of the second kind (Hobson) we obtain:

$$T=z-2^{5/2}a(\cosh\eta-\mu)^{1/2}\sum_{n=1}^{\infty}\frac{n\sin n\theta}{\pi}Q_{n-\frac{1}{2}}(\cosh\eta)$$

$$+2^{5/2}a(\cosh\eta-\mu)^{1/2}\sum_{n=1}^{\infty}\frac{n\pi\sin\left(n\pi\frac{\theta}{\theta_0}\right)}{\theta_0^2}Q_{n\frac{\pi}{\theta_0}-\frac{1}{2}}(\cosh\eta). \qquad (12)$$

This series expansion is uniformly and absolutely convergent in the domain $0<\eta<\infty$, but convergence is slow close to $\eta=0$. For small values of the argument, the Legendre function $Q_\nu(x)$ diverges, thus invalidating the series representation for the temperature field very close to the axis or far from the origin.

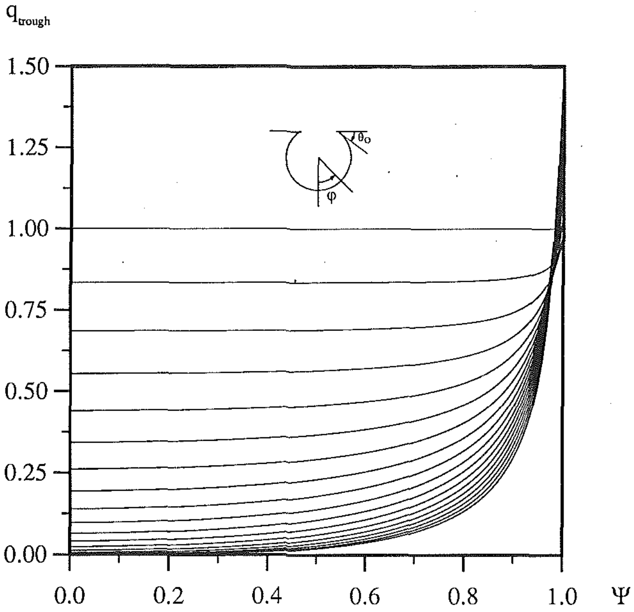

Fig. 2(*e*) **Heat flux distribution on a conducting trough in a conducting plane for various values of the contact angle θ_0: 0(− 10) − 180**

The temperature field in these regions was calculated from Eq. (9), using an expansion for the conical functions derived in the appendix, which are valid for small values of the argument. The integral in Eq. (9) is approximated using a 48-point Gaussian quadrature between consecutive zeros of $K_p(\cosh\eta)$ until the contribution falls below 10^{-6} percent.

The isotherms for $\theta_0 = 30$ are shown in Fig. 2(*a*). From the solution of the temperature distribution, the normalized heat flux distribution on the plane and on the sphere can be obtained by straightforward differentiation:

$$q_{\text{plane}} = \left.\frac{\partial T}{\partial z}\right|_{z=0} = \frac{\cosh\eta - 1}{a}\left.\frac{\partial T}{\partial\theta}\right|_{\theta=0} \tag{13}$$

and on the cap/bowl:

$$q_{\text{sphere}} = -\frac{\cosh\eta - \cos\theta_0}{a}\left.\frac{\partial T}{\partial\theta}\right|_{\theta=\theta_0}. \tag{14}$$

The normalized heat flux distributions on the plane and sphere are depicted in Figs. 2(*c*) and 2(*d*). The solution of the temperature field for negative contact angles, which is the temperature field around a trough, cannot be derived from the solution Eq. (9) since the integrand becomes unbounded for negative θ_0 values. The underlying reason lies in the choice of the coordinate transformation, where θ changes abruptly from π to $-\pi$ if z goes from positive to negative values for $0 < r < a$. A slightly different coordinate transformation avoids this discontinuity:

$$r = \frac{a\sinh\eta}{\cosh\eta + \mu} \tag{15a}$$

$$z = \frac{a\sin\theta}{\cosh\eta + \mu}. \tag{15b}$$

In this coordinate system, the discontinuity in the θ coordinate along the inside of the circle $r = a$ is alleviated and is placed along the outside of the circle. This means that the extension of the spherical cap $\theta = \theta_0$ below the $z = 0$ plane is given by $\theta = \pi + \theta_0$. In these coordinates, the temperature field around a trough of (negative) contact angle θ_0 is given by:

$$T = z - 2^{3/2}a(\cosh\eta + \mu)^{1/2} \times \int_0^\infty p\,\frac{\sinh p\theta_0 \sinh p(\pi - \theta)}{\cosh p\pi \sinh p(\pi - \theta_0)} K_p(\cosh\eta)\,dp \tag{16}$$

and the series representation of the temperature field is:

$$T = z + 2^{5/2}a(\cosh\eta + \mu)^{1/2}\sum_{n=1}^{\infty}\frac{(-)^n n\sin n\theta}{\pi} Q_{n-\frac{1}{2}}(\cosh\eta) + 2^{5/2}a(\cosh\eta + \mu)^{1/2}\sum_{n=1}^{\infty}\frac{n\pi\sin\left(n\pi\frac{\pi-\theta}{\pi-\theta_0}\right)}{(\pi-\theta_0)^2} Q_{n\frac{\pi}{\pi-\theta_0}-\frac{1}{2}}(\cosh\eta). \tag{17}$$

The solution of the temperature field around a trough can be derived from the solution of the temperature field around a cap by replacing θ by $\pi - \theta$ (and θ_0 by $\pi - \theta_0$). The normalized heat flux distributions on the plane and trough are depicted in Figs. 2(*d*) and 2(*e*). To compare the various heat flux distributions corresponding to different θ_0 values, the curves are shown versus normalized distances. The heat flux distribution on the $z = 0$ plane is plotted versus the normalized distance x from the intersection of the cap or trough and the plane, defined by $x_\nu = 1 + (\nu - 1)r - a/\nu - a$. The heat flux distribution on the surface of the cap or trough is plotted as a function of the normalized polar angle Ψ related to φ (Fig. 1) by $\Psi = \varphi / \pi - \theta_0$. The angle $\Psi = 0$ corresponds with the intersection of the symmetry axis with the cap or trough, while $\Psi = 1$ is the intersection of the cap or trough with the $z = 0$ plane. The top and bottom curves in Figs. 2(*c*-*e*) correspond to the limiting cases $\theta_0 = 0$ and π, respectively, a conducting sphere tangent to the $z = 0$ plane and a disk mounted in a plane. From the plot of the isothermal lines in Fig. 2(*a*), it is evident that the disturbance of the linear temperature field diminishes rapidly as a function of distance from the origin and practically disappears at a dimensionless distance of 3 along the plane. The distance at which the disturbance normal to the $z = 0$ plane disappears is a function of the height of the cap above the plane (and thus of θ_0), never extending farther than three times the height of the cap. The disturbance is even more localized for negative contact angles (troughs), where the influence on the isotherms is negligible at distances greater than 2 from the origin. The interior of the trough is screened off from the temperature field above the plane especially in the case of small, negative contact angles. This is reflected in the heat flux distribution on the surface of the disturbance: Only the surface of the trough near the rim of the hole intercepts any heat. As the absolute value of the contact angle increases, the heat flux distribution on the trough becomes more uniform and more heat enters the trough. This is apparent in the heat flux on the plane around a conducting trough where the largest decrease in the heat flux reaching the $z = 0$ plane is found for a hemispherical trough. This is partially due to the fact that for smaller negative contact angles the size of the hole decreases since the radius of the trough is fixed at 1. For the conducting cap, the area at the base of the bowl is screened by the presence of the sphere overlying the area in the limit for $\theta_0 \to 0$ the heat flux becomes zero on the contact point. As more heat is extracted from the linear gradient, the conducting cap and trough lead to a decrease of the thermal resistance. The cap, however, traps more heat than a trough because it extends into regions of higher temperatures. This is evidenced by a compression of the isotherms near the top of the cap, while a conducting trough increases the distance between the isothermal planes.

3.2 Temperature Field Around a Nonconducting Truncated Sphere. The Laplace conduction equation, governing the temperature field around a truncated insulating sphere in a uniform temperature gradient, cannot be expressed as a Dirichlet problem. On the surface of the nonconducting sphere the heat flux is zero, whereas on the plane surface the temperature is constant. This mixed boundary problem can be transformed into a Dirichlet problem by solving the Stokes equation $E^2\Psi = 0$, where the curl of the stream function Ψ is

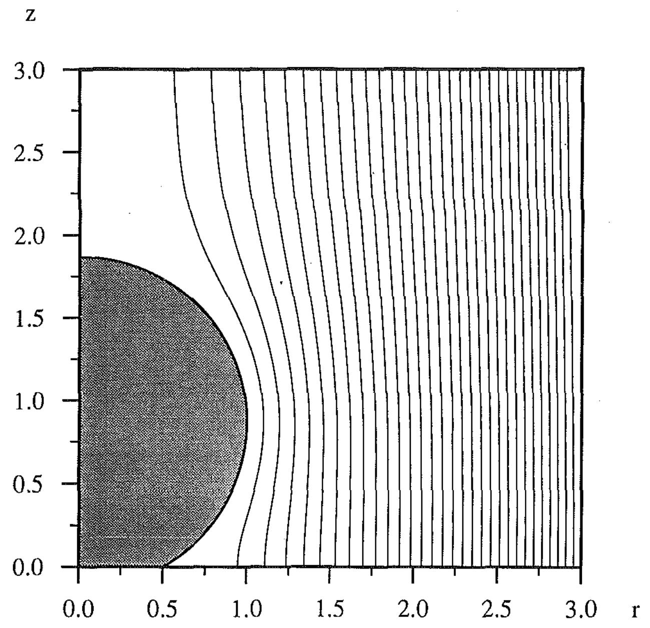

Fig. 3(*a*) Plot of meridian section of the stream surfaces around a nonconductive spherical bowl on a conductive plane placed in a linear temperature gradient, when the bowl makes a contact angle of 30 deg

proportional to the derivative of the temperature field (heat flux). A sufficiently general solution of the Stokes equation $E^2\Psi=0$ can be derived from the solution of the Laplace equation:

$$\Psi=a^2(\cosh\eta-\mu)^{-1/2}\sinh^2\eta\int_0^\infty\{A(p)\sinh p\theta+B(p)\cosh p\theta\}K_p^1(\cosh\eta)dp \qquad (18)$$

where $K_p^1(\cosh\eta)$ is an associated Legendre function defined by:

$$K_p^1(\cosh\eta)=\frac{d}{d\cosh\eta}P_{-\frac{1}{2}+ip}(\cosh\eta). \qquad (19)$$

The uniform, dimensionless temperature gradient $T=z$ corresponds to $\Psi=-r^2/2$ in the Stokes stream function formalism. Exploiting the fact that the E^2 is a linear operator, the problem is decomposed into the uniform heat flow, which is a solution to the Stokes stream function for a linear temperature gradient without a disturbance and a stream function Ψ_d that is a correction due to the presence of the bowl:

$$E^2\left(-\frac{r^2}{2}+\Psi_d\right)=0 \qquad (20)$$

The boundary conditions for the disturbance are:

$$\Psi_d=\frac{r^2}{2}\quad(\theta=\theta_0 \text{ and } \theta=-\theta_0) \qquad (21a)$$

$$\Psi_d=0\quad(\theta=0) \qquad (21b)$$

$$\Psi_d\to 0\quad(\eta,\ \theta\to 0) \qquad (21c)$$

The disturbance stream function is an even function in θ and vanishes far from the origin (Eqs. (21*a*) and (21*c*)). Equation (21*b*) fixes the arbitrary additive constant and makes the disturbance vanish on the symmetry axis. Equation (21*a*) enforces the surface of the bowl to coincide with the stream function $\Psi=0$, which makes the surface impermeable to heat. Boundary condition Eq. (21*a*) is satisfied by expanding $r^2/2$ in suitable harmonics and equating the resulting function to the general solution of the Stokes equation. Using the former identity (Eq. (8)) and comparing like terms with Eq. (18), the total solution becomes:

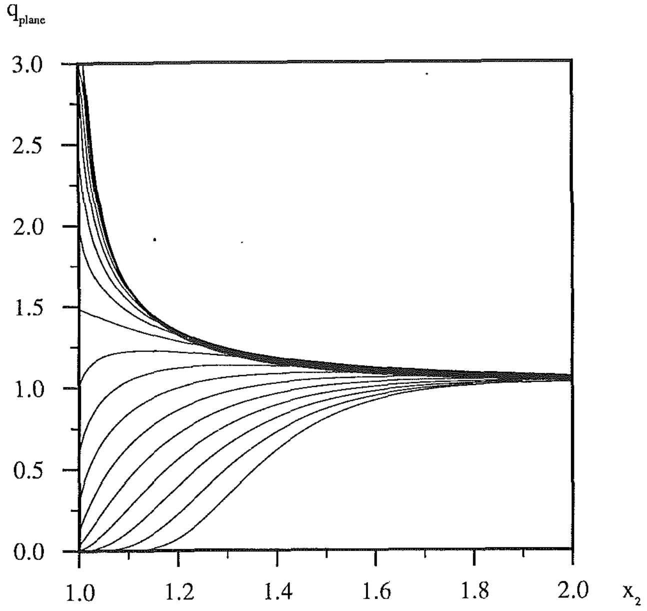

Fig. 3(*b*) Heat flux distribution on the $z=0$ plane around an isolating bowl (cap) for various values of the contact angle θ_0: 0(10)180

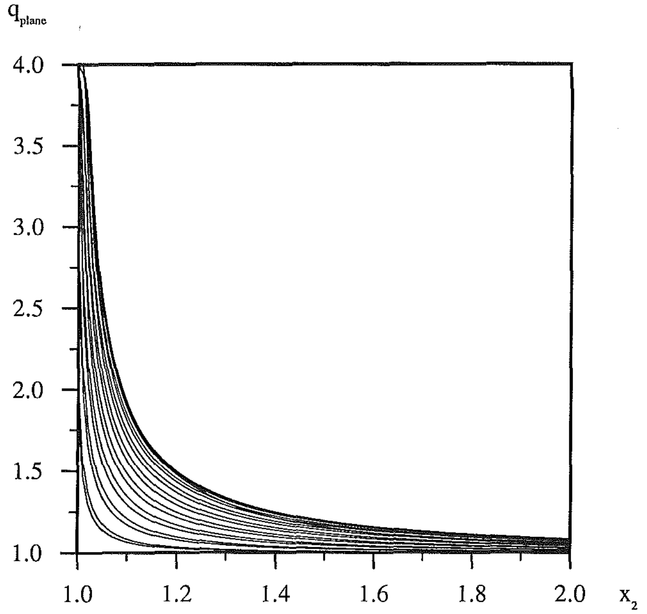

Fig. 3(*c*) Heat flux distribution on the $z=0$ plane around an isolating trough embedded in a conducting plane for various values of the contact angle θ_0: 0(−10)−180

$$\Psi=-\frac{r^2}{2}-\frac{2^{1/2}a^2\sinh^2\eta}{(\cosh\eta-\mu)^{1/2}}\times\int_0^\infty\frac{\cosh p(\pi-\theta_0)\cosh p\theta}{\cosh p\pi\cosh p\theta_0}K_p^1(\cosh\eta)dp \qquad (22)$$

Using the properties of the Mehler-Fock transforms and the recurrence relations of the Legendre functions, and after tedious but straightforward algebra, the following expression for the stream function is found:

$$\Psi=-\frac{r^2}{2}-\frac{2^{1/2}a^2}{(\cosh\eta-\mu)^{1/2}}\sum_{n=0}^{\infty}\frac{\epsilon_n\left(n+\frac{1}{2}\right)\cos n\theta}{\pi}\{Q_{n+\frac{1}{2}}(\cosh\eta)-\cosh\eta\,Q_{n-\frac{1}{2}}(\cosh\eta)\}$$

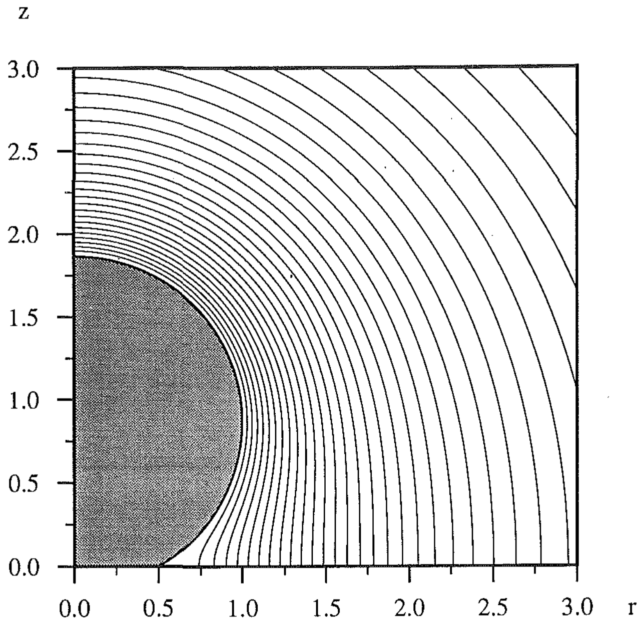

Fig. 4(*a*) Sectional view of the isotherms around a conductive spherical bowl on a nonconductive plane, when the bowl makes a contact angle of 30 deg

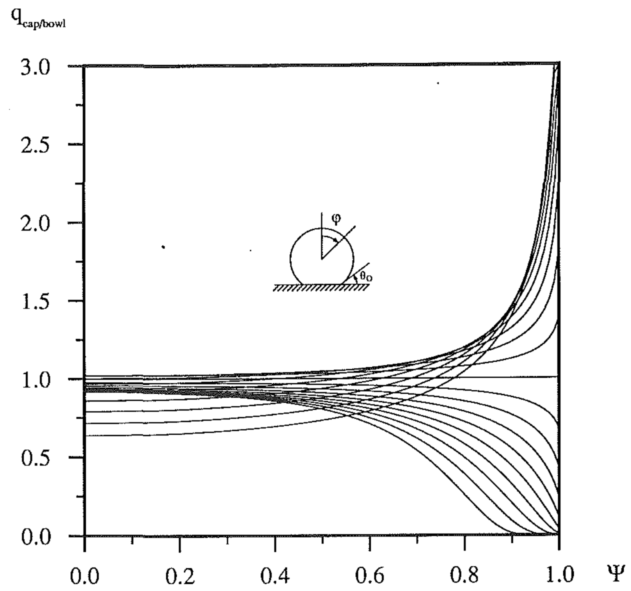

Fig. 4(*c*) Heat flux distribution on a conducting bowl (cap) placed on a isolating plane for various values of the contact angle θ_0: 0(10)180

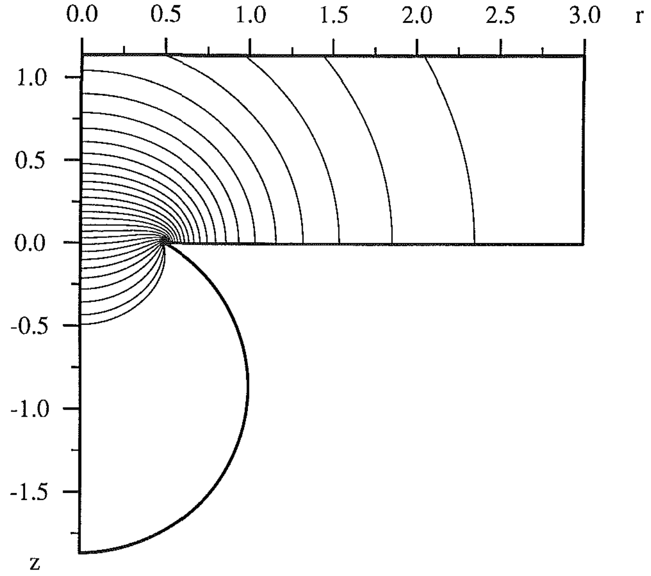

Fig. 4(*b*) Sectional view of the isotherms around a conductive spherical trough in a nonconductive plane, when the trough makes a contact angle of −30 deg with the plane

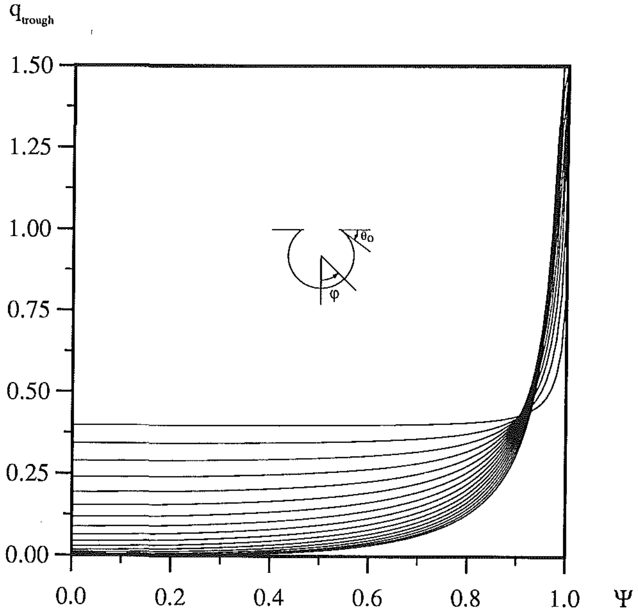

Fig. 4(*d*) Heat flux distribution on a conducting trough situated in a nonconducting plane for various values of the contact angle θ_0: 0(−10)−180

$$+\frac{2^{1/2}a^2}{(\cosh\eta-\mu)^{1/2}}\sum_{n=0}^{\infty}\frac{2\left[\left(n+\frac{1}{2}\right)\frac{\pi}{\theta_0}+\frac{1}{2}\right]\cos\left[\left(n+\frac{1}{2}\right)\pi\frac{\theta}{\theta_0}\right]}{\theta_0}\cdot$$

$$\{Q_{\left(n+\frac{1}{2}\right)\frac{\pi}{\theta_0}+\frac{1}{2}}(\cosh\eta)-\cosh\eta\, Q_{\left(n+\frac{1}{2}\right)\frac{\pi}{\theta_0}-\frac{1}{2}}(\cosh\eta)\}$$

From the temperature distribution, the normalized heat flux distribution on the $z=0$ plane can be derived, knowing that:

$$q_{\text{plane}}=\left.\frac{\partial T}{\partial z}\right|_{z=0}=\left.\frac{(\cosh\eta-1)^2}{a^2\sinh\eta}\frac{\partial\Psi}{\partial\eta}\right|_{\theta=0} \tag{24}$$

Replacing $\theta_{(0)}$ with $\pi-\theta_{(0)}$, the solution for a nonconducting trough embedded in a conducting plane is obtained. The stream lines (lines of constant Ψ) for this problem are shown in Fig. 3(*a*) for a value of θ_0 of 30 deg. Far from the origin, the stream lines are close together since $2\pi(\Psi_1-\Psi_2)$ constitutes the total heat flowing between the stream tubes $\Psi=\Psi_1$ and $\Psi=\Psi_2$. The stream lines are pushed sideways because no heat enters the isolating bowl or cap. The influence of the disturbance on the stream lines falls off rapidly with distance from the origin. For the same projected area, the magnitude of the disturbance is greater for a bowl than for a cap. The heat flux distribution on the $z=0$ plane, as a function of dimensionless distance, appears in Fig. 3(*b*). Since the temperature field is normalized, the heat flux approaches a limiting value of 1.0 far from the origin. The area around the intersection of sphere and plane becomes less effectively screened from the heat flux with increasing contact angle, and disappears once θ_0 equals $\pi/2$. For larger contact angles the heat flux distribution on the $z=0$ plane is maximal on the rim of the cap and this maximum increases until it becomes infinite for a nonconducting disk in a conducting plane.

3.3 Temperature Field Around a Conducting Truncated Sphere or Trough. The temperature field around a truncated sphere or a conducting trough of uniform temperature T_0 on an isolated plane requires the solution of $\nabla^2 T=0$, given by:

$$T=(\cosh\eta-\mu)^{1/2}\int_0^\infty \{A(p)\cosh p\theta + B(p)\sinh p\theta\}K_p(\cosh\eta); \quad (25)$$

which, after dividing the temperature field by T_0, is subject to the following boundary conditions:

$$T=1 \quad (\theta=\theta_0) \quad (26a)$$

$$\frac{\partial T}{\partial\theta}=0 \quad (\theta=0) \quad (26b)$$

$$T\to 0 \quad (\eta,\ \theta\to 0) \quad (26c)$$

The temperature vanishes far from the sphere (Eq. (26*c*)); Eq. (26*a*) governs the surface temperature on the sphere. The zero gradient condition on the plane Eq. (26*b*) can be replaced by the condition that a second bowl, forming the mirror image of the first in the plane, has the same temperature as the first:

$$T=1 \quad (\theta=-\theta_0) \quad (26d)$$

This makes the temperature field an even function in θ and sets $B(p)=0$. The unknown function $A(p)$ is obtained by inspection of the boundary condition Eq. (26*a*) and Eq. (8). Hence the total solution is:

$$T=2^{1/2}(\cosh\eta-\mu)^{1/2}\int_0^\infty \frac{\cosh p(\pi-\theta_0)\cosh p\theta}{\cosh p\pi\cosh p\theta_0}K_p(\cosh\eta)dp \quad (27)$$

Apart from the associated Legendre function, the integrand is identical to the former case. Employing the same line of reasoning and using the properties of the Mehler-Fock transforms of the zeroth order and the definition integral of the Legendre functions of the second kind, the following expression for the temperature around a truncated sphere is obtained:

$$T=2^{1/2}(\cosh\eta-\mu)^{1/2}\sum_{n=0}^{\infty}\frac{\epsilon_n}{\pi}\cos n\theta\, Q_{n-\frac{1}{2}}(\cosh\eta)$$
$$-2^{1/2}(\cosh\eta-\mu)^{1/2}\sum_{n=0}^{\infty}\frac{2}{\theta_0}\cos\left[\left(n+\frac{1}{2}\right)\pi\frac{\theta}{\theta_0}\right]$$
$$\times Q_{\left(n+\frac{1}{2}\right)\frac{\pi}{\theta_0}-\frac{1}{2}}(\cosh\eta) \quad (28)$$

The isotherms for this problem are shown in Fig. 4(*a*) for θ_0 equal to 30 deg. The heat flux distribution on the sphere is depicted in Fig. 4(*c*). The temperature map for $\theta_0=-30$ deg appears in Fig. 4(*b*). Because the $z=0$ plane is nonconducting, the isotherms meet the plane at right angles. As a consequence, very steep temperature gradients arise in the vicinity of the junction between the plane and the bowl or trough, especially for (small) negative contact angles (Fig. 4*b*). This is also reflected in the heat distribution profiles; the area around the rim conducts most of the total heat flow. The maximum of the heat distribution profiles lies near the top of the conducting cap for $\theta_0<\pi/2$ while for larger values of the contact angle more heat flows through the rim of the cap.

4 Discussion and Conclusion

The thermal resistance decrease or increase, caused by a single particle or trough of radius a embedded in a plane, is proportional to the integral of the temperature disturbance T_d over a plane parallel to the $z=0$ plane (Sides and Tobias, 1980).

$$\Delta T\propto 2\pi\int_0^\infty rT_d dr, \quad z=\text{const} \quad (29)$$

It can be shown that this integral is independent of the location of the plane as long as the plane doesn't cut the particle. Evaluation of the integral is best done in the limit for $z\gg 0$. Far from the origin, η, $\theta\to 0$ and thus:

$$(\cosh\eta-\cos\theta)^{1/2}\simeq\sqrt{2}\frac{a}{\rho} \quad (30a)$$

$$\sinh\eta\simeq\frac{2a\sin\psi}{\rho} \quad (30b)$$

$$\sin\theta\simeq\frac{2a\cos\psi}{\rho} \quad (30c)$$

where (ρ, ψ, ϕ) are spherical coordinates with the same origin and azimuthal angle ϕ as the toroidal coordinates and related to these through:

$$\rho^2=\frac{(\cosh\eta+\cos\theta)}{(\cosh\eta-\cos\theta)} \text{ and } \tan\psi=\frac{\sinh\eta}{\sin\theta}. \quad (31)$$

Using these expressions and knowing that $K_p(1)=1$ (see appendix), the following limiting expansions for the disturbance temperature field around a conducting cap on a conducting surface are obtained:

$$T_d=2^{3/2}a(\cosh\eta-\cos\theta)^{1/2}\int_0^\infty p\frac{\sinh p(\pi-\theta_0)\sinh p\theta}{\cosh p\pi\sinh p\theta_0}K_p(\cosh\eta)dp \quad (32a)$$

$$\simeq\frac{8a^3\cos\psi A_0}{\rho^2} \quad (32b)$$

with

$$A_0=\int_0^\infty p^2\frac{\sinh p(\pi-\theta_0)}{\cosh p\pi\sinh p\theta_0}dp. \quad (33)$$

yielding the following expression for the incremental resistance: $\Delta T=\pi a^3 A_o$. A conducting trough results in a similar expression, with A_o given by:

$$A_0=\int_0^\infty p^2\frac{\sinh p\theta_0}{\cosh p\pi\sinh p(\pi-\theta_0)}dp.$$

Since the integrand in Eqs. (33) and (34) is continuous, monotonically decreasing and single-valued in the domain, the integrals Eqs. (33) and (34) were numerically approximated by a Simpson rule with an interval of 0.01.

For an isolated bowl on a conducting surface, the limiting form of the correction to the temperature (i.e., the expansion as $\rho\to\infty$ where ρ is the distance from the origin) is sought. In the far field both η and θ approach zero and:

$$\Psi_d=-\frac{\sqrt{2}a^2\sinh^2\eta}{(\cosh\eta-\cos\theta)^{1/2}}\int_0^\infty\frac{\cosh p(\pi-\theta_0)\cosh p\theta}{\cosh p\pi\cosh p\theta_0}\times K_p^1(\cosh\eta)dp \quad (35a)$$

$$\simeq\frac{2a^3\sin^2\theta A_1}{\rho} \quad (35b)$$

where

$$A_1=\int_0^\infty\left(p^2+\frac{1}{4}\right)\frac{\cosh p(\pi-\theta_0)}{\cosh p\pi\cosh p\theta_0}dp \quad (36)$$

for a nonconducting cap/bowl on a conducting plane or

$$A_1=\int_0^\infty\left(p^2+\frac{1}{4}\right)\frac{\cosh p\theta_0}{\cosh p\pi\cosh p(\pi-\theta_0)}dp \quad (37)$$

for a nonconducting trough in a conducting plane. With the limiting expressions Eqs. (30*a*-*c*), and the value of $K_p^1(1)$ derived in Appendix A, the far field expansion of the correction to the temperature is found, using:

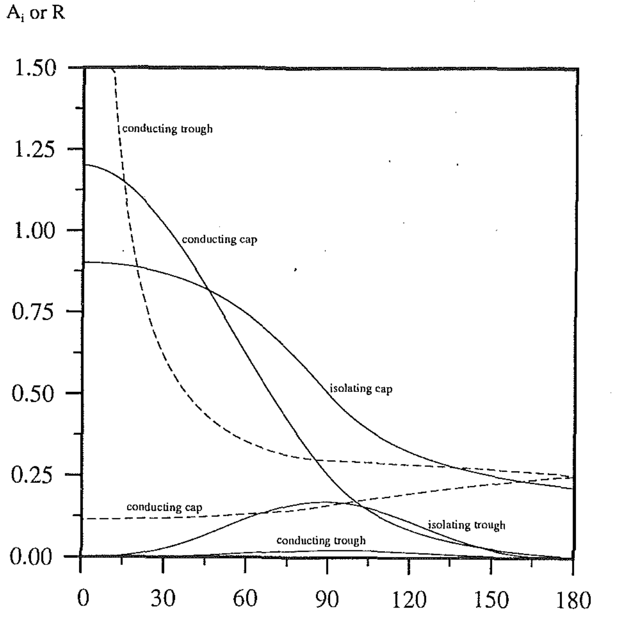

Fig. 5 Integral of the temperature disturbance with area A_i for the various configurations mentioned in the text; also shown (broken lines) are the resistance $\mathcal{R}$ for the flow of heat from a conducting trough (top) or a conducting bowl (bottom)

$$\frac{\partial T_d}{\partial \rho} = -\frac{1}{\rho^2 \sin\theta}\frac{\partial \Psi_d}{\partial \theta} \quad \text{and} \quad \frac{\partial T_d}{\partial \theta} = \frac{1}{\sin\theta}\frac{\partial \Psi_d}{\partial \rho}. \tag{38}$$

The incremental thermal resistance caused by the presence of an isolating cap (or trough) is thus: $\Delta T = \pi a^3 A_1$. In the limit of $|\theta_0| \rightarrow 0$ these results coincide with the values reported earlier for a tangent sphere (Fransaer). The integrals A_0 and A_1 for cap and trough are shown in Fig. 5 as a function of the contact angle θ_0. The maximum disturbance for the heat flow around a cap is obtained for $\theta_0 = 0$, while the temperature disturbance for a trough is greatest for $\theta_0 = \pi/2$. The influence on the temperature distribution vanishes as $\theta_0 \rightarrow \pi$, except for an isolating cap, where the influence on the heat flow of a nonconducting circular disk in a conducting plane is obtained.

The thermal resistance $\mathcal{R}$ of a conducting particle on, or trough in, an isolating surface is: $\mathcal{R} = T_0/Q$ where Q, the total heat radiated by the sphere, is given by:

$$Q = 2\pi \int_\gamma r \frac{\partial T}{\partial n} d\gamma \tag{39}$$

and the integral is taken around any meridian γ. On the surface of the sphere $\theta = \theta_0$

$$d\gamma = -\frac{a}{\cosh\eta - \cos\theta_0} d\eta \quad \text{and}$$

$$\frac{\partial}{\partial n} = -\frac{\cosh\eta - \cos\theta_0}{a}\frac{\partial}{\partial \theta}. \tag{40}$$

Using these relations, the thermal resistance is given by:

$$\frac{1}{\mathcal{R}} = 2\pi a \int_0^\infty \frac{\sinh\eta}{\cosh\eta - \cos\theta_0} \left. \frac{\partial T}{\partial \theta} \right|_{\theta=\theta_0} d\eta. \tag{41}$$

The resistance, calculated with this formula, agrees, in the limit of $\theta_0 \rightarrow 0$, with the value $1/4\pi\kappa \ln 2$ for the conducting sphere tangent to a conducting plane, and for $\theta_0 = \pi/2$ with the resistance $1/2\pi\kappa a$ of a hemisphere of radius a mounted in an insulating plane. The dashed lines in Fig. 5 represent the resistances of a conducting cap and a conducting trough for values of the contact angle $|\theta_0|$ between 0 and π. To compare the added resistances on an equivalent basis, the radius of the cap (or trough) projected on the $z = 0$ plane is taken as a unit length.

The resistance of an array of truncated particles or troughs cannot be obtained by analytical means; it requires the solution of the Laplace equation in a complicated three-dimensional geometry. It is possible, however, to derive an approximation to the resistance of a dilute array of such particles or holes from the thermal disturbances of single truncated particles or troughs. The thermal effect exerted by an array of particles of effective radius a and mean number density n per unit area of the thermal resistance is approximately n times the effect of a single particle. The increment of the thermal resistance $\Delta\mathcal{R}$ caused by a collection of truncated spheres or troughs with a number density n per unit area on a heat exchange surface of area S, is then given by the thermal disturbance integrated with area and then divided by the total heat flow to the plane, κS (Sides and Tobias): $\Delta\mathcal{R} = \pi a^3 A_i/\kappa S$ where κ is the thermal conductivity and A_i given by Eqs. (33), (34), (36), and (37). These approximations remain valid as long as the individual temperature disturbance fields of adjacent particles do not significantly overlap.

Acknowledgments

This work was supported by the Belgian Government and was carried out within the framework of the interuniversity networks for fundamental research (Contract IUAP No. 4).

References

Fransaer, J., Degraef, M., and Roos, J. R., 1990, "The Temperature Disturbution Around a Spherical Particle on a Planar Surface," ASME JOURNAL OF HEAT TRANSFER, Vol. 112, pp. 561-566.

Gradshteyn, I. S., and Ryzhik, I. M., 1980, *Tables of Integrals, Series and Products*, 4th ed., Academic Press, Inc., Orlando, FL.

Hobson, E. W., 1931, *The Theory of Spherical and Ellipsoidal Harmonics*, 4th ed., Cambridge University Press, Chelsea, New York.

Miloh, T., 1981, "Wave Slam on a Sphere Penetrating a Free Surface," *J. Eng. Math.*, Vol. 15, pp. 221-240.

Sides, P., and Tobias, C. W., 1980, "Primary Potential and Current Distribution Around a Bubble on an Electrode," *J. Electrochem. Soc.*, Vol. 127, pp. 288-291.

Sneddon, I. N., 1972, *The Use of Integral Transforms*, 4th ed., McGraw-Hill, New York.

Witze, C. P., Schrock, V. E., and Chambré, P. L., 1968, "Flow About a Growing Sphere in Contact With a Plane Surface," *Int. J. Heat Mass Transfer*, Vol. 11, pp. 1637-1652.

APPENDIX

Approximation for $K_p^{0,1}$ (cosh η) for $\eta \rightarrow 0$

Hobson gives the following integral expressions for the conal functions:

$$K_p(\cosh\eta) = \frac{2^{1/2}}{\pi}\cosh p\pi \int_0^\infty \frac{\cos pu}{(\cosh u + \cosh\eta)^{1/2}} du \tag{42a}$$

$$= \frac{2^{1/2}}{\pi}\coth p\pi \int_\eta^\infty \frac{\sin pu}{(\cosh u - \cosh\eta)^{1/2}} du \tag{42b}$$

$$= \frac{2^{1/2}}{\pi}\int_0^\eta \frac{\cos pu}{(\cosh\eta - \cosh u)^{1/2}} du \tag{42c}$$

These expressions are not convenient for numerical evaluation because the kernel of the integral is singular for $u = \eta$ and/or the kernel is highly oscillatory for large values of p. Moreover, the limit of the integrals is also inconvenient for numerical integration. When $\eta \rightarrow 0$ these shortcomings can be circumvented in the following manner[3]:

---

[3] Note that a similar expression can be derived from Eq. (42*b*) in the case where $\eta \rightarrow \infty$.

$$\frac{2^{1/2}}{\pi}\int_0^{\eta}\frac{\cos pu}{(\cosh\eta-\cosh u)^{1/2}}du$$

$$=\frac{2^{1/2}}{\pi}\cos p\eta\int_0^{\eta}\frac{du}{(\cosh\eta-\cosh u)^{1/2}}$$

$$-\frac{2^{1/2}}{\pi}\int_0^{\eta}\frac{\cos p\eta-\cos pu}{(\cosh\eta-\cosh u)^{1/2}}du \quad (43)$$

Using the l'Hôpital rule, it can be shown that the kernel of the second integral of the right-hand side is bounded if $u\rightarrow\eta$, while the first integral on the right-hand side, after some algebraic manipulation, converts to:

$$\frac{2}{\pi}\frac{\cos p\eta}{\cosh\frac{\eta}{2}}K\left(\tanh\frac{\eta}{2}\right) \quad (44)$$

where $K(x)$ is the complete elliptical integral of the first kind. The second integral of the right-hand side was calculated using a 48-point Gaussian quadrature between the consecutive zeros of the denominator.

The expression for the stream function around a nonconductive bowl also requires the associated conal function $K_p^1(\cosh\eta)$. These were derived using the recurrence relation for the Legendre functions:

$$(2\nu+1)(z^2-1)\frac{dP_\nu(z)}{dz}=\nu(\nu+1)[P_{\nu+1}(z)-P_{\nu-1}(z)] \quad (45)$$

yielding the following expression for $K_p^1(\cosh\eta)$:

$$K_p^1(\cosh\eta)=\frac{2^{1/2}(4p^2+1)}{4p\pi\sinh^2\eta}\int_0^{\eta}\frac{\sin pu\sinh u}{(\cosh\eta-\cosh u)^{1/2}}du \quad (46)$$

Using the same method as used for the calculation of $K_p(\cosh\eta)$:

$$K_p^1(\cosh\eta)=\frac{4(p^2+1)\sin p\eta}{2p\pi\sinh\eta\cosh\frac{\pi}{2}}K\left(\tanh\frac{\eta}{2}\right)$$

$$+\frac{2^{1/2}(4p^2+1)}{4p\pi\sinh^2\eta}\int_0^{\eta}\frac{\sin pu\sinh u-\sin p\eta\sinh\eta}{(\cosh\eta-\cosh u)^{1/2}}du \quad (47)$$

where the second integral is again piecewise integrated using a 48-point Gaussian quadrature between consecutive zeros of the integrand.

Thermal Contact Conductance of a Bone-Dry Paper Handsheet/Metal Interface

J. Seyed-Yagoobi
Assistant Professor of Mechanical Engineering.
Mem. ASME

K. H. Ng
Research Assistant.

L. S. Fletcher
Thomas A. Dietz Professor.
Fellow ASME

Department of Mechanical Engineering,
Texas A&M University,
College Station, TX 77843-3123

An apparatus was constructed for determination of the thermal contact conductance for a paper handsheet/metal interface and for measurement of the effective thermal conductivity of handsheet samples. Bone-dry Bleached Southern Mixed Kraft handsheets with a water retention value of 1.832 were used to study the effect of pressure on thermal contact conductance and to measure the effective thermal conductivity of samples at various sheet density levels. A regression model describing the interface thermal contact conductance as a function of pressure and basis weight was derived. The contact conductance increases with increasing pressure or with decreasing basis weight. At a pressure of 2.3 kPa, the value of the interface contact conductance for the bone-dry samples considered ranges from approximately 97 W/m^{2}K for a sheet of 348.7 g/m^2 basis weight to 200 W/m^{2}K for a sheet of 68.0 g/m^2 basis weight. For pressures near 300 kPa, these values increase to 146 and 452 W/m^{2}K, respectively. The effective thermal conductivity of the handsheet samples was derived from measured values of overall joint conductance and interface contact conductance. The results indicate that the thermal conductivity of the bone-dry samples increases with increasing sheet density, ranging from 0.14 W/mK to 0.70 W/mK for sheet densities of 90 kg/m^3 to 500 kg/m^3, respectively, for the samples considered.

Introduction

Papermaking is one of the most energy and capital-intensive industrial processes in the nation and is the leading industry in terms of energy consumption for drying. In 1985, the massive dehydration operation of paper drying consumed over 3.95×10^{14} kJ of energy (Salama et al., 1987). Since the drying process is the major energy-consuming process in paper making, a small improvement in paper drying would result in significant energy savings.

A better understanding of the parameters associated with the paper-drying process would permit more accurate design and control of the drying process. Paper board is generally dried by threading a continuous wet web of pulp through a multicylinder drying section, and the cylinder dryers are internally heated by condensing steam. In a conventional two-tiered drying configuration, the dryers are arranged so that the wet web is in contact with the cylinders for approximately 75 percent of the drying time and is between the cylinders in open draws for approximately 25 percent of the time. Hence, the overall heat transfer rate between the steam and web significantly affects the overall drying rate. The thermal resistance between the cast-iron cylinder surface and the paper web is one of the resistances affecting the overall heat transfer rate.

There have been very few published experimental studies dealing with the thermal contact conductance between the paper web and dryer drum under various operating conditions, as noted in Table 1. In some of these studies, only selected data are provided, limiting the usefulness of the results.

The overall joint conductance, $h_{o,c}$, of a paper handsheet/metal interface can be expressed in terms of the two interface thermal contact conductances and the bulk conductance of the interfacial paper:

$$\frac{1}{h_{o,c}}=\frac{1}{h_{c,u}}+\frac{1}{h_b}+\frac{1}{h_{c,l}} \tag{1}$$

If the surface roughness is approximately the same on both sides of the paper and if the two surfaces in contact have approximately the same asperities, then the two interface thermal contact conductances can be assumed equal. This simplifies Eq. (1) to the following:

$$\frac{1}{h_{o,c}}=\frac{2}{h_i}+\frac{1}{h_b} \tag{2}$$

where h_i represents the interface contact conductance at either the lower or upper surface. Recognizing that the bulk con-

Table 1 Summary of thermal conductivity and contact conductance results

Author	Paper Grade	Moisture Content (wet basis)	Pressure (kPa)	Heated Surface Temp (°C)	Thermal Conductivity (W/mK)	Thermal Contact Conductance (W/m^{2}K)
Han & Ulmanen (1958)	Sulphite Pulp Handsheet	0%-67%	---	---	0.07-0.79^1	794-1362^2
Redfern (1963)	Bleached Sulfate	0%-70%	0.57-2.9	70-100	---	78-1078
Sundberg & Osterberg (1966)	Unbleached Sulfate	5%-23%	---	---	---	400-4500
Lau & Pratte (1969)	Newsprint	0%-70%	---	24-30^3	0.027-0.195	---
Han (1970)	Tissue Paper Board	wet dry wet dry wet dry	--- --- --- --- --- ---	--- --- --- --- --- ---	0.216^4 0.144^4 0.288^4 0.115^4 0.577^4 0.072^4	2271 1987 1420 1136 1136 568
Kirk & Tatlicibasi (1972)	Bleached Sulphite^6	6.7%-7.9%	0	---	0.084-0.117	---
Kerekes (1980)	Newsprint uncalendared calendared	 7.4% 7.4%	 --- ---	 72.5-78 68-73.5	 0.127 0.169	 875 1610
Lee & Hinds (1981)	Bleached Douglas Fir Kraft	0%-55.6%	2.8	105	0-0.57	226-475
Byrd (1982)	Linerboard	40% 65%	13.8 13.8	121-288 121-288	--- ---	191-1565^5 205-1806^5
Burnside & Crotogino (1984)	Newsprint	5.7%-7%	---	53-83	0.102-0.126	540-1760
Present Study (1991)	Bleached	0%	0-300	85	0.12-0.68	90-450

[1] Apparent Thermal Conductivity
[2] Estimated
[3] Sheet Average Temperature
[4] Calculated
[5] Apparent Heat Transfer Coefficient
[6] Front Surfaces Coated with Graphite

Contributed by the Heat Transfer Division for publication in the JOURNAL OF HEAT TRANSFER. Manuscript received by the Heat Transfer Division October 24, 1990, revision received August 20, 1991. Keywords: Conduction, Direct-Contact Heat Transfer, Thermophysical Properties.

ductance can be expressed as a function of effective thermal conductivity and thickness of the paper yields:

$$\frac{1}{h_{o,c}}=\frac{2}{h_i}+\frac{t}{k_{\mathrm{eff}}} \tag{3}$$

Hence, the interface thermal contact conductance of the paper/metal interface and the effective thermal conductivity of the interfacial handsheet can be derived using Eq. (3) when the overall joint conductance is known.

The limited experimental data that have been published for interface thermal contact conductances and the effective thermal conductivity of paper apply only to a small range of contact pressures and temperatures, as noted in Table 1. Additional data for the interface thermal contact conductance between a paper web and dryer surface are needed for a variety of operating conditions in order to accurately predict changes in the drying rate throughout a paper drying section. This paper reports contact conductance values for a paper handsheet/metal interface and effective thermal conductivities of bone-dry handsheets, which have been determined using a specially designed experimental contact conductance apparatus.

Experimental Program

An experimental investigation was conducted to determine both the thermal contact conductance of a bone-dry paper handsheet/metal interface and the effective thermal conductivity of paper handsheets. A similar study is currently under way to include the effect of moisture on the thermal contact conductance and the effective thermal conductivity of moist handsheets. The experimental facilities, method of handsheet preparation, and experimental procedures are discussed below.

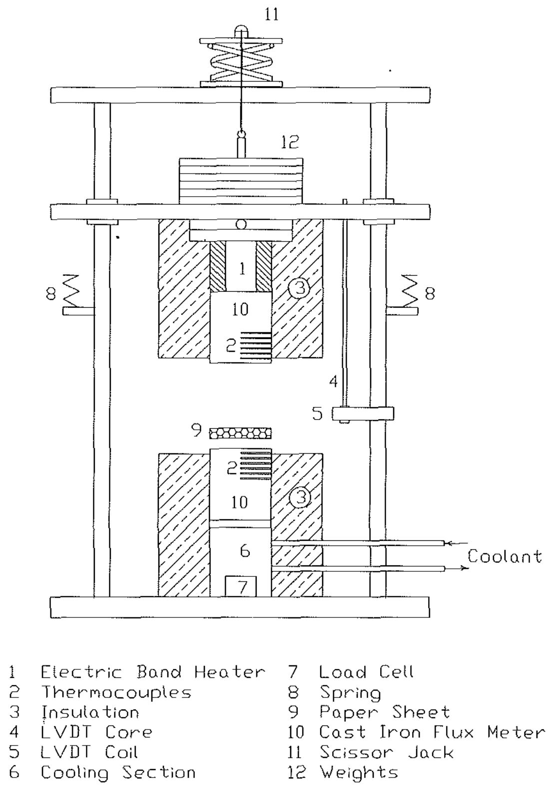

Fig. 1 Schematic of contact conductance measurement apparatus

Apparatus Design and Setup. A schematic of the apparatus is shown in Fig. 1; the apparatus consists of two flux meters, a heat source and heat sink, a temperature measurement system, a loading system, a thickness measurement system, and a mechanism for removing the top half of the assembly.

Each component has been described in detail by Ng et al. (1991). The two heat flux meters, made of cast iron (class No. 40), were designed with lengths sufficient to ensure a uniform, one-dimensional heat flux through the face of the two meters. The surfaces of the flux meters were machined and polished to provide surfaces comparable to a typical cast-iron dryer drum. The temperature distortion in the two heat flux meters resulting from the presence of thermocouples was negligible. The contact pressure was measured with a BLH Model C2M1 compression load cell coupled with a BLH load cell instrument. Maximum applied loads were approximately 1350 N. The thickness of the handsheet was measured throughout the experiments using a linear variable differential transformer (LVDT), Schaevitz Model MHR 500, which had a range from zero to 127 mm and a rated accuracy of 0.25 percent of the calibration range of zero to 12.7 mm.

Preparation of Handsheets. The Technical Association of Pulp & Paper Industries (TAPPI) standard handsheet facility, manufactured by Noram Quality Control and Research Equipment Limited, was used to prepare handsheets in accordance with TAPPI procedure T-205. The handsheets, made of Bleached Southern Mixed Kraft, were placed in a room temperature environment at about 24°C for 10 hours. Samples of 7.62-cm diameter were cut from the 15.24-cm diameter manufactured handsheets in order to be used in the contact conductance apparatus. Immediately prior to commencing the experiments, the handsheets were dried in a microwave for approximately three minutes as a final drying to ensure a bone-dry condition. A bone-dry condition was considered achieved if less than a 1 percent difference in handsheet weight occurred during drying.

Experimental Procedure. Prior to data acquisition, the test section of the contact conductance measurement apparatus was aligned, and the surfaces of the flux meters were cleaned with a soft cloth. Following thermocouple connections, an appropriate power was supplied to the heater in order to obtain a large temperature drop between each thermocouple. The temperature of the constant-temperature bath was kept sufficiently low to remove all the heat. Both the heater and cooling bath were operated for a sufficient length of time prior to handsheet insertion to ensure a steady-state heat transfer through the heat

Nomenclature

A = area, m^2
Bulk = apparent specific volume, cm^3/g
h = heat transfer coefficient, W/m^2K
k = thermal conductivity, W/mK
P = gage contact pressure, Pa
Q = rate of heat flow, W
Q'' = heat flux, W/m^2
R = thermal resistance, K/W
t = thickness of the material, m
ΔT = temperature change, K
W = basis weight; weight of bone-dry handsheet/handsheet area, g/m^2
WRV = water retention value; (weight of retained water)/(weight of dry fibers)

Subscripts

a = air or apparent
b = bulk material
c,u = interface contact at upper surface
c,l = interface contact at lower surface
eff = effective or equilibrium
i = interface or interior
o = overall
o,c = overall joint
s = steam

flux meters. The power to the heater and the temperature setpoint of the cooling water bath were both adjusted during the experiments in order to maintain the desired handsheet temperature. During these experiments, the average handsheet temperature was kept constant at approximately 85°C while the temperature drop across the handsheet averaged around 145°C.

The load cell was zeroed to include the weight of the lower test section and the handsheet. This allowed the load cell to measure only the weight of the upper test section and any weights placed on it, which was the applied load on the handsheet. A combination of the springs and weights was used to vary the applied pressure from 1 kPa to 300 kPa for each test. The experiments were conducted in order of increasing pressure to avoid any precompression of the handsheet fibers.

A data-acquisition program recorded the temperature profiles in the flux meters and calculated the heat flux through each meter. The temperature drop across the handsheet was determined by subtracting the upper interface temperature from the lower interface temperature. The handsheet temperature was taken as the average of the two interface temperatures. The overall joint conductance across the two interfaces and the handsheet was calculated by dividing the average heat flux (in the top and bottom flux meters) by the temperature drop across the sheet.

Experimental data were recorded when steady-state conditions were achieved after approximately one-half hour following each increased loading step. The recorded data included the temperatures of the upper and lower flux meters, handsheet thickness, applied load, overall joint conductance, and uncertainty in overall joint conductance measurements. The uncertainty associated with any single overall joint conductance measurement was a function of the uncertainty in measurements of the temperature profile and thermal conductivity of the cast-iron flux meters and ranged from 4.78 to 4.93 percent for the samples considered.

Results and Discussion

Experiments were conducted to determine the thermal contact conductance and effective thermal conductivity of bone-dry paper handsheets. The handsheets used in this investigation were Bleached Southern Mixed Kraft, composed of 70 percent softwood and 30 percent hardwood, with a water retention value of 1.832 and a Canadian standard freeness of 7.35 millimeters. (Freeness indicates the rate at which water drains from a stock suspension through a wire mesh screen or a perforated plate.) Handsheets with basis weights of 68.0, 85.5, 120.6, 162.3, 236.8, 254.4, and 348.7 g/m^2 were used for data analysis.

The overall joint conductance, representing the sum of the conductances of the handsheet and the upper and lower handsheet/metal interfaces, was measured between the lower and upper flux meters. The overall joint conductance is plotted as a function of the applied pressure for different basis weights in Fig. 2. The thicknesses of the handsheet samples, measured using the LVDT, are shown as a function of applied load in Fig. 3. The samples had thicknesses that varied from 0.123 mm to 2.83 mm, and the data indicated a logarithmic dependence of handsheet thickness on applied pressure. At a given pressure when steady state was reached, the handsheet thickness under compression changed by less than 4 percent, indicating negligible creeping effect with these bone-dry handsheets.

The overall joint conductance increases with increased pressure or decreased basis weight. A logarithmic relation exists between the overall joint conductance and the applied pressure while the conductance changes almost linearly with respect to the basis weight of the handsheet. Handsheet thickness also affects the overall joint conductance by changing the thermal resistance of the sheet. Therefore, any expression for the overall joint conductances measured using the contact conductance apparatus must be a function of applied pressure, handsheet thickness, and basis weight.

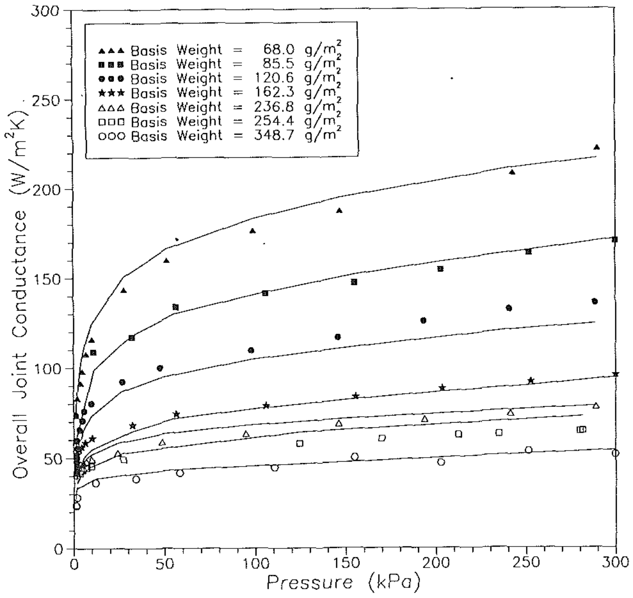

Fig. 2 Effect of basis weight and pressure on overall joint conductance

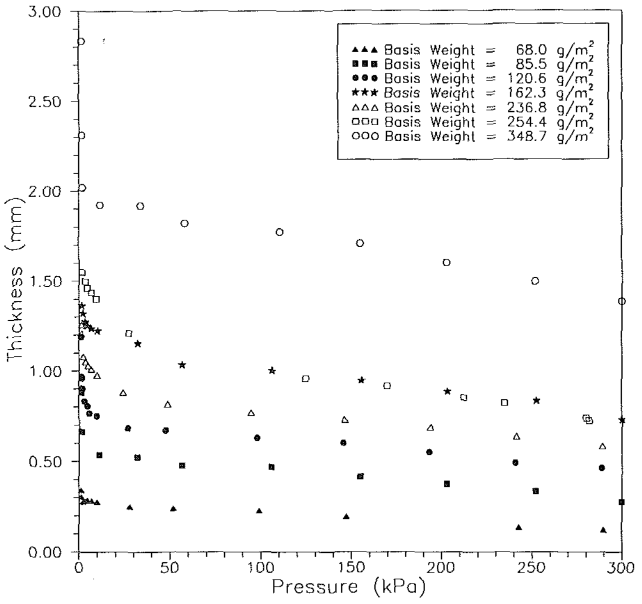

Fig. 3 Effect of basis weight and pressure on handsheet thickness

A well-known statistical computer package, Statistical Analysis System (SAS) (Ray, 1988), was used to determine a regression model for the overall joint conductance. The interface thermal contact conductance and the effective thermal conductivity of the handsheets were then derived from this model. The multiple regression of the overall joint conductance on handsheet thickness, basis weight, and applied load was corrected for multicollinearity among the variables and autocorrelation between the observations. For the samples considered, the best-fit linear model for overall joint conductance is:

$$h_{o,c} = 35.84 + 2912.80/W - 2096136\, t/W + 1756.29 \ln(P)/W - 463807 t * \ln(P)/W \qquad (4)$$

where $1 \leq P \leq 300$ kPa, $68.0 \leq W \leq 348.7$ g/m^2, and

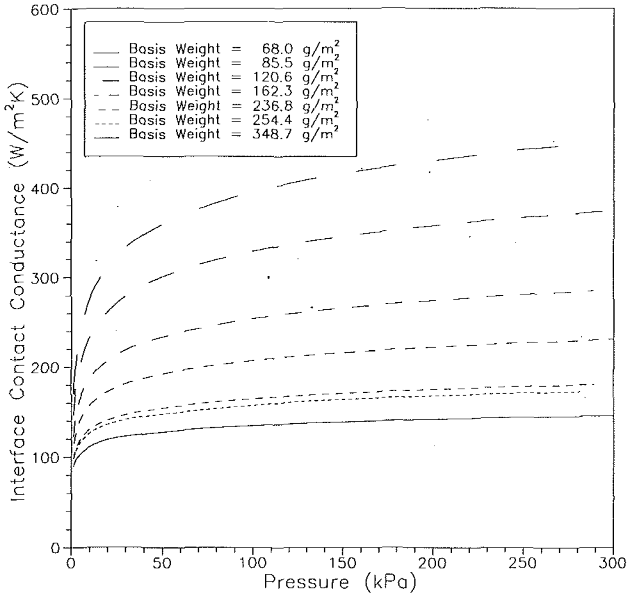

Fig. 4 Interface thermal contact conductance of a paper handsheet/metal interface

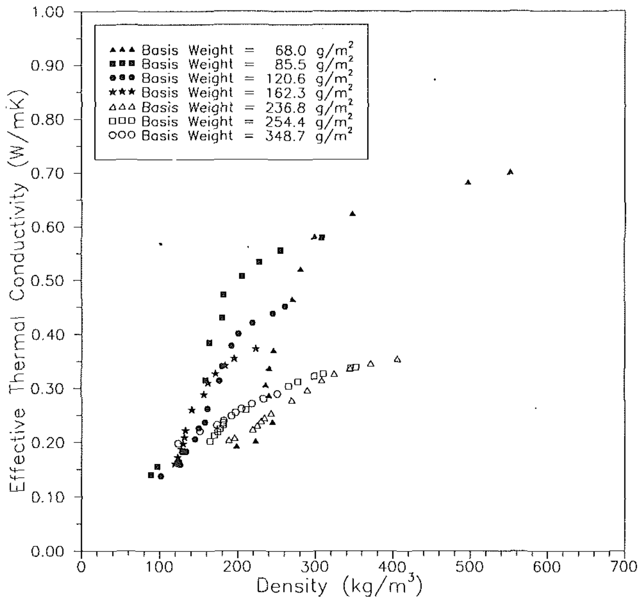

Fig. 5 Effective thermal conductivity for bone-dry Bleached Southern Mixed Kraft handsheets

$0.123 \leq t \leq 2.830$ mm at an average sheet temperature of 85°C. The standard error of the estimate is 3.59 W/m^{2}K, and the adjusted coefficient of determination, $\bar{R}^2$, is 0.9936 for the above regression model.

The interface thermal contact conductance for the paper handsheet/metal interface can be calculated from Eq. (3). At a handsheet thickness of zero, the contact conductance is equal to twice the overall joint conductance. Therefore, using the best-fit expression for $h_{o,c}$, Eq. (4), the interface thermal contact conductance can be expressed as:

$$h_i = 71.68 + 5825.60/W + 3512.58 \ln(P)/W \qquad (5)$$

where $1 \leq P \leq 300$ kPa and $68.0 \leq W \leq 348.7$ g/m^2 at an average sheet temperature of 85°C. Based on Eq. (5), the interface contact conductance is plotted in Fig. 4 for the basis weights and applied pressures used in this study. The contact conductance increases with increasing pressure or decreasing basis weight. As the applied pressure increases, the handsheet/metal contact area increases, resulting in better heat transfer across the interface. In addition, the method of handsheet preparation results in a smoother sheet surface at low basis weights. As a result, sheets of lower basis weight make better contact with the flux meter surface, thereby improving the contact conductance.

At a pressure of 2.3 kPa, the value of the interface contact conductance for the bone-dry samples considered ranges from approximately 97 W/m^{2}K for a sheet of 348.7 g/m^2 basis weight to 200 W/m^{2}K for a sheet of 68.0 g/m^2 basis weight. Paper passed around conventional, 5-ft diameter dryer drums typically has a felt tension of 10 lb/in., which results in an applied load of approximately 2.3 kPa on the web. For pressures near 300 kPa, these values increase to 146 and 452 W/m^{2}K, respectively.

When compared to the previously published contact coefficients listed in Table 1, the predicted values of interface contact conductance are lower. One possible explanation is that the samples used were bone-dry. A completely dry contact zone will offer a considerably greater resistance to heat transfer than one that includes a partial water interface. In addition, the basis weights considered here are greater than the basis weight associated with newsprint or paper manufactured for photocopiers, and the interface contact conductance increases rapidly at low basis weights. Furthermore, the surface roughness of the handsheets may be greater than the asperity of paper webs considered in other studies. The surface roughness of handsheets made for this study was high due to very limited pressing, as indicated by the low handsheet densities. Finally, the low values of interface contact conductance, derived using Eq. (3), could be caused by errors resulting from the assumption that the interface contact conductance is equal at both the top and bottom interfaces. This assumption may not be quite accurate because the temperature of the upper heat flux meter is much greater than the temperature of the bottom flux meter.

The effective thermal conductivity of the handsheets can be determined from Eq. (3) as follows:

$$k_{\text{eff}} = \left(\frac{1}{h_{o,c}} - \frac{2}{h_i} \right)^{-1} t \qquad (6)$$

where $h_{o,c}$ and h_i are given by Eqs. (4) and (5), respectively. The effective thermal conductivity was calculated from Eq. (6) using the values for pressure, thickness, and basis weight. These predicted conductivity values for the handsheets under consideration are plotted as a function of handsheet density in Fig. 5. The sheet density is determined by dividing the basis weight by the sheet thickness.

The predicted handsheet effective thermal conductivity ranges from 0.14 W/mK to 0.70 W/mK for sheet densities of 90 kg/m^3 to 550 kg/m^3, respectively, for all samples considered. Increases in handsheet density were the result of increases in the applied load. The thermal conductivity increases with increasing handsheet density because of the reduction of air within and between the fibers of the handsheet. The low conductivity of air (0.0306 W/mK at 85°C) provides a large resistance to heat flow through the sheet.

The portion of the heat resistance due to heat transfer through the handsheets is indicated by the ratio of bulk resistance to overall joint resistance, $R_b/R_{o,c}$. For the bone-dry handsheets considered in this study, $R_b/R_{o,c}$ ranges from 4 to 30 percent, with a median ratio greater than 20 percent. The ratio decreases with increasing pressure or handsheet density and with decreasing basis weight. The high ratios indicate that the bulk resistance of the handsheet can be significant and may become the controlling resistance for sheets of higher basis weight such as paperboard.

The values of effective thermal conductivity cited in this study are somewhat larger than published values listed in Table

1. However, determination of k_{eff} from Eq. (6) is very sensitive to the predicted value of the interface contact conductance and the handsheet thickness. Further, an uncertainty of 0.032 mm in thickness measurements could contribute to an overestimation of the effective thermal conductivity. Also from Eq. (6), any decreases in the predicted interface contact conductance result in higher estimates for handsheet thermal conductivity. Consequently, errors associated with the prediction of the interface thermal contact conductance appear in thermal conductivity evaluations.

The thermal interface contact conductance and effective thermal conductivity values derived in this study apply to only one set of handsheets. These handsheets were made from a specific pulp and were considered completely bone-dry. The methods discussed, however, can be used to determine the contact conductance and thermal conductivity of a variety of handsheets under varying experimental conditions.

Acknowledgments

This project was sponsored by the Texas Higher Education Coordinating Board Advanced Technology and Energy Research Applications Programs. Sincere appreciation goes to Ms. M. C. Asensio and Ms. Shana O'Pella for their assistance. The pulp was provided by the Simpson Paper Company.

References

Burnside, J. R., and Crotogino, R. H., 1984, "Some Thermal Properties of Newsprint and Their Variations With Bulk," *Journal of Pulp and Paper Science*, Nov., pp. J144–J150.

Byrd, V. L., 1982, "Drying and Heat Transfer Characteristics During Bench-Scale Press Drying of Linerboard," *Drying 1982*, A. S. Mujumdar, ed., McGraw-Hill, New York.

Han, S. T., 1970, "Drying of Paper," *TAPPI*, Vol. 53, No. 6, pp. 1034–1046.

Han, S. T., and Ulmanen, T., 1958, "Heat Transfer in Hot-Surface Drying of Paper," *TAPPI*, Vol. 41, No. 4, pp. 185–189.

Kerekes, R. J., 1980, "A Simple Method for Determining the Thermal Conductivity and Contact Resistance of Paper," *TAPPI*, Vol. 63, No. 9, pp. 137–140.

Kirk, L. A., and Tatlicibasi, C., 1972, "Measurement of Thermal Conductivity of Paper by a Heat Pulse Method," *TAPPI*, Vol. 55, No. 12, pp. 1697–1972.

Lau, Y. L., and Pratte, B. D., 1969, "Measurements of Thermal Conductivity of Wet Paper," NRC, Division Mechanical Engineering Report No. LTR-HY-8.

Lee, P. F., and Hinds, J. A,. 1981, "Optimizing Dryer Performance: Modeling Heat and Mass Transfer Within a Moist Sheet of Paper or Board," Engineering Conference, TAPPI Press, Atlanta, GA, pp. 117–124.

Ng, K. H., Seyed-Yagoobi, J., Asensio, M. C., and Fletcher, L. S., 1991, "An Apparatus for the Measurement of the Thermal Contact Conductance of a Paper Handsheet/Metal Interface," Report No. ME-CHTL-7063-1, Texas A&M University, College Station, TX, Apr.

Ray, A. A., ed., 1988, *Statistical Analysis System* (*SAS*), Release 5.18, SAS Institute, Inc., Cary, NC.

Redfern, A. P., 1963, "Heat Transfer Characteristics in the Drying of Paper," *Papermaker*, Vol. 45, No. 6, pp. 57–60.

Salama, S. Y., Minsker, B. S., and Olsen, K. G., 1987, "Competitive Position of Natural Gas: Industrial Solids Drying," Energy and Environmental Analysis, Inc., Arlington, VA.

Sundberg, T., and Osterberg, L., 1966, "Thermal Resistance Between Drying Cylinders and Paper," *Svensk Papperstid*, Vol. 24, pp. 854–855.

V. Motevalli
Center for Firesafety Studies,
and
Mechanical Engineering Department,
Worcester Polytechnic Institute,
Worcester, MA 01609

C. H. Marks
Department of Mechanical Engineering,
University of Maryland,
College Park, MD 20742

B. J. McCaffrey[1]
Mechanical Engineering,
University of Maryland,
Baltimore, MD 21228

Cross-Correlation Velocimetry for Measurement of Velocity and Temperature Profiles in Low-Speed, Turbulent, Nonisothermal Flows

A technique utilizing thermocouple pairs as sensors to measure velocity and temperature profiles in low-speed, turbulent, nonisothermal flows is described here. In this technique, Cross-Correlation Velocimetry (CCV), the temperature-time records from a pair of thermocouples, one downstream of the other, are cross-correlated to determine the flow's preferred mean velocity while temperature is measured directly. The velocity measurements have undergone extensive verification using hot-wire, pitot tube, and Laser-Doppler Velocimetry to determine the degree of confidence in this technique. This work demonstrates that the CCV technique is quite reliable and can measure the mean preferred component of the convective velocity with better than ±5 percent certainty. Application of this technique to the measurement of velocities in a ceiling jet induced by a fire plume is briefly presented here.

Introduction

This paper describes a technique that can be used to obtain mean velocity and temperature measurements, nearly simultaneously, in low-speed, turbulent, nonisothermal flows that have a preferred velocity component. The motivation for this work was the study of the transient characteristics of a plume-driven ceiling jet. The ceiling jet forms when a buoyant plume from a fire impinges on the ceiling. For small fires, the ceiling jet has a very low speed (less than 1.0 m/s) and is turbulent with large eddy structures. It also has large temperature gradients and its characteristics are affected by the ceiling being heated. The ceiling jet characteristics are mainly determined using velocity and temperature measurements at several locations within the jet. As demonstrated by Cox (1979), conventional measurement techniques such as hot wires and pitot tubes may not be suitable to measure accurately the velocity of low-speed, nonisothermal, turbulent flows containing large-scale eddies.

Cox (1976, 1977) proposed the use of a cross-correlation technique to measure mean velocity and temperature profiles simultaneously using a single probe. The present work and a previous effort by the authors (Motevalli et al., 1987) verify and provide a quantitative assessment of this measurement method. In this technique, hereafter referred to as Cross-Correlation Velocimetry (CCV), the temperature of fluid particles is used as a tracer and the mean velocity of the fluid particles is obtained from the measured travel time from one sensor to another, the second being located at a known distance downstream of the first. A pair of thermocouples, used as temperature sensors, separated by a distance, d, in the flow direction, produce two temperature-time records. The mean temperature of the fluid can be obtained directly from the thermocouples with excellent accuracy. The flow mean velocity is obtained through the cross-correlation of the two temperature-time records with good accuracy as described later.

In general, it is very cumbersome to perform multipoint measurements using Laser-Doppler Velocimetry (LDV) and hot-wire anemometry. Simultaneous velocity and temperature measurements using lasers have been developed only recently and are very expensive and complicated. Hot-wire measurements in highly nonisothermal flows with large eddies and temperature fluctuations are not very easy to perform and are not reliable due to the effect of variable heat transfer along the wire and rapid temperature compensation needed. Furthermore, other known measurement techniques such as bidirectional or pitot tubes have been determined to be generally ineffective or unreliable for low-speed, turbulent, nonisothermal flows. Furthermore, pitot tubes and bidirectional probes are highly disruptive to the flow.

Other investigators such as Bradbury and Castro (1971) and Gaster and Bradbury (1976) have used a similar concept employing a pulsed-wire technique for velocity measurements in highly turbulent flows. Their approach, although successful, does not produce a true flow temperature measurement. Furthermore, in order to perform the velocity measurement, they heat the fluid using a pulsed wire, thus producing a thermal signature that is detected by the downstream sensor. This tends to disturb the flow locally and certainly disallows a true measurement of the flow temperature.

Mesch and co-workers (Mesch et al., 1971a, 1971b; Fritsche and Mesch, 1973) have also used the concept of cross-correlation between two sensors and applied it to two-phase flow and solid object translation. They have discussed the theoretical and statistical nature of this technique. While their work is useful as additional background literature, it has little direct relation to the CCV technique. In addition, work by Lee et al., (1974) may be related to this topic, again only as background material, as they measured turbulent fluctuating velocity gradients at the wall of a pipe and discussed the fluid structures and eddies in the isothermal flow.

Fundamental Theory of Cross-Correlation Velocimetry

Cross-Correlation Velocimetry is based, in principle, on the "frozen eddy" concept in turbulent flows put forward by Sir

---

[1] Deceased in April 1990; this paper is dedicated in his memory.

Contributed by the Heat Transfer Division for publication in the JOURNAL OF HEAT TRANSFER. Manuscript received by the Heat Transfer Division December 1990; revision received September 1991. Keywords: Enclosure Flows, Measurement Techniques, Turbulence.

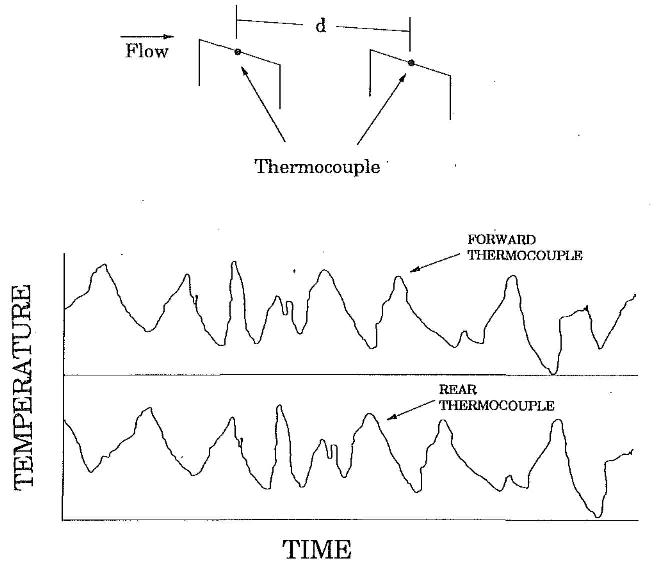

Fig. 1 Graphic illustration of the basis for the Cross-Correlation Velocimetry technique

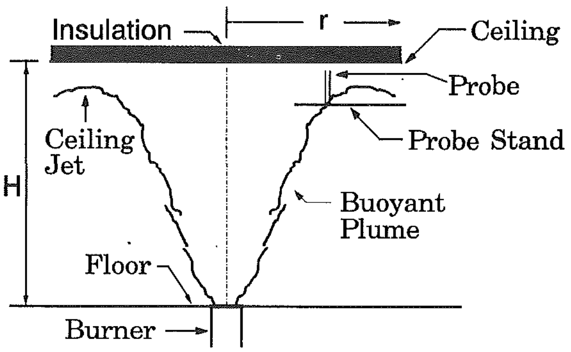

Fig. 2 Schematic of the apparatus simulating a ceiling jet flow

G. I. Taylor (1938). While the use of this concept has been demonstrated in the past through similar techniques, as noted in this paper, the theory is presented here for completeness. Taylor stated that in a turbulent flow there are "eddy structures" that retain their shape and characteristics over a time period and space. He suggested that when the turbulence level is low enough, the evolution in spatial pattern of a fluid structure, especially large-scale, remains effectively "frozen" during this translation (Taylor, 1938). If these eddy structures within a flow can be identified and traced, then the most probable mean velocity of the flow may be estimated as the weighted average of the velocities with which the eddies are moving. This weighing is inherent in the cross-correlation technique since the larger eddies have a more profound effect on the correlation results.

Investigating Taylor's approximation, Favré et al. (1952) and later Comte-Bellot and Corrsin (1971) used two hot-wire probes displaced streamwise by a distance Δx, and recorded the ensuing signals. Their results showed that when delaying the downstream probe record in time by the amount $\Delta t = \Delta x/U$, maximum correlation would be attained.

These investigations showed that for a particular time shift, the mean flow velocity produces a flow displacement exactly equal to the probe spatial separation. These experiments also demonstrated that the corresponding correlation function from these two probes is precisely that measured as auto-correlation by a probe traveling steadily at the mean velocity. It is conceptually the simplest Eulerian correlation function in time.

In nonisothermal turbulent flows with a preferred velocity component, such as ceiling jets, the eddy structure can easily be traced since the fluid particles' temperature acts as a very good marker for the flow. As long as the eddy structure remains relatively unchanged, i.e., approximately "frozen" along the streamwise direction, this concept can be used for velocity measurements based on the Taylor's hypothesis. Therefore, the "frozen eddy" concept is all that is needed to implement the Cross-Correlation Velocimetry technique. The mean ceiling jet flow in this particular case is radially symmetric and the dominant velocity component is the streamwise radial velocity.

It is then clear that for a known separation distance between two sensors, d, there ought to be a time shift, τ, which corresponds to the mean flow velocity, Fig. 1. At that time shift, the maximum correlation between the two signals is obtained. This time shift is the weighted average time needed for the turbulent eddies to travel the distance between the thermocouple pairs. The mean streamwise velocity of the fluid is thus determined by dividing the distance d by time τ. The degree of correlation between a record pair is determined by the correlation function, $R_{X_1X_2}$, which is defined as follows:

$$R_{X_1X_2} = \lim_{t_s\to\infty} \frac{1}{t_s}\int_0^{t_s} X_1(t)X_2(t+\tau)dt \qquad (1)$$

where X_1 and X_2 are the fluctuating components of the data records (i.e., $X = x - \bar{x}$, the mean value subtracted from the original signal) and t_s is the sampling time. Since data are collected over a finite time, the correlation function is normalized to eliminate the effect of amplitude variations of the temperature records. These variations are due to the diffusion of energy taking place while eddies travel between the sensor pairs. The normalized correlation function is called the correlation coefficient, ρ_{X_1,X_2}, and can be written in the following numerical form (Lee, 1960; Motevalli, 1989).

$$\rho_{X_1,X_2} = \frac{R_{X1,X2}}{\left[\frac{1}{N-m}\sum_{n=1}^{N-m} X_1^2(n)\right]^{1/2}\left[\frac{1}{N-m}\sum_{n=m}^{N} X_2^2(n)\right]^{1/2}} \qquad (2)$$

where

$$R_{X_1,X_2}(m) = \frac{1}{N-m}\sum_{n=1}^{N-m} X_1(n)X_2(n+m) \qquad (3)$$

and N is the total number of data points.

Nomenclature

d = separation distance of probe sensors (thermocouples)
H = height of ceiling above burner
l_v = ceiling jet Gaussian momentum thickness
m = number of data points corresponding to a given time shift
n = data point index
N = total number of data points in a record
r = radial distance from the plume impingement point on the ceiling
R = cross-correlation function
Re_{l_v} = ceiling jet Reynolds number
Δt = time shift
t_s = sampling time
ΔT = temperature difference with respect to the ceiling
U = mean velocity
V = ceiling jet velocity
Δx = spatial distance
X_1 = forward thermocouple's record
X_2 = rear thermocouple's record
ρ = cross-correlation coefficient
τ = time shift between thermocouple records corresponding to a maximum correlation

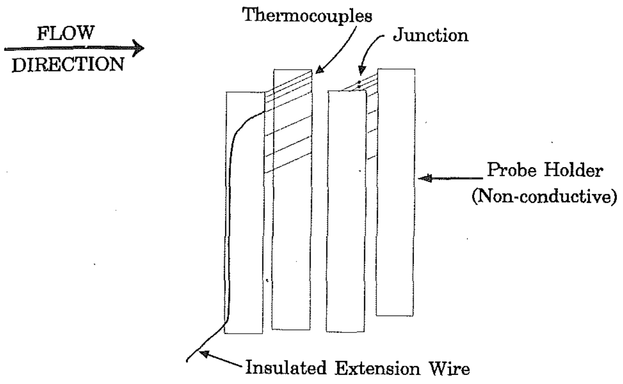

Fig. 3 Schematic of the CCV probe

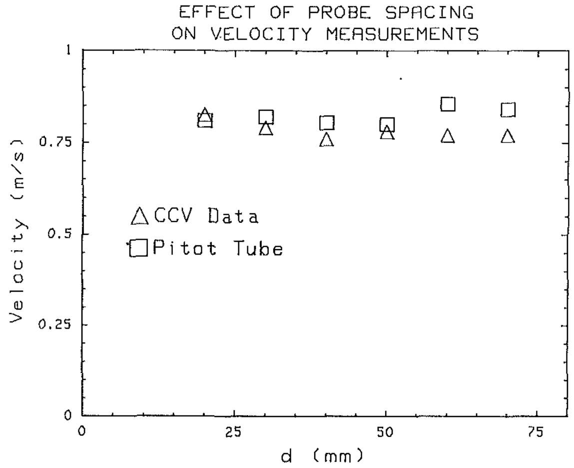

Fig. 4 CCV probe spacing effects on velocity measurement accuracy

The integer number, *m*, corresponds to the time shift translated into number of data points by which one record is shifted with respect to the second for a known sampling rate. The correlation coefficient, ρ_{X_1,X_2}, varies between 0 and 1.0, corresponding to zero and 100 percent correlations, respectively. The procedure outlined in this paper describes how the average time shift over the record length and, consequently, the mean flow velocity (averaged over the sampling time and over the distance between the sensors) are obtained.

Experimental Apparatus and Procedure

The experiment setup is shown in Fig. 2. It consists of a premixed methane-air burner whose outlet is level with an artificial floor, an insulated ceiling, the probe, and a probe stand, which are described in detail by Motevalli (1989).

Probe. The probe consisted of eight pairs of 0.0254-mm-dia, type-E (chromel-constantan) thermocouples stretched between vertical supports as shown in Fig. 3. Using this configuration, nearly simultaneous measurements can be made at eight different locations within the ceiling jet vertically spaced at approximately 3 mm (Motevalli, 1989). Type-E thermocouples have a high sensitivity and the size selected provides a fast response time. The calculated time constant of the thermocouples based on a steady-flow convection coefficient at 0.5 m/s is approximately 0.05 seconds. The time constant, however, is strongly affected by the convection coefficient.

The vertical supports of the probe were separated by 10.16 cm. The thermocouple beads were positioned at midpoint between the holder arms and aligned one behind the other to an accuracy of 0.4 mm. The ceiling jet passed between these arms, which were far enough apart that they did not disturb the flow about the beads. The probe was held in place by a stand that provides three-dimensional positioning of the probe under the ceiling.

Data Collection and Processing. Mean flow temperatures measured by thermocouple sensors in a pair were averaged to obtain a single value. To calculate the velocity, Eq. (2) was used to determine a shift in time domain that maximized ρ_{X_1,X_2}. The golden section method (Press et al., 1986) is used to find this maximum value within the time interval of interest with the least number of coefficients actually calculated. Use of this method reduced the data processing time by a factor of 10 compared to the time required to compute the correlation coefficient for every time-shift increment.

Considerations in Data Analysis. The uncertainty in velocity is mostly due to the uncertainty in τ, since the distance, *d*, can be measured within ±0.5 mm (±2.5 percent uncertainty when $d = 20$ mm and ±1.0 percent for $d = 50$ mm). The uncertainty in τ depends on the sampling frequency and expected velocity. For example, for a velocity of 0.5 m/s and $d = 25$ mm, $\tau = 50$ ms is found with an uncertainty of ±5 percent at a sampling frequency of 400 Hz.

The maximum value of ρ_{X_1,X_2} indirectly affects the uncertainty in the velocity, since as it decreases so does the confidence in the correlation. The correlation coefficient decreases as *d* is increased because the turbulent eddies are not frozen as they move, but instead change their shape and size. This causes the temperature-time records from the thermocouples in a pair to become increasingly dissimilar.

To examine the limits of the sensor separation beyond which the "frozen eddy" concept would not hold, *d* was varied in the CCV probe while measured velocities were compared to those obtained by a pitot tube (pitot tube measurements are discussed in the results section). Figure 4 shows the results of this investigation, where *d* is varied between 20 to 70 mm. The cross-correlation coefficient decreased from 90 to 69 percent with increasing *d* (Motevalli, 1989). The difference between the pitot tube velocity measurement and the CCV technique for the worst case ($d = 60$ mm) was about 10 percent. However, the pitot tube measurements would be more suspect than the CCV measurements since at these low velocities the error in measuring the pressure difference increases.

Because τ is obtained numerically, it cannot be determined with any greater precision than the sampling period (inverse of the sampling frequency) between successive readings from a given thermocouple. The percent error in determining τ, and consequently the error in computing the velocity, decreases for larger values of τ.

Consider a "typical" case with $d = 20$ mm and $V = 0.5$ m/s. The time shift, $\tau = (0.02 \text{ m})/(0.5 \text{ m/s}) = 0.04$ seconds, would result. As an example, in order to make the error in τ less than 5 percent, the sampling period per thermocouple would have to be no more than 5 percent of 0.04 seconds, or 2 milliseconds. This corresponds to a sampling frequency per thermocouple of 500 Hz. Therefore, the combined maximum uncertainty in velocity due to measurement of *d* and determination of τ is approximately 5.6 percent.

Generally, a correlation coefficient of larger than 0.5 is desired to ensure a good correlation. Therefore, the selection of *d* is also controlled by the degree of correlation, i.e., *d* can be increased to any distance only if the correlation coefficient does not fall below a desired value and spatial resolution does not suffer.

The length of data record is another factor in analysis of data. It has to be long enough to include a sufficient number of fluctuations, so that a representative mean velocity can be obtained. However, if the record length is too long, the transient characteristics of the mean flow may be lost since the

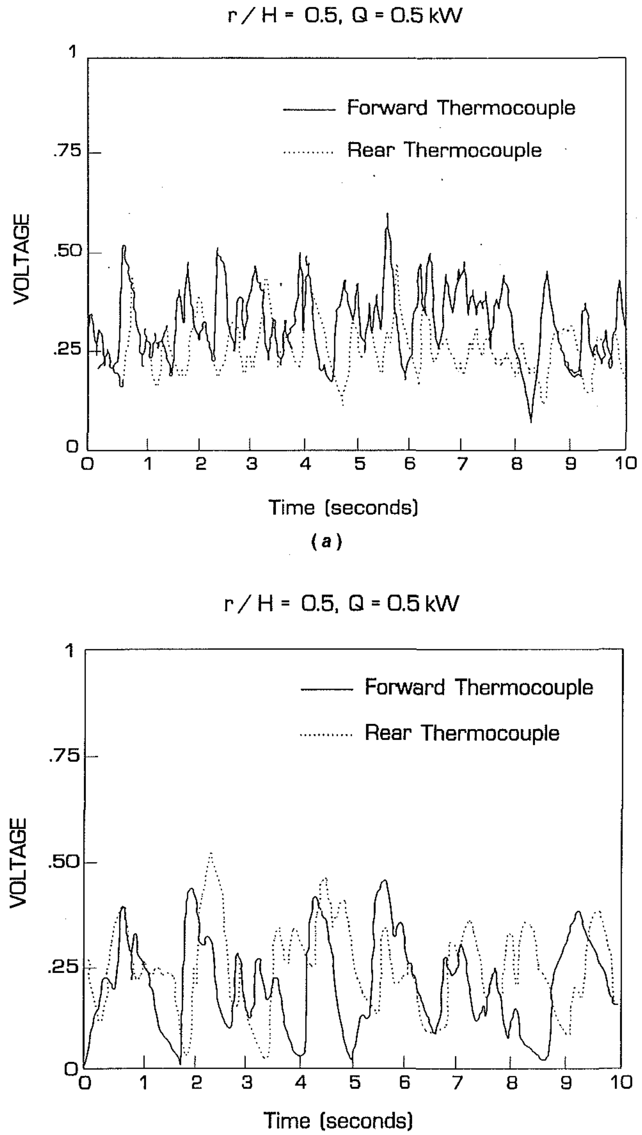

(*a*)

(*b*)

Fig. 5 Thermal fluctuations in the ceiling jet flow and observable correlation: (*a*) 2 mm below the ceiling; (*b*) 60 mm below the ceiling

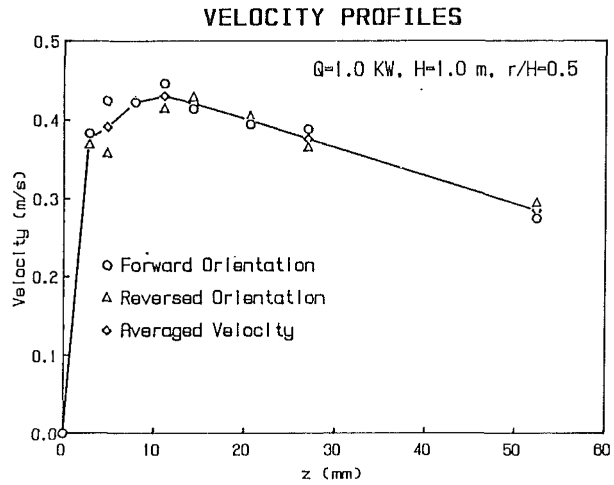

Fig. 6 Effect of thermocouple bead size difference on the CCV measurement

changes in the velocity (in this case due to ceiling heating) may be smoothed out.

Because of the large number of factors to be considered, the selection of the sampling rate, record length, and distance between thermocouples in a pair is a function of the desired results and controllable by the researcher (Motevalli, 1989).

In this work, the separation distance, *d*, between the forward and rear thermocouples was varied from 20 to 50 mm. The distance was selected through a series of experiments (such as those discussed in relation to Fig. 4) performed at the ceiling steady-state conditions and based on the expected velocity and sampling requirements. The cross-correlation coefficient along with the observation of temperature–time plots were used to determine how well the thermal fluctuations were preserved while traveling between the forward and rear thermocouples. In addition, the actual radial location of velocity and temperature measurements and uncertainty in velocity measurements were two major considerations in selecting *d*. The radial location for the measurements is assumed to be at the midpoint between the rear and forward thermocouples. For small radial locations, a larger *d* would represent a mean velocity averaged over a significant portion of the radius.

Furthermore, *d* must be selected such that it is smaller than the characteristic thickness of the ceiling jet, so that the eddies do not distort appreciably during the time they move from the forward to the rear thermocouple. Comparison of *d* with the ceiling jet thickness estimated from Cooper's equations (1987), Alpert's measurements (1971), and Motevalli and Marks (1990) show that this requirement was satisfied for the measurements reported herein. The Gaussian thickness of the ceiling jet, l_v, varied between 0.0375 m at the smallest height and radial location to 0.2 m at the largest radius and height. Hence, the ceiling jet thickness, estimated to be at least twice the Gaussian thickness (Motevalli and Marks, 1990), would be larger than *d*. The Kolmogorov length scale ($l_v \, \mathrm{Re}_{lv}^{-3/4}$) for the flow was estimated to be on the order of 10^{-4} m. The Reynolds number, based on the Gaussian ceiling jet thickness, was between 1500 and 3000. The Kolmogorov scale indicates that the small-scale eddy structures are much smaller than the sensor separation distance. The large-scale eddies are generally on the order of the ceiling jet thickness, which is larger than the *d* selected.

To demonstrate the observable correlation between forward and rear thermocouple signals at different locations within the ceiling jet, the actual temperature–time (represented here as thermocouple voltage-time) records are plotted in Figs. 5(*a*) and 5(*b*). These figures show the temperature–time records at two distances below the ceiling of 2 and 60 mm (d = 50 mm), and for the smallest fire of 0.5 kW (the largest being 2.0 kW). Both figures indicate that there are large-scale turbulent fluctuations in the flow. The correlation between the records seems to be quite good. Higher scatter in velocity measurements observed at larger distances from the ceiling (as discussed later) may be due to a decrease in the thermal fluctuations (i.e., distinct features in the record) and a lower magnitude of thermal fluctuations about the mean. These effects may be observed in Fig. 5(*b*).

Results

Analysis of the Velocity Measurement Technique. The single most important factor that can cause an error in velocity measurements is the difference between bead sizes of thermocouple junctions in a pair. Any such difference affects the time constant of the thermocouples, consequently producing an error in measurements of the true convection time of the flow. Other errors due to sampling rate and signal quality have already been discussed.

To estimate the effect of bead-size difference, two velocity profiles in a ceiling jet under steady-state conditions were ob-

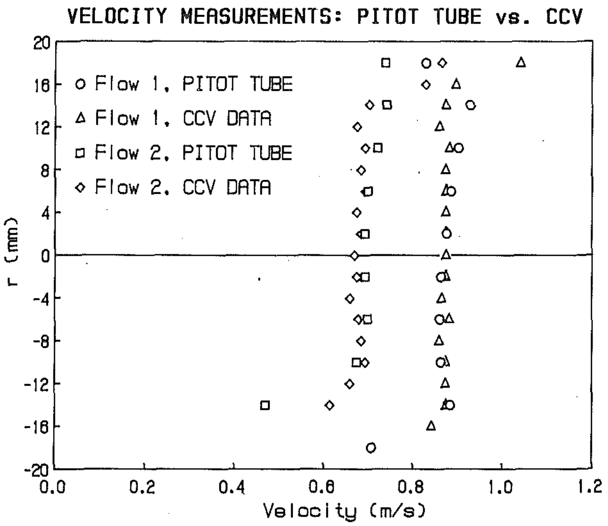

Fig. 7 Comparison of the CCV versus pitot tube measurements for pipe flow at the pipe exit

Table 1 CCV calibration results: individual thermocouple pair velocity measurement versus pitot tube velocity measurement

Pair No.	Flow #1, 62.7 l/min Pitot Tube (m/s)	Flow #1, 62.7 l/min CCV Probe (m/s)	Flow #2, 47.9 l/min Pitot Tube (m/s)	Flow #2, 47.9 l/min CCV Probe (m/s)
1	0.83	0.89	0.67	0.65
2	0.89	0.88	0.70	0.67
3	0.90	0.92	0.69	0.73
4	0.89	0.91	0.73	0.72
5	0.88	0.92	0.72	0.73
6	0.93	0.92	0.72	0.75
7	0.93	0.93	0.76	0.74
8	0.92	0.86	0.75	0.68

Table 2 Calibration of CCV measurements using hot-wire anemometry

CCV Probe Pair No.	Average CCV Velocity (m/s)	Correlation Coefficient	Hot-wire Velocity (m/s)
1	0.40	0.70	before: 0.41 m/s after : 0.43 m/s average: 0.42 m/s
2	0.41	0.72	
3	0.42	0.85	
1	0.75	0.89	before: 0.76 m/s after : 0.74 m/s average: 0.75 m/s
2	0.79	0.97	
3	0.79	0.30	
1	1.08	0.89	before: 1.02 m/s after : 1.06 m/s average: 1.04 m/s
2	1.06	0.80	
3	1.01	0.81	

tained while reversing the thermocouple orientation. This test was carried out using a small fire, approximately 1.0 kW, and measurements were performed at an *r/H* value of 0.5. The results are shown in Fig. 6. Each data point represents a mean velocity value averaged over 3 minutes using twelve 10 second long data records collected every 5 seconds. It is clear that the differences in the measured velocity due to the thermocouple orientation are small. These differences are less than 5 percent, except for one pair with a velocity difference of 9 percent with respect to the average value of the two orientations, which was replaced. Errors due to bead size differences are to some extent controllable. It is possible to either make certain that the selected thermocouple beads are of nearly equal size (by conducting a similar experiment) or to measure the error in the velocity due to the bead-size differences and correct the data.

Calibration of the Velocity Measurements. To verify the CCV, other velocity measurement techniques were employed and a nonisothermal, turbulent flow was simulated using a "flow generator."

The flow generator was constructed from a short horizontal PVC pipe, with a 40.77 mm i.d. Air supplied at the inlet of the pipe was monitored by a calibrated flowmeter. Several fine mesh screens in the pipe were used to straighten the flow. At two pipe diameters upstream of the outlet of the pipe a helical shaped heating coil with a diameter of 4.8 mm, made of nichrome wire, was placed with its central axis aligned approximately with the centerline of the pipe. More screens were place downstream of the heating coil, at the pipe exit, to eliminate any velocity deficit caused by the coil. The heated wire-induced thermal fluctuations needed to trace the flow by the thermocouple sensors.

The velocity at the pipe exit was measured by a 3.175-mm-dia pitot-static tube connected to a capacitance differential pressure sensor with a range as low as 10^{-4} mm Hg. The CCV probe was placed at the pipe exit with *d* set at 30 mm. Two different flow rates, 62.7 liters/min (flow #1) and 47.9 liters/min (flow #2) were selected for the calibration.

The pitot tube and CCV measurements were performed simultaneously for both flow rates. The pitot tube was positioned behind the top thermocouple pair and the pipe was traversed vertically to obtain the velocity profile. The sampling rate was set at 3240 Hz, thus providing a resolution of 1 percent on selecting the correct τ. The results of this experiment showed excellent agreement between the pitot tube and thermocouple measurements, Fig. 7. The measurements for the lower flow rate displayed a higher difference between the CCV and pitot tube data. This may be due to buoyancy effects or limitations of the pitot-tube pressure transducer.

It has been stated that the strength of the thermal fluctuations is an important factor in obtaining good correlation and by extension reliable velocity measurements. Near the edge of the pipe, the amplitude of thermal fluctuations is reduced, resulting in reduced temperature gradients. In Fig. 7, the data points close to the top edge of the pipe seem to indicate the effect of buoyancy, as well as smaller thermal fluctuations, on the velocity measurements. This also indicates that the CCV technique may suffer in the wall shear layer region where the small eddies tend to be much smaller than *d* and also dissipate quickly. This should only affect the velocity measurements, since the temperature measurements in these regions can be made using only one of the thermocouples. The average value from a thermocouple pair may misrepresent the desired point temperature measurement in the wall region.

To examine every thermocouple pair in the probe, individual pairs were aligned with the centerline of the pipe one at a time. Table 1 contains the results of this experiment. The pitot tube measurements and thermocouple values are in agreement to less than 5 percent of the average of the two measurements for all pairs.

Table 3 Calibration of CCV measurements using Laser-Doppler Velocimetry

Average CCV Velocity (m/s)	LDV (m/s)	(%) Diff.
0.207	0.212	2.40
0.228	0.227	-0.44
0.247	0.258	4.26
0.355	0.373	4.83
0.398	0.397	-0.25
0.562	0.567	0.88
0.639	0.619	-3.23
0.671	0.666	-0.75
0.675	0.669	-0.90
0.845	0.865	2.31
0.850	0.862	1.39
0.875	0.898	2.56
1.090	1.130	3.54
1.106	1.141	3.07
1.435	1.498	4.21

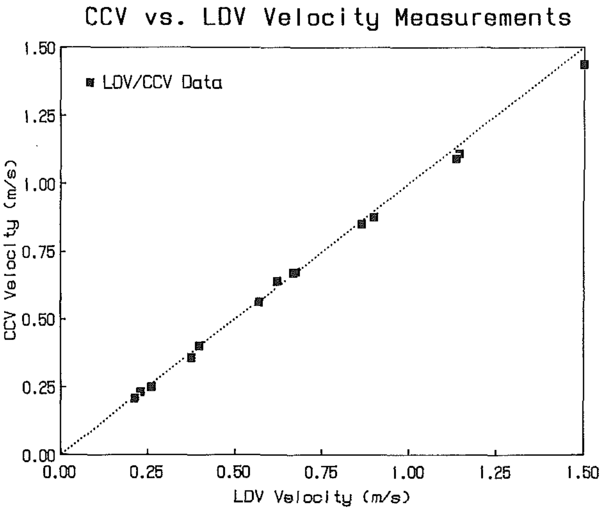

Fig. 8 Calibration results for the CCV technique compared to the LDV measurements

Calibration Using Laser-Doppler Velocimetry (LDV) and Hot-Wire Anemometry

In order further to verify the CCV technique, a separate calibration program was devised (Marrion, 1989). A similar "flow generation" device to that described previously was constructed with a 101.6-mm-dia PVC tube. The air flow was generated using an electric fan. The flow was again passed through a number of screens and air-straighteners prior to it flowing over a heating coil. Using three thermocouple pairs separated by a 19-mm distance, hot-wire velocimetry and LDV measurements were performed. For all measurements, the thermocouple pairs were placed about the central axis of the pipe spaced approximately 3 mm apart vertically and 25 mm from the pipe exit.

Hot-Wire Measurements. Velocity measurements were obtained for a constant cold flow, i.e., before the heating coil was turned on, using a hot-wire probe. For these measurements, the hot-wire probe was placed midway between the thermocouple pairs. The heating coil was then turned on and the measurements were repeated using the CCV probe individual thermocouple pairs. Two to three CCV measurements were performed using 7-10 second long data records and the velocity measurements were averaged between the 2-3 separate measurements. The hot-wire measurements were repeated after the heating coil was turned off and cooled. This test was performed for velocities varying between 0.4 and 1.05 m/s. Results shown in Table 2 indicate that the difference between the two measurements were less than ±5 percent (compared to the average of the velocities measured by the two techniques). These were certainly encouraging yet inconclusive results. Clearly, simultaneous measurements of the velocity using the CCV and a baseline technique were desirable.

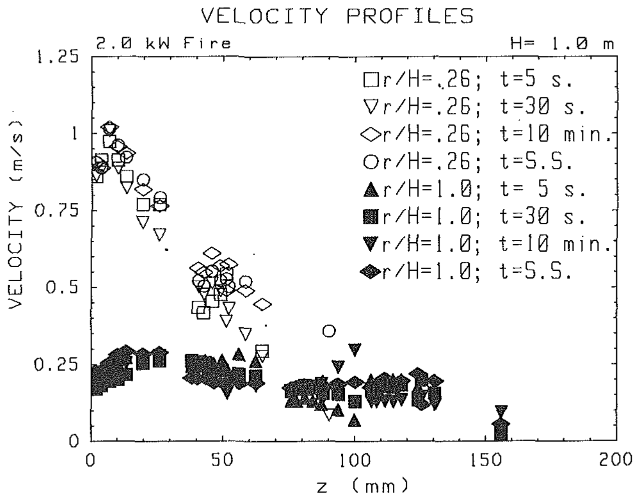

Fig. 9 Velocity profiles in a ceiling jet flow, measurements using the CCV technique

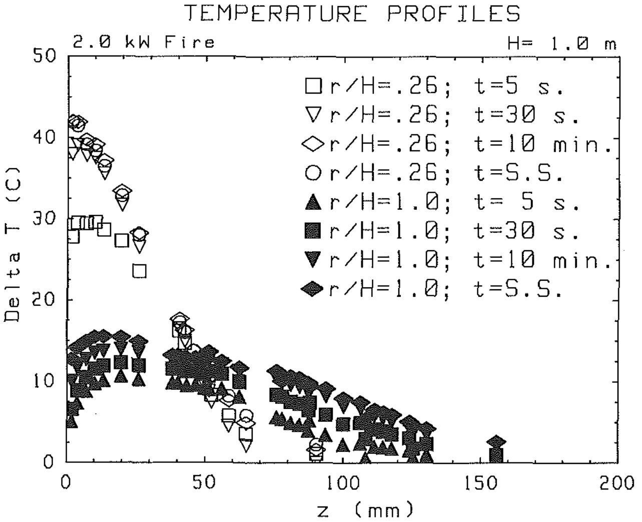

Fig. 10 Temperature profiles in a ceiling jet flow, measurements using the CCV technique

Laser-Doppler Velocimetry Measurements. An LDV system consisting of an argon-ion laser and associated optics was next used as a reliable baseline velocity measurement technique. The flow was seeded using incense sticks and the LDV measurements were obtained at the midpoint between the CCV probe sensors. The thermocouples were sampled at 250 to 1000 Hz for low to high velocities, respectively, over a 7 second period. Each data set for a given velocity represents an average of two to five measurements of the LDV and CCV. The LDV measurements were obtained when 1000 particles crossed the laser control volume over 5 to 20 seconds with the increased sample time occurring at lower velocities.

Table 3 contains the results of this calibration for velocities between 0.2 and 1.4 m/s. These results are also plotted in Fig. 8, where the 45 deg line indicates how closely the CCV and LDV measurements compare. The percent difference between the LDV and CCV measurements is less than ±5 percent for all the measured velocities.

The two separate and independent verification programs using pitot tube, hot-wire anemometry, and LDV measurements ensure that the CCV is quite accurate within less than ±5 percent of the preferred velocity component of a nonisothermal turbulent flow. The two flow generation devices, along with the ceiling jet flow, which contain large-scale eddies, produced different flow regimes and different scales of turbulence covering a reasonable range of low-velocity, low-intensity turbulent flows.

Velocity and Temperature Profiles

Some results from the ceiling jet measurements for a 2.0 kW fire are presented here. The velocity and temperature profiles for times of 5 and 30 seconds (time zero was the start of the fire), 10 minutes, and the ceiling steady-state condition are plotted in Figs. 9 and 10. The data record length was 10 seconds. A number of records were used to generate average profiles at the 10-minute and steady-state condition. The steady-state condition was reached after approximately 35–40 minutes. Data were sampled such that the resolution in selecting τ was better than 5 percent for $d = 5$ cm. The temperature difference, Fig. 10, represents the difference between the absolute temperature of the ceiling jet and the ambient temperature. The data yield well-formed profiles and the scatter seems to be mostly due to combining the data from three runs where the probe vertical position had to be changed three times to obtain the necessary data over a 155 mm vertical span in the ceiling jet.

To demonstrate the transient measurement capability of this technique, Figs. 9 and 10 contain the velocity and temperature profiles at 5 seconds into the run. Each of these profiles is formed from a 10-second-long data record (hence no averaging performed), and it should be noted again that the probe had to be lowered to two new positions to obtain all the data points. Some of the scatter is due to a possible timing difference in initiating the data collection in each of the runs. Yet, remarkably well-formed profiles are obtained. The results have been compared to some limited data obtained by workers who have used other velocity measurement techniques (Motevalli, 1989). These comparisons indicate a reasonable agreement between this work and previous efforts.

Conclusions

The technique presented here is deemed to be quite suitable for low-speed, low turbulent intensity, nonisothermal flow measurements. Among its important advantages are the capability to measure flow velocity and temperature simultaneously and obtain multipoint measurements rather simply. Furthermore, disturbance of the flow by the sensors is almost as low as that by hot wires. In addition, it has been demonstrated that the CCV can be used to measure the flow velocity component in the preferred flow direction reliably while the pitot tube and hot-wire measurements can be suspect due to the effect of other velocity components.

Extensive comparisons of the Cross-Correlation Velocimetry technique with the Laser-Doppler Velocimetry, hot-wire anemometry and pitot-static tube measurements demonstrate that the CCV technique provides accurate velocities that agree with the most reliable baseline technique, namely the LDV, within less than ±5 percent.

The limitations of the CCV technique have been extensively discussed here. The CCV can be used for nonisothermal flows with a preferred velocity component and thermal fluctuations that are distinct enough to provide a higher than 50 percent correlation. In this particular study, thermal fluctuations of at least ±2°C about the flow mean temperature seem to have satisfied the above requirement. This limitation is, however, controllable through instrumentation, and provides high signal-to-noise ratios.

Finally, the CCV offers a relatively simple, inexpensive and accurate multipoint velocity measurement technique with the added capability of simultaneous temperature measurements.

Acknowledgments

The funding for this research, provided by the Center for Fire Research at the National Institute for Standards and Technology under grant No. 70NANB5H0551, is greatly appreciated. The authors would also like to thank Mr. Chris Marrion for conducting the LDV and hot-wire measurements.

References

Alpert, R. L., 1971, "Fire Induced Turbulent Ceiling Jet," Technical Report, Factory Mutual Research Corp., FMRC Serial No. 19722-2.

Bradbury, L. J. S., and Castro, I. P., 1971, "A Pulsed Wire Technique for Velocity Measurements in Highly Turbulent Flows," *J. Fluid Mech.*, Vol. 39, pp. 657–691.

Comte-Bellot, G., and Corrsin, S., 1971, "Simple Eulerian Time Correlation of Full- and Narrow-Band Velocity Signals in Grid-Generated 'Isotropic' Turbulence," *J. Fluid Mech.*, Vol. 48, pp. 273–337.

Cooper, L. Y., 1987, "Ceiling Jet-Driven Wall Flows in Compartment Fires," NBSIR 87-3535.

Cox, G., 1976, "Some Measurements of Fire Turbulence," *Fire and Materials*, Vol. 1, pp. 116–122.

Cox, G., 1977, "Gas Velocity Measurement in Fires by the Cross-Correlation of Random Thermal Fluctuations—A Comparison With Conventional Techniques," *Combustion and Flame*, Vol. 28, pp. 155–163.

Favré, A., Gaviglio, J., and Dumas, R., 1952, *Proc. 8th Int'l. Cong. for Appl. Mech.*, Istanbul, pp. 304–324.

Fritsche, R., and Mesch, F., 1973, "Non-contact Speed Measurement—a Comparison of Optical Systems," *Measurements & Control*, Vol. 6, pp. 293–300.

Gaster, M., and Bradbury, L. J. S., 1976, "The Measurement of the Spectra of Highly Turbulent Flows by a Randomly Triggered Pulsed-Wire Anemometer," *J. Fluid Mech.*, Vol. 77, pp. 499–509.

Lee, Y. W., 1960, *Statistical Theory of Communications*, Wiley, New York.

Lee, M. K., Eckelman, L. D., and Hanratty, T. J., 1974, "Identification of Turbulent Wall Eddies Through the Phase Relation of the Components of the Fluctuating Velocity Gradient," *J. of Fluid Mechanics*, Vol. 66, Part 1, pp. 17–33.

Marrion, C., 1989, "Lag Time Modelling and Effects of Ceiling Jet Velocity on the Placement of Optical Smoke Detectors," Master's Thesis, Worcester Polytechnic Inst., Worcester, MA.

Mesch, F., Daucher, H. H., and Fritsche, R., 1971a, "Correlation Method of Velocity Measurements, Part I—Principles; Application to Two-Phase Flow," *Messtechnik*, Vol. 79, No. 7, pp. 152–157.

Mesch, F., Daucher, H. H., and Fritsche, R., 1971b, "Speed Measurements by Correlation Methods, Part II," *Messtechnik*, Vol. 79, No. 8, pp. 163–168.

Motevalli, V., Marks, C. H., and McCaffrey, B. J., 1987, "Measurement of Velocity and Temperature Profiles in Low-Speed, Turbulent Non-isothermal Flows," ASME Paper No. 87-WA/HT-16.

Motevalli, V., 1989, "A Study of the Characteristics of Small-Scale, Unconfined Fire-Induced Ceiling Jets," Ph.D. Dissertation, University of Maryland, College Park, MD; also appears as a National Inst. for Stds. and Tech. Rpt. NIST-GCR-90-574 (with C. H. Marks, 1990).

Motevalli, V., and Marks, C. H., 1990, "Transient and Steady State Study of Small-Scale, Fire Induced Unconfined Ceiling Jets," *Heat and Mass Transfer in Fires*, J. G. Quintiere and L. Y. Cooper, eds., ASME HTD-Vol. 141, pp. 49–61.

Press, W. H., Flannery, B. P., Tenkolsky, S. A., and Vertterling, W. T., 1986, *Numerical Recipes*, Cambridge University Press, United Kingdom, p. 277.

Taylor, G. I., 1938, "The Spectrum of Turbulence," *Proc. Roy. Soc.*, Vol. A164, pp. 476–490.

Free-Stream Turbulence and Concave Curvature Effects on Heated, Transitional Boundary Layers

J. Kim
Senior Mechanical Engineer,
Calspan Corporation,
Buffalo, NY 14225

T. W. Simon
Professor.

S. G. Russ
Research Assistant.

Department of Mechanical Engineering,
University of Minnesota,
Minneapolis, MN 55455

An experimental investigation of transition in concave-curved boundary layers at two free-stream turbulence levels (0.6 and 8.6 percent) was performed. For the lower free-stream turbulence intensity case, Görtler vortices were observed in both laminar and turbulent flows using liquid crystal visualization and spanwise velocity and temperature traverses. Transition is thought to occur via a vortex breakdown mode. The vortex locations were invariant with time but were nonuniform across the span in both the laminar and turbulent flows. The upwash regions between two vortices were more unstable than were the downwash regions, containing higher levels of u′ and u′v′, and lower skin friction coefficients and shape factors. Turbulent Prandtl numbers, measured using a triple-wire probe, were near unity for all post-transitional profiles, indicating no gross violation of Reynolds analogy. No streamwise vortices were observed in the higher turbulence intensity case. This may be due to the high eddy viscosity, which reduces the turbulent Görtler number to subcritical values, thus eliminating the vortices, or due to an unsteadiness of the vortex structure that could not be observed by the techniques used. Based upon these results, predictions that assume two-dimensional modeling of the flow over a concave wall with high free-stream turbulence levels, as on the pressure surface of a turbine blade, seem to be adequate—there is no time-average, three-dimensional structure to be resolved. High levels of free-stream turbulence superimposed on a free-stream velocity gradient (which occurs within curved channels) cause a cross-stream transport of momentum within the flow outside the boundary layer. The total pressure within this region can rise above the value measured at the inlet to the test section.

Introduction

Due to the sensitivity of transition to many factors (e.g., free-stream acceleration, the level of free-stream turbulence and its characteristics, surface roughness, surface curvature, surface heating, wall suction, compressibility, and unsteadiness), an understanding of transition is far from complete. A study of the effects of streamline curvature and free-stream turbulence intensity on transition, with applications to flows in gas turbines, has been undertaken at the University of Minnesota. The program began with a study of the effects of two levels of free-stream turbulence (0.68 and 2.0 percent) on flat-plate transition (Wang et al., 1985). Streamline convex curvature effects were then studied by Wang and Simon (1987). Kim et al. (1989) revisited free-stream turbulence intensity effects on transition over flat plates using conditional sampling on the intermittency function, including direct measurements of the turbulent Prandtl number. In the present paper, the effects of streamline concave-curvature and free-stream turbulence intensity (0.6 and 8.6 percent) on boundary layer transition and heat transfer are presented. Numerous hydrodynamic studies on the vortex breakdown process have been performed. A few studies have looked at heat and momentum transfer within turbulent boundary layers that were suddenly introduced to concave curvature. However, to the authors' knowledge, no work to date has focused on measuring heat transfer levels in boundary layers undergoing transition on concave surfaces, especially at higher free-stream turbulence intensity levels. This flow is important, as much of the flow over the pressure side of some turbine blades is known to be undergoing transition. The present study was undertaken with this application in mind. A brief review of the literature follows.

Taylor–Görtler vortices that form on the concave wall (first predicted by Görtler, 1940, see Fig. 1) hasten the transition process by producing unstable cross-span and cross-stream inflection point velocity profiles. The formation of these vortices is controlled by the Görtler number, defined as

$$G=\frac{U_{pw}\delta_2}{\nu}\sqrt{\frac{\delta_2}{R}}.$$

Clauser and Clauser (1937) and Liepmann (1943) concluded that concave curvature has a destabilizing effect on the flow, showing transition to occur earlier than on a flat plate. Wortmann (1969), in a flow visualization study, identified three

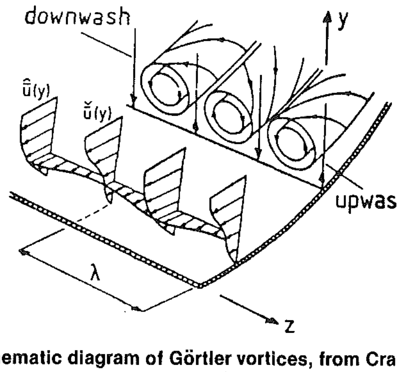

Fig. 1 Schematic diagram of Görtler vortices, from Crane and Sabzvari (1984)

Contributed by the Heat Transfer Division for publication in the JOURNAL OF HEAT TRANSFER. Manuscript received by the Heat Transfer Division October 1990; revision received January 1992. Keywords: Flow Instability, Turbines, Turbulence.

modes of instability where Görtler vortices represented the primary instability. The secondary instability manifested itself as a tilting of the vortex structure, resulting in highly unstable double inflection point velocity profiles. In a third-order instability, the vortex structure oscillated. Bippes (1978) also observed a meandering of the vortex structure prior to breakdown to turbulence. The critical Görtler number (G_c) for onset of the primary instability ranged from 6 to 10, decreasing with increasing free-stream turbulence intensity. Pressure gradients in the direction of the flow had little effect on stability. Swearingen (1985), using smoke visualization and hot-wire rakes, found that the breakdown of vortices occurs via either a horseshoe vortex mode or a sinuous mode. Breakdown to turbulence, which destroyed the coherent structure of the field, occurred shortly downstream. Inflection points in the spanwise direction were more unstable than inflection points in the cross-stream direction. McCormack et al. (1970), who studied the effects of Görtler vortices on heat transfer in a duct, found Nusselt numbers 30 to 190 percent greater on the curved wall than on the corresponding flat plate.

The effects of concave curvature on turbulent boundary layers are well documented. One of the first to study this was Tani (1962), who proposed replacing the molecular diffusivity in the Görtler number with the eddy diffusivity to obtain a turbulent Görtler number. So and Mellor (1975) found a system of longitudinal vortices that were unstable, disintegrating to high turbulence levels downstream. Ramaprian and Shivaprasad (1977) found the outer region of the boundary layer to be very sensitive to wall curvature, reaching a self-preserving form very soon after entry into the curve. Mean profiles agreed with the log-law, the extent of the turbulent core being increased by concave curvature. Shizawa and Honami (1983) found similar results, noting that the Coles profile parameter (Π) decreases to zero and becomes negative. In a later paper, Shizawa and Honami (1985) suggested that the Görtler numbers may be reduced to the stable regime if the eddy viscosity becomes large enough, as the vortex structure within the boundary layer disappears. Barlow and Johnston (1988a, 1988b) found longitudinal vortices that appeared and disappeared randomly in space and time. When vortex generators were placed upstream of the curve, however, the vortex motion stabilized. Bursting was suppressed in the downwash region and enhanced in the upwash region. Although lower velocities near the wall in the upwash suggest decreased local skin friction, increased bursting compensated for the drop, resulting in a relatively constant skin friction coefficient across the span. They felt that a two-dimensional simulation of the flow would be sufficient. Similar conclusions were reached by Simonich and Moffatt (1982) in a heat transfer study in which they found that the Stanton number varied by only 15 percent, even under the most energetic downwash.

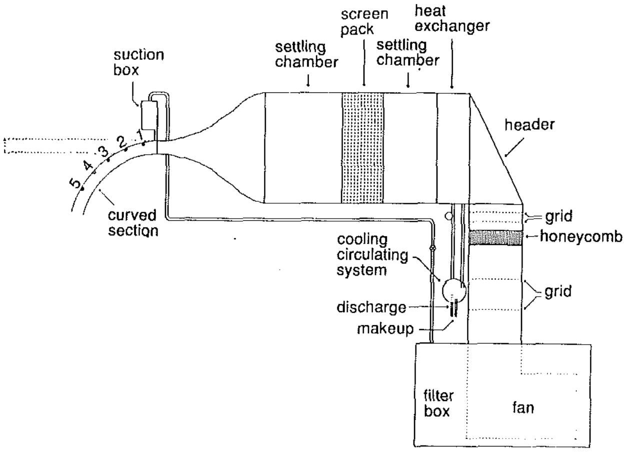

Fig. 2 Schematic of the test facility (plan view)

A description of the test facility and a summary of the results obtained for the low and high free-stream turbulence intensity cases are presented below. Flow parameters and profiles describing the heat and momentum transfer levels at the upwash and downwash locations associated with the vortex pairs are presented.

Test Facility, Measurement Techniques, and Qualification

A schematic of the test facility is shown on Fig. 2. The tunnel was originally designed and built by Wang (1985) and modified as described by Kim et al. (1989). Details of the test facility may be found from Wang (1985). The test channel was rectangular, 68 cm wide, 11.4 cm deep, and 137 cm long. The nominal free-stream turbulence intensity, measured using a cross-wire thermal anemometer probe oriented in two perpendicular directions, was 0.6 percent. Mean velocity was uniform to within 3 percent, and turbulence intensity was uniform to within 6 percent of its value at the beginning of the test section.

Nomenclature

b = bar width
C_f = skin friction
C_p = specific heat
G = Görtler number
Gr = Grashof number
P = production of shear stress
Pr_t = turbulent Prandtl number
$\dot{q}''$ = heat flux per unit time and area
R = wall radius of curvature or resistance, depending on context
r = local radius of curvature
Re = Reynolds number
St = Stanton number
T = temperature, mean value
t = time or instantaneous temperature, depending on context
TI = turbulence intensity
U = mean streamwise velocity
u = instantaneous streamwise velocity
v = instantaneous cross-stream velocity
w = instantaneous cross-span velocity
$\overline{u'v'}$ = turbulent shear stress, time averaged
$\overline{v't'}$ = cross-stream turbulent transport of heat, time averaged
x = streamwise distance
y = cross-stream distance
z = cross-span distance
δ_2 = momentum thickness
λ = wavelength of vortices
ν = kinematic viscosity
Π = Coles wake parameter
ρ = autocorrelation or density, depending on context
τ = shear stress or time delay, depending on context

Subscripts

c = critical or computed value, depending on context
e = eddy value
p = local potential flow value
pw = potential value at wall
t = turbulent
tr = transition
w = wall value or wall, depending on context
x = based on streamwise distance
∞ = free-stream value

Superscripts

$'$ = fluctuating component, instantaneous or rms, depending on context
$+$ = wall coordinates
$\bar{}$ = (overbar) mean value

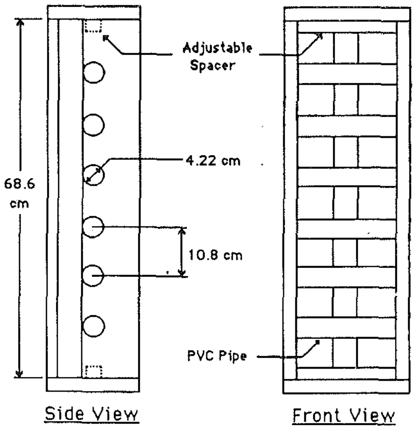

Fig. 3 Jet-grid turbulence generator (from Russ, 1989). Flow is from left to right in the side view.

A free-stream turbulence level of 8.6 percent at the entrance of the test section was achieved with an insert section downstream of the contraction nozzle. This insert, shown on Fig. 3, is a biplane grid of 4.2 cm o.d. polyvinyl chloride (PVC) pipes on 10.8 cm centers. A 96.5-cm-long downstream length before the test section allows turbulence development. The grid is similar to that of O'Brien and vanFossen (1985). A rotating slant wire (Russ, 1989), used to measure all three components of velocity, showed that $u' \sim 1.06v'$ and $u' \sim w'$. The turbulence was, thus, quite isotropic.

The evaluation of uncertainties in hot-wire measurements is very difficult. Even if the uncertainty in the hot-wire calibration is made arbitrarily small, there is always the doubt whether the hot-wire response inferred from a static calibration is applicable over the frequency range of interest. Perry (1982) states that errors as high as 10 percent in the mean square energy distribution of the turbulence are possible, but that the broadband turbulence results are much less affected since the energy-containing components of the turbulent motions are mainly weighted toward the low-frequency end. The reader is referred to Perry (1982) for further discussion of uncertainty in hot-wire measurements. Based upon Perry's discussion and the authors' experience during qualification runs, an uncertainty for the single-wire measurements of 5 percent is assigned as is 10 percent for the cross-correlation measurements ($\overline{u'v'}$ and $\overline{v't'}$). These values are also consistent with the scatter in the measurements as observed by the authors.

Local values of the skin friction coefficient (C_f) were found from the mean velocity profiles measured using a single hot wire. In laminar flows, C_f was determined by fitting the near-wall data to the equation

$$U^+ = y^+$$

where

$$U^+ = \frac{U/U_{pw}}{\sqrt{C_f/2}},\ y^+ = \frac{yU_{pw}\sqrt{C_f/2}}{\nu}.$$

In turbulent flows, the data were also fit to the law of the wall, given by

$$U^+ = 2.44\ln(y^+) + 5.0$$

and the van Driest damping region in the buffer layer (see Kays and Crawford, 1980). Within transition, skin friction values were determined by fitting the near-wall data points in the viscous sublayer to the $U^+ = y^+$ curve.

Table 1 Summary of boundary layer parameters for the lower turbulence intensity case; upwash and downwash are denoted by (u) and (d), respectively; stations 1 and 2 are pre-transitional

Station	x (m)	U_{pw} (m/s)	δ_2 (mm)	Re_x $x10^{-5}$	$Re_{\delta 2}$	C_f $x10^3$	ΔT_w (°C)	Q_w'' (W/m^2)
1	.089	16.53	0.213	.917	219	2.23	---	---
2 (d)	.356	17.24	0.164	3.76	173	4.60	---	---
2 (u)	.356	17.23	0.531	3.757	561	2.10	---	---
3 (d)	.610	17.08	0.996	6.389	1044	4.80	3.95	147.8
3 (u)	.610	17.11	1.124	6.403	1181	4.15	4.23	147.8
4 (d)	.876	17.14	1.167	9.244	1231	5.20	3.88	148.3
4 (u)	.876	17.13	1:820	9.234	1917	4.20	4.20	148.3
5 (d)	1.130	16.76	1.898	11.64	1954	4.70	4.15	146.6
5 (u)	1.130	16.76	2.718	11.65	2801	3.70	4.31	146.6

Qualification of the bendable test wall (while in a flat configuration) was discussed in a previous paper (Kim et al., 1989). In the present experiment, the test wall was bent to a radius of curvature of $R = 97$ cm, and the shape of the outer, flexible wall was adjusted such that the static pressure coefficient (referenced on the upstream static pressure) at the test wall was uniform to within 3 percent. Qualification of the test facility was performed in the low *TI* configuration. Measured free-stream velocity variations within the curve at stations 3 and 4 (see Table 1 for boundary layer parameter values at these stations) were compared with the theoretical velocity distribution given by:

$$Ur = \text{const} = U_{pw}R.$$

Although they agreed quite well, there was a slight discrepancy (the source will be discussed when describing the high free-stream turbulence intensity case in which the discrepancy is more severe). Because of this discrepancy, calculation of boundary layer thicknesses were not precise; distances normal to the wall were therefore normalized on the wall radius of curvature, *R*.

Wall heating destabilizes the flow in two ways. First, heating increases the viscosity near the wall, leading to inflectional velocity profiles (see Schlichting, 1979). Second, the fluid density near the wall decreases, causing heated fluid to move away from the concave wall under the influence of centrifugal forces. The second effect is discussed by Lin et al. (1982) who studied the effect of wall heating on a horizontally oriented concave curved wall. They found that when

$$\frac{\mathrm{Gr}}{\mathrm{G}^2} > 2.99,$$

buoyancy forces dominate centrifugal forces and vortices grow. The Grashof number, Gr, is based on gravitational acceleration. Since the centripetal acceleration in the present test is much larger than the gravitational acceleration (approximately 25 times), the gravitational acceleration in the above Grashof number may be replaced by the centripetal acceleration to determine whether the vortices grow. This yields

$$\frac{\mathrm{Gr}}{\mathrm{G}^2} \cong 5.5 \times 10^{-3}$$

implying that the buoyancy term has little effect on the instability. The main destabilizing effect of heating on the flow is the increase in fluid viscosity near the wall. This is minimized by using the minimal heat flux, dictated by requirements on uncertainty.

Temperature profiles were normalized to wall coordinates, T^+ versus y^+, where

$$T^+ = \frac{T_w - T}{\dot{q}_w''/\rho C_p}\sqrt{\frac{\tau_w}{\rho}},$$

which required local wall heat flux and temperature values. Thermocouples were embedded ~1 mm (40 mil) into the wall behind a lexan/liquid crystal composite, which tended to smooth temporal and spatial variations in wall temperature. Effects of this smoothing were significant only when the vortex spacing was comparable to the composite thickness. The vortex wavelength in the late laminar flow was ~4 mm, giving a vortex wavelength to composite thickness ratio of ~4. Although this was encouragingly large, some smoothing of the temperature and wall heat flux variation was expected. The

Table 2 Summary of boundary layer parameters for the higher turbulence intensity case

Station	x (m)	U_{pw} (m/s)	Re_x $x10^{-5}$	C_f $x10^3$	ΔT_w (°C)	Q_w'' (W/m^2)
1	0.089	17.70	0.965	6.00	3.09	216.9
2	0.356	17.70	3.861	5.90	3.67	213.8
3	0.610	17.70	6.635	5.30	4.11	211.4
4	0.876	17.70	9.543	5.30	4.04	211.8
5	1.13	17.70	12.34	5.00	4.21	210.8

vortex wavelength increased to 10–25 mm after transition; thus, the problem essentially disappeared. Because of these problems, only post-transitional temperature profiles are presented. At these locations, uncertainty values of about 10 percent on T^+ are estimated.

The Stanton number is a nondimensional form of the heat transfer coefficient defined as

$$\mathrm{St} = \frac{\dot{q}_w''}{\rho C_p U_\infty (T_w - T_\infty)}.$$

The wall heat flux was computed by measuring the current through the heater along with the corresponding voltage drop. The power factor was measured to be unity. Corrections were made for back heat loss (through the fiberglass insulation), streamwise conduction, and radiation. The conductivity of the lexan/liquid crystal composite and the emissivity of the liquid crystal surface were measured as described by Kim (1990). Wall temperatures were computed from the thermocouple voltages and the heat flux. Since the thermocouples were located behind the lexan/liquid crystal composite, corrections were made for the temperature drop within the composite.

The uncertainty in Stanton number is 6 percent. This number was calculated using the uncertainty propagation methodology of Kline and McClintock (1953) and a 95 percent confidence level. Sensitivity coefficients for the analysis were evaluated by slightly perturbing the values of the input parameters to the data reduction program one by one and observing their effects on St, as described by Moffat (1980).

The embedded thermocouples at the centerline of the test wall lie directly beneath a downwash for the post-transitional stations. To find the wall temperatures at the upwash, two stick-on foil thermocouples 0.0127 mm (0.5 mils) thick (made by Rdf Corporation), configured to give the temperature difference between the two junctions, were taped onto the wall at the upwash and downwash locations.

Relevant parameters for the present study are shown on Tables 1 and 2.

Results and Discussion

The Low TI Case—TI = 0.6 percent. Shown on Fig. 4 is a schematic of the liquid crystal pattern on the test wall showing transition to turbulence. The spanwise variation in heat flux seen on the liquid crystal surface is believed to be caused by Görtler vortices. Observations of the liquid crystal show that the vortices change spacing at the point of transition. It is felt that the flow undergoes transition through a vortex breakdown process. A streaky pattern remains after transition, however, indicating that the large-scale vorticity persists into the turbulent flow. The unevenness of the streamwise position of the color-sensitive zone from vortex to vortex across the span implies that the vortices transition to turbulence independently of one another. This is consistent with the observations of Swearingen (1985), who used smoke to visualize the vortex breakdown. The transition pattern is quite unlike that observed on the flat wall, in which very little spanwise irregularity was observed. The spanwise temperature variation in the laminar flow was stable in time and space, indicating that the vortices had preferred spanwise locations in the time-averaged flow.

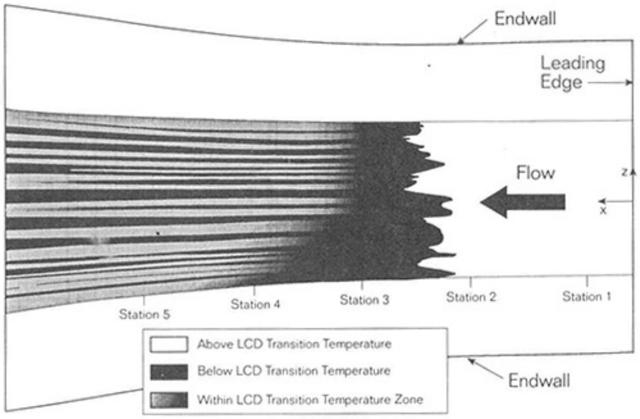

Fig. 4 Schematic of liquid crystal pattern showing the post-transitional vortex pattern on a heated, concave wall. Endwalls are straight; the apparent curvature is due to perspective.

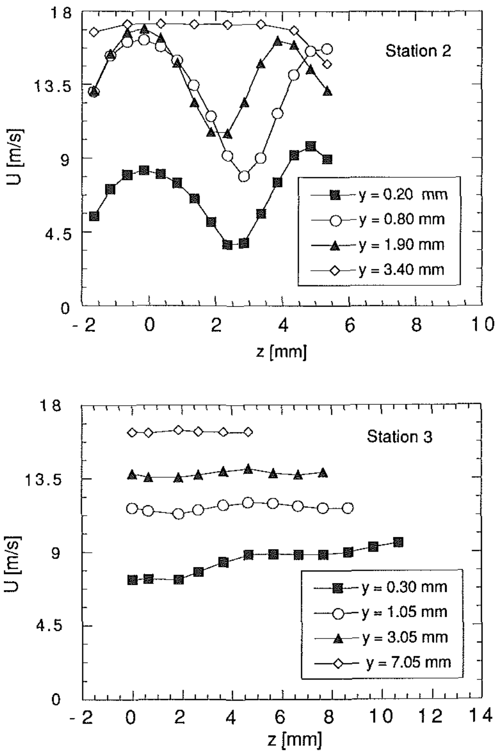

Fig. 5 Spanwise variation in velocity at various normal distances from the wall: (*a*) station 2, (*b*) station 3

If the vortices did move, they did so at a higher frequency than the liquid crystal (~1 Hz) response frequency and with an amplitude that was small relative to the vortex wavelength. There also are spanwise variations in temperature downstream of transition (stations 3 to 5), implying that some vortex structure may exist in the turbulent flow. Simonich and Moffatt (1982) found no stable three-dimensional vortex structure on the concave wall when a fully turbulent boundary layer was introduced to concave curvature. Barlow and Johnston (1988a, 1988b), in a similar study, found that vortices appeared and disappeared randomly across the span. When vortex generators were used upstream of the curve, the Görtler pattern became stationary. It appears that in the present study, the stable vortex structure is established "naturally" using the laminar flow structure to provide preferred spanwise locations for downstream evolution of the vortices. Figure 4 shows that the vortex wavelength is somewhat irregular in the turbulent flow from

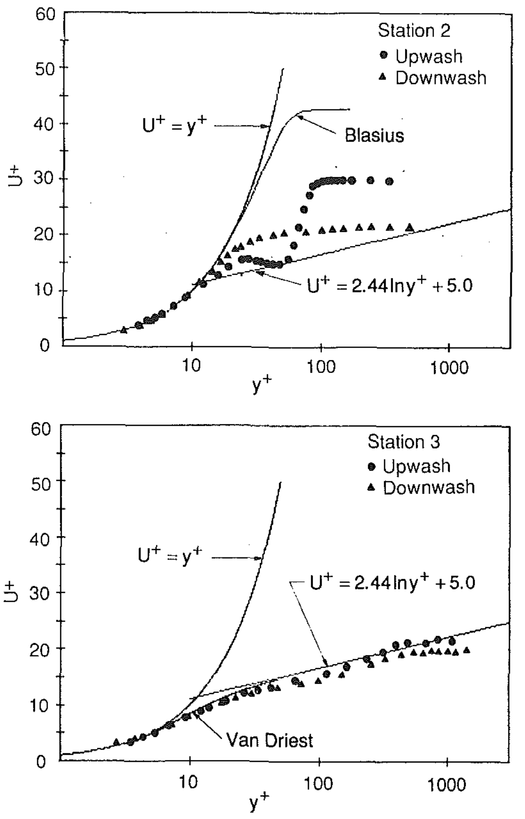

Fig. 6 Velocity profiles at the upwash and downwash normalized on wall coordinates: (*a*) station 2, (*b*) station 3

vortex pair to vortex pair across the span. Similar observations showed similar behavior in the laminar flow. The parameter controlling this spacing may have been the geometry of the last screen upstream of the nozzle, as observed by other researchers (e.g., Swearingen, 1985; Bippes, 1978).

Mean and Fluctuating Velocity. Results of various spanwise traverses of the hot wire at constant y distances from the wall for stations 2 and 3 (pre-transition and post-transition stations, respectively) are shown on Fig. 5. The spanwise variation of the mean velocity (shown) and fluctuating velocity (not shown) in the laminar flow (station 2) is especially pronounced, with a peak in velocity corresponding to a dip in fluctuating velocity, and vice versa, illustrating the unstable nature of the velocity profile in the upwash location. It is further seen that the vortex spacing from row to row in the late laminar flow (station 2) is quite irregular, as observed in the liquid crystal visualization, and that the upwash and downwash do not align, indicating a tilted vortex structure in the time-averaged flow. Also, close inspection of the fluctuating velocity revealed a double peak in u' within the vortex, consistent with the observations of Swearingen (1985). The differences in the spanwise profiles between the upwash and downwash positions (Fig. 5) become much less pronounced after transition (station 3), possibly due to increased mixing in the boundary layer. Movement of the vortices from side to side may also have contributed to the reduction in differences between the upwash and downwash profiles. The vortex wavelength at station 3 became much larger than that at station 2, and no double peak in u', as seen in the laminar flow, appeared.

Table 3 Görtler numbers computed at each station using the appropriate viscosity (molecular or eddy)

Station	G	G_t
2 (upwash)	13.1	-----
2 (downwash)	2.23	-----
3 (upwash)	-----	1.29
3 (downwash)	-----	1.52
4 (upwash)	-----	0.59
4 (downwash)	-----	1.53
5 (upwash)	-----	1.35
5 (downwash)	-----	1.81

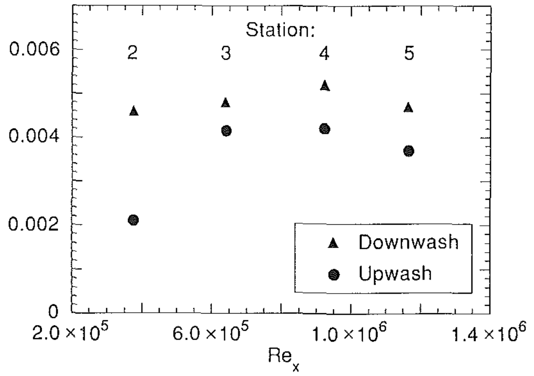

Fig. 7 Skin-friction variation along the wall at upwash and downwash locations

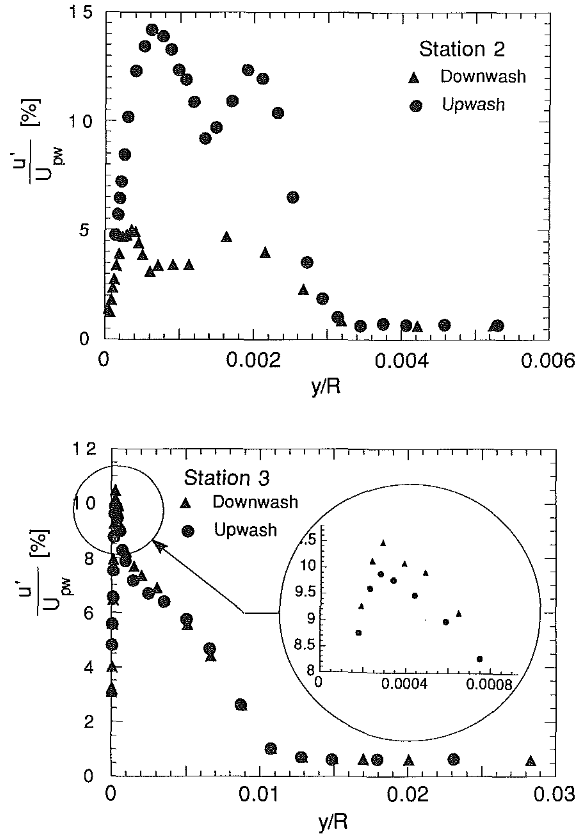

Fig. 8 *Turbulence intensity profiles along the wall at the upwash and downwash locations: (a) station 2, (b) station 3*

The mean velocities normalized on wall coordinates at the upwash and downwash locations near the tunnel centerline are shown on Fig. 6. The upwash profile at station 2 is distinctly inflectional and a dramatic difference between the upwash and downwash profiles is seen. Again, much of this difference disappears after transition. Although it appears that the upwash profiles have a fuller shape than the downwash profiles,

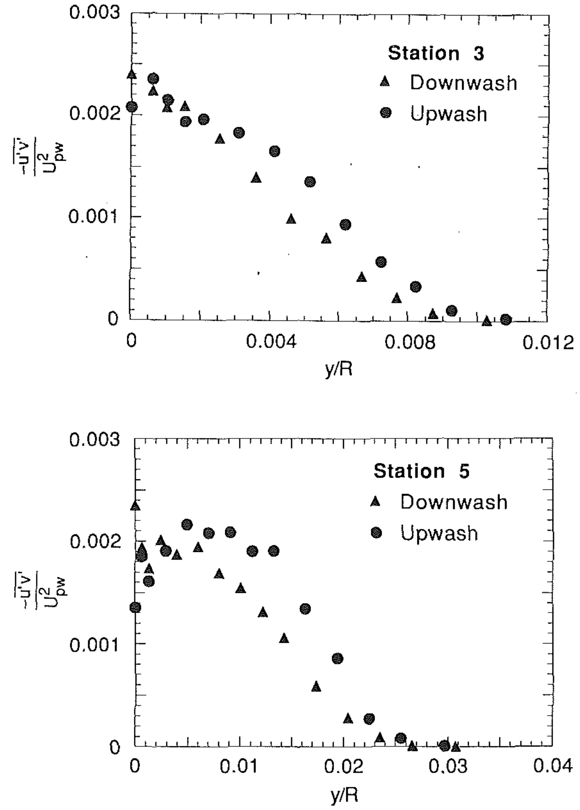

Fig. 9 Shear stress profiles along the wall at the upwash and downwash locations: (*a*) station 3, (*b*) station 5

this is an artifact of the normalization (skin friction values for the upwash are smaller than for the downwash, resulting in higher U^+ values in the upwash).

Plots of skin friction coefficients versus Re_x are shown on Fig. 7. Differences between the upwash and downwash values are larger in the late-laminar region (station 2) and smaller in the turbulent flow (stations 3, 4, and 5), consistent with the trends seen in the streamwise velocity and rms velocity profiles. This led to speculation that in the turbulent flow, the behavior may be better described in terms of a "turbulent" Görtler number (G_t) (the Görtler number with the eddy viscosity replacing the molecular viscosity). Values of G_t based upon measured eddy viscosity values are shown on Table 3. The eddy viscosity value chosen for this computation is the average value across the boundary layer. Values of G_t decrease to ~ 1.3–1.5 immediately after transition. The differences in G_t between the upwash and downwash locations after transition become much smaller than the difference before transition, supporting the observation of smaller differences in u and u' values between the upwash and downwash in post-transitional flow.

Profiles of u' are shown on Fig. 8. The large variations in the late laminar flow (station 2) between profiles taken at the upwash and downwash locations completely disappear after transition (station 3). The near-wall peak in u' is consistently near 11 percent for all the post-transitional profiles, indicating a near-wall, curved-asymptotic situation, i.e., a situation in which the profiles do not change further with axial distance.

Shear Stress Profiles. Profiles of the shear stress $(\overline{u'v'})$ for two post-transitional stations are shown on Fig. 9. The data in the laminar flow are not reliable since the spacing between the wires of the X-wire probe is comparable to the vortex wavelength; when the probe is traversed in the spanwise direction in the boundary layer at that location, the wires were not simultaneously in an upwash or downwash.

The shear stresses at the wall plotted on these figures were computed from skin friction values deduced from mean velocity profiles. Generally good agreement between the wall values and the profile values is seen. Turbulent shear stresses away from the wall in the upwash locations are greater than the shear stresses in the downwash locations in the turbulent flow, a reversal from the wall shear values (C_f in the upwash location is smaller than in the downwash location). A distinction must be made between the near-wall flow and the wake flow, however. The wake flow is more affected by the large vortical motion which convects turbulent fluid toward the upwash.

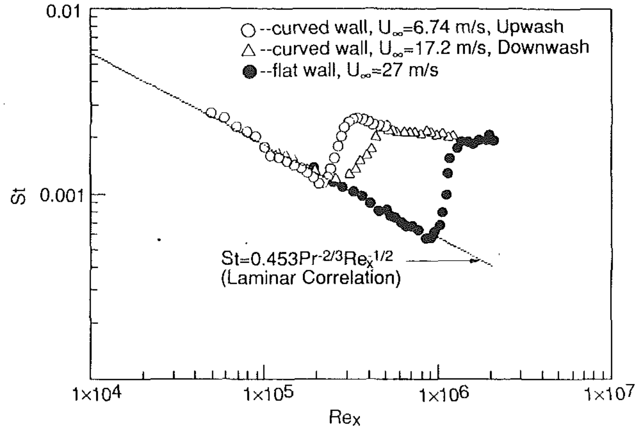

Fig. 10 Stanton number variation on the test wall

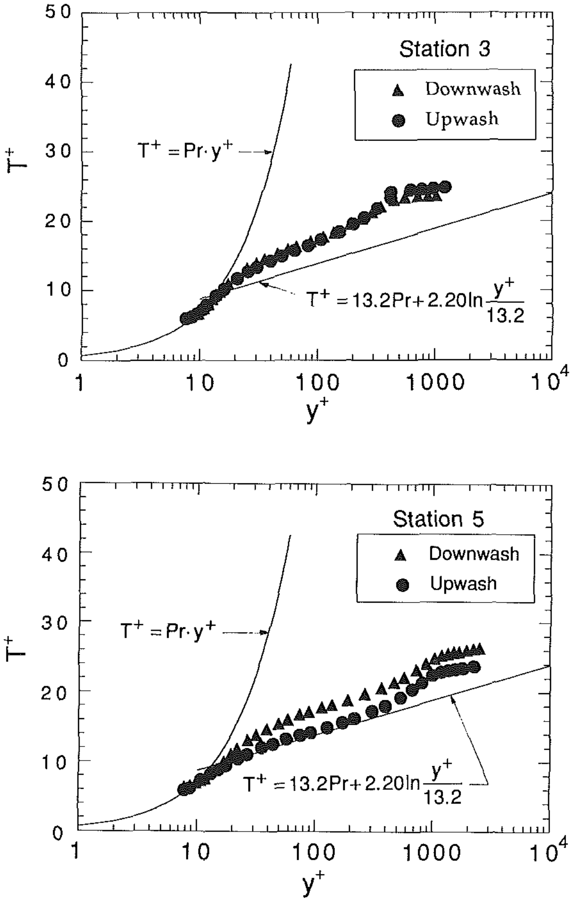

Fig. 11 Mean temperature profiles along the wall at the upwash and downwash locations: (*a*) station 3, (*b*) station 5

Stanton Number. The Stanton number variation along the

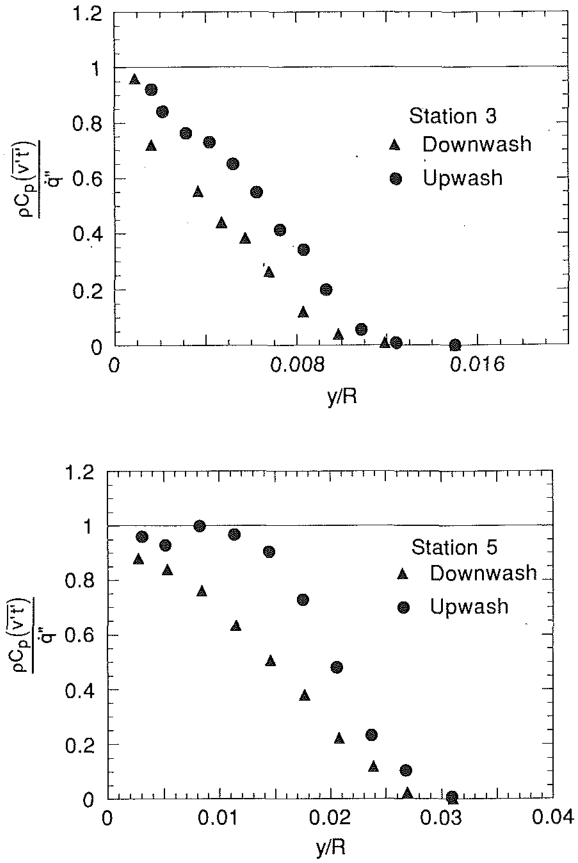

Fig. 12 Cross-stream heat flux profiles along the wall at the upwash and downwash locations: (*a*) station 3, (*b*) station 5

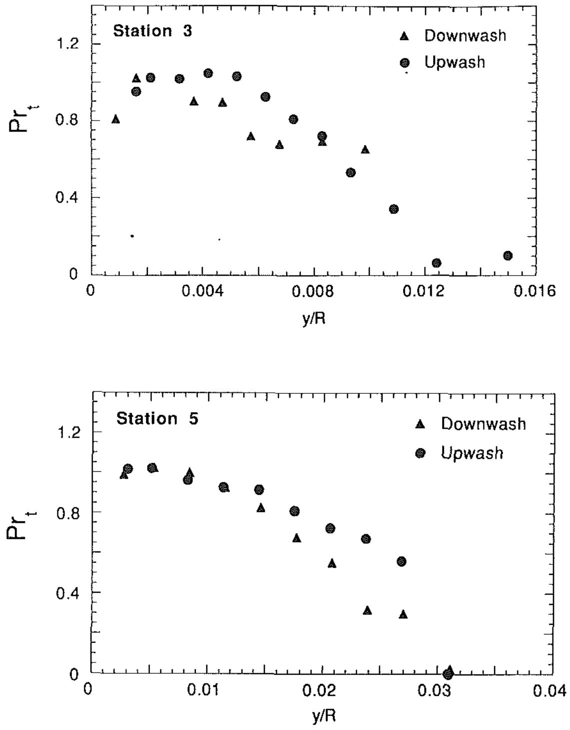

Fig. 13 Turbulent Prandtl number profiles along the wall at the upwash and downwash locations: (*a*) station 3, (*b*) station 5

concave wall is plotted on Fig. 10 along with [the corresponding] flat-plate results taken with nominally the same free-stream turbulence level (Kim et al., 1989). Concave curvature is highly destabilizing, causing transition to occur earlier than on the flat plate. The transition start, path, and length vary depending on whether the centerline thermocouples are beneath a downwash or an upwash, however. Measurements at different locations relative to the vortices were made by changing the free-stream velocity to change the boundary layer thickness and thus the vortex wavelength, enabling the embedded thermocouples along the centerline, used to gather the Stanton number data, to lie under an upwash for the 6.74 m/s case or under a downwash for the 17.2 m/s case. Transition occurs over a shorter length under an upwash than under a downwash. Stanton number values for the upwash locations in the laminar flow lie slightly below the laminar correlation while the downwash values lie slightly above the correlation. Both are influenced by slight wall heating and unheated starting length effects.

Mean and Fluctuating Temperature Profiles. Mean temperature profiles normalized on wall coordinates are shown on Fig. 11. The striking feature of these profiles is their deviation from the thermal law-of-the-wall. While investigating a single pair of vortices with the common flow toward the wall in a turbulent boundary layer, Pauley and Eaton (1988) found increases in T^+ in general, but decreases in the upwash region. The increase in T^+ values in both the present case and in the Pauley and Eaton study may be due to enhanced mixing of the heated boundary layer flow with the free stream, resulting in an overall lowering of the temperature in the boundary layer. The present results and those of Pauley and Eaton (1988) indicate that the thermal law-of-the-wall is not valid in boundary layers that have strong, streamwise vortices embedded within them.

Turbulent Heat Flux and Turbulent Prandtl Number. Profiles of cross-stream heat flux normalized on the wall heat flux are shown on Fig. 12. The profiles approach unity near the wall, as expected. The cross-stream diffusion of heat is greater in the upwash than in the downwash, similar to the behavior observed in the shear stress profiles. Again, this occurs due to spanwise convection of heat to the upwash locations. Values of $\overline{v't'}$ in the upwash are greater than those in the downwash, even though Stanton numbers under the upwash regions are lower than those under the downwash regions, similar to that seen for turbulent shear stress profiles and wall shear stress values.

Profiles of the turbulent Prandtl number deduced from $\overline{u'v'}$, $\overline{v't'}$, and the gradients in velocity and temperature (see Kim, 1990 for a summary of the measurement technique) are shown on Fig. 13. Near-wall values are near unity, indicating no gross violation of Reynolds analogy. The data in the outer part of the boundary layer are not reliable due to the small values of $\overline{u'v'}$ and $\overline{v't'}$ and the very shallow gradients in velocity and temperature.

The High TI Case—TI = 8.6 percent. This case deals with the effects of concave curvature on transitional low Reynolds number boundary layers under high free-stream turbulence conditions. The free-stream turbulence at the test section entrance, generated using the biplane grid generator described earlier, was 8.6 percent. The power spectral distribution was smooth, with no significant spikes over the range from 10 Hz to 10 kHz. Velocity and turbulence intensity profiles just upstream of the test section entrance showed a mean velocity variation across the span of 3 percent and a variation in turbulence intensity of 6 percent of its nominal value. The free-stream autocorrelation, given by

$$\rho(\tau)=\frac{\overline{u'(t)u'(t+\tau)}}{\overline{u'^2(t)}}$$

measured at the beginning of the test region and the center of

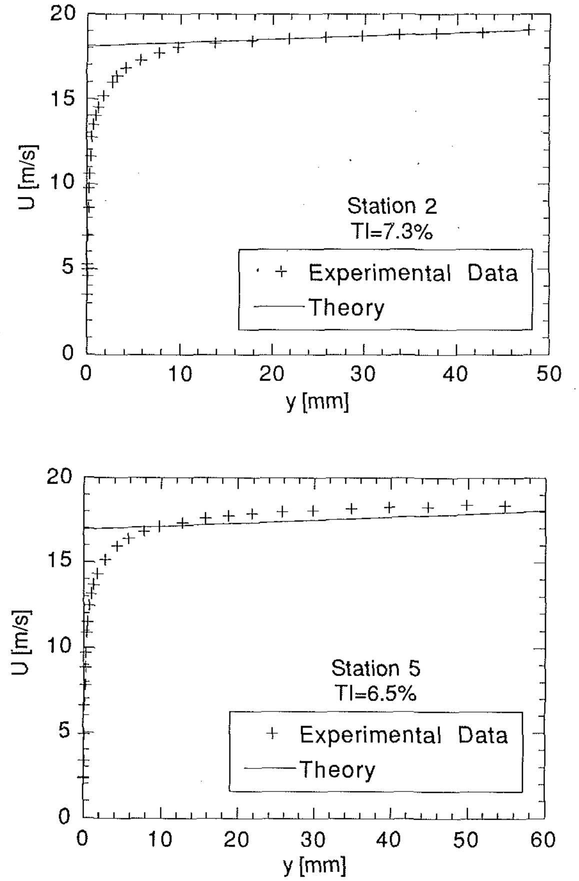

Fig. 14 Mean velocity profiles across the test section at various locations along the test wall: (*a*) station 2, (*b*) station 5; the test section is approximately 115 mm wide

the channel, was used to find two turbulence scales. The area under the autocorrelation curve, called the integral scale (3.3 cm), represents the average size of the turbulent eddies. The Taylor microscale (0.61 cm), which is related to the turbulent dissipation, was determined from the curvature of the autocorrelation curve at the origin ($\tau = 0$). A description of this measurement is given by Kim (1990). Scale measurements were not taken in the low-*TI* case.

Perhaps the most startling find of this case was the cross-stream transport of momentum within that portion of flow that was considered to be a potential core (the flow outside the boundary layer that would be expected to behave according to potential flow theory). Data to be presented indicate that the combination of a high free-stream turbulence intensity superimposed on a free-stream velocity gradient (due to the curve) causes a transport of momentum within the "potential core." As a result, the velocity profile in the core is flatter than predicted by potential theory (specifically, $U(y)r(y) = \text{const}$) due to this transport. Mean velocity profiles, measured across the flow normal to the test wall at each station (Fig. 14) are seen to deviate increasingly from the potential flow distribution with downstream distance. In contrast, similar measurements made for the low free-stream turbulence case (not shown) showed excellent agreement between the measured and theoretical potential velocity profiles. The deviation is seen as early as station 2, where one would expect the boundary layer to be thin. The disagreement of the data with the potential flow theory may be due to a large momentum transport in the "core" flow. This is supported by the shear stress profiles (Fig. 15) where large values of shear stress are seen even at the channel centerline ($Y = 60$ mm). It seems that the high turbulence intensity in the core, when superimposed on a velocity gradient, causes transport of momentum from the flow near the convex wall (higher velocities) toward the flow near the concave wall (lower velocities). The production term in the shear stress budget equation, given by

$$P = \overline{v'^2}\,\frac{\partial U}{\partial y} - (2\overline{u'^2} - \overline{v'^2})\,\frac{U}{r}$$

shows that the production of shear stress can be positive for nonzero free-stream turbulence when streamline curvature is present (note that for this equation, $r < 0$ for concave curvature). The parameters thought to govern this phenomenon are the free-stream mean velocity gradient and turbulence level, and the wall curvature. The channel width is also a parameter. Consider two curved channels, one of which is wider than the other, with the concave wall being the radius of curvature shown on Fig. 2. Assume that the velocity at the concave wall (the wall at radius R) has been set up to give the same potential velocity, i.e., the same U_{pw}, in both cases. Since the flow is irrotational, the potential flow velocity profile must be given by $Ur = \text{const}$. If the inlet turbulence intensity is high, cross-stream transport of momentum occurs, resulting in an averaging (flattening) of the velocity profile. Since the velocity at the convex wall is higher in the wider channel, the average

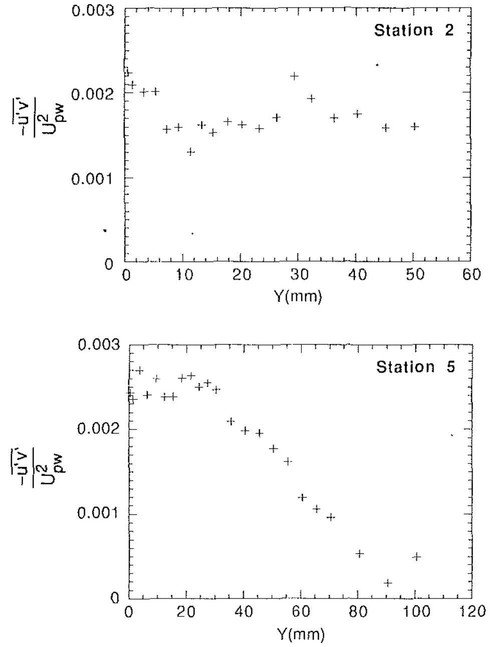

Fig. 15 Shear stress profiles across the test section at various locations along the test wall: (*a*) station 2, (*b*) station 5; the test section is approximately 115 mm wide

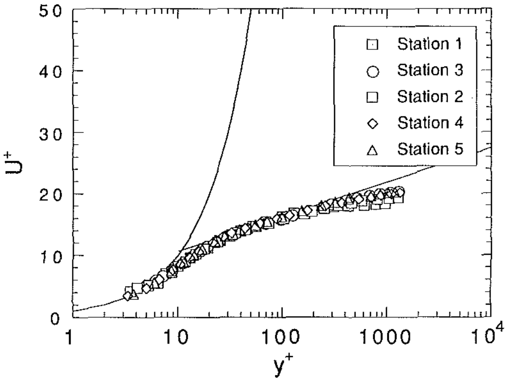

Fig. 16 Mean velocity profiles normalized on wall coordinates along the test wall

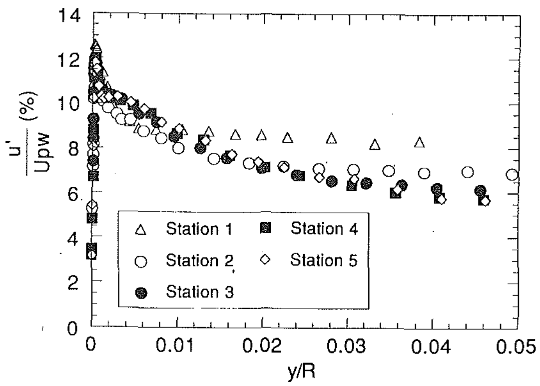

Fig. 17 Turbulence intensity profiles along the test wall

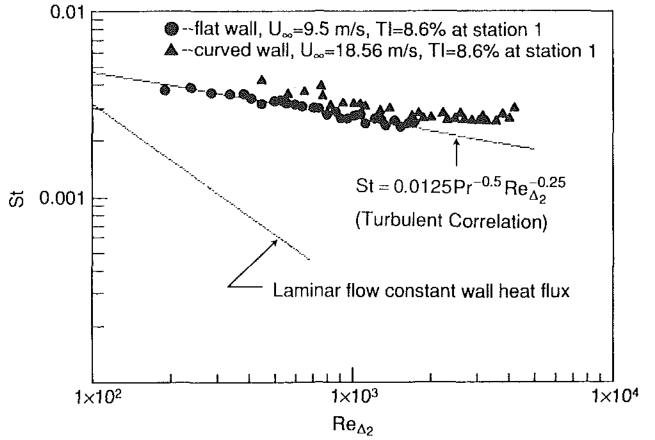

Fig. 18 Stanton numbers on the curved and flat walls at elevated free-stream turbulence intensity

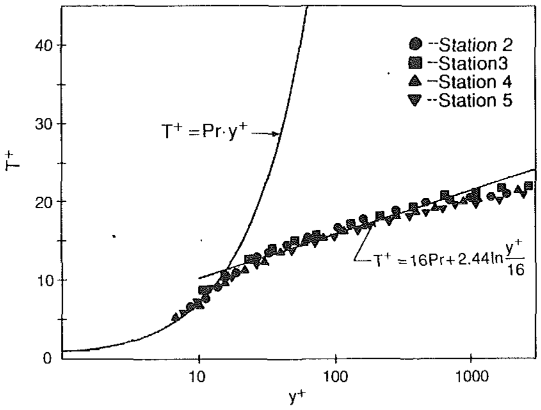

Fig. 19 Mean temperature profiles along the test wall

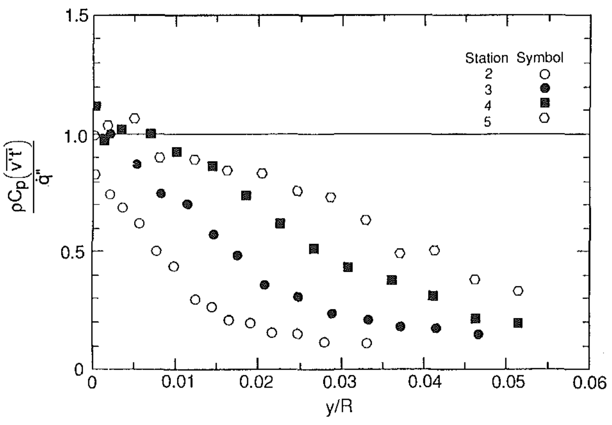

Fig. 20 Cross-stream heat flux profiles along the test wall

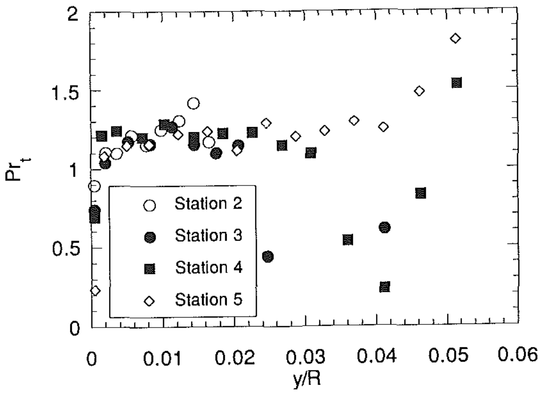

Fig. 21 Turbulent Prandtl number profiles along the test wall

velocity and the velocities near the concave wall will be higher across the wider channel. These higher velocities lead to higher cross-stream transport.

A consequence of this is that the usual normalizing techniques applied to boundary layers are not applicable since neither a potential velocity at the wall nor a boundary layer thickness exists. The quantity selected to normalize velocities was a computed potential velocity at the wall determined by the upstream total pressure, a local static pressure, and the radius of curvature of the wall. Distances from the wall were normalized on the wall curvature, R. Momentum balances were not attempted in this case, due to the cross transport of momentum. Energy balances were successful, however.

No evidence of streamwise vortices was seen. The turbulent Görtler number (G_t) could not be calculated for this case as no momentum thickness could be obtained. The values of the eddy viscosity in this case were, however, from 10 to 100 times the viscosity of the lower turbulence intensity case, suggesting that if G_t could have been calculated, they would have been much lower than the values computed for the lower turbulence intensity case. Thus, G_t is reduced to the stable region on the Görtler map and no vortices are expected. This is consistent with the measurements and the liquid crystal surface temperature visualization. Alternatively, it could have been that vortices exist, but that they appear and disappear randomly in time and space faster than the frequency response of the liquid crystal. Clearly, the near-wall flow appeared to be two-dimensional.

Mean and Fluctuating Velocity. Measurements of the mean velocity normalized on wall coordinates, Fig. 16, show no wakes, and a very short log-linear region. Both concave curvature and high free-stream turbulence reduce the size of the wake. Skin friction (C_f) values deduced from the near-wall velocity profiles show a monotonic decrease with Re_x.

Turbulence intensity profiles, Fig. 17, show near-wall peaks that decay slowly with streamwise distance. Turbulence intensity in the outer part of the flow decays rapidly from station 1 to station 2, essentially stopping its decay beyond station 3. Baines and Peterson (1951) found that the decay of free-stream turbulence behind a grid of square bars is expressed by the equation

$$\frac{u'}{u_\infty} = 1.12\left(\frac{x}{b}\right)^{-5/7}$$

where x is the distance from the grid generator and b is the bar width. The above equation was used with the station 1 data to find an effective bar width of 2.78 cm for the present flow (note that cylinders of 4.45 cm diameter were used instead of square bars in the turbulence generator). The equation was then used to obtain what the turbulence decay rate would have been had the test section been straight. When compared to the curved wall data, it was found that the turbulence decay rate appropriate for a straight channel was significantly greater than in the curved-wall flow.

Stanton Numbers. Stanton numbers, Fig. 18, are compared to the corresponding high turbulence intensity, flat-wall case values (Kim et al., 1989). Concave curvature significantly increases heat transfer from the wall, suggesting increased mixing of the near-wall flow. Vortex activity may be responsible for this increase, although the high eddy viscosity would imply that there are no coherent vortices. Concave curvature is expected to lead to increased instability and more frequent turbulent bursting, but did not lead to coherent cellular structures in this case. Thus, this concave-wall flow appeared two dimensional. An energy balance for this flow showed excellent closure.

Mean and Fluctuating Temperature Profiles. Mean temperature profiles normalized on wall coordinates are shown on Fig. 19. As in the lower turbulence intensity case, measured values of T^+ differ from the thermal law of the wall. The discrepancy is much smaller in the present case, however, illustrating the effect of increased turbulence intensity and two-dimensional behavior.

Fluctuating temperature (t') profiles, measured using the triple-wire probe, approached zero in the isothermal outer portion of the flow. This illustrates a fundamental difference between the momentum and heat transfer processes. The boundary conditions for the two processes are different. Due to this nonsimilarity, the turbulent Prandtl number is expected not to equal unity.

Turbulent Heat Flux and Turbulent Prandtl Numbers. Profiles of the cross-stream transport of heat, Fig. 20, show near unity values near the wall, as expected. In contrast to the shear stress profiles, which remain high across the test section, the turbulent heat flux profiles approach zero in the outer party of the flow. The difference in boundary conditions between the heat and momentum transfer processes is again illustrated.

Turbulent Prandtl numbers deduced from the triple-wire measurements, Fig. 21, are slightly higher than unity. This increase in Pr_t in the outer flow is not surprising given the difference in boundary conditions discussed above.

Conclusions

The main conclusions of this transitional flow study are:

1 Vortices with preferred spanwise locations exist in both the laminar and turbulent boundary layers for the low free-stream turbulence intensity case. No coherent vortices were found for the higher turbulence intensity case.

2 Concave curvature destabilizes the flow, causing transition earlier than on the flat wall. This is a confirmation of earlier findings.

3 No gross violation of Reynolds analogy occurs for the post-transitional profiles in both the low and high turbulence intensity cases, although small deviations from an exact analogy were noted.

4 High levels of free-stream turbulence superimposed on a free-stream velocity gradient were found to cause a cross-stream transport of momentum and a production of turbulent kinetic energy within the "potential core" of the flow.

5 Under high levels of free-stream turbulence, the concave-curved transitional and turbulent boundary layers become two dimensional in the time-mean.

References

Baines, W. D., and Peterson, E. G., 1951, "An Investigation of Flow Through Screens," *Trans. ASME*, Vol. 73, pp. 467–480.

Barlow, R. S., and Johnston, J. P., 1988a, "Structure of a Turbulent Boundary Layer on a Concave Surface," *Journal of Fluid Mechanics*, Vol. 191, pp. 137–176.

Barlow, R. S., and Johnston, J. P., 1988b, "Local Effects of Large-Scale Eddies on Bursting in a Concave Boundary Layer," *Journal of Fluid Mechanics*, Vol. 191, pp. 177–195.

Bippes, H., 1978, "Experimental Study of the Laminar-Turbulent Transition of a Concave Wall in a Parallel Flow," NASA TM-75243.

Clauser, M., and Clauser, F., 1937, "The Effect of Curvature on the Transition From Laminar to Turbulent Boundary Layer," NACA TN-613.

Crane, R. I., and Sabzvari, J., 1984, "Laser-Doppler Measurements of Görtler Vortices in Laminar and Low Reynolds Number Turbulent Boundary Layers," *Laser Anemometry in Fluid Mechanics*, R. J. Adrian et al., eds., Ladoan-Instituto Superior Technico, Lisbon, pp. 19–35.

Görtler, H., 1940, "Uber ein Dreidimensionale Instabilitat Laminarer Grenzschichten an Konkaven Wanden," *Math.-Phys.*, K1.2:1; also NACA TM-1375, 1954.

Kays, W. M., and Crawford, M. E., 1980, *Convective Heat and Mass Transfer*, 2nd ed., McGraw-Hill, New York.

Kim, J., Simon, T. W., and Kestoras, M., 1989, "Fluid Mechanics and Heat Transfer Measurements in Transitional Boundary Layers Conditionally Sampled on Intermittency," *Heat Transfer in Convective Flows*, ASME HTD-Vol. 107, pp. 69–81.

Kim, J., 1990, "Free-Stream Turbulence and Concave Curvature Effects on Heated, Transitional Boundary Layers," Ph.D Thesis, Department of Mechanical Engineering, University of Minnesota, Minneapolis, MN.

Kline, S. J., and McClintock, F., 1953, "Describing Uncertainties in Single-Sample Experiments," *Mechanical Engineering*, Vol. 75, pp. 3–8.

Liepmann, H. W., 1943, "Investigations on Laminar Boundary-Layer Stability and Transition on Curved Surfaces," NACA ACR No. 3H30.

Lin, J. K., Kamotani, Y., and Ostrach, S., 1982, "Effect of Heating on Görtler Instability," Department of Mechanical and Aerospace Engineering, Case Western Reserve University, Report FTAS/TR-82-162.

McCormack, P. D., Welker, H., and Kelleher, M., 1970, "Taylor-Görtler Vortices and Their Effect on Heat Transfer," ASME JOURNAL OF HEAT TRANSFER, Vol. 92, pp. 101–112.

Moffatt, R. J., 1980, "Contributions to the Theory of Uncertainty Analysis for Single-Sample Experiments," in: *Complex Turbulent Flows*, Vol. I, Proceedings of the 1980–1981 AFOSR-HTTM-Stanford Conference on Complex Turbulent Flows, S. J. Kline, B. J. Cantwell, and G. M. Lilley, eds., Thermoscience Division, Mechanical Engineering Dept., Stanford University, CA.

O'Brien, J. E., and vanFossen, G. J., 1985, "The Influence of Jet Grid Turbulence on Heat Transfer From the Stagnation Region of a Cylinder in Crossflow," ASME Paper No. 85-HT-58.

Pauley, W. R., and Eaton, J. K., 1988, "The Fluid Dynamics and Heat Transfer Effects of Streamwise Vortices Embedded in a Turbulent Boundary Layer," Thermosciences Division, Dept. of Mechanical Engineering, Stanford University, Report MD-51.

Perry, A. E., 1982, *Hot-Wire Anemometry*, Clarendon Press, Oxford, United Kingdom.

Ramaprian, B. R., and Shivaprasad, B. G., 1977, "Mean Flow Measurements in Turbulent Boundary Layers Along Mildly Curved Surfaces," *AIAA Journal*, Vol. 15, No. 2, pp. 189–196.

Russ, S. G., 1989, "The Generation and Measurement of Turbulent Flow Fields," MSME Thesis, Dept. of Mechanical Engineering, University of Minnesota, Minneapolis, MN.

Schlichting, H., 1979, *Boundary Layer Theory*, 7th ed., McGraw-Hill, New York.

Simonich, J. C., and Moffatt, R. J., 1982, "Local Measurements of Turbulent Boundary Layer Heat Transfer on a Concave Surface Using Liquid Crystals," Rept. HMT-35, Thermosciences Division, Dept. of Mechanical Engineering, Stanford University, CA.

Shizawa, T., and Honami, S., 1983, "Experiment on Turbulent Boundary Layers Over a Concave Surface—Effects of Introduction of Curvature," *Proc. of the 4th Symposium on Turbulent Shear Flows*, pp. 6.38–6.43.

Shizawa, T., and Honami, S., 1985, "Experiments on Turbulent Boundary Layers Over a Concave Surface—Response of Turbulence to Curvature," *Proc. of the 5th Symposium on Turbulent Shear Flows*, pp. 14.7–14.12.

So, R. M., and Mellor, G. L., 1975, "Experiment on Turbulent Boundary Layers on a Concave Wall," *The Aeronautical Quarterly*, Vol. 26.

Swearingen, J. D., 1985, "The Growth and Breakdown of Streamwise Vortices in the Presence of a Wall," Ph.D. Thesis, University of Southern California.

Tani, I., 1962, "Production of Longitudinal Vortices in the Boundary Layer Along a Concave Wall," *J. of Geophysical Research*, Vol. 67, p. 3075.

Wang, T., 1985, "An Experimental Investigation of Curvature and Free-Stream Turbulence Effects on Heat Transfer and Fluid Mechanics in Transitional Boundary Layer Flows," Ph.D. thesis, University of Minnesota, Minneapolis, MN.

Wang, T., Simon, T. W., and Buddhavarapu J., 1985, "Heat Transfer and Fluid Mechanics Measurements in Transitional Boundary Layer Flows," ASME *Journal of Engineering for Gas Turbines and Power*, Vol. 107, pp. 1007–1015.

Wang, T., and Simon, T. W., 1987, "Heat Transfer and Fluid Mechanics Measurements in a Boundary Layer Undergoing Transition on a Convex-Curved Wall," ASME *Journal of Turbomachinery*, Vol. 109, No. 3, pp. 443–452.

Wortmann, F. X., 1969, "Visualization of Transition," *Journal of Fluid Mechanics*, Vol. 38, Part 3, pp. 473–480.

Turbulent Heat Transfer Augmentation Using Microscale Disturbances Inside the Viscous Sublayer

H. Kozlu[1]

B. B. Mikic

A. T. Patera

Massachusetts Institute of Technology,
Department of Mechanical Engineering,
Cambridge, MA 02139

We report here on an experimental study of heat transfer augmentation in turbulent flow. Enhancement strategies employed in this investigation are based on the near-wall mixing processes induced in the sublayer through appropriate wall and near-wall streamwise-periodic disturbances. Experiments are performed in a low-turbulence wind-tunnel with a high-aspect-ratio rectangular channel having either (a) two-dimensional periodic microgrooves on the wall, or (b) two-dimensional microcylinders placed in the immediate vicinity of the wall. It is found that microdisturbances placed inside the sublayer induce favorable heat-transport augmentation with respect to the smooth-wall case, in that near-analogous momentum and heat transfer behavior are preserved; a roughly commensurate increase in heat and momentum transport is termed favorable in that it leads to a reduction in the pumping power penalty at fixed heat removal rate. The study shows that this favorable performance of microcylinder-equipped channel flows is achieved for microcylinders placed inside $y^+ \simeq 20$, implying a dependence of the optimal position and size on Reynolds number. For microgrooved channel flows, favorable augmentation is obtained for a wider range of Reynolds numbers; however, optimal enhancement still requires a matching of geometric perturbation with the sublayer scale.

1 Introduction

Studies on heat transfer augmentation are motivated by several important factors; in general terms, from the thermal-hydraulic design point of view, transport enhancement leads to a reduction in momentum-transport penalties at a fixed heat removal rate; on a specific level, in certain applications such as aerospace designs and high-power-density electronic equipment, enhancement assures high heat removal rates that are required for functionality and safety of these systems. For these reasons a large number of augmentation techniques (e.g., augmentation hardware modifications, rough surfaces, and flow oscillation) are employed as heat transfer intensification strategies for laminar and turbulent flows (Bergles, 1986).

An important class of heat transfer augmentation techniques is based on the enhancement of *mixing* processes by generation of *hydrodynamic instabilities* in the region of highest resistance to heat transport. This method has been successfully applied to laminar and turbulent flows in recent studies (Karniadakis et al., 1988; Kozlu et al., 1988; Mikic et al., 1988). Intensification of turbulent heat transfer plays a significant role in technological applications since many engineering systems operate under turbulent flow conditions. The most effective enhancement technique for turbulent flows is based on the augmentation of near-wall mixing processes in the sublayer through appropriate wall and near-wall streamwise-periodic disturbances.

There are a large number of studies on heat transfer augmentation employing this type of enhancement procedure. Although they are geometrically different, in all systems the common physical phenomenon is a change in the structure of the viscous sublayer, which is the region extending about 50 wall units away from the wall (Coles, 1987).

- Brouillette et al. (1957) studied the thermal-hydraulic behavior of the 60-deg V-shaped internally grooved tubes. The measured values of heat transfer coefficients and friction factors were 10–100 percent and 15–400 percent higher than those of smooth channels for a Prandtl number of about 7.0, respectively. They found that the heat transfer coefficient was greatly influenced by the groove depth rather than the groove spacing.
- Fortescue and Hall (1957) conducted experiments on the longitudinal-finned and transverse-finned fuel elements for the design of the Calder Hall nuclear reactor. Their heat transfer and pressure drop measurements for transverse-finned fuel rods for a Prandtl number of 0.71 indicated that fins should be closely placed to achieve a better reduction in momentum-transport penalties.
- Dipprey and Sabersky (1963) experimentally investigated the heat and momentum transfer in smooth and rough tubes at several Prandtl numbers using water as the working fluid. Their three-dimensional roughness was formed by sand grains. They observed an increase in the heat transfer coefficient as high as 270 percent. These increases were, in general, associated with larger increases in the friction factor except that the increase in the heat transfer coefficient was more than the increase in the friction factor at the high Prandtl numbers. Their data mostly covered the "fully rough" flow regime.
- Han et al. (1978) investigated the heat transfer and friction characteristics of the rib-roughened surfaces in an air channel. They studied the effects of rib shape, angle of attack, and pitch-to-height ratio on friction factor and heat transfer. A general correlation using the surface roughness parameters was developed to predict the thermal hydraulic behavior of these flows. Ribs at a 45-deg angle of attack were found to have a favorable heat transfer and friction behavior compared to ribs at 90-deg angle of attack and to sand grain roughness.

---

[1] Current address: Creare, Inc., Etna Road, Hanover, NH 03755.

Contributed by the Heat Transfer Division and presented at the National Heat Transfer Conference and Exposition, Philadelphia, Pennsylvania, August 6–9, 1989. Manuscript received by the Heat Transfer Division November 8, 1989; revision received July 11, 1991. Keywords: Augmentation and Enhancement, Flow Instability.

- Sparrow and Tao (1983) performed a study in a smooth channel having streamwise-periodic cylinders attached to the wall. They obtained highly detailed axial distributions of the local mass transfer coefficient using naphthalene sublimation. They studied the effect of the pitch-to-height ratio of the disturbance elements and the effect of the ratio of the disturbance height to the duct height on thermal-hydraulic data. They also investigated the effect of microdisturbances on the opposite smooth wall.
- Kawaguchi et al. (1985) studied the heat transfer phenomena in a turbulent boundary layer having a cylinder array. They reported the optimum spacing between successive cylinders, and distance of the cylinders from the wall required to achieve the maximum heat transfer rate. They found that the performance of the cylinders in improving heat transfer enhancement is better when they are placed closer to the wall.

Most of the work on turbulent heat transfer augmentation has focused on the enhancement of heat transfer and the associated unavoidable increase in the friction factor with respect to smooth channel flow. Increases in the heat transfer coefficient as high as 400 percent were achieved with accompanying changes in the friction factor rising as much as 58 times over the smooth wall case at the same Reynolds number (Bergles, 1986). However, in these studies, the effect of microdisturbances located near or on the wall on the thermal-hydraulic behavior of these flows was not adequately explained in terms of governing variables, such as the placement and spacing of hardware modifications as a function of roughness Reynolds number.

The aim of the present work is to investigate heat and momentum transfer in turbulent flows under the presence of controlled wall and near-wall disturbances. To gain a better understanding of scalar transport phenomena in turbulent flows, two kinds of streamwise-periodic microdisturbances are employed: (*a*) wall disturbances (microgrooves), and (*b*) near-wall disturbances (microcylinders). A parametric study for microcylinders is conducted by changing the distance between successive microcylinders, the diameter of the microcylinders, and the distance of the microcylinders from the heated wall. The purpose of the paper is to establish the underlying physical basis for the turbulent transport phenomena, which permits choice of the proper enhancement scheme for turbulent flows at a given thermal load.

The outline of the paper is as follows: In Section 2 we present the experimental setup and geometric characteristics of the microdisturbances employed. In Section 3 we present and analyze the thermal-hydraulic data for the augmentation schemes of interest. In Section 4 we compare microgroove and microcylinder equipped turbulent channel flows with respect to minimum-dissipation heat removal. Lastly, in Section 5, conclusions of the study are presented.

2 Experimental Apparatus

We shall consider two heat transfer augmentation schemes of (*a*) streamwise-periodic microgrooves, and (*b*) streamwise-periodic microcylinders in a smooth channel as shown schematically in Figs. 1(*a*) and 1(*b*), respectively. The base geometry, smooth channel flow is obtained using the experimental setup of Fig. 1(*b*) with microcylinders removed. We denote the base geometry as Z_0 and describe the two augmentation geometries by sets Z_n: $Z_1=\{e/H, a/H, c/H\}$ for the microgrooved channels, and $Z_2=\{d/H, b/H, l/H\}$ for the microcylindered channels. Here H is the channel height (see Figs. 1*a* and 1*b*); e is the microgroove depth, a the streamwise groove length, and c the distance between successive grooves; d is the microcylinder diameter, b the distance between the microcylinders and the wall, l the distance between successive microcylinders in the array. Microcylinders are made of stainless steel. They are supported at both ends and at the center to prevent vibration for the Reynolds number range of experiments. Plexiglass side walls are used.

We consider one microgroove geometry (denoted by $Z_1=\{e/H=0.025,\ a/H=0.035,\ c/H=0.015\}$). The ranges of the wall variables e^+, a^+, and c^+ for the microgroove geometry were $9.5\le e^+\le 89.1$, $13.3\le a^+\le 124.7$, and $5.7\le c^+\le 53.4$ for the Reynolds number range of experiments. We define the wall variables using the friction velocity and kinematic viscosity: $e^+=u_*e/\nu$, where u_* is the friction velocity ($u_*=\sqrt{\tau_w/\rho}$ where τ_w is the shear stress at the wall) and ν is the kinematic viscosity of the fluid. For the shear stress τ_w, we use the value for smooth channel flow at the same Reynolds number. Seven different microcylinder geometries are studied (denoted by Z_2^m, $m=1,\ldots,7$) as given in Table 1. Experiments for microcylinders were conducted using one heated wall. As shown in Table 1, microcylinder disturbances were employed at the heated and/or at the unheated wall depending on the microcylinder geometry of interest. In this study, it is shown that the opposite wall does not have a significant effect on the

Nomenclature

a = groove length (Fig. 1*a*)
b = distance of the microcylinders from the wall (Fig. 1*b*)
c = distance between successive grooves (Fig. 1*a*)
d = diameter of the microcylinders (Fig. 1*b*)
D_H = channel hydraulic diameter $=4WH/2(W+H)$
e = groove depth (Fig. 1*a*)
f = friction factor
h = heat transfer coefficient
H = channel height (Figs. 1*a* and 1*b*)
j = modified Colburn analogy factor $=1/2f(\mathrm{Re}/\mathrm{Nu})\mathrm{Pr}^{1/3}$
k = thermal conductivity
l = distance between successive microcylinders (Fig. 1*b*)
L = channel length
Nu = Nusselt number $=hD_H/k$
ΔP = pressure drop
Pr = Prandtl number $=\nu/\alpha$
q'' = heat flux per unit area
Re = Reynolds number $=VD_H/\nu$
Re_k = roughness Reynolds number $=u_*e(b)/\nu$
T = temperature
δT = total temperature difference $=T_{w_{out}}-T_{m_{in}}$
u_* = friction velocity $=\sqrt{\tau_w/\rho}$
V = channel-average velocity
W = channel width (Figs. 1*a* and 1*b*)
x, y, z = Cartesian coordinates
y^+ = nondimensional y coordinate $=yu_*/\nu$
Z_n = set of geometric parameters for channel geometry n
Λ = nondimensional thermal load $=q''L/k\delta T$
μ = dynamic viscosity
ν = kinematic viscosity
ρ = density
τ_w = shear stress at the wall
Ψ = nondimensional pumping power per unit width of the channel

Subscripts

in = inlet
m = mixed mean
n = channel geometry
out = exit
w = wall
0 = base geometry, smooth channel
1 = periodic microgrooved channel
2 = periodic microcylindered channel

Superscripts

m = microcylinder geometry (see Table 1)

Table 1 Characteristics of microcylinder geometries

Geometry	d/H	b/H	l/H	Micro-cylinder equipped wall
Z_2^1	0.015	0.025	0.140	heated wall
Z_2^2	0.015	0.025	0.280	heated wall
Z_2^3	0.015	0.025	0.390	heated wall
Z_2^4	0.032	0.060	0.132	heated wall
Z_2^5	0.015	0.025	0.390	heated and unheated wall
Z_2^6	0.015	0.025	0.390	unheated wall
Z_2^7	0.049	0.059	0.424	unheated wall

Table 2 Ranges of the wall variables d^+, b^+, and l^+ for microcylinder geometries

Geometry	d^+	b^+	l^+
Z_2^1	7.0 - 21.3	11.6 - 35.5	65.1 - 198.8
Z_2^2	8.0 - 15.6	13.3 - 26.0	149.0 - 291.5
Z_2^3	8.2 - 20.0	13.7 - 33.4	213.9 - 520.7
Z_2^4	16.1 - 71.3	30.2 - 133.7	66.6 - 294.6
Z_2^5	8.2 - 17.6	13.7 - 29.3	213.3 - 457.0
Z_2^6	12.4 - 20.1	20.7 - 33.5	322.1 - 523.3
Z_2^7	39.3 - 73.7	47.3 - 88.8	339.8 - 637.7

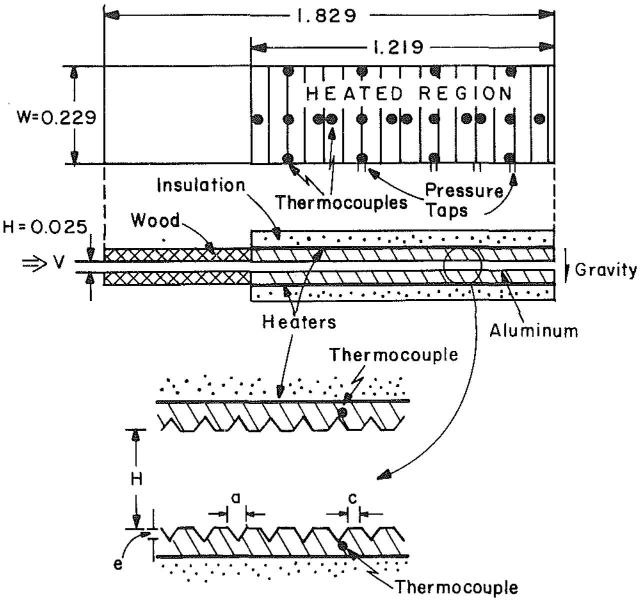

Fig. 1(*a*) Details of the test section for geometry Z_1. The microgrooves are machined on the aluminum plates to high precision using a shaper. All units are in meters.

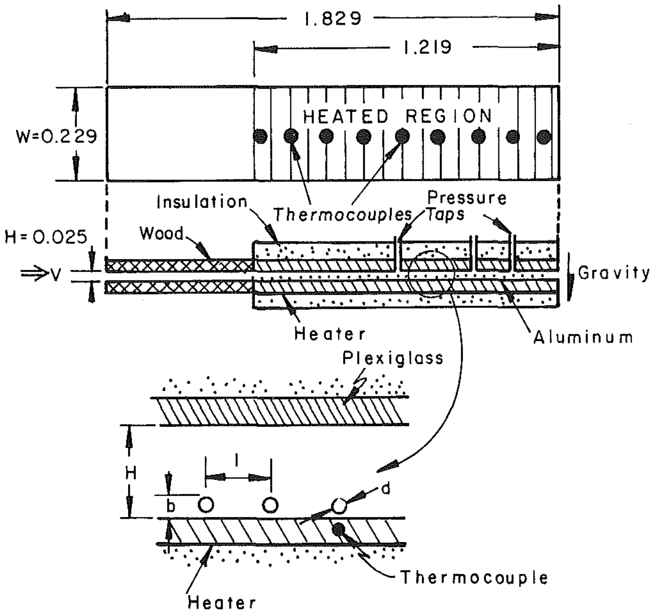

Fig. 1(*b*) Details of the test section for geometry Z_2. For geometry Z_0 the same test section is used with the microcylinders removed. All units are in meters.

heat transfer characteristics of the augmented wall of interest. The ranges of the wall variables d^+, b^+, and l^+ for microcylinder geometries are presented in Table 2. The ratio of the width of the channel W to the channel height H is $W/H = 9.0$. The channel was fitted with electrical strip heaters on both channel walls for microgrooves, and only one channel wall for microcylinders, to deliver the necessary uniform heat flux q''. The test sections shown in Figs. 1(*a*) and 1(*b*) were connected to an open-circuit double-contraction wind tunnel operated in the blower mode. The mixed mean air temperature at the tunnel inlet was maintained constant during the experiments using a heat exchanger. This temperature was in the range of 19°C–23°C depending on the test conditions.

For the augmentation studies of interest we require a set of Nu, f for each Z_n. Reynolds number, Nusselt number, and friction factor are defined in the conventional way as $\mathrm{Re} = VD_H/\nu$, $\mathrm{Nu} = hD_H/k$, and $f = (\Delta P/L)(D_H/4)(2/\rho V^2)$, respectively. Here D_H is the hydraulic diameter for the channel, $\Delta P/L$ the pressure gradient, ρ the fluid density, V the average velocity; h is the heat transfer coefficient, k the fluid thermal conductivity. Air properties were evaluated at local mixed mean temperature. To avoid difficulties with the influence of temperature-dependent air properties, local temperature differences were kept below 15°C. Flow rate is varied to achieve a range of Reynolds numbers. The Mach number range for the experiments was 0.01-0.14. Natural convection was negligible since the highest $\mathrm{Gr}/\mathrm{Re}^2$ for the experiments conducted was about 2×10^{-4} (Eckert and Drake, 1979). For each Reynolds number the pressure drops and wall temperatures at several x locations (Figs. 1*a* and 1*b*) and fluid temperatures at inlet and exit were measured, thus allowing the evaluation of Nu(Re, $\mathrm{Pr} = 0.71$; Z_n) and f(Re; Z_n). The pressure drop was measured with a MKS Baratron differential pressure transducer, and the flow rate was calculated from traversed pitot-static velocity measurements at inflow. Temperature measurements were made using copper-constantan thermocouples. Due to the small length scale of microdisturbances, thermocouples were positioned to measure the average heat transfer coefficients; therefore, periodic variations in the wall temperature were not measured. The inner walls in the heated region were made of high-conductivity aluminum, and thermocouples were placed close to the surface to insure that the error between the thermocouple and the surface temperature was less than 0.2 percent of the difference between the wall temperature and the mixed mean air temperature.

Lastly, we note that the flow is allowed to become hydraulically and thermally fully developed in the streamwise direction x before any measurements are taken. All measurements are taken after a distance of roughly 65 H from the inlet of the channel, and roughly 35 H from the beginning of the heated region. The resulting entrance regions are sufficient to obtain hydraulically and thermally fully developed smooth channel turbulent flows, and the entrance length for geometries Z_1 and Z_2^m is much shorter than the flat channel Z_0 as a result of destabilization (Sparrow and Tao, 1983). In addition to these theoretical considerations of entrance-length effects, it has also been verified directly from measurements that both the time-averaged wall temperature and pressure vary linearly (with the proper slope) with x, consistent with fully developed flow.

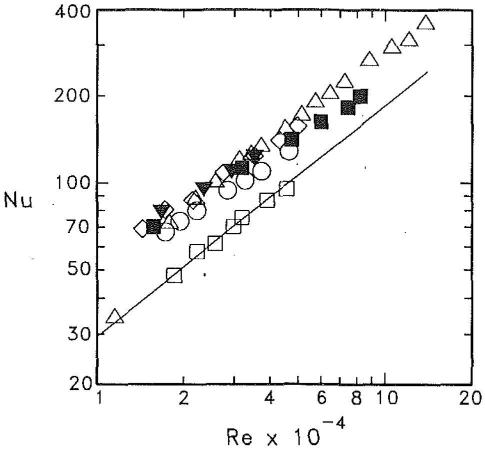

Fig. 2 **Heat transfer data for Pr = 0.71. Z_0 (smooth channel): □, experiment; ——, turbulent correlation (Kays and Crawford, 1980). Z_1 (microgrooves): △. Z_2^m, $m = 1, 2, 3, 4$ (microcylinders, see Table 1): ◇, Z_2^1; ▼, Z_2^2; ○, Z_2^3; ■, Z_2^4.**

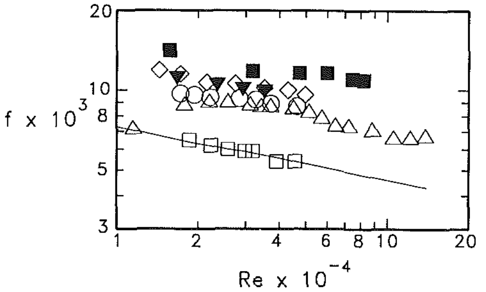

Fig. 3 **Friction coefficient data. Z_0 (smooth channel): □, experiment; ——, turbulent correlation (Hussain and Reynolds, 1975). Z_1 (microgrooves): △. Z_2^m, $m = 1, 2, 3, 4$ (micro-cylinders, see Table 1): ◇, Z_2^1; ▼, Z_2^2; ○, Z_2^3; ■, Z_2^4.**

An uncertainty analysis using the uncertainty estimation method of Kline and McClintock (1953) showed that the uncertainties in the Nusselt number and in the average friction factor were 8 percent and 6 percent, respectively.

3 Results and Discussion

We plot in Figs. 2 and 3 the Nu(Re, Pr = 0.71; Z_n) and f(Re; Z_n) curves for the smooth channel flow and augmentation schemes of interest. First we compare our one-wall heated smooth channel data with existing two-wall heated smooth channel correlations. Note that the heat transfer data for two heated smooth walls are about 5 percent higher than those for one heated smooth wall for the Reynolds number range of interest (Sparrow and Tao, 1983). As can be seen from Fig. 2, the heat transfer data agree well (the largest difference is about 4 percent) with the equation given by Kays and Crawford (1980)

$$\mathrm{Nu} = \frac{0.152\,\mathrm{Re}^{0.9}\mathrm{Pr}}{0.833\,[2.25\ln(0.114\mathrm{Re}^{0.9}) + 13.2\,\mathrm{Pr} - 5.8]}. \qquad (1)$$

The present experimental data are also within the ±6 percent that is given for the Petukhov-Popov equation for Pr = 0.71 (Petukhov, 1970). The friction factor data are compared with the relationship (Hussain and Reynolds, 1975)

$$f = \frac{0.046}{\mathrm{Re}^{0.2}}, \qquad (2)$$

and the experimental data all lie within 2 percent of the above equation.

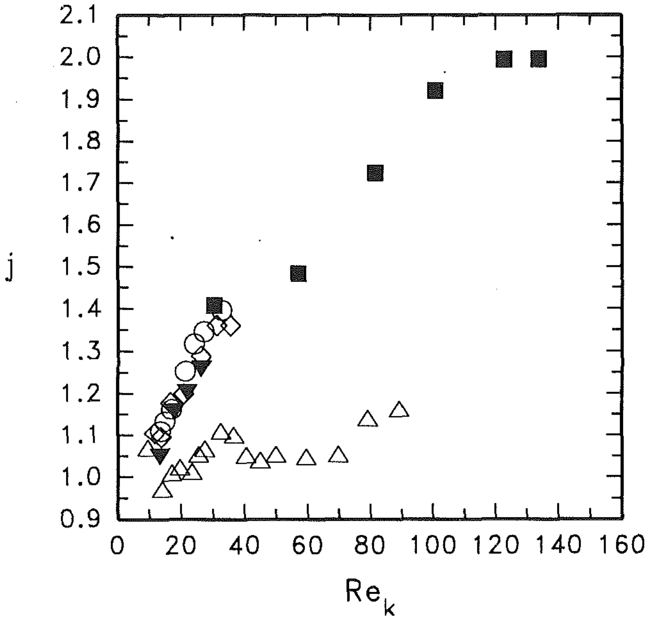

Fig. 4 **Modified Colburn analogy factor as a function of roughness Reynolds number. Z_1 (microgrooves): △. Z_2^m, $m = 1, 2, 3, 4$ (microcylinders, see Table 1): ◇, Z_2^1; ▼, Z_2^2; ○, Z_2^3; ■, Z_2^4.**

As seen in Figs. 2 and 3, for microgroove-equipped channel flows (Z_1), microgrooves have negligible effect on transport augmentation for a Reynolds number of about 11,500. The roughness Reynolds number corresponding to this Reynolds number microgroove data point is 9.5. We define the roughness Reynolds number for the microgroove geometry as $\mathrm{Re}_k = u_* e/\nu$, where u_* is the friction velocity ($u_* = \sqrt{\tau_w/\rho}$, where τ_w is the average shear stress at the wall) and ν the kinematic viscosity of the fluid. For the shear stress τ_w, we use the value for smooth channel flow at the same Reynolds number; this is a lower bound for the roughness Reynolds number and is a reasonable assumption since we do not measure the wall shear stress directly. Therefore, the roughness numbers are calculated for each data point in Figs. 2 and 3 utilizing Eq. (2). When we increase the Reynolds number (or the roughness Reynolds number above 10) the effect of microgrooves becomes significant on scalar transport as the length scale of microgrooves geometrically scale with the sublayer. These observations are consistent with past studies on the effect of roughness in the transport processes (Tennekes and Lumley, 1972).

In Fig. 4 we plot the modified j factor (defined as $j = (f/2)(\mathrm{Re}/\mathrm{Nu})\,\mathrm{Pr}^{1/3}$) for the augmentation schemes of interest shown in Figs. 2 and 3 as a function of the roughness Reynolds number. For flows in which analogous heat and momentum transfer are preserved, the modified Colburn analogy (Colburn, 1933) factor has a value of one. Figure 4 shows that for microgrooves a roughly equal relative increase in heat and momentum transfer is obtained for $\mathrm{Re}_k \leq 80$. As we continue to increase the Reynolds number ($\mathrm{Re}_k \geq 80$), the microgrooves will cease to match the sublayer scale, and the nonanalogous form drag will start dominating in the ensuing fully rough regime. Thus, the relative increase in pressure drop will be larger than the increase in heat transfer. The behavior of thermal-hydraulic data for microgrooves reconfirms the fact that the roughness Reynolds number is the critical parameter governing the scalar transport, and that there is an optimal placement of microdisturbances to increase the heat transfer with a comparable increase in the friction factor. This optimal placement of microdisturbances requires a matching of geometric perturbation with sublayer scale.

For microcylinders, we obtain the following results from comparisons of four different data sets (Z_2^1–Z_2^4). First, as seen

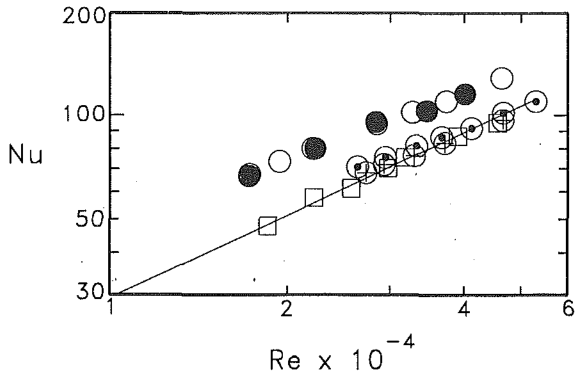

Fig. 5 Heat transfer data for Pr = 0.71. Z_0 (smooth channel): □, experiment; ——, turbulent correlation (Kays and Crawford, 1980). Z_2^m, $m = 3$, 5, 6, 7 (microcylinders, see Table 1); ○, Z_2^3; ●, Z_2^5; ⊕, Z_2^6; ⊙, Z_2^7.

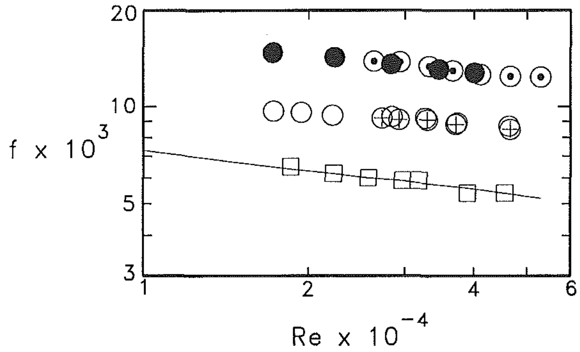

Fig. 6 Friction coefficient data. Z_0 (smooth channel): □, experiment; ——, turbulent correlation (Hussain and Reynolds, 1975). Z_2^m, $m = 3$, 5, 6, 7 (microcylinders, see Table 1): ○, Z_2^3; ●, Z_2^5; ⊕, Z_2^6; ⊙, Z_2^7.

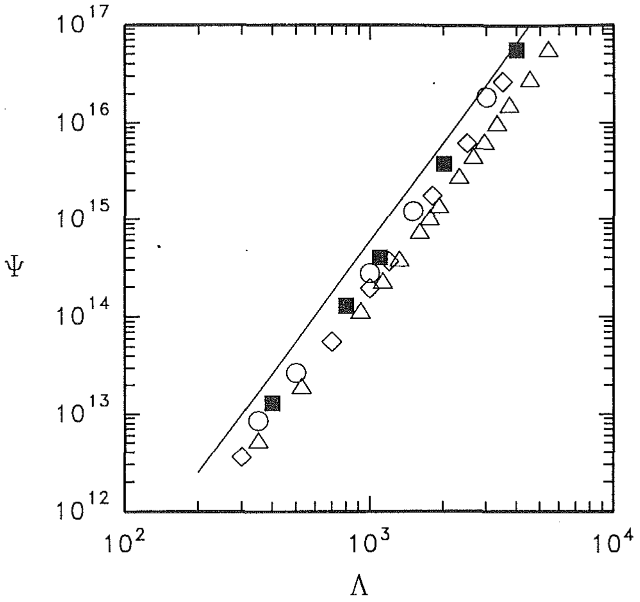

Fig. 7 A plot of minimum dissipation as a function of thermal load. The plot is based on the data sets of Figs. 2 and 3. Z_0 (smooth channel correlations): ——. Z_1 (microgrooves): △. Z_2^m, $m = 1, 3, 4$ (microcylinders, see Table 1): ◇, Z_2^1; ○, Z_2^3; ■, Z_2^4.

in Figs. 2 and 3, l/H has a small effect for the values b and d studied until $l/H = 0.280$. It is observed that the results of $l/H = 0.140$ and $l/H = 0.280$ are almost the same, whereas for $l/H = 0.390$ we see a decrease in heat and momentum transfer compared to the previous two cases. This is consistent with the expected trend of diminished transport augmentation as $l \rightarrow \infty$. As we decrease the distance between the microcylinders and increase the diameter of microcylinders (geometry Z_2^4), an increase in the transport rates is observed.

Referring again to our plot of the modified j factor as a function of the roughness Reynolds number (for microcylinders we define the roughness Reynolds number based on b, $\mathrm{Re}_k = u_* b/\nu$) in Fig. 4, the data show a similar behavior, and the effectiveness of microcylinders (in enhancing heat transfer without generating an unduly high friction loss) is increased when they are placed inside $y^+ \simeq 20$ (i.e., $\mathrm{Re}_k = 20$). This is the reason that Z_2^4 is not favorable compared to other geometric configurations, Z_2^1 and Z_2^2, since the microcylinders in the former case (i.e., $b \simeq 2.5$ times larger) were outside the $y^+ = 20$ region for the whole range of Reynolds numbers tested, thereby contributing to form drag and nonanalogous dissipation.

Achievement of favorable heat transfer augmentation by matching the geometric scale of the augmentation hardware modification to that of the sublayer is consistent with the theory of *scale matched destabilization for optimal scalar transport* enhancement described by Kozlu et al. (1988): Microdisturbances placed inside the sublayer increase the heat transfer while simultaneously controlling the increase of nonanalogous drag. The increase in scalar transport rates is a result of the local changes in the sublayer structure (Mikic, 1988).

To show the effect of microdisturbances on the opposite (from the heated) wall, we conducted three different sets of experiments. Thermal-hydraulic data of these tests are presented in Figs. 5 and 6. First for the geometry Z_2^3 we use microcylinders at both the heated wall and unheated wall (geometry Z_2^5). Figure 5 illustrates that there is no change in the heat transfer coefficient compared to the geometry Z_2^3, indicating that microdisturbances affect the flow locally; they have no effect on the core flow, and hence no effect on the opposite wall. To support this conjecture, we have also conducted an experiment with the geometry Z_2^6 in which only the unheated wall was equipped with microcylinders, whereas the heated wall was smooth. As can be seen from Fig. 5, the experimental heat transfer data for Z_2^6 agree very well with the smooth channel heat transfer data, strengthening the above explanation.

When we considerably increase the opposite-wall microcylinder diameter (about three times compared to Z_2^5) in geometry Z_2^7, we see *no effect at higher Reynolds numbers* (Figs. 5 and 6). However, for low Reynolds numbers an increase in heat transfer up to 10 percent compared to the smooth channel flow is observed. An explanation for this behavior might be as follows: An increase in microcylinder diameter causes an asymmetry in the flow (i.e., increases velocity near the smooth wall), which is responsible for altering the transport characteristics of smooth wall for low Reynolds numbers. If we continue to increase the cylinder diameter (about 20–30 percent of the channel height), transport rates for both walls will be affected by the existence of unsteady secondary flows as studied by Karniadakis et al. (1988) for laminar flows, and Kozlu et al. (1988), and Ichimiya and Yokohama (1987) for turbulent flows. This again supports the scale-matched hypothesis for optimal transport. The extent to which the microcylinder high-Reynolds-number and macrocylinder low-Reynolds-number flows are "self-similar" as regards transport remains to be determined.

4 Minimum Pumping Power Heat Removal Considerations

Heat removal from a wall to a flowing fluid stream with minimum pumping power is reported by Karniadakis et al. (1988) and Kozlu et al. (1988). Here, as described in detail by Kozlu et al. (1988), we consider the problem of incompressible flow in a plane channel of length L and height H, with uniform heat flux q'' imposed on the top wall, and an adiabatic bottom surface. The flow is assumed to be hydraulically and thermally fully developed in x. We also chose the maximum wall temperature δT relative to the inlet temperature as our thermal constraint as this is the quantity that typically limits the performance of devices (e.g., computer chips). In terms of these given quantities, a solution of the minimum pumping power heat removal problem is given by Kozlu et al. (1988). In Fig. 7 we plot the nondimensional minimum pumping power (we define the nondimensional pumping power as follows: $\Psi = L^2/\rho\nu^3\, \Delta PVH$) versus thermal load ($\Lambda = q''L/k\delta T$ where δT is the temperature difference between the maximum wall temperature and the inlet mixed mean fluid temperature) for smooth channel flows and the augmentation schemes of interest. The procedure for the construction of Fig. 7 is presented in detail by Kozlu et al. (1988).

Figure 7 illustrates the significant savings in dissipation compared to smooth channel flows. It is important to note that microgrooves perform efficiently for a wider range of thermal load than microcylinders due to the fact that the matching of geometric perturbation and sublayer scale is less sensitive to Reynolds number. For microcylinders placed outside $y^+ \simeq 20$, the relative savings tend to decrease strongly (see Fig. 4), implying a significant Reynolds number dependence on position and size of near-wall microdisturbances.

5 Conclusions

In this experimental study it is shown that turbulent heat transfer augmentation can be effectively achieved by placing wall and near-wall microdisturbances inside the sublayer. It appears that the optimal placement of microdisturbances requires a matching of geometric perturbation with the sublayer scale. The relative performance of microgrooves greatly decreases in the fully rough regime due to the dominant role of the nonanalogous form drag. Significant savings in dissipation are possible through heat transfer augmentation; this is demonstrated in a sample study of minimum pumping power heat-transfer analysis in a channel.

References

Bergles, A. E., 1986, "Techniques to Augment Heat Transfer," in: *Handbook of Heat Transfer Applications*, W. M. Rohsenow, J. P. Hartnett, and E. N. Ganic, eds., McGraw-Hill, New York, Chap. 3.

Brouillette, E. C., Mifflin, T. R., and Myers, J. E., 1957, "Heat-Transfer and Pressure-Drop Characteristics of Internal Finned Tube," ASME Paper No. 57-A-47.

Colburn, A. P., 1933, "A Method of Correlating Forced Convection Heat Transfer Data and a Comparison With Fluid Friction," *Trans. Am. Inst. Chem. Eng.*, Vol. 29, pp. 174–210.

Coles, D., 1987, "Coherent Structures in Turbulent Boundary Layers," in: *Perspectives in Turbulence Studies*, H. U. Meier and P. Bradshaw, eds., Springer-Verlag, New York, pp. 93–114.

Dipprey, D. F., and Sabersky, R. H., 1963, "Heat and Momentum Transfer in Smooth and Rough Tubes at Various Prandtl Numbers," *Int. J. Heat Mass Transfer*, Vol. 6, pp. 329–353.

Eckert, E. R. G., and Drake, R. M., 1979, *Heat and Mass Transfer*, McGraw-Hill, New York.

Fortescue, P., and Hall, W. B., 1957, "Heat-Transfer Experiments on the Fuel Elements," *J. Brit. Nucl. Energy Conf.*, Session 2, pp. 83–91.

Han, J. C., Glicksman, L. R., and Rohsenow, W. M., 1978, "An Investigation of Heat Transfer and Friction for Rib-Roughened Surfaces," *Int. J. Heat Mass Transfer*, Vol. 21, pp. 1143–1156.

Hussain, A. K. M. F., and Reynolds, W. C., 1975, "Measurements in Fully-Developed Turbulent Channel Flow," ASME *Journal of Fluids Engineering*, Vol. 97, pp. 568–580.

Ichimiya, K., and Yokoyama, M., 1987, "Effects of Artificial Roughness Elements for Heat Transfer and Flow on a Smooth Heated Wall in a Parallel Plate Duct," *Heat Transfer—Japanese Research*, Vol. 16, pp. 24–39.

Karniadakis, G. E., Mikic, B. B., and Patera, A. T., 1988, "Minimum Dissipation Transport Enhancement by Flow Destabilization: Reynolds' Analogy Revisited," *J. Fluid Mech.*, Vol. 192, pp. 365–391.

Kawaguchi, Y., Suzuki, K., and Sato, T., 1985, "Heat Transfer Promotion With a Cylinder Array Located Near the Wall," *Int. J. Heat Fluid Flow*, Vol. 6, pp. 249–255.

Kays, W. M., and Crawford, M. E., 1980, *Convective Heat and Mass Transfer*, McGraw-Hill, New York.

Kline, S. J., and McClintock, F. A., 1953, "The Description of Uncertainties in Single-Sample Experiments," *Mechanical Engineering*, Vol. 75, pp. 3–9.

Kozlu, H., Mikic, B. B., and Patera, A. T., 1988, "Minimum-Dissipation Heat Removal by Scale-Matched Flow Destabilization," *Int. J. Heat Mass Transfer*, Vol. 31, pp. 2023–2032.

Mikic, B. B., Kozlu, H., and Patera, A. T., 1988, "A Methodology for Optimization of Convective Cooling Systems for Electronic Devices," submitted to XXth International Symposium of the International Centre for Heat and Mass Transfer, Yugoslavia.

Mikic, B. B., 1988, "On Destabilization of Shear Flows: Concept of Admissible System Perturbations," *Int. Comm. Heat Mass Transfer*, Vol. 15, pp. 799–811.

Petukhov, B. S., 1970, "Heat Transfer and Friction in Turbulent Pipe Flow With Variable Physical Properties," *Advances in Heat Transfer*, Academic Press, Vol. 6, pp. 503–564.

Sparrow, E. M., and Tao, W. Q., 1983, "Enhanced Heat Transfer in a Flat Rectangular Duct With Streamwise-Periodic Disturbances at One Principal Wall," ASME JOURNAL OF HEAT TRANSFER, Vol. 105, pp. 851–861.

Tennekes, H., and Lumley, J. L., 1972, *A First Course in Turbulence*, MIT Press, Cambridge, MA.

Local Heat Transfer in a Rotating Serpentine Flow Passage

Wen-Jei Yang

Nengli Zhang

Jeff Chiou

Department of Mechanical Engineering and
Applied Mechanics,
University of Michigan,
Ann Arbor, MI 48109

An experimental study is performed on the internal cooling of a rotating serpentine flow passage of square cross section with throughflow. The test section is not proceeded by a hydrodynamic calming region, i.e., a leading arm, and is rotated at low Rossby numbers. The local heat transfer coefficients along the flow passage, including the leading wall, trailing wall, and sidewalls, are determined together with the circumferentially averaged values. The Reynolds, Rossby, and rotating Rayleigh numbers are varied to determine their effects on heat transfer performance. It is disclosed that heat transfer augmentation is significant at all sharp turns due to the presence of strong secondary flow. The rotational effect is very obvious and complicated in the local heat transfer performance but it is very minor on the average heat transfer performance. The throughflow rate plays an important role on the heat transfer performance. The results may serve as a baseline for comparison with the results from a model with a leading arm to determine the effects of a hydrodynamic calming section on the heat transfer performance of a rotating serpentine flow passage.

Introduction

Gas turbines are presently responsible for generating the majority of electric power. In current advanced gas turbine power plants, increased speeds, pressures, and temperatures are used to reduce specific fuel consumption. Hence, turbine blades are subjected to increased heat loads, which, in turn, escalate the amount of cooling required. The efficient use of cooling air requires that the local geometry and flow conditions be adequately modeled to predict the heat loads and their corresponding heat transfer coefficients. Improved turbine blade local temperature predictions (and hence, life predictions) can be realized by accurately accounting for the effects of rotation on internal cooling, which give rise to large Coriolis and buoyancy forces. However, these effects are currently not adequately considered in thermal design of blades. Experimental data are particularly needed for the high Rayleigh and Reynolds number conditions that are characteristic of turbine blade cooling passages. These data are crucial for both the development and the verification of design correlations and computer codes. Accurate prediction of local heat transfer coefficients enables a designer to minimize both metal temperatures and thermal gradients by optimizing the cooling configuration of the turbine blade, thus significantly improving blade life and turbine efficiency. Results can also be applied to the internal forced convective heat transfer of other rotating systems.

It is not an easy task to study convective heat transfer in rotating flow passages. Experimentally, slip rings are required as bridges between the rotating and stationary systems in order to transfer temperature data and power to heat the fluid. In theoretical study, the Coriolis and centrifugal force terms in the rotating coordinates substantially complicate the solution of rotational problems. Hence, little effort has been directed to heat transfer problems involving rotating channels. It is only in recent years that literature (for example, [1-3]) pertinent to this type of problem has begun to surface. However, while this literature has provided a data base, the flow phenomena are still not yet clearly understood. Heat transfer enhancement was studied with the use of rib turbulators in the stationary case but has not been treated in the rotating system.

The project is to conduct both experimental and theoretical studies of the heat and fluid flows in the internal cooling of rotating gas turbine blades. The flow passage in an actual blade of a typical gas turbine engine (Fig. 1) is idealized as four-pass serpentine-type channel, without a leading arm (Fig. 2). In the first stage of the experimental study, attention was focused on the effects of the Reynolds, Rossby, and Rayleigh numbers on the local and circumferentially averaged heat transfer coefficients. The effect of geometry on the heat transfer characteristics is left for the next stage of study. The physical limitations of the test device result in rotations at low Rossby numbers. The absence of a leading arm provides test results that will serve as a baseline to determine the effects of a hydrodynamic calming region on the heat transfer performance in a rotating serpentine flow passage.

Experimental Apparatus and Procedure

Rotating Facility and Heat Transfer Model. The experimental apparatus used in the study is shown schematically in Fig. 3. It was comprised of a test section, a blower, a motor, a heat source, two slip rings, and a data logger. The test section consisted of a four-pass serpentine flow channel with a 2.54 cm square cross section mounted on a shaft supported by two bearings.

Two methods involving heating are used to determine the internal heat transfer performance of a rotating body. One method is to use a thin film electrical resistance-type heater instrumented with thermocouples (for example, [1, 4]). The other is to pass a hot air steam through an internal flow passage coated with liquid crystal. A no-heating method is to utilize naphthalene sublimation to determine the heat transfer characteristics in the coolant passage through the use of heat and mass transfer analogy [5, 6]. The electrical resistance heating method was employed in the present study. The test core (Fig. 2) was made from two pieces of Grade G-10 Garolite plate held together by screws. The flow passage had a square cross section, 25.4 mm by 25.4 mm, and was 913.5 mm long. The serpentine passage was mounted on a metal shaft hollow on

---

Contributed by the Heat Transfer Division for publication in the JOURNAL OF HEAT TRANSFER. Manuscript received by the Heat Transfer Division August 1990; revision received October 1991. Keywords: Augmentation and Enhancement, Forced Convection, Turbines.

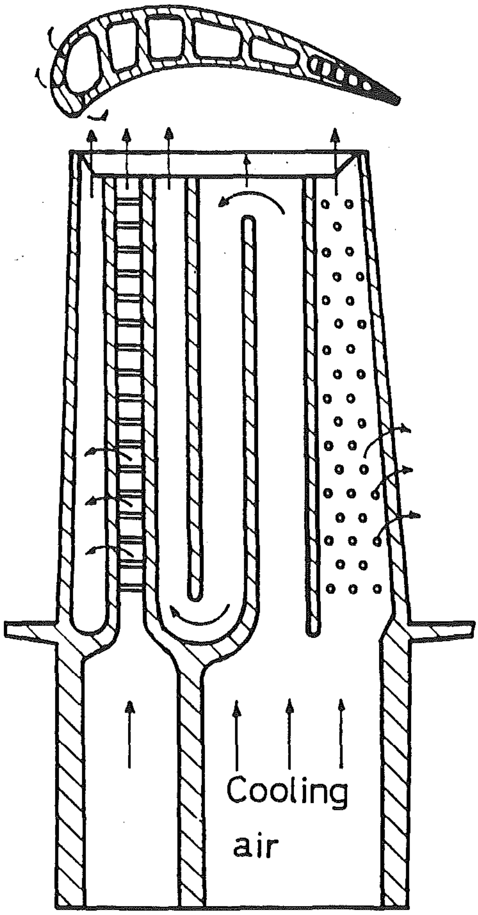

Fig. 1 Cooling concepts of a turbine blade

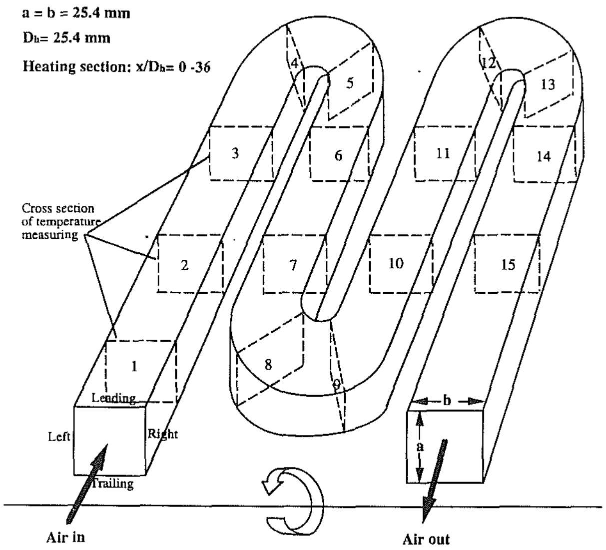

Fig. 2 Schematic diagram of test section

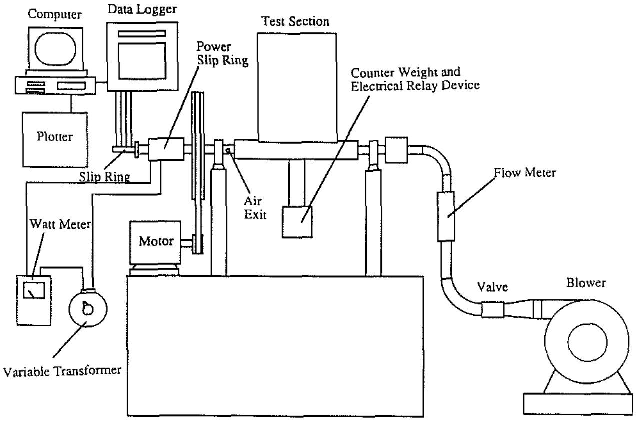

Fig. 3 Schematic of experimental setup

both ends to allow air flow. A counterweight and electrical relay device were mounted on the shaft opposite the test core.

Squares 1-13 of Fig. 2 show the location of the thermocouples used to monitor the wall temperature of the flow passage. Four thermocouples were installed at each cross section, one on each sidewall, to measure the wall temperature. Two thermocouples were installed in the middle of the square cross sections at the beginning and end of the flow passage to determine the inlet and outlet fluid temperatures.

Figure 4 illustrates: (*a*) the cross section of the test section in the flow direction, (*b*) the position of the four stainless-steel

Nomenclature

C_p = specific heat at constant pressure of fluid, kJ(kg-°C)
D_h = hydraulic diameter of flow passage, m
G = air flow rate, kg/h
h = local heat transfer coefficient, as defined by Eq. (1), W/(m^2=°C)
I = heating current, A
k = thermal conductivity of fluid, W/(m-°C)
L = length of one of the four parallel ducts in the test section, m
Nu = local Nusselt number as defined by Eq. (2); Nu_0, the value of Nu for stationary case; $\overline{\mathrm{Nu}}$, circumferentially averaged Nu value; $\overline{\mathrm{Nu}}_{\mathrm{TL}}$, the value of Nu averaged over the trailing and leading walls of the first passage; $\overline{\mathrm{Nu}}_{\mathrm{TL}_0}$, the value of Nu_0 averaged over the trailing and leading walls of the first passage
Pr = Prandtl number
Q' = heat loss, W
q'' = wall heat flux, W/m^2
R = length of arm in rotation, m
Ra = Raleigh number, as defined by Eqs. (9) and (11)
Re = Reynolds number, as defined by Eq. (9)
Ro = Rossby number, as defined by Eq. (9)
T = temperature, °C
ΔT = temperature difference, as defined by Eq. (10)
u = mean flow velocity in flow passage, m/s
V = voltage, V
W = result uncertainty interval
w = uncertainty interval of variables
x = distance along flow passage measured from flow entrance, m
β = coefficient of thermal expansion, 1/K
ν = kinematic viscosity, m^2/s
Ω = rotational speed, r/s

Subscripts

g = gas
in = inlet condition of gas to test section
out = outlet condition of gas in test section
w = wall

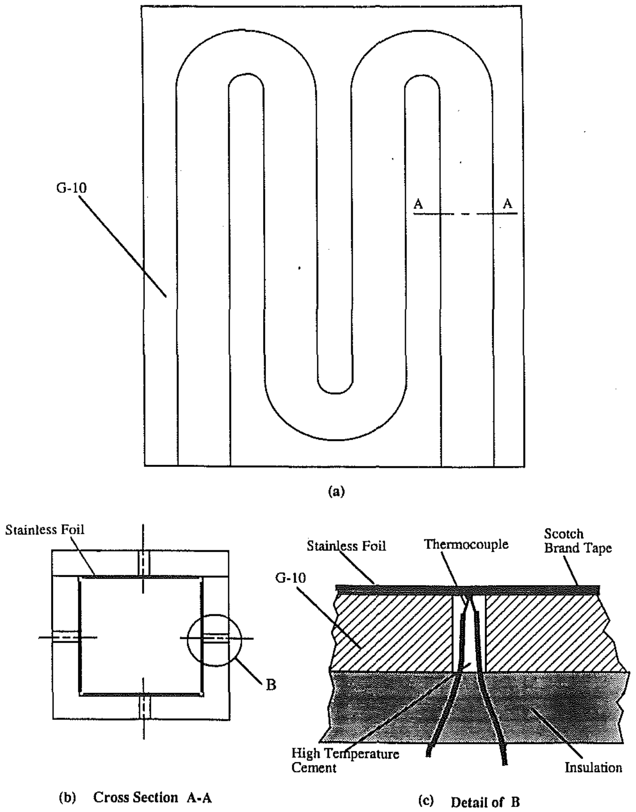

(a)

(b) Cross Section A-A (c) Detail of B

Fig. 4 Structure of test section

heating foils and the four thermocouple wells, one on each sidewall, and (*c*) the detail of an individual thermocouple well, illustrating the installation of the thermocouples.

Electrical power was supplied to the film heaters by a variable current power source through a slip ring. The temperature readings of the wall thermocouples were transmitted from the test piece to the data logger via another slip ring. The cooling air from the blower was supplied through one end of the hollow shaft to the serpentine passage and then exhausted through the other end of the shaft. A valve was installed for regulating the air flow rate, which was measured by means of a flow meter. A protective metal cover enclosed the rotating system.

The nearly constant heat flux experiment was conducted instead of a constant wall temperature case because of its simplicity of construction and ease of operation. The advantage of the more uniform wall-to-air temperature difference is more uniform uncertainty in the results. It should be noted that real turbine blades operate under a condition in between the constant heat flux and constant wall temperature cases.

Data Reduction. The local heat transfer performance is determined as follows: Let q'' be the heat flux of passage walls. q'' was calculated by subtracting conducted heat losses from the total energy supplied and verified by an energy balance through measurement of the air temperatures at outlet and inlet. The conductive heat losses were measured under steady-state rotational conditions without throughflow in which the temperature at a strategic position (the left wall at the first turn, i.e., section 4 in Fig. 2) was maintained at the same temperature as in the corresponding throughflow case. The resulting calculated heat loss showed that both methods for calculating the energy supplied to the air (total energy supplied – heat loss, and measuring air inlet/outlet temperatures) obtained the same results within a variation of 5 percent. The local heat transfer coefficient $h(x)$ is evaluated as follows:

$$h(x)=q''/\Delta T(x) \qquad (1)$$

where $\Delta T(x) = T_w(x) - T_g(x)$, and $T_w(x)$ and $T_g(x)$ denote the local wall and air temperatures, respectively. The local Nusselt number $\mathrm{Nu}(x)$ is defined as

$$\mathrm{Nu}(x)=h(x)D_h/k \qquad (2)$$

in which D_h is the hydraulic diameter, equal to one side of a square flow cross section, and k is the fluid thermal conductivity. It should be noted that the value of $\mathrm{Nu}(x)$ at the same cross section varies between the sidewalls of the flow passage. The right, left, leading, and trailing sidewalls have different heat transfer coefficients because of different flow conditions.

In order to assure the data reliability, all measurements were made and continuously sampled after the stable condition had been reached. The temperatures stabilized approximately 40 minutes after the heater power and motor were turned on.

Uncertainty Analysis. The method of single sample experiments [10] was utilized to estimate the uncertainties in the heat transfer coefficients. In the present study, the result function is Nu in Eq. (2). Substituting the expression given in Eq. (1) for $h(x)$,

$$\begin{aligned}\mathrm{Nu}(x)&=q''D_h/[k\Delta T(x)]\\&=(IV-Q')/[D_hk\Delta T(x)]\end{aligned} \qquad (3)$$

or

$$\mathrm{Nu}(x)=(0.278\ G\ C_p\Delta T_g)/[D_hk\Delta T(x)] \qquad (4)$$

Here, I is the heating current supplied to the film heaters; V, the voltage applied across the heaters; Q', the heat loss; G, the air flow rate; C_p, the specific heat of the air; $\Delta T_g = T_{\mathrm{out}} - T_{\mathrm{in}}$; T_{out} and T_{in}, the air temperatures at the outlet and inlet of the test section, respectively. All thermocouple measurements were recorded using a model DFP 38 trend recorder/data logger (by Wahl Instruments Inc.). The uncertainty in these temperature measurements is estimated to be ±1°C. Typical values of $\Delta T(x)$ are 14°C and 18°C at the inlet and outlet, respectively. The value of ΔT_g is around 15°C. The uncertainty in the heat transfer coefficient depends more strongly on $\Delta T(x)$ than on ΔT_g. The typical nondimensional uncertainty intervals for the variables in Eq. (4) are estimated as follows:

Specific heat of air	C_p	±0.5 percent
Hydraulic diameter of flow passage	D_h	±0.5 percent
Air flow rate	G	±5.0 percent
Thermal conductivity of air	k	±0.5 percent
Temperature	T	±5.5–8.3 percent

The dimensionless uncertainty interval for the Nusselt number is found to be in the range of ±12.6 to ±14.1 percent. It is disclosed that heat transfer performance under constant heat flux conditions is characterized by more uniform uncertainty over the entire flow passage than the uniform wall temperature case because of more uniform wall-to-air temperature differences. The uncertainty in the Nusselt number increases with a decrease in heat flux, implying a reduction in ΔT_g. Furthermore, the uncertainty along x/D_h is different for different values of $\Delta T(x)$. A maximum uncertainty of Nusselt number up to 23 percent occurs at the lowest heat transfer coefficient on the leading surface in the rotational case.

Results and Discussion

The convective heat transfer performance inside of a rotating serpentine flow passage is governed by the flow velocity, wall heat flux, and rotational speed. In other words,

$$\mathrm{Nu}=f(\mathrm{Re},\ \mathrm{Ro},\ \mathrm{Ra}) \qquad (5)$$

where

$$\begin{aligned}&\mathrm{Re}=\text{Reynolds number}=uD_h/\nu\\&\mathrm{Ro}=\text{Rossby number}=\Omega D_h/u\\&\mathrm{Ra}=\text{rotational Rayleigh number}=\Delta TR(\mathrm{Ro\ Re})^2\ \mathrm{Pr}/(T\ D_h)\end{aligned} \qquad (6)$$

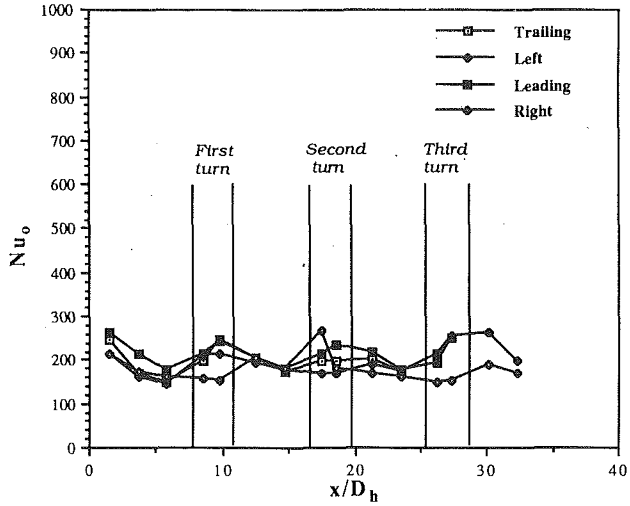

(a) Re=4.4 X 10^4 and Ro=0

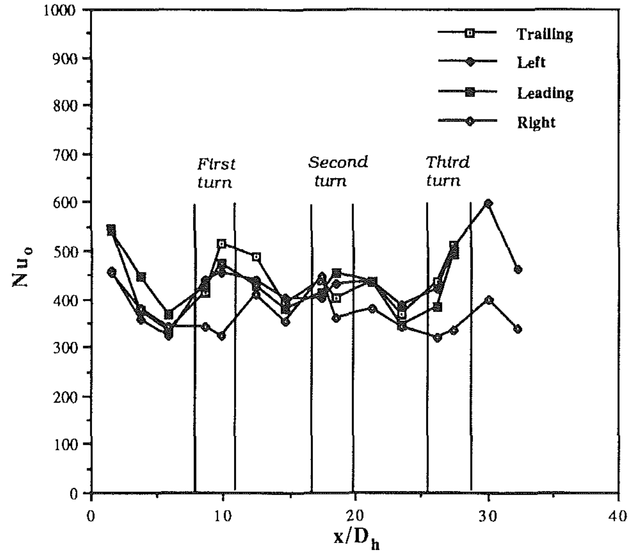

(b) Re=1.1 X 10^5 and Ro=0

Fig. 5 Local heat transfer performance in a stationary (Ro = 0) serpentine flow passage, at (*a*) Re = 4.4 × 10^4 and (*b*) Re = 1.1 × 10^5

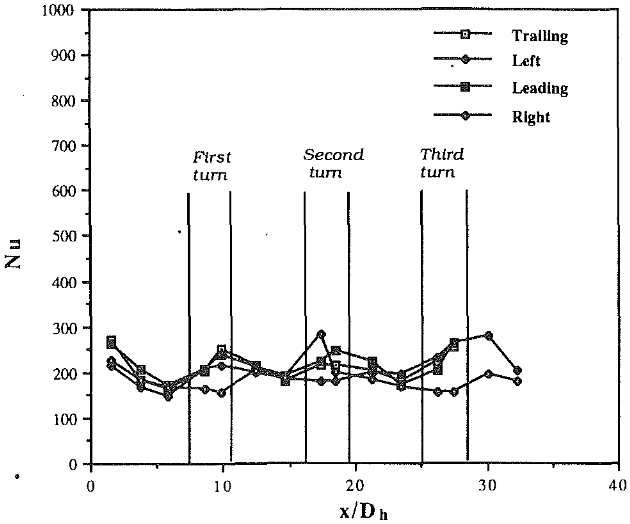

(a) Re=4.4 X 10^4 and Ro=0.017

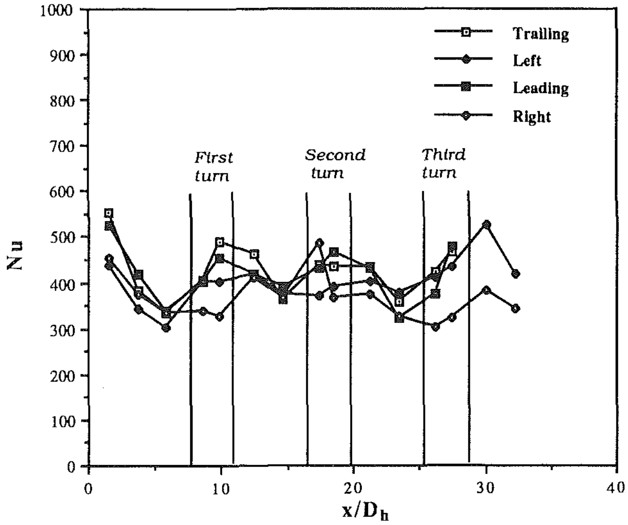

(b) Re=1.1 X 10^5 and Ro=0.017

Fig. 6 Local heat transfer performance in a rotating (Ro = 0.017) serpentine flow passage, at (*a*) Re = 4.4 × 10^4 and (*b*) Re = 1.1 × 10^5

u denotes the mean flow velocity in the flow passage; ν, kinematic viscosity; Ω, rotational speed; ΔT, difference between the wall temperature and the bulk air temperature; R, mean radius of rotation; and Pr, Prandtl number. T in the absolute scale is equal to the reciprocal of β, the coefficient of thermal expansion. ΔT is defined as

$$\Delta T = q''\ D_h/k \tag{7}$$

Therefore,

$$\mathrm{Ra} = \beta q'' R(\mathrm{Re\ Ro})^2 \mathrm{Pr}/k \tag{8}$$

The fluid flow rate, heating rate, and rotational speed of the rotor were varied to produce various values of Re, Ro, and Ra. Both stationary and rotating cases were investigated. The former served as the basis to determine the effects of rotation on the heat transfer performance. Representative results are presented in Figs. 5–10. The abscissa denotes the ratio of the distance x to the hydraulic diameter D_h, with x being measured along the centerline from the flow entrance. In the first straight pass (from the entrance to $x/D_h = 7.5$), the fluid flows radially outward. It is followed by the first turn, in which the flow makes a 180-deg turn. The succeeding flow is radially inward until the second 180-deg turn, and so on. At the end of the fourth straight pass, the fluid exits into a hollow portion of the rotating axis, and is exhausted into the atmosphere.

Figure 5 shows the heat transfer characteristics in a nonrotating four-pass serpentine square channel. It serves as the reference case (no rotation) so that the effects of rotation may be determined by comparison. In the first straight pass (with radially outward flow), all four side walls exhibit the effects of a thermal entrance region: decreasing Nu_0 with increasing nondimensional distance, x/D_h, from the entrance. Nu_0 on the right wall drops continuously to a minimum in the first turn. In contrast, Nu_0 at the three other sidewalls increases and peaks in the first turn, with greatest Nu_0 at the trailing surface. This significant enhancement in heat transfer is due to the presence of secondary flow in the bend. In the second straight pass (radially inward flow), only the right sidewall shows an increase in Nu_0 due to the impingement of a secondary flow coming from the outside corner of the bend. The other three sidewalls experience "quasi-entrance region effect" induced by the second flow. The heat transfer performance in the second turn is the same as that in the first turn, except that the performance of the left and right walls are switched. The heat transfer performance in the first turn and first and second straight passes is repeated in the third turn and third and fourth straight passes. In short, significant enhancement in heat transfer performance is observed only in the sharp turns, due to the generation of secondary flows. The local Nusselt number Nu_0 of each sidewall remains practically the same in all straight passes.

A comparison of Figs. 5(*a*) and 5(*b*) reveals the effect of flow rate on local heat transfer performance: An increase in Re raises but preserves the shape of the Nu_0 versus x/D_h curve.

Figure 6 illustrates the local heat transfer performance for the rotating case of Ro = 0.017. A comparison of Figs. 5(*a*) and 6(*a*) for flow at $Re = 4.4 \times 10^4$ indicates that rotation fails to alter the nature of heat transfer phenomena in the serpentine passage. The magnitude of the local Nusselt number is changed only slightly by the rotation. This is also true at $Re = 1.1 \times 10^5$, as seen by comparing Figs. 5(*b*) and 6(*b*). However, a comparison of Figs. 6(*a*) and 6(*b*) reveals that an increase in Re causes a significant increase in Nu, although the shape of the Nu-Re curve is practically unchanged. A similar situation is observed at a higher rotational speed, Ro = 0.042 (not shown).

The ratio of Nu for rotating cases to Nu for stationary cases, Nu/Nu_0, is shown in Fig. 7. The deviation of this ratio from unity indicates the change in local heat transfer performance due to rotation. A ratio of greater than unity signifies an enhancement, while that of less than unity signifies a retardation. Results are presented in Fig. 7 for three cases: (*a*) $Re = 4.4 \times 10^4$, Ro = 0.017, (*b*) $Re = 4.4 \times 10^4$, Ro = 0.042, and (*c*) $Re = 1.1 \times 10^5$, Ro = 0.017. A comparison of cases (*a*) and (*b*) reveals the effect of rotation, Ro, on Nu/Nu_0, and a comparison of cases (*a*) and (*c*) reveals the effect of throughflow rate, Re, on Nu/Nu_0. It is seen in Fig. 7(*a*) that the heat transfer performances on the left and right walls are enhanced at different levels. The maximum enhancement due to rotation is about 12 percent (i.e., $Nu/Nu_0 \cong 1.12$) for the left and right sidewalls located at the third straight pass and at the second turn, respectively.[†] The local heat transfer coefficient on the trailing wall is enhanced greatly in the first straight pass, slightly at the first turn, and strongly at the

---

[†] Three repeated experiments were made and it was found that the variation between them is within 3.7 percent.

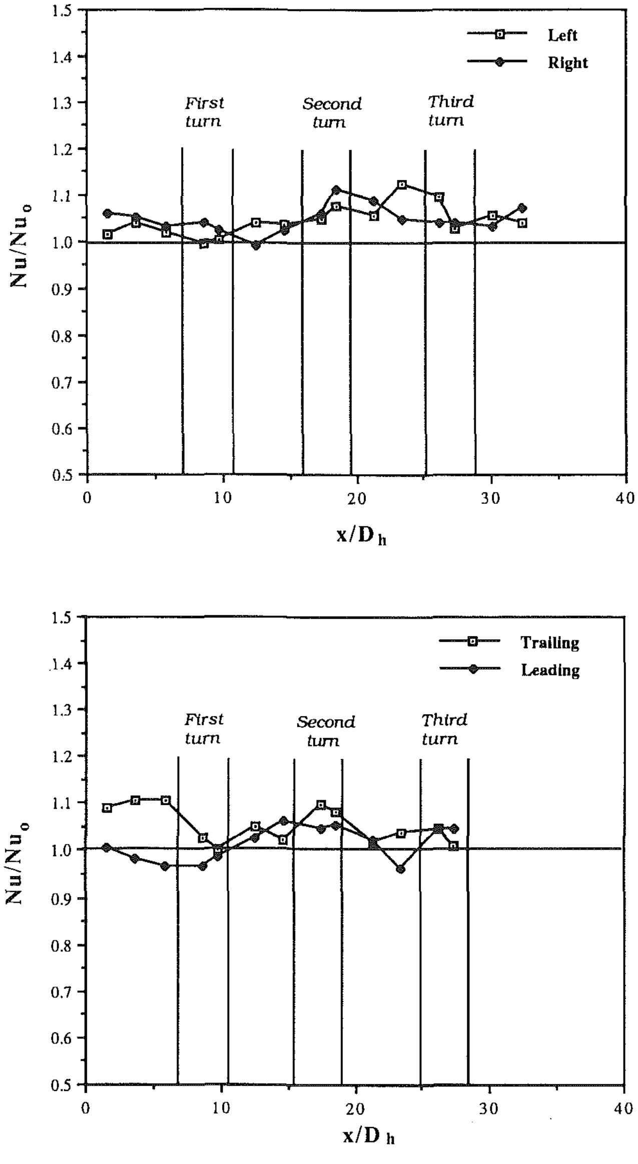

Fig. 7(a)

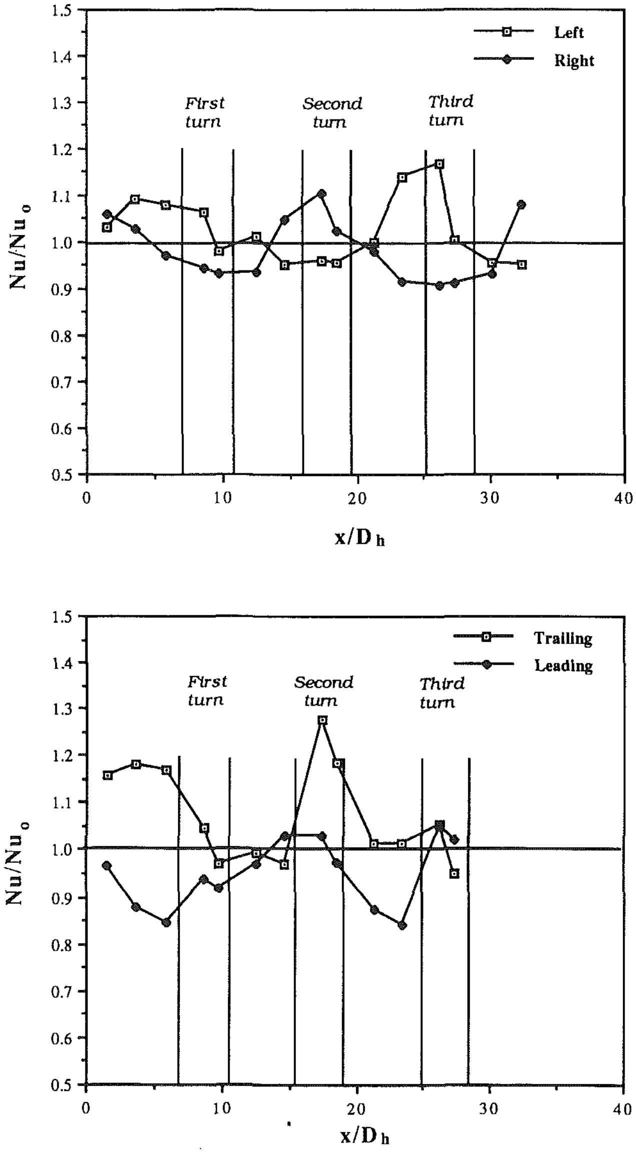

Fig. 7(b)

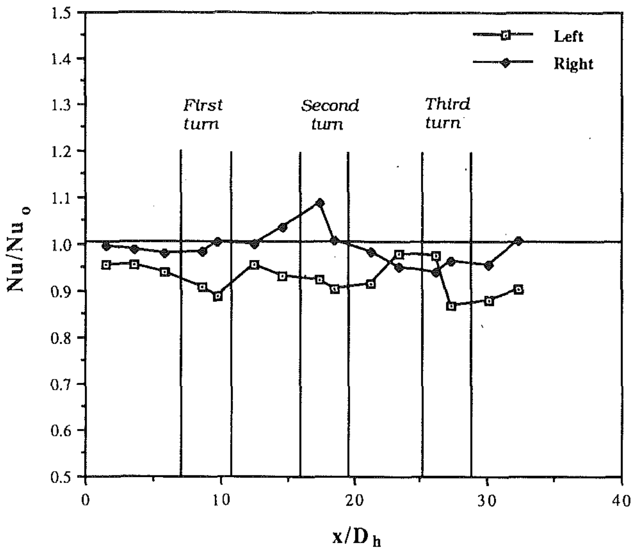

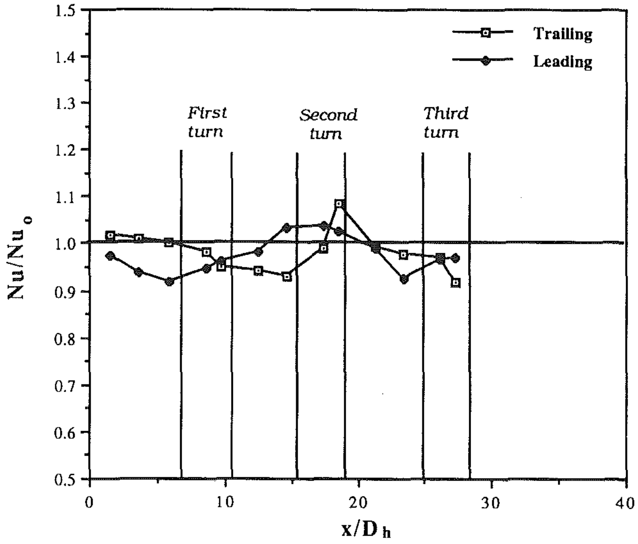

Fig. 7(c)

Fig. 7 Effect of rotation on local heat transfer performance for (*a*) Re = 4.4 × 10^4, Ro = 0.017, (*b*) Re = 4.4 × 10^4, Ro = 0.042, and (*c*) Re = 1.1 × 10^5, Ro = 0.017

second turn. At both the first straight pass and the second turn, the enhancement reaches a maximum value of 10 percent. The coefficient distribution on the leading wall follows a different pattern: It is gradually retarded in the first straight pass but recovers at the first turn, followed by an increase until the second turn. It then repeats the same cycle but with more rigorous change. The minimum enhancement on the left and right sidewalls as well as on the trailing surface (pressure side) is zero. About 5 percent retardation in heat transfer performance due to rotation occurs on the leading surface (suction side). As the rotational speed is increased to Ro = 0.042, Fig. 7(*b*), heat transfer retardation takes place on both the left and right sidewalls. More than one half of the right sidewall in the flow direction suffers severe retardation: almost 10 percent at the worst section. The local heat transfer performance is enhanced on the left wall in the first and third straight passes (centrifugal channels) but retarded in the second straight pass (centripetal channel). However, it undergoes a practically opposite cycle on the right wall. Meanwhile, the distribution patterns of the local heat transfer coefficient on the trailing and the leading walls are the same as the patterns of Ro = 0.017, but are of much larger amplitude (i.e., both enhancement and retardation are greatly increased). The worst retardation is experienced by the leading surface, with retardation as high as 16 percent. Conversely, the trailing surface experiences up to 27 percent heat transfer enhancement. It is obvious that the Coriolis force plays an important role. Figure 7(*b*) gives the best evidence of the effects of the Coriolis force. In this case, the leading and trailing surfaces compensate for each other, i.e., a significant loss on the leading surface is made up for by an equally significant gain on the trailing surface. The net effect of rotation on Nu/Nu_0 is almost nil. Note that the curves of Nu/Nu_0 versus x/D_h for the leading and trailing surfaces cross at every sharp turn, as seen in Fig. 7(*c*). The case of Re = 1.1 × 10^5 and Ro = 0.017 is even less favorable to heat transfer performance than the stationary case of Re = 1.1 × 10^5. The benefits of higher Re (1.1 × 10^5 versus 4.4 × 10^4) realized in the case of Fig. 5(*b*) has been suppressed by the increase in Ro.

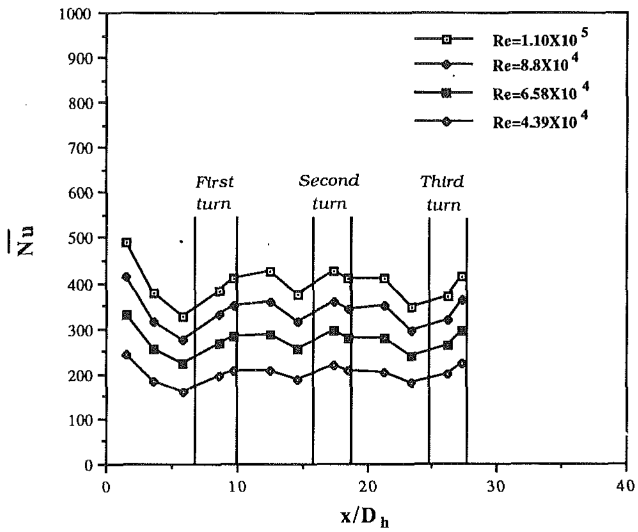

Fig. 8 Effect of Re on circumferentially averaged Nu at Ro = 0.017

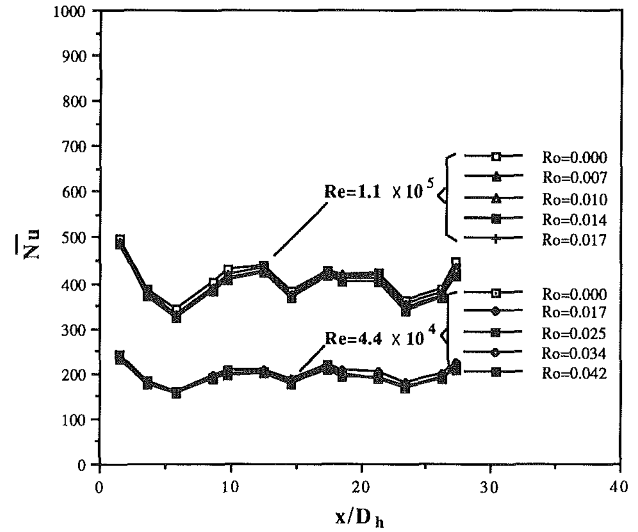

Fig. 9 Effect of Ro on circumferentially averaged Nu at Re = 4.4 × 10^4 and 1.1 × 10^5

Although the local heat transfer performance on each wall is very important, sometimes circumferentially averaged heat transfer coefficients are more relevant. The distribution of the circumferentially averaged Nusselt number, $\overline{Nu}$, is plotted in Fig. 8 for a constant Ro (= 0.017) and various values of Re.

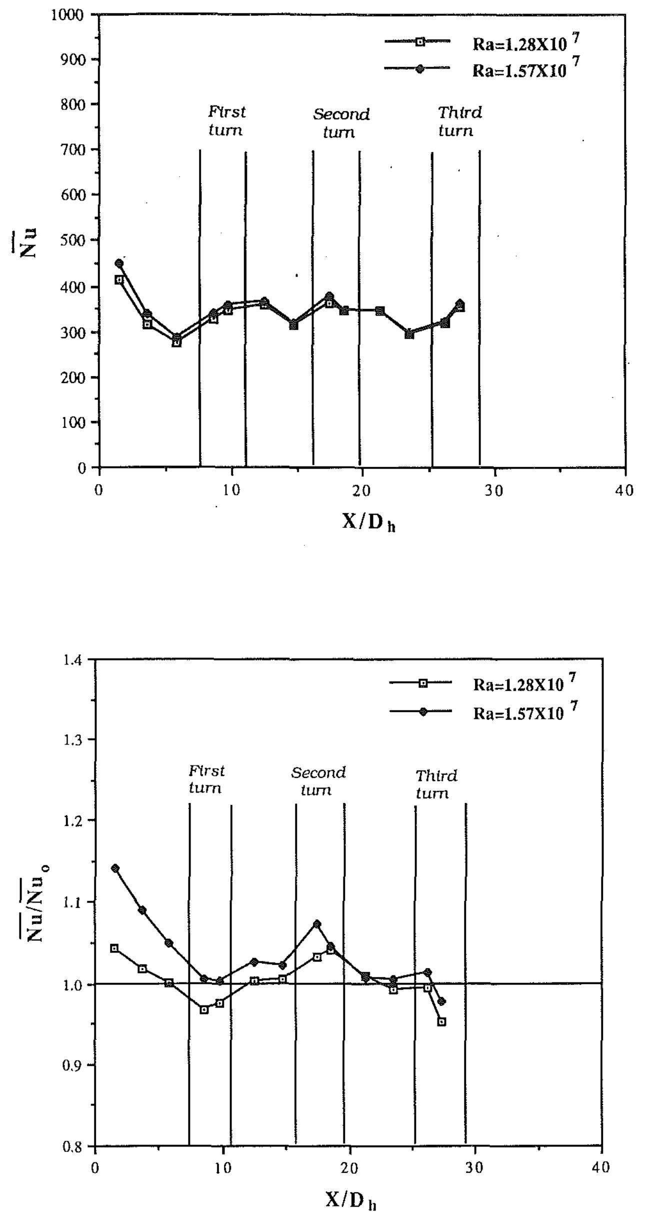

Fig. 10 Effect of Ra on circumferentially averaged Nu at Ro = 0.021 and Re = 8.85 × 10^4

One observes that $\overline{Nu}$ decreases with x/D_h in the first straight pass due to the entrance region effect. After reaching a minimum value, it increases in the first turn due to secondary flow. The pattern repeats at every straight pass-sharp turn cycle. The value of $\overline{Nu}$ increases with an increase in Re, with the distribution curve, i.e., $\overline{Nu}$ versus x/D_h, being parallel for the different values of Re.

The effect of rotation on the distribution of $\overline{Nu}$ is depicted in Fig. 9 for two different values of Re, 4.4 × 10^4 and 1.1 × 10^5. The effect of rotation on the $\overline{Nu}$ distribution is negligible at both Reynolds numbers. The values of $\overline{Nu}$ for Re = 4.4 × 10^4 fluctuate about 200, while the value of $\overline{Nu}$ for Re = 1.1 × 10^5 fluctuate about 400. The variation of $\overline{Nu}$ along the flow passage is small and nearly periodic.

Figure 10 shows the effect of Ra on $\overline{Nu}$ and $\overline{Nu}/\overline{Nu}_0$ at Ro = 0.021 and Re = 8.85 × 10^4. $\overline{Nu}$ reflects the effects of buoyancy gradients. One observes that the effect is most prominent in the first straight pass and diminishes along the flow passage. This trend holds for other combinations of Ro and Re.

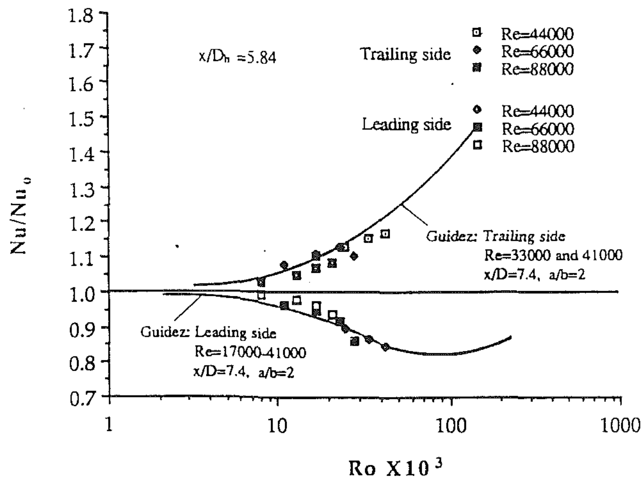

Fig. 11 Variation of local heat transfer performance with Rossby number Ro for centrifugal channel (first passage) and a comparison with Guidez [3]

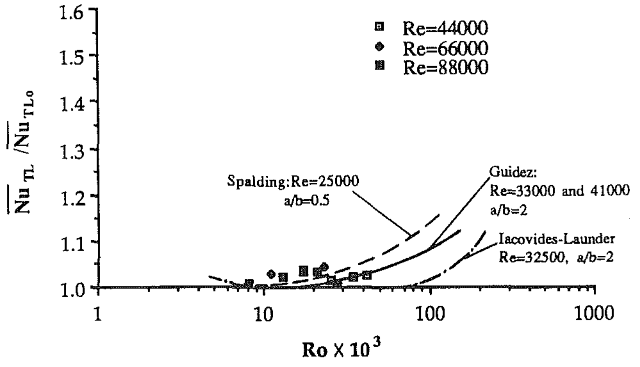

Fig. 12 $\overline{Nu}_{TL}/\overline{Nu}_{TL_0}$ versus Rossby number Ro for centrifugal channel (first passage) and a comparison with Guidez [3], Spalding [7], and Iacovides-Launder [8]

A comparison between the results of the present study and the results of the study performed by Guidez [3] (solid lines) is shown in Fig. 11. The two results agree quite well. The discrepancy is probably due to the difference in aspect ratios, 1 in the present study and 2 in the Guidez's case. Figure 12 plots $\overline{Nu}_{TL}/\overline{Nu}_{TL_0}$ against Ro. Here, $\overline{Nu}_{TL}$ is the value of Nu averaged over the trailing and leading walls of the first passage, $\overline{Nu}_{TL_0}$ is the value of Nu_0 averaged over the trailing and leading walls of the first passage, and Ro is the Rossby number. The results of Guidez [3], Spalding [7], and Iacovides-Launder [8] are superimposed on the figure for comparison. It should be noted that the Coriolis force has opposite effects on the trailing and leading sides. Hence, the enhancement in heat transfer performance on the trailing side by the Coriolis force is partly offset by a reduction in the heat transfer performance on the leading side.

A comparison between the present study and the study by Wagner et al. [2, 9] is not possible due to a lack of a common reference basis. Nevertheless, it is noted that the two studies have yielded a similar trend in the heat transfer performance in rotation.

The effects of the ratio L/R (L is the length of each of the four parallel ducts in the test section, and R is the length of arm in rotation) on heat transfer performance is not investigated in the present study due to the physical limitations of the experimental setup. The construction of a new setup is under way to determine the effects of various geometric and operational parameters on heat transfer performance. Iacovides and Launder [8] theoretically predicted the distribution of the local normalized Nusselt number (Nu/Nu_0) around square and rectangular cross sections and showed that the value at the middle is higher than that at the corners. This result needs further experimental verification, which is a very difficult task because measurements must be made of both the wall and air temperature distributions across the flow cross section at each location in the duct. In the present work, the temperatures on the centerline of each wall were used as the representative local wall temperatures of each wall at the cross sections. This may cause a little error, which cannot be accurately estimated.

Conclusions

The internal (i.e., convective) cooling of turbine blades is idealized by the cooling of a four-pass serpentine passage. The local heat transfer coefficients of the passage surface are determined together with their circumferentially averaged values. It is disclosed from the study that:

(*i*) A significant enhancement in heat transfer performance is achieved at all sharp turns due to strong secondary flow.

(*ii*) The variation of Nusselt numbers, both local and circumferentially averaged, along the flow passage is nearly periodic. This signifies the achievement of the thermally developed condition at the first turn.

(*iii*) Although rotation has a great effect on the local heat transfer performance, it has little effect on the circumferentially averaged heat transfer coefficients for the rotational speeds tested. This may imply that for a given flow rate, the thermal condition has been fully developed by the complex secondary flow at the sharp turns. Therefore, additional disturbance by rotation can no longer augment the performance.

(*iv*) The throughflow rate can significantly enhance the heat transfer performance, as it is known that the Nusselt number is a function of the Reynolds number in convective heat transfer.

(*v*) The enhancement of the local heat transfer performance due to an increase in the rotational Rayleigh number is most prominent near the entrance but diminishes along the flow passage.

Acknowledgments

This study was supported by the Electric Power Research Institute under Contract No. 8006-11.

References

1 Hajek, T. J., and Higgins, A. W., "Coolant Passage Heat Transfer With Rotation," NASA Contract NAS 3-23691, United Technologies Corporation, 1984, pp. 187–201.

2 Wagner, J. H., Johnson, B. V., and Hajek, T. J., "Heat Transfer in Rotating Passages With Smooth Walls and Radial Outward Flow," ASME *Journal of Turbomachinery*, Vol. 113, 1991, pp. 42–51.

3 Guidez, J., "Study of the Convective Heat Transfer in a Rotating Coolant Channel," ASME *Journal of Turbomachinery*, Vol. 111, 1989, pp. 43–50.

4 Mochizuki, S., and Yang, W. J., "Local Heat Transfer Performance and Mechanisms of Radial Flow Between Parallel Disks," *Journal of Thermophysics and Heat Transfer*, Vol. 1, 1987, pp. 112–116.

5 Sakamoto, M., "Research on Convective Cooling of Rotating Electric Machinery," Report, Toshiba Central Research Institute, 1973.

6 Chyu, M. K., "Regional Heat Transfer in Two-Pass and Three-Pass Passages With 180-deg Sharp Turns," ASME JOURNAL OF HEAT TRANSFER, Vol. 113, 1991, pp. 63–70.

7 Spalding, D. B., and Skiadaressis, D., "Heat Transfer in Ducts Rotating Around a Perpendicular Axis," *6th Int. Heat Transfer Conference*, Vol. 2, Toronto, Canada, 1978, pp. 91–95.

8 Iacovides, H., and Launder, B. E., "Parametric and Numerical Study of Fully Developed Flow and Heat Transfer in Rotating Rectangular Ducts," ASME *Journal of Turbomachinery*, Vol. 113, 1991, pp. 331–338.

9 Wagner, J. H., Johnson, B. V., and Kopper, F. C., "Heat Transfer in Rotating Serpentine Passages With Smooth Walls," ASME *Journal of Turbomachinery*, Vol. 113, 1991, pp. 321–330.

10 Kline, S. J., and McClintock, F. A., "Describing Uncertainties in Single Sample Experiments," *Mechanical Engineering*, Vol. 75, 1953, pp. 3–8.

J. H. Lienhard V
Associate Professor.
Mem. ASME

X. Liu
Research Assistant.
Student Mem. ASME

L. A. Gabour
Research Assistant.

Department of Mechanical Engineering,
Massachusetts Institute of Technology,
Cambridge, MA 02139

Splattering and Heat Transfer During Impingement of a Turbulent Liquid Jet

Splattering and heat transfer due to impingement of an unsubmerged, fully turbulent liquid jet is investigated experimentally and analytically. Heat transfer measurements were made along a uniformly heated surface onto which a jet impacted, and a Phase Doppler Particle Analyzer was used to measure the size, velocity, and concentration of the droplets splattered after impingement. Splattering is found to occur in proportion to the magnitude of surface disturbances to the incoming jet, and it is observed to occur only within a certain radial range, rather than along the entire film surface. A nondimensional group developed from inviscid capillary disturbance analysis of the circular jet successfully scales the splattering data, yielding predictive results for the onset of splattering and for the mass splattered. A momentum integral analysis incorporating the splattering results is used to formulate a prediction of local Nusselt number. Both the prediction and the experimental data reveal that the Nusselt number is enhanced for radial locations immediately following splattering, but falls below the nonsplattering Nusselt number at larger radii. The turbulent heat transfer enhancement upstream of splattering is also characterized.

1 Introduction

Liquid jets are often directed onto hot surfaces to provide simple and efficient cooling. Such jets typically issue from a nozzle at the terminus of a pipe, or similar manifolding system, and may be encountered in a wide range of manufacturing, laser-heated, or electronic systems. Quenching of steels during rolling processes, or, conversely, cooling of the rollers themselves during hot rolling, are just two common examples. Circular liquid jets are of particular value in creating extremely high heat transfer coefficients over relatively localized areas. The corresponding piping systems have the added attraction of being inexpensive and easy to install.

In our previous papers (Liu and Lienhard, 1989; Liu et al., 1991), we discussed the heat transfer characteristics of an unsubmerged, impinging laminar liquid jet issuing from a sharp-edged orifice. In the latter paper, disturbances to the experimental liquid supply were carefully damped so as to create uniform-velocity profile, laminar jets having very stable, undisturbed free surfaces. While that configuration is well suited for examining the physical mechanisms of jet impingement cooling, in applications such as those mentioned above, the piping or manifolding systems are likely to generate turbulence in the liquid supply. The resultant liquid jets are turbulent and have heavily disturbed surfaces, which make them susceptible to the highly undesirable effect of splattering after they strike the target surface (Fig. 1).

When a jet splatters, much of the incoming liquid can become airborne, as droplets, within a few jet diameters of the point of impact. Airborne liquid no longer contributes to the cooling of the liquid surface, and in consequence, cooling is far less efficient than it could be if splattering were suppressed. Understanding the causes and scaling of splattering is thus an essential element in jet cooling system design.

The basic physical mechanism of splattering has been described by Errico (1986). Disturbances to the surface of the incoming jet are strongly amplified as the jet spreads into a liquid film along a wall normal to the axis of the jet (Fig. 1*b*, *c*). The associated flow regimes along the surface can be characterized in an average sense as follows (Fig. 2):

1. *Stagnation Zone*: A very thin wall boundary layer with a turbulent free stream above it.
2. *Region Before Splattering*: Disturbances to the liquid sheet are strongly amplified in this region. As in the stagnation zone, the wall boundary layer is affected by turbulent and capillary disturbances to the flow above it.
3. *Region of Splattering*: A portion of the liquid sheet breaks free as droplets, owing to the instability of the disturbed liquid sheet. The effective radial size of this zone is fairly small.
4. *Region After Splattering*: Having lost both mass and momentum in the splattering process, the remaining liquid sheet continues to flow outward. The liquid sheet is fully turbulent.

Errico's experiments on the splattering of impinging jets demonstrated that jet splatter is directly tied to the surface roughness or deformation of the incoming liquid jet, that jet splatter is reduced by making the jet shorter (so that disturbances to the liquid jet have less time to develop), and that jet stability is related to the specific nozzle design. Errico also found that onset of splattering in jets forced at their breakup frequency varies with Re_d, We_d, and the ratio of jet length to jet diameter.

Splattering and turbulence both produce additional mixing in the liquid sheet, which will tend to enhance heat transfer relative to a laminar sheet. Conversely, the wall friction will be generally lower for laminar flow, which should result in larger velocities at a given downstream radius. The relative cooling efficiency of these cases is not obvious *a priori*, apart from the expectation that turbulence enhances heat transfer in the stagnation zone. Additionally, turbulence and splattering are closely related, with splattering both being driven by turbulence and adding fluctuating disturbances to the film, so that these effects must be accounted for simultaneously in attempting to model the heat removal. Presumably, the jet Reynolds and Weber numbers will appear as controlling parameters.

Since the initial condition of the jet and the subsequent flow

---

Contributed by the Heat Transfer Division and presented at the 27th National Heat Transfer Conference, Minneapolis, Minnesota, July 27–29, 1991. Manuscript received by the Heat Transfer Division April 1, 1991; revision received July 31, 1991. Keywords: Forced Convection, Jets, Sprays/Droplets.

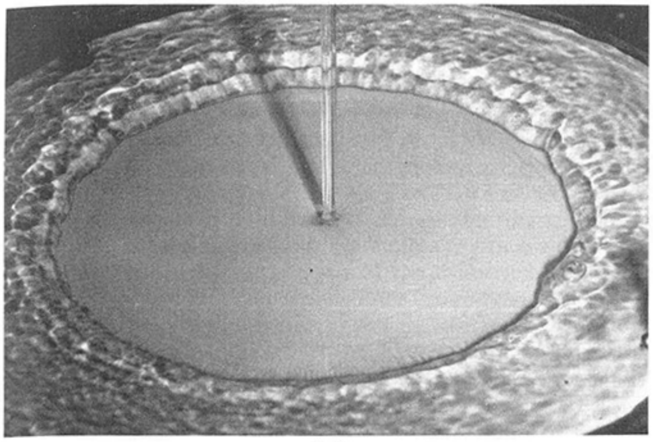
(*a*)

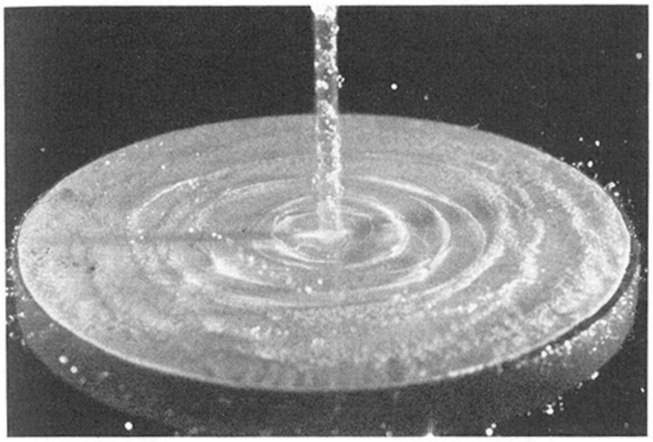
(*b*)

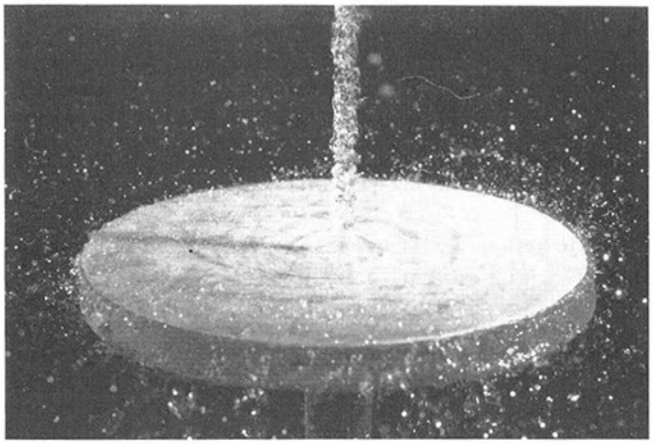
(*c*)

Fig. 1 (*a*) Laminar jet at $\mathrm{Re}_d = 51{,}500$ (depth of 9.2 mm beyond hydraulic jump); (*b*) splattering jet at $\mathrm{Re}_d = 28{,}400$, $\omega = 4550$, and $\xi = 0.108$; (*c*) splattering turbulent jet at $\mathrm{Re}_d = 48{,}300$, $\omega = 8560$, $\xi = 0.311$ (no jump)

behavior are strongly dependent on the specific nozzle configuration, there arises the question of how best to explore the heat transfer performance of different nozzles. Most nozzle systems seek to minimize pressure drop by using a relatively large diameter liquid supply line followed by a contracting nozzle. The liquid supply may reasonably be assumed to have reached fully developed turbulent flow, and this turbulence will be partially damped by the nozzle. Actual nozzle conditions are thus bounded at one extreme by a stable laminar jet (as achieved by a sharp-edged orifice nozzle by Liu et al., 1991) and at the other extreme by a fully developed turbulent jet (as achieved by a sufficiently long tube with no outlet contraction). Other types of nozzles will generally fall between these two, having a somewhat lower turbulence intensity than in fully developed pipe flow, and their heat transfer behavior should be bounded by the laminar and fully turbulent jets.

The mean velocity profile of the jet will also affect convective heat removal, particularly in the stagnation zone. The sharp-edged orifices used in our previous studies are known to produce a uniform velocity profile about one diameter downstream of the orifice. The turbulent pipe jets studied herein have a relatively flat velocity profile as well. A recent study of planar jets (Wolf et al., 1990) concluded that velocity profile effects on stagnation zone heat transfer were pronounced for laminar flows, but suggested that, for turbulent jets, the velocity profile was relatively unimportant in comparison to the stronger influence of turbulent mixing. In this light, we expect that velocity-profile effects are less important in what follows than are the effects of turbulence. However, measurements independently varying turbulence intensity and velocity profile are needed to resolve fully the role of mean velocity profile in

Nomenclature

a = liquid jet radius
A_{rms} = mean jet-radius disturbance amplitude when jet strikes plate
C = scaled nozzle-outlet turbulence intensity = $0.195 \times \sqrt{2}(q'/u_f)^2$
C_s = const
C_f = friction factor = $\tau_w/(1/2\,\rho u_{\max}^2)$
c_p = specific heat capacity per unit mass at constant pressure
d = liquid jet diameter
D = temporal volumetric mean diameter of splattered droplets at a given height
$h(r)$ = local mean thickness of liquid sheet
h_c = equivalent mean thickness of liquid sheet containing same momentum as actual sheet after splattering
h_s = mean liquid sheet thickness at the position just before splattering occurs
h^* = mean thickness of liquid sheet at the position just after splattering occurs
k = liquid thermal conductivity
l = distance between nozzle and target
Nu_d = local Nusselt number = $q_w d/k(T_w - T_f)$
p' = rms turbulent fluctuation of liquid pressure
$p'_{\max}$ = pressure disturbance amplitude at wavelength of maximum instability
Pr = liquid Prandtl number
q' = rms magnitude of turbulent velocity vector at nozzle outlet
q_w = wall heat flux, uniform
Q = total volume flow rate of jet = $\pi/4\,d^2 u_f$
Q'' = volume flow rate of splattered liquid per unit height above the plate
r = radius, measured from point of jet impact
r_m = radius of droplet profile measurement
r_s = effective radius of splattering region
R_1, R_2 = principal radii of curvature for liquid surface
Re_d = Reynolds number of the jet = $u_f d/\nu$

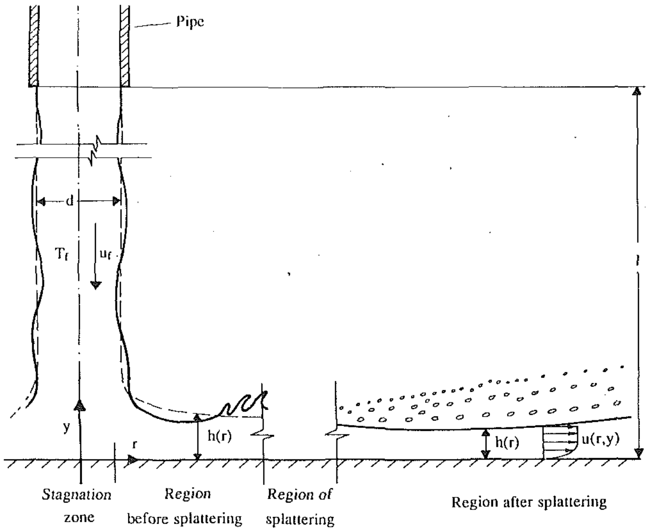

Fig. 2 Regions for turbulent incoming jet: ——— instantaneous liquid surface; --- mean liquid surface

turbulent jets, particularly for those jets having a large nonuniformity of mean velocity.

In this work, we investigate heat removal by fully turbulent liquid jets both with and without splattering. Our method is to combine relatively simple models of the mechanism of liquid splattering with phase-Doppler measurements of the splattered droplets' size and velocity to create a predictive model for the mass lost to splattering and the radial location of splatter. We then use this information to model the consequences of splattering for the efficiency of convective heat removal by the jet-induced liquid sheet, and we compare the model's results to measurements of the local Nusselt number along the wall.

Our analysis employs the momentum integral procedure, reflecting our attention to the average behavior of a physical process that is far too complex for exact analytical solution. Moreover, the momentum integral procedure has been found to facilitate relatively clear and general descriptions of the varying radial characteristics of the film flow (Liu and Lienhard, 1989); alternative, numerical procedures cannot provide any useful generality for the whole range of radius, although they show some promise for the stagnation zone (Liu et al., 1992).

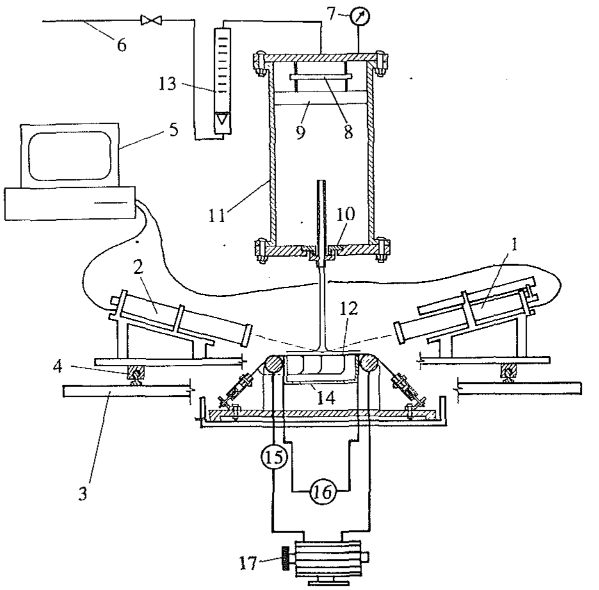

Fig. 3 Experimental apparatus: (1) PDPA laser transmitter; (2) PDPA receiver; (3) vertical traversing table; (4) horizontal rail bearings; (5) PDPA electronics; (6) water supply line; (7) pressure gage; (8) strike plate; (9) honeycomb; (10) tube support plate; (11) plenum; (12) instrumented heater sheet; (13) flowmeter; (14) insulating box; (15) electrical leads; (16) voltmeter; (17) high-current, low-voltage electric generator, 25 kW

2 Experiments

Experiments were performed to measure the splattered mass and heat transfer for a fully developed, turbulent liquid jet. The experimental jets were produced using long tubes (50 to 100 dia long; 3.2–9.5 mm dia), which received liquid water from a pressurized plenum and issued into still air (Fig. 3). The outlet of each pipe was carefully smoothed and deburred so that surface disturbances in the liquid jets were produced solely by the turbulence of the jets. The initial conditions for the jet should thus depend only on Reynolds number. Contraction of the turbulent jets causes less than a 1.5 percent reduction in diameter, in contrast to the large contraction for sharp-edged orifice jets. Jet velocity was determined using a flow meter (primary calibration of the meter was performed). The jets struck a thin, uniformly electrically heated plane target, which was instrumented for local temperature measurement. The nozzle to plate separation was adjustable over the

Nomenclature (cont.)

s, $s_{\max}$ = growth rate of capillary disturbances, maximum growth rate
St = local Stanton number = $q_w/(\rho c_p u_{\max}(T_w - T_{sf}))$
t = time
T_f = incoming jet temperature, before impingement
$T_{sf}(r)$ = free surface temperature distribution of liquid sheet
$T_w(r)$ = wall temperature distribution
$u(r, y)$ = mean radial velocity distribution in liquid film
u_f = velocity of impinging jet (bulk velocity of flow exiting nozzle)
$u_{\max}$ = local maximum film velocity (liquid free surface velocity); mean value is near u_f in boundary layer region
$u^*, u^*_{\max}$ = liquid velocity, liquid maximum velocity just after splattering
v = mean radial velocity component of splattered droplets at a given height
We_d = jet Weber number = $\rho u_f^2 d/\sigma$
x = fraction of liquid sheet contained in boundary layer at given radius
y = distance normal to the wall
δ = viscous boundary layer thickness
ϵ, $\epsilon_{\max}$ = amplitude, mean amplitude of initial surface of displacement
θ = angle in cylindrical coordinate system
Θ = constant in momentum balance, Eq. (26)
λ, $\lambda_{\max}$ = capillary-disturbance wavelength for jet, most unstable wavelength
ν = kinematic viscosity
ξ = ratio of splattered-liquid volume flow rate to incoming jet volume flow rate
ρ = liquid density
σ = surface tension
Φ = constant in momentum balance, Eq. (18) or (28)
ω = dimensionless group = $\mathrm{We}_d \exp(0.971/\sqrt{\mathrm{We}_d}\cdot l/d)$

range $1.2 \leq l/d \leq 28.7$. The remainder of the experimental apparatus consists of the water jet loop, a refrigerating system, and an electrical heating system. Full details of this equipment, the heater, the instrumentation, and the error analysis are given by Liu et al. (1991).

The distribution of the splattered droplets' velocities and diameters above the target plate were measured using a Phase Doppler Particle Analyzer (PDPA). The PDPA (Aerometrics, Inc.) is an advanced laser-Doppler velocimeter that produces concurrent measurements of an individual particle's diameter and velocity through an analysis of the measured amplitude and phase of the Doppler burst. Since the splattered droplets travel at only a small angle with respect to the target surface (about 20 deg off horizontal), the PDPA was configured to record the radial component of velocity; this component is also that required in the momentum integral analysis below. Owing to ambiguities in the instrument's probe-area correction for the number density calculation, the measured volume flux was independently calibrated by direct measurement of the splattered mass (following Errico, 1986), as shown in Fig. 4; the incoming-jet volume flow and the volume flow remaining in the liquid sheet after splattering were measured at radii corresponding to those used in the PDPA measurements.

The wall temperature increases with radius, and the local Nusselt number is based on the difference between the local wall temperature and the temperature of the incoming jets. The incoming jet temperature was measured using the stagnation point thermocouples with the heater power off (i.e., the adiabatic-wall temperature). As in our previous experiments (Liu and Lienhard, 1989; Liu et al., 1991), evaporative cooling was suppressed by limiting the maximum liquid temperature along the test heater. At the stagnation point, the temperature differences are the smallest and the uncertainty in Nusselt number is the largest when the previously mentioned heater is employed. Thus, a narrower heater strip (3.8 cm wide rather than 15.2 cm wide) was used for separate stagnation zone measurements. This enabled the use of higher heat fluxes (up to 300 kW/m^2) without concern for liquid surface temperature or burning of the test heater; the temperature differences were thus raised to accurately resolvable values for the stagnation point, providing stagnation Nusselt numbers with uncertainties of 10 percent or less. Downstream, the reported Nusselt numbers have uncertainties of only 5 percent. The estimated uncertainty for Re_d is 5 percent and that for r is 0.5 mm.

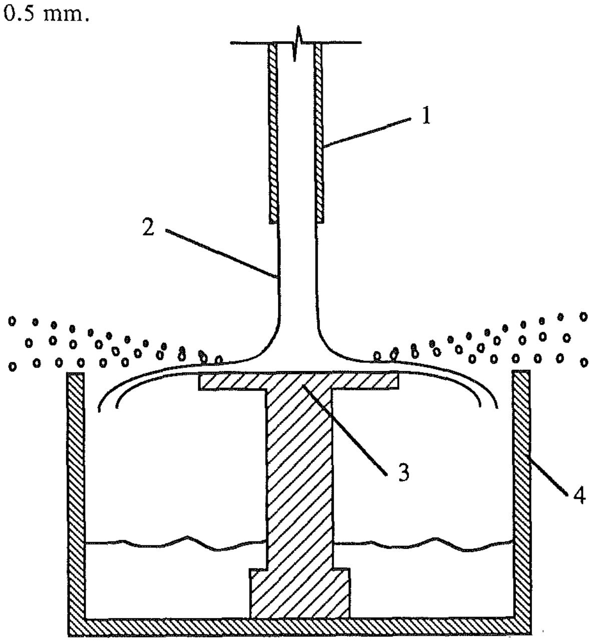

Fig. 4 Direct measurement of splattered mass: (1) tube; (2) liquid jet; (3) target disk; (4) capture tank for unsplattered liquid

Both the wide and narrow heaters were made from 0.1-mm-thick 304SS sheet. Corrections were applied for the conductive temperature difference across the Joule-heated sheet, as described by Liu et al. (1991). These corrections are quite important when Nu_d is large. Omitting them, as some authors apparently have (Faggiani and Grassi, 1990), may cause large errors.

3 Splattering

The vertical distribution of the radial volume flux of splattered droplets was measured for a variety of jet Reynolds numbers, Re_d, jet-to-plate separations, l/d, and radial measuring stations, r_m/d. Representative profiles are presented in Fig. 5(a); the droplet volume flow rate in the radial direction per unit height, Q'' (m^3/s m), is normalized with the total volume flow rate of the incoming jet, Q (m^3/s), and plotted as a function of the vertical distance from the plate surface at given radius. Decreasing the Reynolds number shifts the whole profile to the left. Decreasing the nozzle height has a similar effect, reducing the splattering at all vertical positions. When the profile is measured at larger radius, its basic shape changes;

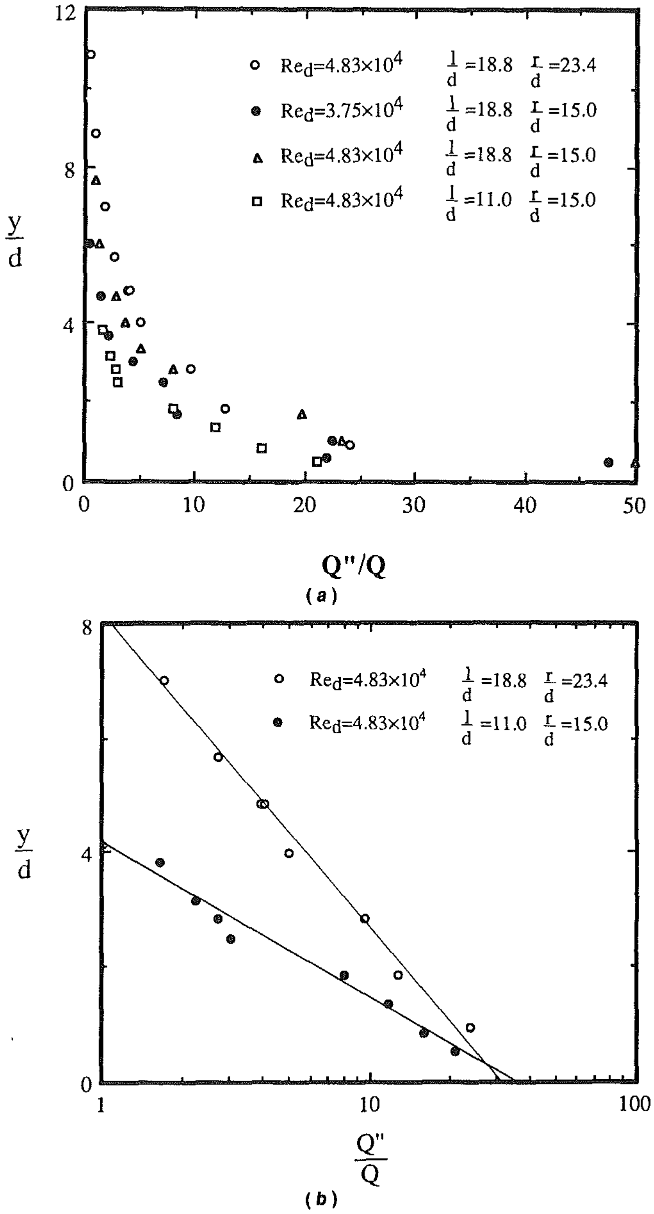

Fig. 5 Vertical distribution of splattered radial liquid volume flow rate divided by total jet volume flow rate, Q''/Q (m^{-1}): (a) linear coordinates; (b) semilogarithmic coordinates

near the wall (small y) the splattered volume flux decreases with increasing radius, but farther from the wall (larger y), the flux decreases less and may even increase. The shape distortion occurs because the droplets travel at an angle relative to the plate, and at larger radius the droplets are spread over a larger area than at small radius.

In semilogarithmic coordinates (Fig. 5*b*), the volume flux distribution is almost a straight line. A line fit may be applied to these curves, corresponding to an exponentially decaying vertical distribution of splattered mass, and the total volume flow rate of splattered droplets may then be obtained by integration. The total volume flow is then used to calibrate the volume flux measurements, as described above.

For the data shown in Fig. 5(*b*), the ratio of total splattered droplet volume flow to total incoming volume flow (which is 0.34) decreases by only about 2.6 percent when the measuring radius is increased from $r_m/d = 15$ to $r_m/d = 24$, holding other variables constant. This difference is within the uncertainty of the measurements, although some decrease may occur as a few large droplets fall back to the liquid sheet under gravity. However, both these measurements and stroboscopic observations by Errico (1986) and by our group show that the actual splattering occurs within a certain radial band around the point of impact; beyond this band, splattering no longer occurs. Hence, the total splattered mass flow, as observed beyond the radius of splattering, will not depend on r/d, but only upon Reynolds number, Weber number, and l/d.

3.1 A Model for Splattering.

The splattering of an impinging jet depends strongly upon the disturbances present on the incoming jet when it reaches the plate. These initial disturbances are sharply amplified when the fluid flows into the thin liquid film surrounding the point of impact, and their magnitude determines both whether or not the jet splatters and the magnitude of the actual splattering. The disturbances undergo substantial distortion upon entering the liquid sheet, with changes in amplitude, wavelength, and wavespeed; rigorous analysis of that development is beyond our present scope. However, we may make substantial progress by considering only the size of the disturbances that the jet delivers to the liquid sheet. Here, we present a model that relates the initial turbulence in the jet to the initial surface disturbances on the jet and their subsequent growth by capillary instability. In this way, we scale the disturbances reaching the liquid sheet that drive actual splattering.

Surface shape is related to the difference between liquid and gas phase pressure, Δp, via the Laplace relation:

$$\Delta p = \sigma\left(\frac{1}{R_1} + \frac{1}{R_2}\right) \tag{1}$$

We assume that the surface disturbances at the nozzle outlet are due primarily to turbulent pressure fluctuations within the jet, which have an rms value of

$$p' \cong \frac{1}{2}\rho(q')^2 = \frac{1}{2}\rho u_f^2\left(\frac{q'}{u_f}\right)^2 \tag{2}$$

The turbulent pressure fluctuations will be distributed over a broad spectrum of wavelengths. The corresponding surface disturbances also show a range of wavelengths, some of which are more unstable than others. Rayleigh's normal mode analysis of circular jet capillary instability (Drazin and Reid, 1981) showed that a disturbance of wavelength λ evolves in time from an initial amplitude ϵ to an amplitude A given by

$$A = \epsilon\exp\left(i[2\pi y/\lambda + m\theta] + st\right) \tag{3}$$

and that the disturbance of maximum growth rate has $\lambda_{\max} = 4.51d$ and $m = 0$. From Eq. (1), the associated initial pressure disturbance amplitude is (Drazin and Reid, 1981)

$$p'_{\max} = -0.514\frac{\sigma\epsilon}{a^2} \tag{4}$$

and the corresponding growth rate may be shown to be

$$s_{\max} = 0.3433\sqrt{\frac{\sigma}{a^3\rho}} \tag{5}$$

Thus, if we equate the rms turbulent pressure disturbance, p', to rms capillary pressure disturbance, $|p'_{\max}|/\sqrt{2}$, we obtain an rms initial surface displacement

$$\frac{\epsilon_{\mathrm{rms}}}{a} \cong 0.781\sqrt{2}\left(\frac{\rho u_f^2 a}{\sigma}\right)\left(\frac{q'}{u_f}\right)^2 \tag{6}$$

The spectral distributions of the turbulent pressure fluctuations and the surface disturbances have been lumped into a single mean disturbance amplitude, so no direct significance should be attached to the coefficient $0.781\sqrt{2}$. However, the physical mechanism relating intensity of pressure fluctuations to the surface displacement should scale as shown irrespective of this approximation.

The liquid travels from the nozzle to the plate in a time $t = l/u_f$, during which the surface disturbance grows from the initial ϵ_{rms} to

$$A_{\mathrm{rms}} = \epsilon_{\mathrm{rms}}\exp(s_{\max}t) = \epsilon\exp\left(0.3433\frac{l}{u_f}\sqrt{\frac{\sigma}{\rho a^3}}\right) \tag{7}$$

Nondimensionalizing yields

$$\frac{A_{\mathrm{rms}}}{d} = C\,\mathrm{We}_d\exp\left(\frac{0.9710}{\sqrt{\mathrm{We}_d}}\frac{l}{d}\right) \tag{8}$$

where the jet Weber number is

$$\mathrm{We}_d = \frac{\rho u_f^2 d}{\sigma} \tag{9}$$

and

$$C = 0.195\sqrt{2}\left(\frac{q'}{u_f}\right)^2 \tag{10}$$

Hence, the disturbance reaching the point of impact, which drives subsequent splattering, should scale with the dimensionless group

$$\omega = \mathrm{We}_d\exp\left(\frac{0.971}{\sqrt{\mathrm{We}_d}}\frac{l}{d}\right) \tag{11}$$

and the fraction of the total incoming liquid flow which is splattered, ξ, is a function of ω, which must be found experimentally.

The total turbulence intensity, q'/u_f, has an average value of approximately 0.080 in turbulent pipe flow (at $\mathrm{Re}_d = 5 \times 10^4$) and varies only weakly with Reynolds number (roughly as $\mathrm{Re}_d^{1/8}$; Laufer, 1954; Tennekes and Lumley, 1972). The Reynolds number range of the present splattering experiments (19,000 to 69,000) is narrow enough that a constant value of $C \approx 0.0018$ is an adequate initial condition for our jets. The turbulence decays under viscous influence as the jet travels to the plate; a homogeneous-turbulence decay estimate predicts a 50 percent drop in turbulence intensity if the jet is 20 diameters above the target. However, the capillary disturbances that turbulence induces at the jet outlet have grown exponentially during the journey to the target.

Figure 6 shows the ω at which we observed onset of splattering as a function of Reynolds number.[1] For all Reynolds numbers, the data show ω to be about 2120 at the onset of splattering. Thus, the jet disturbance found from the above analysis does control the stability of the liquid sheet, and ω is

---

[1] Our observations were both visual and tactile; "onset" is the point at which we observed *any* droplets to leave the liquid sheet.

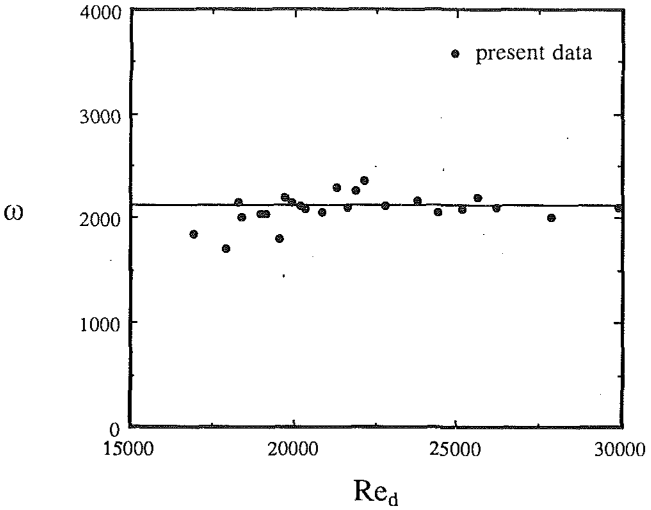

Fig. 6 The critical ω for onset of splattering as a function of Reynolds number

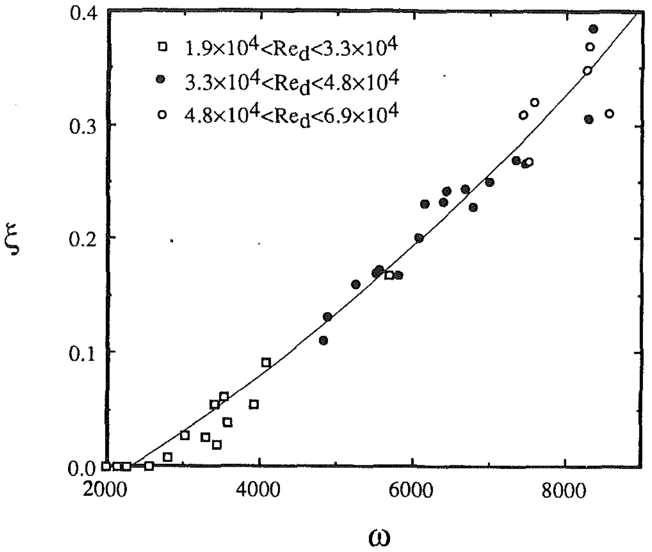

Fig. 7 The fraction of incoming mass splattered, ξ, as a function of ω; ——— curve fit

a good measure of that stability. From the definition of ω, this shows that splattering occurs whenever $We_d > 2120$, irrespective of l/d, although splattering may occur at lower values of We_d when l/d is nonzero. This graph ends at Re_d of 30,000 because our higher Re_d jets all exceeded $We_d = 2120$.

Figure 7 shows the total fraction of liquid splattered from the sheet as a function of ω. The ratio of the splattered flow to the total flow increases monotonically with ω. The amount of splattering is very small in the range $2120 \leq \omega \leq 3000$, with $\xi \leq 2.5$ percent; in engineering applications, splattering may be neglected in this range. For $2200 \leq \omega \leq 8500$, splattering increases rapidly; the splattering ratio is well represented by the curve fit

$$\xi = -0.0935 + 3.41\times10^{-5}\omega + 2.25\times10^{-9}\omega^2 \qquad (12)$$

No data are available beyond $\omega = 8500$, but we can assume that ξ will flatten, since it is necessarily less than one. For these data, the uncertainty is 8 percent for ω and 1 percent for ξ.

The onset of splattering is fairly flat in the sense of ξ versus ω. Hence, the reported "onset" may vary among observers, depending on how much mass must be splattered before splattering is noticed. Few outside data are currently available for comparison to the present criterion. Womac et al. (1990) cite three observations of onset for tube nozzles 20-40 diameters in length, which may be nondimensionalized using present terminology. For water, onset was noted for a 0.978 mm nozzle at $\omega \approx 2600$–3800 with $Re_d = 13900$; for FC-77, onset was noted for a 0.978 mm nozzle at $\omega \approx 2900$–4200 with $Re_d = 5800$ and for a 0.4 mm at $\omega \approx 6600$–8300 with $Re_d = 5900$. The first pair of observations is consistent with the present results, given the smallness of ξ at those values of ω and the low (marginally turbulent) Reynolds numbers involved. The last observation is well above present results; however, the volume of splattered liquid at observed onset would have been roughly the same as for the larger nozzles, making an issue of the operating definition of "onset." From a practical viewpoint, the curve $\xi(\omega)$ itself is of greatest importance, and onset may be best defined in terms of a threshold value of ξ below which splattering can be ignored.

Bhunia and Lienhard (1992) present more detailed results for the onset of splattering and an improved version of Eq. (12).

3.2 Droplet Departure Radius. The distribution of droplet diameter, D, typically ranges from a few microns to almost a millimeter. However, most droplets passing a particular point have essentially the same velocity irrespective of their size. Very small droplets (less than about 20 μm) suffer significant

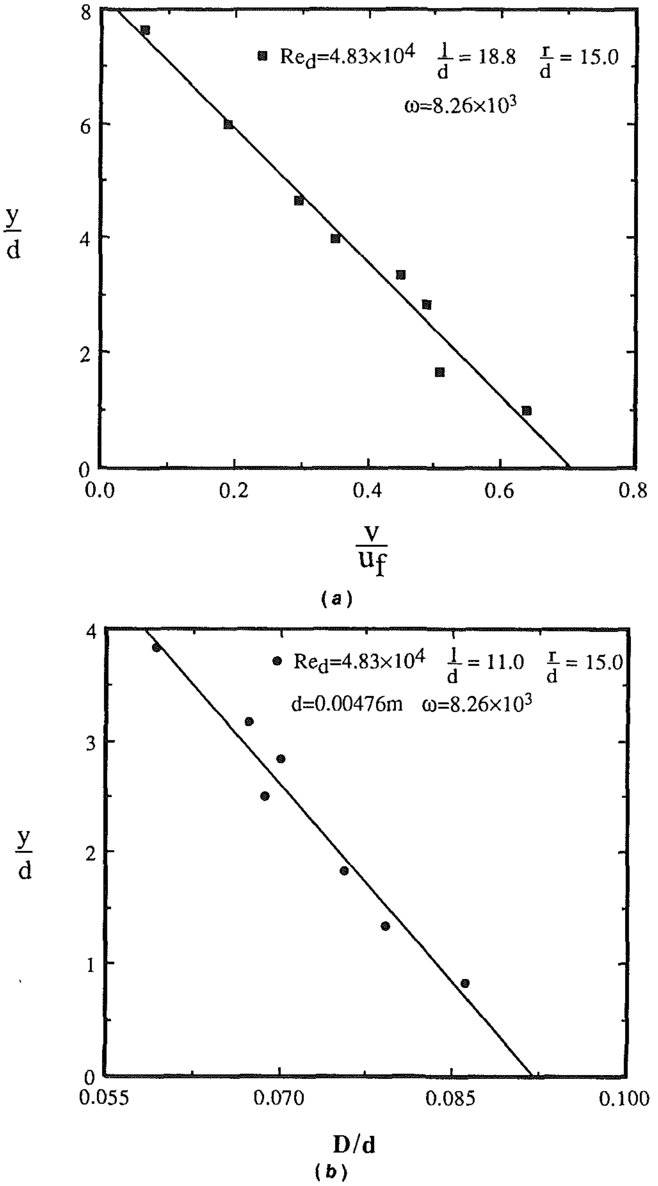

Fig. 8 (a) Droplet radial velocity profile above plate; (b) droplet diameter profile; ——— curve fits

viscous drag and move slower, but these droplets contribute little to the mass-averaged velocity. The mean droplet velocity, v, near the plate is fairly represented by a linearly decreasing velocity profile (Fig. 8*a*). The mean droplet diameter also decreases with increasing distance from the plate (Fig. 8*b*).

We may infer the radial position at which the droplets separated from the liquid surface, r_s, by assuming that the large droplets near the liquid surface maintain the radial velocity they had at the point of departure from the liquid sheet (neglecting air drag) and that the departure velocity is equal to the mean surface velocity; the droplets' velocity then determines the radial position where the liquid surface had that velocity. This estimate sets the position of breakaway at about $r_s = 5.7d$. Since the wavelength of maximum capillary instability for a circular jet is $\lambda_{\max}/d = 4.51$, the estimated breakaway position is slightly more than one $\lambda_{\max}$. In his experiments, Errico (1986) observed that the radius where the disturbances to the liquid sheet reach maximum height (droplet departure point) was between 0.73 cm and 1.46 cm, which appeared to be about 4 jet diameters.[2] The heat transfer data also verify this estimate indirectly, as will be discussed later. The present data do not clearly show a dependence of the breakaway radius upon Re_d, d, or ω, but more detailed measurements are unquestionably required to resolve such influences and to set a more precise value for r_s. For modeling purposes, we take $r_s \approx \lambda_{\max}$ in what follows.

A few very fine droplets were observed around the incoming jet when the Reynolds number was large. These droplets appear to be generated at the jet nozzle, and are formed by a different mechanism than considered here. They have a very small contribution to the total liquid volume flow. In addition, aerodynamic drag on the jet will become increasingly important for Reynolds numbers above 50,000 and will alter the capillary growth as modeled here.

4 Mean Flow Field and Heat Transfer

For turbulent jets, and especially for those that splatter, the flow field of the liquid sheet is highly unsteady and irregular. However, for the purpose of modeling the jet heat convection, we may focus on the mean flow field and consider separately the region before splattering and the region after splattering.

Visual observation shows that the capillary disturbances create very large, highly unsteady disturbances to the liquid film. Stroboscopic observations show that the disturbances grow larger up to the point of droplet separation, where tall, sharp crests are observed; these crests break into a spray of droplets (Errico presents excellent photographs of the breakup). The capillary disturbances greatly exceed in magnitude the free-stream turbulence in the incoming jet and will promote the rapid transition to a fully turbulent film downstream.

In the region upstream of droplet breakaway, we may suppose the flow to be composed of a thin, *laminar* wall boundary layer and a turbulent, fluctuating free stream above it. We may further suppose that the capillary disturbances to the liquid surface have essentially the same effect on the boundary layer as does the free stream turbulence. This region extends to only about 5 jet diameters from the point of impact.

To gain some idea of free stream turbulence effects on wall boundary layer heat transfer, we can refer to previous studies of the problem. A general survey of free stream turbulence effects was given by Kestin (1966); the stagnation zone of a *submerged* jet was investigated numerically by Traci and Wilcox (1975). Local measurements in the laminar stagnation zone of a cylinder show an unexpectedly large effect of free stream turbulence, reaching an enhancement of more than 80 percent in $\mathrm{Nu}_d/\mathrm{Re}_d^{1/2}$ at the stagnation point for a change of turbulence intensity from 0 percent to only 2.7 percent. Laminar boundary layer heat transfer can be substantially increased if the pressure gradient is nonzero, but for zero pressure gradient (as in the present flow, *away* from the stagnation point), free-stream turbulence does not affect the local heat transfer coefficient up to a turbulence intensity of at least 3.82 percent. The turbulence intensities of these past experiments are similar to those estimated for the present case, in the absence of capillary contributions. The magnitudes of the present capillary disturbances are not known precisely; however, we compare the present measurements to the undisturbed, laminar predictions (Liu et al., 1991) below, so as to gage the magnitude of the combined turbulent and capillary augmentation.

The splattering region itself is relatively small and may be modeled as if splattering occurs at a single radius. The large disturbances associated with droplet departure may reasonably be presumed to induce fully turbulent flow in the liquid sheet after splattering. We may estimate the thickness and velocity variation of the turbulent residual sheet by accounting for the loss of mass and momentum associated with splattering. Having the velocity and thickness of the turbulent liquid sheet, we may then use the thermal law of the wall to estimate the local Nusselt number.

We emphasize that the model that follows is directed at the average behavior of the sheet, rather than a precise prediction of velocity profile and film thickness.

4.1 Mass and Momentum Conservation. At the radial location just before splattering (here taken as $r_d/d = 4.51$), the ratio of mass in the boundary layer to total incoming mass in the jet is

$$x = \frac{2\pi r \int_0^\delta u\,dy}{\frac{\pi}{4} d^2 u_f} = 13.34 \left(\frac{r_s}{d}\right)^{3/2} \mathrm{Re}_d^{-1/2} = 128.3\,\mathrm{Re}_d^{-1/2} \tag{13}$$

where, from Sharan (1984),

$$u(y) = u_f \left[\frac{3}{2} \frac{y}{\delta} - \frac{1}{2} \left(\frac{y}{\delta}\right)^3 \right] \tag{14}$$

and

$$\frac{\delta}{d} = 2.679 \left(\frac{r}{d\,\mathrm{Re}_d} \right)^{1/2} \tag{15}$$

These expressions assume a laminar wall boundary layer beneath a turbulent free stream with mean velocity u_f. Stevens and Webb (1991) measured radial surface speeds for a non-splattering turbulent jet and found surface speeds near u_f (as would be expected from streamline momentum conservation); speeds up to 20 percent larger were measured for small diameter, low Reynolds number jets. As discussed below, this acceleration may be associated with surface tension effects on those small, slow jets.

If $(1-\xi) \geq x$, the splattered liquid does not include fluid in the boundary layer. In this case, the liquid sheet remaining after splattering has an effective thickness, h_c (Fig. 9), of

$$h_c = h_s - \frac{\xi d^2}{8 r_s} \tag{16}$$

where h_s is the mean film thickness prior to splattering and the second term is the loss of (inviscid) fluid due to splattering. The remaining mass flow, $(1-\xi)\pi/4 d^2 u_f$, carries momentum

$$2\pi r_s \rho \left[\int_0^\delta u^2 dy + \int_\delta^{h_c} u_f^2 dy \right] = 2\pi r_s \rho u_f^2 \Phi d \tag{17}$$

where

---

[2] Errico's water jet diameter was not specified, since he observed the splattering radius to be independent of jet size. From a Kelvin-Helmholtz instability analysis of the liquid sheet, Errico estimated that this radial position was one to two disturbance wavelengths.

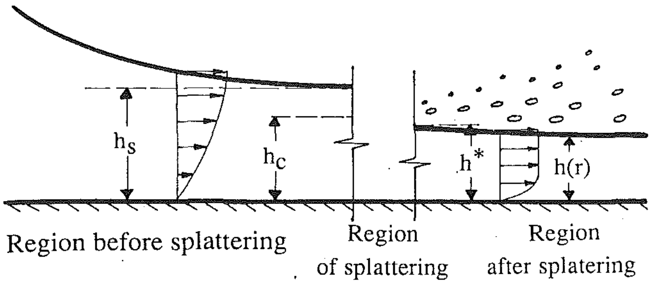

Fig. 9 Mean flow field during splattering (schematic)

$$\Phi = 0.125(1-\xi)\frac{d}{r_s} - 0.373\left(\frac{r_s}{d\mathrm{Re}_d}\right)^{1/2} \tag{18}$$

These results do not account for the transition to turbulent flow after splattering, which will change the velocity profile and alter the film thickness from h_c to another value, h^*.

Azuma and Hoshino (1984) measured the velocity distributions in the sheet for both laminar and turbulent flow; they showed that a 1/7th power law is a good approximation in the turbulent sheet:

$$u(y) = u_{\max}\left(\frac{y}{h}\right)^{1/7} \tag{19}$$

for h the thickness of the turbulent sheet and $u_{\max}$ the free surface speed. We assume the adjustment from the laminar boundary layer to turbulent sheet velocity distributions occurs within a small radial region at the zone of splattering. In terms of the turbulent thickness just after splattering, h^*, the mass flow in the sheet after splattering is

$$2\pi r_s \rho \int_0^{h*} u dy = \frac{7}{4}\pi r_s \rho h^* u^*_{\max} \tag{20}$$

and the momentum flow in the sheet after splattering is

$$2\pi r \rho \int_0^{h*} u^{*2} dy = \frac{14}{9}\pi r_s \rho h^* u^{*2}_{\max} \tag{21}$$

for u^* the mean velocity distribution in the sheet just after splattering and $u^*_{\max}$ its maximum. Then, with Eqs. (16)–(18), mass and momentum balances on the region of adjustment (at radius r_s) give

$$\frac{h^*}{d} = \frac{(1-\xi)^2 d^2}{63 r_s^2 \Phi} \tag{22}$$

At larger radii, solution of the momentum integral equation gives the variation of turbulent liquid sheet thickness as

$$\frac{h}{d} = \frac{0.02091}{[(1-\xi)\mathrm{Re}_d]^{1/4}}\left(\frac{r}{d}\right)^{5/4} + C_s\frac{d}{r} \tag{23}$$

where

$$C_s = \frac{h^* r_s}{d^2} - \frac{0.02091}{[(1-\xi)\mathrm{Re}_d]^{1/4}}\left(\frac{r_s}{d}\right)^{9/4} \tag{24}$$

Note that the above mass and momentum balances across the splattering region provided the initial conditions used in solving the momentum integral equation for $r > r_s$.

For the case $(1-\xi) < x$, the mass in the sheet after splattering is

$$(1-\xi)\frac{\pi}{4}d^2 u_f = 2\pi r \int_0^{h_c}\left(\frac{3}{2}\left(\frac{y}{\delta}\right) - \frac{1}{2}\left(\frac{y}{\delta}\right)^3\right)dy \tag{25}$$

so that

$$\frac{h_c}{\delta} \equiv \Theta = \sqrt{3 - 3\sqrt{1 - \frac{(1-\xi)d^2}{9 r_s \delta}}} \tag{26}$$

The momentum remaining within the liquid sheet is

$$2\pi r_s \rho \int_0^{h_c} u^2 dy = 2\pi r_s \rho u_f^2 \delta\left(\frac{3}{4}\Theta^3 - \frac{3}{10}\Theta^5 + \frac{1}{28}\Theta^7\right) \tag{27}$$

We obtain the same results for h^* and h, Eqs. (22) and (23), except that Φ is not given as Eq. (18), but is instead

$$\Phi = \left(\frac{3}{4}\Theta^3 - \frac{3}{10}\Theta^5 + \frac{1}{28}\Theta^7\right)\frac{\delta}{d} \tag{28}$$

4.2 Heat Transfer. We may now apply the thermal law of the wall to calculate the heat transfer in the film after splattering, following Liu et al. (1991). According to the law of the wall

$$\mathrm{St} = \frac{q_w}{\rho c_p u_{\max}(T_w - T_{sf})} = \frac{C_f/2}{1.07 + 12.7(\mathrm{Pr}^{2/3} - 1)\sqrt{C_f/2}} \tag{29}$$

The friction coefficient in the liquid sheet, from the Blasius law, is

$$C_f = 0.045\left(\frac{\nu}{h u_{\max}}\right)^{1/4} \tag{30}$$

and for a turbulent sheet,

$$u_{\max} h = \frac{1}{7}\frac{u_f d^2(1-\xi)}{r} \tag{31}$$

If we define the local Nusselt number as

$$\mathrm{Nu}_d = \frac{q_w d}{k(T_w - T_f)} \tag{32}$$

then, letting $T_{sf} = T_f$ at $r = r_s$ and taking the free surface to essentially adiabatic (Liu et al.), a calculation yields

$$\mathrm{Nu}_d = \frac{8\mathrm{Re}_d \mathrm{Pr}\,\mathrm{St}}{49(hr/d^2) + 28(r/d)^2\mathrm{St}} \tag{33}$$

This expression for Nu_d may be evaluated in conjunction with Eqs. (23), (29), (30), (31), and (12).

Figure 10 shows the Nusselt number predicted above. The Nusselt number from the laminar prediction is also shown. As shown below (Figs. 13*a*, *b*), the turbulent prediction agrees reasonably well with our experimental results.

Splattering has a strong effect on heat transfer, especially immediately after the breakaway radius. Increasing the amount of mass splattered (raising ξ) deteriorates the heat transfer. Splattering thins the film, and the resultant, increased skin friction creates a rapid decay in the Nusselt number with radius. Far downstream, the heat transfer is substantially worse than for the laminar case. Similarly, as more mass is splattered (ξ increasing), the remaining film has less momentum, and slows more quickly. At radii close to the radius of splattering, however, the heat transfer is larger than for laminar flow; this results from the assumption that turbulent transition accompanies splattering. This enhancement is stronger when less mass is splattered, leaving more momentum in the film.

For the case without splattering ($\xi = 0$), the prediction and data still show an enhancement from capillary disturbances, which is caused by the turbulent transition. For $\omega < 5000$, the prediction overestimates the Nusselt number relative to measurements immediately after the "splattering" radius (19 percent higher for $\omega \approx 2400$), but farther downstream the disagreement disappears (after about $5d$ for $\omega \approx 2400$). The overprediction may occur because turbulent transition is not completed at the splattering radius; Liu et al. showed that turbulent transition can occur over a significant radial band. However, these estimates are still much closer to the data than is the laminar prediction; even in the absence of actual splattering, the liquid sheet is still highly disturbed by the capillary fluctuations.

Liu et al. (1991) showed that the stagnation zone of a uni-

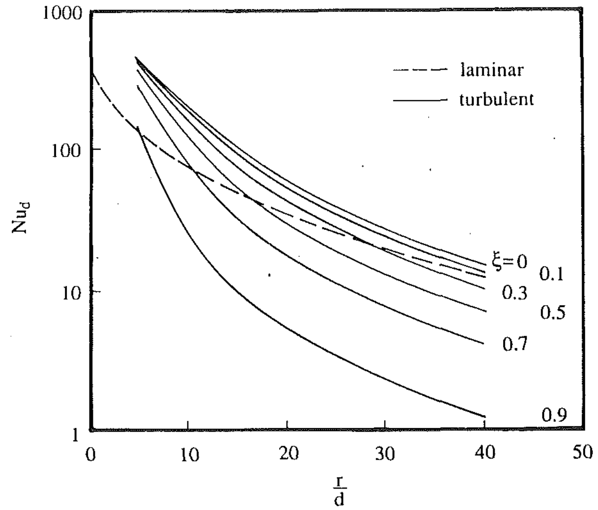

Fig. 10 Estimated Nusselt number for region after splattering as a function of fraction of mass splattered: Eq. (33); ——— ; laminar results (Liu et al.) ---

form-velocity-profile, laminar incoming jet covers the region $r/d \leq 0.787$ and that the Nusselt number there may be estimated from

$$\mathrm{Nu}_d = \begin{cases} 0.715\mathrm{Re}_d^{1/2}\mathrm{Pr}^{0.4} & 0.15 \leq \mathrm{Pr} \leq 3 \\ 0.797\mathrm{Re}_d^{1/2}\mathrm{Pr}^{1/3} & \mathrm{Pr} > 3 \end{cases} \tag{34}$$

For a turbulent incoming jet, both free stream turbulence and capillary disturbances may affect the stagnation zone heat transfer. Figure 11(*a*) shows the ratio of measured Nusselt number to 0.797 $\mathrm{Re}_d^{1/2}\mathrm{Pr}^{1/3}$ as a function of ω. The stagnation zone heat transfer appears to be essentially independent of ω. This is not surprising given that the stagnation zone is well separated from the free surface and its capillary disturbances. However, the turbulent stagnation zone heat transfer is still much higher than for a laminar impinging jet; the data show an augmentation factor of about 1.55. Turbulent disturbances are not directly separated from capillary disturbances in this presentation. However, as mentioned previously, variations in outlet turbulence intensity show only a weak additional dependence on Reynolds number beyond the u_f dependence of ω, and viscous damping of turbulence during travel to the plate may well be offset by growth of the fluctuating capillary disturbances to the fluid flow. Indeed, Fig. 11(*b*) shows the augmentation factor to be essentially independent of jet Reynolds number in this range of Re_d and ω.

The stagnation zone Nusselt number for the present experiments is represented by the following expression to an accuracy of about ±10 percent:

$$\mathrm{Nu}_d = 1.24\mathrm{Re}_d^{1/2}\mathrm{Pr}^{1/3} \tag{35}$$

This equation should apply for any Prandtl number greater than 3, although the present experiments, for $7 < \mathrm{Pr} < 11$, do not verify the Pr range.

Stevens and Webb (1989) and Jiji and Dagan (1988) present results for the turbulent stagnation zone of an unsubmerged jet. The parameter ω is generally small for both studies, given their low ranges of either Reynolds number or l/d; neither study appears to have used splattering jets. Jiji and Dagan's jets were confined to low Re_d and were produced by very short tubes, some six diameters in length. The turbulence intensity in their jets should thus be lower than for the fully developed turbulence of the present, long tubes, leading to a somewhat lower stagnation point Nusselt number. Their results are shown for comparison in Fig. 11(*a*); their data are in fact somewhat below the present data. Stevens and Webb's prediction is considered below.

For liquid jet impingement, the pressure gradient in the

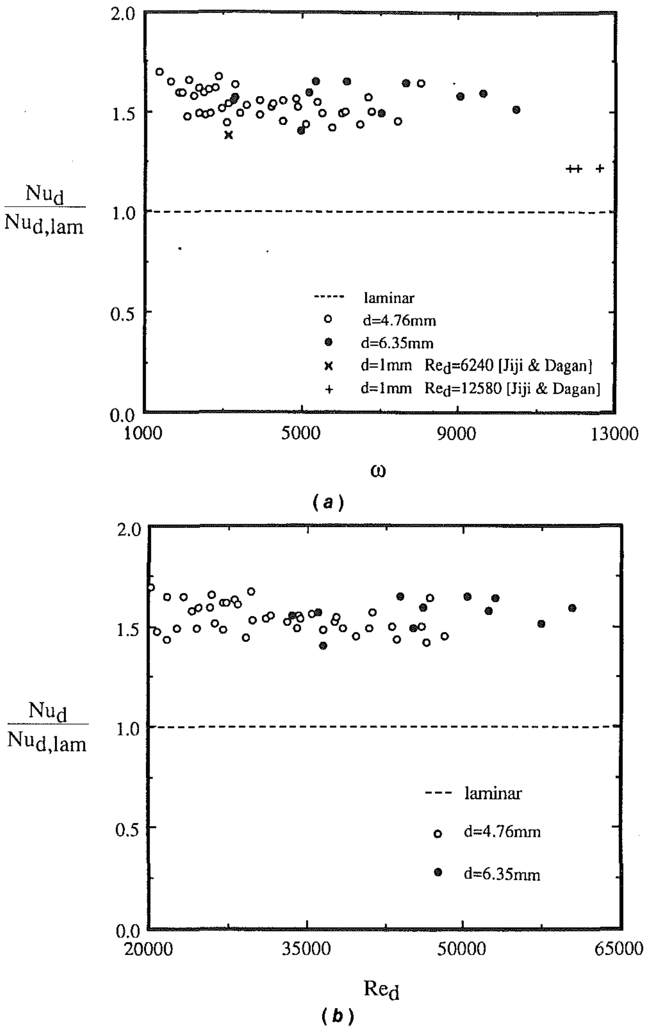

(*a*)

(*b*)

Fig. 11 Nusselt number in stagnation zone for turbulent, splattering jets relative to Nusselt number for laminar jets from Eq. (34)

region between the stagnation zone and the splattering radius is negligible, and, as noted above, previous studies (Kestin, 1966) suggest that no turbulent augmentation of the boundary layer heat transfer should occur. However, the presence of strong capillary disturbances before the radius of droplet separation provides an alternative mechanism for heat transfer enhancement. To show the effect of capillary disturbances, the Nusselt number between stagnation and splattering was averaged, and the ratio between this average Nusselt number and the averaged laminar prediction (Liu and Lienhard, 1989) was calculated. Figure 12 shows this ratio as a function of ω. The enhancement by capillary disturbances is apparent, in contrast to the stagnation zone heat transfer, and enhancement appears to be independent of Reynolds number. Capillary augmentation reaches a factor of three at $\omega = 9000$.

We may predict the Nusselt number over the entire range of radius by using Eq. (33) for the region after splattering ($r/d > 5.7$), using Eq. (35) for the stagnation zone ($r/d < 0.787$), and applying the augmentation factor (Fig. 12) to the laminar prediction between the stagnation zone and the splattering radius. This composite prediction is compared to two sets of data in Fig. 13(*a*,*b*), and the agreement is generally good. Many other cases are shown by Gabour (1991). In Fig. 13(*a*), in the region just after splattering, the data show a lower value than the prediction. The reason, as mentioned above, is that for this case ω is about 4003 and the turbulent transition is not completed in the splattering region; this disagreement disappears downstream as the transition is completed. In the figure,

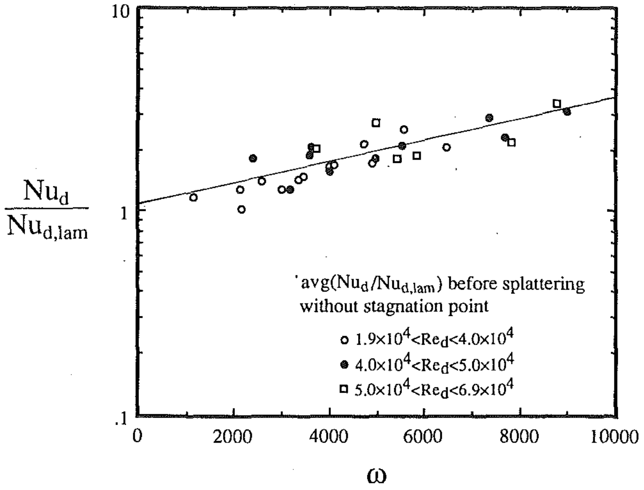

Fig. 12 Augmentation of Nu_d in boundary layer region upstream of the splattering radius as a function of ω; turbulent results normalized with laminar results of Liu and Lienhard (1989)

the correlation of Stevens and Webb (1989) underestimates the Nusselt number for $r/d > 3$, consistent with its expected range of validity. Our data are somewhat higher than that correlation at small r. Figure 13(*b*) shows similar results at a larger ω.

5 Other Nozzles

Other nozzle configurations may have different outlet turbulence intensities. A tentative suggestion for adapting the present results to such nozzles is to rescale the present values of ω to values appropriate to such nozzles. Since the initial *disturbance to the sheet is proportional to* $C\omega$, the procedure is to determine the values of C and ω for the new nozzle and then find an effective value of ω as:

$$\omega_{\mathrm{eff}}=\frac{(C\omega)_{\mathrm{new}}}{C_{\mathrm{present}}} \tag{36}$$

The value ω_{eff} may be used in calculations based on the present results.

Additional considerations for other nozzles include variations in the coefficient of contraction and nonuniform velocity profiles. While velocity-profile influence on heat transfer has been clearly established for laminar jets, Wolf et al. (1990) suggested that for planar, fully developed turbulent jets, the velocity profile itself has far less effect on turbulent heat transfer than does turbulence. However, measurements that independently vary turbulence intensity and mean velocity profile are needed in order to quantify and settle this issue.

Likewise, the precise effect of a nonuniform velocity distribution on the evolution of surface disturbances has yet to be clearly identified, although the present results work well for the levels of nonuniformity found in turbulent pipe jets. Until further data are obtained, a tentative recommendation is to ignore velocity profile effects on splattering, unless the nozzle produces a mean velocity profile markedly different than that for normal pipe flow.

Nonunity contraction coefficients should be taken into account when calculating jet velocity and diameter, although they seem unlikely to have a strong influence on capillary or turbulent disturbances such as are considered here. For low Reynolds number jets of small diameter, surface tension (and gravitational acceleration) can alter the flow field of the jet near the plate. Liu et al. (1992) find some evidence of such effects in the stagnation zone of laminar jets.

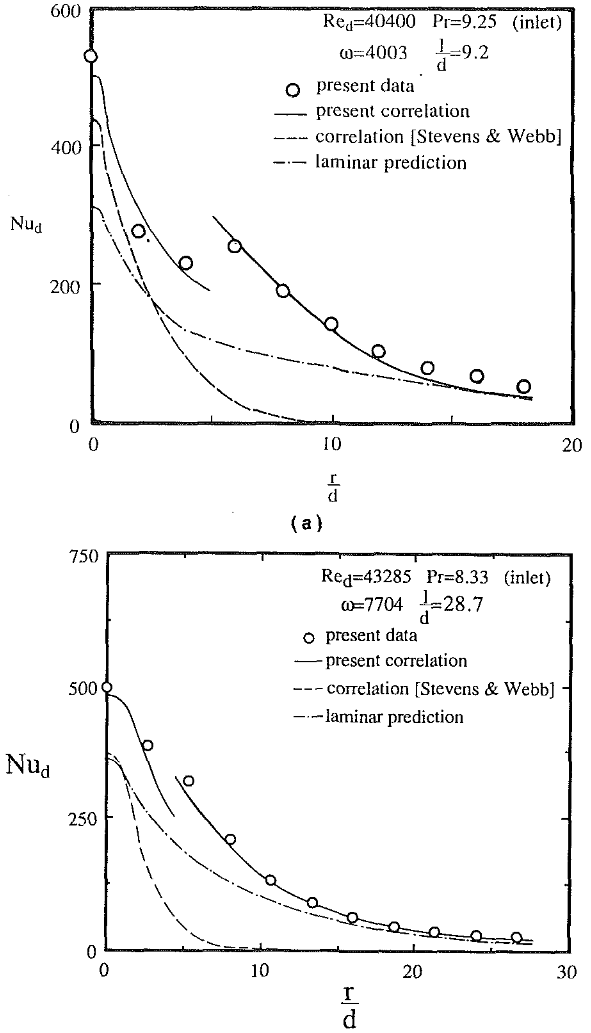

Fig. 13 Comparison of measurements to the present model: ——— from Eq. (33) and Figs. (10) and (12); laminar theory from Liu et al.

6 Conclusions

Splattering and heat transfer have been investigated for unsubmerged, circular, fully turbulent impinging liquid jets. Predictive results have been developed for the local Nusselt number along a uniform heat flux surface and for the onset of splattering and the total mass splattered.

- The occurrence of splattering is well characterized by the group ω (Eq. (11)) when: (*a*) the initial disturbances to the jet are produced by turbulence in the liquid exiting the nozzle; and (*b*) the jet Reynolds number is low enough that capillary instability guides the growth of these disturbances. The present results validate ω for $19{,}000 < \mathrm{Re}_d < 69{,}000$; breakdown of the model is likely at higher Reynolds numbers due to aerodynamic drag. Differences are also expected when the turbulence is less than fully developed, as at lower Reynolds numbers. The data cover jet-to-target separations of $7.6 \le l/d \le 26.4$ and $1000 < \mathrm{We}_d < 5000$; the present model is likely to fail if the jet is long enough to undergo breakup prior to impact.
- Splattering occurs within a narrow radial band, rather than being distributed at all radii in the liquid sheet. The breakup radius, r_s, is about one $\lambda_{\max}$ (roughly $4.51d$), although further study of the scaling of both r_s and splattered droplet profiles are needed. Splattering appears to be an inviscid phenomenon.
- Jets begin to splatter when $\omega > 2120$ (or for $\mathrm{We}_d > 2120$ for any l/d). The fraction of incoming mass splattered, ξ, is

given by Eq. (12) for $\omega < 8500$. These results apply for $7.6 \leq l/d \leq 26.4$ and $1000 < We_d < 5000$.

- Local Nusselt number depends on Re_d, r/d, and ω for turbulent, splattering jets. The present results facilitate prediction of local wall temperature from the stagnation zone to radii well past the splattering radius.
- Both turbulent and capillary disturbances to the free-stream flow strongly augment heat transfer in the laminar wall boundary layers in the stagnation zone and film region upstream of the splattering radius. Results are shown in Figs. 11 and 12.
- After droplet breakaway, heat transfer is further enhanced by complete turbulent transition of the viscous film. However, heat transfer drops quickly thereafter as a result of the higher skin friction in the film. Nusselt number may be estimated with Eq. (33) for $r > r_s$ and is shown in Figs. 10 and 13.
- In the stagnation zone, capillary disturbances appear to have no direct effect on the heat transfer. Augmentation by the turbulence in the incoming jet appears to increase the heat transfer by a factor of 1.55 over that for a laminar jet. Augmentation is independent of ω and Re_d over the range of those variables covered in these experiments ($1.2 \leq l/d \leq 28.7$). The stagnation zone Nusselt number ($r/d \leq 0.787$) is well represented by Eq. (35), $Nu_d = 1.24 Re_d^{1/2} Pr^{1/3}$.

Acknowledgments

The authors are grateful to Mr. John A. Simo for his assistance with the Phase Doppler equipment. This work was supported by the A. P. Sloan Foundation and the National Science Foundation under grant No. CBT-8858288. The Phase Doppler Particle Analyzer was purchased under Electric Power Research Institute contract No. RP8000-41.

References

Azuma, T., and Hoshino, T., 1984, "The Radial Flow of Thin Liquid Film, Part 3: Velocity Profile," *Trans. Japan Soc. Mech. Engrs.*, Paper No. 50-1126.

Bhunia, S. K., and Lienhard V, J. H., 1992, "Splattering of Turbulent Liquid Jets Impinging on Solid Targets: Parametric Studies," *28th AIChE/ASME Nat. Heat Transfer Conf.*, San Diego, to appear.

Drazin, P. G., and Reid, W. H., 1981, *Hydrodynamic Stability*, Cambridge University Press, United Kingdom.

Errico, M., 1986, "A Study of the Interaction of Liquid Jets With Solid Surfaces," Ph.D. Thesis, University of California, San Diego.

Faggiani, S., and Grassi, W., 1990, "Round Liquid Jet Impingement Heat Transfer: Local Nusselt Numbers in the Region With Nonzero Pressure Gradient," *Proc. Ninth Int. Heat Transfer Conf.*, Jerusalem, Vol. 4, pp. 197-202.

Gabour, L. A., 1991, "Heat Transfer to Turbulent and Splattering Impinging Liquid Jets," S.B. Thesis in Mechanical Engineering, MIT, Cambridge, MA.

Jiji, L. M, and Dagan, Z., 1988, "Experimental Investigation of Single-Phase Multijet Impingement Cooling of an Array of Microelectronic Heat Sources," *Cooling Technology for Electronic Equipment*, Hemisphere, New York.

Kestin, J., 1966, "The Effect of Free-Stream Turbulence on Heat Transfer Rates," *Adv. Heat Transfer*, Vol. 3, pp. 1-32.

Laufer, J., 1954, "The Structure of Turbulence in Fully Developed Pipe Flow," NACA Tech. Report No. 1174.

Liu, X., and Lienhard V, J. H., 1989, "Liquid Jet Impingement Heat Transfer on a Uniform Flux Surface," *Heat Transfer Phenomena in Radiation, Combustion, and Fires*, ASME HTD-Vol. 106, pp. 523-530.

Liu, X., Lienhard V, J. H., and Lombara, J. S., 1991, "Convective Heat Transfer by Impingement of Circular Liquid Jets," ASME JOURNAL OF HEAT TRANSFER, Vol. 113, pp. 571-582.

Liu, X., Gabour, L. A., and Lienhard V, J. H., 1992, "Stagnation Point Heat Transfer During Impingement of Laminar Liquid Jets: Analysis With Surface Tension," *28th AIChE/ASME Nat. Heat Transfer Conf.*, San Diego, to appear.

Lombara, J. S., 1990, "An Experimental Investigation of Liquid Jet Impingement Heat Transfer Theories," S.B. Thesis in Mechanical Engineering, MIT, Cambridge, MA.

Sharan, A., 1984, "Jet-Disc Boiling: Burnout Predictions and Application to Solar Receivers," Master's Thesis, University of Houston, TX.

Stevens, J., and Webb, B. W., 1989, "Local Heat Transfer Coefficients Under an Axisymmetric, Single-Phase Liquid Jet," *Heat Transfer in Electronics—1989*, ASME HTD-Vol. 111, pp. 113-119.

Stevens, J., and Webb, B. W., 1991, "Measurements of the Free Surface Flow Structure Under an Impinging, Free Liquid Jet," presented at the 3rd ASME/JSME Thermal Engineering Joint Conference, Reno, NV.

Tennekes, H., and Lumley, J. L., 1972, *A First Course in Turbulence*, MIT Press, Cambridge, MA.

Traci, R. M., and Wilcox, D. C., 1975, "Freestream Turbulence Effects on Stagnation Point Heat Transfer," *AIAA J.*, Vol. 13, pp. 890-896.

Wolf, D. H., Viskanta, R., and Incropera, F. P., 1990, "Local Convective Heat Transfer From a Heated Surface to a Planar Jet of Water With a Nonuniform Velocity Profile," ASME JOURNAL OF HEAT TRANSFER, Vol. 112, pp. 899-905.

Womac, D. J., Aharoni, G., Ramadhyani, S., and Incropera, F. P., 1990, "Single Phase Liquid Jet Impingement Cooling of Small Heat Sources," *Proc. Ninth Int. Heat Transfer Conf.*, Jerusalem, Vol. 4, pp. 149-154.

Heat Transfer in Thin, Compact Heat Exchangers With Circular, Rectangular, or Pin-Fin Flow Passages

D. A. Olson
Chemical Engineering Division,
National Institute of Standards
and Technology,
Boulder, CO 80303-3328
Assoc. Mem. ASME

We have measured heat transfer and pressure drop of three thin, compact heat exchangers in helium gas at 3.5 MPa and higher, with Reynolds numbers of 450 to 36,000. The flow geometries for the three heat exchanger specimens were: circular tube, rectangular channel, and staggered pin fin with tapered pins. The specimens were heated radiatively at heat fluxes up to 77 W/cm^2. Correlations were developed for the isothermal friction factor as a function of Reynolds number, and for the Nusselt number as a function of Reynolds number and the ratio of wall temperature to fluid temperature. The specimen with the pin fin internal geometry had significantly better heat transfer than the other specimens, but it also had higher pressure drop. For certain conditions of helium flow and heating, the temperature more than doubled from the inlet to the outlet of the specimens, producing large changes in gas velocity, density, viscosity, and thermal conductivity. These changes in properties did not affect the correlations for friction factor and Nusselt number in turbulent flow.

Introduction

Compact heat exchangers are widely used in many applications, including gas turbines, the aerospace industry, and cryogenics. The problem motivating this work is cooling the engine struts of the National Aerospace Plane (NASP). The engine struts are expected to receive a normal (perpendicular) heat load of the order of 2000 W/cm^2 due to aerodynamic heating and thermal radiation from the combustion of the hydrogen gas fuel (Scotti et al., 1988). The present concept for cooling the strut is to attach a heat exchanger to the surface facing the high heat flux, through which hydrogen gas will flow prior to entering the engine. Due to limitations of size and weight, the heat exchanger must be thin and compact. The pressure will be high (7 MPa or greater) to reduce the pressure drop for a given gas flow rate. Temperatures will increase substantially from the inlet to outlet (56 K to 890 K) to minimize the gas flow rate for a given incident heat flux. The outlet temperature is determined by temperature limits of the materials used in constructing the heat exchanger.

Thermal-fatigue studies of concepts for cooling the strut (Shore, 1986) have shown that the life of the engine increases as the temperature difference between the wall and fluid of the heat exchanger decreases. This implies maximizing the product of the heat transfer coefficient and the internal wall area of the exchanger. For applications other than the NASP strut, high heat transfer coefficients allow either reducing the coolant flow or reducing the size of the heat exchanger to achieve the same heat transfer.

In this work, three compact heat exchangers were tested in a helium flow apparatus to measure their heat transfer and pressure drop. All had approximately the same heated normal area, were thin perpendicular to the flow direction (5 mm or less), and were made of commercially pure nickel (UNS 02200). Two specimens used conventional flow geometries, while the third had a novel, "pin-fin" geometry for which there were no performance data. The "tube" specimen consisted of 20 tubes, 1.02 mm i.d., lying in parallel on a base plate. The "channel" specimen contained 12 rectangular channels in parallel, 3.18 mm wide by 0.56 mm deep, milled in a base plate. In the pin-fin specimen, tapered circular cylinders spanned the height of the cooling passage. The centers of the pins were located at the corners of equilateral triangles.

Pin-fin banks have been used in the gas turbine industry to cool turbine blades or vanes (Armstrong and Winstanley, 1988). In that application, the length-to-diameter ratio of the pins varies from 1/2 to 4, and the pin diameter is constant across the span of the channel. Long pin fins (length-to-diameter ratio of 8 or greater) have been used by the heat exchanger industry and were studied by Kays and London (1964). In all past applications, the pin diameter has been constant across the channel. For our work, the pins were tapered; the length-to-diameter ratio varied from 1/4 to 1/2 on each pin. Pin banks of past works are often "staggered" in the flow direction to break up the flow path. The pins of our work were also staggered, but the layout angle was different.

The tube and channel specimens were constructed to test alternative fabrication techniques to those of the pin fin, because initial attempts to build a pin-fin specimen were unsuccessful. Because the heat transfer in tube and channel geometries has been measured before (albeit in a single tube at low heat flux and easily measured wall and fluid temperatures), testing these specimens allowed us to determine whether variable properties, axial flow acceleration, flow nonuniformities, or errors in temperature measurement were significant. Neither the tube nor channel specimens were optimized for heat transfer, a fact that should be remembered when comparing their performance to that of the pin-fin specimen.

Description of the Apparatus

We mounted the heat exchanger specimens in an apparatus that provided steady flow of helium at constant inlet temperature and pressure, and heated the specimens radiatively (Olson, 1989, 1990). The apparatus was designed to test specimens at heating rates of 0 to 80 W/cm^2 and gas temperatures from ambient to 810 K. In testing with helium we could match the

---

Contributed by the Heat Transfer Division for publication in the JOURNAL OF HEAT TRANSFER. Manuscript received by the Heat Transfer Division May 1991; revision received January 1992. Keywords: Augmentation and Enhancement, Forced Convection, Heat Exchangers.

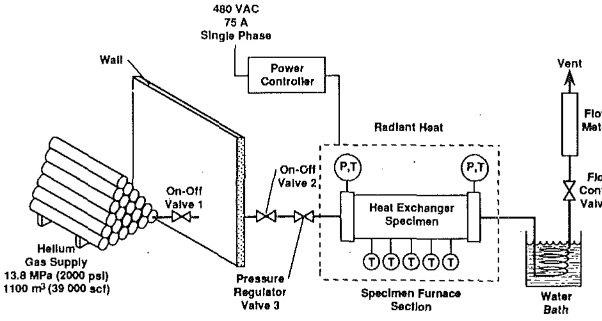

Fig. 1 Helium flow apparatus

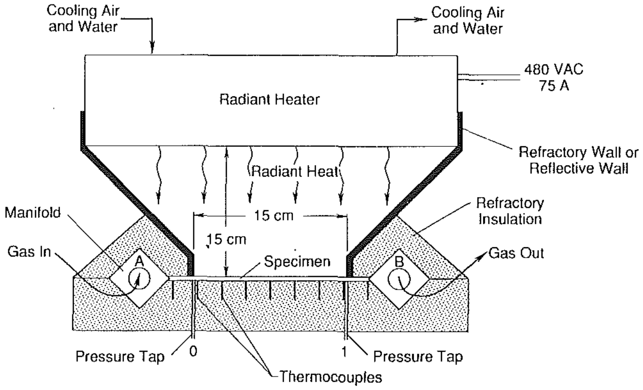

Fig. 2 Specimen furnace, showing location of inlet gas temperature (A), upstream pressure (0), outlet gas temperature (B), and downstream pressure (1)

Reynolds number, Prandtl number, and temperature rise from the specimen inlet to outlet to those of hydrogen, because of the similarities in specific heat, thermal conductivity, and dynamic viscosity between the two gases.

Flow Apparatus. The helium flow apparatus is shown in Fig. 1, with the details of the specimen furnace section shown in Fig. 2. Helium gas at 17 MPa (2500 psi) or less was supplied from a tube trailer outside the laboratory. System pressure was set by the dome-loaded pressure regulator (valve 3).

Within the furnace (Fig. 2), the gas flowed into an inlet manifold, which distributed it to the heat exchanger specimen. A similar manifold collected the gas exiting the specimen and directed it to the outlet tubing. The specimen was located in the target area of the furnace (7.8 cm wide by 15.2 cm long). The x coordinate is aligned with the direction of gas flow in the specimen, with $x/L=0$ at the (upstream) furnace wall where the heating of the gas begins, and $x/L=1$ at the (downstream) furnace wall where heating ends. The furnace consisted of a high-intensity infrared radiant heater, surrounded by focusing walls, which directed the heat to the specimen. For the tube specimen, the walls were made of refractory insulation (Olson, 1989). For the channel and pin-fin specimens, the walls were made of polished aluminum (Olson, 1990). The aluminum walls were watered cooled. The heater contained six high-temperature infrared lamps mounted in an aluminum housing. The aluminum surface behind the lamps was polished to reflect the light. Quartz windows placed in front of the lamps and

Nomenclature

A = location of inlet manifold
A_f = flow normal area $= V_0/L$, m^2
A_n = specimen normal area $= L \cdot w$, m^2
A_w = wetted wall area (total wall area exposed to fluid), m^2
B = location of outlet manifold
Bi = Biot number $= h_w \cdot D_h / k_{ni}$
c_p = specific heat at constant pressure, J/(kg•K)
D_h = specimen hydraulic diameter $= 4V_0/A_w$, m
f = isothermal friction factor (Eq. (2))
f_M = friction factor used by Metzger et al. (1982) (Eq. (20))
f_q = heat flux distribution function
G = mass flow rate per unit flow normal area $= \dot{m}_w w / A_f$, kg/(s•m)
h = heat transfer coefficient (Eq. (7)), W/(m^2•K)
h = enthalpy, J/kg
H = thickness of specimen, m
h_n = normalized heat transfer coefficient (Eq. (16)), W/(m^2•K)
h_w = heat transfer coefficient based on temperature of wall-fluid interface (Eq. 14)), W/(m^2•K)
k = thermal conductivity, W/(m•K)
k_{ni} = thermal conductivity of nickel, W/(m•K)
L = heated length of specimen, m
$\dot{m}$ = mass flow rate, kg/s
$\dot{m}_w$ = mass flow rate per unit width of specimen, kg/(s•m) $= \dot{m}/w$ if the flow is uniform with y
N = number of rows of pins in flow direction in Metzger friction factor
Nu = Nusselt number $= h \cdot D_h / k$
Nu$_m$ = modified Nusselt number $= (h \cdot D_h/k) \cdot (T_w/T_f)^{0.55}$
Nu$_w$ = Nusselt number based on temperature of wall-fluid interface $= (h_w \cdot D_h/k) \cdot (T_w/T_f)^{0.55}$
P = pressure, Pa
P_w = wall perimeter perpendicular to flow direction, m
Pr = Prandtl number $= \mu \cdot c_p / k$
q_n = local normal heat flux, W/m^2
Q_{px} = fraction of total heat flow on specimen added up to position x = integration of furnace calibration function f_q, from 0 to x
Q_T = total heat transfer to specimen, W
q_w = local wall heat flux based on total wetted-wall area of the specimen, W/m^2
r = recovery factor $= (T_{aw} - T_f)/(V^2/2c_p)$, taken as Pr$^{1/3}$ for turbulent flow
ref = reference conditions
Re = Reynolds number $= \rho V D_h / \mu$
T = temperature, K
T_{aw} = adiabatic wall temperature of cooling fluid, K
T_f = temperature of local bulk fluid, K
T_w = temperature of specimen wall, K
V = velocity, m/s
$V_{\max}$ = maximum velocity in specimen, m/s
V_0 = open volume in specimen, m^3
w = width of specimen, m
x = position coordinate parallel to flow direction, m
y = position coordinate perpendicular to flow direction, m
β = coefficient of thermal expansion
ΔP_n = normalized pressure drop (Eq. (4)), Pa•(s•m)^2/kg^2
η = pin efficiency
μ = dynamic viscosity, kg/(s•m)
ρ = density, kg/m^3
σ = standard deviation
0 = location where heating begins ($x/L=0$)
1 = location where heating ends ($x/L=1$)

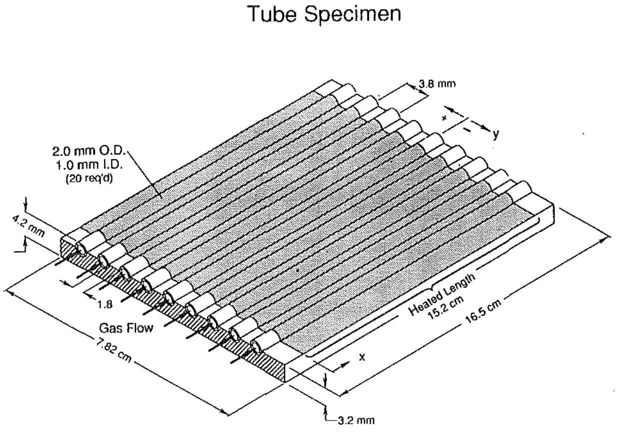

Fig. 3 Tube specimen

mounted in the aluminum housing provided an enclosure for air to flow around the lamps and prevent over heating. The aluminum housing of the heater was water cooled.

Downstream of the furnace section, the hot gas flowed through a cooling coil immersed in a water bath. The rate of gas flow was manually adjusted at the bath outlet by valve 4. Beyond the valve, we measured helium flow rate with a heated-tube thermal mass flow meter with an uncertainty of ±1 percent. After exiting the flow meter the gas was vented outside the laboratory.

Tube Specimen. The tube specimen consisted of 20 small-diameter tubes lying in parallel in channels machined on a base plate, as shown in Fig. 3. Both the tubes and the base plate were made of commercially pure nickel. The outer diameters of the tubes were 2.03 mm and the inner diameters were 1.02 mm. Adjacent tubes were 3.81 mm between centers, leaving 1.78 mm of flat between the tubes. The base plate was 7.82 cm wide, 16.5 cm long, and 3.18 mm thick. The overall thickness of the specimen was 4.19 mm.

The tubes (1.2 cm longer than the base plate on each end) were brazed into the channels in the base plate using a braze alloy foil containing 70 percent gold, 8 percent palladium, and 22 percent nickel (AMS-4786, 1310 K liquidus). Header pieces of commercially pure nickel, with holes drilled to match the tube locations, were slipped onto the protruding tubes on each end of the base plate. The header pieces were brazed to the tubes and base plate using an alloy of 82 percent gold and 18 percent nickel (AMS-4787, 1223 K liquidus).

Channel Specimen. The channel specimen is shown in Fig. 4. It consisted of 12 parallel-flow channels of rectangular cross section milled in a lower plate of commercially pure nickel, with a cover plate of commercially pure nickel brazed to it. The channel width and height were 3.18 mm and 0.56 mm, respectively. The ridge between channels was 3.18 mm wide. The lower plate was 3.12 mm thick, and the cover plate was 1.93 mm thick, for a total thickness of 5.05 mm. The specimen was 7.86 cm wide and 19.1 cm long.

The cover plate was brazed to the base plate in a vacuum oven using a 0.025-mm-thick braze alloy foil of 50 percent gold, 25 percent palladium, and 25 percent nickel (AMS-4784, 1394 K liquidus). Prior to brazing, the inner facing surface of each plate was lapped to a flatness of ±0.01 mm. An X-ray of the specimen after brazing showed that large braze fillets formed in 4 of the 12 channels, which partially occluded the flow passages. For the channel with maximum blockage, the reduced width of the channel was about 30 percent of the unblocked width, and the blockage extended over 20 percent of the channel length.

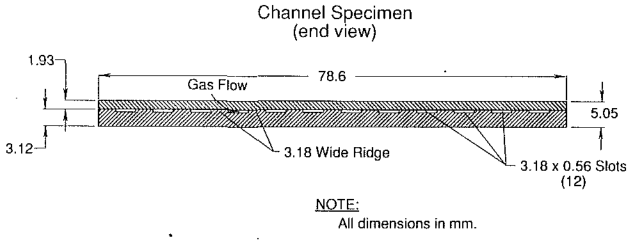

Fig. 4 Channel specimen

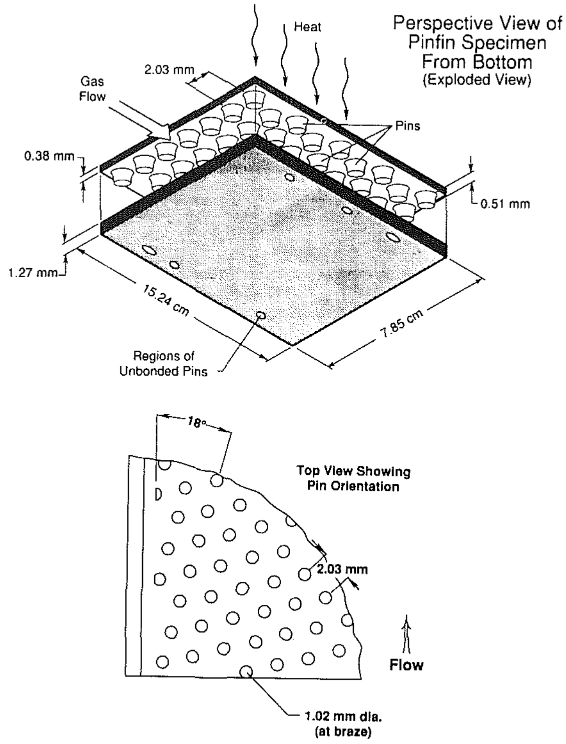

Fig. 5 18 deg pin-fin specimen

18 deg Pin-Fin Specimen. The pin-fin specimen was constructed at NASA Langley Research Center and is shown in Fig. 5. The specimen consisted of an upper plate with integral pins, and a lower plate to which the pins of the upper plate were brazed. Both plates were made of commercially pure nickel. The total thickness of the upper plate was 0.89 mm, with 0.51-mm-high pins and 0.38 mm plate thickness above the pins. The lower plate was 1.27 mm thick. The pins were formed in the upper plate in a photochemical etching process. The pin diameter varied from 2.03 mm at its base to 1.02 mm at the point of braze to the bottom plate; the ratio of pin height to diameter varied from 1/4 to 1/2. The centers of the pins were located at the corners of equilateral triangles. The separation from pin center to pin center was 2.03 mm. The angle of a line drawn through the pin centers, with respect to the flow direction, was 18 deg. (Refer to Fig. 5: The angle for maximum channeling of the flow would be 0 deg; the angle for maximum stagger would be 30 deg.)

The top and bottom plates were brazed together in a vacuum oven using a 0.025-mm-thick braze alloy foil of 50 percent gold, 25 percent palladium, and 25 percent nickel (AMS-4784, 1394 K liquidus). Prior to brazing, the inner facing surface of both plates was lapped to a flatness of ±0.01 mm. After brazing, the specimen was pressurized by NASA Langley to 10.3 MPa (1500 psi). This caused the top plate to deflect from the bottom plate at six spots where the pins had not brazed to the lower plate. The locations of the unbounded spots were as shown in Fig. 5. The normal area occupied by the disbonds was less than 1 percent of the total normal area of the specimen.

All Specimens. After the specimens were built, they were installed in slots in the inlet and outlet manifolds. The tube specimen was welded to the manifolds. The channel and pin-fin specimens were brazed to the manifolds using a braze alloy of 82 percent gold and 18 percent nickel (AMS-4787, 1223 K liquidus). For the channel and pin-fin specimens, the pressure tap tubes (1.5 mm o.d., 1.0 mm i.d.,) were brazed to the specimen during this braze cycle. We pressurized the manifold and specimen assemblies to a pressure about 3.5 MPa (500 psi) above the maximum test pressure prior to installing them into the flow apparatus, and there were no leaks. We painted the top side of the specimens a very-high-temperature, flat black paint over the 15.2 cm length to establish a uniform and highly absorptive surface over the heated area. The manufacturer of the paint listed the total, normal emissivity as 0.85 ± 0.05.

The geometry of the three specimens is summarized in Table 1. The hydraulic diameter and flow area were based on the open volume in the specimen, which is the method used by VanFossen (1982) for analyzing his pin-fin data. The definition for D_h reduces to $D_h = 4A_f/P_w$ when the open volume does not change with length, which is the case for the tube and channel specimens. The hydraulic diameters are all on the order of 1mm. The tube specimen has the smallest flow are, so for similar pressure, density, and gas flow it had the highest velocities. Because the Reynolds number scales as D_h/A_f, the pin-fin specimen will have the lowest Reynolds numbers for the same gas flow. The wall area is much greater for the pin-fin specimen; if the Nusselt numbers are about the same for all specimens, the pin-fin specimen should have the smallest wall-to-fluid temperature difference for a given heat flux and gas flow.

Measurements and Instrumentation. We determined the distribution of normal heat flux on the specimen by calibrating the furnace prior to installing the specimen. Absolute heat flow on the specimen was determined by using the distribution function obtained from the calibration in conjunction with the heat gain of the helium flowing through the specimen. Because up to 75 percent of the calculated radiant energy, generated by the lamps in the heater, was absorbed by the water and air cooling the lamp and furnace walls, we did not perform an energy balance between the radiation heat flow from the furnace and the heat gain of the helium.

To calibrate the furnace, a heat flux gage, which measured normal heat flux, was soldered to a water-cooled copper plate. We painted the heat flux gage and copper plate with the same paint applied to the three specimens. We placed the plate in the target area of the furnace, prior to installing the specimen. The heat flux gage was traversed across the target area of the furnace, measuring the heat flux as a function of position. The furnace was calibrated both with the refractory, insulating walls and with the reflective, cooled walls. The heat flux was constant in the direction perpendicular to flow, y, for both sets of walls. In the direction parallel to the flow, x, the heat flux varied by no more that ±15 percent for the refractory walls; for the reflective walls, the heat flux varied by no more than ±7 percent, except within 6 percent of the end walls. We rechecked the calibration periodically, and there was no change in calibration. The uncertainty of the measurement was ±4 percent.

The temperature of the gas in the inlet and outlet manifolds was measured with platinum resistance thermometers (PRTs), 4.8 mm diameter, inserted at locations A and B of Fig. 2. The uncertainty in the measurement was ±0.5 K. We measured the upstream gas pressure (location 0 for the channel and pin-fin specimens, location A in the tube specimen) with a variable-reluctance pressure transducer. The uncertainty was ±0.25 percent. Difference in pressure between the upstream and downstream (locations 0 and 1 in the channel and pin-fin specimens, locations A and B in the tube specimen) was measured with a differential pressure transducer, also a variable-reluctance type. The uncertainty in the pressure measurement was ±0.5 percent of the reading or ±0.1 percent of full scale, whichever was greater.

Table 1 Summary of geometry for specimens

Parameter	Specimen		
	Tube	Channel	18° Pin-fin
L (cm)	15.24	15.24	15.24
w (cm)	7.82	7.86	7.85
H (mm)	4.19	5.05	2.16
D_h (mm)	1.016	0.950	0.715
A_f (cm^2)	0.162	0.213	0.253
A_w (cm^2)	97.3	136.6	215.8
A_n (cm^2)	119.2	119.8	119.6
A_w/A_n	0.816	1.140	1.804
D_h/A_f (cm^{-1})	0.627	0.446	0.283

We measured temperatures of the unheated (insulated) sides of the specimens with thermocouples made from type-N wire, which had a wire diameter of 0.25 mm. We spotwelded at least 29 thermocouples to the surface. The uncertainty in the measured temperature was the greater of: (*a*) ±1.1 K, or (*b*) ±0.4 percent of the difference between the measured temperature and a reference temperature (≈300 K). Temperatures measured with the insulated-side thermocouples were used to determine the heat transfer coefficient, as the installation technique did not disturb the specimen temperatures and conduction errors were insignificant.

Description of Experiments and Analysis Techniques

Experiments Conducted. A summary of the conditions for the experiments conducted on the tube, channel, and 18 deg pin-fin specimens is shown in Table 2. Complete tables for the measured and calculated parameters at each data point for each experiment are found in Olson and Glover (1990) (tube specimen), Olson (1990) (channel specimen), and Olson (1991) (pin-fin specimen). The tube and pin-fin specimens were tested at system pressures of 3.5 MPa (500 psi), while the channel specimen was tested at pressures of 3.5 MPa and 7.1 MPa. We determined the friction factor from the experiments with zero heat flux. Reynolds numbers were lower for the pin-fin specimen because the hydraulic diameter was less, and because the maximum helium flow rate was less (due to the higher pressure drop). We allowed the specimens and manifolds to reach thermal steady state before taking data. Gas inlet temperature and pressure, furnace heating, and helium flow rate remained sufficiently steady while taking data to ignore thermal transients in the data analysis. Duplicate heat transfer measurements on the pin-fin specimen two months apart showed no shift in the data, indicating negligible change in the emissivity of the surface.

Data Analysis. For the experiments conducted, we analyzed the measured data to determine the Nusselt number, Nu, from the tests with heating, and the isothermal friction factor, f, from the tests without heating. A modified Nusselt number, Nu_m, was calculated to include the effects of variations in thermophysical properties between the wall and the fluid. For the pin-fin specimen, we calculated a wall Nusselt number, Nu_w, in which we extrapolated the temperature of the insulated side to the temperature of the wall-fluid interface. Nu, Nu_m, and Nu_w were calculated at each location of an insulated-side thermocouple and were correlated with the Reynolds number, Re.

Friction Factor. The isothermal friction factor, f, is de-

Table 2 Summary of experimental conditions for specimens

Parameter	Specimen		
	Tube	Channel	18° Pin-fin
Inlet Pressure (kPa)	3500	3450, 7100	3500
Normal Heat Flux (W/cm²)	0 - 54	0 - 77	0 - 74
Helium Flow Rate (kg/h)	2.6 - 40	2.4 - 40	1.1 - 31
Reynolds Number	2200 - 36 000	1400 - 28 000	450 - 12 000
Prandtl Number	0.66 - 0.67	0.66 - 0.67	0.66 - 0.67
Range in Helium Temperatures (K)	277 - 647	291 - 710	284 - 742
Maximum Specimen Temperature (K)	743	784	761
Uncertainty in Flow Distribution (%)	5	5	2
Uncertainty in Re (%)	11.6	11.3	10.7
Uncertainty in f (%)	14 - 16 for Re > 3000	17 - 18 for Re > 4000	22 - 23 for Re > 500
Uncertainty in Nu (%)	6.6 - 13.8	7.6 - 13.8	13.6 - 43.8

rived from integrating the one-dimensional momentum equation in the flow direction:

$$P_0-P_1=G^2\left(\frac{1}{\rho_1}-\frac{1}{\rho_0}\right)+2\frac{G^2}{D_h}\int_0^L\frac{f}{\rho}\,dx \qquad (1)$$

In the tube specimen, the pressure was measured at points A and B in the inlet manifold, and the pressure was estimated for points 0 and 1 by subtracting inlet and outlet losses.

When the specimen is not heated, Re is constant from the inlet to the outlet, so f is constant and can be removed from the integral. For the tube and channel specimens, the change in density was small compared to the absolute density and the integral could be approximated as a constant. The resulting expressing for f is

$$f=\frac{(P_0-P_1)-G^2\left(\frac{1}{\rho_1}-\frac{1}{\rho_0}\right)}{2G^2\frac{L}{D_h}\bullet\frac{2}{(\rho_0+\rho_1)}}. \qquad (2)$$

For the pin-fin specimen, even with no heating, at high helium flow rate the pressure drop could be 40 percent of the inlet pressure. By assuming a linear pressure drop and density drop through the specimen, we can evaluate the integral, and the resulting expression for f is

$$f=\frac{(P_0-P_1)-G^2\left(\frac{1}{\rho_1}-\frac{1}{\rho_0}\right)}{2G^2\frac{L}{D_h}\bullet\frac{\ln\frac{\rho_0}{\rho_1}}{(\rho_0-\rho_1)}}. \qquad (3)$$

To compare the pressure drop between the various specimens in a way that removes differences in absolute density, macroscopic length and width, and the internal flow geometry, we calculate a "normalized" pressure drop, ΔP_n, which is

$$\Delta P_n=\frac{P_0-P_1}{\left(\frac{\dot{m}}{W}\right)^2}\bullet\frac{\rho_0}{\rho_{0,\mathrm{ref}}}\bullet\frac{L_{\mathrm{ref}}}{L}. \qquad (4)$$

The measured pressure drop is divided by the square of the mass flux because to first order the pressure drop varies with the square of the mass flux. The (arbitrary) reference density is the density at $P_0=3.5$ MPa and $T_0=293.16$ K; the reference length is 15.24 cm, and L is the length between the locations 0 and 1.

Heat Transfer. The heat transfer coefficient, h is defined through the equation

$$q_w=h\bullet(T_w-T_{aw}), \qquad (5)$$

where q_w is the local heat flux (heat flow per unit area) into the cooling fluid based on total wetted-wall area of the specimen; T_w is the specimen temperature of the insulated wall; and T_{aw} is the adiabatic wall temperature of the cooling fluid. The adiabatic wall temperature was used since adiabatic heating was as much as 2 K at the high flow rates and heating rates. The local heat flux was obtained by using the calibration of the furnace in conjunction with the measured enthalpy rise of the helium in the specimen. We express q_w in terms of the total heat transfer to the specimen Q_T, the furnace calibration function f_q and the wall area of the specimen:

$$q_w=\frac{Q_T}{A_n}\bullet\frac{A_n}{A_w}\bullet f_q\,. \qquad (6)$$

The calibration function f_q is on the order of 1, and if the heat flux were constant then f_q would be 1 everywhere. Measured wall temperature indicate that heat conduction was negligible both perpendicular to the flow direction (y), and in the flow direction (x), except near the end manifolds.

Combining Eqs. (5) and (6), and substituting for T_{aw}, the equation for the heat transfer coefficient, h, is

$$h=\frac{\frac{Q_T}{A_w}\bullet f_q}{T_w-\left(T_f+\frac{rV^2}{2c_p}\right)}, \qquad (7)$$

where T_f is the local bulk fluid temperature and r is the recovery factor.

The total heat absorbed by the specimen, Q_T, was calculated from the first law of thermodynamics using the enthalpy, h, of the gas at the inlet and outlet manifolds, and the helium flow rate:

$$Q_T=\dot{m}\bullet(h_B-h_A). \qquad (8)$$

The enthalpy was evaluated from the functions given by McCarty (1973), using the measured temperatures in the inlet and outlet manifolds and the gas pressure drop:

$$h=h(T_f,P). \qquad (9)$$

For the channel and pin-fin specimens, the pressure at A and B was estimated by assuming a linear pressure along the specimen and extrapolating the pressure from 0 and 1. This assumption introduces less than 0.1 percent error in Q_T. The total uncertainty in Q_T was less than ±3 percent.

For the tube specimen in the refractory furnace, the measured heat flow was adjusted to account for heat conducted from the furnace to the manifolds. This heat leak was insignificant for the reflective furnace, so adjustment was not necessary for the channel and pin-fin specimens. Kinetic energy changes from A to B were insignificant compared to the uncertainties in the enthalpy produced by uncertainties in the measured gas temperatures.

The fluid temperature, T_{fx}, was calculated by integrating the flow energy equation from the inlet manifold up to x, now including kinetic energy:

$$T_{fx}=T_A+\frac{Q_TQ_{px}}{\dot{m}_wwc_p}+\frac{\int_A^x\left(\frac{1-\beta T_f}{\rho}\right)dP}{c_p}-\frac{V_x^2}{2c_p}+\frac{Q_{m,in}}{\dot{m}c_p}. \qquad (10)$$

Q_{px} is the fraction of the total heat flow added from 0 to position x, which is calculated by integrating the furnace calibration function f_q, 0 to x. $Q_{m,in}$ is the heat leak through the furnace to the inlet manifold. For the channel and pin-fin specimens in the reflective furnace, this term was negligible. The pressure term was included for the slight deviation from the ideal gas state. Over the range of temperatures and pressures tested the specific heat changes by less than 0.1 percent. The velocity at x, V_x, is given by

$$V_x = \frac{\dot{m}_w w}{A_f \rho_x} . \tag{11}$$

The density at x, ρ_x, is given by the equation of state (McCarty, 1973) as

$$\rho_x = \rho_x(T_{fx}, P_x) . \tag{12}$$

To evaluate the pressure term in Eq. (10) and the density in Eq. (12), we assumed the pressure varied linearly between locations 0 and 1. This assumption introduced a maximum error in T_f of less than 0.15 K for the pin-fin specimen, and less for the tube and channel specimens. The equations for temperature, velocity, and density were solved through iteration.

The gas flow, $\dot{m}_w$, can vary in the y direction, which we did not measure directly. If this variation is not accounted for, it translates into an error in the fluid temperature, which propagates as errors in h and Nu. An approximate method for estimating how $\dot{m}_w$ varies in the y direction is described by Olson (1990). This method uses the measured wall temperatures across the specimen at constant x. Since the incident heat flux does not vary in the y direction, the product of the local gas flow and the temperature difference between the fluid at the inlet and x does not vary with y (variations in the kinetic energy term and the pressure term of Eq. (10) in the y direction are negligible compared to uncertainties in the wall temperature). We also assume that the product of the local mass flow rate and the local wall-to-fluid temperature difference is constant; this is equivalent to requiring that the exponent on the Nu-versus-Re correlation is 1.0, which introduces less than a 1 percent error on the calculated Nu. We then require that the gas flow integrated across the specimen width equals the measured total gas flow. For the channel and tube specimens the calculation was performed at $x/L = 0.5$. For the pin-fin specimen, the variation in T_w with y at constant x was of the same order as the uncertainty in wall temperature, indicating the flow was constant with y within experimental uncertainty. The adjusted flow was used in calculating f and h.

After determining T_f and V at location x, the heat transfer coefficient was calculated using Eq. (7). We evaluated transport properties at T_f using the functions given in McCarty (1972). The Nusselt number was calculated from the heat transfer coefficient of Eq. (7), based on the actual finite $T_w - T_{aw}$. In correlating heat transfer results with high wall-to-fluid temperature differences, we accounted for differences in viscosity and thermal conductivity between the wall and the fluid. We used the temperature ratio method of Rohsenow and Hartnett (1973):

$$\mathrm{Nu}_m = \mathrm{Nu} \cdot \left(\frac{T_w}{T_f}\right)^{0.55} . \tag{13}$$

We *defined* the heat transfer coefficient, h, in terms of the insulated wall temperature, which was the temperature we measured. However, h is commonly defined in terms of a solid-fluid interface temperature. Because the specimens were heated from one side only, solid temperatures will vary between the heated side, the insulated side, and the solid-fluid interface. For the tube and channel specimens, a finite element analysis with approximate heat transfer coefficients indicated that the fluid convection compared to the solid conduction was low enough that the temperature variations in the solid were small compared to the temperature difference between the wall and the fluid; that is, the "fin" efficiency was 1. In the pin-fin specimen, the convection heat transfer was higher, and temperature variations in the solid were not insignificant (the fin efficiency was less than 1).

To calculate a heat transfer coefficient that accounted for temperature variations in the pin, we analyzed the heat conduction in the pin using the finite element method. The boundary conditions to the analysis were the anticipated values of the wall heat transfer coefficient, h_w, anticipated normal heat fluxes, and the adiabatic wall temperature. Because there are no detailed measurements of the local h_w, we assumed h_w was uniform around a pin and on top and bottom plates. From the heat conduction analysis, we calculated a pin efficiency, η, defined by

$$\eta = \frac{\dfrac{Q_T}{A_n}}{h_w \cdot (T_w - T_{aw})} . \tag{14}$$

The temperature of the insulated wall, T_w, was calculated in the analysis. The analysis was repeated for the range of h_w expected experimentally. η was then correlated as a function of the Biot number, where $\mathrm{Bi} = h_w D_h / k_{ni}$. h_w was calculated for the *experimental* data by using Eq. (14) with the measured values of Q_T/A_n, T_w, T_{aw}, and the function η versus Bi. h_w was normalized as a wall Nusselt number:

$$\mathrm{Nu}_w = \frac{h_w D_h}{k} \cdot \left(\frac{T_w}{T_f}\right)^{0.55} . \tag{15}$$

To compare heat transfer between specimens in a way that directly indicates the magnitude of $T_w - T_f$ for a given normal heat flux and gas flow, we define a "normalized" heat transfer coefficient as

$$h_n = \frac{\dfrac{Q_T}{A_n}}{T_w - T_f} . \tag{16}$$

This parameter ignores the details of the internal geometry of the specimens.

Uncertainty Analysis. Uncertainties for the calculated quantities were obtained by Taylor series error propagation as described by ASME (1986). This technique generally produces the same level of confidence in a calculated result as the level of confidence in the measurements that contribute to the result (Kline and McClintock, 1953). A summary of the uncertainties for the flow distribution, Nu, Re, and f is listed in Table 2. The uncertainty in flow distribution was based on the wall temperatures measured along a line perpendicular to the flow direction. The largest contributor to the uncertainty in Nu was the uncertainty in flow distribution, and the uncertainty in Nu was greatest near the exit of the specimen. Even though we estimate that the uncertainty in the flow distribution was smallest for the pin-fin specimen, because the wall-to-fluid temperature difference was at least 5 times smaller for the pin-fin specimen, the uncertainty in Nu was much higher.

Results of Experiments

Friction Factor and Pressure Drop. The variation of the isothermal friction factor with Reynolds number is shown for the three specimens in Fig. 6. The isothermal friction of the pin-fin specimen is much higher than either the channel or tube specimens. Shown also is the von Karman-Nikuradse correlation (Rohsenow and Hartnett, 1973) for flow in a smooth tube. The correlations for the three specimens, the Reynolds number range, and the standard deviations, σ, between the data and the correlation are

$$\text{Tube (Re} > 5000\text{)}: f = 0.07532 \cdot \mathrm{Re}^{-0.2693} \quad \sigma = 2.78 \text{ percent}, \tag{17}$$

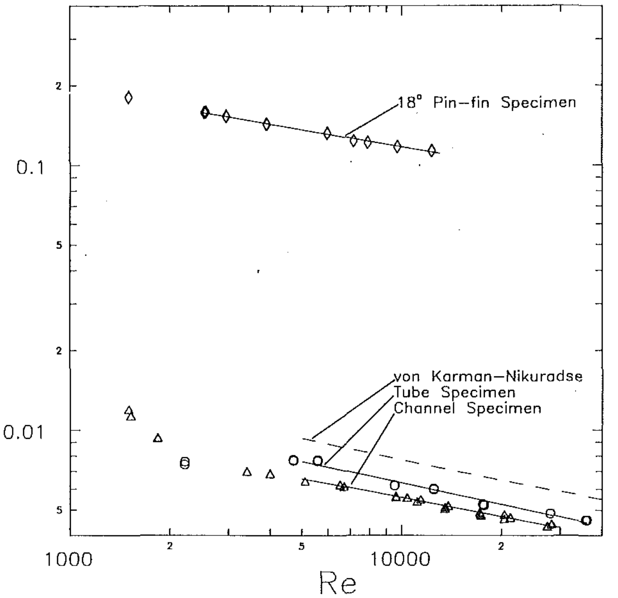

Fig. 6 Isothermal friction factor (*f*) as a function of Reynolds number (Re) for all specimens, no heating

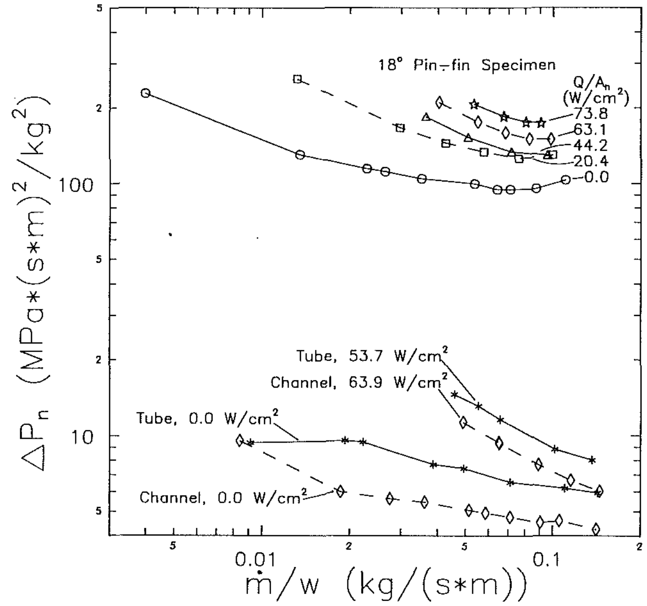

Fig. 7 Normalized pressure drop (ΔP_n) as a function of gas flow per unit width ($\dot{m}/w$) for all pin-fin experiments, and for tube and channel experiments at no heating and high heating

Channel (Re>5000): $f = 0.05058 \cdot \text{Re}^{-0.2397}$ $\sigma = 1.26$ percent, (18)

18 deg pin fin(Re>2500):

$$f = 0.8561 \cdot \text{Re}^{-0.2160} \quad \sigma = 0.92 \text{ percent}, \tag{19}$$

The tube and channel specimen data lie 18 to 20 percent and 27 to 30 percent, respectively, below the smooth tube correlation. Although the uncertainties in f are nearly as high as the deviation from the smooth tube correlation, we believe the cause of the difference between our measurements and the accepted values is that the specimens are too "short" to make an accurate measurement of friction factor. For both specimens, $4fL/D_h \approx 3$, and the dynamic head, $\rho V^2/2$, is about 30 percent of the total pressure drop. The pressure taps were located near regions of rapid flow area changes, making an accurate static pressure measurement difficult. Losses of 1 or more times the dynamic head would account for the discrepancy between our data and the smooth tube correlation.

For the pin-fin specimen, the uncertainty in our measured values of f is believed to be 22–23 percent for Re>450. The largest source of uncertainty for f was the uncertainty in the height of the pins, which we estimated as 0.025 mm. This could not be confirmed without sectioning the specimen, which would render it unusable for future tests. If the uncertainty in height of the pins were half as much, or 0.013 mm, then the uncertainty in f would be 12–13 percent. Because the dynamic head was 1 percent or less of the total pressure drop, it is not likely that installation errors were significant for the pin-fin.

Metzger et al. (1982) measured friction factors of staggered pin fins with constant diameter, which had length-to-diameter ratios of 1, using air. They correlated the data in the same format as for long cylinders, where the hydraulic diameter is the pin diameter, the characteristic velocity is the maximum velocity in the channel (which occurs at the minimum area), and the pressure drop scales with the number of rows of pins the flow passes between the pressure taps. Or,

$$f_M = \frac{(P_0 - P_1) - G^2\left(\dfrac{1}{\rho_1} - \dfrac{1}{\rho_0}\right)}{2\rho V_{\max}^2 N}. \tag{20}$$

Metzger et al. found, for $10^3 < \text{Re} < 10^4$,

$$f_M = 0.317 \cdot \text{Re}^{-0.132}. \tag{21}$$

We can compare our measurements of friction factor to their results, making some assumptions about minimum flow area and number of rows. If the angle of the pins to the flow for our specimen were 30 deg instead of 18 deg, then there would be 87 rows in the flow direction. If we use as the minimum flow area the open area along a row of pins, at Re = 8000, we calculate a pressure drop that is 23 percent lower using the Metzger correlation than what we measure. This agreement is probably reasonable because both N and $V_{\max}$ are approximations, due to the differences in geometry between our specimen and that of Metzger et al. Metzger et al. indicate that the exponent of the Re term changes to -0.318 for $10^4 < \text{Re} < 10^5$, which makes our exponent approximately midway between what they report.

Figure 7 shows the measured, normalized pressure drop, ΔP_n, for all heating levels in our pin-fin specimens, along with the tube and channel specimens at conditions of no heating and high heating. ΔP_n was plotted against the flow rate per unit width; in the NASP application, the mass flow will be the same regardless of the heat exchanger chosen due to constraints on the gas outlet temperature. The pressure drop in the 18 deg pin-fin specimen was much greater than in either the tube or channel specimens. For example, interpolating from the measured data to $\dot{m}/w = 0.1 \text{kg}/(\text{s} \cdot \text{m})$, at the reference density, reference length, and no heating, the pressure drop for the various specimens would be: pin-fin specimen, 1000 kPa (145 psi); tube specimen, 62 kPa; and channel specimen, 45 kPa.

The pressure drop for all specimens increased as the heat flux increased. As the heat flux increased, the gas temperature increased and the density decreased. This produced higher velocities and the higher pressure drop. The friction factor does not, however, appear to depend on the heating rate. Using the correlation of f versus Re developed for the tests without heating, we integrated Eq. (1) along the specimen for the tests with heating, and evaluated ρ, Re, and f at each location where T_w was measured. The predicted pressure drop agreed to within experimental uncertainty of the measured pressure drop.

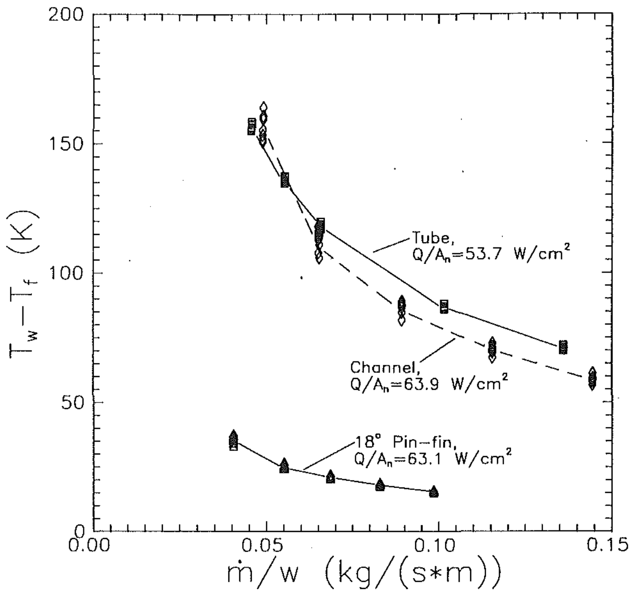

Fig. 8 Wall-to-fluid temperature difference ($T_w - T_f$) as a function of gas flow per unit width ($\dot{m}/w$) for a single heat flux for the tube, channel, and pin-fin specimens

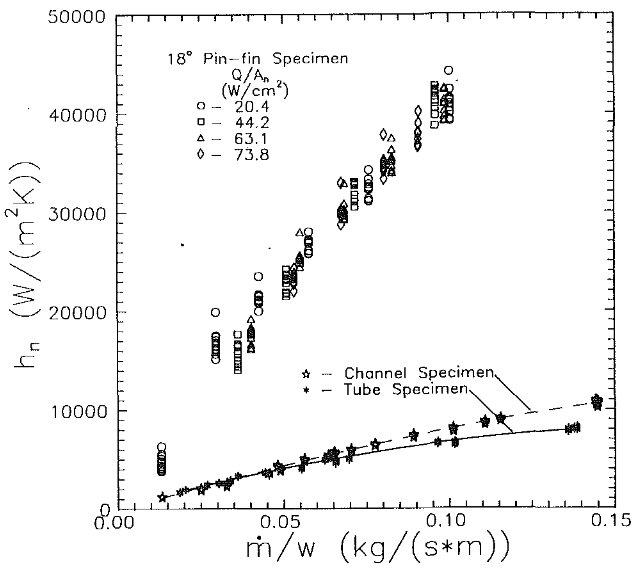

Fig. 9 Normalized heat transfer coefficient (h_n) as function of gas flow per unit width ($\dot{m}/w$) for all specimens

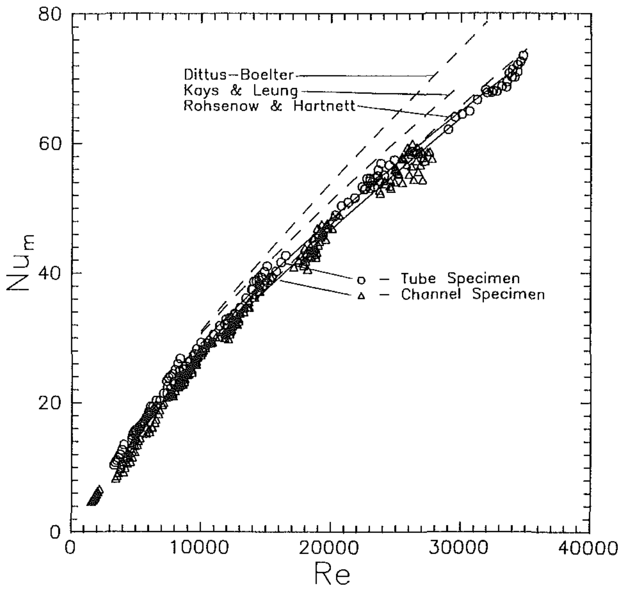

Fig. 10 Modified Nusselt number (Nu_m) as a function of Reynolds number (Re) for tube and channel specimens

Heat Transfer. When the specimens were heated, the gas temperature increased almost linearly from the inlet to the outlet. The maximum outlet temperature was 2.6 times the inlet temperature. Higher flow rate for the same heating rate reduced this temperature increase. The density decreased and the velocity increased along the specimen due to the temperature rise and pressure drop. Gas thermal conductivity and viscosity increased from the inlet to the outlet due to the temperature increase. Re and Nu decreased from the inlet to the outlet. The maximum Mach number was 0.14, which occurred in the tube specimen at the highest heat flux and flow rate.

The relative performance of the three specimens can be seen in Fig. 8, which shows the measure wall-to-fluid temperature difference ($T_w - T_f$) as a function of gas flow rate per unit width; a single heat flux setting is shown for each specimen. $T_w - T_f$ is smallest for the pin-fin specimen, showing that it has better heat transfer performance than the tube or channel specimens. Because $T_w - T_f$ is linear with heat flux, if the tube specimen had been tested around a heat flux of 63 W/cm^2, $T_w - T_f$ would be 30 percent higher than it is for the channel specimen. Uncertainties in Nu are much higher for the pin-fin specimen than for the tube or channel specimen because the temperature differences are so small. For example, at $\dot{m}/w = 0.1$ kg/(s•m), $T_w - T_f = 15$ K. Uncertainties in T_w and T_w can easily be 1 K and 4 K, respectively.

In Fig. 9 we have plotted the normalized heat transfer coefficient, h_n, as a function of the gas flow per unit width, $\dot{m}/w$. This figure contains data for all the heat fluxes tested. For the pin-fin specimen, h_n is 5 to 6 times higher than it is for the tube or channel specimens, for a given $\dot{m}/w$, reflecting a $T_w - T_f$ that is 5 to 6 times lower for the pin-fin specimen when compared to the tube or channel specimen. The scatter in h_n for the pin-fin specimen represents Re effects that are ignored in the definition of h_n. h_n was slightly higher for the channel specimen because the channel specimen had more wall surface area.

Results of experiments with heat transfer on the tube and channel specimens are shown in Fig. 10, where we plot both the measured Nu_m and the correlations of the data against Re. Also plotted are several correlations from the literature for turbulent flow in single tubes in which the heat transfer coefficient is based on the wall-fluid interface temperature. Temperatures of the wall measured transverse to the flow direction indicated that the velocities were highest in the center channels or tubes. Heat conduction from the specimen to the inlet and outlet manifold was found to be significant from $x/L = 0$ to 0.2, and from $x/L = 0.8$ to 1.0. The data plotted and used in the correlation are at $y/w = 0$ and $0.2 < x/L < 0.8$. The tube and channel correlations, along with the standard deviations between the data and correlation, are

Tube (Re > 10,000):

$$\mathrm{Nu}_m = 0.0442 \cdot \mathrm{Re}^{0.731} \cdot \mathrm{Pr}^{0.6} \quad \sigma = 1.8 \text{ percent}, \tag{22}$$

Channel (Re > 10,000):

$$\mathrm{Nu}_m = 0.0298 \cdot \mathrm{Re}^{0.768} \cdot \mathrm{Pr}^{0.6} \quad \sigma = 2.6 \text{ percent}. \tag{23}$$

In terms of Nu, the correlations are

$$\text{Tube (Re} > 10{,}000\text{):} \quad \mathrm{Nu} = 0.0442 \cdot \mathrm{Re}^{0.731} \cdot \mathrm{Pr}^{0.6} (T_w/T_f)^{-0.55}, \tag{24}$$

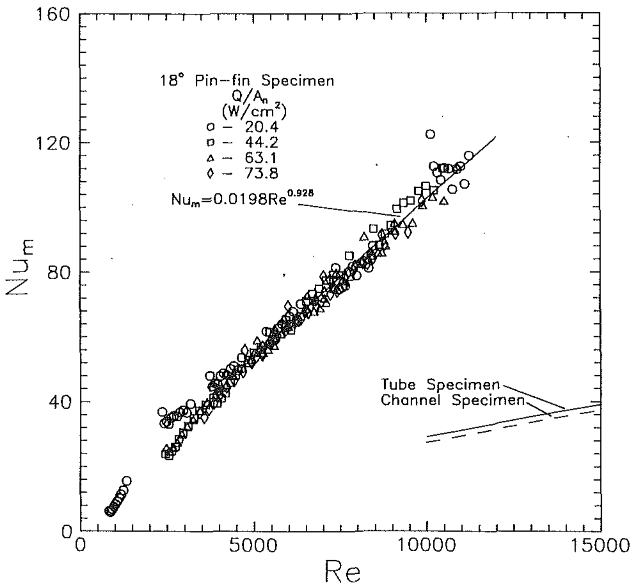

Fig. 11 Modified Nusselt number (Nu_m) as a function of Reynolds number (Re) for pin-fin specimen, plus correlations for tube and channel specimens

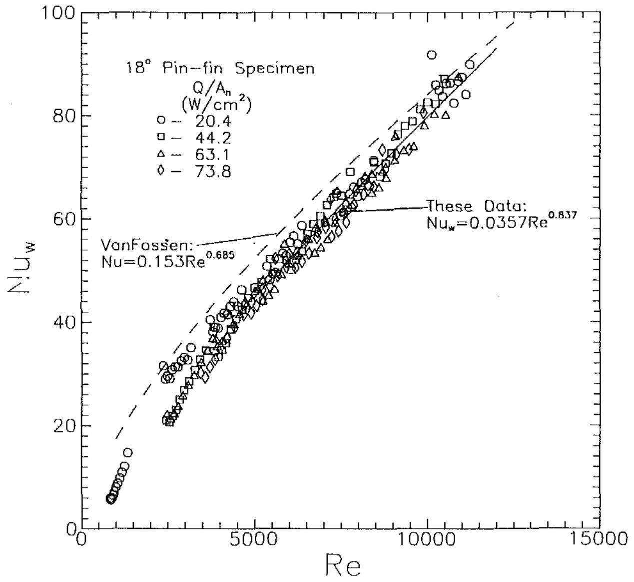

Fig. 12 Wall Nusselt number (Nu_w) as a function of Reynolds number (Re) for pin-fin specimen

Channel ($Re > 10{,}000$):

$$Nu = 0.0298 \cdot Re^{0.768} \cdot Pr^{0.6} (T_w/T_f)^{-0.55}. \quad (25)$$

The correlations from the literature for single tubes are:

Dittus-Boelter: $Nu = 0.023 \cdot Re^{0.8} \cdot Pr^{0.4}$, (26)
(in Rohsenow and Choi, 1961)

Rohsenow and Hartnett (1973):

$$Nu = 0.022 \cdot Re^{0.8} \cdot Pr^{0.6}, \quad (27)$$

Kays and Leung (1962): $Nu = 0.0422 \cdot Re^{0.74} \cdot Pr^{0.56}$. (28)

Equation (28) is a curve-fit of the theoretical analysis of Kays and Leung over the range $0.5 < Pr < 0.7$ and $10^4 < Re < 3 \times 10^4$. The boundary conditions of Eqs. (27) and (28) are constant heat flux along the direction of flow. Rohsenow and Hartnett (1973) indicate that the Dittus-Boelter correlation overpredicts Nu for $0.5 < Pr < 1.0$, which can be seen in Fig. 10.

We have assumed a 0.6 power variation on Pr, and the leading coefficient and exponent on Re were calculated from a least-squares fit. The uncertainty on Nu_m was 6.6 to 13.8 percent for the tube specimen, and 7.6 to 13.8 percent for the channel specimen. For both sets of data, the temperature ratio varied from 1.06 to 1.41, making Nu_m 3 to 21 percent higher than Nu. To within experimental uncertainty, the tube and channel specimen correlations and data agree with one another and with the correlations for single tubes. This indicates that the temperature of the wall on the insulated surface is representative of the wall-fluid interface temperature (fin efficiency of 1), that the effects of variable thermophysical properties are accounted for adequately in this method of correlation, and that flow acceleration (produced by the high heat flux) does not measurably affect the heat transfer.

Heat transfer for the pin-fin specimen is shown in Fig. 11. Plotted are the data and correlation for Nu_m, along with the correlations of the tube and channel specimens. For the pin-fin specimen, the region where conduction to the end manifolds was insignificant was $0.07 < x/L < 0.93$. As is the convention for the pin-fin literature, we include the Prandtl number effect in the leading coefficient of the correlation:

Pin-fin ($Re > 5000$): $Nu_m = 0.0198 \cdot Re^{0.928}$ $\sigma = 3.7$ percent, (29)

$$Nu = 0.0198 \cdot Re^{0.928} \cdot (T_w/T_f)^{-0.55} \quad (30)$$

The uncertainty in our experimental data was 13.6 to 43.8 percent, with the highest uncertainty occurring near the specimen outlet for low heat flux and high helium flow (conditions of the smallest $T_w - T_f$).

Heat transfer for the pin fin was much higher than heat transfer in the tube or channel specimens. The improvement in Nu_m beyond the tube or channel specimen correlations represents the enhancement due to the pins breaking up the flow path and increasing the turbulence.

When we extrapolated our data using Eq. (14) to calculate h_w, which includes the effect of fin efficiency, we got the results shown in Fig. 12. Plotted for comparison is the correlation of VanFossen (1982) from data on staggered circular pins with length-to-diameter ratios of 1/2 and 2; his data also include the effect of fin efficiency. The correlation for Nu_w is:

$$Nu_w = 0.0357 \cdot Re^{0.837} \qquad \sigma = 4.0 \text{ percent}, \quad (31)$$

VanFossen (1982): $Nu_w = 0.153 \cdot Re^{0.685}$. (32)

The correlation of our data agrees with that of VanFossen to within 15 percent at low Re and to within 3 percent at high Re, which is within the estimated uncertainty of our data. The good agreement suggests that at least to first order the tapered pin fins of our study are dynamically similar to straight pin fins of approximately the same length-to-diameter ratio.

For the NASP application, the amount of coolant available is limited, so a "good" heat exchanger is one with high heat transfer for a given flow rate. In other applications we might want to minimize pumping power. A comparison of the relative performance of the three specimens for constant pumping power is shown in Fig. 13. We have plotted Nu_w against $f \cdot Re^3$; pumping power is proportional to $f \cdot Re^3$ if flow acceleration is small compared to frictional losses and the gas temperature rise is small. This comparison also requires that the flow area be the same, and the heat transfer area be the same, for the specimens; hence we are considering hypothetical designs that are slightly different than these. The correlations from our data are used to calculate f and Nu_w for the pin fin; Nu_m is used for Nu_w for the tube and channel since the efficiency is 1. The Karman-Nikuradse correlation is used for f for the tube and channel since f for our data was systematically low. Figure 13 shows that the pin-fin specimen also is the best surface for high heat transfer at constant pumping power.

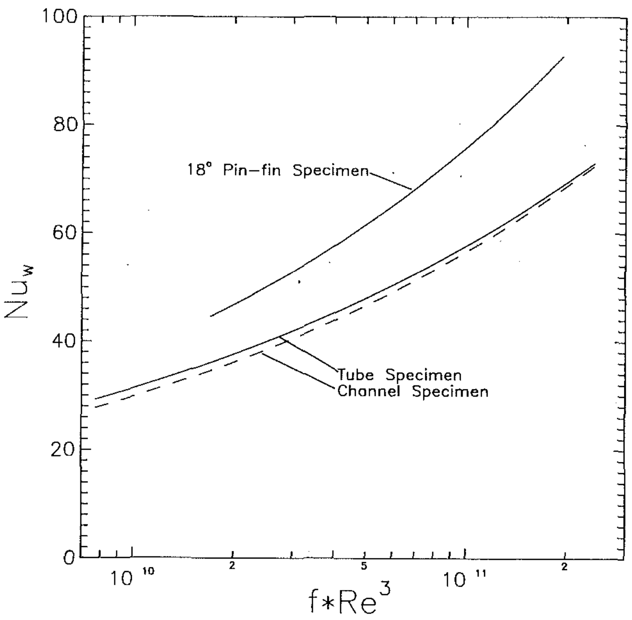

Fig. 13 Wall Nusselt number (Nu_w) as a function of pumping power ($f \cdot Re^3$) for pin-fin, tube, and channel specimens

Summary and Conclusions

We have measured the pressure drop and heat transfer in three compact heat exchangers, all of which have the same length and width, and which are radiatively heated on one side. The pin-fin specimen has a novel internal geometry that has never before been tested. For constant mass flow rate, this geometry transfers heat 5 to 6 times better than the tube specimen or the channel specimen geometries (which, however, were not optimized for heat transfer). The reasons for the improvement are the increased heat transfer area per unit surface area, and the higher levels of turbulence in the pin-fin passages. The pin-fin specimen also has a much higher pressure drop than either the tube or channel specimens, both when the specimens are heated and when they are isothermal.

The measured Nusselt numbers for the tube and channel specimen agree within experimental uncertainty with each other and to literature correlations for turbulent flow in a single tube. We accounted for variations in thermophysical properties between the wall and fluid due to the temperature difference between the wall and fluid. The heat transfer coefficient, h, was defined using the temperature of the insulated wall, since that temperature was the easiest and most accurate to measure. This did not introduce significant error between our data and past correlations in which h was based on the wall-fluid interface temperature.

For the pin-fin specimen, we report the heat transfer as a modified Nusselt number, which should be used for design purposes to predict the temperature on the insulated side of the specimen. We also report the heat transfer as a wall Nusselt number, which includes the fin efficiency and which we compared to the performance of past work on pin-fin configurations. Our measured wall Nusselt number agrees with the correlation of VanFossen to within experimental uncertainty for $Re > 5000$. For conditions of constant pumping power, the pin-fin design transfers heat better than the tube or channel geometry.

Acknowledgments

This work was supported by NASA Langley Research Center under contract L7400C. We greatly appreciate the efforts of Robert McWithey, Henry Elksnin, and Paul Sandefur in constructing the pin-fin specimen and brazing the channel specimen. We thank Michael P. Glover for constructing the tube specimen.

References

Armstrong, J., and Winstanley, D., 1988, "A Review of Staggered Array Pin Fin Heat Transfer for Turbine Cooling Applications," ASME *Journal of Turbomachinery*, Vol. 110, pp. 94–103.

ASME, 1986, "ASME Performance Test Codes Supplement on Instruments and Apparatus—Part 1—Measurement Uncertainty," ANSI/ASME PTC 19.1-1985.

Kays, W. M., and Leung, E. Y., 1962, "Heat Transfer in Annular Passages—Hydrodynamically Developed Turbulent Flow With Arbitrarily Prescribed Heat Flux," *Int. J. of Heat Mass Transfer*, Vol. 6,, pp. 537–557.

Kays, W., and London, A. L., 1964, *Compact Heat Exchangers*, McGraw-Hill, New York.

Kline, S. J., and McClintock, F. A., 1953, "Describing Uncertainties in Single-Sample Experiments," *Mechanical Engineering*, Vol. 75, pp. 3–8.

McCarty, R. D., 1972, "Thermophysical Properties of Helium-4 From 2 to 1500 K With Pressures to 1000 Atmospheres," NBS-TN-631.

McCarty, R. D., 1973, "Thermodynamic Properties of Helium 4 From 2 to 1500 K at Pressures to 10^8 Pa," *J. Phys. Chem. Ref. Data*, Vol. 2, No. 4, pp. 923–1042.

Metzger, D. E., Fan, Z. X., and Shepard, W. B., 1982, "Pressure Loss and Heat Transfer Through Multiple Rows of Short Pin Fins," in: *Heat Transfer 1982*, U. Grigull et al., eds., Vol. 3, pp. 137–142.

Olson, D. A., 1989, "Apparatus for Measuring High-Flux Heat Transfer in Radiatively Heated Compact Exchangers," NISTIR 89-3926, National Institute of Standards and Technology, Boulder, Co.

Olson, D. A., 1990, "Heat Transfer in a Compact Heat Exchanger Containing Rectangular Channels and Using Helium Gas," NISTIR 3959, National Institute of Standards and Technology, Boulder, Co.

Olson, D. A., and Glover, M. P., 1990, "Heat Transfer in a Compact Tubular Heat Exchanger With Helium Gas at 3.5 MPa," NISTIR 3941, National Institute of Standards and Technology, Boulder, Co.

Olson, D. A., 1991, "Heat Transfer and Pressure Drop in a Compact Pin-Fin Heat Exchanger With Pin Orientation at 18° to the Flow Direction," NISTIR 3965, National Institute of Standards and Technology, Boulder, Co.

Rohsenow, W. M., and Choi, H., 1961, *Heat, Mass, and Momentum Transfer*, Prentice-Hall, Englewood Cliffs, NJ.

Rohsenow, W. M., and Hartnett, J. P., 1973, *Handbook of Heat Transfer*, McGraw-Hill, New York.

Scotti, S. J., Martin, C. J., and Lucas, S. H., 1988, "Active Cooling Design for Scramjet Engines Using Optimization Methods," NASA TM-100581.

Shore, C. P., 1986, "Review of Convectively Cooled Structures for Hypersonic Flight," NASA TM-87740.

VanFossen, G. J., 1982, "Heat-Transfer Coefficients for Staggered Arrays of Short Pin Fins," ASME *Journal of Engineering for Power*, Vol. 104, pp. 268–274.

Numerical Simulation of the Fluid Flow and Heat Transfer Processes During Scavenging in a Two-Stroke Engine Under Steady-State Conditions

M. de Castro Gouveia

J. A. dos Reis Parise

A. O. Nieckele

Department of Mechanical Engineering,
Pontifícia Universidade Católica
do Rio de Janeiro,
22453, Rio de Janeiro, RJ, Brazil

A numerical simulation of the scavenging process in a two-stroke flat-piston model engine has been developed. Air enters the cylinder circumferentially, inducing a three-dimensional turbulent swirling flow. The problem was modeled as a steady-state axisymmetric flow through a cylinder with uniform wall temperature. The steady-state regime was simulated by assuming the piston head fixed at the bottom dead center. The calculation was performed employing the κ–ϵ *model of turbulence. A comparison of the results obtained for the flow field with available experimental data showed very good agreement, and a comparison with an available numerical solution revealed superior results. The effects of the Reynolds number, inlet port angles, and engine geometry on the flow and in-cylinder heat transfer characteristics were investigated. The Nusselt number substantially increases with larger Reynolds numbers and a smaller bore-to-stroke ratio. It is shown that the positioning of the exhaust valve(s) is the main parameter to control the scavenging process.*

Introduction

Scavenging is a critical area in the development of two-stroke diesel engines. In a very short period of time the air stream, coming from intake ports near the bottom dead center, must displace all the remaining products of combustion from the cylinder. Premature opening of the exhaust valves helps diminish the mass of combustion gases left in the cylinder, even though the bulk of the process is actually left to the air charge. In reality the scavenging process is, as illustrated by Meintjes (1987), an air/combustion product mixing process where the objective is to reduce the exhaust residual concentration.

The process requires a minimum of losses and is, of course, greatly affected by flow conditions. Swirl and recirculation flows can either improve or impart scavenging, depending on their intensity and location inside the cylinder.

Concerning in-cylinder flow conditions, a number of studies can be found in the literature. One could mention recent reviews, by Heywood (1987), Arcoumanis and Whitelaw (1987), Kamimoto and Kobayashi (1988), as well as conferences and symposia entirely devoted to the subject (Morel et al., 1987; Uzkan and Bailey, 1988; Uzkan, 1989).

Recent research involves the development of multidimensional computer codes to model the flow conditions inside reciprocating machinery. One early example is the CONCHAS (Butler et al., 1979) and the CONCHAS-SPRAY (Cloutman et al., 1982) computer codes, from Los Alamos National Laboratory, USA. Having the application to internal combustion engines specifically in mind, both codes were developed to generate numerical solutions to multicomponent reactive fluid flow problems in two space dimensions. CONCHAS-SPRAY is a descendant of CONCHAS, presenting new features such as the capability of modeling fuel spray and improved numerical algorithms.

Diwakar (1984, 1985) utilized the CONCHAS-SPRAY code to analyze the turbulent flow field inside some typical internal combustion engine chambers under motoring conditions. The study showed that the scavenging efficiency could be improved with minor alterations to the intake port swirl angle. The same model was utilized by Kuo and Duggal (1984) to assess the effect of engine design parameters, such as piston bowl shape, on air motion inside the cylinder. Two-dimensional models, in spite of the many assumptions that have to be made regarding the geometry of the engine, in order to make it axisymmetric, have been used extensively by several authors. These include Gosman et al. (1980), Zhang (1985), Chiu et al. (1986, 1987), and Chiu and Wu (1990).

Other examples of multidimensional models are provided by Kondoh et al. (1985), Ikegami et al. (1986), Inoge and Kobayashi (1987), Carapanayotis and Salcudean (1988), and Uzkan (1988).

Undoubtedly, a major progress in the prediction of in-cyl-

Contributed by the Heat Transfer Division for publication in the JOURNAL OF HEAT TRANSFER. Manuscript received by the Heat Transfer Division January 31, 1990; revision received July 22, 1991. Keywords: Forced Convection, Turbulence.

inder gas flow was achieved with the use of three-dimensional models. Reports on such models are provided in the literature by Gosman et al. (1984) and Diwakar (1987). Both codes made use of the k–ϵ turbulence model and the latter specifically aimed at the study of the gas exchange process in a uniflow-scavenged two-stroke engine. One important conclusion from Diwakar (1987) was that two-dimensional models, although providing less realistic results than three-dimensional codes, could still be useful in predicting trends regarding the influence of intake port angle on scavenging.

Measurements involving steady-state flow in model engines have also been carried out by Das (1974), Sung and Patterson (1982), Itoh et al. (1985), Vafidis et al. (1987), Doan et al. (1988), Basters et al. (1988), Borée et al. (1989), and Sher et al. (1988). These works provide a useful data base for validation of the models.

Another important aspect of flow and heat transfer studies for in-cylinder geometry is that they can be readily applied to other piston machines, such as the reciprocating compressor and the Stirling engine. In particular, there have been studies reported by West (1986) and Martini (1986) on the application of so-called "isothermalized" Stirling engines, whose main feature is that their heat exchangers are removed. It means that the energy conversion efficiency of such engines will rely entirely upon heat transfer conditions between the working gas and the cylinder walls.

The scavenge process in the two-stroke internal combustion engine and the isothermalization of the Stirling engine are two examples where the use of a computer code, capable of simulating in detail the flow and heat transfer characteristics for different geometries and operating conditions, can become a powerful and cost-effective tool in the design and development stages of the equipment.

The purpose of this paper is to present a numerical study of turbulent flow and heat transfer during the scavenging process in a two-stroke engine in which the piston head and cylinder walls are maintained at constant temperature. The model adopts simplifying assumptions (steady state, air flow only, axisymmetric geometry), which make it less accurate than the most up-to-date codes now available, such as that of Diwakar (1987). Results and conclusions were, therefore, limited to those that should not be very much affected by the model limitations. The idea was to present, with a simple and less costly computer code, a first assessment of the effects that some controlling parameters (geometry and flow conditions) have on the process.

Analysis

A cross section of the two-stroke engine under consideration is shown in Fig. 1. During the scavenging process, simultaneous inflow and outflow streams pass through the open ports. Fresh air is admitted with an axial and tangential component (given by the α and β angles), and scavenges the products of combustion through the exhaust valve. During the process the piston is near the bottom dead center and, although the crank angle varies by about 40 deg, the volume of the cylinder can be considered as being approximately constant. With this approximation and assuming that only air flows through the cylinder, it is possible to study the flow and heat transfer characteristics of the process in a steady-state regime.

Air enters the cylinder circumferentially (Fig. 1*c*), inducing a three-dimensional turbulent swirling flow where u, v, and w are the velocity components in the x, r, and θ coordinates, and leaves the domain through the exhaust port, which can be one of the three types shown in Fig. 1(*a*). Due to symmetry considerations of the cylinder and port assembly, the flow can be considered axisymmetric. With respect to the thermal boundary conditions, the piston head and the cylinder liner are assumed to be at constant temperature, since the variations of the gas temperature during the scavenge process are usually small when compared with the gas to wall temperature difference. It is further assumed that the flow is incompressible.

Governing Equations. The numerical calculation of the flow field and heat transfer are based on the time-averaged Navier–Stokes and energy equations. The κ–ϵ model of turbulence was selected to represent the turbulence behavior of the fluid. Appropriate dimensionless variables for this problem can be defined as

$$X=\frac{x}{D},\quad R=\frac{r}{D},\quad U=\frac{u}{V_m},\quad V=\frac{v}{V_m},\quad W=\frac{w}{V_m}$$

$$K=\frac{\kappa}{V_m^2},\quad E=\frac{\epsilon D}{V_m^3},\quad P=\frac{p^*}{(\rho V_m^2)},\quad \phi=\frac{(T-T_{in})}{(T_w-T_{in})} \tag{1}$$

Nomenclature

A = cross-sectional area
c_1, c_2, c_μ = constants in κ–ϵ turbulence model
C_d = discharge coefficient
D = cylinder diameter
E = dimensionless dissipation rate of turbulent kinetic energy
G = production term
K = dimensionless turbulent kinetic energy
k = thermal conductivity
L = cylinder height
L_1 = inlet aperture
$\dot{m}$ = mass flow rate
$\dot{m}_i$ = isoentropic mass flow rate
Nu = local Nusselt number
$\overline{\mathrm{Nu}}$ = overall Nusselt number
p^* = modified pressure
P = dimensionless modified pressure
q, $\bar{q}$ = local and average rate of heat transfer per unit area
R_{air} = gas constant of the air
R_1, R_2 = internal and external radius of exhaust
Re = Reynolds number
T = temperature
T_{in} = inlet temperature
T_b = exit bulk temperature
T_w = wall temperature
T^+ = dimensionless temperature
u, v, w = axial, radial, and tangential velocity components
U, V, W = dimensionless axial, radial, and tangential velocity components
V_m = mean velocity through the cross section
x, r = axial and radial coordinates
X, R = dimensionless axial and radial coordinates
X_1 = dimensionless inlet port size
y = distance to the wall
y^+ = dimensionless distance to the wall
α = axial inlet angle
β = inlet swirl angle
γ = ratio of the heat capacities at constant pressure and constant volume
ϵ = dissipation rate of turbulent kinetic energy
κ = turbulent kinetic energy
μ = dynamic viscosity
μ_t = turbulent viscosity
ρ = density
σ = Prandtl number
σ_t, σ_ϵ, σ_κ = constants in κ–ϵ turbulence model
τ_w = wall shear stress
ϕ = dimensionless temperature
ψ = dimensionless stream function
Ω = constant in "wall function"

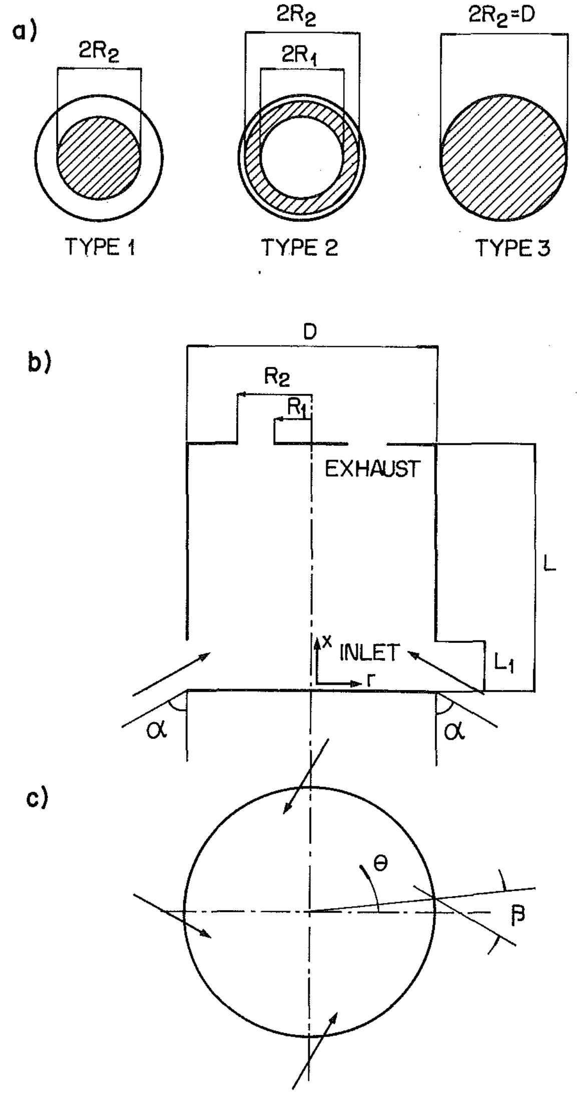

Fig. 1 Cylinder geometry: (*a*) exhaust port type, (*b*) cylinder cross section, (*c*) inlet port

where D is the cylinder diameter and V_m is the mean velocity through the cross section of the cylinder given by $V_m = \dot{m}/(\rho\pi D^2/4)$ where $\dot{m}$ is the mass flow rate of air into the cylinder. κ is the turbulent kinetic energy and ϵ its dissipation rate. T_{in} and T_w are the inflow air temperature and surface temperature (piston head and cylinder walls), respectively. p^* is the modified pressure defined as

$$p^* = p + \frac{2}{3}\rho\kappa \tag{2}$$

where p is the thermodynamic pressure, and ρ is the density.

For steady, incompressible flow in the axisymmetric situation, the flow field inside the cylinder can be determined by the simultaneous solution of the following equations expressing conservation of mass and momentum and transport of turbulent kinetic energy and its dissipation rate. The energy equation can be solved once the flow field is known.

Conservation of mass

$$\frac{\partial U}{\partial X} + \frac{1}{R}\frac{\partial (RV)}{\partial R} = 0 \tag{3}$$

Conservation of momentum (axial, radial, and angular directions)

$$\begin{aligned}\frac{\partial (UU)}{\partial X} + \frac{1}{R}\frac{\partial (RVU)}{\partial R} &= -\frac{\partial P}{\partial X} \\ &+ \frac{1}{\mathrm{Re}}\left\{\frac{\partial}{\partial X}\left[\frac{\mu_t}{\mu}\frac{\partial U}{\partial X}\right] + \frac{1}{R}\frac{\partial}{\partial R}\left[R\frac{\mu_t}{\mu}\frac{\partial U}{\partial R}\right]\right\} \\ &+ \frac{1}{\mathrm{Re}}\left\{\frac{\partial}{\partial X}\left[\frac{\mu_t}{\mu}\frac{\partial U}{\partial X}\right] + \frac{1}{R}\frac{\partial}{\partial R}\left[R\frac{\mu_t}{\mu}\frac{\partial V}{\partial X}\right]\right\}\end{aligned} \tag{4}$$

$$\begin{aligned}\frac{\partial (UV)}{\partial X} + \frac{1}{R}\frac{\partial (RVV)}{\partial R} &= \\ -\frac{\partial P}{\partial R} &+ \frac{1}{\mathrm{Re}}\left\{\frac{\partial}{\partial X}\left[\frac{\mu_t}{\mu}\frac{\partial V}{\partial X}\right] + \frac{1}{R}\frac{\partial}{\partial R}\left[R\frac{\mu_t}{\mu}\frac{\partial V}{\partial R}\right]\right\} \\ &+ \frac{1}{\mathrm{Re}}\left\{\frac{\partial}{\partial X}\left[\frac{\mu_t}{\mu}\frac{\partial U}{\partial R}\right] + \frac{1}{R}\frac{\partial}{\partial R}\left[R\frac{\mu_t}{\mu}\frac{\partial V}{\partial R}\right] - 2\frac{\mu_t}{\mu}\frac{V}{R^2}\right\} + \frac{W^2}{R}\end{aligned} \tag{5}$$

$$\begin{aligned}\frac{\partial (UW)}{\partial X} + \frac{1}{R}\frac{\partial (RVW)}{\partial R} &= \frac{1}{\mathrm{Re}}\left\{\frac{\partial}{\partial X}\left[\frac{\mu_t}{\mu}\frac{\partial W}{\partial X}\right] + \frac{1}{R}\frac{\partial}{\partial R}\left[R\frac{\mu_t}{\mu}\frac{\partial W}{\partial R}\right]\right\} \\ &+ \frac{1}{\mathrm{Re}}\left\{\frac{W}{R}\frac{\partial}{\partial R}\left[\frac{\mu_t}{\mu}\right] - \frac{\mu_t}{\mu}\frac{W}{R^2}\right\} - \frac{VW}{R}\end{aligned} \tag{6}$$

Conservation of turbulent kinetic energy

$$\begin{aligned}\frac{\partial (UK)}{\partial X} + \frac{1}{R}\frac{\partial (RVK)}{\partial R} &= \frac{1}{\mathrm{Re}}\left\{\frac{\partial}{\partial X}\left[\frac{\mu_t}{\mu\sigma_\kappa}\frac{\partial K}{\partial X}\right]\right. \\ &\left. + \frac{1}{R}\frac{\partial}{\partial R}\left[R\frac{\mu_t}{\mu\sigma_\kappa}\frac{\partial K}{\partial R}\right] + \frac{\mu_t}{\mu}G\right\} - E\end{aligned} \tag{7}$$

Conservation of dissipation rate

$$\begin{aligned}\frac{\partial (UE)}{\partial X} + \frac{1}{R}\frac{\partial (RVE)}{\partial R} &= \frac{1}{\mathrm{Re}}\left\{\frac{\partial}{\partial X}\left[\frac{\mu_t}{\mu\sigma_\epsilon}\frac{\partial E}{\partial X}\right]\right. \\ &\left. + \frac{1}{R}\frac{\partial}{\partial R}\left[R\frac{\mu_t}{\mu\sigma_\epsilon}\frac{\partial E}{\partial R}\right]\right\} + \frac{1}{Re}\left\{c_1\frac{\mu_t}{\mu}G\frac{E}{K}\right\} - c_2\frac{E^2}{K}\end{aligned} \tag{8}$$

Conservation of energy

$$\begin{aligned}\frac{\partial (U\phi)}{\partial X} + \frac{1}{R}\frac{\partial (RV\phi)}{\partial R} &= \frac{1}{\mathrm{Re}}\left\{\frac{\partial}{\partial X}\left[\frac{\mu_t}{\mu\sigma_t}\frac{\partial \phi}{\partial X}\right]\right. \\ &\left. + \frac{1}{R}\frac{\partial}{\partial R}\left[R\frac{\mu_t}{\mu\sigma_t}\frac{\partial \phi}{\partial R}\right]\right\}\end{aligned} \tag{9}$$

where G is the production of turbulent kinetic energy given by

$$\begin{aligned}G = 2&\left\{\left[\frac{\partial U}{\partial X}\right]^2 + \left[\frac{\partial V}{\partial R}\right]^2 + \left[\frac{V}{R}\right]^2\right\} \\ &+ \left[\frac{\partial V}{\partial X} + \frac{\partial U}{\partial R}\right]^2 + \left[\frac{\partial W}{\partial X}\right]^2 + \left[R\frac{\partial}{\partial R}\frac{W}{R}\right]^2\end{aligned} \tag{10}$$

and Re is the Reynolds number defined by

$$\mathrm{Re} = \frac{\rho V_m D}{\mu} \tag{11}$$

The dimensionless turbulent viscosity given by the κ-ϵ model is

$$\frac{\mu_t}{\mu} = \frac{c_\mu K^2}{E}\mathrm{Re} \tag{12}$$

The constants in the turbulence model are taken directly from Launder and Spalding (1974). These are:

$$c_\mu = 0.09, \quad c_1 = 1.44, \quad c_2 = 1.92, \quad \sigma_\kappa = 1.00, \quad \sigma_\epsilon = 1.30, \quad \sigma_t = 0.9 \tag{13}$$

Boundary Conditions

Inlet Conditions. It can be assumed that air enters the domain with a known mass flow rate and constant temperature. The dimensionless inlet velocities will depend only on the inlet port size $X_1 = L_1/D$, and angles α and β. The κ-ϵ turbulence model requires the numerical values of κ and ϵ at the inlet cross section. The value of κ was taken as 2 percent of the mean kinetic energy and the corresponding ϵ value was specified by assuming the mixing length to be 4.5 percent of the inlet port size, as suggested by Gosman in Zhang (1985). Computational trials indicated that the results were insensitive to the inlet values of κ and ϵ. The inlet conditions ($R = 0.5$, $X \leq X_1$) were:

$$U=\frac{\cos\alpha}{4X_1},\quad V=\frac{1}{4X_1},\quad W=\frac{\tan\beta}{4X_1\sin\alpha}$$
$$K=\frac{0.01}{(4X_1\cos\beta\sin\alpha)^2},\quad E=\frac{c_\mu^{3/4}K^{3/2}}{0.045X_1},\quad \phi=0 \tag{14}$$

Symmetry Line. Along the symmetry line, for $R = 0$, we have

$$V=W=0,\quad \frac{\partial U}{\partial R}=\frac{\partial K}{\partial R}=\frac{\partial E}{\partial R}=\frac{\partial \phi}{\partial R}=0 \tag{15}$$

Exit Conditions. At the exhaust opening, the usual condition of neglecting the diffusion flux of all variables was adopted. Thus, for $X = L/D$ and $R_1/D \leq R \leq R_2/D$:

$$\frac{\partial U}{\partial X}=\frac{\partial V}{\partial X}=\frac{\partial W}{\partial X}=\frac{\partial K}{\partial X}=\frac{\partial E}{\partial X}=\frac{\partial \phi}{\partial X}=0 \tag{16}$$

The Wall Regions. The κ-ϵ model is used everywhere except in the narrow regions near the walls, where the "wall function" method is used, as suggested by Launder and Spalding (1974). In this method the region between the node P, closest to the wall, and the wall is linked by the logarithmic velocity profile

$$\frac{u_P}{\sqrt{\tau_w/\rho}}=2.5\ \ln 9y_P^+ \tag{17}$$

where u_P is the velocity component parallel to the wall at node P, τ_w is the wall shear stress and y_P^+ is the dimensionless distance of the node P to the wall given by

$$y_P^+=\frac{\sqrt{\tau_w\rho}}{\mu}\,y \tag{18}$$

Assuming that the generation and dissipation are in balance in the narrow layer between node P and the wall and using the log relation, the constant shear stress can be written as

$$\tau_w=\rho c_\mu^{1/2}\kappa_P \tag{19}$$

where κ_P is the near-wall kinetic energy of turbulence, which is found from its transport equation with diffusion set equal to zero at the wall, in accordance with the above expression.

The value of the dissipation of kinetic energy ϵ_P is determined by substituting the log velocity profile into the turbulence kinetic energy balance near the wall, resulting in

$$\epsilon_P=\frac{c_\mu^{3/4}\kappa^{3/2}}{(0.4y)} \tag{20}$$

The "wall function" can also be applied for the energy equation, as described by Patankar and Spalding (1970), where the following dimensionless temperature profile can be used to link the boundary to the near-wall temperature:

$$T_P^+=\sigma_t\left[\frac{u_P}{\sqrt{\tau_w/\rho}}+\Omega\right] \tag{21}$$

where

$$T_P^+=(T_P-T_w)\,\frac{\sqrt{\tau_w\rho}}{\left[\dfrac{\mu}{\sigma}\left(\dfrac{\partial T}{\partial y}\right)_w\right]}$$
$$\Omega=9.0\left[\frac{\sigma}{\sigma_t}-1\right]\left[\frac{\sigma}{\sigma_t}\right]^{-1/4} \tag{22}$$

and σ is the Prandtl number.

Computational Details. The set of equations (3)–(10) was solved numerically by the method described by Patankar (1980). The coupling between the axial and radial momentum equations and continuity was handled by the SIMPLER algorithm. Furthermore, the turbulent viscosity was underrelaxed since all equations are connect through its value.

Exploratory calculations on a finer grid were employed to provide guidance for the selection of the appropriate grid for the several cases studied. A typical grid test result is presented in the appendix. A 22 × 12 uniform grid in the axial and radial direction was selected for the calculation domain. Since it is known that the log law is valid for values of y^+ greater than about 11.5, the wall adjacent nodes in the finite difference grid were positioned so that their y values satisfied this constraint.

Results and Discussion

Comparison With Available Solutions. Initially numerical solutions were obtained for the three exhaust opening types shown in Fig. 1(*a*), as used by Sung and Patterson (1982) in their experimental simulation of a two-stroke engine under steady-state condition. As mentioned before, the working fluid selected was air ($\sigma = 0.69$). The Reynolds number was maintained at 43,113 and the aspect ratio $L/D = 1.057$. The inlet port angle α was set equal to 90 deg, implying no axial velocity component at the inlet port. The inlet size X_1 was set equal to 0.114 in order to furnish the same entrance area as the 18 uniformly spaced windows of the experimental apparatus.

The inlet angle β, which causes the swirl, was obtained experimentally by drilling the windows with the desired inclination. However, the effective β angle is smaller than the geometric inclination of the windows, especially if the thickness of the cylinder wall is smaller than 80 percent of the width of the windows, in accordance with Annand and Roe (1974). In the experimental apparatus of Sung and Patterson (1982), the inlet β angle was specified as 25 deg; but since the thickness of the cylinder wall was only 31.25 percent of the width of the windows, the effective β angle is much smaller. Zhang (1985) has solved this problem numerically, using an effective β angle of 20 deg. In the present work, the effective angle β was determined by solving the problem for different β angles and comparing the resulting velocity profiles with the experimental results. The effective β angle was then selected as the one that presented the best agreement.

The comparison of tangential and axial velocity component profiles along the radius at the cross section $X = 0.73$ with the experimental results of Sung and Patterson (1982) and with the numerical results of Zhang (1985) are presented in Figs. 2–4.

The velocity profile comparison for the Type 1 exhaust opening can be seen in Fig. 2. For this case $R_1/D = 0$ and $R_2/D = 0.30$. The velocity profile was obtained for three different swirl angles β (β = 10, 15, and 18 deg). It can be observed in Fig. 2(*a*) that the effect of the β angle on the axial velocity component is quite small. The profiles are nearly coincident close to the cylinder wall, presenting a small deviation near the symmetry line. This is not true for the tangential velocity component shown in Fig. 2(*b*). Note that the level of the velocity is significantly affected by the swirl angle β. It can also be observed that the numerical solution of Zhang (1985) for

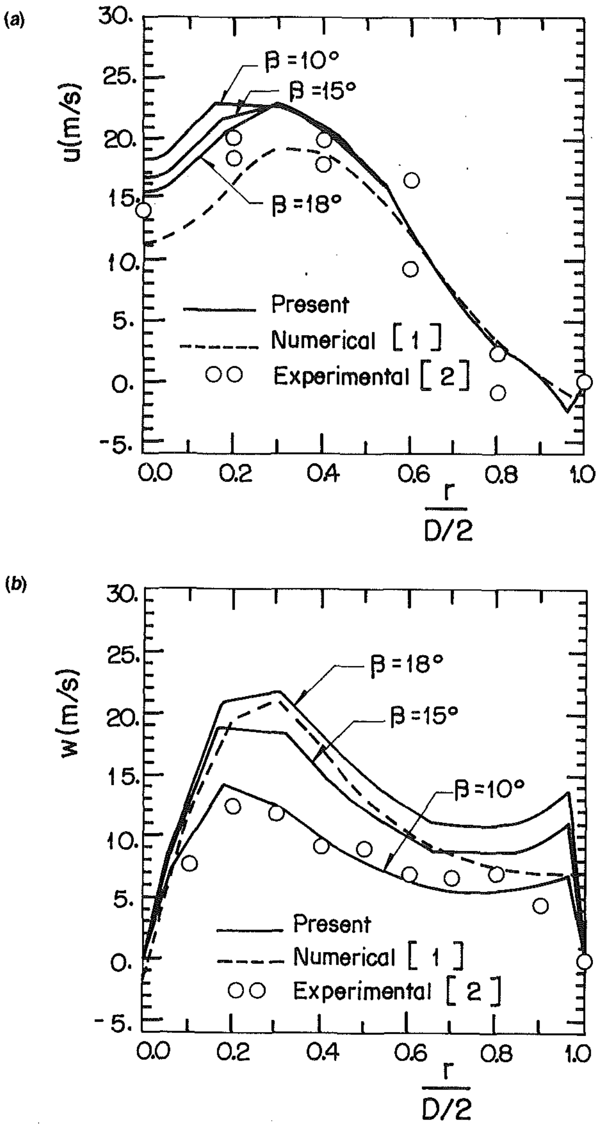

Fig. 2 Velocity profiles at section $X = 0.73$ for Type 1 exhaust port: (*a*) axial velocity, (*b*) tangential velocity; [1] Zhang (1985); [2] Sung and Patterson (1982)

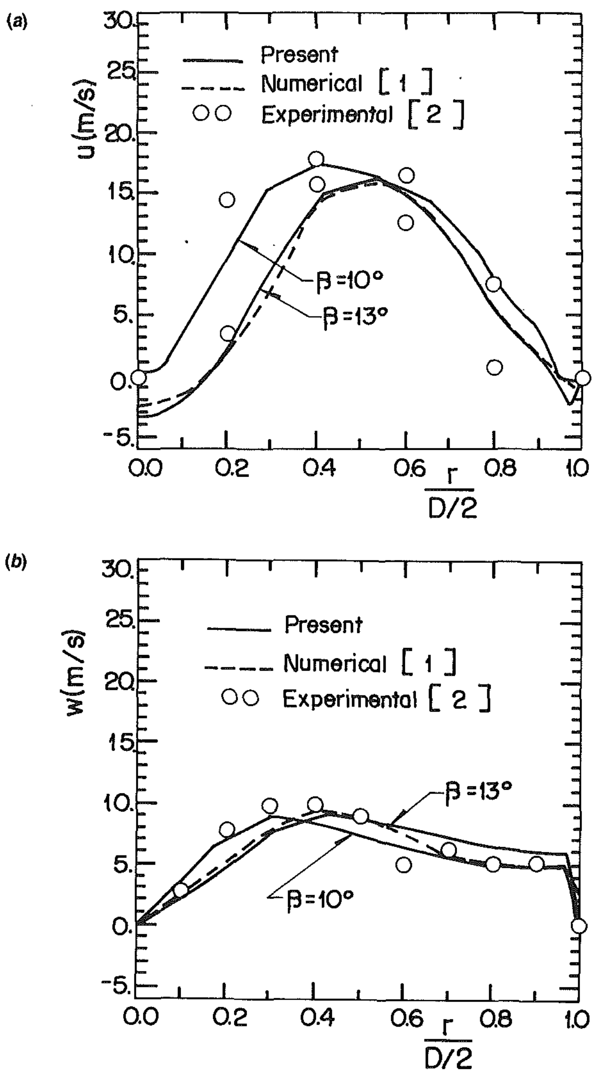

Fig. 3 Velocity profiles at section $X = 0.73$ for Type 2 exhaust port: (*a*) axial velocity, (*b*) tangential velocity; [1] Zhang (1985) [2] Sung and Patterson (1982)

$\beta = 20$ deg is quite similar to the present solution for $\beta = 18$ deg. However, the best agreement between the numerical and experimental results for both velocities components occurs for $\beta = 10$ deg, which was selected as the correct effective swirl angle β.

Figure 3 presents velocity profiles for the Type 2 exhaust opening ($R_1/D = 0.36$ and $R_2/D = 0.47$) for β equal to 10 and 13 deg. In this case the effect of the swirl angle β on the velocities profiles is smaller. Once again the numerical results of Zhang (1985) are closer to the present solution for the higher β value, and $\beta = 10$ deg can be selected as the effective swirl angle β, since it gives the best agreement with the experimental results.

Finally, the velocities profiles for the Type 3 exhaust opening ($R_1/D = 0$, $R_2/D = 0.5$) can be seen in Fig. 4. The following β angles were tested: β equal to 10, 13, and 15 deg. For this type of exhaust geometry, the effective swirl angle $\beta = 10$ deg is also recommended. The numerical results of Zhang (1985) for this case presented poor agreement; he had some convergence problems and failed to obtain a reasonable solution. Note that the velocity profile distribution for a totally open exhaust port is similar to the profiles for Type 1, indicating that an increase in the exhaust port area has little effect on the flow pattern inside the cylinder, as also observed by Sher et al. (1988), who investigated different combinations of R_2/D of Type 1 exhaust opening.

Observing the present numerical results in Figs. 2–4 for the tangential velocity profile, a peak on the velocity near the cylinder wall can be noted. Although there are no experimental data on this region, it seems unlikely that this peak really exists. Thus, one is led to believe that this velocity profile distortion is due to the "wall function" and grid distribution near the wall.

Local Results

Axial and Tangential Velocities. In order to have a better understanding of the flow field, the tangential and axial velocity profiles for the exhaust port of Type 1 are also examined for a cross section at $X = 0.20$ (near the piston head) on Fig. 5.

It can be observed in Fig. 5(*a*) that the axial velocity profile is almost independent of the swirl angle β for radius $2R$ greater than 0.20 near the piston head and 0.30 for a section closer to the exhaust (Fig. 2*a*). The depression on the axial velocity near the symmetry line increases as β increases at both sections. Note the existence of a recirculating zone by the negative values of the axial velocity. Further, note that the axial velocity increases as one moves away from the inlet port region.

The tangential velocity profile can be seen in Fig. 5(*b*). As mentioned before the level of velocity increases with an increase in the swirl angle β. There is a strong peak in the tangential

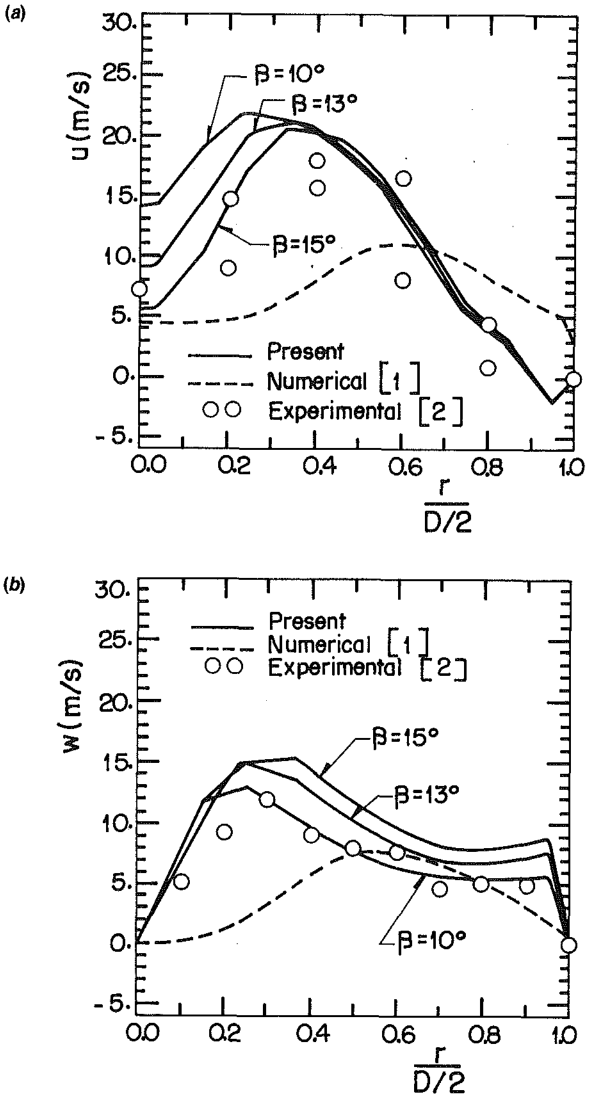

Fig. 4 Velocity profiles at section X = 0.73 for Type 3 exhaust port: (a) axial velocity, (b) tangential velocity; [1] Zhang (1985); [2] Sung and Patterson (1982)

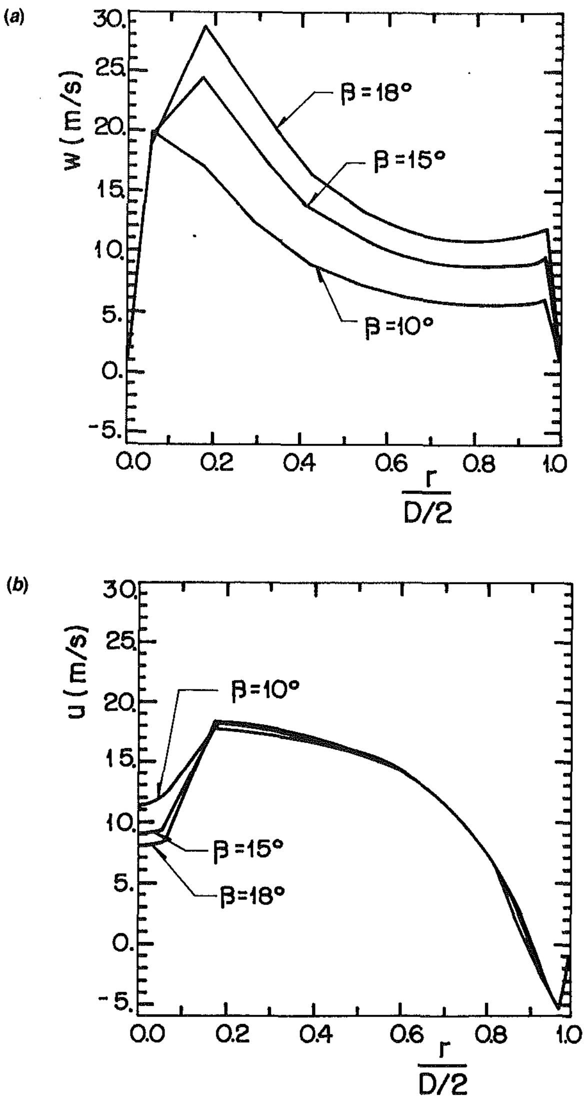

Fig. 5 Velocity profiles at section X = 0.20 for Type 1 exhaust port: (a) axial velocity, (b) tangential velocity; [1] Zhang (1985); [2] Sung and Patterson (1982)

velocity near the symmetry line close to the piston head due to the encounter of the inlet circular jet. As one moves downstream (Fig. 2*b*) this peak is reduced. Note that, as the tangential velocity decreases, the axial velocity increases as one moves downstream inside the cylinder, indicating that there is a transfer of tangential momentum to axial momentum.

Streamlines. Figures 6 and 7 show the streamlines inside the cylinder for the Type 1 and Type 2 exhaust opening, respectively. The following parameters were maintained constant for both cases: Re = 5×10^4, $L/D = 1$, α = 90 deg, β = 10 deg, $X_1 = 0.10$. The exhaust port parameters were: Type 1—$R_1/D = 0.00$, $R_2/D = 0.30$; Type 2—$R_1/D = 0.36$, $R_2/D = 0.47$.

The dimensionless stream function ψ was calculated from

$$\psi = \int_0^R URdR \tag{23}$$

Figure 6 shows the flow pattern for a Type 1 exhaust opening. The inlet circular swirling jet, normal to the cylinder liner, is deviated to the axial direction near the symmetry line, due to the encounter of the jet inducing a weak secondary flow along the cylinder wall. This recirculating zone is undesirable for the scavenging process, since the combustion products can be trapped in this region. The streamlines for Type 2 exhaust can

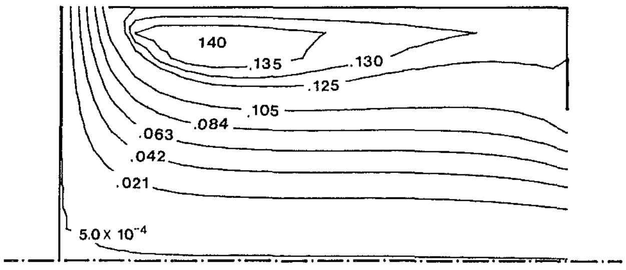

Fig. 6 Streamlines for exhaust port of Type 1

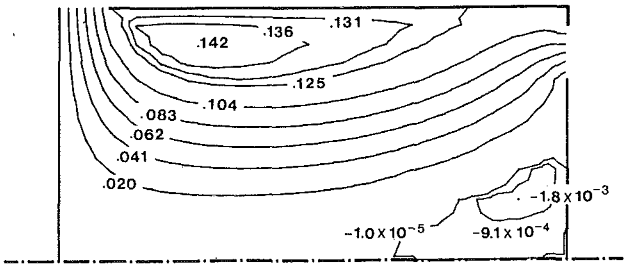

Fig. 7 Streamlines for exhaust port of Type 2

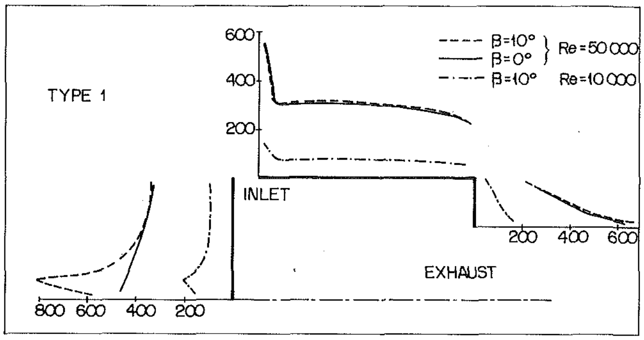

Fig. 8 Local Nusselt number distribution around the cylinder for exhaust port of Type 1

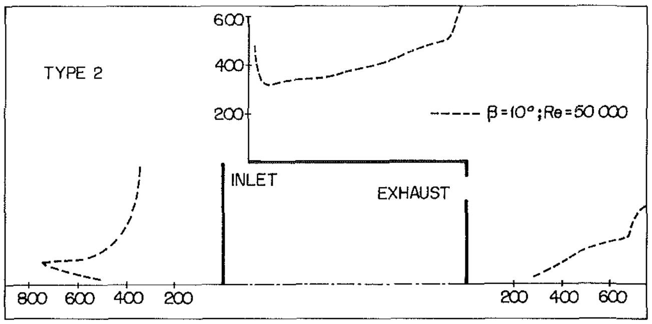

Fig. 9 Local Nusselt number distribution around the cylinder for exhaust port of Type 2

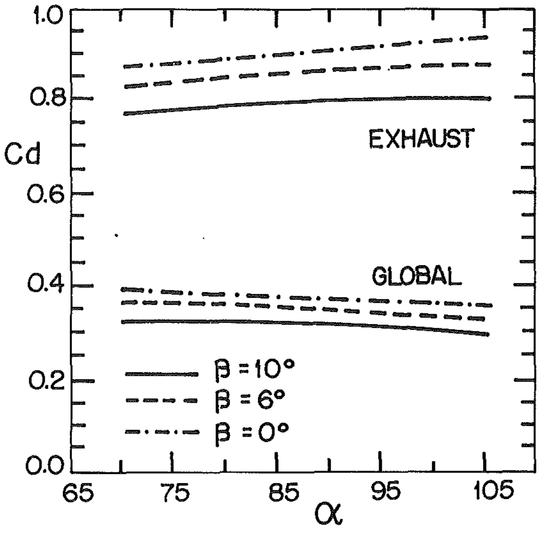

Fig. 10 Discharge coefficient versus inlet α angle

be seen in Fig. 7. Since the inlet angles are the same for these two cases, the flow pattern near the entrance is similar, but as one moves downstream the main stream is deviated to the direction of the exhaust port, causing a reduction on the recirculating region and inducing a new secondary flow near the symmetry line close to the exhaust port. Note, however, that the overall volume of trapped fluid will be smaller for Type 2 exhaust geometry, since the volume is proportional to the radius squared, and near the symmetry line the radius is very small.

Local Heat Transfer Coefficient. Due to the patterns of velocity and temperature inside the chamber, local heat transfer is not constant along the piston head, cylinder liner, and cylinder head end. The local and average Nusselt number are defined as

$$\mathrm{Nu}=\frac{qD}{k(T_w-T_b)}$$

$$\overline{\mathrm{Nu}}=\frac{\overline{q}D}{k(T_w-T_b)} \tag{24}$$

where q and $\overline{q}$ are the local and average heat flux at the solid walls, and T_b is the bulk temperature of the air at the exhaust port. T_b is calculated from

$$T_b=\frac{\int Turdr}{\int urdr} \tag{25}$$

where the integral is evaluated at the exhaust port area.

Figures 8 and 9 show the variation of Nu with the position around the cylinder chamber for the same exhaust port Type 1 and Type 2 used for the streamline presentation. For Type 1 exhaust port, different Reynolds numbers and β angles were investigated. By examining Figs. 8 and 9, one can observe a peak on the Nusselt number at the piston head near the symmetry line when the swirl angle β is different from zero. This peak is caused by the high intensity of the tangential velocity at this region due to the encounter of the inlet jet. Note that for the same inlet conditions, the Nusselt number along the piston head is not affected by the different exhaust port types.

The local Nusselt number distribution along the cylinder liner is affected by the type of exhaust port, since the recirculating zone is quite different for the two cases. Nu is higher outside the recirculating zones, as can be noted by observing Figs. 8 and 9 with the flow pattern distribution in Figs. 6 and 7.

Note that an increase in the Reynolds number maintains the same distribution of the local Nusselt number, but increases its level, as can be seen in Fig. 8 for the Type 1 exhaust port.

It should be mentioned that even when Nu decreases with the radial position along the piston head and exit surface, heat transfer increases since heat transfer area increases with the radius.

Overall Results. The effect of the inlet angles α and β, the Reynolds number, and the aspect ratio L/D on the overall characteristics of the flow and heat transfer inside the cylinder are examined next. These parameters were varied from the following configuration: $X_1 = 0.1$, $R_1/D = 0$, $R_2/D = 0.3$, $\mathrm{Re} = 5 \times 10^4$, $L/D = 1$, $\alpha = 90$ deg and $\beta = 10$ deg.

Discharge Coefficient. To assess the effectiveness of the scavenging process, the discharge coefficient can be a useful parameter. It can be defined as the ratio between the actual mass flow rate $\dot{m}$ through the cylinder and an isentropic mass flow rate of a perfect gas between two sections of the cylinder, $\dot{m}_i$,

$$C_d=\frac{\dot{m}}{\dot{m}_i} \tag{26}$$

where

$$\dot{m}_i=A_2\left\{\frac{2P_1\gamma\left(\frac{p_1}{p_2}\right)}{R_{\mathrm{air}}(\gamma-1)}\left[\frac{\left(\frac{p_2}{p_1}\right)^{2/\gamma}-\left(\frac{p_2}{p_1}\right)^{(\gamma+1)/\gamma}}{1-\left(\frac{p_2}{p_1}\right)^{2/\gamma}\left(\frac{A_3}{A_1}\right)^2}\right]\right\}^{1/2} \tag{27}$$

and the subscripts 1 and 2 indicate the two sections.

To analyze the results better a global and an exhaust discharge coefficient were defined. The global coefficient can be a measure of the overall friction loss inside the chamber between the inlet port (section 1) and the exhaust valve (section 2). The exhaust coefficient gives an indication of the losses due to the expulsion of the gases. For the exhaust coefficient, section 1 was selected as a generic section inside the cylinder and section 2 the exhaust port.

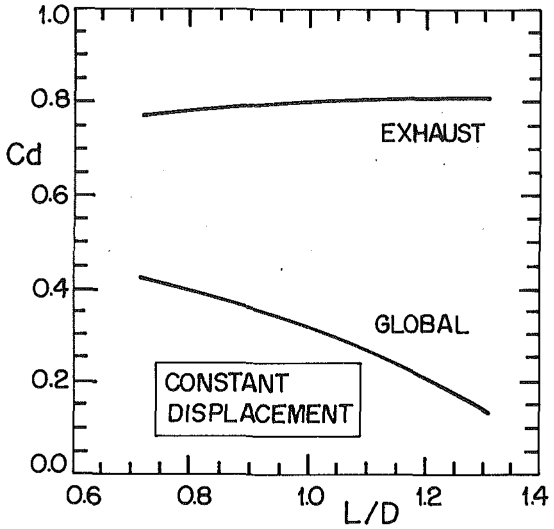

Fig. 11 Discharge coefficient versus aspect ratio

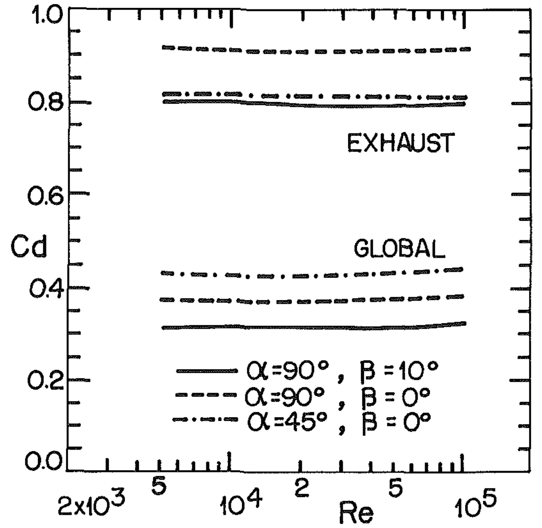

Fig. 12 Discharge coefficient versus Reynolds number

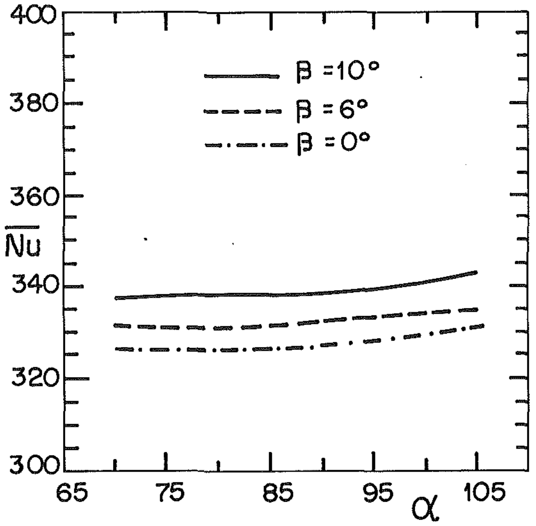

Fig. 13 Overall Nusselt number versus inlet α angle

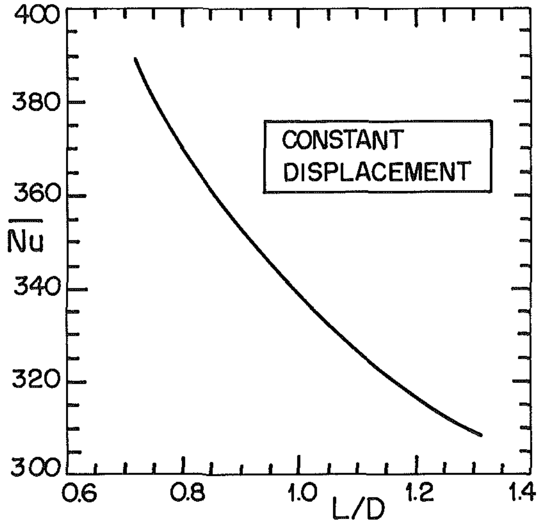

Fig. 14 Overall Nusselt number versus aspect ratio

Properties at the exhaust were evaluated as mean values along the area, while properties at a generic section of the cylinder were taken as mean values inside the whole calculation domain.

Figure 10 shows the small influence of the inlet angles α and β on the discharge coefficients. It can be seen that C_d decreases as the swirl angle β increases, indicating that the losses are higher when the swirl is stronger. It can also be observed that the global C_d decreases when the axial angle α increases, while the exit C_d increases. It can then be concluded that when the inlet jet is directed to the piston (α greater than 90 deg) the losses near the entrance region are higher due to the encounter of the inlet jet near the symmetry line of the cylinder.

The effect of the bore-to-stroke ratio (here represented by aspect ratio D/L) on the flow pattern was investigated maintaining the displaced volume of the cylinder constant. The ratio between the inlet port size and exhaust port size in relation to the volume were also maintained constant. Therefore, three dimensionless parameters of the problem were altered simultaneously: L/D, L_1/D, and R_2/D. The last two parameters are proportional to $(L/D)^{1/3}$ for the present situation.

The effect of the aspect ratio on the discharge coefficient can be seen in Fig. 11. Note that the global C_d decreases when L/D increases, since for smaller diameters the encounter of the inlet jet near the symmetry line will be stronger, causing higher losses. On the other hand, the exhaust C_d is approximately constant with L/D once the exhaust area also increases when L/D increases, thus reducing losses on this region.

Figure 12 shows that the discharge coefficients are independent of the Reynolds number. It can also be seen the effect of the inlet angles on C_d as already discussed.

Overall Heat Transfer Coefficient. The variation of $\overline{\mathrm{Nu}}$ with the inlet angles α and β is shown in Fig. 13. Note that when the swirl angle β increases, the Nusselt number also increases, due to the peak on the local Nusselt number at the piston head, as seen in Fig. 8. The effect of α on $\overline{\mathrm{Nu}}$ is very small, showing an increase on $\overline{\mathrm{Nu}}$ when the inlet jet is directed to the piston head (α greater than 90 deg).

Figure 14 shows the effect of the aspect ratio L/D on $\overline{\mathrm{Nu}}$ while maintaining constant the displaced volume, as explained before. It can be seen that there is an increase in the Nusselt number when the aspect ratio decreases, since for a larger diameter the inlet jet induces a stronger secondary flow near the cylinder liner, enhancing the heat transfer coefficient at that region.

The Reynolds number significantly affects the Nusselt number as can be seen in Fig. 15. It can also be seen that the variation of the $\overline{\mathrm{Nu}}$ as a function of the inlet angles is less significant in comparison with the effect of Re. The following

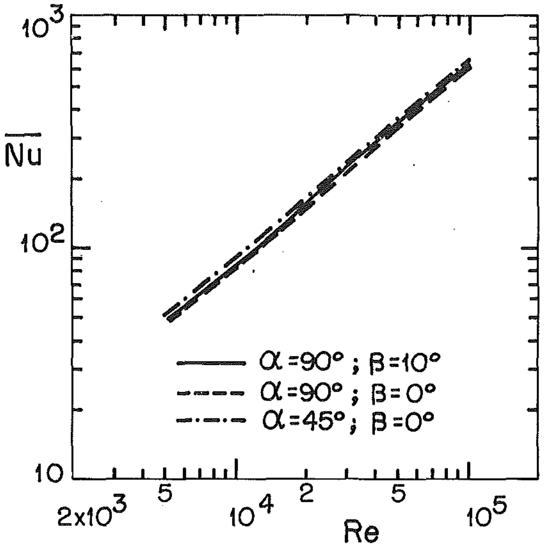

Fig. 15 Overall Nusselt number versus Reynolds number

equation was found best to fit the $\overline{\mathrm{Nu}} \times \mathrm{Re}$ curve in Fig. 15:

$$\overline{\mathrm{Nu}} = 0.030\ \mathrm{Re}^{0.863} \tag{28}$$

Conclusion

The present numerical study of the scavenging process on a two-stroke engine under steady-state condition showed good agreement with available experimental results. The effective value of the swirl angle β differs from the geometric one for reasons given by Annand and Roe (1974), so that special care should be taken on its specification for numerical simulation. The use of an effective value for β emphasizes the influence that flow conditions of the inlet plenum have on the cylinder boundary conditions. On the other hand, it is believed that Zhang (1985) and Sher et al. (1988) could achieve better agreement with experimental data should they explore the effects of the swirl angle β in more depth, even using the same κ–ϵ model.

The inlet angles α and β showed a small influence on the flow pattern and heat transfer characteristics for the situation where only air flows through the cylinder. It has been shown that exhaust port location controls the size of the recirculating zones where the combustion products will eventually be trapped. The Reynolds number is the principal parameter to control the heat transfer characteristics of the process.

It should be stressed that simplifying assumptions, notably steady-state and single component flow, were introduced in order to make the model simple and easy to handle. This restricted the production of results of realistic value. Scavenging efficiency is, for example, one parameter that the model, in its present form, would be unable to quantify.

Yet, other relevant results were produced. For example, the discharge coefficient and the overall Nusselt number will find application in lumped-parameter models, for performance prediction. These models, although in use for nearly two decades (Benson and Galloway, 1969), are quite accurate in predicting the pressure history inside the cylinder. Balance equations in their time-derivative form are applied to prescribed control volumes with uniform gas properties. These control volumes can take the form of the entire cylinder, regions within the fuel jet (Chiu et al., 1976) or zones comprising fresh air, combustion products and a mixture of the two, during scavenging (Kyrtatos and Koumbarelis, 1988). No spatial variations are considered, so velocity or gas property distributions are unimportant, except for the evaluation of overall parameters such as discharge coefficients across ports and valve passages and gas to wall heat transfer coefficients. The resulting ordinary differential equations are then integrated to give the variation of in-cylinder gas properties with time, or crank angle degree. Equations for instantaneous mass flow rate, Eq. (27), or heat transfer rate, are taken, in those lumped parameter models, as those for steady-state conditions, for each time step. Since the time interval for integration is rather small (0.2 deg), this "quasi-steady" approach does not represent any error of significance. This shows that values for C_d and $\overline{\mathrm{Nu}}$, produced by the present model, even with the steady-state limitation, are quite adequate for use in lumped-parameter models.

References

Arcoumamis, C., and Whitelaw, J. H., 1987, "Fluid Mechanics of Internal Combustion Engines: A Review," *Proc. IMechE*, Part C, Vol. 201, No. C1, pp. 57–72.

Annand, W. J. D., and Roe, G. E., 1974, *Gas Flow in the Internal Combustion Engine*, G. T. Foulis, United Kingdom.

Basters, A. V., Lebedev, O. N., Titkov, V. I., and Chiekov, S. N., 1988, "Investigation of Aerodynamics in Internal Combustion Engines by Laser Doppler Anemometry," *Soviet J. Applied Physics*, Vol. 2, No. 1, pp. 55–59.

Benson, R. S., and Galloway, K., 1969, "An Experimental and Analytical Investigation of the Gas Exchange Process in a Multi-cylinder Pressure-Charged Two-Stroke Engine," *Proc. IMechE*, Vol. 183, Pt. 1, No. 14, pp. 253–279.

Borée, J., Charnay, G., and Nuglish, H. J., 1989, "Experimental Modelisation of the Piston Engine's Internal Aerodynamics," *Entropie*, Vol. 25, No. 148, pp. 5–12.

Butler, T. D., Cloutman, L. D., Dukowicz, J. K., and Ramshaw, J. D., 1979, "CONCHAS: An Arbitrary Lagrangian-Eulerian Computer Code for Multicomponent Chemically Reactive Fluid Flow at All Speeds," Los Alamos Scientific Laboratory, Report LA-8129-MS.

Carapanayotis, A., and Salcudean, M., 1988, "Mathematical Modeling of the Scavenging Process in a Two-Stroke Diesel Engine," ASME *Journal of Engineering for Gas Turbines and Power*, Vol. 110, pp. 538–546.

Chiu, C. P., Wu, T. S., and Chou, H. M., 1986, "Numerical Simulation of In-Cylinder Air Motion," *3rd Conference of CSME*, pp. 380–400.

Chiu, C. P., Wu, T. S., and Chou, H. M., 1987, "Numerical Simulation of Turbulent and Laminar Flow in Internal Combustion Engines," *4th Conference of CSME*, pp. 175–190.

Chiu, C. P., and Wu, T. S., 1990, "Study of Air Motion in Reciprocating Engine Using an Algebraic Grid Generation Technique," *Numerical Heat Transfer*, Part A, Vol. 17, pp. 309–327.

Chiu, W. S., Shahed, S. M., and Lyn, W. T., 1976, "A Transient Spray Mixing Model for Diesel Combustion," SAE Paper No. 760128.

Cloutman, L. D., Dukowicz, J. K., Ramshaw, J. D., and Amsden, A. A., 1982, "CONCHAS-SPRAY: A Computer Code for Reactive Flows With Fuel Sprays," Report No. LA-9294-MS, Los Alamos National Laboratories, NM.

Das, D. K., 1974, "An Investigation of the Vortex Flow Inside a Model Diesel Engine Cylinder," PhD Thesis, UMIST, Mechanical Engineering Department, Manchester, United Kingdom.

Diwakar, R., 1984, "A Motoring Study of Global Turbulence Characteristics in Some Engines With Axially Symmetric Combustion Chambers," *Flows in Internal Combustion Engines—II*, ASME FED-Vol. 20, pp. 1–7.

Diwakar, R., 1985, "Multidimensional Modeling of the Gas Exchange Processes in a Uniflow-Scavenged Two-Stroke Diesel Engine," *International Symposium on Flows in Internal Combustion Engines—III*, T. Uzkan et al., eds., ASME FED-Vol. 28, pp. 125–134.

Diwakar, R., 1987, "Three-Dimensional Modeling of the In-Cylinder Gas Exchange Processes in a Uniflow-Scavenged Two-Stroke Engine," SAE Technical Paper Series 870596.

Doan, T. D., Crawford, E. F., and Hinkle, S. J., 1988, "Steady-State Air Motion Study in a V-6 Uniflow Scavenged Two-stroke Diesel Engine," ASME *Journal of Engineering for Gas Turbines and Power*, Vol. 110, pp. 503–508.

Gosman, A. D., Johns, R. J. R., and Watkins, A. P., 1980, "Development of Prediction Methods for In-Cylinder Processes in Reciprocating Engines," *Combustion Modelling in Reciprocating Engines*, J. N. Mattavi and C. A. Amann, eds., Plenum Press, New York, pp. 69–124.

Gosman, A. D., Tsui, Y. Y., and Watkins, A. P., 1984, "Calculation of Three Dimensional Air Motion Model Engines," SAE Technical Papers Series 840229.

Heywood, J. B., 1987, "Fluid Motion Within the Cylinder of Internal Combustion Engines: The 1986 Freeman Scholar Lecture," ASME *Journal of Fluids Engineering*, Vol. 109, pp. 3–35.

Ikegami, M., Kidoguchi, Y., and Nishiwaki, K., 1986, "A Multidimensional Model Prediction of Heat Transfer in Non-fired Engine," SAE Technical Paper Series 860467.

Inoge, S., and Kobayashi, K., 1987, "Prediction of In-Cylinder Flow and Heat Transfer in Direct-Injection Diesel Engines," *JSME Int. J.*, Vol. 30, No. 264, pp. 950–957.

Itoh, T., Takagi, Y., Ishida, T., Ishikawa, S., and Ishikawa, T., 1985, "Analysis of In-Cylinder Air Motion With LDV Measurement and Multi-dimensional Modeling," Proc. Int. Symp. *Diagnostic and Modeling of Combustion in Reciprocating Engines*, Tokyo, Japan, pp. 185–192.

Kamimoto, T., and Kobayashi, H., 1988, "In-Cylinder Fluid Dynamics of Diesel Engines," *JSME Int. J.*, Series II, Vol. 31 II, pp. 199–208.

Kondoh, T., Fukumoto, A., Ohsawa, K., and Ohkubo, Y., 1985, "An Assessment of a Multi-dimensional Numerical Method to Predict the Flow in Internal Combustion Engines," SAE Technical Paper Series 850500.

Kuo, T. W., and Duggal, V. K., 1984, "Modelling of In-Cylinder Flow Characteristics—Effect of Engine Design Parameters," *Flows in Internal Combustion Engines—II*, ASME FED-Vol. 20, pp. 9–18.

Kyrtatos, N. P., and Koumbarelis, I., 1988, "Three-Zone Scavenging Model for Two-Stroke Uniflow Engines," ASME *Journal of Engineering for Gas Turbines Power*, Vol. 110, pp. 531–537.

Launder, B. E., and Spalding, D. B., 1974, "The Numerical Computation of Turbulent Flows," *Computer Methods in Applied Mechanics and Engineering*, Vol. 3, pp. 269–289.

Martini, W. R., 1986, "Investigation of the Isothermalization of the Hot and Cold Gas Spaces Using Numerical Analysis," *3rd International Stirling Engine Conference*, Rome, Italy, June 25–27, pp. 683–697.

Morel, T., Dudenhoefer, J. E., and Uzkan, T., eds., 1987, *Fluid Flow and Heat Transfer in Reciprocating Machinery*, ASME FED-Vol. 62, 96 pp.

Meintjes, K., 1987, *Engine Combustion Modeling: Prospects and Challenges*, Cray Channels, Winter.

Patankar, S. V., and Spalding, D. B., 1970, *Heat and Mass Transfer in Boundary Layers*, Intertext Books.

Patankar, S. V., 1980, *Numerical Heat Transfer and Fluid Flow*, Hemisphere, Washington, DC.

Shah, P., 1987, "Computer Simulation of Turbulence in Internal Combustion Engines," *Int. J. Numerical Methods in Fluids*, Vol. 7, pp. 927–952.

Sher, E., Hossain, I., Zhang, Q., and Winterbone, D. E., 1988, "Calculations and Measurements in the Cylinder of a Two Stroke Uniflow-Scavenge Engine Under Steady State Flow Conditions," *Proceedings of the First World Conference on Experimental Heat Transfer, Fluid Mechanics and Thermodynamics*, Dubrovnik, Yugoslavia, Elsevier.

Sung, N. W., and Patterson, D. J., 1982, "Air Motion in a Two Stroke Engine Cylinder—The Effects of Exhaust Geometry," *SAE Trans. 820751*, pp. 2534–2544.

Uzkan, T., 1988, "Effects of Engine Speed on the Scavenging Characteristics of a Two-Cycle Engine," ASME *Journal of Engineering for Gas Turbines and Power*, Vol. 110, pp. 523–530.

Uzkan, T., and Bailey, J. M., eds., 1988, *Basic Processes in Internal Combustion Engines 1988*, ASME ICE-Vol. 3.

Uzkan, T., ed., 1989, *Basic Processes in Internal Combustion Engines 1989*, ASME ICE-Vol. 6.

Vafidis, C., Vorropoulos, G., and Whitelaw, J. H., 1987, "Effects of Intake Port and Combustion Chamber Geometry on In-Cylinder Turbulence in a Motored Reciprocating Engine," *Fluid Flow and Heat Transfer in Reciprocating Machinery*, T. Morel et al., eds., ASME FED-Vol. 62.

West, C. D., 1986, "Stirling Machines—Adiabatic to Isothermal," *3rd International Stirling Engine Conference*, Rome, June 25–27, pp. 557–570.

Zhang, Q., 1985, "Flow Modeling of Scavenging Process in a Two Stroke Cycle Engine Cylinder," M.Sc. Thesis, UMIST, Mechanical Engineering Department, Manchester, United Kingdom.

APPENDIX

To assess the numerical accuracy of the present work quantitatively, an exploratory computation on different mesh sizes was performed. A typical grid test case was selected for presentation. The governing parameters were: $\beta = 3$ deg, $\alpha = 90$ deg, $X_1 = 0.1$, $R_1/D = 0$, $R_2/D = 0.3$, $\mathrm{Re} = 5 \times 10^4$, $L/D = 1$, and $\sigma = 0.69$.

Table 1 presents the average Nusselt number and the discharge coefficient for three different mesh sizes. The percent

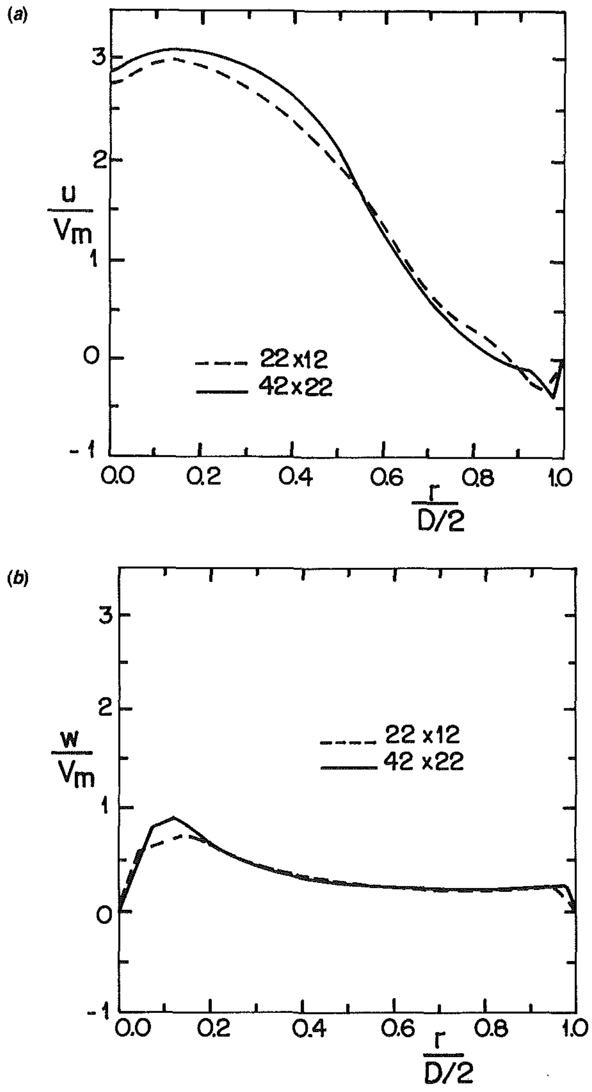

Fig. A1 Grid test for Type 1 exhaust port; velocity profiles at section $X = 0.73$: (*a*) axial velocity, (*b*) tangential velocity

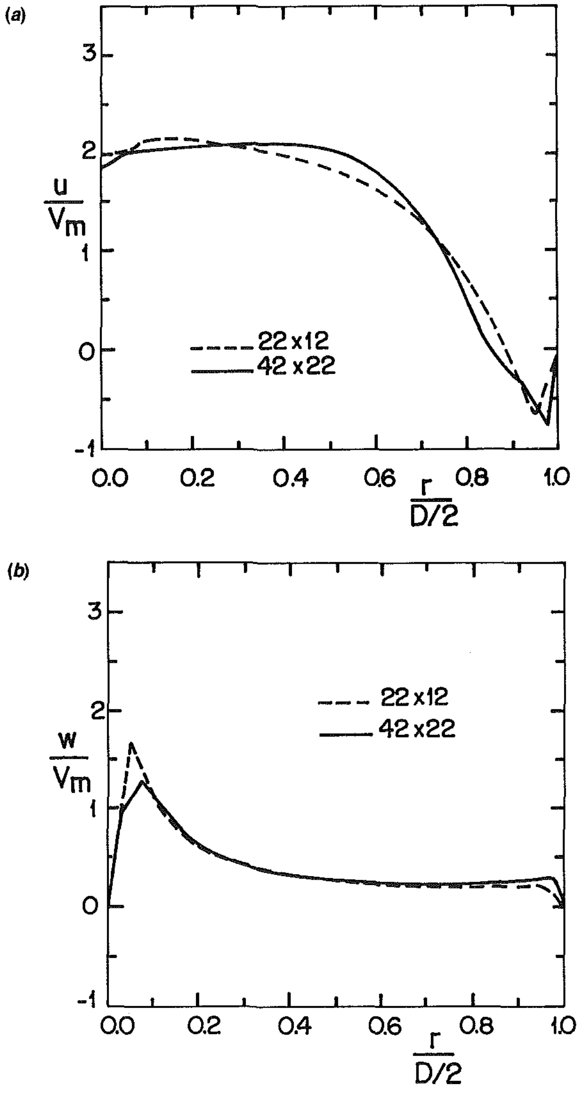

Fig. A2 Grid test for Type 1 exhaust port; velocity profiles at section $X = 0.20$: (*a*) axial velocity, (*b*) tangential velocity

Table A.1 Grid test

Grid	42 × 22	32 × 17	Δ percent	22 × 12	Δ percent
$\overline{Nu}$	304.7	314.0	3.1	329.2	8.0
C_d (global)	0.341	0.349	2.2	0.362	7.5
C_d (exhaust)	0.841	0.858	1.9	0.899	6.8

differences shown were calculated in relation to the finer mesh results. A significant reduction on the variation of the results when the mesh size is made finer can be observed. Note also that for a 22 × 12 there is a maximum of 8 percent variation on the results.

Figures A1 and A2 show the axial and tangential velocity profiles at two different sections, for the mesh size 42 × 22 and 22 × 12. It can be seen in both figures that the agreement between the results is very good. The main difference on the tangential velocity results is on its maximum value. Note, however, that the position of the peak is correctly predicted on the coarser grid. The axial velocity results also compared well. The recirculation flow region, which can be identified by the negative velocities, was also reasonably well predicted with the coarser mesh.

It should be mentioned here, that a uniform mesh was selected, since each velocity component presents steep gradient in different regions of the calculation domain.

Since experimental results of turbulent situations, such as the ones studied, involve uncertainties of approximately 10 percent (Sher et al., 1988), and it is much faster and cheaper to obtain the numerical solution in a coarser mesh, the mesh size of 22 × 12 was selected to investigate the flow and heat transfer characteristics in a two-stroke engine.

An Experimental Study of Free Convection Heat Transfer From an Array of Horizontal Cylinders Parallel to a Vertical Wall

T. R. Al-Alusi
R&D Senior Engineer,
General Dynamics,
Sterling Heights, MI
Mem. ASME

D. J. Bushnell
Associate Professor,
Department of Mechanical Engineering,
Oregon State University,
Corvallis, OR 97331

An experimental investigation of heat transfer from an array of three horizontal cylinders aligned vertically parallel to a single wall is presented. Three different cylinder center-to-center spacings for the array cylinders were examined, $CC = 1.5D$, $2D$, and $4D$. The wall-array spacings were varied from $0.081D$ to infinity. The cylinders were placed in a still air medium at atmospheric pressure and maintained at constant heat flux. Modified Rayleigh number, based on the diameter of the cylinders, ranged from 6.2×10^4 to 1.2×10^6. Results indicate that heat transfer is generally enhanced, but for some wall spacing to cylinder configurations the heat transfer can be minimally decreased. For cases where the heat transfer was enhanced the top cylinder in the array was observed to have the highest enhancement (22 percent) and the lowest cylinder was enhanced the least (5 percent). Flow visualization studies showed that the wall generated a chimney effect between the wall and the cylinders.

1 Introduction

Array of horizontal cylinders confined by a single wall occur in numerous heat exchangers and storage devices. Heat transfer engineering designers prefer the natural convection mode because it is more reliable due to the elimination of the cooling/heating fluid circulation parts [1]. The characteristics of natural convection heat transfer from a heated isothermal horizontal cylinder parallel to an adiabatic wall(s) were examined by Sparrow and Ansari [2]. Their results showed a degradation in the heat transfer from the cylinder at $S/D < 0.25$, where S and D are defined in the nomenclature section. McCoy [3] studied the convection heat transfer behavior from an isothermal heated horizontal cylinder parallel to an isothermal vertical wall in water. It was found that the ratio of the Nusselt number of the cylinder to the Nusselt number of a free single cylinder at the same Rayleigh number, Nu/Nu_S, increased slowly as the wall-cylinder distance was decreased. This enhancement reached its maximum at approximately $S/D = 0.2$. Then Nu/Nu_S dropped off sharply for closer spacings.

The objective of the present study is to investigate heat transfer by natural convection from three horizontal cylinders, at constant heat flux, aligned vertically parallel to a vertical wall, as shown in Fig. 1. During the course of the experiment, the effect of the wall spacing, S, on natural convection from the cylinders was studied. The effect of cylinder-to-cylinder spacing, CC, on natural convection was also investigated. Increased understanding of the fluid flow around the cylinders was obtained by videotaping and taking photographs of the flow field. Laser sheets were used to illuminate smoke particles in the test section.

2 Experimental Apparatus and Procedure

2.1 Heat Transfer Experimental Apparatus and Procedure. Three cylinders comprised the main experimental apparatus. These cylinders were fabricated to be identical in all respects (i.e., dimensions and surface radiation conditions). The test section assembly for the cylinders is shown in Fig. 2. The cylinders were fabricated from aluminum tubing with a 2.54 cm (1.0 in.) o.d. and a 2.36 cm (0.93 in.) i.d. Aluminum was chosen as the heat transfer surface because, when polished to a mirrorlike finish, it reduces the radiation heat loss, which competes with natural convection [4]. The high thermal conductivity of aluminum is another important factor as aluminum provides a more uniform heat flux surface.

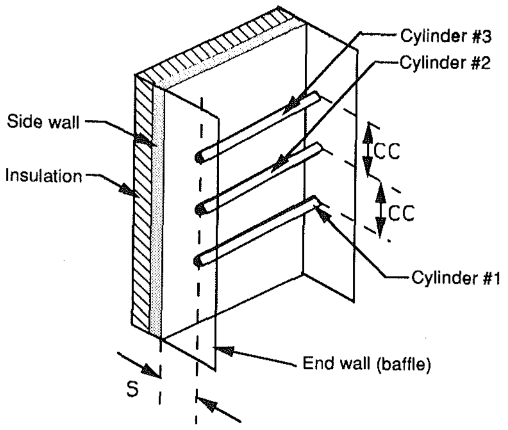

Fig. 1 Schematic of array-wall setting

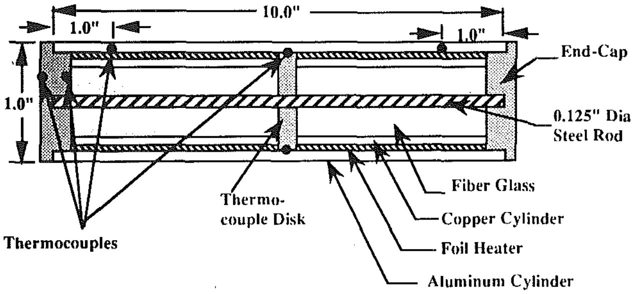

Fig. 2 Test section assembly for the cylinders

Contributed by the Heat Transfer Division for publication in the JOURNAL OF HEAT TRANSFER. Manuscript received by the Heat Transfer Division July 16, 1990; revision received October 14, 1991. Keywords: Flow Visualization, Heat Exchangers, Natural Convection.

Each cylinder had a length-to-diameter ratio equal to 10, allowing for suppression of the axial heat transfer effect. The ends of the cylinders were insulated by solid disks of low thermal conductivity material. These disks will be referred to as end-caps in the text. Eight thermocouples were used for each cylinder. Two were used to measure the axial temperature gradient in the end-cap. The other six thermocouples were used to measure the temperature of the cylinder surface, Fig. 2. Two thermocouples were cemented to the interior surface of the cylinder by using thermocouple epoxy and placed 2.54 cm (1.0 in.) from each cylinder's end, below the top stagnation point of the cylinder. The other four thermocouples were radially positioned at the midlength of the cylinder at 90-deg intervals from the top stagnation point around the inner circumference of each cylinder. These thermocouples were positioned in a thermocouple disk.

The thermocouple disks were placed at the midlength point of each cylinder. Then, two foil heaters were inserted from each end of the cylinder. These heaters were backed up by 2.23 mm (0.875 in.) diameter copper cylinders with a length of 12.065 cm (4.75 in.). The copper cylinders were used to support the heaters against the aluminum cylinders and to prevent hot spots on the heating foils due to loss of contact between the heaters and the cylinders. In order to prevent internal natural convection in the cores of the cylinders, the cores were filled with pressed fiber glass insulation. Then, the ends were sealed with end-caps.

Two types of walls were used in the experiment: side wall, which was parallel to the cylinders' axes, and the end walls (the baffles), which were perpendicular to the cylinders' axes. The side wall was made from 1.27 cm (0.5 in.) thick acrylic and was constructed at a height of 63.5 cm (25 in.) and a width of 25.4 cm (10 in.). It was backed with 2.54 cm (1 in.) thick styrofoam insulation, which was glued on the back surface of the wall. The surfaces of all the walls facing the cylinders were painted with a flat black paint in order to achieve a uniform radiation condition [5].

In order to approximate the experimental conditions of two-dimensional cases [2], baffles made of 3.175 mm (1/8 in.) thick acrylic were used to eliminate the transverse fluid motions associated with the finite length of the cylinders. Three sets of baffles were fabricated to accommodate the three settings ($CC=4D$, $2D$, and $1.5D$). The positions of the top cylinder (cylinder #3) from the top end of the baffles were the same for all sets. This left the positions of the lower (#2 and #1) dependent on the cylinder-to-cylinder spacings. There was no direct contact between the cylinders' surfaces and the baffles, since the baffles supported the end-caps of the cylinders. For each set, two baffles were placed 25.4 cm (10 in.) apart on the main frame to form a C-shaped channel with the side wall.

To reduce the air movement around the testing section, the main frame was placed in a 1.1 m × 0.765 m × 2.134 m (3.5 ft × 2.5 ft × 7 ft) enclosure. The enclosure was made of 1.27 cm (0.5 in.) plywood sheets. The top and bottom ends of the enclosure were open. To prevent air stratification in the enclosure, a 2.54 cm (1 in.) gap between the floor and the bottom end of the enclosure was left open.

There were two systems used in this experiment, each having different functions. The purpose of the first system was to supply power to the heaters in the cylinders and to measure the power supply for each heater. The second system was used to monitor the output of the thermocouples. A regulated power supply was used to supply direct current to heat the heaters. The temperature measurements were accomplished by using a data acquisition system with appropriate computer software. The aim of each experimental run was to establish a thermal equilibrium. The computer program coupled with a data acquisition program was used to display the temperature readings and the percentage of the average temperature difference for each cylinder, $\{\Delta T \text{ percent} = (T_{\text{new}} - T_{\text{old}})\, 100/T_{\text{new}}\}$, every 20 seconds. When the average temperature difference was less than 0.25 percent for 10 minutes, steady-state conditions were considered to be established. The data was recorded one hour after the establishment of the steady-state conditions in order to accommodate the slow thermal response of the side wall.

Once the average temperature of the cylinder(s) and the ambient temperature were recorded and the power supply was determined, the total heat transfer by convection, Q_{cv}, could be calculated from:

$$Q_{cv} = Q - Q_r - Q_{cd} \tag{1}$$

where Q_{cd} is the conduction heat loss from the cylinders' end caps, $\{Q_{cd} = -AK(dT/dX)$, where dT is the temperature drop across the end-cap thickness $dX\}$. The maximum heat loss by conduction was about 0.02 percent of the total input power, $\{(\text{conduction heat loss}) \text{ percent} = (Q_{cd}/Q)\, 100\}$. This occurred when the total input power, Q, was equal to 30 W at center-to-center spacing, $CC=1.5D$, and wall spacing ratio, $S/D = 0.081$. The radiation heat loss, Q_r, ranged from 6 to 8 percent of the total input power for no wall cases and from 4 to 7

Nomenclature

A = surface area of the cylinder = (πDL), m^2
CC = cylinder center-to-center spacing, m
C_p = specific heat, W h/(kg K)
D = cylinder diameter, m
Gr* = modified Grashof number
g = acceleration of gravity, m/s^2
h = average heat transfer coefficient, W/m^2 K
K = thermal conductivity, W/m K
L = cylinder length
Nu = average Nusselt number of the cylinder = $((hD)/K)$
Nu$_{av}$ = average Nusselt number of the whole array for single wall cases, Eq. (9)
Nu$_{av/f}$ = Nusselt number ratio for single wall cases, Eq. (10)
Nu$_{av/s}$ = Nusselt number ratio for single wall cases, Eq. (11)
Nu_i = average Nusselt number for cylinder i
Nu$_{i,f}$ = average Nusselt number for cylinder i in a free array
Nu$_s$ = average Nusselt number for a free single cylinder
Pr = Prandtl number
Q = total power input, W
Q_{cv} = heat flux by convection, W
Q_{cd} = heat flux by conduction, W
Q_r = heat flux by radiation, W
q = heat flux per unit area, W/m^2
Ra* = modified Rayleigh number, Eq. (4)
Ra$^*_i$ = modified Rayleigh number for cylinder i for single wall cases
Ra$^*_{i,f}$ = modified Rayleigh number for cylinder i for free array cases
S = spacing between the array and the wall, m
T = temperature, °C
T_w = surface temperature of the cylinder, °C
$T_{w,i}$ = surface temperature of cylinder i, °C
T_{inf} = ambient temperature, °C
Y_i = distance from the center of the lowest cylinder to the center of cylinder i ($Y_1 = 0.0$)
α = thermal diffusivity, m^2/h
β = coefficient of thermal expansion, K^{-1}
μ = dynamic viscosity, kg/m h
ν = kinematic viscosity, m^2/h
ρ = density, kg/m^3
ϕ = normalized temperature, Eq. (7)

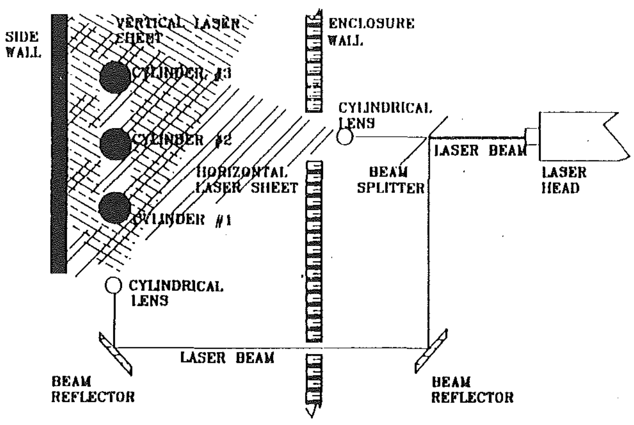

Fig. 3 Laser illumination system

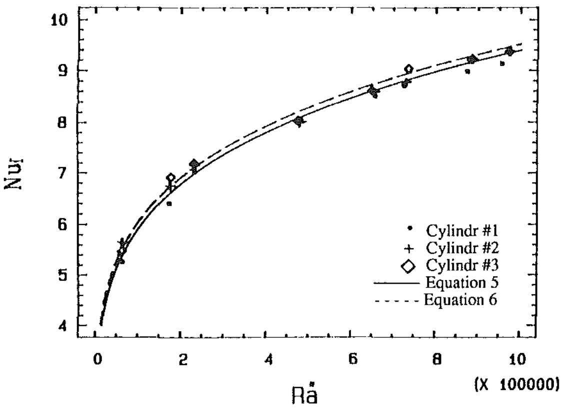

Fig. 4 Nusselt number, Nu_{ll}, versus Ra* for a free single cylinder

percent of the total input power for single wall cases. A detailed radiation heat transfer calculation is presented in [6]. Since the cylinders were polished to mirrorlike surfaces, the emissivity was considered equal to 0.05 [7–10].

Once the convection heat transfer, Q_{cv}, was determined, the average heat transfer coefficient was obtained from:

$$h=\frac{Q_{cv}}{A\,(T_w-T_{\rm inf})} \tag{2}$$

The average Nusselt number, Nu, was determined from:

$$\mathrm{Nu}=\frac{hD}{K}=\frac{Q_{cv}D}{AK(T_w-T_{\rm inf})} \tag{3}$$

For correlating the data, the modified Rayleigh number was calculated from:

$$\mathrm{Ra}^*=\mathrm{Gr}^*\mathrm{Pr}=\frac{G\beta\rho^2C_P\left(\dfrac{Q_{cv}}{A}\right)D^4}{K^2\mu} \tag{4}$$

All the air properties were calculated at the film temperature, $T_f=(T_w+T_{\rm inf})/2$. The uncertainty (based on Kline's approach [11]) in the calculated Nusselt number from the experimental results was 5.0%.

2.2 Flow Visualization Experimental Apparatus and Procedure. Flow visualization was accomplished by illuminating smoke particles with laser sheets perpendicular to the cylinders' axes, as shown in Fig. 3. A 3-W argon and krypton ion laser was used. A beam splitter, two beam reflectors, and two cylindrical lenses were used to generate two laser sheets. These sheets illuminated one vertical plane at the midwidth of the array. The vertical plane, except those sections blocked out by the cylinders themselves, was illuminated by the horizontal sheet. The horizontal sheet was created from the horizontal laser beam. Therefore, a vertical laser sheet created from the vertical laser beam was used to illuminate an opaque area and to enhance the illumination of the other parts of the illuminated plane. Smoke was introduced to the bottom of the main enclosure at very low velocity and at room temperature. The patterns of the flow fields were recorded on video tape and slides.

3 Experimental Results and Discussion

The three cylinders that were used in the array were tested separately as isolated single cylinders in an infinite expanded medium (the surrounding air) and the results are shown in Fig. 4. There are two primary reasons to study the free single cylinder case. First, it was necessary to verify the data-taking process and to check the related equipment setup. This was accomplished by comparing the Nusselt number from this experiment with the available data in the literature. The second reason was to find a correlation equation to represent the average Nusselt number for a single free cylinder, Nu_s, as a function of the modified Rayleigh number, Ra*. This equation would serve as the datum from which the heat transfer in the other cases would be considered enhanced or degraded. The functional relationship between Nu_s and Ra* for these data is shown in Eq. (5):

$$\mathrm{Nu}_s=0.571\ \mathrm{Ra}^{*0.2027} \qquad 3\times10^4<\mathrm{Ra}^*<10^6 \tag{5}$$

This equation lies about 1.6 percent below the following equation, which was obtained experimentally and theoretically by Dyer [12]:

$$\mathrm{Nu}_s=0.6\ \mathrm{Ra}^{*0.2}\ \text{for}\ 10^4<\mathrm{Ra}^*<10^6 \tag{6}$$

Equations (5) and (6) are superimposed on the experimental data as shown in Fig. 4.

3.1 Temperature Distribution Along the Array With Various Wall Spacings. The effect of array-wall spacing, S, and the effect of cylinder center-to-center spacing, CC, on the temperature distribution along the array will be discussed in this section.

The data are presented as the normalized temperature, ϕ, which is defined as the ratio of the excess temperature for each cylinder from the ambient temperature to the excess temperature for the lowest cylinder from the ambient temperature, as shown in Eq. (7).

$$\phi=\frac{T_{w,i}-T_{\rm inf}}{T_{w,1}-T_{\rm inf}} \tag{7}$$

From Eq. (7), the normalized temperature for the lowest cylinder is equal to one in all cases. The normalized temperature, ϕ, for $CC=1.5D$ and $CC=2D$ have a fixed pattern where the highest cylinder always has a higher normalized temperature than the second cylinder (Figs. 5 and 6). The increase in cylinder temperature for cylinders higher in the array is attributed to the balance between the temperature rise of the surrounding air of the upper cylinders and the increase of the plume velocity due to the density change from adding heat from the lower cylinders to the plume [5, 13, 14]. The normalized temperature data for $CC=1.5D$ and $CC=2D$ decrease sharply as the S/D ratio increases from 0.081 to $S/D=0.5$. Then the normalized temperature, ϕ, increase as S/D increases from 0.5 to 2.0. Also, at $S/D=0.5$, the normalized excess temperature difference between cylinders 2 and 3 is very small and sometimes reaches zero. This indicates that the behavior of these cylinders is the same at wall spacing ratio, $S/D=0.5$; as the wall spacing ratio diverts from $S/D=0.5$, in either direction, the normalized temperature difference between the upper cylinders, $(\phi_3-\phi_2)$, increases.

For $CC=4D$ (Figs. 5 and 6), the normalized excess tem-

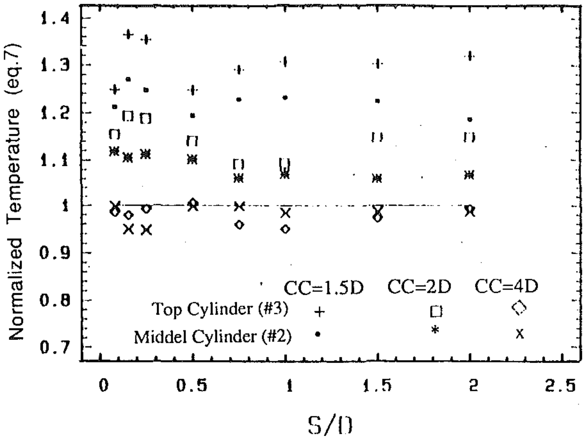

Fig. 5 Effect of wall spacing on the normalized temperature at $q = 49.338$ W/m^2

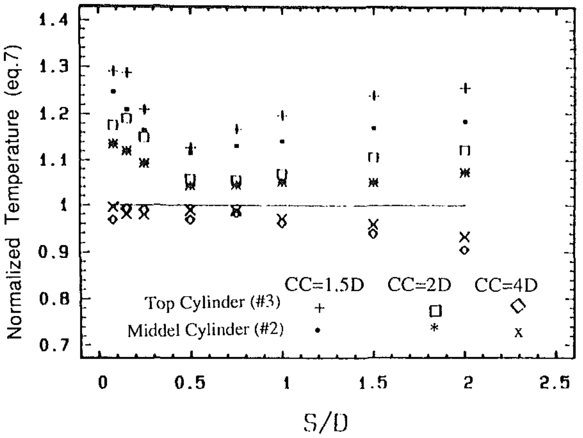

Fig. 6 Effect of wall spacing on the normalized temperature at $q = 493.380$ W/m^2

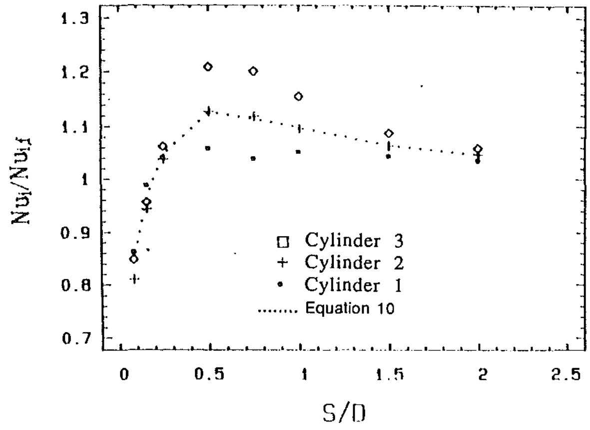

Fig. 7 Effect of wall spacing on the Nusselt number ratio, $Nu_i/Nu_{i,f}$ at $CC = 1.5D$ and $q = 149.014$ (W/m^2)

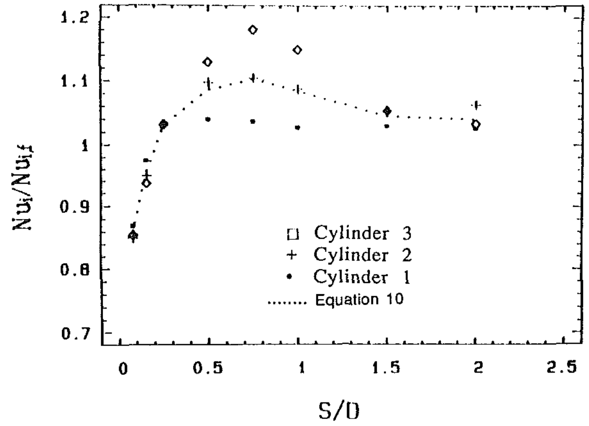

Fig. 8 Effect of wall spacing on the Nusselt number ratio, $Nu_i/Nu_{i,f}$ at $CC = 2D$ and $q = 149.014$ (W/m^2)

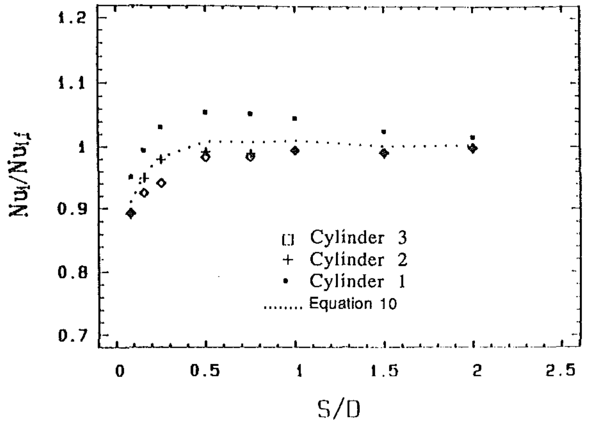

Fig. 9 Effect of wall spacing on the Nusselt number ratio, $Nu_i/Nu_{i,f}$ at $CC = 4D$ and $q = 149.014$ (W/m^2)

perature, ϕ, is less than one for both cylinders (2 and 3). The behavior of these cylinders was not consistent. The change in the normalized temperature is minimal for $S/D < 1.0$, but ϕ decreases as S/D increases above 1.0. In all the cases ($CC = 1.5D$, $CC = 2D$, and $CC = 4D$), the upper cylinders behave more like the lowest cylinder at $S/D \sim 0.5$.

3.2 Heat Transfer Characteristics of the Cylinders in the Array. The effect of the wall-array spacing and the cylinders' center-to-center spacing on the heat transfer capability of each cylinder will be examined by studying the Nusselt number ratio of $Nu_i/Nu_{i,f}$, which is the ratio of the Nusselt number value of each cylinder in the array with a single wall, Nu_i, to the Nusselt number value of the same cylinder in a free array (no wall condition), $Nu_{i,f}$, at the same input heat flux. The ratios $Nu_i/Nu_{i,f}$ at various S/D at the same input heat flux are plotted in Figs. 7–9. For small center-to-center spacings, $CC = 1.5D$ and $CC = 2D$, all the cylinders experience the same percentage of degradation, which is about 20 percent at S/D of 0.081. This degradation decreases as the S/D increases and the values of $Nu_i/Nu_{i,f}$ reach unity at $S/D \sim 0.155$. At $S/D > 0.25$, the effect of the wall spacing on the cylinder depends on the position of the cylinder in the array. The upper cylinders have the highest enhancement at S/D equal to 0.5. At the peak, the highest cylinder in the array has an enhancement between 15 and 22 percent above the no wall case, while the second cylinder has an enhancement between 9 and 15 percent. The lowest cylinder in the array reaches the peak with an enhancement of about 5 percent maximum at $S/D \simeq 0.25$ at all the heat flux values except the lowest value.

Figure 9 shows the effect of wall spacing on the array at $CC = 4D$. The lowest cylinder shows a 10 percent maximum degradation at $S/D = 0.081$. The maximum enhancement in the lowest cylinder was 5 percent at S/D values between 0.25 and 0.5. For the upper cylinders (cylinders 2 and 3), the $Nu_i/Nu_{i,f}$ values were less than one. These degradations are between 12 and 24 percent at $S/D = 0.081$ and they decrease as S/D

Table 1 Coefficients of Eq. (8), $Nu_i/Ra_i^{*0.2} = A_i + A_2\exp[-A(y_i(CC))]$

S/D	CC = 1.5D			CC = 2D			CC = 4D		
	A_1	A_2	A_3	A_1	A_2	A_3	A_1	A_2	A_3
0.081	0.38816	0.12099	1.68782	0.44023	0.08724	1.23577	0.53390	0.00448	-0.86297
0.155	0.42637	0.15017	1.15017	0.46097	0.14512	0.62651	0.49841	0.10969	-0.02341
0.250	0.47994	0.12880	1.08535	0.48866	0.13475	0.46858	0.49055	0.12841	-0.05972
0.500	0.53707	0.07132	1.97020	0.57548	0.04468	0.84132	0.52552	0.08878	-0.11651
0.750	0.52015	0.08865	1.43274	0.86924	-0.25232	-0.06193	0.59267	0.02977	-0.15812
1.000	0.50866	0.10537	1.28668	0.56256	0.05466	0.83912	0.49579	0.12126	-0.10031
1.500	0.47515	0.12910	1.05709	0.36239	0.24567	0.17936	0.39546	0.21512	-0.09113
2.000	0.45226	0.14330	0.89824	0.36551	0.24209	0.19971	0.26659	0.33887	-0.07347
Infinity	0.44692	0.14101	1.13765	0.46811	0.12704	0.51142	0.09139	0.50926	-0.08129

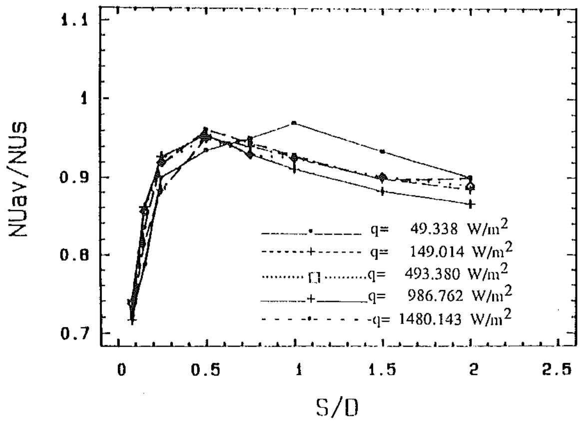

Fig. 10 Effect of wall spacing on the average Nusselt number of the whole array at $CC = 1.5D$

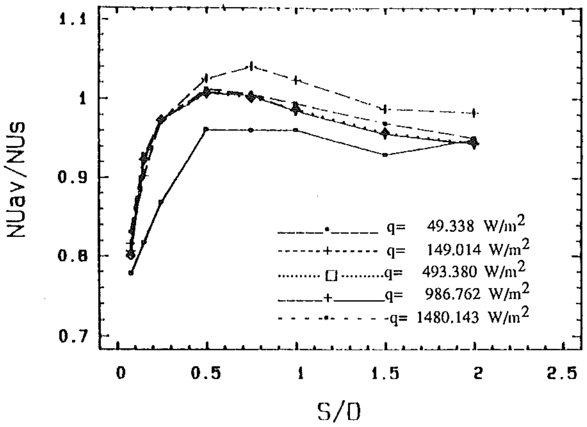

Fig. 11 Effect of wall spacing on the average Nusselt number of the whole array at $CC = 2D$

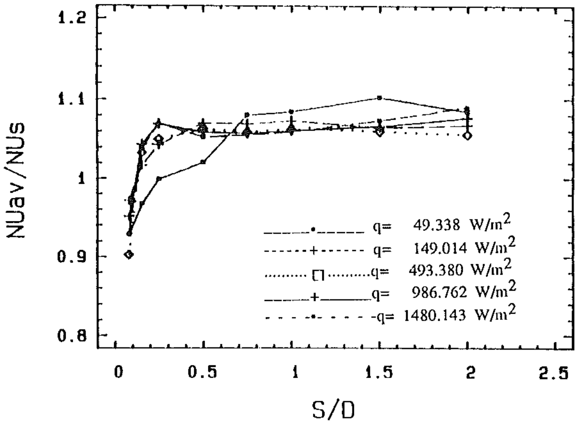

Fig. 12 Effect of wall spacing on the average Nusselt number of the whole array at $CC = 4D$

increases. The reduction of $Nu_3/Nu_{3,f}$ from unity is twice the reduction of $Nu_2/Nu_{2,f}$ from unity. These values, $Nu_i/Nu_{i,f}$ ($i = 2$ and 3), increase to unity as S/D increases to infinity. The Nusselt number for each cylinder can be predicted from Eq. (8) with less than 5 percent error for $q > 49.338$ W/m^2 and with 10 percent or less error for $q = 49.338$ W/m^2.

$$\frac{N_i}{Ra_i^{*0.2}} = A_1 + A_2\exp\left[-A_2\left(\frac{Y_i}{CC}\right)\right] \quad (8)$$

The values of A_1, A_2, and A_3 are shown in Table 1 and Y_i is defined in the nomenclature section.

The effect of wall spacings, S, and center-to-center spacing, CC, on the average Nusselt number of the whole array, Nu_{av}, will be discussed by examining the Nusselt number ratio $Nu_{av/f}$. This ratio, $Nu_{av/f}$, is the ratio of the average Nusselt number of the whole array with presence of the side wall to the average Nusselt number of the whole array without the wall (free array) as shown in Eq. (10). The average Nusselt number of the whole array, Nu_{av}, was compared to the Nusselt number of a free single cylinder, Nu_s, at the same heat flux. The average Nusselt number ratio for the whole array, $Nu_{av/f}$, is superimposed on Figs. 7-9, where $Nu_{av/f}$ is shown by the dotted line, as calculated from:

$$Nu_{av} = \frac{\sum_{i=1}^{3} Nu_i}{3.0} \quad (9)$$

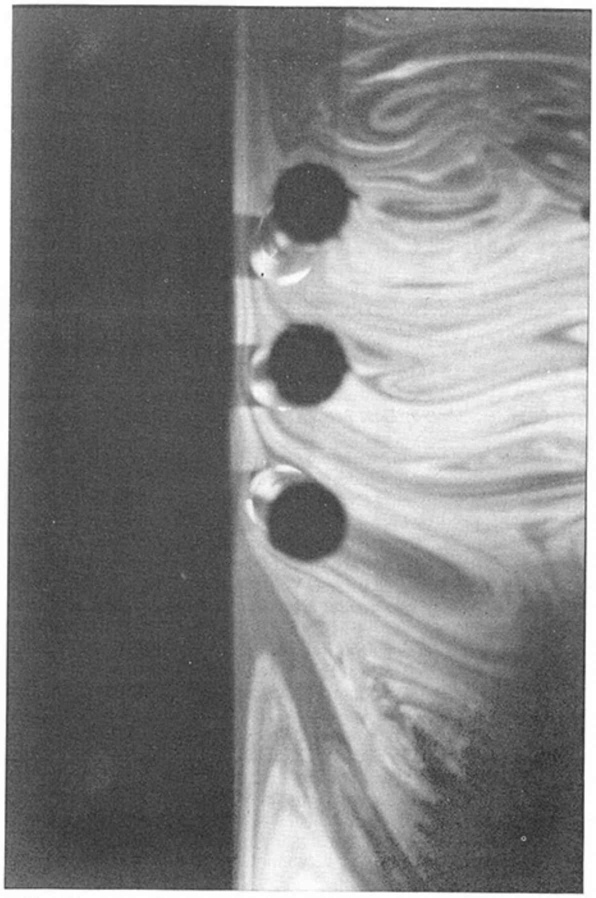

Fig. 13 Flow visualization for $CC = 2D$ with a single wall at $S/D = 0.5$

$$\mathrm{Nu}_{av/f} = \frac{\mathrm{Nu}_{av}}{\dfrac{\sum_{i=1}^{3} N_{i,f}}{3.0}} \tag{10}$$

Although $\mathrm{Nu}_{av/f}$ is plotted as a line, the plot is a point-to-point curve. For $CC = 1.5D$ and $CC = 2D$, the $\mathrm{Nu}_{av/f}$ values have peaks, with 8–12 percent enhancement, at $0.5 \leq S/D < 0.75$. The $\mathrm{Nu}_{av/f}$ ratio decreases sharply as S/D decreases from 0.5 and reaches its lowest values, about 0.82 at $CC = 1.5$ at $S/D = 0.081$, and about 0.84 at $CC = 2D$ at $S/D = 0.081$. At $S/D > 0.75$, the $\mathrm{Nu}_{av/f}$ values decrease slowly and asymptote to a value corresponding to S/D of infinity as shown in Figs. 7 and 8.

The $\mathrm{Nu}_{av/f}$ values for $CC = 4D$ are always less than one, as shown in Fig. 9. Those values increase sharply as S/D increases from 0.081 to 0.5. Then the increments in these values of $\mathrm{Nu}_{av/f}$ become smaller as $\mathrm{Nu}_{av/f}$ asymptotes to a value corresponding to S/D of infinity.

Figures 10–12 show the Nusselt number ratios, $\mathrm{Nu}_{av/s}$, of the Nu_{av} values to the Nusselt numbers of a single cylinder, Nu_s, as calculated from Eq. (5) at Ra* of the lowest cylinder of the array. The $\mathrm{Nu}_{av/s}$ is defined in the following equation:

$$\mathrm{Nu}_{av/s} = \frac{\mathrm{Nu}_{av}}{\mathrm{Nu}_s} = \frac{\dfrac{\sum_{i=1}^{3} \mathrm{Nu}_i}{3.0}}{[0.571\ \mathrm{Ra}_1^{*0.2027}]} \tag{11}$$

The enhancements of Nu_{av} from Nu_s were insignificant and $\mathrm{Nu}_{av/s}$ is mostly equal to or less than one at $CC = 1.5D$ and $CC = 2D$. In both cases, there were peak values at $0.5 \leq S/D < 0.75$, except at the lowest heat flux, where the peaks were at $0.75 \leq S/D < 1.0$. For $CC = 4D$, there was a maximum 8 percent enhancement at Nu_{av} values at $0.25 < S/D \leq 0.5$ in all the input heat flux values, except the lowest heat flux where the maximum enhancement was 10 percent at $1.0 \leq S/D < 1.5$. The average Nusselt number for the whole array, Nu_{av}, can be predicted from Eq. (12) with an error less than 4 percent. Table 2 shows the coefficient B_1.

$$\mathrm{Nu}_{av} = \frac{\sum_{i=1}^{3} \mathrm{Nu}_i}{3.0} = B_1\,\mathrm{Ra}^{*0.2} \tag{12}$$

Table 2 Correlation coefficient B_1 for Eq. (12), $\mathrm{Nu}_{cv} = B_1\ \mathrm{Ra}_l^{*0.2}$

S/D	CC = 1.5D	CC = 2D	CC = 4D
	B_1	B_1	B_1
0.081	0.43243	0.47916	0.55287
0.155	0.49607	0.53926	0.60844
0.250	0.54069	0.56980	0.62368
0.500	0.56403	0.59535	0.62452
0.750	0.55490	0.59425	0.62771
1.000	0.55014	0.58631	0.63009
1.500	0.53139	0.56906	0.63291
2.000	0.52108	0.56284	0.63612
Infinity	0.50840	0.55027	0.64887

3.3 Flow Visualization. The results of the flow visualization are shown in Fig. 13 for cylinder center-to-center spacing equal to $2D$. Figure 13 shows that the space between the cylinders and the wall acts as a chimney where the air particles are at a higher temperature than the ambient. The high temperature zone creates a low density region between the wall and the cylinders of the array. This results in a low-pressure region between the wall and the array. Due to buoyancy forces, this low pressure drives the air particles horizontally toward the wall through the cylinder-to-cylinder spacing and vertically through the lower cylinder-wall space. The flow visualization showed that the presence of a single wall induces more air circulation from the ambient around the highest cylinder in the array. This enhances the heat transfer from the highest cylinder in the array. As the center-to-center spacing increases, the plume from one cylinder to the next higher cylinder has more time to mix with the ambient air particles that were directed toward the wall. Also, as the CC spacing increases, the plume from the lower cylinder(s) has fewer flow restrictions given the geometry of the setup and has more time to be accelerated by the buoyancy forces while it rises. This explains why the highest cylinder in the array at $CC = 4D$ has the highest Nusselt number in the array.

Furthermore, the flow visualization shows that the weak regions above the cylinders were shifted toward the wall. The streamlines of the flow show that the air particles approach the upper cylinders horizontally. For the lowest cylinder, the air particles approach the cylinders in a plane rotating toward the vertical wall. In other words, if there is a single wall at the left side of the array, the upper and lower stagnation points of each cylinder were rotated counterclockwise from the vertical plane (the plane that passes through the axis of each cylinder). This rotation of the stagnation points was at its maximum at $S/D = 0.5$ and the rotation decrease as the wall-array spacing decreases or increases from $S/D = 0.5$. Therefore, there was more ambient air at room temperature mixed with raised plume from the lower cylinder at $S/D \sim 0.5$. This explains why the array has the highest heat transfer rate at $S/D \sim 0.5$.

4 Conclusions

The experiments have shown that the lowest cylinder in the array behaves as a free single cylinder for all cases in which the ratio of wall-array spacing to the cylinder diameter $S/D \geq 0.155$. The heat transfer from the upper cylinders of the array was affected by the wall-array spacing and the cylinder center-to-center spacing. The presence of the wall enhanced the heat transfer from the upper cylinders of the array with cylinder center-to-center spacing equal to $1.5D$ and $2D$ relative to the no wall cases, while there was degradation in the cylinders' heat transfer capability with cylinder center-to-center spacing equal to $4D$. At the two small cylinders' center-to-center spacing values, the maximum enhancement for the free array occurred at $S/D \sim 0.5$. The top cylinder had the maximum enhancement, the middle cylinder had the next highest enhancement, and the lowest cylinder had the lowest enhancement. The space between the array and the wall acts like a chimney and creates a wall jet flow.

References

1 Sloan, J. L., *Design and Packaging of Electronic Equipment*, Van Nostrand Reinhold Company, Inc., New York, 1985.

2 Sparrow, E. M., and Ansari, M. A., "All-Modes Heat Transfer From a Horizontal Cylinder Situated Adjacent to Adiabatic, Partially Enclosing Walls," *Int. J. Heat Mass Transfer*, Vol. 27, No. 10, 1984, pp. 1855-1864.

3 McCoy, T. J., "Natural Convection From a Horizontal Cylinder Parallel to a Heated Vertical Wall," Master's thesis, Mechanical Engineering Department, Oregon State University, 1988.

4 Sparrow, E. M., and Boessneck, D. S., "Effect of Transverse Misalignment on Natural Convection From a Pair of Parallel, Vertically Stacked, Horizontal Cylinders," ASME JOURNAL OF HEAT TRANSFER, Vol. 105, 1983, pp. 241-247.

5 Masters, G. F., and Paulus, G., "Effects of Confining Walls on Heat Transfer From a Vertical Array of Heated Horizontal Cylinders," *Transaction of CSME*, Vol. 1, No. 4, 1972, pp. 219-222.

6 Al-Alusi, T. R., "An Experienced Study of Natural Convection Heat Transfer From a Horizontal Cylinder Array Vertically Aligned to and Confined by a Single Wall and Two Walls," Ph.D. thesis, Mechanical Engineering Department, Oregon State University, 1990.

7 Holman, J. P., *Heat Transfer*, 6th ed., McGraw-Hill, New York, 1986.

8 Sparrow, E. M., Mendes, P. S., Ansari, M. A., and Parta, A. T., "Duct-Flow Versus External-Flow Natural Convection at a Short, Wall-Attached Horizontal Cylinder," *Int. J. Heat Mass Transfer*, Vol. 26, No. 6, 1983, pp. 881-888.

9 Sparrow, E. M., and Niethammer, J. E., "Effect of Vertical Separation Distance and Cylinder-to-Cylinder Temperature Imbalance on Natural Convection for a Pair of Horizontal Cylinders," ASME JOURNAL OF HEAT TRANSFER, Vol. 103, 1981, pp. 638-644.

10 Sparrow, E. M., and Pfeil, D. R., "Enhancement of Natural Convection Heat Transfer From a Horizontal Cylinder Due to Vertical Shrouding Surfaces," ASME JOURNAL OF HEAT TRANSFER, Vol. 106, 1984, pp. 124-130.

11 Holman, J. P., *Experimental Methods for Engineers*, 4th ed., McGraw-Hill, New York, 1986.

12 Dyer, J. R., "Laminar Natural Convection From a Horizontal Cylinder With a Uniform Convective Heat Flux," *Mechanical and Chemical Engineering Transactions*, Institute of Engineers, Australia, Vol. MC1, 1965, pp. 125-128.

13 Marsters, G. F., "Array of Heated Horizontal Cylinders in Natural Convection," *Int. J. Heat Mass Transfer*, Vol. 15, 1972, pp. 921-933.

14 Tokura, I., Saito, H., Kishinami, K., and Muramoto, K., "An Experienced Study of Free Convection Heat Transfer From a Horizontal Cylinder in a Vertical Array Set in Free Space Between Parallel Walls," ASME JOURNAL OF HEAT TRANSFER, Vol. 105, 1983, pp. 102-107.

Natural Convection Liquid Cooling of a Substrate-Mounted Protrusion in a Square Enclosure: A Parametric Study

S. B. Sathe
IBM Corporation
Endicott, NY 13760

Y. Joshi
Department of Mechanical Engineering,
Naval Postgraduate School,
Monterey, CA 93943

The coupled conduction and natural convection transport from a substrate-mounted heat generating protrusion in a liquid-filled square enclosure is numerically examined. The governing steady two-dimensional equations are solved using a finite-difference method for a wide range of Rayleigh numbers, protrusion thermal conductivities and widths, substrate heights, and enclosure boundary conditions. The results presented apply to liquids with $10 \leq Pr \leq 1000$. It was established that in many situations it may be inappropriate to specify simple boundary conditions on the solid surface and decouple the conduction within the substrate or the protrusion. Higher Rayleigh numbers, protrusion thermal conductivities, and widths enhanced cooling. A variation in the substrate height did not affect the maximum protrusion temperature; however, the flow behavior was considerably altered. An empirical correlation for the maximum protrusion temperature was developed for a wide range of parametric values. The enclosure thermal boundary conditions changed the heat transfer in the solid region to only a small extent. Immersion cooling in common dielectric liquids was shown to be advantageous over air cooling only if the thermal conductivity of the protrusion was larger than that of the liquid.

1 Introduction

The increasing interest in the study of thermal control of micro-electronic equipment can perhaps be attributed to the rapid advances in semi-conductor devices fabrication technology. With the incorporation of each generation of new devices into electronic systems, the available cooling technologies are re-examined, often leading to the development of innovative heat removal methods (Chu, 1986). Current designs typically specify device temperatures below 85°C in order to meet overall system reliability goals. A number of thermal management strategies for modern mainframe computers are discussed by Chu (1986) and Nakayama (1988).

Single-phase convection heat transfer is frequently employed in the cooling of electronic systems. Such applications are characterized by geometric complexity, discrete heating, and a multitude of heat transfer paths, which often preclude the use of available heat transfer correlations. A number of studies on single-phase convective cooling applicable to the thermal control of electronic equipment were reviewed by Incropera (1988). Many of these examine natural, mixed, or forced convection air cooling. Due to several desirable features such as low cost, design simplicity, and high reliability, passive air cooling employing natural convection continues to be of interest as discussed by Jaluria (1985a).

Several investigations of natural convection from discrete heat sources in air have been reported. Jaluria (1985b) computationally examined the transport resulting from discrete, uniform flux strips mounted on an adiabatic vertical surface. The effect of component spacing on the surface temperatures was discussed. Afrid and Zebib (1989) considered protruding heat sources on an adiabatic vertical surface. The heat conduction within the protrusion and the coupled convection in air were examined. Lee and Yovanovich (1989) also considered the transport from flush uniform flux heat source on a vertical surface. Conduction within the thin substrate was computed using a one-dimensional model. Radiation from the surface was also accounted for.

Compared to air, natural convection in liquids is known to result in significantly larger heat transfer coefficients, making it an attractive cooling option for enclosed electronic systems such as some high dissipation power supplies. Use of liquids both in single-phase and phase-change systems has recently been reviewed by Bergles and Bar-Cohen (1990). A few experimental investigations have examined liquid immersion natural convection in geometries of interest in electronic equipment cooling. These studies have considered discrete heat sources on vertical surfaces (Park and Bergles, 1987), within enclosures (Keyhani et al., 1988), and in vertical channels (Joshi et al., 1989).

Limited numerical simulations of the natural convection transport in liquid-filled enclosures with discrete heating have also been made. Liu et al. (1987) carried out three-dimensional computations of natural convection due to a three by three array of rectangular protrusions in a dielectric liquid filled enclosure. Lee et al. (1987) numerically examined two-dimensional natural convection from a single protrusion in a liquid-filled enclosure. Both of these studies prescribed uniform flux conditions on the protrusion faces. In most applications only the volumetric energy generation rates within the protruding components are avaiable and explicit thermal boundary conditions on their surfaces are therefore unknown.

For a substrate-mounted protrusion in a liquid-filled square enclosure Sathe and Joshi (1990) computed both the conduction in the protrusion and substrate, and the natural convection in the liquid. Results were reported for a single set of Pr, protrusion dimensions and thermophysical properties, and enclosure boundary conditions. The effect of the thermal conductivity of the substrate on the maximum protrusion temperature was also examined. Comparisons with existing experimental data showed favorable agreement. In electronic

---

Contributed by the Heat Transfer Division and presented at the ASME Winter Annual Meeting, Dallas, Texas, November 25–30, 1990. Manuscript received by the Heat Transfer Division November 1, 1990; revision received August 20, 1991. Keywords: Conjugate Heat Transfer, Electronic Equipment, Natural Convection.

component cooling applications, a wide variation in the geometric parameters, thermophysical properties, and enclosure boundary conditions is possible; this area was not addressed.

The present investigation is a detailed numerical parametric study of the coupled conduction and natural convection processes in the cooling configuration considered in our previous study. Two-dimensional computations of flow and heat transfer are carried out for specified rates of volumetric energy generation within the protrusion. The transport characteristics are examined for different thermophysical properties of the protrusion, and protrusion and substrate dimensions. These data are used to obtain an empirical correlation for the maximum protrusion temperature over a wide range of operating parameters. The influence of the enclosure thermal boundary conditions on the temperature levels within the protrusion is also studied.

2 Analysis

A substrate-mounted, uniformly heat-generating protrusion enclosed in a liquid-filled square cavity is considered. A schematic sketch of the configuration is provided in Fig. 1. The protrusion, substrate, and fluid have constant but different thermophysical properties. The fluid is assumed to be Newtonian. For specified rates of volumetric energy generation within the protrusion, the natural convection in the liquid and the coupled conduction processes within the substrate and the protrusion are described by the following set of equations.

2.1 Governing Equations. Assuming a steady-state, laminar flow with negligible viscous dissipation and pressure stress terms and invoking the Boussinesq approximations, the governing equations are:

Fluid Region

$$\frac{\partial u}{\partial x}+\frac{\partial v}{\partial y}=0 \tag{1}$$

$$\frac{\partial(\rho u^2)}{\partial x}+\frac{\partial(\rho uv)}{\partial y}=\mu\left(\frac{\partial^2 u}{\partial x^2}+\frac{\partial^2 u}{\partial y^2}\right)+\rho g\beta(t-t_c)-\frac{\partial p}{\partial x} \tag{2}$$

$$\frac{\partial(\rho uv)}{\partial x}+\frac{\partial(\rho v^2)}{\partial y}=\mu\left(\frac{\partial^2 v}{\partial x^2}+\frac{\partial^2 v}{\partial y^2}\right)-\frac{\partial p}{\partial y} \tag{3}$$

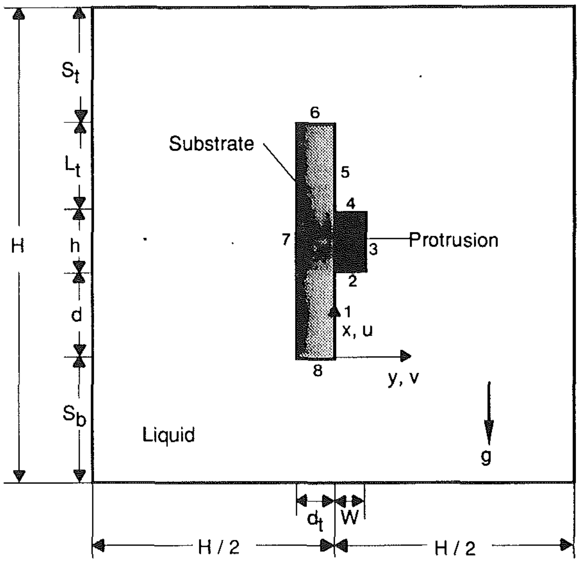

Fig. 1 Schematic diagram of the liquid cooled protruding heat source assembly

$$\frac{\partial(\rho ut)}{\partial x}+\frac{\partial(\rho vt)}{\partial y}=\frac{k_f}{c_p}\left(\frac{\partial^2 t}{\partial x^2}+\frac{\partial^2 t}{\partial y^2}\right) \tag{4}$$

Protrusion

$$k_c\left(\frac{\partial^2 t}{\partial x^2}+\frac{\partial^2 t}{\partial x^2}\right)=\frac{Q}{wh} \tag{5}$$

Substrate

$$\frac{\partial^2 t}{\partial x^2}+\frac{\partial^2 t}{\partial y^2}=0 \tag{6}$$

The boundary conditions include isothermal cavity walls at temperature t_c and the no-slip and impermeable wall conditions for the velocity components; i.e., $u = v = 0$ and $t = t_c$ at the cavity boundaries. Heat fluxes and temperatures are to be

Nomenclature

c_p = specific heat at constant pressure, J/kg-K
d = dimension in Fig. 1, m
d_t = substrate thickness, m
F_1-F_4 = energy fractions leaving the bottom, right, top, and left faces of the protrusion, respectively
g = gravitational acceleration, m/s^2
h = protrusion height, m
H = enclosure height, m
k = thermal conductivity, W/m-K
L_t = dimension in Fig. 1, m
$\mathbf{n}$ = outward unit normal vector at the solid surface
p = pressure, N/m^2
P = nondimensional pressure $= p/\rho U_o^2$
Pr = Prandtl number $= \mu c_p/k_f$
Q = linear heat generation rate, W/m
$\mathbf{Q}$ = nondimensional heat flux crossing the solid surface, Eq. (7)
R_c = protrusion to fluid thermal conductivity ratio $= k_c/k_f$
R_s = substrate to fluid thermal conductivity ratio $= k_s/k_f$
Ra = Rayleigh number $= g\beta Qh^3/\alpha k_f\nu$
s = nondimensional clockwise contour distance along the solid-fluid interface in Tables 2 and 3
S_b, S_t = dimensions in Fig. 1, m
t_c = enclosure wall temperature, K
T = nondimensional temperature $= (t-t_c)/(Q/k_f)$
u = vertical velocity component, m/s
U = nondimensional vertical velocity component $= u/U_o$
U_o = reference velocity $= (g\beta Qh/k_f)^{1/2}$, m/s
v = horizontal velocity component, m/s
V = nondimensional horizontal velocity component $= v/U_o$
w = protrusion width, m
x = vertical coordinate, m
X = nondimensional vertical coordinate $= x/h$
y = horizontal coordinate, m
Y = nondimensional horizontal coordinate $= y/h$
α = fluid thermal diffusivity, m^2/s
β = coefficient of thermal expansion, 1/K
ρ = fluid density, kg/m^3
μ = dynamic viscosity, kg/m-s
ν = kinematic viscosity, m^2/s

Subscripts

c = protrusion (chip)
f = fluid/liquid
max = maximum
s = substrate

matched at the interfaces of dissimilar materials. The following scheme is used to nondimensionalize the governing equations and boundary conditions: $X = x/h$, $Y = y/h$, $U = u/U_o$, $V = v/U_o$, $T = (t-t_c)/(Q/k_f)$, and $P = p/\rho U_o^2$ where $U_o = (g\beta Qh/k_f)^{1/2}$ is a reference velocity. As a result of the nondimensionalization, the governing parameters are: $\Pr = \mu c_p/k_f$, $\mathrm{Ra} = g\beta Qh^3/\alpha k_f \nu$, $R_c = k_c/k_f$, $R_s = k_s/k_f$, S_b/h, d/h, L_t/h, S_t/h, d_t/h, and w/h. The various symbols have been defined in the Nomenclature.

2.2 Numerical Procedure. The governing Eqs. (1)-(6) were discretized using a finite difference technique wherein the control volumes for the temperature were staggered from those for the velocities. The faces of the temperature control volumes coincide with the interfaces of dissimilar materials. Power law variation was used for the interpolation of the dependent variables. Abrupt changes in the diffusivities, such as those encountered in the present problem, were handled effectively by using the harmonic-mean formulation. The details of the numerical procedure can be found from Patankar (1980). The discretized equations were solved iteratively using the line-by-line TDMA (Tri-Diagonal Matrix Algorithm) and the SIMPLER procedure (Patankar, 1980).

Even though separate equations are written in the fluid and solid regions, the solid region was numerically simulated by letting its viscosity be very large. Thus the same momentum equation was solved throughout the computational domain. Similarly, heat sources and property values were appropriately specified in each region and only one energy equation was solved in the entire computational domain. The flux matching conditions were satisfied implicitly in the present formulation.

Test computations were performed on a series of grids ranging from 10 × 10 to 60 × 60 control volumes. The grid points were densely packed above the protrusion after preliminary runs on coarser grids showed that the flow was thermally stratified below the protrusion. It was determined that increasing the grid points from a 45 × 50 to 60 × 60 nonuniform mesh resulted in less than 2 percent changes in the maximum temperature, protrusion heat fluxes, and the maximum fluid velocities. A 45 × 50 nonuniform grid was then used in the rest of the computations. Convergence was assumed when the change in the dependent variables in successive iterations was no more than 0.005 percent. An overall energy balance was computed as the difference between the total heat generation rate and the net rate of energy loss through the cavity boundaries. In most cases, a balance of better than 0.1 percent was achieved, with the energy balance in the worst case being no more than 1 percent.

The computational times on an IBM-370/3033 computer ranged from 200–400 CPU minutes for computations started with $u = v = 0$ and $t = t_c$ throughout the cavity. The run times could be reduced in a few cases when computations were commenced with earlier solutions as initial guesses.

The numerical code was validated by solving the problem of natural convection in an air-filled cavity with vertical isothermal hot and cold walls and horizontal adiabatic surfaces. A comparison of the overall Nusselt numbers with the numerical results of Raithby and Wong (1981) for a cavity aspect ratio 5 and Rayleigh numbers 10^4 and 10^5 yielded agreements better than 0.8 percent.

3 Computational Results

Numerical computations were performed for a range of governing parameters that may be encountered in actual applications. These input levels are collected in Table 1. The upper limit for Ra was restricted to 10^7 due to nonconvergence of the numerical procedure for higher Ra. To get an idea of the Ra values corresponding to given input power levels, for example, 0.1 W generated in a 10 mm × 10 mm × 25 mm long protruding source, would yield Ra of the order of 10^7 and 10^5, respectively, in commercially available dielectric fluids FC-75 and FC-71. The corresponding Ra in water and air are 10^5 and 10^4, respectively.

Table 1 Parameter values used in numerical computations

Parameter	Value(s)
Pr	25 (also, selected computations for 10, 100, 1000)
Ra	10^3-10^7
R_s	10
R_c	0.1-10^3
S_b/h	4.5
S_t/h	4.5
d/h	2
d_t/h	1.5
L_t/h	0-4
w/h	0.25-1.25

The fluorinert liquids FC-75 and FC-71 have Pr of about 25 and 1400 at 300 K, respectively (3M Corp., 1985). A set of calculations was performed with a fixed Ra of 10^7 for Pr = 10, 100, and 10^3 to study the Prandtl number effect. It was revealed that the maximum temperatures changed negligibly when Pr was varied over the wide range mentioned above. All subsequent computations were done for Pr = 25, characteristic of FC-75. However, the dimensionless protrusion temperature levels are applicable to liquids with $10 \leq \Pr \leq 1000$ due to the relatively weak additional dependence of the transport within the solid on Pr, once the fluid properties are incorporated into Ra.

As seen in Table 1, the substrate conductivity was ten times that of the fluid, i.e., $R_s = 10$. Such a ratio represents a substrate made of a combination of epoxy-glass, copper, or ceramic laminates, with an effective thermal conductivity of 0.6 W/m-K; along with the fluid FC-75 that has a thermal conductivity of 0.06 W/m-K (3M Corp., 1985). It was shown in our earlier study (Sathe and Joshi, 1990) that for $R_s > O(1)$, conduction through the substrate is an important cooling mechanism and must be accounted for. The maximum temperature occurring in the chip was shown to decrease with an increasing R_s. For $R_s > 100$ or $R_s < 1$, the maximum temperature changed negligibly with a change in R_s.

In the following, for a fixed R_s of 10, the value of R_c was varied over a wide range, from 0.1 to 10^3. Such a variation may be encountered in practice due to the fact that different packages have widely varying amounts of silicon, air gaps and heat spreading and encapsulation materials. The influence of R_c, L_t/h, and w/h on the heat transfer and fluid flow is studied for different Ra. The resulting trends are first presented for conditions when all enclosure walls are maintained at a uniform temperature of t_c. Effects of changing the enclosure surface thermal conditions on transport from the heat source are then examined.

3.1 Effect of Protrusion Thermal Conductivity, R_c. The streamlines and isotherms for different R_c are shown in Fig. 2 for $\mathrm{Ra} = 10^6$. The flow is characterized by a primary clockwise circulation in the upper right portion of the cavity due to the buoyancy effects arising from the heated protrusion. A secondary counterclockwise cell is evident above the substrate, resulting from a combination of the buoyant force generated due to conduction across the substrate and the splitting of the

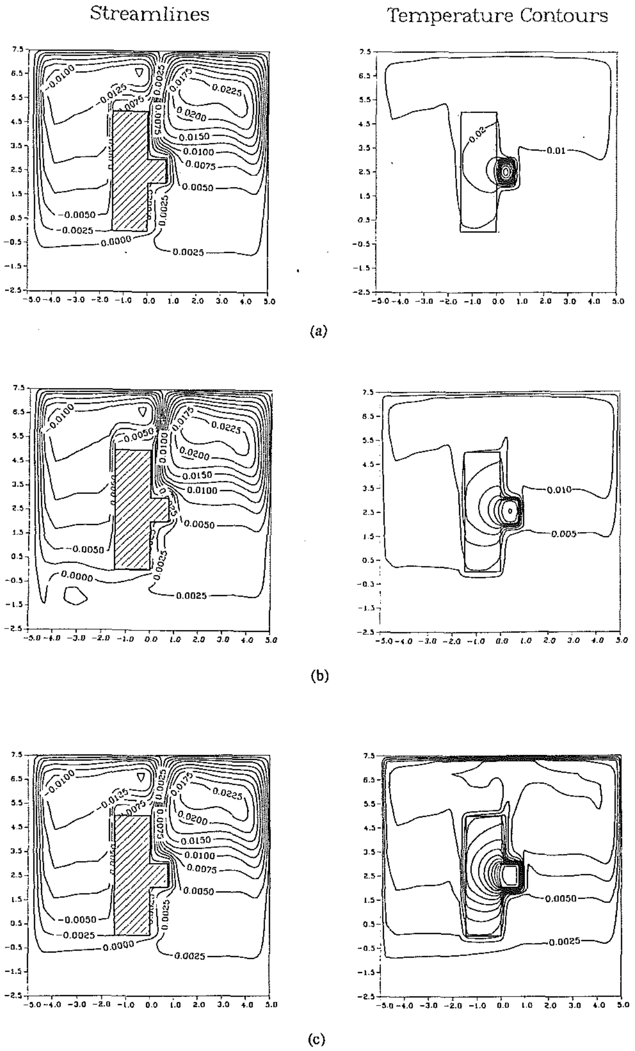

Fig. 2 Streamline and isotherm patterns for various R_c when $\mathrm{Ra} = 10^6$, $w/h = 0.75$, and $L_t/h = 2$: *(a)* $R_c = 1$, *(b)* $R_c = 10$, and *(c)* $R_c = 100$

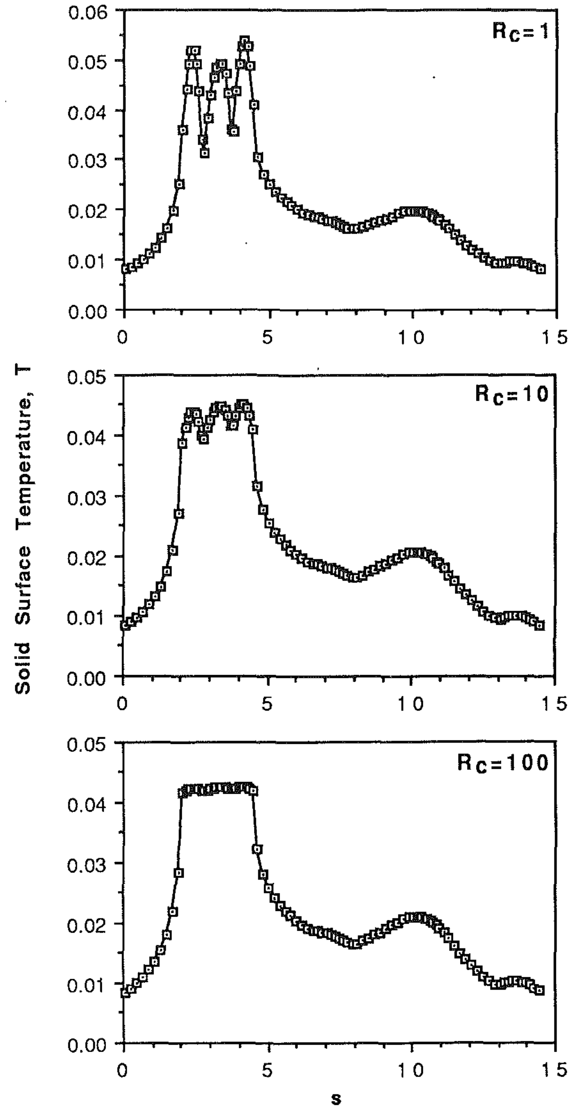

Fig. 3 Solid-Fluid interface temperatures for different R_c. The distance s is the contour length along the interface as defined in Table 2. The computations are for $\mathrm{Ra} = 10^6$, $w/h = 0.75$, and $L_t/h = 2$.

flow at the top boundary. The fluid below the protrusion is almost stagnant and thermally stratified, as indicated by the isotherms. We note that the flow patterns for $1 \leq R_c \leq 100$ are almost identical.

The temperature distribution inside the protrusion is almost symmetric about its centroid. It is interesting to note that the temperatures far away from the protrusion are not affected appreciably by a change in R_c. For $1 \leq R_c \leq 100$, the temperature distribution for $T < 0.03$ is almost identical. A decrease in R_c is associated with an increase in the thermal resistance of the protrusion and hence an increase in the maximum temperature $T_{\max}$ occurring within the protrusion. The isotherms indicate that the temperature drop within the protrusion is as much as 80 percent of the total temperature variation in the enclosure for $R_c = 1$. The corresponding levels are 25 and 5 percent, respectively, for $R_c = 10$ and 100. Thus for $R_c > 100$, the internal thermal resistance of the protrusion is almost negligible.

Interesting heat transfer trends are revealed when the solid surface temperatures are examined for various R_c in Fig. 3. The coordinate s is the clockwise contour distance along the solid-fluid interface starting from the origin. The ranges of s corresponding to the various surfaces in Fig. 1 are provided in Table 2. Higher temperatures occur on the protrusion faces ($2 < s < 4.5$) compared to the substrate surfaces, due to the heat generation within the protrusion. A local maximum is evident at $s \approx 10$ due to heating via substrate conduction.

A low value of R_c results in large temperature variations on the protrusion faces. For example, the temperature deviations are as high as 25 percent about the mean for $R_c = 1$. For $R_c = 10$, the corresponding variation is only 6 percent. The protrusion faces are nearly isothermal for $R_c = 100$. It is thus clearly demonstrated that simplistic conditions cannot be assigned to the solid surfaces for many actual cases. The maximum temperature on a particular protrusion face seems to occur approximately at the midpoint of that face for all R_c. We note that the substrate surface temperatures change only marginally due to a change in R_c, unlike the protrusion face temperatures.

Figure 4 shows the dimensionless heat flux from the solid into the fluid, defined as:

$$\mathbf{Q} = -\frac{R_i}{(\mathrm{RaPr})^{1/2}}\left(\frac{dT}{dN}\right)_i \mathbf{n} \qquad (7)$$

where the subscript i represents either c or s depending upon whether the interface is a protrusion-fluid or substrate-fluid interface, respectively. The quantity $(dT/dN)_i$ is the dimensionless temperature gradient in the direction normal to the

Table 2 Ranges of s corresponding to different solid-fluid interfaces; $w/h=0.75$, $L_t/h=2$

Surface no. in Fig. 1	X	Y	s
1	0 to 2	0	0.00 to 2.00
2	2	0.0 to 0.75	2.00 to 2.75
3	2 to 3	0.75	2.75 to 3.75
4	3	0.0 to 0.75	3.75 to 4.50
5	3 to 5	0	4.50 to 6.50
6	5	-1.5 to 0	6.50 to 8.00
7	0 to 5	-1.5	8.00 to 13.00
8	0	-1.5 to 0	13.00 to 14.50

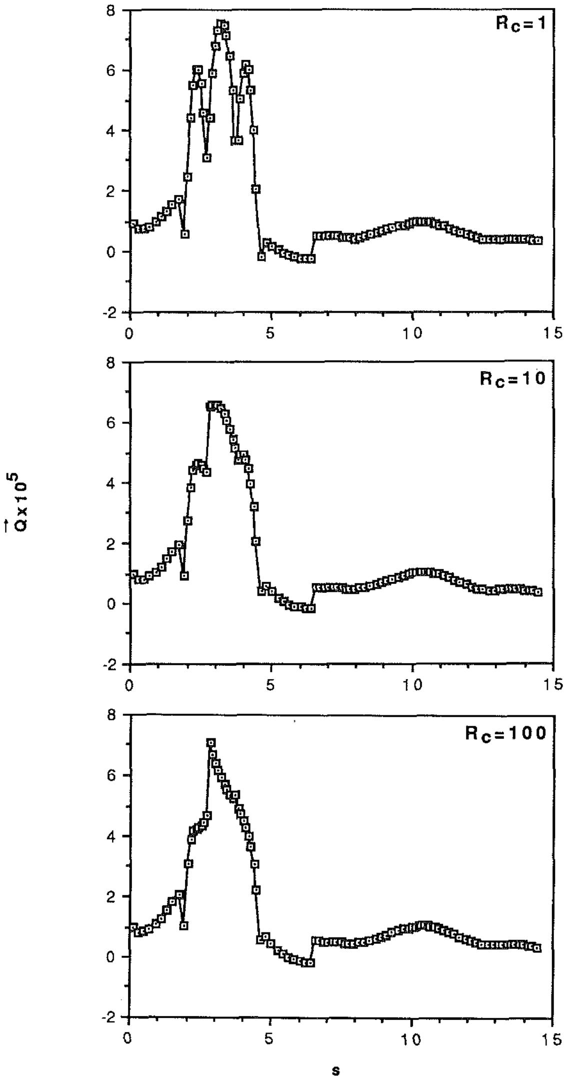

Fig. 4 Effect of R_c on the heat flux across the solid-fluid interface when $\mathrm{Ra}=10^6$, $w/h=0.75$, and $L_t/h=2$; distance s is defined in Table 2

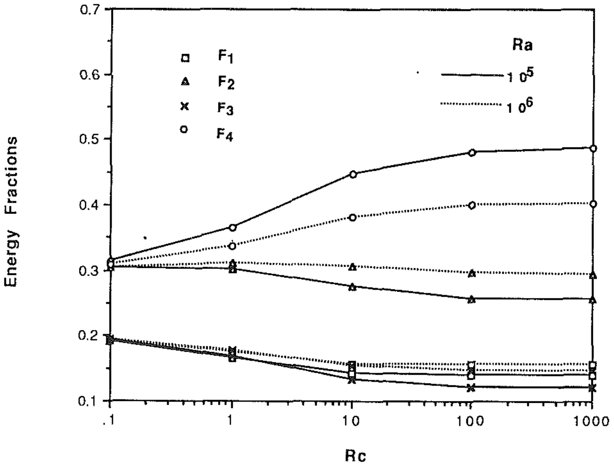

Fig. 5 Energy rate fractions F_1-F_4 leaving the four protrusion faces as a function of R_c and Ra. The subscript 1, 2, 3 and 4 represent the bottom, fluid-side, top, and substrate-side faces of the protrusion, respectively. The computations are for $w/h=0.75$ and $L_t/h=2$.

surface evaluated on the solid side of the interface and **n** is the unit outward normal vector to the solid surface. The heat flux is positive when energy transfer is from the solid to the fluid. The temperature gradient is calculated using the harmonic mean formulation (Patankar, 1980). We note that even though the heat flux is undefined at the corners, the points corresponding to various locations on each surface in the figure are shown joined by straight lines to aid the eye.

The heat fluxes are substantially higher at the protrusion surfaces than at the substrate surfaces. The substrate surface heat fluxes are largely unaffected by a change in R_c, but this is not true for the protrusion surfaces. As for the temperatures, at low R_c the heat flux variations go through local maxima near the protrusion mid-faces owing to the high thermal resistance of the protrusion. However, at higher R_c of 10 and 100, the increased fluid-side thermal resistance compared to that on the solid side is the dominant factor affecting the heat flux distribution.

For $R_c=100$ no extrema are observed in the heat fluxes over the various protrusion faces. The region near $s=2$ is largely diffusion-dominated due to the stagnant flow in that region. The heat flux then increases as s is increased beyond 2 over the bottom face due to an increase in fluid velocity. A sharp increase is observed for larger s due to the substantially higher velocities in the vicinity of the vertical protrusion face. The heat flux then decreases over the vertical protrusion face as s is increased further due to the growth of the thermal boundary layer. The heat flux continues to decrease further when s is increased over the top face due to further warming of the fluid in addition to the slowing of the fluid over the top surface to form another region of low fluid velocities near the vertical substrate surface. It must be noted, however, that the average heat flux values over each protrusion face do not change substantially with a change in R_c. Also, it is interesting that the heat flux in the vicinity of $s=6$ is negative, implying that the fluid is warm enough to lose heat to the substrate in that region.

Shown in Fig. 5 are the fractions of the total power generated that pass through the bottom, right, top, and left sides of the protrusion, represented by F_1, F_2, F_3, and F_4, respectively. For $R_c=0.1$, the internal thermal resistance of the protrusion is high enough so that the heat transfer is symmetric with respect to the centroid of the protrusion resulting in $F_2=F_4$ and $F_1=F_3$. Not that $F_2>F_3$ because $w/h=0.75$, so that more surface area is available on the vertical protrusion face than the horizontal face. Also, for $R_c=0.1$, there is a negligible effect of Ra on the mechanism of heat dissipation from the various protrusion faces due to the large protrusion thermal resistance. When R_c is increased beyond 0.1, substrate conduction becomes the dominant mechanism of heat removal from the protrusion, as seen from the values of F_4.

From Fig. 5 it is clear that the substrate conduction assumes

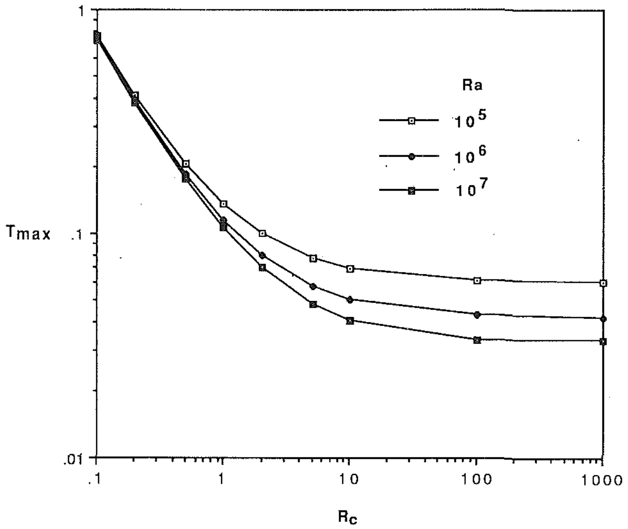

Fig. 6 Maximum temperature T_{max} for various R_c and Ra when $w/h = 0.75$ and $L_t/h = 2$

greater importance for lower Ra due to the reduction on fluid velocities for the same power input. For $\mathrm{Ra} = 10^5$ and $R_c > 10$ as much as 45 percent of the generated energy is being removed via the substrate, clearly demonstrating the importance of substrate conduction in actual cases. For $R_c > 10$ the thermal resistance of the protrusion is negligible so that further increase in R_c does not bring about substantial changes in the various fractions. It is seen that the top and bottom faces each contribute to no more than 20 percent of the input power removal owing to lower fluid velocities near those faces, in addition to smaller face lengths.

The maximum temperature is often of significance to thermal designers from the viewpoint of reliability of electronic components. Such a maximum nondimensional temperature occurring within the protrusion is seen in Fig. 6 for different R_c and Ra. As expected, an increase in R_c decreases the thermal resistance of the protrusion, thereby lowering the maximum temperatures. Only a marginal cooling enhancement results when R_c is increased further beyond 10. The maximum temperatures are more sensitive to Ra when R_c is higher due to lower protrusion thermal resistances. For $R_c < 1$, only a small change in maximum temperatures results when Ra is changed by two orders of magnitude. For $R_c > 10$, the maximum temperatures drop by as much as 40 percent when Ra is increased from 10^5 to 10^7. As explained previously, Ra obtained in air is two orders of magnitude less than those in liquids for the same power input in a chip. This fact implies that liquid immersion cooling would be beneficial compared to air-cooling only for packages whose internal thermal resistances are not too large, such that $R_c > 1$.

3.2 Effect of Protrusion Width, w/h. Figure 7 shows a comparison of the isotherms and streamlines for $w/h = 0.25$ and 1.25, all other parameters being identical. The same rate of net heat generation is applied uniformly over the entire protrusion for both widths. It is noticed that the isotherm pattern is altered only in the vicinity of the protrusion by changing its width. The maximum temperatures occur close to the centroid of the protrusion for the two widths. An examination of the streamline patterns reveals similar flow structures with a main clockwise cell in the right top corner and a secondary anticlockwise circulation above the substrate. A slightly more vigorous flow is evident for the larger width.

The protrusion face temperatures are seen for different w/h and Ra in Fig. 8. The contour distance s along the protrusion face is defined in Table 3. Curves for different w/h span different s ranges, due to changing protrusion face lengths. As seen in Fig. 3, the maximum temperature on each protrusion face occurs near its midpoint. The temperatures are lower for larger protrusion widths due to availability of larger heat transfer area. The vertical face is warmer on the average than the top and bottom faces when $w/h = 0.25$, while it is cooler than the top and bottom faces when $w/h = 1.25$. This follows from the fact that a width smaller than the height results in a lower

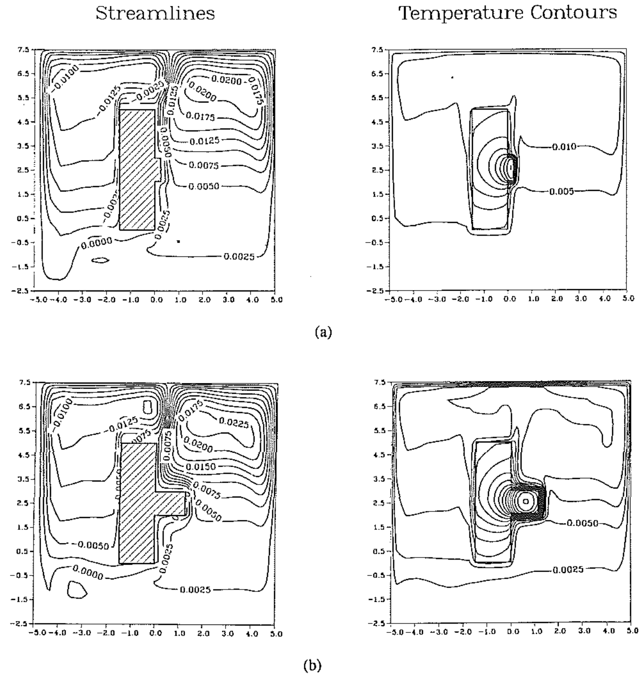

Fig. 7 Streamlines and isotherms for different protrusion widths when $\mathrm{Ra} = 10^6$, $R_c = 10$, and $L_t/h = 2$: *(a)* $w/h = 0.25$ and *(b)* $w/h = 1.25$

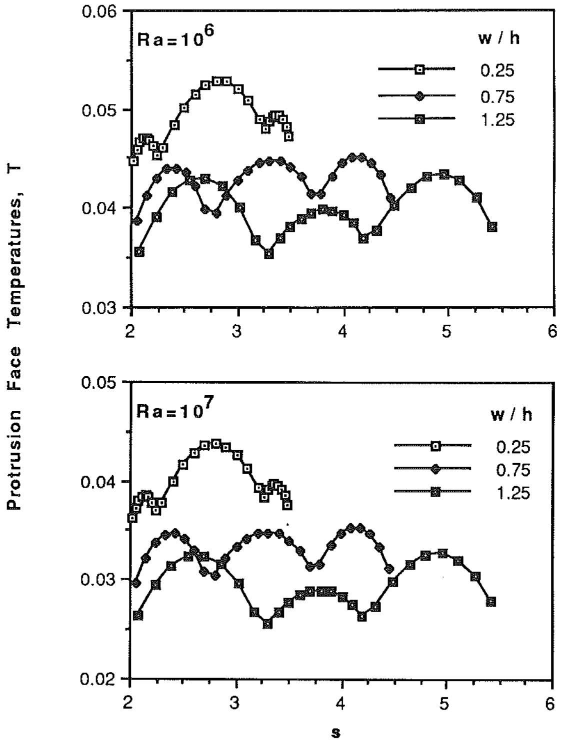

Fig. 8 Effect of Ra and protrusion width on the protrusion face temperatures. The contour distance s along the protrusion faces is defined in Table 3. Computations are for $L_t/h = 2$ and $R_c = 10$

Table 3 Ranges of *s* corresponding to protrusion surfaces for different *w/h*

Surface no. in Fig. 1	s w/h=0.25	 w/h=0.75	 w/h=1.25
2	2.00 to 2.25	2.00 to 2.75	2.00 to 3.25
3	2.25 to 3.25	2.75 to 3.75	3.25 to 4.25
4	3.25 to 3.50	3.75 to 4.50	4.25 to 5.50

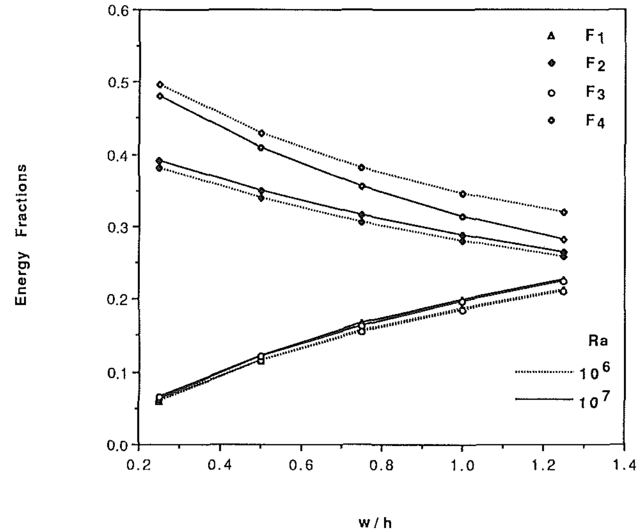

Fig. 9 Energy rate fractions F_1-F_4 passing through the protrusion faces for different Ra and w/h for $L_t/h = 2$ and $R_c = 10$. The subscripts 1-4 denote the bottom, right, top, and left faces of the protrusion, respectively.

protrusion thermal resistance in the horizontal direction compared to in the vertical direction, and vice versa. The top face is always warmer than the bottom face owing to warmer fluid present in the vicinity of the top face. Similar trends are seen for both $\mathrm{Ra} = 10^6$ and 10^7; however, the temperature levels are lower for higher Ra due to enchanced circulation in the cavity.

The energy rate fractions through the four protrusion faces are seen in Fig. 9 for different w/h. The trends and fractional levels are similar for $\mathrm{Ra} = 10^6$ and 10^7. An increase in the protrusion width results in larger surface area at the top and bottom faces. The fractions passing through the bottom and top faces, F_1 and F_3, respectively, increase almost fourfold when w/h is increased from 0.25 to 1.25. The substrate conduction effect is stronger for smaller widths with as much as 50 percent of the total input power being lost through the substrate for $w/h = 0.25$.

Shown in Fig. 10 is the effect of w/h on the maximum temperature occurring within the protrusion. The temperatures drop by approximately 14 and 18 percent for $\mathrm{Ra} = 10^6$ and 10^7, respectively, when w/h is increased from 0.25 to 1.25. The drop is lesser for larger w/h because even though the heat transfer surface area is increasing, the increasing frictional drag on the fluid decreases the rate of cooling enhancement. In actual applications, w/h cannot be increased arbitrarily because of space limitations.

3.3 Effect of Substrate Height, L_t/h. Computations performed for varying substrate heights revealed a negligible change in temperatures within the protrusion when L_t/h was increased from 2 to 4 with $R_c = 10$, and $\mathrm{Ra} = 10^6$ and 10^7. Minor differences in the flow patterns and isotherms were, however, revealed. Shown in Fig. 11 are the isotherms and streamlines for $L_t/h = 4$. We note that the temperature patterns for $L_t/h = 4$ differ from those when $L_t/h = 2$ (Fig. 2*b*), for all other conditions identical, only in the region where the additional substrate material is present. When the substrate length is increased, the flow pattern behind the substrate is modified so that the secondary cell is at the back of the substrate in Fig. 11 instead of on top of it as seen in Fig. 2(*b*).

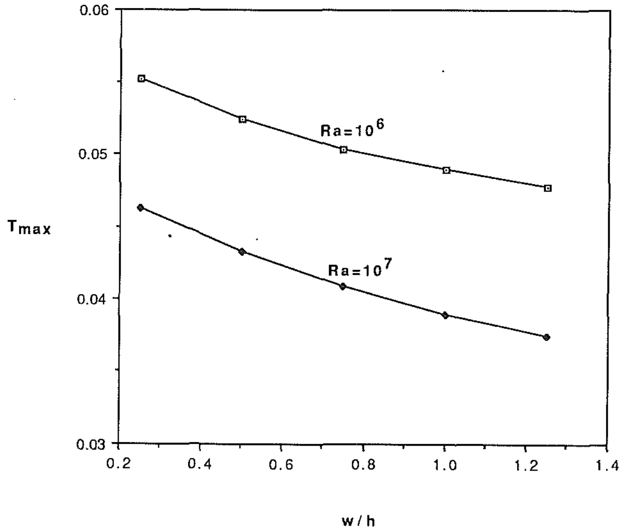

Fig. 10 Effect of Ra and w/h on the maximum temperature T_{max} for $L_t/h = 2$ and $R_c = 10$

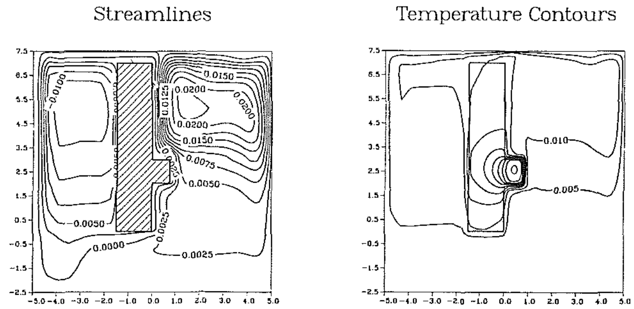

Fig. 11 Streamlines and isotherms for $L_t/h = 4$, $\mathrm{Ra} = 10^6$, $R_c = 10$, and $w/h = 0.75$

An interesting phenomenon was observed for $L_t/h \leq 1$. Flow rising above the protrusion swayed with iterations after a large number of iterations and convergence of the steady-state scheme could not be achieved. For the limiting condition of $L_t = 0$ the present configuration simulates a plume flow. Periodic swaying of thermal plumes above heated line sources is well documented (Eichhorn and Vedhanayagam, 1982). The temperatures within the protrusion did not appear to fluctuate significantly after a large number of iterations, and attained values close to those for $L_t/h > 1$. For $L_t/h > 1$, no swaying was observed, since the presence of the longer wall aids in stabilizing the flow due to the Coanda effect wherein plumes and jets tend to attach themselves to adjacent walls.

3.4 Effect of Enclosure Thermal Boundary Conditions. It is possible to reduce the dimensional temperature t at a location within the protrusion by lowering the sink temperature t_c alone, keeping Q, k_f, and all the nondimensional parameters constant since $t = t_c + QT/k_f$. For higher power inputs in the electronic components, a lower t_c may well be required to maintain the temperature of the component within admissible limits. However, a lower t_c increases the power consumption of the heat exchanger. It is thus of practical

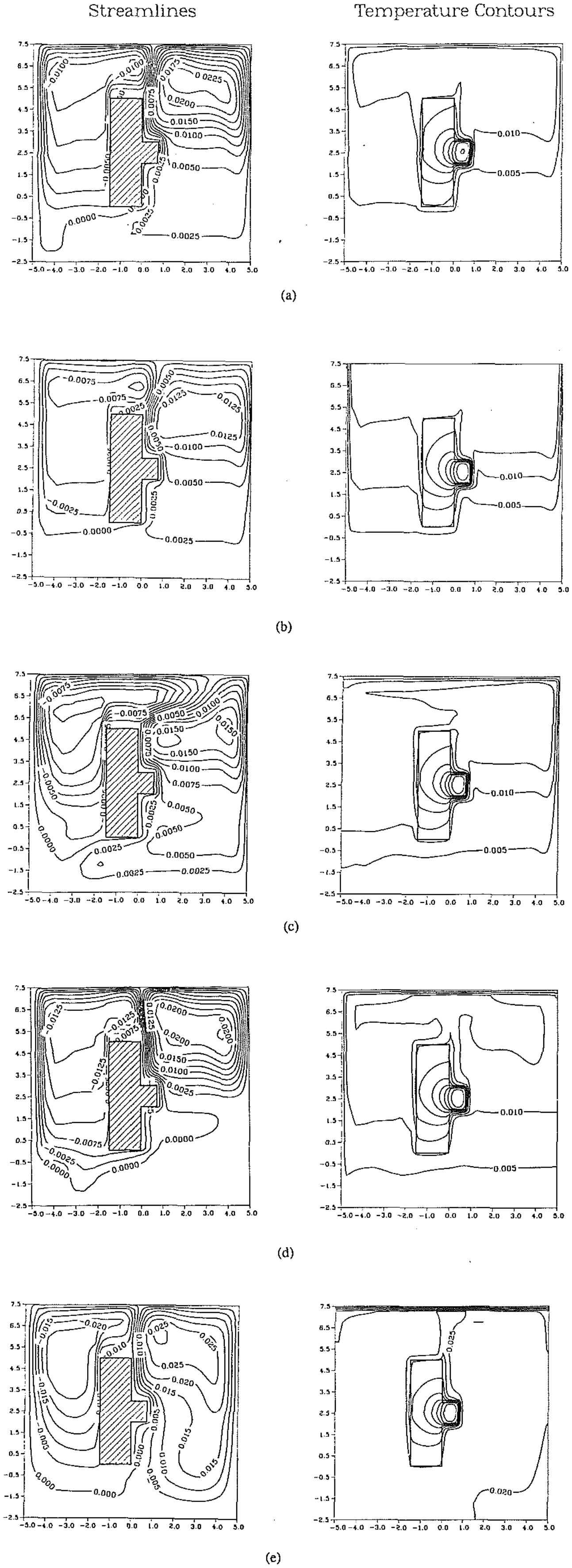

Fig. 12 Effect of enclosure thermal boundary conditions on the heat transfer and fluid flow when Ra = 10^6, $R_c = 10$, $L_l/h = 2$, and $w/h = 0.75$. Streamlines and isotherms are for the conditions defined in Table 4: *(a)* Case 1, *(b)* Case 2, *(c)* Case 3, *(d)* Case 4, and *(e)* Case 5.

Table 4 Description of the thermal boundary conditions at the cavity walls

Case	Wall condition
baseline	$t=t_c$ at all walls
1	adiabatic bottom wall, $t=t_c$ at remaining walls
2	adiabatic top wall, $t=t_c$ at remaining walls
3	adiabatic left vertical wall, $t=t_c$ at remaining walls
4	adiabatic right vertical wall, $t=t_c$ at remaining walls
5	$t=t_c$ at top wall, all other walls adiabatic

interest to determine the changes in the protrusion temperatures if one or more walls were insulated instead of being maintained at t_c, so that fewer than four heat exchangers are utilized. Table 4 summarizes the different types of thermal boundary conditions investigated.

Figure 12(*a*) shows the streamlines and isotherms for case 1 when the bottom wall is insulated. A comparison with Fig. 2(*b*), the baseline case, reveals almost identical temperature and flow distribution. This is somewhat expected since the fluid is almost thermally stratified below the protrusion and hence the bottom heat exchanger contributes negligibly to the overall cooling. When the top wall is adiabatic as in Fig. 12(*b*), the overall circulation strength drops due to the accumulation of warmer fluid in the vicinity of the top wall compared to the baseline case. Large horizontal temperature gradients are observed near the top portion of the vertical walls where the fluid loses heat to the enclosure. The maximum protrusion temperature $T_{\max}$ is only 6.6 percent higher than for the baseline case.

The streamlines and isotherms for the cases when the left and right vertical walls are insulated are depicted in Figs. 12(*c*) and 12(*d*), respectively. For both of these conditions the fluid in the bottom half of the cavity is warmer than in the baseline case. The temperature distribution inside the solid for these two cases is almost identical. When the left vertical wall is insulated, the fluid between the substrate and the left wall is warmer than the baseline case. This results in a lower buoyant force and velocities in that region, thus increasing the pressure. Thus the main flow above the protrusion is pushed toward the right to a greater extent as it leaves the substrate as compared to the baseline case.

The opposite effect is seen when the right vertical wall is insulated, where the main flow above the protrusion is not pushed to the right to as great an extent as in the baseline case. With equal buoyant forces on each side of the substrate, the stagnation region at the top wall would lie close to the vertical centerline of the substrate. Though the flow patterns show marked difference in Figs. 12(*c*) and 12(*d*), the flow patterns in the vicinity of the protrusion are almost identical and $T_{\max}$ for both cases 3 and 4 is only approximately 7.75 percent higher than in the baseline case.

It was observed for the situations when all the walls were maintained at t_c that temperature gradients at the enclosure boundaries were the largest near the top wall. It is thus of interest to investigate the possibility of only using the top heat exchanger, with other walls insulated. Streamlines and isotherms for such a case are shown in Fig. 12(*e*). The temperature gradients near the top wall are much steeper than in the other cases. The flow does not appear to be stagnant below the protrusion. The maximum temperature within the protrusion is higher by as much as 28 percent, compared to the baseline case.

4 A Correlation For Maximum Protrusion Temperature

Since the maximum protrusion temperature, $T_{\max}$, is of great interest to designers of electronic components, an empirical correlation has been developed for it as a function of all the relevant governing parameters. The resulting correlation for the isothermal walls boundary condition is as follows:

$$T_{\max} = \{(0.1R_c^{-0.86})^{3/2} + (0.277\mathrm{Ra}^{-0.133})^{3/2}\}^{2/3} \times \{0.6 + 0.9e^{-0.1R_s}\}\{1.2 - 0.3(w/h) + 0.1(w/h)^2\} \quad (8)$$

Equation (8) correlates all of our numerical data within ±12 percent, and 67 percent of the numerical data within ±5 percent for the following wide range of governing parameters: $0.1 \le R_c \le 10^3$, $0.1 \le R_s \le 10^3$, $0.25 \le w/h \le 1.25$, $10^5 \le \mathrm{Ra} \le 10^7$, $\mathrm{Pr} \ge 10$, $0.3 \le d_t/h \le 3$, $L_t/h \ge 1$, $d/h \ge 2$, $S_t/h \ge 4.5$, $S_b/h \ge 4.5$. Note that $T_{\max}$ changes by more than an order of magnitude over the ranges mentioned above. For a smaller range of $0.1 \le R_s \le 10$, all the numerical data are correlated within ± 6 percent.

The expression in the first curly bracket in Eq. (8) has been derived using the technique proposed by Churchill and Usagi (1972) for data that have two asymptotic limits. For fixed set of other parameters it predicts independence of $T_{\max}$ with Ra for small R_c and independence of $T_{\max}$ with R_c for large R_c as was seen in Fig. 6. Also, some of the parameters do not appear explicitly in the correlation because for a change in these parameters in their correponding ranges above, $T_{\max}$ changed negligibly. It is noted that for the numerical runs performed in our earlier study (Sathe and Joshi, 1991) for water as the fluid ($\mathrm{Pr} = 8$), $5 \times 10^4 \le \mathrm{Ra} < 6 \times 10^5$, $R_c = 24.2$, $R_s = 0.24$, $w/h = 0.78$, $d_t/h = 1.625$, $d/h = L_t/h = 2.5$, and $S_t/h = S_b/h = 5$, the computed $T_{\max}$ agree with the correlation, Eq. (8), within 5 percent.

Conclusions

Heat transfer and fluid flow arising from a substrate-mounted protruding heat source immersed in a liquid-filled square cavity were examined numerically. The effects of Rayleigh number, Prandtl number, substrate and protrusion dimensions, protrusion properties, and cavity thermal boundary conditions on the steady-state heat transfer and fluid flow were studied. In most cases, the fluid below the protrusion was seen to be thermally stratified with a primary cell in the top right corner of the cavity. A secondary cell was also observed due to weaker buoyant forces at the back of the substrate. Flow oscillations were observed for smaller substrate heights, when $L_t/h < 1$.

It was demonstrated that the solid conduction effects must be included in most situations and simplistic solid surface thermal conditions are inappropriate. It is shown that liquid cooling is preferable to air cooling only if the package internal thermal resistance is small enough, i.e., when $R_c > 1$. The substrate height had a marginal effect on the maximum temperature occurring within the protrusion. A slight cooling enhancement on the order of 10 percent was observed when w/h was changed from 0.25 to 1.25. The results of this parametric study were used to obtain an empirical correlation for the maximum temperature in terms of the relevant nondimensional parameters.

A number of different boundary conditions at the enclosure walls were examined to study their effects on the temperature variation within the protrusion. The protrusion temperatures did not change significantly when any one of the walls was kept insulated instead of at a uniform temperature. Keeping only the top boundary at a fixed temperature and all others insulated resulted in protrusion temperatures higher by as much as 28 percent.

Acknowledgments

The authors gratefully acknowledge the support of this work by a grant from the U.S. Naval Weapons Support Center, Crane, IN.

References

Afrid, M., and Zebib, A., 1989, "Natural Convection Air Cooling of Heated Components Mounted on a Vertical Wall," *Numerical Heat Transfer*, Part A, Vol. 15, pp. 243–259.

Bergles, A. E., and Bar-Cohen, A., 1990, "Direct Liquid Cooling of Microelectronic Components," *Advances in Thermal Modeling of Electronic Components and Systems*, Vol. 2, A. Bar-Cohen and A. D. Kraus, eds., ASME Press, pp. 233–342.

Chu, R. C., 1986, "Heat Transfer in Electronic Systems," *Proc. Eighth Int. Heat Trans. Conf.*, San Francisco, CA, pp. 293–305.

Churchill, S. W., and Usagi, R., 1972, "A General Expression for the Correlation of Rates of Transfer and Other Phenomena," *A.I.Ch.E. Journal*, Vol. 18, pp. 1121–1128.

Eichhorn, R., and Vedhanayagam, M., 1982, "The Swaying Frequency of Line Source Plumes," *Proc. Seventh Int. Heat Trans. Conf.*, Munich, Fed. Rep. of Germany, Vol. 2, pp. 407–412.

Incropera, F. P., 1988, "Convection Heat Transfer in Electronic Equipment Cooling," ASME JOURNAL OF HEAT TRANSFER, Vol. 110, pp. 1097–1111.

Jaluria, Y., 1985a, "Natural Convective Cooling of Electronic Equipment," *Natural Convection Fundamentals and Applications*, S. Kakac, W. Aung, and R. Viskanta, eds., pp. 961–986.

Jaluria, Y., 1985b, "Interaction of Natural Convection Wakes Arising From Thermal Sources on a Vertical Surface," ASME JOURNAL OF HEAT TRANSFER, Vol. 107, pp. 883–892.

Joshi, Y., Willson, T., and Hazard, S. J., 1989, "An Experimental Study of Natural Convection From an Array of Heated Protrusions in a Vertical Channel in Water," ASME *Journal of Electronic Packaging*, Vol. 111, pp. 33–40.

Keyhani, M., Prasad, V., and Cox, R., 1988, "An Experimental Study of Natural Convection in a Vertical Cavity With Discrete Heat Sources," ASME JOURNAL OF HEAT TRANSFER, Vol. 110, pp. 616–624.

Lee, J. J., Liu, K. V., Yang, K. T., and Kelleher, M. D., 1987, "Laminar Natural Convection in a Rectangular Enclosure Due to a Heated Protrusion on One Vertical Wall—Part II: Numerical Simulation," *Proc. Second ASME/JSME Therm. Engr. Joint Conf.*, Honolulu, HI, pp. 179–185.

Lee, S., and Yovanovich, M. M., 1989, "Conjugate Heat Transfer From a Vertical Plate With Discrete Heat Sources Under Natural Convection," ASME Paper No. 89-WA/EEP-9.

Liu, K. V., Yang, K. T., and Kelleher, M. D., 1987, "Three Dimensional Natural Convection Cooling of an Array of Heated Protrusions in an Enclosure Filled With a Dielectric Fluid," *Proc. Int. Symp. on Cooling Technology for Electronic Equipment*, Honolulu, HI, pp. 486–497.

Nakayama, W., 1988, "Thermal Management of Electronic Equipment: A Review of Technology and Research Topics," *Advances in Thermal Modeling of Electronic Components and Systems*, Vol. 1, A. Bar-Cohen and A. D. Kraus, eds., Hemisphere, pp. 1–78.

Park, K. A., and Bergles, A. E., 1987, "Natural Convection Heat Transfer Characteristics of Simulated Microelectronic Chips," ASME JOURNAL OF HEAT TRANSFER, Vol. 109, pp. 90–96.

Patankar, S. V., 1980, *Numerical Heat Transfer and Fluid Flow*, Hemisphere/McGraw-Hill, New York.

Raithby, G. D., and Wong, H. H., 1981, "Heat Transfer by Natural Convection Across Vertical Air Layers," *Numerical Heat Transfer*, Vol. 4, pp. 447–457.

Sathe, S. B., and Joshi, Y., 1991, "Natural Convection Arising From a Heat Generating Substrate-Mounted Protrusion in a Liquid-Filled Two-Dimensional Enclosure," *International Journal of Heat and Mass Transfer*, Vol. 34, pp. 2149–2163.

3M Corporation, 1985, "Product Manual: Fluorinet Liquids," Minneapolis, MN.

K. C. Karki

P. S. Sathyamurthy

Innovative Research, Inc.,
Minneapolis, MN 55414

S. V. Patankar

Department of Mechanical Engineering,
University of Minnesota,
Minneapolis, MN 55455

Natural Convection in a Partitioned Cubic Enclosure

Numerical solutions are obtained for fluid flow and heat transfer in a cubic enclosure with a vertical adiabatic partition. The two zones of the enclosure are connected by a single rectangular opening. The partition is oriented parallel to the isothermal sidewalls, one of which is heated and the other cooled while the remaining walls are adiabatic. Results have been presented for air for the Rayleigh numbers in the range 10^4*–*10^7*. The width of the opening is held fixed while the height, relative to the enclosure height, is varied from 0.25 to 0.75. The effects of various parameters on the flow structure and heat transfer are investigated. The results of the three-dimensional simulation have also been compared with those for the corresponding two-dimensional configurations.*

Introduction

Natural convection in partitioned enclosures with differentially heated sidewalls is of importance in many engineering applications. These include: energy transfer in rooms and buildings, nuclear reactor cooling, solar collectors, and electronic equipment cooling. A number of studies, both experimental and numerical, are available on natural convection in partitioned enclosures. Nansteel and Greif (1981, 1984) have reported experimental studies of natural convection in a water-filled enclosure of aspect ratio of 0.5 with both two-dimensional and three-dimensional partitions. The Rayleigh numbers considered in these studies are in the range 10^{10}–10^{11}. Boardman et al. (1989) and Neymark et al. (1989) have reported experiments for natural convection in a partitioned cubic enclosure with a doorway-like opening. In these studies, the effect of opening height and width on the heat transfer rate has been presented. These experiments are directed toward heat transfer in buildings; consequently, the Rayleigh numbers considered are greater than 10^{11}. Bajorek and Lloyd (1982) have reported a series of experiments in an air-filled two-dimensional enclosure with two partial dividers attached to the top and bottom walls of the enclosure (i.e., a central opening). Rayleigh numbers ranging from 10^5 to 10^6 were studied. Subsequently, Bilski et al. (1986) obtained velocity data for the same configuration. In addition to these experimental investigations, several numerical studies have also been reported on natural convection in partitioned enclosures. These studies have been restricted to laminar flows in two-dimensional configurations. Chang et al. (1982) and Zimmerman and Acharya (1985) have presented numerical results for the geometry of Bajorek and Lloyd (1982). Jetli et al. (1986) have studied the effect of partition position on heat transfer. Kelkar and Patankar (1990) have reported numerical results for two partition arrangements; one of these is similar to that of Bajorek and Lloyd (1982), while in the other, the partition is located vertically at the center of the enclosure.

The purpose of this paper is to present a numerical study of laminar natural convection in a partitioned cubic enclosure. The configuration considered is shown in Fig. 1. The enclosure is divided into two zones by a vertical partition, which is oriented parallel to and located midway between the sidewalls. The two zones of the enclosure are connected by a single rectangular opening as shown in Fig. 1. The heat transfer process in this configuration is dependent on the thermal boundary conditions and the geometric configuration, e.g., the opening height and width. In the present investigation, results have been obtained for a range of Rayleigh numbers and geometric parameters. Detailed local and overall results are presented over the range of the parameters considered. Computations have also been made for the corresponding two-dimensional configurations. A comparison of the results for two- and three-dimensional enclosures provides an insight into the effect of three dimensionality on the heat transfer and flow characteristics.

Mathematical Formulation

The governing equations are solved for only one-half of the cubic enclosure since the flow is symmetric about $z = B/2$. The vertical sidewalls at $x = 0$ and $x = L$ are maintained at temperatures T_h and T_c, respectively. The horizontal walls and the endwalls are considered to be adiabatic. The partition is also regarded as adiabatic. The flow is considered to be steady and laminar, and the fluid properties as uniform except for density. The variation of density with temperature is calculated using the Boussinesq approximation and considered only in the buoyancy term in the momentum equation. The governing equations are nondimensionalized by using the following definitions of nondimensional variables:

$$X = \frac{x}{H} \qquad Y = \frac{y}{H} \qquad Z = \frac{z}{H} \tag{1a}$$

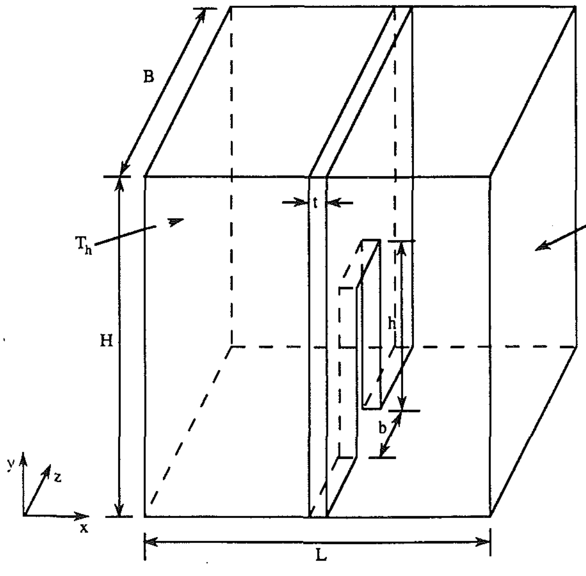

Fig. 1 The geometry considered

Contributed by the Heat Transfer Division for publication in the Journal of Heat Transfer. Manuscript received by the Heat Transfer Division May 1991; revision received October 1991. Keywords: Enclosure Flows, Natural Convection.

$$U=\frac{u}{(\nu/H)} \qquad V=\frac{v}{(\nu/H)} \qquad W=\frac{w}{(\nu/H)} \tag{1b}$$

$$P=\frac{(p+\rho_0 gy)}{\rho_0(\nu/H)^2} \qquad \theta=\frac{T-T_0}{T_h-T_c} \tag{1c}$$

$$A_x=\frac{L}{H} \qquad A_z=\frac{B}{H} \tag{1d}$$

$$h^*=\frac{h}{H} \qquad b^*=\frac{b}{H} \qquad t^*=\frac{t}{H} \tag{1e}$$

The resulting governing equations are as follows.

Continuity

$$\frac{\partial U}{\partial X}+\frac{\partial V}{\partial Y}+\frac{\partial W}{\partial Z}=0 \tag{2}$$

x Momentum

$$U\frac{\partial U}{\partial X}+V\frac{\partial U}{\partial Y}+W\frac{\partial U}{\partial Z}=-\frac{\partial P}{\partial X}+\nabla^2 U \tag{3}$$

y Momentum

$$U\frac{\partial V}{\partial X}+V\frac{\partial V}{\partial Y}+W\frac{\partial V}{\partial Z}=-\frac{\partial P}{\partial Y}+\nabla^2 V+\frac{\mathrm{Ra}}{\mathrm{Pr}}\theta \tag{4}$$

z Momentum

$$U\frac{\partial W}{\partial X}+V\frac{\partial W}{\partial Y}+W\frac{\partial W}{\partial Z}=-\frac{\partial P}{\partial Z}+\nabla^2 W \tag{5}$$

Energy

$$U\frac{\partial \theta}{\partial X}+V\frac{\partial \theta}{\partial Y}+W\frac{\partial \theta}{\partial Z}=\frac{1}{\mathrm{Pr}}\nabla^2\theta \tag{6}$$

where

$$\mathrm{Ra}=\frac{g\beta(T_h-T_c)H^3}{\nu\alpha} \qquad \mathrm{Pr}=\frac{c_p\mu}{k} \tag{7}$$

The boundary conditions are as follows:

On all bounding walls:

$$U=V=W=0 \tag{8a}$$

$$\theta(0,Y,Z)=0.5 \tag{8b}$$

$$\theta(A_x,Y,Z)=-0.5 \tag{8c}$$

$$\frac{\partial\theta}{\partial Y}=0 \text{ at } Y=0,1 \tag{8d}$$

$$\frac{\partial\theta}{\partial Z}=0 \text{ at } Z=0 \tag{8e}$$

On the symmetry plane, $Z=A_z/2$:

$$\frac{\partial U}{\partial Z}=\frac{\partial V}{\partial Z}=W=0 \tag{9a}$$

with $U=V=W=0$ on the partition surface, and

$$\frac{\partial\theta}{\partial Z}=0 \tag{9b}$$

Computational Details

The governing equations were solved using the finite-volume method described in detail by Patankar (1980). The coupling between the velocity and pressure fields was handled by the SIMPLER algorithm. All computations were performed on a $44\times42\times22$ (x, y, z) nonuniform grid. The grid for two-dimensional problems was identical to that in the x-y plane of a three-dimensional configuration. A fine grid was employed near the solid surfaces. This final grid was decided on the basis of a series of exploratory calculations on grids of varying fineness.

Extensive tests were performed to establish the adequacy of the chosen grid. First, results were obtained for natural convection in a two-dimensional square cavity. The predicted average Nusselt numbers were within 0.05 percent of the reference values given by de Vahl Davis (1983). Next, computations were performed for several two-dimensional partitioned enclosures, and the results were compared with available numerical solutions and experimental data. The results from the present study were in good agreement with other numerical solutions. Figure 2 shows a typical comparison of the present numerical solution at $\mathrm{Ra}=1.1\times10^6$ with experimental data of Bilski et al. (1986) for a partitioned cavity with a central opening. The agreement between calculation and experiment is good. The differences are attributed to the use of the Boussinesq ap-

Nomenclature

A_x = aspect ratio, Eq. (1*d*)
A_z = aspect ratio, Eq. (1*d*)
B = enclosure width, Fig. 1
b = width of opening in the partition, Fig. 1
b^* = nondimensional width of opening, Eq. (1*e*)
c_p = specific heat
g = acceleration due to gravity
H = enclosure height, Fig. 1
h = height of opening in partition, Fig. 1
h^* = nondimensional height of opening, Eq. (1*e*)
k = thermal conductivity of the fluid
L = enclosure length, Fig. 1
Nu = local Nusselt number, Eq. (10)
$\overline{\mathrm{Nu}}$ = average Nusselt number, Eq. (11)
$\overline{\mathrm{Nu}}_{2D}$ = average Nusselt number for two-dimensional enclosure
$\overline{\mathrm{Nu}}_{2D,0}$ = average Nusselt number for nonpartitioned two-dimensional enclosure
$\overline{\mathrm{Nu}}_{3D}$ = average Nusselt number for partitioned cubic enclosure
$\overline{\mathrm{Nu}}_{3D,0}$ = average Nusselt number for nonpartitioned cubic enclosure
P = nondimensional pressure, Eq. (1*c*)
p = pressure
Pr = Prandtl number, Eq. (7)
Q = total heat transfer across the enclosure
q = local heat transfer rate
Ra = Rayleigh number, Eq. (7)
T = temperature
t = thickness of the partition wall, Fig. 1
t^* = nondimensional thickness of partition, Eq. (1*e*)
T_0 = reference temperature = $(T_h+T_c)/2$
T_c = temperature of the cold wall
T_h = temperature of the hot wall
U = dimensionless velocity in x direction, Eq. (1*b*)
u = dimensional velocity in x direction
V = dimensionless velocity in y direction, Eq. (1*b*)
v = dimensional velocity in y direction
W = dimensionless velocity in z direction, Eq. (1*b*)
w = dimensional velocity in z direction
X, Y, Z = dimensionless Cartesian coordinates, Eq. (1*a*)
x, y, z = Cartesian coordinates
β = coefficient of thermal expansion
θ = nondimensional temperature, Eq. (1*c*)
μ = fluid viscosity
ν = kinematic viscosity
ρ = fluid density
ρ_0 = fluid density at reference temperature

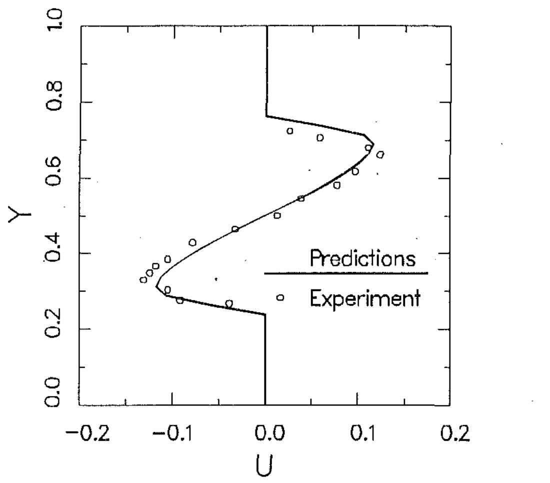

Fig. 2 Comparison of predicted velocity profile at Ra = 1.1 × 10^6 with the experimental data of Bilski et al. (1986)

proximation and the assumption of constant fluid properties in the calculations. The computer program was also used to solve the natural convection problem in a differentially heated cubic cavity. The results are in good agreement with other numerical solutions. For example, the average Nusselt number at $\mathrm{Ra}=10^6$ is within 1 percent of the value reported by Le Peutrec and Lauriat (1990), who employed the vorticity-vector potential formulation for the Navier-Stokes equations. For the present problem, initial computational experiments on finer grids and grids of different nonuniformity indicated that the average Nusselt numbers are accurate to within 2 percent.

The iterative solution procedure was terminated when the sum of the absolute values of the residuals over all the grid points, normalized by suitable reference quantities, for each equation fell below 0.01 percent. At this stage, the average Nusselt numbers on the hot and cold sidewalls differed by less than 0.1 percent.

Solutions were obtained for a cubic enclosure, i.e., $A_x=A_z=1$. The thickness of the partition t^* was kept fixed at 0.1. The width of the opening b^* was maintained constant at 0.2 and the height of the opening h^* was varied from 0.25 to 0.75. (Incidentally, the value of b^* was erroneously quoted as 0.25 in the earlier version of this paper (Karki et al., 1991).)

Results and Discussion

In the present investigation, the Rayleigh number was varied from 10^4 to 10^7. The Prandtl number was fixed at 0.7 (corresponding to air).

From the wealth of information generated by the numerical solution, only a selection can be presented here. The results to be presented include, in addition to the overall heat transfer results, some local details of the flow and temperature fields, which give insight into the interacting physical processes. Computations have also been made for partitioned two-dimensional enclosures. A comparison of the results for three-dimensional configurations with those for the corresponding two-dimensional geometries will provide an indication of the three-dimensional nature of the flow.

Velocity Field. The main features of the flow field will be described, via velocity vectors, with reference to the case $\mathrm{Ra}=10^6$ and $h^*=0.5$. To avoid crowding and overlapping, vectors at all grid points have not been shown; instead, they are plotted at 15 points in the x direction, 14 points in the y direction, and 10 points in the z direction. Figure 3 shows the velocity vectors in four x-y ($Z=$ const) planes for this particular flow. In the plane $Z=0.093$, which is close to the endwall, the fluid motion is limited to the narrow regions adjacent to the hot and cold sidewalls. In general, the fluid velocities near the cold wall are larger than those near the hot wall. The bulk fluid motion is inhibited by the presence of the endwall and the partition. The flow pattern at $Z=0.093$ is typical of the flow patterns in the x-y planes that include the complete partition. The flow becomes more intense as the opening is approached. This is seen from the velocity vectors in the plane $Z=0.307$. The location $Z=0.41$ is just after the beginning of the opening in the partition. The velocities in the upper left quadrant are relatively small. It is worth noting that there is no discernible flow recirculation in this quadrant. At this Rayleigh number, there are two sources for the hot fluid in the opening: the downward flow along the partition and the horizontal flow originating due to flow separation at the hot wall. The horizontal flow accelerates as it moves through the opening and exits as a jet at an angle. The hot fluid also creeps upward along the cold side of the partition. As expected, there is a downflow along the cold wall of the enclosure. Along the bottom horizontal wall, the fluid moves toward the hot wall. The velocity vectors in the symmetry plane ($Z=0.5$) show a well-defined fluid jet exiting from the opening and impinging on the top wall of the enclosure. The fluid velocities in this plane are significantly larger than the velocities in other x-y planes. It is interesting to note that the velocities in the cold zone are larger than those in the hot zone.

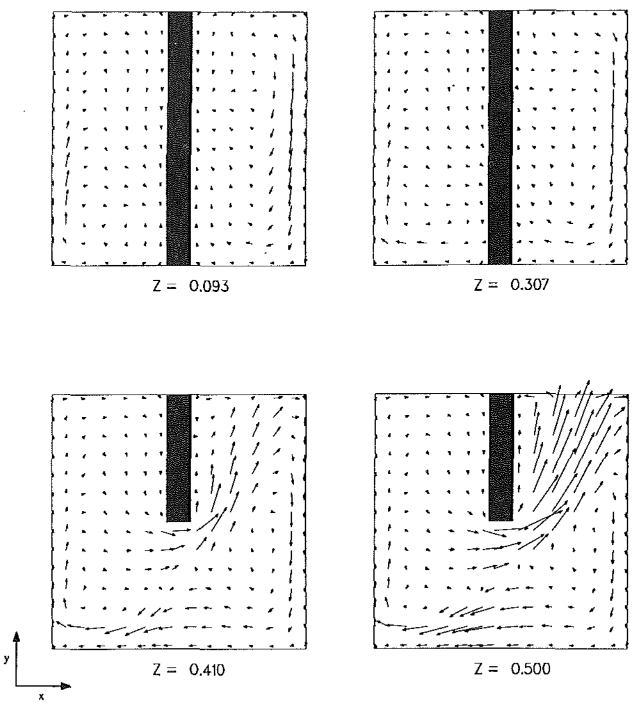

Fig. 3 Flow patterns in x-y planes, $\mathrm{Ra}=10^6$, $h^*=0.5$

A comparison of the flow patterns in the four x-y planes discussed above clearly indicates the presence of strong three-dimensional effects. The three-dimensional nature of the flow becomes more evident by examining the flow patterns in the y-z ($X=$ const) planes. The velocity vectors in four representative planes are shown in Fig. 4. The fluid in the plane $X=0.08$ is rising due the presence of the hot sidewall in its vicinity. The velocities in the region $Y>0.5$ are relatively small. The velocity vector distribution at $X=0.413$ depicts a typical flow pattern in a y-z plane near the partition in the hot zone. Now the presence of the opening in the partition causes the fluid to move toward the symmetry plane ($Z=0.5$). Also note that in this plane, the fluid is falling near the $Z=0$ endwall, whereas in the y-z planes close to the hot sidewall, the fluid rises near this endwall. On the y-z planes near the partition in the cold zone (e.g., $X=0.587$), there is a distinct vortex structure in

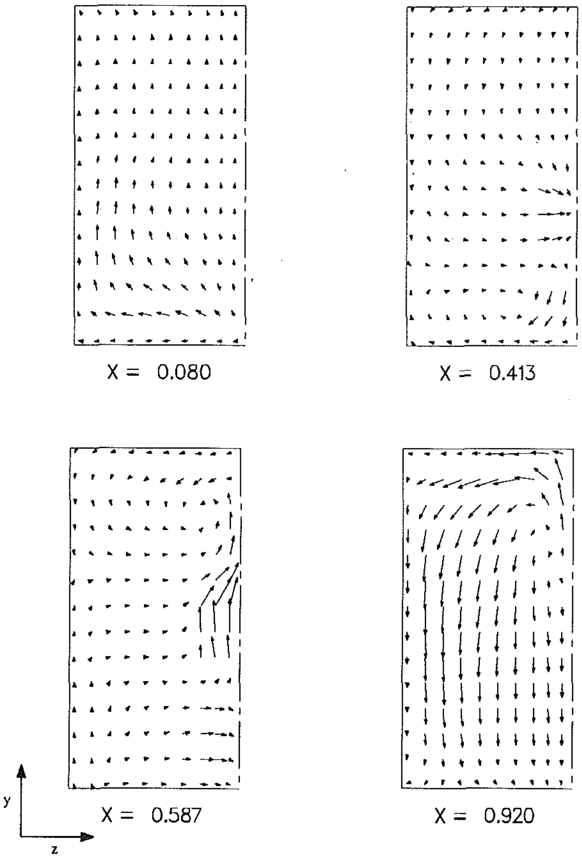

Fig. 4 Flow patterns in y-z planes, $\mathrm{Ra}=10^6$, $h^*=0.5$

the upper half. This vortex is caused by the high-velocity jet that leaves the opening at an angle, and it becomes stronger and more distinct in the y-z planes away from the partition. However, near the cold sidewall, the fluid has a global tendency to flow downward. This is seen from the velocity vectors in the y-z plane $X=0.92$. Even in this plane, the residual effect of the vortex is evident in the upper right corner. Subsequently, the vortex structure is completely destroyed by the strong downflow near the cold sidewall. This downflow is much stronger than the upflow near the hot sidewall.

Figure 5 shows the velocity vectors in the symmetry plane ($Z=0.5$), at different values of Ra, for the configuration with $h^*=0.5$. This figure along with the appropriate plot in Fig. 3 shows the influence of the Rayleigh number on the flow field. It should be noted that the velocity scale for each Rayleigh number is based on the corresponding maximum resultant velocity. Consequently, the magnitude of the velocity represented by a vector of a given length increases with the Rayleigh number. These flow patterns differ primarily in three respects: the extent to which the hot fluid penetrates into the low-velocity region in the upper left quadrant, the manner in which the fluid exits from the opening into the cold zone, and the nature of the flow near the opening.

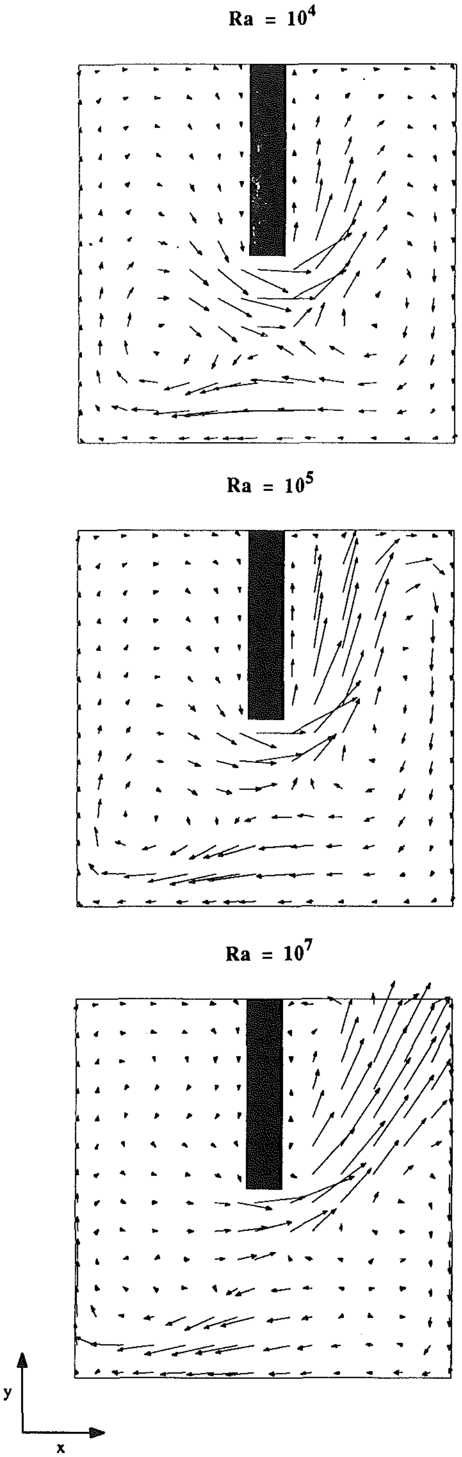

Fig. 5 Effect of the Rayleigh number on the flow field for $h^*=0.5$

The extent of the low-velocity region to the left of the partition increases with the Rayleigh number. There is a tendency for the boundary layer to separate from the hot wall at higher Rayleigh numbers. The location at which the boundary layer begins to separate from the wall is independent of the Rayleigh number. At lower Rayleigh numbers, the hot fluid negotiates the partition wall smoothly, turning nearly 180 deg. However, at Rayleigh numbers of 10^6 and above, the fluid exits from the opening as a jet at an angle. The inclination of the fluid jet from the vertical direction increases as the Rayleigh number increases. This flow behavior can be attributed to the increased inertial forces caused by the stronger buoyancy effects at high Rayleigh numbers. Further, at $\mathrm{Ra}=10^4$, the flow pattern exhibits two eddies, one on either side of the partition. As the Rayleigh number increases, the structure of these eddies becomes less well defined.

Figure 6 shows the flow fields at $\mathrm{Ra}=10^6$ for two opening heights. The symmetry plane ($Z=0.5$) has been selected to show these results because major differences in the flow behavior occur in the region close to the opening. This figure, supplemented by the appropriate plot in Fig. 3, presents the influence of the opening height on the flow field. The region to the left of the partition is inactive at all opening heights. The boundary layer on the hot wall begins to separate at a

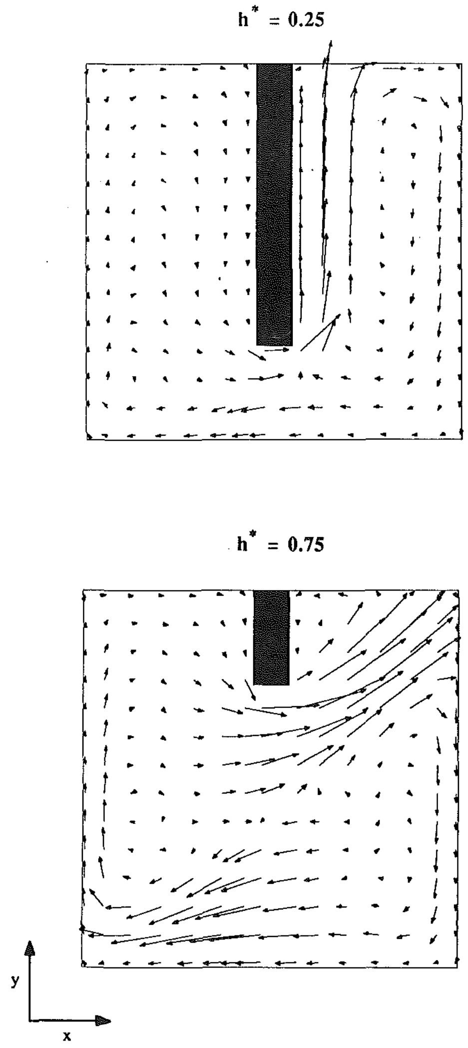

Fig. 6 Effect of the opening height on the flow field at Ra = 10^6

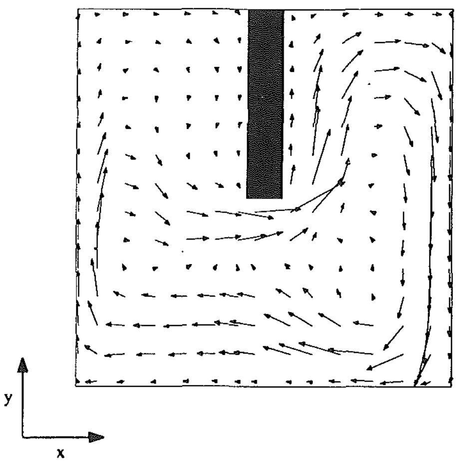

Fig. 7 Flow field at Ra = 10^6 for two-dimensional enclosure with $h^* = 0.5$

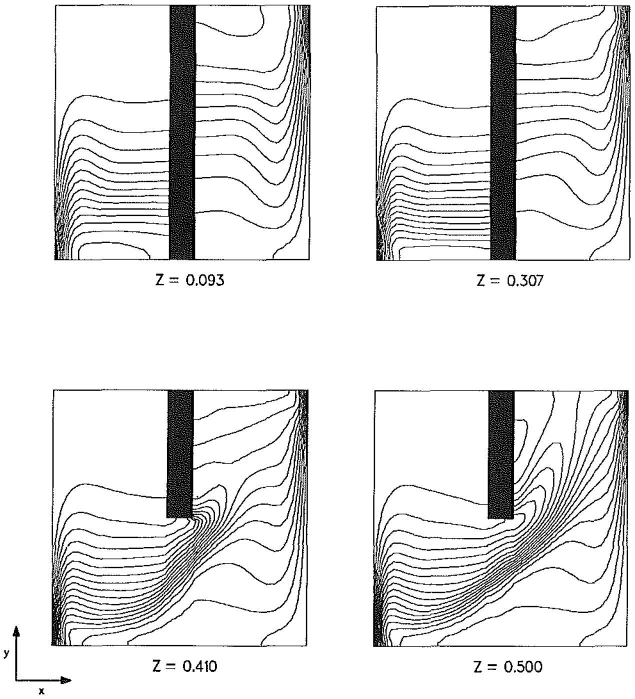

Z = 0.093
Z = 0.307
Z = 0.410
Z = 0.500

Fig. 8 Isotherms in x-y planes, Ra = 10^6, $h^* = 0.5$

location that roughly corresponds to the beginning of the opening. A major influence of the opening height is on the behavior of the fluid after it enters the cold zone. For small openings, the flow negotiates the partition wall smoothly. As the opening height is increased, the hot fluid cannot turn around the partition wall and exits as a jet, which impinges on the top wall and the cold sidewall. This flow behavior is a consequence of the increased throughflow that results from a decrease in the flow resistance, as the opening is made larger at a fixed Rayleigh number. The inclination of the hot-fluid jet with reference to the vertical axis increases with an increase in the opening height. These trends are similar to those noticed when the Rayleigh number is increased at a given opening height.

At this point, it is interesting to compare the flow pattern in the x-y symmetry plane ($Z = 0.5$) of the three-dimensional enclosure with the flow pattern in the corresponding two-dimensional enclosure. The velocity vectors at Ra = 10^6 for the two-dimensional enclosure with $h^* = 0.5$ are shown in Fig. 7. The two flow patterns are markedly different. In the two-dimensional situation, the fluid near the hot wall penetrates deeper into the upper left quadrant leading to a smaller inactive zone. Also, there is a significant difference in the manner in which the fluid exits from the opening. In the three-dimensional case, the fluid enters the cold region as a jet at an angle that hits the top wall; in the two-dimensional case, the hot fluid is able to flow around the partition wall and it then rises along the cold side of the partition.

Temperature Field. The temperature distribution in the enclosure is presented via isotherms in selected x-y planes. The isotherms are displayed with increments of 0.05 in the nondimensional temperature. Again, the general characteristics will be discussed for the specific case of Ra = 10^6 and $h^* = 0.5$.

Figure 8 shows the isotherms on four x-y planes. The temperature distribution conforms to the velocity field discussed earlier. In general, the temperature gradients are large near the base of the hot wall and near the top of the cold wall. This indicates that heat transfer through these parts of the walls is greater. In the hot zone, the isotherms are nearly horizontal, approximating the temperature distribution in a stably stratified fluid. The fluid in the upper left quadrant is nearly at the temperature of the hot wall. This trapped hot fluid inhibits heat transfer from the upper half of the hot wall. In the x-y planes that include the full partition, the fluid near the partition in the cold zone is also stably stratified. The temperature distributions in other x-y planes that include the full partition are very similar to that shown for $Z = 0.093$. The only major difference is that the extent of the inactive region in the upper

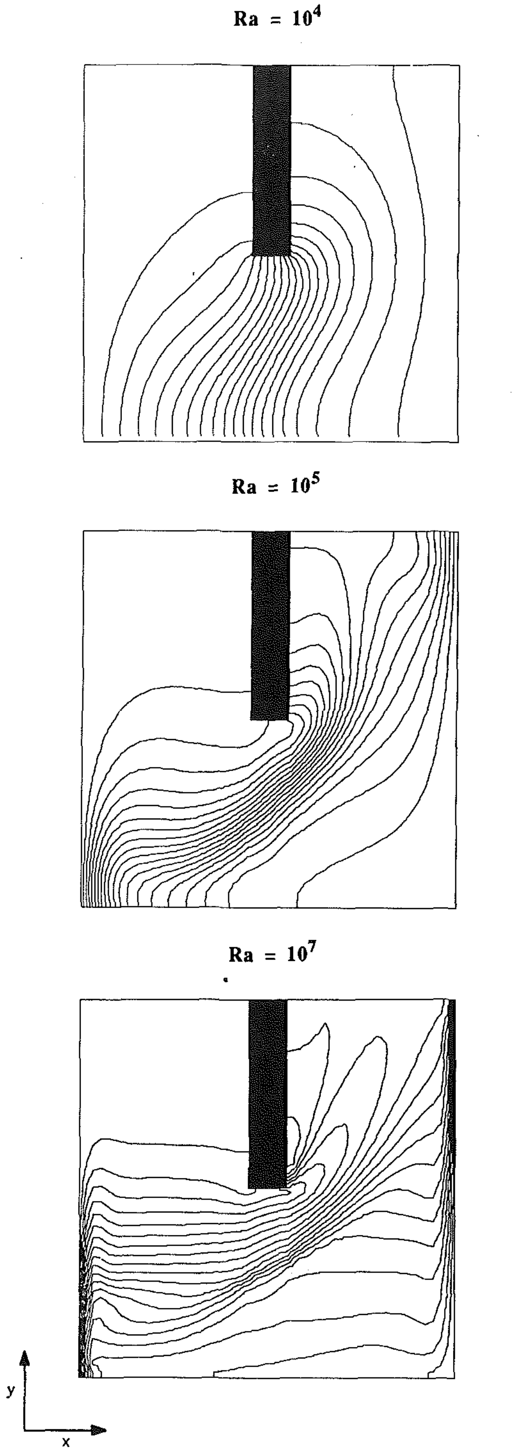

Fig. 9 Effect of the Rayleigh number on the temperature field for $h^* = 0.5$

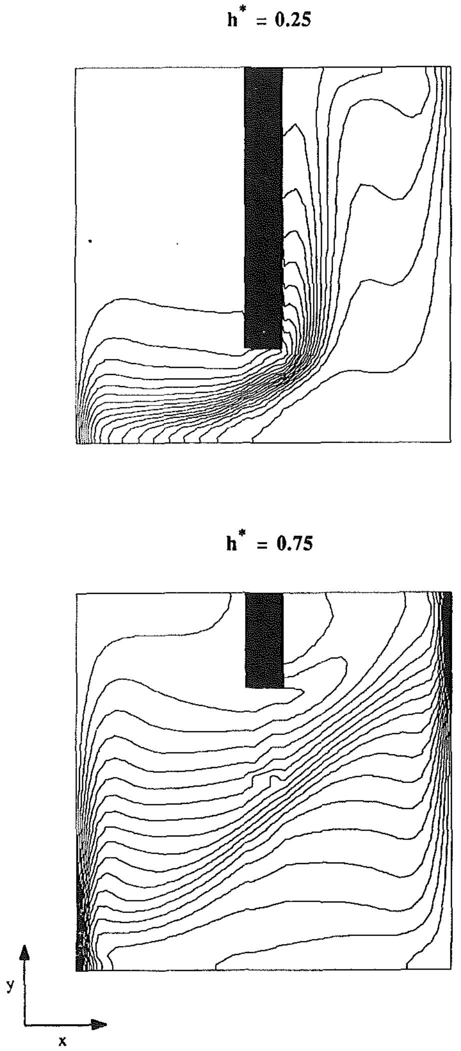

Fig. 10 Effect of the opening height on the temperature field at Re = 10^6

left quadrant increases slightly, as can be seen from the temperature distribution on the $Z = 0.307$ plane. The effect of the opening on the temperature distribution is depicted in the x–y plane $Z = 0.410$. As described earlier, for the particular case considered, the hot fluid exits from the hot zone as a jet at an angle. This hot-fluid jet disrupts the stable stratification in the cold zone. The jet impingement results in large temperature gradients near the top of the cold sidewall, as is evidenced by the clustering of isotherms in that region. The effect of the hot-fluid jet becomes more prominent on the planes closer to the symmetry plane ($Z = 0.5$). The thickness of the thermal boundary layer on the lower region of the hot sidewall decreases for increasing values of Z. Also note that on the symmetry plane, there is no indication of thermal stratification in the cold zone.

Figure 9 shows the isotherms on the symmetry plane for different Rayleigh numbers for a fixed opening height. This figure, along with the plot corresponding to $Z = 0.5$ in Fig. 8, shows the effect of the Rayleigh number on the temperature distribution. At $\mathrm{Ra} = 10^4$, there is no indication of thermal stratification in either zone of the enclosure. At such a low Rayleigh number, the boundary layers on the hot and cold sidewalls are thick, and the temperature gradients across the opening are large. As the Rayleigh number is increased, the boundary layers on the heat transfer surfaces become progressively thinner and the temperature gradients across the opening become less steep. This trend is expected, since now most of the temperature drop across the enclosure takes place in the boundary layers on the sidewalls, and there is less temperature drop across the opening. At high Rayleigh numbers, there is a tendency for stable thermal stratification in the hot zone and there is a distinct region in the upper left quadrant, where the fluid temperature is nearly the same as the hot wall temperature. The influence of the hot-fluid jet becomes more pronounced as the Rayleigh number is increased. At $\mathrm{Ra} = 10^7$, the isotherms in the lower half of the cold region are nearly horizontal, indicating stable thermal stratification in that region also.

Figure 10 is intended to show the influence of the opening height on the temperature distribution. This figure, supple-

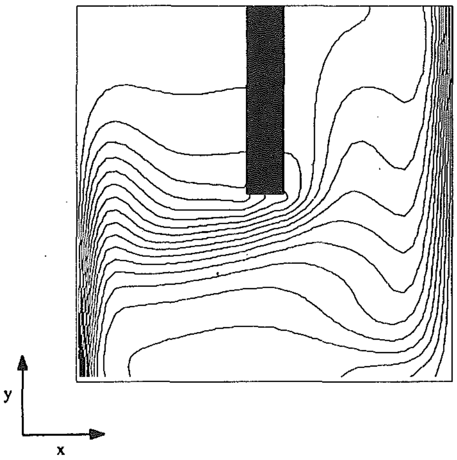

Fig. 11 Isotherms at $\mathrm{Ra} = 10^6$ for two-dimensional enclosure with $h^* = 0.5$

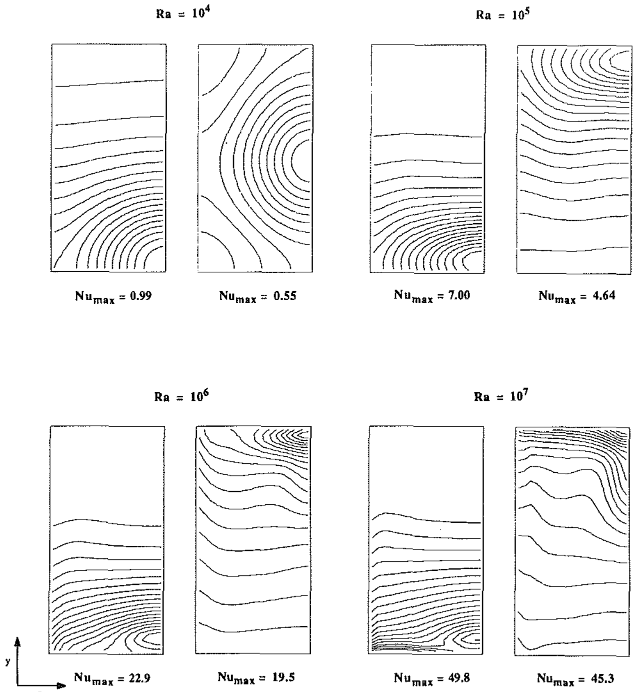

Fig. 12 Effect of the Rayleigh number on the local Nusselt number on the side walls: hot wall (left), cold wall (right)

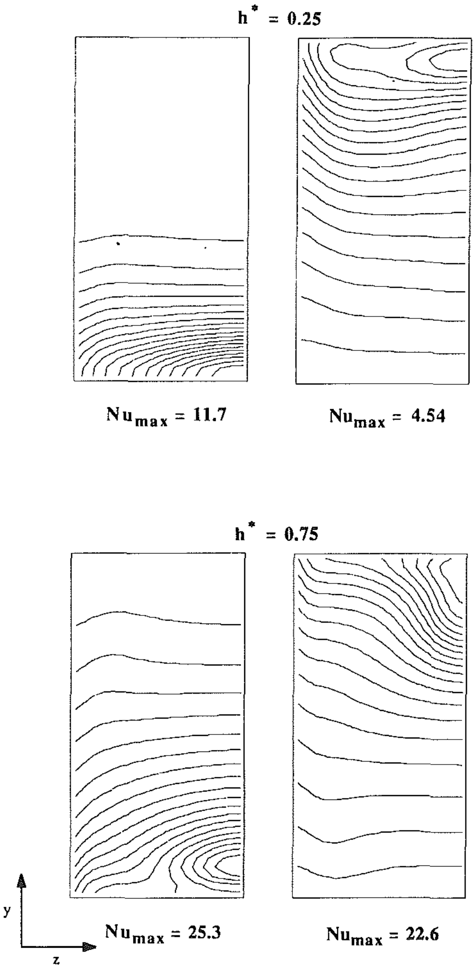

Fig. 13 Effect of the opening height on the local Nusselt number on the side walls: hot wall (left), cold wall (right)

mented by the appropriate isotherm plot in Fig. 8, indicates that as the opening height is increased, the thermal boundary layers on the heated and cooled sidewalls become thinner, and the temperature gradients across the opening become less steep. For larger opening heights ($h^* = 0.5$, 0.75), the temperature distribution exhibits jetlike characteristics as it enters the cold zone. It is observed that, while the fluid in the hot zone is stably stratified at all opening heights, stable stratification in the cold zone occurs only at larger opening heights.

Figure 11 shows the temperature distribution at $\mathrm{Ra} = 10^6$ for a two-dimensional configuration with $h^* = 0.5$. The isotherm pattern for the two-dimensional configuration is very different from that on the symmetry plane of the three-dimensional configuration. The extent of the inactive region in the upper left quadrant is much smaller in the two-dimensional enclosure. The thermal boundary layer near the top of the cold wall is much thinner in the three-dimensional configuration, due to the hot-fluid jet impinging on the cold wall. There is no such jet in the two-dimensional enclosure. Further, the temperature gradients across the opening are much smaller in the two-dimensional case. This is the result of smaller flow resistance associated with the larger opening area in the two-dimensional enclosure.

Local Heat Transfer Results. In this section, local heat transfer results along the hot and cold sidewalls are presented. These results are presented in terms of a local Nusselt number, defined as

$$\mathrm{Nu} = \frac{qH}{k(T_h - T_c)} \tag{10}$$

where q is the local heat flux.

Figure 12 presents the contours of constant local Nusselt number on the hot and cold sidewalls at different Rayleigh numbers for the configuration with $h^* = 0.5$. In these plots, $\mathrm{Nu}_{\max}$ is the maximum value of the Nusselt number.

In conformity with the temperature distribution discussed earlier, the heat transfer rates are high on the lower part of the hot wall and on the top part of the cold wall. The location of maximum heat transfer on both walls is close to the symmetry plane ($Z = 0.5$). On the hot wall, the region $Y > h^*$ is nearly inactive in the heat transfer process. The locally large heat transfer rates in the top region of the cold wall result due to the impingement of the hot-fluid jet on the cold wall.

Figure 13 shows the influence of the opening height on the local Nusselt number distribution. The opening height primarily affects the local heat transfer distribution on the cold wall; locally large heat transfer rates are encountered as the opening height is increased. As explained earlier, these heat

Table 1 Average Nusselt numbers for $h^* = 0.5$

Ra	10^4	10^5	10^6	10^7
$\overline{Nu}_{3D}$	0.33	1.50	5.00	11.65
$\overline{Nu}_{3D,0}$	1.83	4.36	8.76	–
$\overline{Nu}_{2D}$	0.97	3.32	7.04	13.68
$\overline{Nu}_{2D,0}$	2.24	4.52	8.80	–

Table 2 Average Nusselt numbers at $Ra = 10^6$

h^*	0.25	0.50	0.75
$\overline{Nu}_{3D}$	1.68	5.0	7.32

transfer rates depend on whether the hot fluid leaving the hot zone is able to negotiate the partition wall or exits as a jet that impinges on the cold sidewall.

Overall Heat Transfer Results. In this section, overall heat transfer results are presented in terms of an average Nusselt number, which is defined as

$$\overline{Nu} = \frac{Q}{kW(T_h - T_c)} = \frac{H}{W} \int \left(\frac{\partial \theta}{\partial X}\right)_{X=0} dYdZ \qquad (11)$$

It should be noted that for the thermal boundary conditions employed in this analysis, the integrated heat transfer rate is independent of the position x.

The average Nusselt numbers at different Rayleigh numbers for the configuration with $h^* = 0.5$ are presented in Table 1. For reference, the average Nusselt numbers for the cubic cavity, and partitioned and nonpartitioned two-dimensional cavities are also included.

The heat transfer rate increases with an increase in the Rayleigh number. This increase is the direct result of larger throughflow at higher Rayleigh numbers. A comparison of the average Nusselt numbers for two-dimensional and three-dimensional partitioned enclosures indicates that the three-dimensional effects are more prominent at lower Rayleigh numbers. In terms of a relative difference, defined as $(\overline{Nu}_{2D} - \overline{Nu}_{3D})/\overline{Nu}_{2D}$, for this particular configuration, the approximation of two dimensionality leads to an overprediction of average Nusselt number by about 66 percent at $Ra = 10^4$. However, at $Ra = 10^7$ this difference reduces to about 15 percent. Here it is of interest to note that the relative difference between the average Nusselt numbers for a cubic cavity (three-dimensional) and that for a square cavity (two-dimensional) is less than 5 percent for Rayleigh numbers larger than 10^5. The heat transfer results also indicate that the reduction in the cross-cavity heat transfer due to the presence of partitions is much more significant in three-dimensional configurations. Of course, a three-dimensional enclosure will approach the two-dimensional limit as the aspect ratio (B/H) and the width of the opening are increased.

The average Nusselt numbers, at $Ra = 10^6$, for the three opening heights considered are given in Table 2. As expected, the total heat transfer increases with an increase in the opening height.

Concluding Remarks

Natural convection in a cubic enclosure with a vertical partition has been studied. Results have been presented for a range of the values of the Rayleigh number and the opening height. Both these parameters have a significant effect of the fluid flow and heat transfer characteristics in the enclosure. The three-dimensional effects are significant for the Rayleigh numbers considered in this study. The heat transfer rate increases with increasing Rayleigh number and opening height. The average Nusselt numbers for three-dimensional enclosures are 15 to 66 percent smaller than those for two-dimensional enclosures with the same relative opening height.

Acknowledgments

The authors are grateful to Professor J. R. Lloyd for bringing to their attention the paper by Bilski et al. (1986). This research was partially funded by a grant from the Minnesota Supercomputer Institute.

References

Bajorek, S. M., and Lloyd, J. R., 1982, "Experimental Investigation of Natural Convection in Partitioned Enclosures," ASME JOURNAL OF HEAT TRANSFER, Vol. 104, pp. 527–532.

Bilski, S. M., Lloyd, J. R., and Yang, K. T., 1986, "An Experimental Investigation of the Laminar Natural Convection Velocity Field in Square and Partitioned Enclosures," *Proceedings, 8th International Heat Transfer Conference*, Hemisphere Publishing Corp., Washington, DC, pp. 1513–1518.

Boardman, C. R., Kirkpatrick, A., and Anderson, R., 1989, "Influence of Aperture Height and Width on Interzonal Natural Convection in a Full-Scale Air-Filled Enclosure," ASME *Journal of Solar Energy Engineering*, Vol. 111, pp. 278–285.

Chang, L. C., Lloyd, J. R., and Yang, K. T., 1982, "A Finite Difference Study of Natural Convection in Complex Enclosures," *Proceedings, 7th International Heat Transfer Conference*, Hemisphere Publishing Corp., Washington, DC, pp. 183–188.

de Vahl Davis, G., 1983, "Natural Convection of Air in a Square Cavity: A Benchmark Numerical Solution," *International Journal of Numerical Methods in Fluids*, Vol. 3, pp. 249–264.

Jetli, R., Acharya, S., and Zimmerman, E., 1986, "Influence of Baffle Location on Natural Convection in a Partially Divided Enclosure," *Numerical Heat Transfer*, Vol. 10, pp. 521–536.

Karki, K. C., Sathyamurthy, P., and Patankar, S. V., 1991, "Natural Convection in a Partitioned Cubic Enclosure," in: *Mixed Convection Heat Transfer 1991*, ASME HTD-Vol. 163, D. W. Pepper et al., eds., pp. 139–151.

Kelkar, K. M., and Patankar, S. V., 1990, "Numerical Prediction of Natural Convection in Square Partitioned Enclosures," *Numerical Heat Transfer*, Vol. 17, pp. 269–285.

Le Peutrec, Y., and Lauriat, G., 1990, "Effects of the Heat Transfer at the Side Walls on Natural Convection in Cavities," ASME JOURNAL OF HEAT TRANSFER, Vol. 112, pp. 370–378.

Nansteel, M. W., and Greif, R., 1981, "Natural Convection in Undivided and Partially Divided Rectangular Enclosures," ASME JOURNAL OF HEAT TRANSFER, Vol. 103, pp. 623–629.

Nansteel, M. W., and Greif, R., 1984, "An Investigation of Natural Convection in Enclosures With Two- and Three-Dimensional Partitions," *International Journal of Heat and Mass Transfer*, Vol. 27, No. 4, pp. 561–571.

Neymark, J., Boardman, C. R., Kirkpatrick, A., and Anderson, R., 1989, "High Rayleigh Number Natural Convection in Partially Divided Air and Water Filled Enclosures," *International Journal of Heat and Mass Transfer*, Vol. 32, No. 9, pp. 1671–1679.

Patankar, S. V., 1980, *Numerical Heat Transfer and Fluid Flow*, Hemisphere Publishing Corp., Washington, DC.

Zimmerman, E., and Acharya, S., 1987, "Free Convection Heat Transfer in a Partially Divided Vertical Enclosure With Conducting End Wall," *International Journal of Heat and Mass Transfer*, Vol. 30, No. 2, pp. 319–331.

C. J. Ho
Professor.
Mem. ASME

F. J. Tu
Graduate Student.

Department of Mechanical Engineering,
National Cheng Kung University,
Tainan, Taiwan 701

Laminar Mixed Convection of Cold Water in a Vertical Annulus With a Heated Rotating Inner Cylinder

A numerical investigation is made to evaluate the perturbing effect of forced convection due to axial rotation of the inner cylinder on natural convection heat transfer of cold water with density inversion effects in a vertical cylindrical annulus. The mixed convection heat and fluid flow structures in the annulus are found to be strongly affected by the density inversion effects. The centrifugally forced convection can result in significant enhancement of the buoyant convection heat transfer of cold water with the density inversion parameter being equal to 0.4 or 0.5; thus the slow axial rotation of the inner cylinder can be a viable means for heat transfer augmentation of cold water natural convection in a vertical annulus.

Introduction

Thermally driven convection of cold water is well known to be characterized with the existence of a nonlinear density temperature relationship having a density maximum at about 4°C at atmospheric pressure. This density inversion phenomenon commonly results in a rather peculiar convection behavior from that observed for ordinary fluids, which follow a linear density temperature relationship. Natural convection of cold water in enclosures has been studied considerably for various fundamental geometries. Some of the representative studies of this aspect are those of Seki et al. (1975); Vasseur et al. (1983); Inaba and Fukuda (1984); Lin and Nansteel (1987a, 1987b); Ho and Lin (1988, 1990). It has been established from these works that a minimum heat transfer rate arises under the influence of the density inversion at which a bicellular flow structure of approximately equal strength and size prevails across the enclosure.

From a standpoint of heat transfer engineering, feasible treatment to circumvent the aforementioned inherently minimum heat transfer characteristics of cold water may be quite desirable. To this purpose, consideration is given in the present study to the possible modification in the fluid flow structures and heat transfer characteristics of natural convection of cold water enclosed in a vertical cylindrical annulus by imposing an axial rotation of constant speed Ω on the inner cylinder, as depicted schematically in Fig. 1. It follows that a buoyant rotating (mixed) convection flow arises in a vertical annulus. The problem of mixed convection heat transfer in such a physical configuration has recently received considerable attention due to its relevance to a wide range of engineering applications as well as natural occurrences, such as cooling of rotating machinery, rotating heat exchangers, chemical vapor deposition processes, atmospheric circulation, and so on. Few works have been reported concerning mixed convection heat transfer within a rotating vertical annulus. de Vahl Davis et al. (1984) and Hessami et al. (1987) studied numerically the laminar mixed convection for air contained in a vertical annulus with the inner cylinder and one of the horizontal endwalls rotating about the vertical axis in order to simulate the heat transfer behavior of a small air-cooled, electric motor. Ball and Farouk (1987) conducted a numerical simulation of the buoyant rotating convection for air contained in a vertical annulus with emphasis on the interaction of buoyancy and centrifugal forces. Recently, Ball et al. (1989) supplemented this work with an experimental study and made a qualitative description of the transition from a buoyancy-dominated flow regime to one dominated by rotation. With increasing rotation a greater increase of the heat transfer rate could be obtained in an annulus of narrow gap.

There have been extensive works concerning the classical problem of hydrodynamic stability of isothermal flow in an annulus between rotating vertical cylinders (Taylor vortex flow). Comprehensive reviews of the literature on various aspects of this flow problem are available in the papers of DiPrima and Swinney (1985) and Anson et al. (1989). The effects of buoyancy induced by the radial temperature gradient on the stability of the Couette flow are the subjects of renewed interest to research workers. A numerical study dealing with the buoyancy effects on bifurcation phenomenon in annuli of small-to-moderate aspect ratio was presented by Ball and Farouk (1988). Moreover, Ball and Farouk (1989) performed a flow visualization study of buoyancy-induced instability on the development and structure of Taylor vortices in a wide-gap vertical annulus of moderate aspect ratio.

To the authors' best knowledge, there is no other study concerning the mixed convection heat transfer of cold water enclosed in a vertical annulus with a rotating inner cylinder. The present study will therefore focus attention on the perturbing effect of slow rotation of the inner cylinder on the buoyancy convection of cold water, considering the density inversion effect via a numerical simulation.

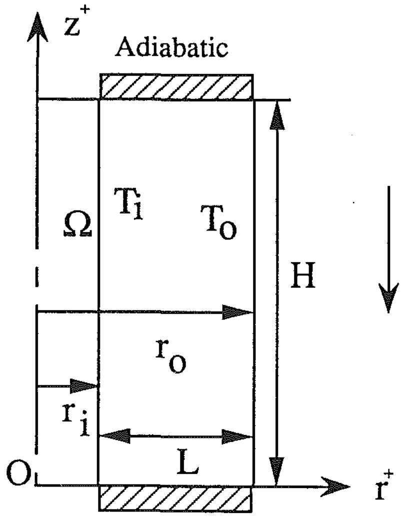

Fig. 1 Schematic view of the physical configuration

Contributed by the Heat Transfer Division for publication in the JOURNAL OF HEAT TRANSFER. Manuscript received by the Heat Transfer Division December 1990; revision received September 30, 1991. Keywords: Enclosure Flows, Mixed Convection, Rotating Flows.

Problem Statement and Formulation

The vertical annular enclosure as shown in Fig. 1 is formed by two concentric cylinders and two horizontal endwalls. The inner cylinder of radius r_i has an axial rotation of constant speed Ω and is isothermally heated at a fixed temperature T_i. Meanwhile, the outer cylinder of radius r_o is the cold wall of the annulus at an isothermal surface temperature $T_o (< T_i)$ and the horizontal endwalls are assumed adiabatic. Moreover, the outer cylinder and the horizontal endwalls are stationary.

The flow of cold water inside the cylindrical annulus is assumed axisymmetric, steady, and laminar. According to the experimental observations of Snyder and Karlson (1964), Karlson and Snyder (1965), and Snyder (1965), the flow configuration under consideration remains axisymmetric when the magnitude of the radial temperature gradient across the annular gap is less than 5°C/cm. Here the temperature gradient considered is restricted to be of the order of 1°C/cm across a 5-cm annular gap. The thermophysical properties of water, except density, are temperature independent, adhering to the Boussinesq approximation. The Boussinesq approximation holds for slow rotating flow with small centrifugal acceleration (Ball and Farouk, 1987). In the present study the rotation speed of the inner cylinder considered is of the order of one revolution per minute. Viscous dissipation is negligible. Moreover, the body forces considered here include those due to the gravitational, centrifugal, and Coriolis accelerations. In terms of the vorticity, stream function, swirl velocity, and temperature, the flow field and temperature distribution of cold water within the annulus are governed by the following dimensionless partial differential equations:

$$\frac{\partial(u\zeta)}{\partial r}+\frac{\partial(w\zeta)}{\partial z}-\frac{\mathrm{GrFr}}{\mathrm{Re}^2}\frac{\Gamma}{r^3}\left(\Gamma\frac{\partial\theta^*}{\partial z}+2\theta^*\frac{\partial\Gamma}{\partial z}\right)-\frac{2}{r^3}\frac{\partial\Gamma}{\partial z}+\frac{\mathrm{Gr}}{\mathrm{Re}^2}\frac{\partial\theta^*}{\partial r}=\frac{1}{\mathrm{Re}}\left(\frac{\partial^2\zeta}{\partial r^2}+\frac{1}{r}\frac{\partial\zeta}{\partial r}-\frac{\zeta}{r^2}+\frac{\partial^2\zeta}{\partial z^2}\right) \tag{1}$$

$$\frac{1}{r}\frac{\partial(ru\Gamma)}{\partial r}+\frac{\partial(w\Gamma)}{\partial z}=\frac{\mathrm{GrFr}}{\mathrm{Re}^2}\frac{u\theta^*\Gamma}{r}+\frac{1}{\mathrm{Re}}\left(\frac{\partial^2\Gamma}{\partial r^2}-\frac{1}{r}\frac{\partial\Gamma}{\partial r}+\frac{\partial^2\Gamma}{\partial z^2}\right) \tag{2}$$

$$\frac{\partial}{\partial r}\left(\frac{1}{r}\frac{\partial\psi}{\partial r}\right)+\frac{1}{r}\frac{\partial^2\psi}{\partial z^2}=-\zeta \tag{3}$$

$$\frac{\partial(u\theta)}{\partial r}+\frac{\partial(w\theta)}{\partial z}=\frac{1}{\mathrm{RePr}}\left(\frac{\partial^2\theta}{\partial r^2}+\frac{1}{r}\frac{\partial\theta}{\partial r}+\frac{\partial^2\theta}{\partial z^2}\right) \tag{4}$$

where

$$u=-\frac{1}{r}\frac{\partial\psi}{\partial z} \tag{5a}$$

$$w=\frac{1}{r}\frac{\partial\psi}{\partial r} \tag{5b}$$

$$\zeta=\frac{\partial u}{\partial z}-\frac{\partial w}{\partial r} \tag{5c}$$

$$\theta^*=|\theta-\theta_m|^a \tag{5d}$$

The nonlinear density-temperature relationship of cold water was based on the correlation proposed by Gebhart and Mollendorf (1974) given as:

$$\rho(T)=\rho_m(1-rsp\,|T-T_m|^a) \tag{6}$$

where $\rho_m = 999.9720$ kg/m^3, $T_m = 4.29325$°C, $a = 1.894816$, and $rsp = 9.297173\times10^{-6}(°\mathrm{C})^{-a}$

The dimensionless boundary conditions for the problem under consideration are:

$$z=0 \text{ or } A,\quad u=w=\Gamma=\psi=0,\quad \frac{\partial\theta}{\partial z}=0 \tag{7a}$$

$$r=\frac{1}{RR-1},\quad u=w=\psi=0,\quad \Gamma=\frac{1}{(RR-1)^2},\quad \theta=1 \tag{7b}$$

$$r=\frac{RR}{RR-1},\quad u=w=\psi=\Gamma=\theta=0 \tag{7c}$$

Numerical Method

The governing equations, together with the boundary conditions, were solved numerically by the finite difference method. A pseudotransient formulation approach (Peyret and Taylor, 1983) was employed to obtain the solution to the steady-state equations. The partial differential equations were discretized using the central difference formulae for the spatial derivatives, except the convective terms, and a forward difference formula for the pseudo-time derivatives. For the convective terms, the second upwind scheme (Roache, 1976) was used. Moreover, the boundary conditions for the vorticity were derived using the Thom formula (Roache, 1976). The resulting finite difference equations were then solved by the ADI scheme until a relative convergence criterion (10^{-5}) was met for all the field variables of the problem. Furthermore, the steady-state solutions were checked with an energy balance across the annulus to within at least 2 percent.

In the present study various uniform meshes that subdivide the r and z directions into 41-65 by 41-81 grid points were

Nomenclature

a = exponent of density equation
A = aspect ratio $= H/L$
Fr = Froude number $= L\Omega^2/g$
g = gravitational acceleration
Gr = Grashof number $= g(rsp)\,|T_i-T_o|^a L^3/(\nu^2)$
h = heat transfer coefficient
H = height of the annulus
k = thermal conductivity
k_{eq} = equivalent thermal conductivity $= \mathrm{Nu}\cdot\ln(RR)/(RR-1)$
L = annulus gap $= (r_o - r_i)$
Nu = Nusselt number
Pr = Prandtl number
r^+ = radial coordinate
r = dimensionless radial coordinate $= r^+/L$
Ra = Rayleigh number = PrGr
Re = rotational Reynolds number $= L\Omega^2/\nu$
r_i = radius of inner cylinder
r_o = radius of outer cylinder
RR = radius ratio $= r_o/r_i$
rsp = coefficient of density equation
T = temperature
u = radial velocity component
v = angular velocity component
w = axial velocity component
z^+ = axial coordinate
z = dimensionless axial coordinate $= z^+/L$
α = thermal diffusivity
Γ = swirl velocity $= rv$
ζ = dimensionless vorticity
θ = dimensionless temperature $= (T-T_o)/(T_i-T_o)$
θ_m = density inversion parameter $= (T_m-T_o)/(T_i-T_o)$
ν = kinematic viscosity
ρ = density
ψ^+ = stream function
ψ = dimensionless stream function $= \psi^+/(L^3\Omega)$
Ω = rotational speed of inner cylinder

Subscripts

b = pure natural convection
i = inner cylinder
m = extreme temperature
o = outer cylinder

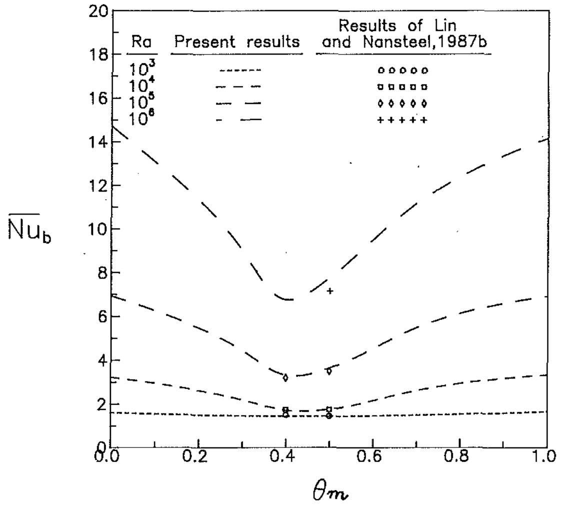

Fig. 2 Relation of average Nusselt number of pure natural convection of cold water versus the density inversion parameter in a unit-aspect-ratio annulus

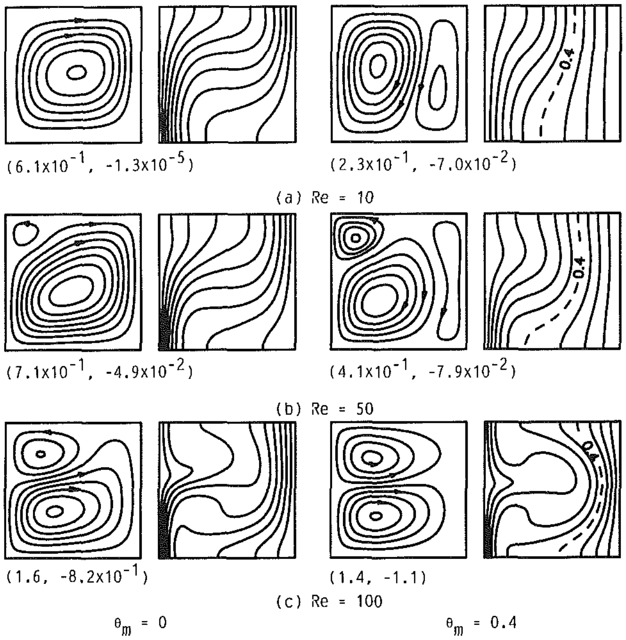

(6.1x10^{-1}, -1.3x10^{-5}) (2.3x10^{-1}, -7.0x10^{-2})

(a) Re = 10

(7.1x10^{-1}, -4.9x10^{-2}) (4.1x10^{-1}, -7.9x10^{-2})

(b) Re = 50

(1.6, -8.2x10^{-1}) (1.4, -1.1)

(c) Re = 100

θ_m = 0 θ_m = 0.4

Fig. 3 Influence of Re on streamlines and isotherms at Ra = 10^4 and $A = 1$

Table 1 Average heat transfer results of the buoyant rotating convection of air in a vertical annulus of $A = 10$ with Re = 100 and $RR = 2$

Gr	$\overline{Nu}$	$\bar{k}_{eq}$
0	2.127	1.477(1.473)**
10^2	2.048	1.420(1.370)*
500	1.828	1.267(1.324)*
10^3	1.749	1.212(1.258)*
10^4	2.095	1.452

* From Ball and Farouk(1987)

** From the empirical correlation in Ball et al.(1989)

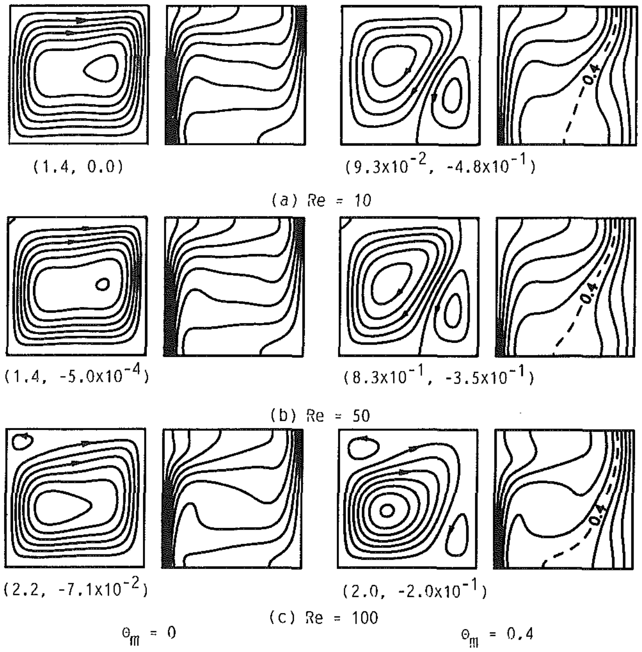

(1.4, 0.0) (9.3x10^{-2}, -4.8x10^{-1})

(a) Re = 10

(1.4, -5.0x10^{-4}) (8.3x10^{-1}, -3.5x10^{-1})

(b) Re = 50

(2.2, -7.1x10^{-2}) (2.0, -2.0x10^{-1})

(c) Re = 100

θ_m = 0 θ_m = 0.4

Fig. 4 Influence of Re on streamlines and isotherms at Ra = 10^5 and $A = 1$

employed, depending on either the aspect ratio or the Rayleigh number. The selected meshes were a compromise between the computational cost and the resolution of the details of the heat and fluid flow fields through a series of grid size tests. For instance, for $RR = 2$, $A = 1$, $\theta_m = 0.4$, Re = 100, and Ra = 10^6, the differences in the average heat transfer rate and the maximum stream function are less than 1 percent between the 65×51 and 81×65 grids. The calculations were performed on a workstation (Silicon Graphics Personal Iris 4D/20) and required less than 1000 CPU seconds for a typical case. Furthermore, validation studies were performed by generating solutions for both the pure natural convection of cold water and the buoyant rotating convection of air in a vertical annulus, and comparing, respectively, with the published results (Lin and Nansteel, 1987b; Ball and Farouk, 1987; Ball et al., 1989). Temperature distribution, flow patterns, and heat transfer results of the present calculations were found to be in good agreement with their results as exemplified in Fig. 2 for the results of the average Nusselt number of the pure natural convection of cold water, $\overline{Nu}_b$, and in Table 1 for the average equivalent conductivity of the buoyant rotating convection of air, $\bar{k}_{eq}$.

Results and Discussion

From the foregoing mathematical formulation, it can be seen that the flow field and temperature distribution for the problem under consideration are governed by the following parameters: the rotational Reynolds number Re, the Rayleigh number Ra, the Froude number Fr, the density inversion parameter θ_m, the aspect ratio A, and the radius ratio RR. Similar to the findings by de Vahl Davis et al. (1984) and Ball and Farouk (1987), the numerical calculations in the present work also indicate that the solutions of the problem considered here are insensitive to the variation of Fr in the ranges of Re and Ra investigated. This is expected from the fact that at low rotational speeds considered in the present study, the centrifugal and Coriolis components of the buoyancy force are much smaller than that induced by the gravitational acceleration. Therefore, the numerical results will be presented for Fr = 0 with the following values of the relevant parameters: Re = 10, 50, 100, 200; Ra = 10^3 to 10^6; $\theta_m = 0$ to 1; $A = 1$ to 8; and $RR = 2$.

Flow Structure and Temperature Distribution. The flow structures and temperature distributions of cold water inside the vertical annulus will be presented by means of contour

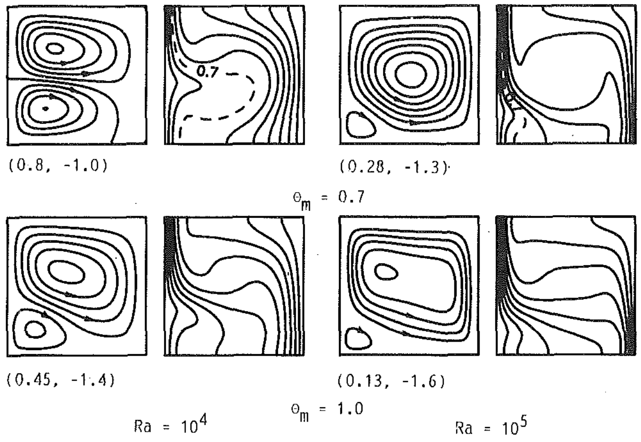

Fig. 5 Effect of density inversion on flow structure and temperature field at $A=1$ and $\mathrm{Re}=100$

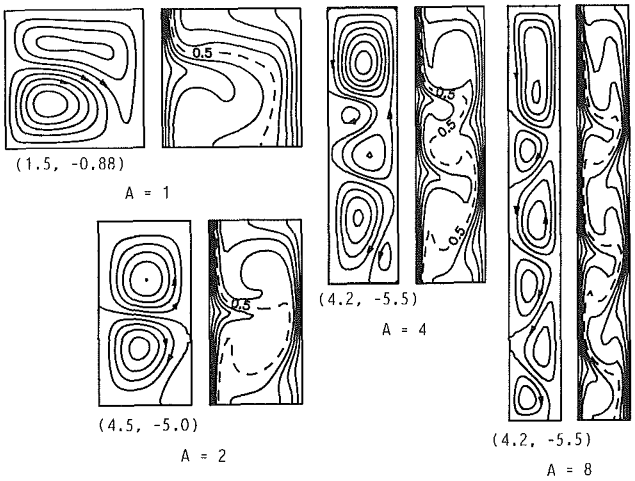

Fig. 6 Streamlines and isotherms at $\theta_m=0.5$ and $\mathrm{Ra}=10^5$, and $\mathrm{Re}=100$ for various aspect ratios

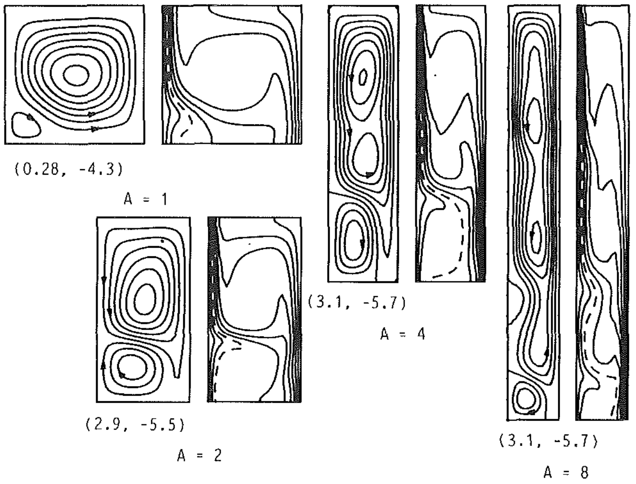

Fig. 7 Streamlines and isotherms at $\theta_m=0.7$, $\mathrm{Ra}=10^5$, and $\mathrm{Re}=100$ for various aspect ratios

maps of streamlines and isotherms, respectively. Moreover, on the isotherm plots the temperature contour corresponding to the density extreme, θ_m, is traced by a dashed line, when it exists. In all the following contour plots the rotating heated inner cylinder is on the left; the two numbers within the parentheses beneath the streamline plots denote, respectively, the maximum and minimum values of the stream function (multiplied by the Reynolds number in order to provide a better indication of the flow strength).

Figures 3 and 4 illustrate the influence of forced convection due to the rotating inner cylinder on the buoyant convection flow structure and temperature field for fixed Rayleigh number but varying Reynolds number in a unit-aspect-ratio annulus with two different values of the density inversion parameter. At $\mathrm{Ra}=10^4$ it can be seen from Fig. 3 that with $\theta_m=0$ as an ordinary fluid, the clockwise circulation and the isotherm distribution at $\mathrm{Re}=10$ resemble closely the pure natural convection, indicating a buoyancy-dominated flow regime. With increasing Reynolds number, the resulting greater centrifugal force not only induces a growing counterclockwise secondary eddy (Taylor vortex) near the upper left corner of the annulus but also strengthens the originally buoyancy-driven clockwise circulation. As a result, a pattern of bicellular flow is formed at $\mathrm{Re}=100$ for $\theta_m=0$, shown in Fig. 3(*c*). On the other hand, in the presence of the density inversion effect, the buoyancy-driven flow structures appear to be rather susceptible to the influence of the centrifugal force, as can be seen in Fig. 3 for $\theta_m=0.4$. The two counterrotating buoyant circulations due to the density inversion effect of cold water are seen to be affected differently by the centrifugal force. At $\mathrm{Re}=50$ the clockwise circulation near the inner cylinder (inner circulation) is intensified together with the growth of a counterclockwise secondary vortex due to the centrifugal force near the upper corner of the annulus, thereby suppressing the buoyancy-driven counterclockwise circulation near the outer cylinder (outer circulation). With Re increasing up to 100, it can be seen that the outer buoyant circulation is diminished and a structure of layered counterrotating vortices is detected, resembling the Taylor vortex pair observed in isothermal flow configuration. This is a clear indication of a centrifugally dominated flow regime. Accordingly, the isotherm distribution in Fig. 3 for $\theta_m=0.4$ is seen to change from the buoyancy-dominated pattern to one dominated by the centrifugally forced convection. Further, as is expected, the above effect of the centrifugally forced convection is markedly diminished as the Rayleigh number is increased. This can be observed in Fig. 4 for $\mathrm{Ra}=10^5$, by comparison with Fig. 3. Another important fact that can be drawn from Figs. 3 and 4 is that the effect of the centrifugally forced convection on the buoyancy-driven convection of cold water in the annulus is a function of the density inversion parameter as well.

The dependence of the combined buoyantly and centrifugally driven flow and temperature fields of cold water on the density inversion parameter is considered next in Fig. 5 (supplemented with Figs. 3 and 4 for Re fixed at 100 with $\mathrm{Ra}=10^4$ and 10^5). A scrutiny of the streamline patterns and isotherm distributions for $\mathrm{Ra}=10^4$ reveals an interesting influence of the density inversion parameter. As the density inversion parameter is increased from 0 to 0.4, the heat and fluid flow structures in the annulus are seen to change from a buoyancy-dominated regime into one that is controlled by the centrifugally forced convection. By further increasing the density inversion parameter, as shown in Fig. 5, the forced convection effect is seen to degrade progressively; and at $\theta_m=1$, buoyancy-dominated convection heat and fluid flow structures are essentially recovered but in an opposite sense of the ordinary fluid as $\theta_m=0$ displayed in Fig. 3. Moreover, the increase of Rayleigh number tends to promote the foregoing density inversion effect; a convective inversion phenomenon can be readily detected at $\theta_m=0.7$ for $\mathrm{Ra}=10^5$ (Fig. 5).

Next, the flow structure and temperature distribution for various values of the aspect ratio ($A \geq 1$) are exemplified in Figs. 6 and 7, respectively, for $\theta_m=0.5$ and 0.7 keeping Ra and Re constant. In general, the increase of the aspect ratio of the annulus results in eddy splitting of the flow structure. In the tall annulus, as shown in Fig. 6 ($A \geq 4$), the eddy-splitting flow structure becomes increasingly pronounced, yielding a staggered multicellular flow pattern at $A=8$. A closer exam-

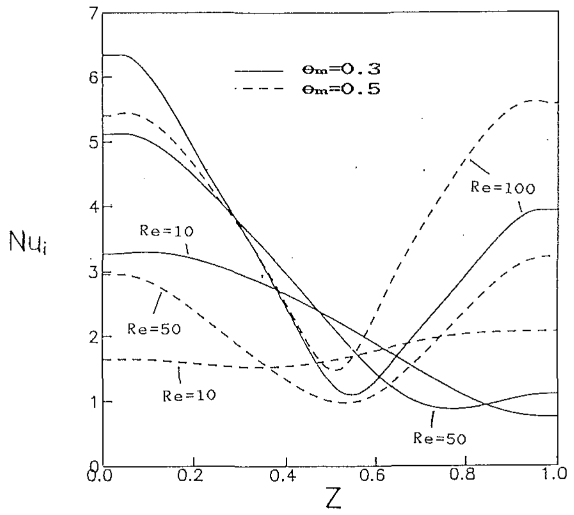

Fig. 8 Variation of local Nusselt number along the inner cylinder at Ra = 10^5 for various Reynolds numbers

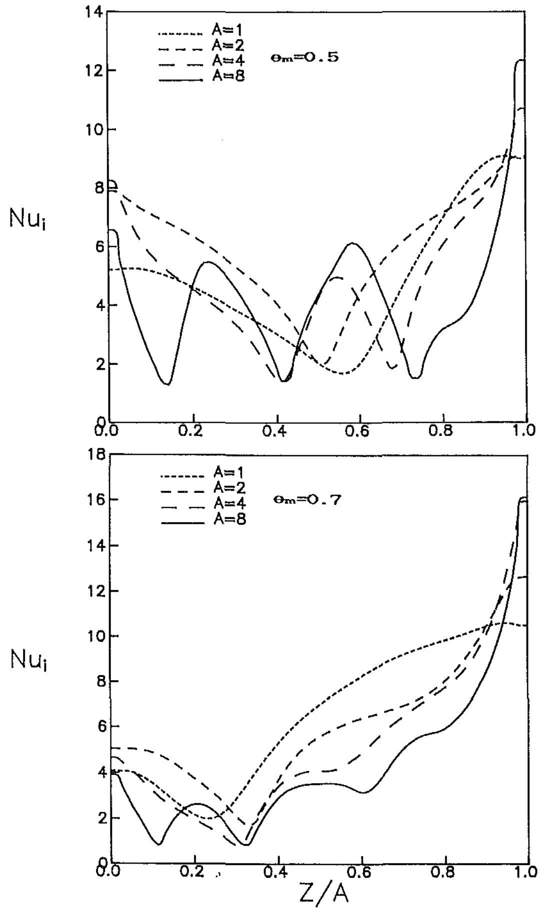

Fig. 9 Variation of local Nusselt number along the inner cylinder at Ra = 10^5 for various aspect ratios

ination of the flow structure for $A = 8$ indicates that the counterclockwise circulations are relatively stronger, reflecting the presence of the density inversion effect. The isotherms display accordingly a wavy distribution. As for $\theta_m = 0.7$, Fig. 7, the foregoing dominance of the split counterclockwise circulation near the outer cylinder becomes more distinctive, where the clockwise eddy is mainly confined to the lower end of the annulus for $A = 8$. As a result, a natural-convection-dominated heat transfer mechanism prevails across the tall annulus, as witnessed by the isotherm pattern displayed in Fig. 7.

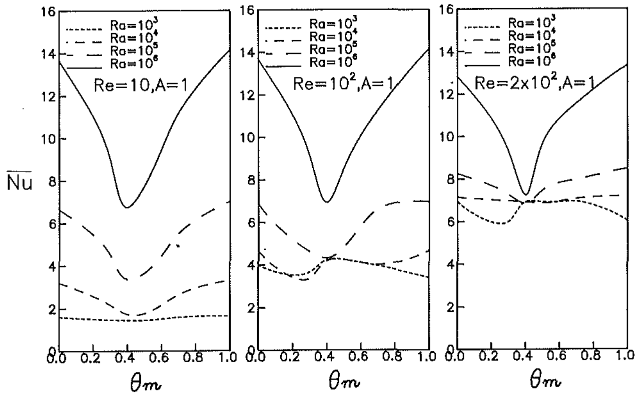

Fig. 10 Relation of average Nusselt number versus the density inversion parameter

Heat Transfer Results. Figure 8 presents the local heat transfer coefficient on the inner cylinder of a unit-aspect-ratio annulus by means of a local Nusselt number defined as

$$\text{Nu}_i = \frac{hL}{k} = \frac{\partial\theta}{\partial r}\bigg|_{r=\frac{1}{RR-1}} \tag{8}$$

An overview of the figure finds that the increase in Re causes the variation of the heat transfer coefficient along the inner cylinder to change from a somewhat monotonic (natural-convection-dominated) trend into a rather sinusoidal behavior with a minimum value occurring in the vicinity of midplane of the annulus. This is another evidence for the transition from the natural-convection-dominated regime into that dominated by the centrifugally forced convection. In particular, one can notice that the increase in the centrifugal force, namely Re, can lead to a drastic increase in heat transfer rate for $\theta_m = 0.5$, which apparently fulfills the main objective of the present study to enhance the inherently lower buoyant convection heat transfer of cold water due to the density inversion effect.

In Fig. 9 the variation of the local heat transfer rate, Nu$_i$, with the aspect ratio of the annulus is depicted for $\theta_m = 0.5$ and 0.7. In general the heat transfer coefficient distributions simply reflect the wavy isotherm distributions shown in Figs. 6 and 7.

Next, the average heat transfer rate through the inner cylinder of a unit-aspect-ratio annulus is presented in Fig. 10 in terms of average Nusselt number versus the density inversion parameter for three different values of the Reynolds number. For Re = 10, the average Nusselt number displays a humpy variation with the density inversion parameter similar to that commonly observed for the pure natural convection heat transfer of cold water as displayed in Fig. 2, featuring a minimum heat transfer rate at a certain value of the density inversion parameter (Lin and Nansteel, 1987b; Ho and Lin, 1990). This clearly reflects that natural convection still remains as the dominant heat transfer mechanism in the annulus. With Re increasing up to 100, a significant modification due to centrifugally forced convection in the Nusselt number curves can be readily discerned in Fig. 10 for Ra ≤ 10^5. Particularly noteworthy is the drastic enhancement of heat transfer rate for Ra = 10^3 and 10^4; the Nusselt number curves exhibit a local maximum at a critical density inversion parameter around which a minimum natural convection heat transfer occurs. At higher Re = 200 as shown in Fig. 10 the foregoing influence of the centrifugal force on the cold water heat transfer characteristics becomes further pronounced. This again demonstrates the viability of the heat transfer augmentation induced by the perturbing rotation of the inner cylinder in the aspect of coping with the inherently minimum heat transfer characteristic of natural convection of cold water enclosed in the annulus.

Table 2 Values of $\overline{Nu}/\overline{Nu}_b$ for $A=1$ and $RR=2$

Ra	Re	Re^2/Ra	$\overline{Nu}/\overline{Nu}_b$ $\theta_m=0$	0.3	0.4	0.5	0.7	1.0
10^3	10	0.1	1.000	1.001	1.001	1.001	1.057	0.992
	50	2.5	1.204	1.361	1.388	1.355	1.277	1.145
	100	10.0	2.403	2.488	2.923	2.769	2.633	2.060
	200	40.0	4.303	4.723	4.786	4.782	4.602	4.193
10^4	10	0.01	0.994	0.989	1.006	0.999	1.004	0.990
	50	0.25	1.059	1.179	1.252	1.178	1.071	1.005
	100	1.00	1.443	1.534	2.434	2.238	1.523	1.400
	200	4.00	2.210	3.182	4.026	3.903	2.693	2.154
10^5	10	0.001	0.960	1.016	1.015	1.001	1.000	1.057
	50	0.025	0.968	1.011	0.994	1.081	0.993	0.995
	100	0.1	1.000	1.041	1.328	1.326	1.201	1.009
	200	0.4	1.192	1.644	2.067	2.049	1.450	1.229
10^6	10	0.0001	0.927	0.999	1.001	1.001	1.000	0.999
	50	0.0025	0.927	1.007	1.007	1.022	0.999	0.998
	100	0.01	0.939	1.014	1.028	1.099	1.007	1.001
	200	0.04	0.871	1.038	1.074	1.243	1.033	0.944

Table 3 Constants of Eq. (9) for $RR=2$ and $A=1$

θ_m	C	n	Ra	Max. Deviation(%)	Correlation Coefficient
0.0	0.1727	0.3209	10^3-10^6	2.71	0.99982
0.3	0.1301	0.3065	10^4-10^6	0.16	0.99999
0.4	0.1097	0.2970	10^4-10^6	3.58	0.99894
0.5	0.0900	0.3223	10^4-10^6	1.00	0.99992
0.7	0.1457	0.3145	10^4-10^6	0.97	0.99992
1.0	0.1903	0.3117	10^3-10^6	0.70	0.99989

To quantify further the effect of the centrifugally forced convection on the pure natural convection heat transfer of cold water in the annulus, the heat transfer results of the mixed convection are presented by means of a ratio of the average Nusselt number to that for the pure natural convection, $\overline{Nu}_b$, as tabulated in Table 2 for a unit-aspect-ratio annulus. Inspection of the table reveals that the influence of the centrifugally forced convection is a rather complicated function of the Rayleigh number and the density inversion parameter. The imposed axial rotation of the inner cylinder does not always result in enhancement of the natural convection heat transfer of cold water; that is, under certain combinations of Re, Ra, and θ_m, the opposing effect of the centrifugal and the buoyancy forces causes the ratio $\overline{Nu}/\overline{Nu}_b$ to be less than unity. In the absence of the density inversion effect, $\theta_m=0$, the table indicates an aiding mixed convection heat transfer for the parameter $Re^2/Ra>0.1$; but under the influence of the density inversion, $\theta_m>0$, no such simple quantitative trend can be observed. Nevertheless, it can be noticed from the table that the greatest contribution of the forced convection in the heat transfer enhancement over the buoyant convection occurs with the density inversion parameter being 0.4 or 0.5. For instance, with $\theta_m=0.5$ and $Re=200$, the enhancement can be more than 100 percent at $Ra=10^5$ and about 24 percent at $Ra=10^6$.

Finally, by means of least-squares regression analysis, the results of the average Nusselt number for the pure natural convection of cold water in a unit-aspect-ratio annulus can be well correlated in the form of

$$\overline{Nu}_b=C(Ra)^n \tag{9}$$

where C and n are presented in Table 3 for various density inversion parameter. Little success was obtained in an attempt to attain a correlation for the mixed convection heat transfer results obtained in the present study.

Concluding Remarks

The perturbing influence of forced convection driven by the axial rotation of the inner cylinder on the buoyancy-driven convection of cold water enclosed in a vertical cylindrical annulus is studied via a numerical simulation. Numerical results obtained in the present study indicate that the mixed convection of cold water due to the combined centrifugal and buoyancy forces in a vertical annulus is rather complicated by the presence of the density inversion effect. The effect of the centrifugally forced convection on the cold water natural convection is therefore a function of the Rayleigh number as well as the density inversion parameter. Under certain combinations of the Reynolds number, the Rayleigh number, and the density inversion parameter, opposing effects of the forced and buoyant convection arise, resulting in a lower heat transfer rate than that of the pure natural convection. On the other hand, the heat transfer augmentation due to the aiding forced convection appears to be most significant for the density inversion parameter being 0.4 or 0.5, around which the minimum heat transfer of cold water occurs for the pure natural convection in the annulus. Therefore, the imposed slow rotation of the inner cylinder can be a viable means to enhance the natural convection heat transfer of cold water in a vertical annulus with the density inversion effect.

Acknowledgments

The constructive comments of the reviewers are highly appreciated. The necessary computing facility and time for this study were provided by the National Cheng Kung University Computing Center.

References

Anson, D. K., Mullin, T., and Cliffe, K. A., 1989, "A Numerical and Experimental Investigation of a New Solution in the Taylor Vortex Problem," *J. Fluid Mech.*, Vol. 207, pp. 475–487.

Ball, K. S., and Farouk, B., 1987, "On the Development of Taylor Vortices in Vertical Annulus With a Heated Rotating Inner Cylinder," *Int. J. Numer. Meth. Fluids*, Vol. 7, pp. 857–867.

Ball, K. S., and Farouk, B., 1988, "Bifurcation Phenomena in Taylor-Couette Flow With Buoyancy Effects," *J. Fluid Mech.*, Vol. 197, pp. 479–501.

Ball, K. S., and Farouk, B., 1989, "A Flow Visualization Study of the Effects of Buoyancy on Taylor Vortices," *Phys. Fluids A*, Vol. 1, pp. 1502–1507.

Ball, K. S., Farouk, B., and Dixit, V. C., 1989, "An Experimental Study of Heat Transfer in a Vertical Annulus With a Rotating Inner Cylinder," *Int. J. Heat Mass Transfer*, Vol. 32, pp. 1517–1527.

de Vahl Davis, G., Leonardi, E., and Reizes, J. A., 1984, "Convection in a Rotating Annular Cavity," in: *Heat and Mass Transfer in Rotating Machinery*, D. E. Metzger and N. H. Afgan, eds., Hemisphere Publishing Corp., Washington, DC, pp. 131–142.

DiPrima, R. C., and Swinney, H. L., 1985, *Hydrodynamic Instabilities and the Transition to Turbulence*, H. L. Swinney and J. P. Gollub, eds., Springer, New York, pp. 139–180.

Gebhart, B., and Mollendorf, J., 1974, "A New Density Relation for Pure and Saline Water," *Deep-Sea Research*, Vol. 24, pp. 831–848.

Hessami, M. A., de Vahl Davis, G., Leonardi, E., and Reizes, J. A., 1987, "Mixed Convection in Vertical Cylindrical Annulus," *Int. J. Heat Mass Transfer*, Vol. 30, pp. 831–848.

Ho, C. J., and Lin, Y. H., 1988, "Natural Convection Heat Transfer of Cold Water Within an Eccentric Horizontal Cylindrical Annulus," ASME JOURNAL OF HEAT TRANSFER, Vol. 110, pp. 894–900.

Ho, C. J., and Lin, Y. H., 1990, "Natural Convection of Cold Water in a Vertical Annulus With Constant Heat Flux on the Inner Wall," ASME JOURNAL OF HEAT TRANSFER, Vol. 112, pp. 117–123.

Inaba, H., and Fukuda, T., 1984, "Natural Convection in an Inclined Square Cavity in Regions of Density Inversion of Water," *J. Fluid Mech.*, Vol. 42, pp. 363–381.

Karlson, S. K. F., and Snyder, H. A., 1965, "Observations on a Thermally Induced Instability Between Rotating Cylinders," *Ann. Phys.*, Vol. 31, pp. 314–324.

Lin, D. S., and Nansteel, M. W., 1987a, "Natural Convection Heat Transfer in a Square Enclosure Containing Water Near Its Density Maximum," *Int. J. Heat Mass Transfer*, Vol. 30, pp. 2319–2329.

Lin, D. S., and Nansteel, M. W., 1987b, "Natural Convection in a Vertical Annulus Containing Water Near the Density Maximum," ASME JOURNAL OF HEAT TRANSFER, Vol. 109, pp. 899–905.

Peyret, R., and Taylor, T. D., 1983, *Computational Methods for Fluid Flow*, Springer-Verlag, New York.

Roache, P. J., 1976, *Computational Fluid Dynamics*, Hermosa, Albuquerque, NM.

Seki, N., Fukusako, S., and Nakoroka, M., 1975, "Experimental Study on Natural Convection Heat Transfer With Density Inversion of Water Between Two Horizontal Concentric Cylinders," ASME JOURNAL OF HEAT TRANSFER, Vol. 97, pp. 556–561.

Snyder, H. A., and Karlson, S. K. F., 1964, "Experiments on the Stability of Couette Motion With a Radial Thermal Gradient," *Phys. Fluids*, Vol. 7, pp. 1696–1706.

Snyder, H. A., 1965, "Experiments on the Stability of Two Types of Spiral Flow," *Ann. Phys.*, Vol. 31, pp. 292–313.

Vasseur, P., Robillard, L., and Chandra Shekar, B., 1983, "Natural Convection Heat Transfer of Water Within a Horizontal Cylindrical Annulus With Density Inversion Effects," ASME JOURNAL OF HEAT TRANSFER, Vol. 105, pp. 117–123.

Nucleate Boiling Characteristics of R-113 in a Small Tube Bundle

P. J. Marto
Fellow ASME.

C. L. Anderson

Department of Mechanical Engineering,
Naval Postgraduate School,
Monterey, CA 93943

Heat transfer measurements were made during nucleate boiling of R-113 from a bundle of 15 electrically heated, smooth copper tubes arranged in an equilateral triangular pitch. The bundle was designed to simulate a portion of a refrigeration system flooded-tube evaporator. The outside diameter of the tubes was 15.9 mm, and the tube pitch was 19.1 mm. Five of the tubes that were oriented in a vertical array on the centerline of the bundle were each instrumented with six wall thermocouples to obtain an average wall temperature and a resultant average heat transfer coefficient. All tests were performed at atmospheric pressure. The majority of the data were obtained with increasing heat flux to study the onset of nucleate boiling and the influence of surface "history" upon boiling heat transfer. Data taken during increasing heat flux showed that incipient boiling was dependent upon the number of tubes in operation. The operation of lower tubes in the bundle decreased the incipient boiling heat flux and wall superheat of the upper tubes, and generally increased the boiling heat transfer coefficients of the upper tubes at low heat fluxes where natural convection effects are important. The boiling data confirmed that the average heat transfer coefficient for a smooth-tube bundle is larger than obtained for a single tube.

Introduction

In recent years significant progress has been made in understanding nucleate boiling heat transfer on the shell side of tube bundles in order to design improved evaporators for the process and refrigeration industries. Leong and Cornwell (1979) and Cornwell et al. (1980) conducted a photographic investigation of circulation effects in a thin slice of a reboiler tube bundle containing 241 electrically heated, 19-mm-dia tubes arranged in a square in-line pitch of 25.4 mm. While boiling R-113 at atmospheric pressure, they were able to view the boiling process in the bundle through one side of the boiler, which was made of glass. They deduced the circulation pattern within the bundle and observed that the flow pattern changed from bubbly flow in the bottom of the bundle to frothy flow near the top. The measured heat transfer coefficients showed an increasing trend from the bottom of the bundle toward the top.

Yilmaz and Westwater (1980) measured the effect of velocity on heat transfer to boiling R-113 on the outside of a single, 6.5-mm-dia horizontal tube. They found that velocity increases improved the nucleate boiling heat transfer coefficients. Cornwell and Schuller (1982) pointed out that the high values of the heat transfer coefficients at the top of a tube bundle cannot be entirely explained by an increase in liquid velocity. Using high-speed photography, they observed that numerous bubbles sliding over and around the top tubes in a bundle create a sliding bubble microlayer between the bubble and the tube wall, and these sliding bubbles can account for increases in the heat transfer coefficient on the upper tubes of as much as four times that on the lower tubes. Further work by Cornwell and Scoones (1988) and Cornwell (1989) has indicated that nucleation occurs only on the lower tubes in a bundle and that sliding bubbles and liquid forced convection can account for all the heat transfer in the top part of the bundle.

The influence of tube position within a bundle of smooth tubes has been studied extensively by Wallner (1974), Fujita et al. (1986), and Chan and Shoukri (1987). These investigators, using both square and staggered tube arrangements with a tube pitch-to-diameter ratio of between 1.2 and 2.0, verified that the influence of the lower tubes in a bundle can significantly increase the heat transfer from the upper tubes, and this increase can be predicted by combining pool boiling predictions with liquid forced convection predictions. Similar results have been obtained for finned tube bundles by Hahne and Müller (1983), Müller (1986), and Fujita et al. (1986). The influence of two-phase convection effects in a bundle has also been studied by Wege and Jensen (1984), Hwang and Yao (1986), and Jensen and Hsu (1988).

From the abovementioned results, it is apparent that the two-phase interactions that occur in tube bundles during boiling can be very complex and can change with heat flux level, fluid properties, tube bundle layout, etc. For example, Webb et al. (1989) point out that the boiling mechanism in a flooded refrigerant evaporator is different from that which occurs in a kettle reboiler used in the process industry. This is due to a different tube layout in a refrigerant evaporator that restricts natural circulation effects and to the presence of vapor quality (approximately 15 percent) in the inlet feed at the bottom of the bundle. As a result, it is very difficult to use information from one type of bundle and fluid combination, and apply it to another situation. Instead, a complete range of experimental data is needed in the open literature that covers various fluids, tube bundle geometries, heat fluxes, and inlet qualities, so that theoretical models can be formulated and appropriately evaluated. This is particularly important in the refrigeration industry where new, alternative refrigerants and refrigerant–oil mixtures are being proposed. In addition, no information is available regarding the onset of nucleate boiling in a bundle, bundle hysteresis effects, and the influence of past history upon the incipient boiling condition. These phenomena may be very important during startup of a refrigeration or process plant.

The purpose of the present paper is, therefore, to establish additional baseline nucleate boiling data of R-113 from a small bundle of smooth tubes that represents a section of a refrigerant evaporator. Emphasis is placed on the influence of tube position in the bundle upon the incipient boiling point and any hysteresis effects common in nucleate boiling processes. The data obtained are expected to serve as reference data for comparison with other refrigerants and refrigerant–oil mixtures from bundles of both smooth as well as new enhanced tubes.

Contributed by the Heat Transfer Division for publication in the JOURNAL OF HEAT TRANSFER. Manuscript received by the Heat Transfer Division December 1990; revision received October 1991. Keywords: Boiling, Multiphase Flows, Refrigeration.

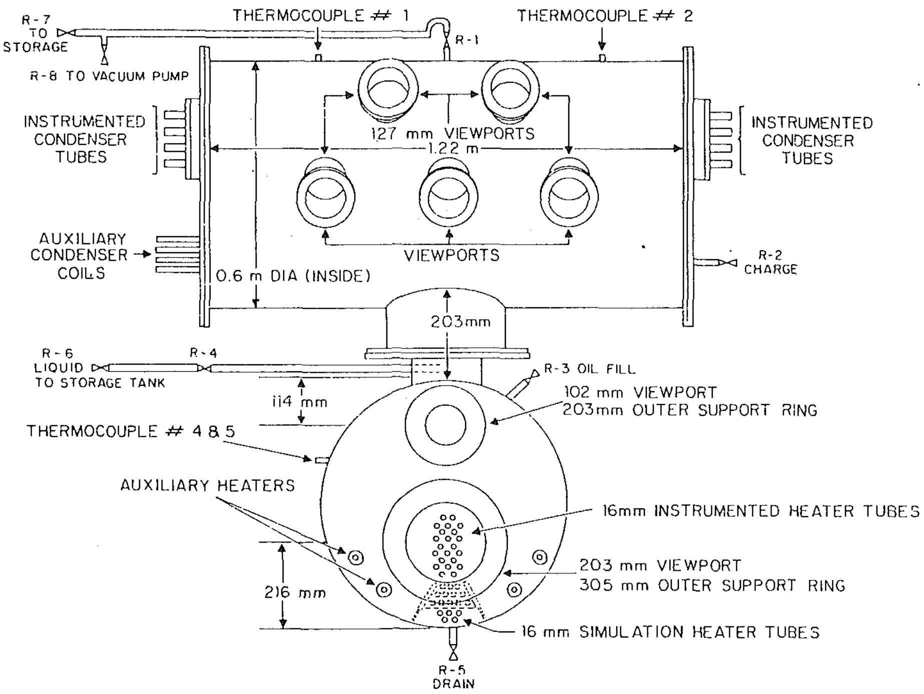

Fig. 1 Experimental apparatus

Experimental Apparatus

The basic experimental apparatus used during this investigation is shown in Fig. 1. It consisted of an evaporator and condenser arranged to provide reflux operation. The condenser included four instrumented test tubes and five auxiliary coils, all cooled by a refrigerated mixture of water and ethylene glycol. It was designed to permit independent condensation studies while using the evaporator as a source of vapor. During the present investigation, the condenser was used simply to maintain the system pressure near atmospheric conditions.

The evaporator was designed to simulate a portion of a refrigerant-flooded evaporator. It was fabricated from stainless steel plate and formed into a short cylinder 610 mm in diameter and only 241 mm long. Electrically heated tubes were cantilever-mounted from the back wall of the evaporator to permit viewing the boiling phenomena along the axis of the tubes through the lower of two glass windows mounted in the front. Figure 2 is a schematic sectional view of the evaporator that shows four sets of heated tubes. Two auxiliary heaters, each capable of 4 kW, were installed on each side of the test bundle to maintain the liquid pool at saturated conditions and to provide system pressure control. Five simulation heaters, each also capable of 4 kW, were mounted below the test bundle in order to simulate additional tube rows in a larger bundle and to provide inlet vapor quality into the bottom of the test bundle. The test bundle consisted of two types of heated tubes: active tubes (marked "A") which contained 1 kW heaters, and instrumented tubes (marked "I") which, in addition to 1 kW heaters, contained wall thermocouples. The instrumented tubes were thus located along the centerline of a symmetric, staggered tube bundle. All the bundle tubes were made from commercially available, 15.9-mm-dia, smooth copper tubing. They were arranged in an equilateral triangular pitch (i.e., centerline-to-centerline spacing) of 19.1 mm, giving a pitch-to-diameter ratio of 1.20. Each set of auxiliary tubes, simulation tubes, and test bundle tubes could be heated independently using three separate rheostat controllers. The bundle also contained a number of unheated dummy tubes (marked "D") that were used to guide the two-phase mixture through the bundle. Two vertical baffle plates were installed to restrict side circulation into and out of the bundle. An open space was left, however, on the lower part of each side of the dummy tube bundle, adjacent to the simulation heaters, to permit side entry of liquid into the bottom of the simulation bundle. Thus, liquid circulation was vertically upward over the test tubes with no net horizontal component. The liquid–vapor mixture at the top of the bundle split symmetrically, with the liquid returning down the outside of each of the baffle plates. Vapor from the evaporator flowed upward through a riser section and was distributed axially and circumferentially to the top of the condenser by a vapor shroud. The condensate collected in the bottom of this shroud and returned to the evaporator by gravity. The two-phase mixing and the condensate return flow were observed through the top window.

In measuring boiling heat transfer coefficients, great care must be exercised with the cartridge heater and temperature measuring instrumentation to ensure good accuracy. Various installation techniques were recently reviewed by Jung and Bergles (1989). Based upon extensive pool boiling data with R-113, they concluded that the heat transfer coefficient of a single tube in pool boiling is not sensitive to variation in the cartridge heater heat flux provided that enough thermocouples are used to measure an average wall temperature. During this investigation, the instrumented test tubes were fabricated in a similar way to those used by Hahne and Müller (1983) and Wanniarachchi et al. (1986). Figure 3 is a cross-sectional sketch

Nomenclature

c_4 = coefficient in Eq. (1)

q = heat flux

T_{sat} = saturation temperature

$\bar{T}_{wo}$ = average tube wall outside temperature

α = heat transfer coefficient

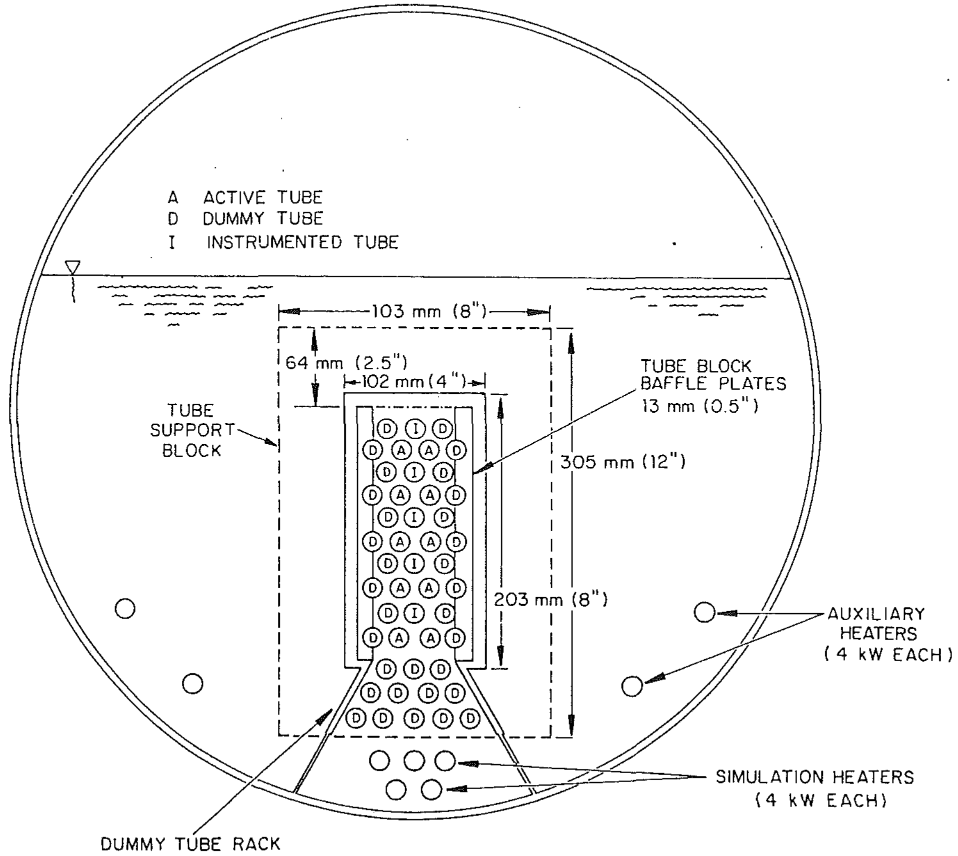

Fig. 2 Sectional view of evaporator

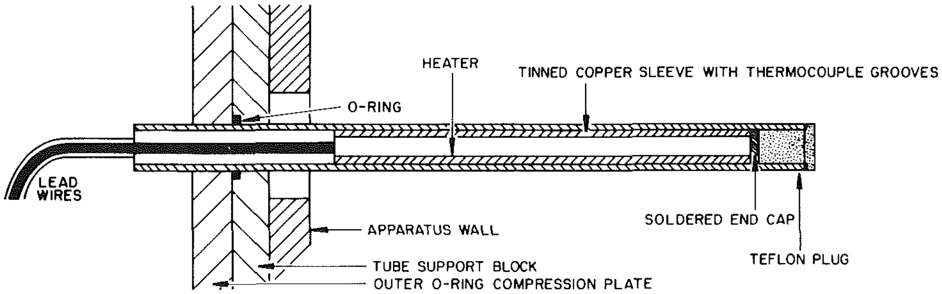

(a) BUNDLE HEATER TUBE SECTIONAL VIEW

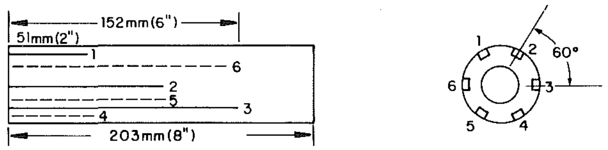

(b) THERMOCOUPLE LOCATIONS ALONG HEATED LENGTH

Fig. 3 Instrumented tube construction

of an instrumented tube, showing the construction details and the location of the wall thermocouples. To smooth out any nonuniformities in heat flux caused by the cartridge heater and to provide a convenient method to install wall thermocouples, a copper sleeve was used inside the test tube into which the cartridge heater was inserted with a tight mechanical fit. The outer diameter of the sleeve was machined to a diameter that was about 0.1 mm less than the inside diameter of the test tube. Its center was bored out to accommodate the cartridge heater. Six 1-mm-square longitudinal slots, spaced 60 deg apart, were milled into the outside wall of the sleeve to create channels for the wall thermocouples. They were milled to different lengths to provide temperature measurement at three different axial positions (50.8 mm from each end of the sleeve and in the middle). Type-T copper-constantan, Teflon-insulated, thermocouple wire was placed in each channel and secured in place by peening over the edges of the grooves in different locations using a blunt punch. The resulting imperfections were then removed with fine (400 grit) emery paper. Following this assembly procedure, the cartridge heater was inserted into the copper sleeve. The outer surface of the sleeve and the inner surface of the test tube were then brushed with solder flux solution to insure good wetting. The evaporator tube was then heated in an oven while the sleeve was heated by applying electrical power to the cartridge heater. The temperature of each component was brought up to about 200°C. This temperature was maintained while a eutectic 60:40 lead-tin solder was applied to both surfaces. Following the tinning process of both surfaces, the copper sleeve was inserted into the evaporator test tube while both pieces were hot. Prior to cooling, a copper end cap was soldered in position using a torch. After cooling, a Teflon end plug was inserted to minimize axial heat losses from the heater. Each test tube was installed into the tube support block using an O-ring. An outer compression plate was then bolted to the support block to seal each tube. Once all the evaporator tubes were installed, the support block was bolted into the rear wall of the evaporator unit. During this assembly, care was taken to insure that each tube was properly aligned in the bundle and was pushing against the inside face of the lower front viewing window.

Measurements and Procedures

Vapor temperatures were measured by two thermocouples at the top of the condenser and one thermocouple near the top of the evaporator. Liquid temperatures were measured by two thermocouples located close to the free surface of the liquid. During operation, these two thermcouples were located in a frothy, two-phase mixture and were considered to be well representative of T_{sat} at the free surface. The average outer wall temperature of the instrumented test tubes was obtained by averaging the six wall thermocouples in the copper sleeve and correcting for the small radial temperature drop due to conduction across the copper wall. The temperature drop across the 0.05-mm-thick solder joint between the copper sleeve and the test tube was neglected. The voltage and amperage to each of the test tubes were measured using voltage and current sensors. For a given tube, the heat flux was calculated by dividing the electrical power (after it was corrected for small axial losses out each end of the test tube) by the smooth tube surface area based upon an active heating length of 203 mm. During all the tests, the pressure was kept near atmospheric and the liquid level was kept approximately 100 mm above the top row of tubes. In order to calculate the local saturation temperature for each tube in the bundle, a hydrostatic pressure correction was made between the tube location and the free surface of the liquid. All the data were obtained and reduced with a computer-controlled data acquisition system.

Prior to filling with R-113, the system was evacuated and leak checked. Once the system was felt to be vacuum tight, R-113 was added to the evaporator by drawing it into the evaporator under vacuum. Prior to operating the evaporator, the ethylene glycol-water coolant for the condenser was cooled down using an 8-ton refrigeration system. Circulating pumps were then turned on to get a desired flow through the condenser tubes and cooling coils. During this investigation, nucleate boiling data were obtained following four different surface aging procedures similar to those used by Bergles and Chyu (1982) and Marto and Lepere (1982). With the first procedure (surface aging A), the tubes were preboiled at 30 kW/m^2 for 1 hour followed by immediate operation with increasing heat flux. The second procedure (surface aging B) was similar to the first except, after preboiling, the power to the bundle was turned off for 30 minutes while maintaining the pool at saturated conditions with the auxiliary heaters prior to increasing the heat flux. With the third procedure (surface aging C), the evaporator power was turned off overnight. The following morning, the system was slowly brought to saturated conditions using the auxiliary heaters, before operation of the tubes was commenced with increasing heat flux. The last procedure (surface aging D) consisted of boiling at 100 kW/m^2 for 30 minutes followed by immediate operation with decreasing heat flux. In this way, boiling incipience and bundle start up problems could be investigated. It should be noted that the recirculation pattern that existed in the evaporator vessel (and, therefore, across the test bundle) prior to the commencement of each experiment may have been affected by the four different aging procedures. However, once system operation was begun, data were not taken until 10-15 minutes after start up. Therefore, most of the recirculation variations would have disappeared prior to the process of actually taking data. Nevertheless, the uncertainty of the first one or two data points taken at very low heat fluxes, following aging procedures A, B, and C, may be larger than the uncertainties stated later in the paper.

Results and Discussion

All data were obtained with R-113 at a pressure of 1 atm. During increasing heat flux runs, the onset of nucleate boiling was observed through the lower viewing window. This "point" was defined as the applied heat flux where first nucleation was observed on the instrumented tubes. When heat flux is plotted versus ($\overline{T}_{wo} - T_{\text{sat}}$), the "incipient boiling" condition is indicated by a change in slope since the heat transfer mechanism changes from single-phase convection to two-phase convection with the activation, growth, and departure of vapor bubbles. Throughout this investigation, the instrumented tubes located along the centerline of the tube bundle were numbered consecutively from the top downward as tubes 1, 2, 3, 4, and 5, respectively. At each operating point, the values of the six wall thermocouples were recorded and compared to examine variations in wall temperature caused either by nonuniformities in the cartridge heater coils or by the test tube soldering and assembly procedure. This problem has been explored in more detail by Wanniarachchi et al. (1986). The maximum variation of the six measured wall temperatures was 3.7°C at the maximum heat flux (approximately 10^5 W/m^2) and 0.3°C at the minimum heat flux (approximately 10^3 W/m^2). This variation appeared to be random and independent of thermocouple orientation, and was probably caused by the tube soldering process. As a percentage of the corresponding wall superheats, the above values correspond to 17 and 10 percent, respectively. This variation in wall temperature created an estimated uncertainty in the wall superheat of ± 1.5°C at high fluxes and ± 0.3°C at low fluxes. The corresponding uncertainty in the measured heat flux was estimated to be ± 1 percent.

Figure 4 shows the data for tube 1 operating alone as a single tube, during increasing heat flux. The data were obtained following aging procedure C where the pool of R-113 was not preboiled, but was allowed to sit overnight. Prior to taking data, the pool temperature was slowly brought up to saturation conditions using the auxiliary heaters. Typical uncertainty bands are included at low and high heat fluxes. The data of Marto and Lepere (1982) for pool boiling of R-113 at 1 atm from a single short (50 mm heated length), 15.8-mm-dia copper tube, aged following the same procedure C and operated in an "as-received" condition, are included for comparison. In the natural convection region at low heat fluxes, the data from the two investigations have the same slope, but the present data show a smaller superheater of approximately 1-2°C. It may be that the bundle geometry in the present investigation, with the inactive, closely spaced ($p/D = 1.20$) neighboring tubes and the vertical baffles, generated a different liquid circulation pattern over tube 1, than occurred over the single tube used by Marto and Lepere (1982). The incipient boiling heat flux is remarkably close for the two investigations (about 7000 W/m^2). The wall superheat in the present investigation at the incipient boiling condition was approximately 13°C and the corresponding temperature overshoot was about 6°C. This was less than the measured superheat of 20°C by Marto and Lepere (1982) with an overshoot of about 10°C. When surface aging

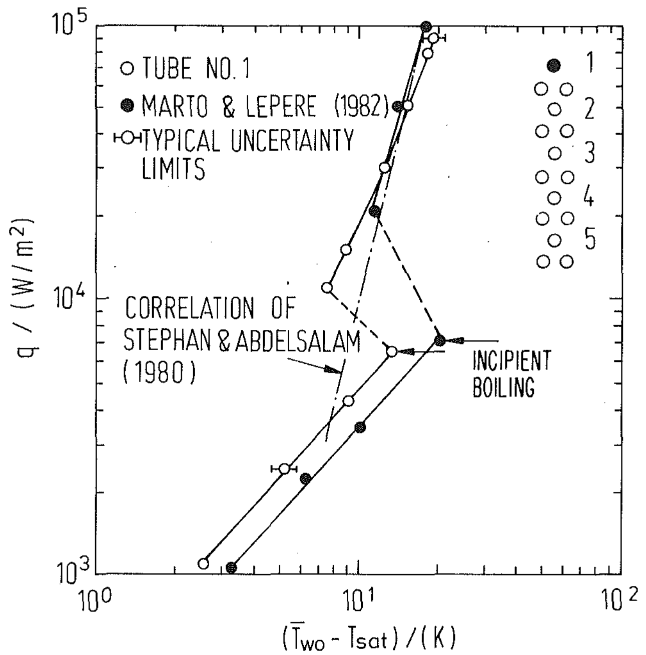

Fig. 4 Boiling data for tube 1 operating as a single tube (aging procedure C)

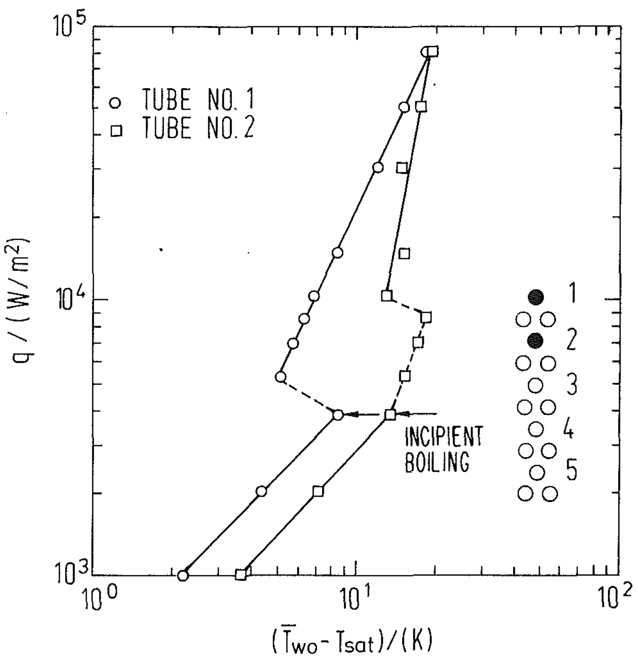

Fig. 5 Boiling data for tubes 1 and 2 operating simultaneously (aging procedure C)

procedure A was followed, the incipient boiling point occurred at a very low heat flux near 1000 W/m^2 and there was no discernible overshoot, while with aging procedure B, both the incipient boiling superheat and the resulting overshoot were less than shown. Clearly, in addition to variations in local flow conditions, the incipient boiling characteristics depend upon the active site distribution on the boiling surface and this can be very different depending upon the immediate past history of the heating surface. Figure 4 also shows that at higher heat fluxes, when nucleate boiling is completely developed, both sets of data are in good agreement with one another and with the empirical correlation of Stephan and Abdelsalam (1980) for refrigerants:

$$\alpha = \frac{q}{(\overline{T}_{wo} - T_{\rm sat})} = c_4 q^{0.745} \tag{1}$$

where the coefficient c_4 is provided as a function of pressure for various refrigerants. For R-113 at a pressure of 1 atm, c_4 equals 1.02, so with this correlation, the heat flux may be expressed in terms of the superheat as:

$$q = 1.08\ (\overline{T}_{wo} - T_{\rm sat})^{3.92} \tag{2}$$

Figure 5 shows the results for tubes 1 and 2 operating simultaneously, during increasing heat flux. Again, the tubes were subjected to aging procedure C prior to taking data. The natural convection data of tube 1, compared to the data in Fig. 4 when operating as a single tube, show that there appears to be no influence of the lower heated tube (tube 2) upon the heat transfer of the upper tube (tube 1). However, the natural convection heat transfer coefficient for the lower tube is less than the upper tube. The exact reason for this behavior is unknown, but may be due to the influence of the closely spaced tubes upon the velocity and temperature fields in the wake region of a heated tube. There is very little published information in the open literature for natural convection in tube bundles. Marsters (1972) studied the heat transfer characteristics of a vertical array of heated cylinders in air and found that the upper cylinders displayed reduced Nusselt numbers at small spacings and increased Nusselt numbers at large spacings. This behavior was explained by the fact that an upper tube in a vertical array of tubes experiences two phenomena that act in different directions to affect the heat transfer. First of all, the upper tubes feel a warmer fluid due to the heated tubes below. This warmer fluid decreases the local thermal driving potential for buoyancy-induced flow. On the other hand, the upper tubes are also exposed to a moving fluid due to the heated tubes below. This moving fluid enhances the natural convection effects due to the resulting mixed convection (Gebhart et al., 1988). Marsters (1972) went on to point out that in an array of tubes, the characteristic length of the process may not be the tube diameter but rather the position in the array. As a result, a local Grashof number formed with the characteristic length as the vertical distance from the bottom of the array to the local position of interest may reflect a transition in flow from laminar to turbulent somewhere in the array that implies a change in the local heat transfer characteristics. In a tightly spaced bundle of tubes such as used in this investigation, the flow may behave more as an internal one than an external one, and a characteristic length may be very difficult to select. As a consequence, it is clear that natural convection in a bundle is a complex process and needs further research attention to unravel the mysteries behind the observed trends.

Figure 5 also shows that the incipient boiling heat flux is reduced to about 4000 W/m^2 for both tubes, although the tube 2 data show an irregular nucleation process until higher heat fluxes are reached. This irregular behavior has been observed by Wanniarachchi et al. (1987) during boiling of R-114 from a single enhanced tube containing numerous nucleation sites. They attributed this behavior to incomplete nucleation along the boiling surface due to non-uniform heat flux or non-uniform cavity openings. Tube 1 displays a small characteristic temperature overshoot (about 4°C) and then a consistent trend with increasing heat flux in the developed nucleate boiling region. Tube 2 shows a somewhat erratic superheat behavior with increasing heat flux, which displays a very steep slope. When the results for tube 1 are compared to the data in Fig. 4 for tube 1 *acting as a single tube*, it is clear that boiling from a lower tube enhances the performance of an upper tube. Therefore, the influence of bubbles from a lower tube impacting on an upper tube is an important mechanism to enhance the heat transfer process. Microscopic bubbles from the lower

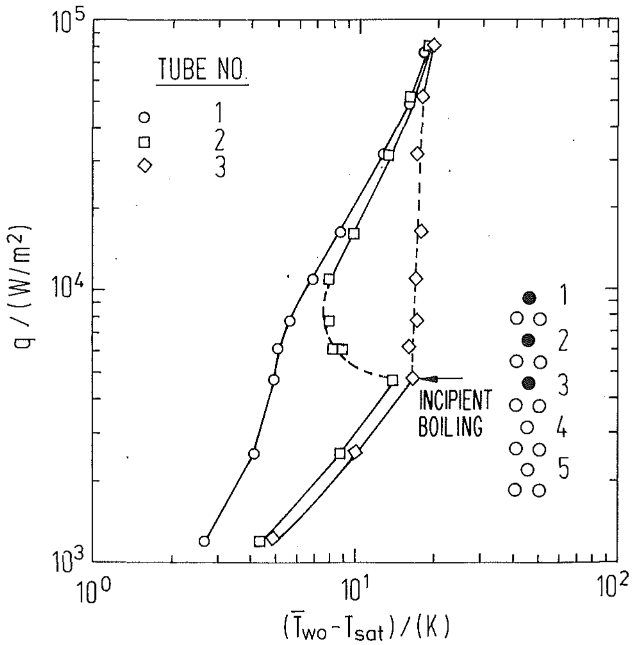

Fig. 6 Boiling data for tubes 1, 2, and 3 operating simultaneously (aging procedure C)

tube impacting upon the surface of the upper tube can reduce boiling incipient superheat significantly, as shown by Bergles and Kim (1988). In addition, it is well known that "bubble pumped" convection can enhance natural convection heat transfer rates by more than 100 percent (Bergles and Bar-Cohen, 1990).

Figure 6 shows similar data for three heated tubes. With tube 3 in operation, there is no apparent influence on the natural convection data of tube 2, confirming the abovementioned results of Fig. 5 that a lower heated tube does not seem to influence the natural convection behavior of an upper tube. However, the data of tube 1 indicate the presence of nucleate boiling at very low heat fluxes. A discrete incipient boiling point for tube 1 was never observed, even though tubes 2 and 3 did not show definite nucleation until a heat flux of about 5000 W/m^2. The reason for this behavior is not clear. Local variations in liquid subcooling could have caused this behavior, as reported by Bar-Cohen and Simon (1988), even though the inlet flow to the bundle is mixed by the presence of the lower dummy tubes. Perhaps the two heated lower tubes generated small bubbles at very low heat fluxes since the liquid pool came to room temperature conditions overnight and contained some absorbed air. These air bubbles could have aided the nucleation process for tube 1 as described previously. Tube 2 shows a dramatic shift compared to Fig. 5 because of the heated tube 3 below it, confirming again the important influence of a lower neighboring heated tube. Once tube 3 nucleates, it exhibits a nearly vertical slope with increasing heat flux similar to that shown by tube 2 in Fig. 5, when it was the bottom tube. This behavior is similar to the forced convection nucleate boiling data described by Auracher (1990). Similar results to the above-described phenomena were obtained when bundles of both 4 and 5 tubes were heated simultaneously. The lowest tube demonstrated a nearly vertical slope in the nucleate boiling regime. From these results several important observations may be made:

1 During natural convection in a bundle of tubes, the heated lower tubes do not have much influence on the upper tubes, and the lower tubes exhibit a decreased heat transfer coefficient when compared to the top tube operating as a single tube.

2 The presence of heated lower tubes reduces the incipient boiling point and the accompanying temperature overshoot for upper tubes. After the lowermost tube nucleates, it exhibits a very steep slope on a q versus ΔT plot (thus, the nucleate boiling heat transfer coefficient in this region is very sensitive to wall superheat).

3 The presence of heated lower tubes enhances the nucleate boiling heat transfer coefficients of upper tubes at low heat fluxes, and the most important influence appears to be from the heated tube immediately below the tube of interest.

Although some of the above observations are not readily explainable at this time, the nucleate boiling results summarized in observation 3 are in good agreement with the earlier experimental and theoretical results of Fujita et al. (1986), Chan and Shoukri (1987), Cornwell and Scoones (1988), Chen et al. (1989), and Cornwell (1989). Cornwell (1989) postulates that in a tube bundle, the local heat transfer coefficient may be written as:

$$\alpha = \alpha_{fc} + \alpha_{sb} + \alpha_{nb} \tag{3}$$

where the first term on the right is due to local liquid forced convection, the second is due to approaching bubbles striking the tube surface from below, and the third term is due to bubble nucleation on the surface itself. He further states that at medium heat fluxes, the first two terms alone can account for all the heat transfer. Cornwell (1989) points out that the second term will depend upon the size of the bubbles. For small bubbles, such as in R-113, the impacting bubbles cause additional turbulence in the liquid boundary layer and can also create an evaporating microlayer that is caught between the heating surface and the sliding bubble. Tong et al. (1988) also propose that sweeping bubbles can strip superheated liquid off the surface to enhance the heat transfer.

Another entirely different mechanism may be occurring in a boiling tube bundle that could explain some of the above observations and consequently deserves mention. It is well known that nucleate boiling in thin films exhibits higher heat transfer coefficients than when boiling in a deep pool (Nishikawa et al., 1967 Mesler, 1976; Marto et al., 1977). Mesler and Mailen (1977) found that when a bubble bursts through a thin liquid film, many new bubbles grow from that location, indicating that the bursting process was creating new vapor nuclei in the vicinity of the heating surface that served as sources for additional vapor bubbles to grow, thereby enhancing the heat transfer. Bergman and Mesler (1981) showed that bubble nuclei are also formed when a vapor bubble bursts through the surface of a pool of superheated water. Carroll and Mesler (1981) found through photographic evidence that when a vapor bubble bursts through a free surface, vortex rings occur and microscopic vapor bubbles are entrained in these vortex rings. These bubbles were estimated to be only a few hundred microns in diameter and could only be seen under special lighting conditions. Gopalen and Mesler (1990) found that a threshold superheat exists for this secondary nucleation to occur. Thus, it is reasonable to postulate that whenever nucleate boiling occurs and a bubble bursts through a liquid-vapor interface, the possibility of forming microscopic vapor nuclei to serve as a source for new vapor bubbles exists. In a bundle of tubes, especially with a small pitch-to-diameter ratio, a chaotic two-phase mixture flows upward through the bundle, and some bubbles can be carried back down into the bundle due to intense recirculation around the sides. Under these conditions, a growing bubble on a tube surface meeting another vapor bubble flowing past the heater surface (especially on the underside of a tube) could burst through the surface of the larger bubble and create conditions favorable for the formation of these microscopic vapor nuclei. Therefore, lower tubes in a bundle could assist in causing more numerous bubbles to flow past the upper tubes. This larger number of bubbles would help to accelerate the flow and stimulate any bubble sweeping effect. In addition, more bubbles could produce a foamy flow near the top of the bundle, enhancing the heat transfer in that region (Udomboresuwan and Mesler, 1986).

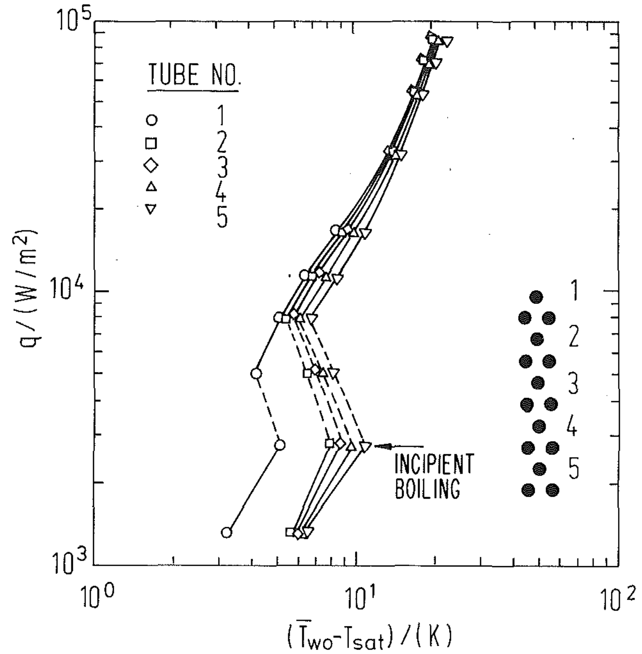

Fig. 7 Tube bundle data with no simulation heaters in operation (aging procedure C)

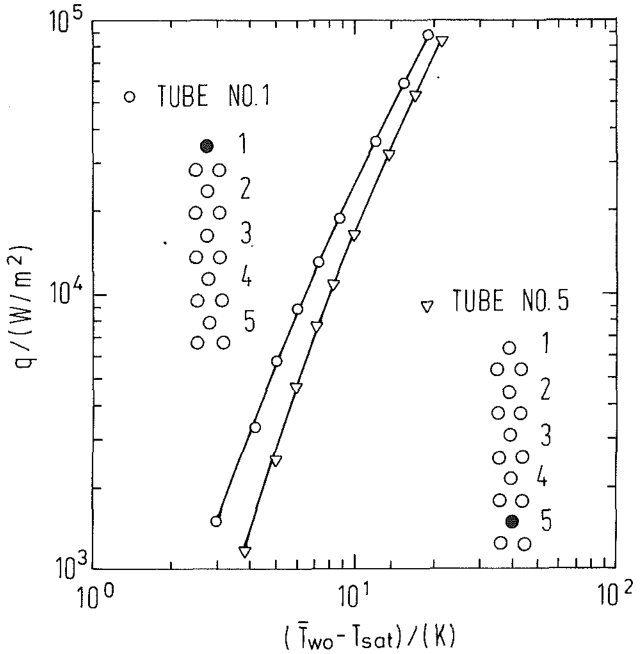

Fig. 9 Single tube data for tubes 1 and 5 (aging procedure D)

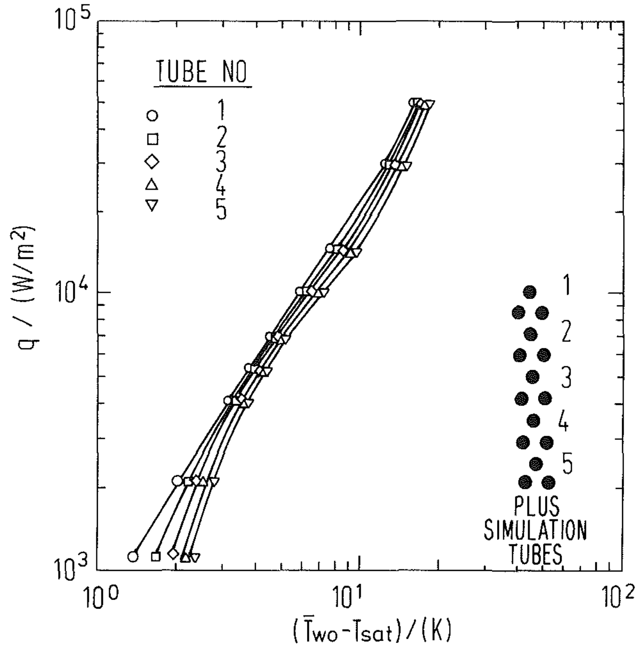

Fig. 8 Tube bundle data with simulation heaters in operation (aging procedure C)

Figures 7 and 8 show the behavior of tubes 1–5 when all 15 active tubes are heated as a bundle and when the bundle plus the lower simulation tubes are all heated. The data were obtained for increasing heat flux following aging procedure C. The results in Fig. 7 show that the entire bundle seems to nucleate at about the same heat flux (3000 W/m^2). The best performing tube is always the top tube and the worst performing is always the lowest. Above a heat flux of 25,000 W/m^2, all tubes approach the single tube performance. When the additional simulation tubes are also heated (representing 15 more active tubes), as shown in Fig. 8, there is no evidence of any incipient boiling in the upper bundle at all, indicating that boiling is occurring even at very low heat fluxes. Once again, there is significant enhancement at low fluxes and this enhancement decreases as the flux increases. This suggests that the presence of two-phase flow at the entry of the bundle (with a quality greater than zero) eliminates boiling incipience problems in the bundle and enhances heat transfer as well. Recently, Webb and Apparao (1990) calculated the performance of enhanced tubes in an R-11 flooded refrigerant evaporator. They found that the effect of entering flash gas on thermal performance was different depending upon the type of boiling surface used. For a finned tube bundle, the heat duty increased by 3 percent when the entering quality was increased from 0 to 16 percent, whereas for a structured enhanced surface, there was a 4 percent decrease in the heat duty. They attributed these two different trends to a balance between two-phase pressure drop in each case, and to the difference between the importance of liquid convection versus bubble nucleation between the integral fin tube and the structured surface. In the present investigation, the smooth tubes would be expected to behave closer to the finned tube bundle of Webb and Apparao (1990) rather than to their enhanced tube bundle, and show an increase in thermal performance with inlet quality because with smooth tubes there is less nucleation and significant liquid convection.

Figure 9 shows the data for tube 1 and tube 5 when each is operating separately as a single tube. The data were taken for decreasing heat flux, following aging procedure D. Although the difference is small, tube 1 exhibits a higher heat transfer coefficient than tube 5. Perhaps the liquid circulation pattern is different for the two tubes because of their location relative to the rest of the bundle and to the free surface. The data for tube 1 during decreasing heat flux, when compared to the data for tube 1 during increasing heat flux (Fig. 4), show very good agreement at high heat fluxes, within the uncertainties of the measurements, and a definite hysteresis pattern at low heat fluxes. Figure 10 shows the data for all five instrumented tubes in operation during decreasing heat flux. When compared to the previous figure, enhancement is evident at low heat fluxes ($q < 20$ kW/m^2). However, a deterioration in relative performance occurs for larger heat fluxes. Further improvement was evident when the entire bundle was operated together with the simulation tubes, creating conditions close to an actual refrigerant evaporator. In this later case, at a heat flux of 3 kW/m^2, the relative performance of tube 1 in the complete bundle

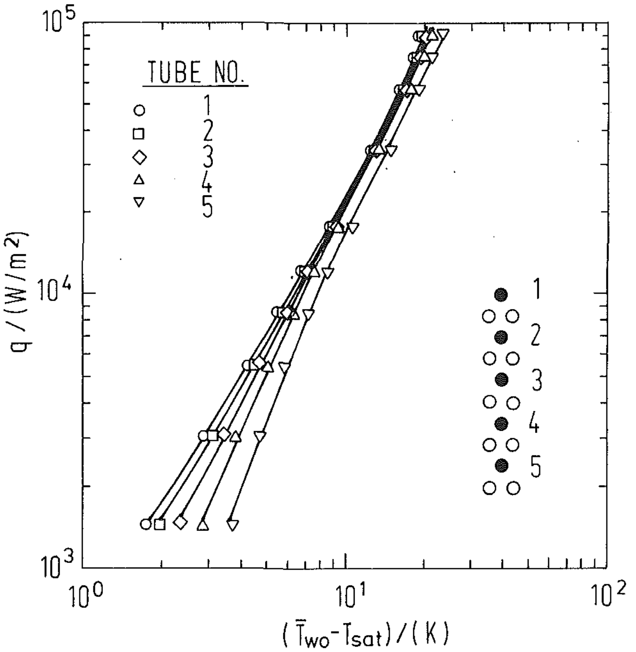

Fig. 10 Boiling data for tubes 1, 2, 3, 4, and 5 operating simultaneously (aging procedure D)

compared to its performance as a single tube was approximately 60 percent greater. A similar 60 percent increase occurred for tube 5. However, at a flux of 30 kW/m^2, the benefit of bundle operation was completely eliminated. These results confirm that a "bundle factor" that predicts greater performance than the single tube results must be used in the design of flooded evaporators. This "bundle factor," however, will depend upon the type of boiling surface being used, the tube bundle layout, the operating heat flux, and, of course, the type of liquid being boiled.

Conclusions

Nucleate boiling data of R-113 at atmospheric pressure were obtained using a small bundle of smooth copper tubes. The data were obtained after subjecting the bundle to different preboiling (i.e., aging) conditions, and with either increasing or decreasing heat flux. Based upon the results obtained, the following conclusions may be made:

1 During natural convection in a bundle of tubes, heated lower tubes do not have much influence on heat transfer from the upper tubes. Natural convection in tube bundles is a complex phenomenon and deserves further research attention.

2 The presence of heated lower tubes in a bundle reduces the incipient boiling point and the accompanying temperature overshoot for upper tubes.

3 The lowest tube in a bundle gives the poorest heat transfer. After this tube nucleates during increasing heat flux, it exhibits a nearly vertical slope on a heat flux versus superheat plot, similar to forced convection nucleate boiling.

4 During nucleate boiling, the presence of heated lower tubes enhances the heat transfer coefficients of upper tubes at low heat fluxes. This enhancement leads to a "bundle factor" that depends upon heat flux and the number of heated tubes in the bundle.

5 Using simulation heaters at the bottom of a test bundle to provide inlet vapor quality eliminates any boiling hysteresis in the test bundle; otherwise, a hysteresis pattern exists between increasing and decreasing heat flux. Therefore, flooded tube refrigerant evaporators with entering flash gas should experience negligible hysteresis effects.

6 In a bundle of tubes experiencing nucleate boiling, chaotic two-phase bubble motion may create favorable conditions for secondary nucleation, as discovered by Bergman and Mesler (1981) and Carroll and Mesler (1981), to exist.

Acknowledgments

This work was prepared for the David Taylor Research Center and funded by the Naval Postgraduate School. The paper was written while the first author was in residence at the Institut für Technische Thermodynamik und Thermische Verfahrenstechnik, Universität Stuttgart, as an Alexander von Humboldt U.S. Senior Scientist. He would, therefore, like to express his gratitude to the Alexander von Humboldt-Stiftung, Germany.

References

Auracher, H., 1990, "Transition Boiling," *Proceedings 9th International Heat Transfer Conf.*, Jerusalem, Vol. 1, pp. 69–90.

Bar-Cohen, A., and Simon, T. W., 1988, "Wall Superheat Excursions in the Boiling Incipience of Dielectric Fluids," *Heat Transfer Engineering*, Vol. 9, No. 3, pp. 19–31.

Bergles, A. E., and Chyu, M. C., 1982, "Characteristics of Nucleate Pool Boiling From Porous Metallic Coatings," ASME JOURNAL OF HEAT TRANSFER, Vol. 104, pp. 279–285.

Bergles, A. E., and Kim, C. J., 1988, "A Method to Reduce Temperature Overshoots in Immersion Cooling of Electronic Devices," *Proceedings of the Intersociety Conf. on Thermal Phenomena in the Fabrication and Operation of Electronic Components*, IEEE, New York, pp. 100–105.

Bergles, A. E., and Bar-Cohen, A., 1990, "Direct Liquid Cooling of Microelectronic Components," *Advances in Thermal Modelling of Electronic Components and Systems*, A. Bar-Cohen and A. D. Kraus, eds., ASME Press, New York, pp. 282–288.

Bergman, T., and Mesler, R., 1981, "Bubble Nucleation Studies, Part I: Formation of Bubble Nuclei in Superheated Water by Bursting Bubbles," *AIChE Journal*, Vol. 27, No. 5, pp. 851–853.

Carroll, K., and Mesler, R., 1981, "Bubble Nucleation Studies, Part II: Bubble Entrainment by Drop-Formed Vortex Rings," *AIChE Journal*, Vol. 27, No. 5, pp. 853–855.

Chan, A. M. C., and Shoukri, M., 1987, "Boiling Characteristics of Small Multitube Bundles," ASME JOURNAL OF HEAT TRANSFER, Vol. 109, pp. 753–760.

Chen, Q., Windisch, R., and Hahne, E., 1989, "Pool Boiling Transfer on Finned Tubes," *Proceedings of Eurotherm Seminar No. 8, Advances in Pool Boiling Heat Transfer*, May 11–12, Paderborn, Germany, pp. 126–141.

Cornwell, K., Duffin, N. W., Schuller, R. B., 1980, "An Experimental Study of the Effects of Fluid Flow on Boiling Within a Kettle Reboiler Tube Bundle," ASME Paper No. 80-HT-45.

Cornwell, K., and Schuller, R. B., 1982, "A Study of Boiling Outside a Tube Bundle Using High Speed Photography," *Int. J. Heat Mass Transfer*, Vol. 25, pp. 683–690.

Cornwell, K., and Scoones, D. J., 1988, "Analysis of Low Quality Boiling on Plain and Low-Finned Tube Bundles," *Proceedings 2nd UK Heat Transfer Conf.*, Vol. 1, pp. 21–32.

Cornwell, K., 1989, "The Influence of Bubbly Flow on Boiling From a Tube in a Bundle," *Proceedings of Eurotherm Seminar No. 8, Advances in Pool Boiling Heat Transfer*, May 11–12, Paderborn, Germany, pp. 177–183.

Fujita, Y., Ohta, H., Hidaka, S., and Nishikawa, K., 1986, "Nucleate Boiling Heat Transfer on Horizontal Tubes in Bundles," *Proceedings of 8th Int. Heat Transfer Conf.*, San Francisco, Vol. 5, pp. 2131–2136.

Gebhart, B., Jaluria, Y., Mahajan, R. L., and Sammakia, B., 1988, *Buoyancy Induced Flows and Transport*, Hemisphere Publishing Co., Inc., New York, pp. 487–495.

Gopalen, B., and Mesler, V. R., 1990, "Surface Nucleate Boiling, Secondary Nucleation and Threshold Superheat," ASME HTD-Vol. 136, New York, pp. 7–12.

Hahne, E., and Müller, J., 1983, "Boiling on a Finned Tube and a Finned Tube Bundle," *Int. J. Heat Mass Transfer*, Vol. 26, pp. 849–859.

Hwang, T. H., and Yao, S. C., 1986, "Crossflow Boiling Heat Transfer in Tube Bundles," *Int. Communication Heat and Mass Transfer*, Vol. 13, pp. 493–502.

Jensen, M. K., and Hsu, J. T., 1988, "A Parametric Study of Boiling Heat Transfer in a Horizontal Tube Bundle," ASME JOURNAL OF HEAT TRANSFER, Vol. 110, pp. 976–981.

Jung, C. J., and Bergles, A. E., 1989, "Evaluation of Commerical Enhanced Tubes in Pool Boiling," Report DOE/ID/12772-1, Rensselaer Polytechnic Institute, Troy, NY.

Leong, L. S., and Cornwell, K., 1979, "Heat Transfer Coefficients in a Reboiler Tube Bundle," *The Chemical Engineer*, UK, Apr., pp. 219–221.

Marsters, G. F., 1972, "Arrays of Heated Horizontal Cylinders in Natural Convection," *Int. J. Heat Mass Transfer*, Vol. 15, pp. 921–933.

Marto, P. J., Mackenzie, D. K., and Rivers, A. D., 1977, "Nucleate Boiling in Thin Liquid Films," *AIChE Symposium Series*, Vol. 73, No. 164, pp. 228–235.

Marto, P. J., and Lepere, V. J., 1982, "Pool Boiling Heat Transfer From Enhanced Surfaces to Dielectric Fluids," ASME JOURNAL OF HEAT TRANSFER, Vol. 104, pp. 292-299.

Mesler, R., 1976, "A Mechanism Supported by Extensive Experimental Evidence to Explain High Heat Fluxes Observed During Nucleate Boiling," *AIChE Journal*, Vol. 22, p. 246.

Mesler, R., and Mailen, G., 1977, "Nucleate Boiling in Thin Liquid Films," *AIChE Journal*, Vol. 23, p. 954.

Müller, J., 1986, "Boiling Heat Transfer on Finned Tube Bundles: The Effect of Tube Position and Intertube Spacing," *Proceedings of 8th Int. Heat Transfer Conf.*, San Francisco, Vol. 5, pp. 2111-2116.

Nishikawa, K., Kusada, H., Yamansaki, K., and Tanaka, K., 1967, "Nucleate Boiling at Low Liquid Levels," *Bulletin JSME*, Vol. 10, p. 328.

Stephan, K., and Abdelsalam, M., 1980, "Heat Transfer Correlations for Natural Convection Boiling," *Int. J. Heat Mass Transfer*, Vol. 23, pp. 73-87.

Tong, W., Simon, T. W., and Bar-Cohen, A., 1988, "A Bubble Sweeping Heat Transfer Mechanism for Low-Flux Boiling on Downward-Facing Inclined Surfaces," ASME HTD-Vol. 104, New York, pp. 173-178.

Udomboresuwan, A., and Mesler, R., 1986, "The Enhancement of Nucleate Boiling by Foam," *Proceedings of 8th Int. Heat Transfer Conf.*, San Francisco, Vol. 6, pp. 2939-2944.

Wallner, R., 1974, "Heat Transfer in Flooded Shell and Tube Evaporators," *Proceedings 5th Int. Heat Transfer Conf.*, Tokyo, Vol. 5, pp. 214-217.

Wanniarachchi, A. S., Marto, P. J., and Reilly, J. T., 1986, "The Effect of Oil Contamination on the Nucleate Pool Boiling Performance of R-114 From a Porous Coated Surface," *ASHRAE Trans.*, Vol. 92, Pt. 2, pp. 525-538.

Wanniarachchi, A. S., Sawyer, L. M., and Marto, P. J., 1987, "Effect of Oil on Pool Boiling Performance of R-114 From Enhanced Surfaces," *Proceedings 2nd ASME-JSME Thermal Engineering Joint Conference*, Honolulu, HI, Vol. 1, pp. 531-537.

Webb, R. L., Choi, K. D., and Apparao, T. R., 1989, "A Theoretical Model for Prediction of the Heat Load in Flooded Refrigerant Evaporators," *ASHRAE Trans.*, Vol. 95, Pt. 1, pp. 326-338.

Webb, R. L., and Apparao, T. R., 1990, "A Performance of Flooded Refrigerant Evaporators With Enhanced Tubes," *Heat Transfer Engineering*, Vol. 11, No. 2, pp. 29-42.

Wege, M. E., and Jensen, M. K., 1984, "Boiling Heat Transfer From a Horizontal Tube in an Upward Flowing Two-Phase Crossflow," ASME JOURNAL OF HEAT TRANSFER, Vol. 106, pp. 849-855.

Yilmaz, S., and Westwater, J. W., 1980, "Effect of Velocity on Heat Transfer to Boiling Freon-113," ASME JOURNAL OF HEAT TRANSFER, Vol. 102, pp. 26-31.

Model of the Evaporating Meniscus in a Capillary Tube

L. W. Swanson[1]
Mem. ASME

G. C. Herdt[2]

Department of Engineering,
University of Denver,
Denver, CO 80208

A mathematical model describing the evaporating meniscus in a capillary tube has been formulated incorporating the full three-dimensional Young-Laplace equation, Marangoni convection, London-van der Waals dispersion forces, and nonequilibrium interface conditions. The results showed that varying the dimensionless superheat had no apparent effect on the meniscus profile. However, varying the dispersion number produced a noticeable change in the meniscus profile, but only at the microscopic level near the tube wall. No change in the apparent contact angle was observed with changes in the dimensionless superheat or dispersion number. In all cases, the dimensionless mean curvature was asymptotic to a value equal to that for a hemispherical meniscus. The local interfacial mass flux and total mass transfer rate increased dramatically as the dispersion number was increased, suggesting that surface coatings can play an important role in improving or degrading capillary pumping. The model also predicted that the local capillary pressure remains constant and equal to $2\sigma/r_c$ regardless of changes in the dimensionless superheat and dispersion number. It should be noted that the results in this study are theoretical in nature and require experimental verification.

Introduction

The capillary forces present in the evaporator and the condenser sections of capillary heat pumps (e.g., heat pipes or capillary pumped loops) constitute the basic driving force for internal fluid circulation. Under normal operating conditions, the rate at which fluid is circulated determines the energy transport capacity of the heat pump. The net capillary force is generated by the integral effect of the evaporating and condensing menisci.

Despite the complicated and interactive nature of these capillary forces, the heat transport capability of capillary heat pumps is usually determined by equating the capillary pressure to the liquid pressure drop in the wick or loop, assuming that the adverse capillary pressure in the condenser is negligible and the capillary pressure in the evaporator is maximum. The capillary pressure is commonly taken as $2\sigma/r_c$, where σ is the vapor-liquid surface tension and r_c is the average capillary radius. This is known as the wicking limitation and presumably represents the point at which dryout begins in the evaporator. In most situations, the maximum capillary pressure cannot be used to evaluate the local interfacial mass transfer rate, which is an intermediate boundary condition between the vapor and liquid phases. This is due to the fact that the transport phenomena in the thin film on the capillary wall, which is coupled to the meniscus, are dramatically affected by either evaporation or condensation. Under certain conditions, the interfacial processes may even be rate limiting.

Although capillary heat pumps have been studied extensively in the past, very little effort has been put forth to understand the basic mechanism describing the evaporating and condensing menisci in capillary structures. For example, the studies of Ambrose et al. (1987) and Beam (1985, 1987), which address the vapor-liquid interface in heat pipes, treat the interface as a macroscopic phenomenon and are semiempirical in nature since they require mass transfer data. This approach is very interesting and useful for predicting dry-out in certain capillary structures; however, a mathematical model derived from first principles should actually generate values for the mass transfer rate since the mass transfer rate is not a true parameter of the system. A second drawback of past macroscopic models describing the vapor-liquid interface is that they neglect microscopic interfacial phenomena taking place near the vapor-liquid-solid contact line, known as the interline. The pioneering work of Wayner and his co-workers (Wayner et al., 1976; Wayner, 1978, 1979, 1986) has shown that these effects significantly influence both the apparent contact angle and the heat flux in an evaporating meniscus for a smooth plane wall as well as a capillary tube. The inclusion of these effects into an integral formulation of the macroscopic interface similar to that derived by Ambrose et al. (1987) will yield a solution that does not require the use of mass transfer data. In capillary heat pumps, this type of integral formulation will also be amenable to formal optimization techniques, which can be used to determine the optimal radial and axial pore size distributions in the capillary structure. These distributions represent fabrication parameters that are essential to the design of advanced capillary structures. The foundation of this design technique, however, must begin with a fundamental understanding of the evaporating and condensing meniscus, preferably for a simple geometry characterizing common wicking material. The capillary tube is one such geometry and is the focus of this study.

Studies specifically addressing evaporation and condensation in capillary tubes have been undertaken by a number of investigators. To our knowledge, the earliest study of evaporation in isolated capillary tubes was conducted by Deryagin et al. (1965). They developed a model that included an adsorption isotherm based on dispersion forces as well as mass transport due to both vapor diffusion and film flow. They found that including mass transport in the thin film near the interline dramatically increased the rate of evaporation over that estimated solely by diffusion theory. They also confirmed their theoretical results with experimental data.

Preiss and Wayner (1976) conducted an experimental study of the evaporating meniscus near the exit of a capillary tube with ethanol as the working fluid. The meniscus was found to be stable over a wide range of evaporation rates and hydrostatic heads. They also concluded that fluid flow to the base of the stable evaporating meniscus was caused by a change in its curvature. Experiments at high evaporation rates demonstrated that sputtering occurred near the wall before the meniscus became unstable.

Wayner (1979) also developed a dispersion-based model of

---

[1] Currently at Heat Transfer Research, Inc., College Station, TX.

[2] Currently at the National Renewable Energy Laboratory, Golden, CO.

Contributed by the Heat Transfer Division and presented at the 3rd ASME/JSME Joint Thermal Engineering Conference, Reno, Nevada, March 17-22, 1991. Manuscript received by the Heat Transfer Division March 1991; revision received October 1991. Keywords: Evaporation, Heat Pipes and Thermosyphons, Thin-Film Flow.

the evaporating meniscus near the exit of a capillary tube. He found that viscous flow in the thin film near the interline significantly affected the entire meniscus profile. The model also predicted that increasing the interline heat flux reduced the capillary pressure by increasing the apparent contact angle. The impact of the dispersion forces on the evaporation process was highlighted by a comparison of the interline heat sink capability for different liquid-solid substrate combinations.

More recently, Meyer (1984) performed very interesting analytical assessments of evaporation in (1) isolated capillaries, (2) two interconnected capillaries of variable cross section, and (3) networks of capillary menisci. He found that large temperature gradients developed in localized neighborhoods of the menisci. For interconnected menisci, evaporation was found to proceed in statically unstable configurations, via so-called Haines jumps (Haines, 1930), due to the dynamic balance of surface tension, local evaporation rate, and viscous shear. His model unfortunately did not include dispersion forces common to the previous analytical studies.

The objectives of this study are to formulate and solve a mathematical model of the evaporating meniscus in a capillary tube to determine how the various forces at the interface influence the meniscus profile, the mass transfer rate, and the capillary pressure. The results will be used to identify what types of modifications should be made to capillary structures to enhance their heat transport capability. The capillary tube configuration was chosen because it represents a pore geometry both compliant to formal mathematical characterization and common to capillary structures.

Formulation of Mathematical Model

The forthcoming mathematical model describes the fluid mechanics, heat transfer, and interfacial phenomena characteristic of an isolated evaporating meniscus in a capillary tube. The formulation includes the full three-dimensional Young-Laplace equation, Marangoni convection, London-van der Waals dispersion forces, and nonequilibrium interface conditions. The formulation of this model has been strongly influenced by the work of Wayner and his co-workers (Wayner et al., 1976; Wayner, 1978, 1979, 1986) as well as the study of Mirzamoghadam and Catton (1988).

Figure 1 shows the various flow regions characterizing the transport processes near the evaporating meniscus in a capillary tube. The origin of the axial coordinate (x) is at the interline while the origin of the radial coordinate (r) is at the tube centerline. r_i is the distance from the axial centerline to the meniscus interface. Each region is briefly described as follows:

1 Thin film region ($<1\ \mu$m): the London-van der Waals forces (intermolecular dispersion forces) are important and significantly affect the transport phenomena in the thin film.

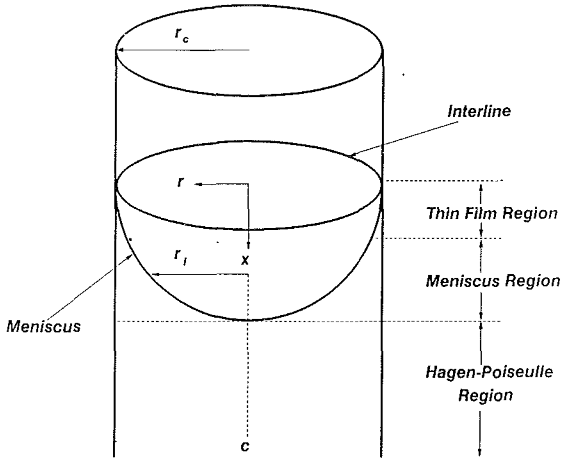

Fig. 1 Flow regions for an isolated evaporating meniscus in a capillary tube

2 Meniscus region ($>1\ \mu$m): London-van der Waals forces are small and the interfacial curvature dominates the capillary pressure creating an attenuated Hagen-Poiseuille flow field.

3 Hagen-Poiseuille region: Hagen-Poiseuille flow.

A mathematical model of the process can be formulated under the following assumptions:

1 Axial symmetry.
2 Steady-state two-dimensional laminar flow.
3 Incompressible flow.
4 The convective terms, with the exception of axial convection in the energy equation, are negligible.
5 The radial pressure gradient is negligible.
6 The temperature in the bulk vapor is equal to the interfacial vapor temperature.
7 The pressure in the bulk vapor is constant.
8 No slip at the wall.
9 The tube wall is smooth and the liquid is pure.
10 σ and $\bar{A}$ are not affected by interfacial curvature.
11 Retardation effects in $\bar{A}$ are negligible.
12 The hydrostatic pressure is negligible.
13 Marangoni effects are important only in the thin-film region.

Under these assumptions, the axial momentum equation describing flow in the meniscus and interline regions is

$$-\frac{dP_{li}}{dx}+\frac{\mu_l}{r}\frac{\partial}{\partial r}\left(r\frac{\partial u_l}{\partial r}\right)=0, \qquad (1)$$

with boundary conditions of

Nomenclature

$\bar{A}$ = dispersion coefficient, J
C = accommodation coefficient
D_1 = change in interface location with respect to position
F = function
G = dimensionless function
h_{fg} = latent heat of vaporization, J/kg
k_l = thermal conductivity in the liquid, W/m K
K = mean interfacial curvature, m^{-1}
$\dot{m}$ = liquid mass flow between the interface and tube wall, kg/s
$\dot{m}''$ = interfacial mass flux, kg/s m^2
P_{li} = pressure on the liquid side of the meniscus, N/m^2
P_{vi} = pressure on the vapor side of the meniscus, N/m^2
r = radial coordinate, m
r_c = tube radius, m
r_i = radial location of the meniscus, m
R = ideal gas constant divided by the molecular weight, J/kg K
T = temperature, K
T_i = interfacial temperature, K
u_l = liquid axial velocity, m/s
w_{li} = liquid interfacial velocity perpendicular to the meniscus, m/s
w_{vi} = vapor interfacial velocity perpendicular to the meniscus, m/s
x = axial coordinate, m
α = thermal diffusivity, m^2/s
θ = local contact angle
μ = viscosity, N s/m^2
ρ = density, kg/m^3
σ = surface tension, N/m

Subscripts

c = capillary
i = interface
l = liquid
v = vapor
w = capillary wall

$$r = r_i, \quad -\mu_l \frac{\partial u_l}{\partial r} = \frac{\partial \sigma}{\partial x},$$

$$r = r_c, \quad u_l = 0.$$

The first boundary condition is the shear stress interfacial condition, which equates the interfacial shear stress to the change in surface tension with respect to position. This condition accounts for Marangoni effects at the interface. The solution to this differential equation is straightforward yielding

$$u_l = \frac{1}{4\mu_l}\frac{dP_{li}}{dx}(r^2 - r_c^2) - \left(\frac{r_i}{\mu_l}\frac{d\sigma}{dx} + \frac{r_i^2}{2\mu_l}\frac{dP_{li}}{dx}\right)\ln\frac{r}{r_c}. \tag{2}$$

Applying l'Hopital's rule shows that this profile correctly reduces to the Hagen-Poiseuille velocity profile when the interface is at the axial center of the tube ($r = r_i = 0$). The liquid pressure in the velocity profile can be evaluated using the normal stress interfacial condition (also known as the modified Young-Laplace equation),

$$P_{li} = P_{vi} - 2\sigma K + \frac{\overline{A}}{(r_c - r_i)^3}. \tag{3}$$

The second term on the right-hand side of the equation is the capillary pressure due to interfacial curvature and the third term is the nonretarded disjoining pressure (Deryagin et al., 1965) for liquids due to the London-van der Waals forces near the interline. $\overline{A}$ is the dispersion coefficient and is negative for a wetting fluid. Note that in the thin film near the interline ($r_i \approx r_c$), the disjoining pressure significantly influences the capillary pressure; the disjoining pressure also decreases rapidly as the interface gets farther away from the tube wall. Equation (3) also assumes that the pressure forces, surface tension forces, and dispersion forces are simply additive at the vapor-liquid interface. This assumption is in accord with the thermodynamic (or force balance) derivation of the standard Young-Laplace equation for an isolated vapor-liquid interface found in Adamson (1982) and is probably accurate to leading order. However, it is important to note that the dispersion coefficient ($\overline{A}$) in the thin film is not only dependent on the dielectric behavior characterizing the liquid and vapor, but also the dielectric behavior of the solid substrate (e.g., see Israelachvili, 1985). The surface tension for an isolated vapor-liquid interface can also be written in terms of the dispersion forces between the vapor and liquid (Ivanov, 1988); thus, a rigorous derivation of the capillary pressure ($P_{vi} - P_{li}$) from first principles should inherently account for solid-liquid-vapor interactions. A unified expression of this type, in effect, will attenuate the vapor-liquid surface tansion in the film due to the presence of the solid substrate and also produce a disjoining pressure for thin films when there is no interfacial curvature.

An expression for the mean interfacial curvature in a capillary tube has been derived by Philip (1977) as

$$K = \frac{1}{2}\left\{\frac{1}{r_i[1 + (dr_i/dx)^2]^{1/2}} - \frac{d^2 r_i/dx^2}{[1 + (dr_i/dx)^2]^{3/2}}\right\}. \tag{4}$$

The mass flowing between the interface and wall (mass transfer rate) at any axial position in the liquid can be found by multiplying the liquid velocity by the liquid density and integrating over the flow cross-sectional area between the meniscus interface and the tube wall. This yields

$$\dot{m} = \frac{1}{F_1}\frac{dP_{li}}{dx} - \frac{F_2}{F_1}\frac{d\sigma}{dT_i}\frac{dT_i}{dx}, \tag{5}$$

where the chain rule has been used in the second term to accentuate the Marangoni effect ($d\sigma/dT_i$). The functions F_1 and F_2 are cumbersome functions of ρ_l, μ_l, r_c, and r_i, and are given in the appendix. The integral form of the mass continuity equation in the liquid is

$$r_i v_{li} = \frac{d}{dx}\int_{r_i}^{r_c} u_l r\,dr + r_i u_{li}\frac{dr_i}{dx}, \tag{6}$$

where the Leibnitz rule has been used to generate the second term on the right-hand side. This expression is essentially the interfacial kinematic condition, which accounts for evaporation at the interface. Multiplying this expression by $2\pi\rho_l$, substituting for u_l, integrating, and solving for v_{li} gives

$$v_{li} = \frac{1}{2\pi\rho_l r_i}\frac{d\dot{m}}{dx} + u_{li}\frac{dr_i}{dx}. \tag{7}$$

The interfacial velocity of the liquid normal to the interface is

$$w_{li} = v_{li}\cos\theta + u_{li}\sin\theta, \tag{8}$$

where θ is the local contact angle given by

$$\theta = \tan^{-1}\left(-\frac{dr_i}{dx}\right). \tag{9}$$

Equations (7), (8), and (9) can be combined to produce

$$w_{li} = \frac{\cos\theta}{2\pi\rho_l r_i}\frac{d\dot{m}}{dx}, \tag{10}$$

which shows the relationship between the liquid velocity normal to the interface, the local contact angle, and the change in the mass transfer rate with respect to position. An expression for the vapor mass flux at the interface has been derived by Schrage (1953) using kinetic theory

$$-\rho_v w_{vi} = \left(\frac{2C}{2-C}\right)\left(\frac{1}{2\pi R}\right)^{1/2}\left(\frac{P_{vi}}{T_{vi}^{1/2}} - \frac{P_v}{T_v^{1/2}}\right).$$

Assuming that the change in temperature between the interface and the bulk vapor is small ($T_v \approx T_i$), this expression reduces to

$$-\rho_v w_{vi} = \left(\frac{2C}{2-C}\right)\left(\frac{1}{2\pi R T_i}\right)^{1/2}(P_{vi} - P_v), \tag{11}$$

where C is the accommodation coefficient. A mass balance at the interface requires that

$$\rho_v w_{vi} = \rho_l w_{li}. \tag{12}$$

Combining Eqs. (10), (11), and (12) gives an expression for the interfacial pressure in the vapor phase,

$$P_{vi} = P_v - \left(\frac{2-C}{2C}\right)\left(\frac{RT_i}{2\pi}\right)^{1/2}\frac{\cos\theta}{r_i}\frac{d\dot{m}}{dx}. \tag{13}$$

Substituting this expression into Eq. (3) yields

$$P_{li} = P_v - \left(\frac{2-C}{2C}\right)\left(\frac{RT_i}{2\pi}\right)^{1/2}\frac{\cos\theta}{r_i}\frac{d\dot{m}}{dx} - 2\sigma K + \frac{\overline{A}}{(r_c - r_i)^3}. \tag{14}$$

Conservation of energy at the interface requires setting the heat flux normal to the interface equal to the latent heat required to evaporate the liquid, or after some manipulation

$$\frac{dT_i}{dx}\frac{dr_i}{dx} - \left.\frac{\partial T}{\partial r}\right|_{r=r_i} = \frac{h_{fg}}{2\pi\rho_l r_i}\frac{d\dot{m}}{dx}. \tag{15}$$

Assuming axial diffusion is small, conservation of energy in the liquid can be expressed as

$$u\frac{\partial T}{\partial x} = \frac{\alpha}{r}\frac{\partial}{\partial r}\left(r\frac{\partial T}{\partial r}\right), \tag{16}$$

with boundary conditions of

$$r = r_i, \quad T = T_i(x),$$

$$r = r_c, \quad T = T_w = \text{const}.$$

The solution to this partial differential equation is approximated using the von Karman integral method assuming a linear temperature profile of

$$T=T_i+\frac{T_w-T_i}{r_c-r_i}\,(r-r_i). \tag{17}$$

The resulting expression is

$$\left(\frac{F_3}{4\mu_l}\frac{dT_i}{dx}-\frac{r_i^2F_5}{2\mu_l}\frac{dT_i}{dx}+\frac{F_4}{4\mu_l}\frac{dr_i}{dx}-\frac{r_i^2F_6}{2\mu_l}\frac{dr_i}{dx}\right)\frac{dP_{li}}{dx}$$
$$+\left(\frac{r_iF_5}{\mu_l}\frac{d\sigma}{dT_i}\frac{dT_i}{dx}+\frac{r_iF_6}{\mu_l}\frac{d\sigma}{dT_i}\frac{dr_i}{dx}\right)\frac{dT_i}{dx}=\alpha(T_w-T_i), \tag{18}$$

where F_3, F_4, F_5, and F_6 are cumbersome functions of r_c, r_i, T_c, and T_i, and are given in the appendix. All equations to this point are now nondimensionalized using the following dimensionless variables:

$$\overline{x}=\frac{x}{r_c},\quad \overline{r}_i=\frac{r_i}{r_c},\quad \overline{T}_i=\frac{T_w-T_i}{T_w-T_v},\quad \overline{K}=Kr_c,$$
$$\overline{P}_{li}=\frac{P_{li}}{P_v},\quad \overline{\dot{m}}=\frac{h_{fg}}{r_ck_l(T_w-T_v)}\,\dot{m},\quad \overline{\sigma}=\frac{\sigma}{\sigma_w(T_w)}.$$

Combining and rearranging the previous equations produce the following set of dimensionless coupled nonlinear ordinary differential equations:

$$\frac{d\overline{r}_i}{dx}-D_1=0, \tag{19}$$

$$G_2\frac{d\overline{\sigma}}{d\overline{T}_i}\frac{d\overline{T}_i}{d\overline{x}}-\pi_1\frac{d\overline{P}_{li}}{d\overline{x}}+\pi_2G_1\overline{\dot{m}}=0, \tag{20}$$

$$\frac{d\overline{\dot{m}}}{d\overline{x}}+2\pi\overline{r}_iD_1\frac{d\overline{T}_i}{d\overline{x}}+\frac{2\pi\overline{r}_i}{1-\overline{r}_i}\overline{T}_i=0, \tag{21}$$

$$(2\overline{r}_i^2G_5-G_3)\frac{d\overline{T}_{li}}{d\overline{x}}\frac{d\overline{P}_{li}}{d\overline{x}}+(G_4-2\overline{r}_i^2G_6)D_1\frac{d\overline{P}_{li}}{d\overline{x}}$$
$$+\pi_3\overline{T}_i-\overline{r}_iG_5\frac{d\overline{\sigma}}{d\overline{T}_i}\left(\frac{d\overline{T}_i}{d\overline{x}}\right)^2+\overline{r}_i^2G_6\frac{d\overline{\sigma}}{d\overline{T}_i}D_1\frac{d\overline{T}_i}{d\overline{x}}=0, \tag{22}$$

$$\frac{dD_1}{d\overline{x}}-\pi_4G_7(1+D_1^2)^{3/2}\frac{\cos\theta}{\overline{\sigma}\,\overline{r}_i}\frac{d\overline{\dot{m}}}{d\overline{x}}-\frac{1+D_1}{\overline{r}_i}$$
$$-(1+D_1^2)^{3/2}\left\{4\pi_1(\overline{P}_{li}-1)+\frac{\pi_5}{(1-\overline{r}_i)^3}\right\}=0, \tag{23}$$

where Eq. (19) results from reducing the order of Eq. (23). The dimensionless functions G_1-G_7 are given in the appendix. Note that the dependent variables in this equation set are $\overline{r}_i$, $\overline{T}_i$, $\overline{\dot{m}}$, $\overline{P}_{li}$, and $D_1 = d\overline{r}_i/d\overline{x}$. The dimensionless initial conditions are specified at the interline ($x = 0$):

$$\overline{r}_{i,0}=1-\left(\frac{-\overline{A}T_v}{\rho_lr_c^3h_{fg}(T_w-T_v)}\right)^{1/3},$$

$$\overline{T}_{i,0}=0,$$

$$\overline{\dot{m}}_0=0,$$

$$\overline{P}_{li,0}=1-\frac{1}{4\pi_1\overline{r}_{i,0}}-\frac{\rho_lh_{fg}(T_w-T_v)}{P_vT_v},$$

$$D_{l,0}=0.$$

The above initial condition for $\overline{P}_{li,0}$ was obtained by evaluating Eq. (23) at $x = 0$, assuming the initial mean curvature was equal to $1/r_c$. This differs from most other theoretical studies, which assume the mean curvature is zero at the interline, even for a capillary tube geometry.

The above expression for $r_{i,0}$ is a modification of that derived by Wayner et al. (1976) for superheated adsorbed layers. One peculiarity in this expression is that the dimensionless adsorbed layer thickness ($1 - \overline{r}_{i,0}$) goes to infinity as the superheat, $T_w - T_v$, goes to zero under isothermal conditions. Adamson and Zebib (1980) showed that adsorbed layers coupled to a meniscus should be on order of 1000 Å for an isothermal system with a hydrostatic head pressure, suggesting that the expression derived by Wayner et al. is accurate only to leading order. A more rigorous derivation of the superheated adsorbed layer thickness using dispersion forces can likely be obtained by applying the theory of physical adsorption pioneered by Hill (1949a, 1949b, 1952). Instead of taking the solution thermodynamic point of view, this approach treats the adsorbed layer and solid substrate as a single phase in equilibrium with a vapor phase.

The dimensionless groupings in Eqs. (19)–(23) are:

$$\pi_1=\frac{r_cP_v}{4\sigma_w},$$

$$\pi_2=\frac{2\mu_lk_l(T_w-T_v)}{\pi r_c\rho_l\sigma_wh_{fg}},$$

$$\pi_3=\frac{\alpha\mu_l}{r_c\sigma_w},$$

$$\pi_4=\left(\frac{2-C}{2C}\right)\frac{R^{1/2}k_l(T_w-T_v)^{3/2}}{(2\pi)^{1/2}\sigma_wh_{fg}},$$

$$\pi_5=\frac{-\overline{A}}{\sigma_wr_c^2}.$$

π_2 is the dimensionless superheat, π_3 is the Crispation number, π_4 represents the mass flux at the interface, and π_5 is a dispersion number, which denotes the magnitude of the dispersion forces in the thin film. The Marangoni effects in Eqs. (19)–(23) are captured by terms containing $d\overline{\sigma}/d\overline{T}_i$.

Solution Method

The numerical technique used to solve Eqs. (19)–(23) incorporated both partial linearization and first-order backward finite differencing. The nonlinear terms in Eq. (22) were first linearized with respect to the first-order derivatives of the dependent variables using a Taylor series expansion around the previous iteration. The resulting equation set was then written in matrix form with the solution vector composed of the current iteration first-order derivatives. The elements in the coefficient matrix (5 × 5) contained constants, dependent variables, and/or previous iteration first derivatives. Similarly, the elements in the constant vector were composed of constants and/or dependent variables. A solution to the matrix equation was obtained at each axial position by solving the linear system, updating the dependent variables with first-order backward finite differencing, and then iterating until the derivative terms and dependent variables converged to a relative error of less than 10^{-8}. In most cases, the numerical scheme converged within 30 iterations. In order to prevent singularities in the matrix equation and initiate the numerical scheme, the initial values of $\overline{T}_{i,0}$, $\overline{\dot{m}}_0$, and $D_{1,0}$ were set equal to 1×10^{-11}, -1×10^{-11}, and -1×10^{-11}, respectively. Magnitudes less than this produced physically unrealistic solutions, i.e., a decreasing thin film thickness. An IBM PS-2 386 computer with a mathematical coprocessor was used to generate the numerical solutions. Run times for a complete solution were on the order of 5 minutes for a step size of 10^{-4}. The solution also converged at the theoretical rate when the step size was decreased.

Solutions using Eqs. (19)–(23) in the above matrix formulation could be attained only for values of $\overline{r}_i > 0.65$, starting from the capillary wall ($\overline{r}_{i,0} \approx 1$). This was due to the fact that the matrix equation became stiff at this point, forcing $dD_1/d\overline{x}$ to go to negative infinity prematurely. For the most part, this problem was alleviated by transforming the terms in the mean curvature as follows:

$$\bar{K}=\frac{1}{2}\left\{\frac{1}{\bar{r}_i[1+D_1^2]^{1/2}}-\frac{dD_1/d\bar{x}}{[1+D_1^2]^{3/2}}\right\}$$

$$=\frac{1}{2\bar{r}_iD_1}\frac{d(w\bar{r}_i)}{d\bar{x}}=\frac{1}{2\bar{r}_i}\frac{d(w\bar{r}_i)}{d\bar{r}_i}. \qquad (24)$$

where

$$w=(1+D_1^2)^{-1/2}.$$

Applying this transformation simply required modifying Eq. (23) and changing one initial condition: at $\bar{x} = 0$, $D_1 = 0$, giving $(w\bar{r}_i)_0 = \bar{r}_{i,0}$. Unfortunately, a solution to the transformed equation set could not be obtained near the interline ($\bar{x} \approx 0$) because the values of D_1, which were on the order of -1×10^{-11}, were too small to produce any change in $w\bar{r}_i$ using either double-precision or extended-precision arithmetic. Quadratic-precision arithmetic was not available to us on this machine.

The problems of both initiating the algorithm and obtaining solutions near the axial centerline were eliminated by starting the solution using the original equations and then at some point changing the equations to the transformed equation set to complete the solution. The value of D_1 at which this transition occurred was chosen as 10^{-3}. Tests of the hybrid algorithm showed that order of magnitude changes on either side of this transition value produced negligible changes in the overall solution. Using the hybrid algorithm, solutions could be attained for values of $\bar{r}_i < 0.20$.

One aspect of the physical problem that has not been discussed yet is the requirement that $D_1 \rightarrow -\infty$ as $\bar{r}_i \rightarrow 0$ (this represents the targeted endpoint for the above shooting method). Arbitrarily selecting combinations of parameters forced the far field meniscus either to curve abruptly and not intersect the axial centerline at all or to form a cusp at the axial centerline. The various parameter combinations also produced different values for the mass transfer rate. Thus, ensuring that the centerline condition is satisfied, which to our knowledge has not been done in any past studies of the evaporating meniscus in a capillary tube, is necessary since the total mass transfer rate is strongly dependent on the system parameters.

Further tests of the hybrid algorithm showed that the mean curvature outside the thin film was rapidly asymptotic to a constant value whose magnitude depended on the values of the parameters. This asymptotic property allowed us to define the various combinations of r_c, ΔT and $\bar{A}$ that ensured that $D_1 \rightarrow -\infty$ as $\bar{r}_i \rightarrow 0$. When the mean curvature is constant, Eq. (24) can be integrated from some initial point on the meniscus to an arbitrary location giving

$$wr_i-(wr_i)_{K=\mathrm{const}}=Kr_i^2-(Kr_i^2)_{K=\mathrm{const}}.$$

Because this expression applies at $r_i = 0$,

$$(r_i)_{K=\mathrm{const}}=\sqrt{\left(\frac{wr_i}{K}\right)_{K=\mathrm{const}}}. \qquad (25)$$

Solutions that satisfy this condition will guarantee that the targeted condition of $D_1 \rightarrow -\infty$ as $\bar{r}_i \rightarrow 0$ is achieved. It is interesting to note that, in all cases, meeting this criterion required that the dimensionless mean curvature be asymptotic to one, a value typically characterizing a hemispherical meniscus. This asymptotic behavior suggests that there is likely some mathematical justification for $\bar{K} \rightarrow 1$ outside the thin film region, although the proof will not be attempted here.

Results/Discussion

As stated earlier, the primary objectives of this study were to determine how the various forces at the interface influence the meniscus profile, the mass transfer rate, and the capillary pressure. As an example, room temperature hexane was chosen as the working fluid and the accommodation coefficient was assumed to be equal to one. The tube radius, superheat, and dispersion coefficient were chosen as independent parameters. Fluid properties were taken from Vargaftik (1975) and the range of values for the dispersion coefficient corresponded to those found in the literature (Wayner, 1978; Israelachvili, 1985). Various combinations of these parameters satisfying the axial boundary condition produced dimensionless parameter ranges of $2.47 \times 10^{-11} < \pi_2 < 1.34 \times 10^{-10}$ and $2.0 \times 10^{-10} < \pi_5 < 1.0 \times 10^{-9}$. Recall, π_2 represents a dimensionless superheat, while π_5 is the dispersion number. Note that all other dimensionless parameters are dependent on the material properties, the capillary radius, and/or the superheat; thus holding π_2 constant fixes all of the other dimensionless parameters except for π_5.

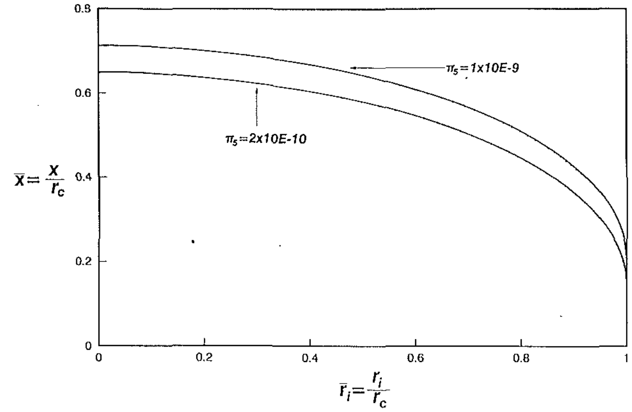

Fig. 2 Meniscus profiles for different values of the dispersion number

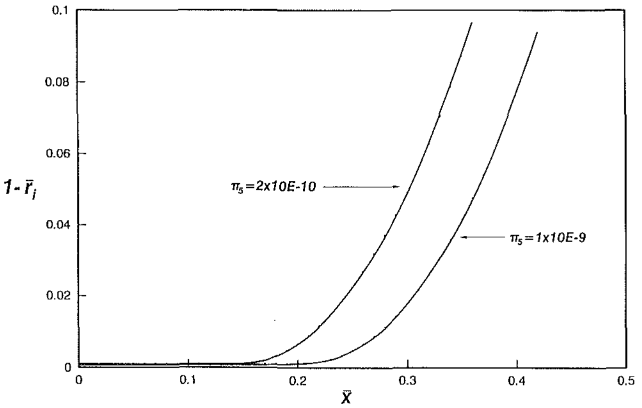

Fig. 3 Microscopic meniscus profiles for different values of the dispersion number

Figure 2 shows meniscus profiles for the extreme values of the dispersion number; all profiles for the intermediate values of the dispersion number fell between the two curves shown. One unexpected result shown in Fig. 2 is that varying the dimensionless superheat, for a constant dispersion number, had no apparent effect on the meniscus profile. However, varying the dispersion number did produce a noticeable change in the meniscus profile, but only at the microscopic level near the tube wall, as shown more explicitly by Fig. 3. This is highlighted by the fact that, under all conditions, the local contact angles become equal beyond about ten adsorbed layer thicknesses ($10[1 - \bar{r}_{i,0}]$). This location also loosely defines the point at which the dimensionless meniscus curvature is asymptotic to one. One noticeable difference in the microscopic characteristics of the menisci is that for larger dispersion numbers, the thin film extends farther down the tube due to the stronger attractive forces between the liquid and the solid sub-

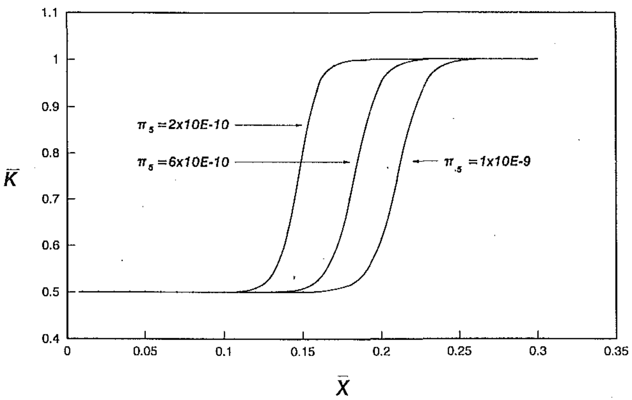

Fig. 4 Dimensionless mean curvature profile for different values of the dispersion number

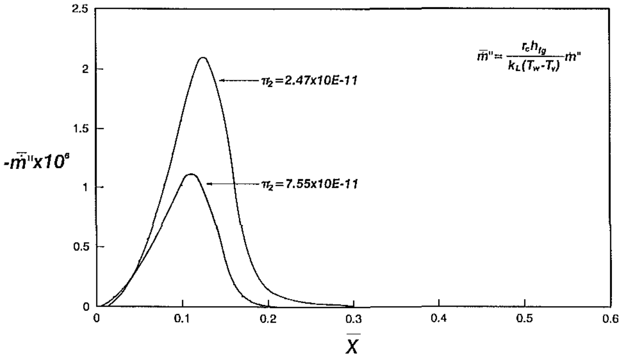

Fig. 5 Dimensionless interfacial mass flux profile for $\pi_5 = 2 \times 10^{-10}$

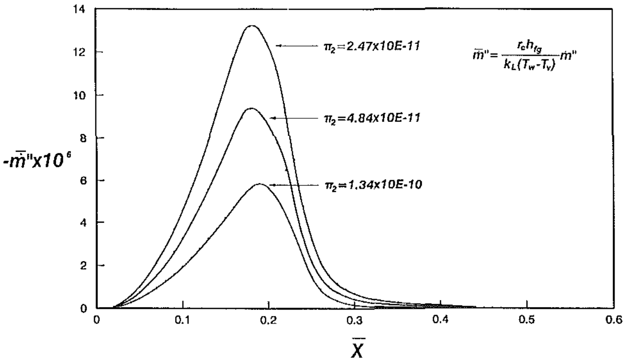

Fig. 6 Dimensionless interfacial mass flux profile for $\pi_5 = 1 \times 10^{-9}$

strate. This has a significant effect on the liquid pumping capability of the capillary tube.

Figure 4 depicts the dimensionless mean curvature as a function of axial position. As the dispersion number increases, the dimensionless mean curvature remains at approximately 0.5 farther down the tube. The first noticeable change in $\bar{K}$ occurs at $\bar{x} \approx 0.11$ for $\pi_5 = 2 \times 10^{-10}$ and $\bar{x} \approx 0.16$ for $\pi_5 = 1 \times 10^{-9}$. It is interesting to note in Fig. 3 that the first recognizable change in the microscopic interface radial location occurs at $\bar{x} \approx 0.15$ for $\pi_5 = 2 \times 10^{-10}$ and $\bar{x} \approx 0.22$ for $\pi_5 = 1 \times 10^{-9}$, corresponding to dimensionless mean curvature values of 0.8 and 0.89, respectively. Thus, the mean curvature is very near its asymptotic value of one before any significant change in the radial interface location can be observed.

The impact of the dispersion forces and superheat on the local interfacial mass flux is shown in Figs. 5 ($\pi_5 = 2 \times 10^{-10}$) and 6 ($\pi_5 = 1 \times 10^{-9}$). Both figures exhibit peaks in the dimensionless mass flux whose magnitudes tend to increase as the dimensionless superheat decreases. The reason for this counterintuitive behavior is that the dimensionless form of the

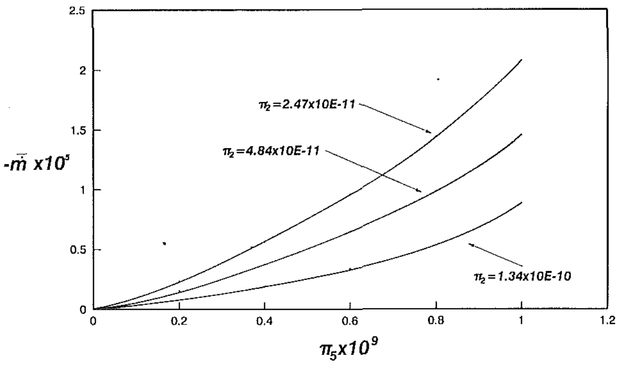

Fig. 7 Dimensionless mass transfer rate as a function of the dispersion number

mass flux (shown in each figure) is inversely proportional to the superheat. Dimensional values of the mass flux do indeed display the correct trends as the superheat increases; in fact, the dimensional mass flux is nearly directly proportional to the superheat.

Figures 5 and 6 also show that the location of the peak mass flux appears nearly constant with respect to the dimensionless superheat, although mild peak shifts occur in both curves. The peaks occur at approximately 0.12 and 0.18 for dispersion numbers of $\pi_5 = 2 \times 10^{-10}$ and $\pi_5 = 2 \times 10^{-10}$. At these locations and dispersion numbers, Fig. 4 shows that the mean curvature lies in the range $0.5 < \bar{K} < 0.55$; thus, most of the evaporation occurs in the thin film region. As expected, larger dispersion numbers, which reflect the fluid's affinity for the wall, produce larger local mass fluxes or tube pumping capability.

Increasing the dispersion number produces a similar trend in the dimensionless total mass transfer rate. Figure 7 depicts the mass transfer rate as a function of the dispersion number for various values of the dimensionless superheat. The counterintuitive decrease in the dimensionless total mass transfer rate with increasing superheat occurs for same reasons discussed earlier. The figure shows that increasing the dispersion number dramatically increases the mass transfer rate. As mentioned earlier, the cause for the increase in mass transfer rate is due to the stronger dispersion forces between the liquid and solid substrate, which increase both the thin film surface area and the liquid pressure difference. These results agree with previous studies, which also show that the dispersion forces in the thin film significantly influence the liquid pumping capability of capillary tubes.

Although experimental verification is still required, these findings, as well as others (Wayner, 1978, 1979), suggest that the presence of surface coatings in capillary structures can either enhance or degrade capillary pumping. For example, simply adding a surface coating that increases the dispersion number over that for the uncoated solid substrate should improve capillary pumping. Similarly, preventing an oxide coating from developing on a metallic capillary structure during heat pump fabrication or due to material/fluid incompatibility should prevent a reduction in capillary pumping.

Another interesting result produced by the model is shown in Fig. 8, which gives the dimensionless capillary pressure difference, $\bar{P}_{vi} - \bar{P}_{li}$, for all values of π_2 and π_5 as a function of capillary radius. The figure shows that the capillary pressure difference is only a function of the capillary radius, and is independent of the dispersion number and dimensionless superheat. This observation bears sharp contrast to the theoretical model of Wayner (1979), which predicts that increasing the interline heat flux reduces the capillary pressure by increasing the apparent contact angle. In our model, neither an increase in apparent contact angle nor a decrease in capillary pressure was observed as the dimensionless superheat was in-

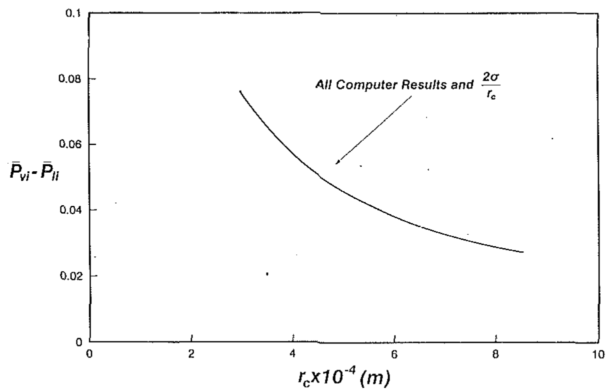

Fig. 8 Dimensionless capillary pressure as a function of the capillary radius for all values of π_2 and π_5

creased. Two possible explanations for the difference between our results and those of Wayner (1979) are: (1) the requirement that $D_1 \rightarrow -\infty$ as $\bar{r}_i \rightarrow 0$ forces the contact angle and capillary pressure to be constant and (2) the significantly lower superheats in our study (10^{-4}–10^{-3} K) are not high enough to show a discernible attenuation in the contact angle and capillary pressure. In fact, the capillary pressure generated by our model was found to be constant locally and equal to $2\sigma/r_c$ up to four decimal places. The local invariance in the capillary pressure and the fact that the dimensionless mean curvature is approximately equal to approximately 0.5 in the thin film leads us to believe that the term accounting for dispersion forces in Eq. (3) compensates for the lower curvature in the thin film. The reason that no significant changes in the capillary pressure in the thin film region were observed as the dispersion coefficient was increased is due to the initial adsorbed layer thickness: The initial adsorbed layer thickness increases as the dispersion coefficient to the 1/3 power. This renders the dispersion term in Eq. (3) constant at the initial condition and produces a constant capillary pressure throughout the thin film region regardless of the magnitude of the dispersion number.

Conclusions

A mathematical model describing the evaporating meniscus in a capillary tube has been formulated incorporating the full three-dimensional Young–Laplace equation, Marangoni convection, London–van der Waals dispersion forces, and nonequilibrium interface conditions. The governing equations and boundary conditions were cast in terms of five coupled nonlinear ordinary differential equations and solved numerically. Material properties characterizing hexane at room temperature and pressure were used to test the model for various values of the dimensionless superheat and dispersion number.

The results showed that varying the dimensionless superheat, for a constant dispersion number (number characterizing the London–van der Waals forces in the thin film region), had no apparent effect on the meniscus profile. However, varying the dispersion number did produce a noticeable change in the meniscus profile, but only at the microscopic level near the tube wall. No change in the apparent contact angle was observed with changes in the dimensionless superheat or dispersion number. In all cases, the dimensionless mean curvature was asymptotic to a value equal to that for a hemispherical meniscus. At the microscopic scale, larger dispersion numbers produced thin films, which extended farther down the tube, increasing the mass transfer surface area. The liquid pressure difference also increased with increasing dispersion number. These combined effects produced increases in the local interfacial mass flux and total mass transfer rate as the dispersion number was increased. Peaks in the mass flux were also observed in the thin film region. This has a significant effect on the liquid pumping capability of the capillary tube and suggests that surface coatings can play an important role in improving or degrading capillary pumping. The model also predicted that the local capillary pressure remains constant and equal to $2\sigma/r_c$ regardless of changes in the dimensionless superheat and dispersion number.

It should be noted that all the results in this work require experimental verification. Unfortunately, performing an experiment on a capillary tube with a radius less than 100 μm is a formidable task. It may be possible to set up an experiment with a bundle of capillary tubes to allow the measurement of an effective mass transfer rate. This would require more extensive modeling to account for the variation in tube wall temperature between the outer wall and the bundle centerline. Similar tests on tubes, or vertical flat plates, with vapor-deposited surface layers of varying thickness and material type, should clarify the effect surface coatings have on meniscus pumping capability.

Acknowledgments

Primary support for this research was provided by Universal Energy Systems, Inc. for the Air Force Office of Scientific Research under Contract F49620-88-C-0053/SB5881-0378. Partial support was furnished by the Space Technology Center for the Strategic Defense Initiative. We would also like to thank Michael Powell at the Edwards Air Force Base Astronautics Laboratory and Professor Roger Salters at the University of Denver for their very stimulating and helpful discussions.

References

Adamson, A. W., and Zebib, A., 1980, "Transition Region Between an Infinite Plane Meniscus and an Absorbed Film," *Journal of Physical Chemistry*, Vol. 84, pp. 2619–2623.

Adamson, A. W., 1982, *Physical Chemistry of Surfaces*, 4th ed., Wiley, New York.

Ambrose, J. H., Chow, L. C., and Beam, J. E., 1987, "Transient Heat Pipe Response and Rewetting Behavior," *Journal of Thermophysics and Heat Transfer*, Vol. 1, No. 3, pp. 222–227.

Beam, J. E., 1985, "Unsteady Heat Transfer in Heat Pipes," Ph.D. Dissertation, School of Engineering, University of Dayton, OH.

Beam, J. E., 1987, "Transient Heat Pipe Analysis," AIAA Paper No. 85-0936.

Deryagin, B. V., Newpin, S. V., and Churayev, N. V., 1965, "Effect of Film Transfer Upon Evaporation of Liquids From Capillaries," *Bull. R.I.L.E.M.*, Vol. 29, pp. 93–98.

Haines, W. B., 1930, "Studies in the Physical Properties of Soils, Part V," *Journal of Agric. Sci. Camb.*, Vol. 20, p. 97.

Hill, T. L., 1949a, "Statistical Mechanics of Adsorption. V. Thermodynamics and Heat of Adsorption," *Journal of Chemical Physics*, Vol. 17, No. 6, pp. 520–535.

Hill, T. L., 1949b, "Thermodynamic Transition From Absorption to Solution," *Journal of Chemical Physics*, Vol. 84, No. 6, p. 507.

Hill, T. L., 1952, "Theory of Physical Adsorption," in: *Advances in Catalysis*, IV, Academic Press, New York, pp. 211–258.

Israelachvili, J. N., 1985, *Intermolecular and Surface Forces With Application to Colloidal and Biological Systems*, Academic Press, New York.

Ivanov, I. B., 1988, *Thin Liquid Films*, Marcel Dekker, Inc., New York.

Meyer, R. E., 1984, "Note on Evaporation in Capillaries," *IMA Journal of Applied Mathematics*, Vol. 32, pp. 236–252.

Mirzamoghadam, A., and Catton, I., 1988, "A Physical Model of the Evaporating Meniscus," ASME JOURNAL OF HEAT TRANSFER, Vol. 110, pp. 201–207.

Philip, J. R., 1977, "Unitary Approach to Capillary Condensation and Adsorption," *Journal of Chemical Physics*, Vol. 66, No. 11, pp. 5069–5075.

Preiss, G., and Wayner, P. C., Jr., 1976, "Evaporation From a Capillary Tube," ASME JOURNAL OF HEAT TRANSFER, Vol. 98, No. 2, pp. 178–181.

Schrage, R. W., 1953, *A Theoretical Study of Interphase Mass Transfer*, Columbia University Press, New York.

Vargaftik, N. B., 1975, *Tables on the Thermophysical Properties of Liquids and Gases*, 2nd ed., Wiley, New York.

Wayner, P. C., Jr., Kao, Y. K., and LaCroix, L. V., 1976, "The Interline Heat-Transfer Coefficient of an Evaporating Wetting Film," *International Journal of Heat and Mass Transfer*, Vol. 19, pp. 487–492.

Wayner, P. C., Jr., 1978, "The Effect of the London-Van der Waals Dispersion Force on Interline Heat Transfer," ASME JOURNAL OF HEAT TRANSFER, Vol. 100, No. 1, pp. 155–159.

Wayner, P. C., Jr., 1979, "Effect of Thin Film Heat Transfer on Meniscus Profile and Capillary Pressure," *AIAA Journal*, Vol. 17, No. 7, pp. 772–776.

Wayner, P. C., Jr., 1986, "The Use of Interfacial Phenomena in Change-of-Phase Heat Transfer," *Heat Transfer in Thermal Systems Seminar—Phase II*, National Cheng Kung University, Tainan, Taiwan.

APPENDIX

The dimensional forms of the mathematical functions ($\{F_i\}$) generated during the formulation of the problem are:

$$F_1=\frac{\dfrac{8\mu_1}{\pi\rho_l}}{-3r_i^4+4r_c^2r_i^2-r_c^4+r_i^4\ln\left(\dfrac{r_i}{r_c}\right)}, \tag{A1}$$

$$F_2=\frac{4\left(r_i^3-r_c^3r_i-2r_i^3\ln\left(\dfrac{r_i}{r_c}\right)\right)}{-3r_i^4+4r_c^2r_i^2-r_c^4+r_i^4\ln\left(\dfrac{r_i}{r_c}\right)}, \tag{A2}$$

$$F_3=-\frac{1}{4}\,(r_c^2-r_i^2)^2-\frac{-\dfrac{2}{5}\,r_c^5+\dfrac{1}{20}\,r_i^5+\dfrac{1}{4}\,r_c^4r_i-\dfrac{1}{6}\,r_c^2r_i^5}{r_c-r_i}, \tag{A3}$$

$$\begin{aligned}F_4=&\,T_i(-r_i^3+r_c^2r_i)+\frac{1}{4}\,\frac{T_w-T_i}{r_c-r_i}\,(r_c^2-r_i^2)^2\\&-\frac{T_w-T_i}{(r_c-r_i)^2}\left(-\frac{2}{15}\,r_c^5+\frac{1}{20}\,r_i^5+\frac{1}{4}\,r_c^4r_i-\frac{1}{6}\,r_c^2r_i^3\right),\end{aligned} \tag{A4}$$

$$\begin{aligned}F_5=&-\frac{1}{2}\,r_i^2\ln\left(\frac{r_i}{r_c}\right)-\frac{1}{4}\,(r_c^2-r_i^2)\\&-\frac{\dfrac{1}{6}\,r_i^3\ln\left(\dfrac{r_l}{r_c}\right)-\dfrac{1}{9}\,r_c^3+\dfrac{1}{4}\,r_c^2r_i-\dfrac{5}{36}\,r_i^3}{r_c-r_i},\end{aligned} \tag{A5}$$

$$\begin{aligned}F_6=&-T_ir_i\ln\left(\frac{r_i}{r_c}\right)+\frac{T_w-T_i}{r_c-r_i}\left\{\frac{1}{2}\,r_i^2\ln\left(\frac{r_i}{r_c}\right)+\frac{1}{4}\,(r_c^2-r_i^2)\right\}\\&-\frac{T_w-T_i}{(r_c-r_i)^2}\left\{\frac{1}{2}\,r_i^3\ln\left(\frac{r_i}{r_c}\right)+\frac{1}{4}\,r_c^2r_i-\frac{1}{4}\,r_i^3\right.\\&\left.-\frac{1}{3}\,r_i^3\ln\left(\frac{r_i}{r_c}\right)-\frac{1}{9}\,(r_c^3-r_i^3)\right\},\end{aligned} \tag{A6}$$

The nondimensional mathematical functions ($\{G_i\}$) found in the dimensionless working equation set (19)–(23) are:

$$G_1=\frac{1}{-3\bar{r}_i^4+4\bar{r}_i^2-1+4\bar{r}_i^4\ln\bar{r}_i}, \tag{A7}$$

$$G_2=(\bar{r}_i^3-\bar{r}_i-\bar{r}_i^3\ln\bar{r}_i)\,G_1, \tag{A8}$$

$$G_3=-\frac{1}{4}\,(1-\bar{r}_i^2)^2-\frac{-\dfrac{2}{5}+\dfrac{1}{20}\,\bar{r}_i^5+\dfrac{1}{4}\,\bar{r}_i-\dfrac{1}{6}\,\bar{r}_i^3}{1-\bar{r}_i}, \tag{A9}$$

$$\begin{aligned}G_4=&\,\frac{T_w}{T_w-T_v}\,(-\bar{r}_i^3+\bar{r}_i)-(-\bar{r}_i^3+\bar{r}_i)\,\bar{T}_i-\frac{1}{4}\,\frac{(1-\bar{r}_i^2)^2}{1-\bar{r}_i}\,\bar{T}_i\\&+\frac{-\dfrac{2}{5}+\dfrac{1}{20}\,\bar{r}_i^5+\dfrac{1}{4}\,\bar{r}_i-\dfrac{1}{6}\,\bar{r}_i^3}{(1-\bar{r}_i)^2}\,\bar{T}_i,\end{aligned} \tag{A10}$$

$$G_5=-\frac{1}{2}\,\bar{r}_i^2\ln\bar{r}_i-\frac{1}{4}\,(1-\bar{r}_i^2)-\frac{\dfrac{1}{6}\,\bar{r}_i^3\ln\bar{r}_i-\dfrac{1}{9}+\dfrac{1}{4}\,\bar{r}_i-\dfrac{5}{36}\,\bar{r}_i^3}{1-\bar{r}_i}, \tag{A11}$$

$$\begin{aligned}G_6=&-\frac{T_w}{T_w-T_v}\,\bar{r}_i\ln\bar{r}_i+\bar{r}_i\bar{T}_i\ln\bar{r}_i+\frac{\dfrac{1}{2}\,\bar{r}_i^2\ln\bar{r}_i+\dfrac{1}{4}(1-\bar{r}_i^2)}{1-\bar{r}_i}\,\bar{T}_i\\&-\frac{\dfrac{1}{6}\,\bar{r}_i^3\ln\bar{r}_i-\dfrac{1}{9}+\dfrac{1}{4}\,\bar{r}_i-\dfrac{5}{36}\,\bar{r}_i^3}{(1-\bar{r}_i)^2}\,\bar{T}_i,\end{aligned} \tag{A12}$$

$$G_7=\left(\frac{T_w}{T_w-T_v}-\bar{T}_i\right)^{1/2}, \tag{A13}$$

H. Honda
Institute of Advanced Material Study,
Kyushu University,
Kasuga, Fukuoka 816, Japan

B. Uchima
Kagawa Technical College,
Marugame, Kagawa 763, Japan

S. Nozu

E. Torigoe

S. Imai

Department of Mechanical Engineering,
Okayama University,
Tsushima, Okayama 700, Japan

Film Condensation of R-113 on Staggered Bundles of Horizontal Finned Tubes

Film condensation of R-113 on staggered bundles of horizontal finned tubes with vertical vapor downflow was experimentally investigated. Two tubes with flat-sided annular fins and four tubes with three-dimensional fins were tested. The condensate flow and heat transfer characteristics were compared with the previous results for in-line bundles of the same test tubes and a staggered bundle of smooth tubes. The decrease in heat transfer due to condensate inundation was most significant for the in-line bundles of the three-dimensional fin tubes, whereas the decrease was very slow for both the staggered and in-line bundles of the flat-sided fin tubes. The predictions of the previous theoretical model for a bundle of flat-sided fin tubes agreed fairly well with the measured data at a low vapor velocity. The highest heat transfer performance was provided by the staggered bundle of flat-sided fin tubes with fin dimensions close to the theoretically determined optimum values.

Introduction

Horizontal finned tubes are commonly used in shell and tube condensers in the refrigeration, air-conditioning, and process industries because of their high heat transfer performance. Systematic experimental data on the effects of fin geometry, tube material, condensing fluid, and vapor velocity on the performance of single horizontal finned tubes have been reported in the recent literature. Theoretical models that can predict the heat transfer coefficient with sufficient accuracy have also been proposed for a tube with flat-sided annular fins. Comprehensive reviews of relevant literature are given by Webb (1988), Marto (1988), and Sukhatme (1990).

A relatively small number of studies have reported on the condensation heat transfer performance of a bundle of horizontal finned tubes, which is subject to the combined effects of tube arrangement, velocity and flow direction of vapor, and condensate inundation from upper tubes. Katz and Geist (1948), Gogonin et al. (1983), Webb and Murawski (1990), and Murata et al. (1990) measured the row-by-row heat transfer coefficient for vapors condensing on the vertical columns of horizontal finned tubes. Mills et al. (1975) and Marto (1988) also obtained the row-by-row data for steam by using a liquid distributor tube for simulating condensate inundation. Nosetani et al. (1989) measured the local overall heat transfer coefficient for steam condensation in a large surface condenser. Smirnov and Lukanov (1972) and Honda et al. (1989a) measured the row-by-row heat transfer coefficient for refrigerants condensing on the staggered and in-line bundles of horizontal finned tubes with vertical vapor downflow, respectively. The former data were, however, affected by the presence of noncondensable gas in the condenser.

Most of the previous studies were concerned with the flat-sided fin tube. Honda et al. (1989a) and Webb and Murawski (1990) tested several finned tubes with distinctly different fin geometry and showed that the row effect was smallest for the flat-sided fin tube. Although these studies provide a considerable amount of information on the effects of various parameters, local heat transfer data obtained under specified conditions of tube arrangements, vapor velocity, and condensate inundation are still limited.

Ishihara and Palen (1983), McNaught and Cotchin (1989), and Honda et al. (1989b) proposed calculation methods for heat transfer during condensation on a bundle of horizontal flat-sided fin tubes. Ishihara and Palen (1983) and McNaught and Cotchin (1989) compared their results to available data for practical condensers and found good to reasonable agreement between predicted and actual surface areas. These theoretical models remain to be verified by direct comparison with the local heat transfer data. Honda et al. (1989b) compared their theoretical predictions to available local heat transfer data (Katz and Geist, 1948; Gogonin et al., 1983; Marto, 1988; Honda et al., 1989a) and found good to reasonable agreement between the two.

The objective of the present study is to obtain the row-by-row heat transfer data during condensation of R-113 on the staggered bundles of horizontal finned tubes with vertical vapor downflow. Following the previous study for in-line bundles (Honda et al., 1989a), two kinds of flat-sided fin tube and four kinds of three-dimensional fin tube are tested and their heat transfer characteristics are compared with the previous results.

Experimental Apparatus and Procedure

The experimental apparatus, which consisted of a natural circulation loop of refrigerant R-113 and a forced circulation loop of cooling water, is schematically shown in Fig. 1. It was basically the same as that used in the previous study for the in-line bundles of horizontal finned tubes (Honda et al., 1989a) with the exception of the test sections. The test sections were 3 × 15 (columns × rows) staggered bundles of horizontal finned tubes made of copper. The odd rows consisted of three active tubes and the even rows consisted of two active tubes and dummy half tubes on the side walls. Both the longitudinal and transverse tube pitches were 22 mm. These values were the same as those for the in-line tube bundles (Honda et al., 1989a). The tube bundles were assembled in a vertical duct with inner dimensions of 66×100 mm^2, as shown in Fig. 2. The side walls parallel to the tube axis were provided with viewing windows. A gutter for collecting the falling condensate on the duct wall was attached to the duct just downstream of the fifteenth row.

Six finned tubes with different fin geometry were tested.

Contributed by the Heat Transfer Division for publication in the JOURNAL OF HEAT TRANSFER. Manuscript received by the Heat Transfer Division March 1991; revision received October 1991. Keywords: Augmentation and Enhancement, Condensation, Finned Surfaces.

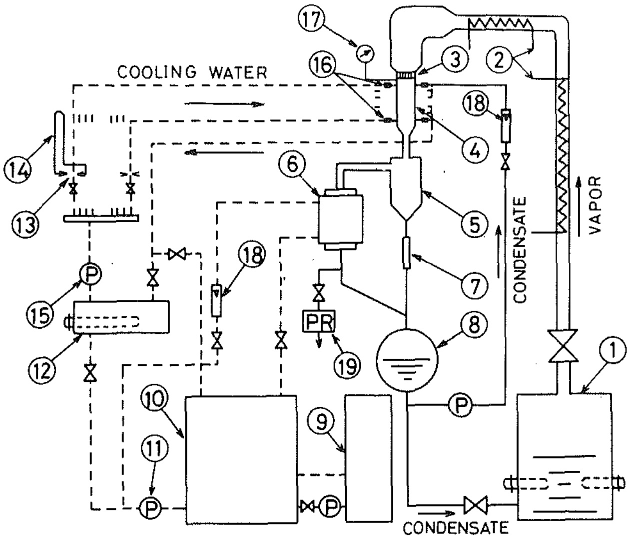

1 Boiler
2 Superheater
3 Calming section
4 Test section
5 Drain separater
6 Dump condenser
7 Condensate measuring tube
8 Condensate receiver
9 Chilling unit
10 Cooling water tank
11 Feed pump
12 Circulation tank
13 Orifice
14 Inverse U-tube manometer
15 Feed pump
16 Mixing chamber
17 Pressure gauge
18 Rotameter
19 Vacuum pump

Fig. 1 Schematic diagram of experimental apparatus

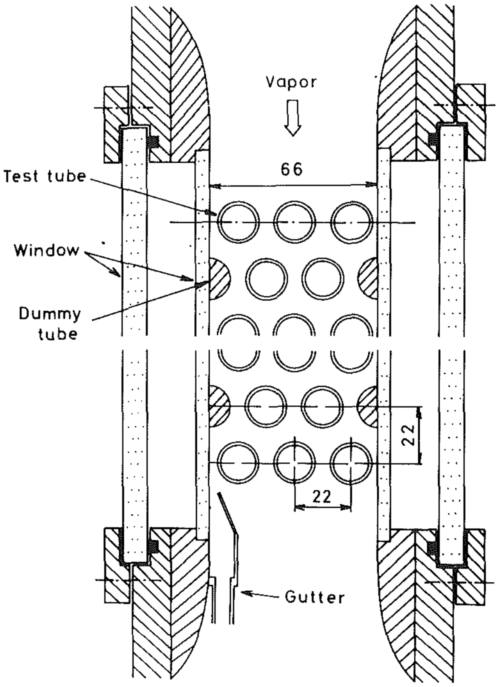

Fig. 2 Cross-sectional view of test section

Table 1 Dimensions of test tubes

Tube designation		A	B	C	D	E	F
Fin pitch	p mm	0.96	0.50	0.73	1.00	0.69	0.95
Fin height	h mm	1.43	1.30	0.99	1.28	1.01	1.14
Fin thickness at fin tip	t mm	0.24	0.05	----	----	----	----
Fin half tip angle	θ rad	0.082	0.047	----	----	----	----
Diameter at fin tip	d mm	15.60	16.10	15.85	15.80	15.86	15.81
Diameter at fin root	mm	12.74	13.50	13.87	13.24	13.84	13.53
Tube inside diameter	mm	11.21	11.80	12.09	11.39	12.22	12.04

These tubes were the same as those tested for the in-line tube bundles (Honda et al., 1989a). The dimensions of the test tubes are listed in Table 1, and the longitudinal cross section and close-up of these tubes are shown in Fig. 3. Tubes A and B had flat-sided annular fins, whereas tubes C–F had three-dimensional fins. Tubes A and C–F were obtained from tube manufacturers. Tube B was machined from a smooth tube. This tube had fin dimensions that were close to the optimum values obtained from the previous theoretical model (Honda et al., 1989b). The procedure for optimizing the fin dimensions is described in detail in Honda and Nozu (1990).

For tube A, two types of test section were used. One of the test sections consisted of 15 rows of active tubes. The other had two rows of inundation tubes at the top and the lower

Nomenclature

d = diameter at fin tip
g = gravitational acceleration
h = fin height
h_{fg} = specific latent heat of evaporation
k = number of active tubes in a tube row
l = effective length of tube
n = number of rows counted from top row
Nu = condensation number = $\alpha(\nu_l^2/g)^{1/3}/\lambda_l$
p = fin pitch
Q = heat transfer rate to coolant
Q_l = heat loss to environment
Re = film Reynolds number, Eq. (5)
T_s = saturation temperature
T_{wm} = average tube wall temperature at fin root for a tube row
ΔT = average condensation temperature difference for a tube row = $T_s - T_{wm}$
t = fin thickness at fin tip
u = vapor velocity based on minimum free cross section
W = flow rate of condensate leaving a tube row
α = average heat transfer coefficient for a tube row based on equivalent smooth tube area, Eq. (1)
γ = ratio of condensate transported to duct wall to total condensate leaving a tube row, Eq. (3)
ϵ = ratio of condensate flow rate on the duct wall to total condensate flow rate at the exit of a tube bundle, Eq. (4)
θ = fin half tip angle
λ_l = thermal conductivity of condensate
μ_l = dynamic viscosity of condensate
ν_l = kinematic viscosity of condensate

Subscripts

N = calculated value by the Nusselt equation for single smooth tube
n = nth row
o = tube bundle inlet

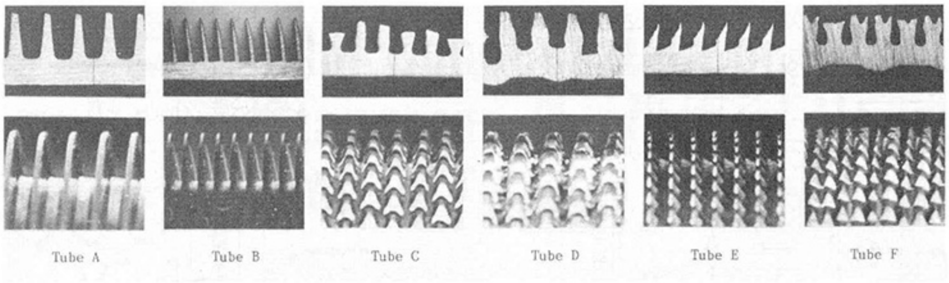

Fig. 3 Longitudinal cross section and close-up of test tubes

rows consisted of tube A. The latter was used to simulate condensation at a large condensate inundation rate. For tubes B–F, experiments were conducted using test sections that had two rows of inundation tubes at the top and one or two rows of these tubes at the twelfth to fourteenth rows. The remaining rows consisted of tube A.

The vapor gage pressure was measured by a precision Bourdon tube gage, reading to 10^2 Pa, connected to a pressure tap on the duct wall located 100 mm upstream of the first row. The atmospheric pressure was measured by a Fortin barometer. The vapor temperature was measured by two 1-mm-o.d. sheathed thermocouples inserted in the test section at 70 mm upstream and 70 mm downstream of the tube bundle, respectively. The temperature of the condensate returning to the boiler was also measured by a 1-mm-o.d. sheathed thermocouple. The cooling water temperatures at the inlet and outlet of each row were measured by two junction thermopiles inserted in mixing chambers. The tube wall temperature was measured by the resistance thermometry. The test tubes and a standard resister of 1 mΩ were connected in series by a lead wire to a 40 A d-c power supply. Voltage taps were soldered at both ends of each test tube. The thermocouple and thermopile outputs and the voltage drops of the test tubes and the standard resistor were read ten times consecutively and recorded by a programmable data logger to 1 μV. In the data reduction, the average values of the ten measurements were adopted as the experimental data. The cooling water flow rate for each tube row was measured using an orifice and an inverse U-tube manometer. The flow rate of condensate on the duct wall, collected by the gutter shown in Fig. 2, was also measured using an orifice and an inverse U-tube manometer.

Two kinds of experiment were performed at the vapor pressure of about 0.11 MPa ($T_s \simeq 323$ K). The first experiment was aimed at obtaining heat transfer data without the effect of condensate inundation. In this experiment the cooling water was passed through only the thirteenth row of the test section. The second experiment was aimed at obtaining heat transfer data under the combined effects of vapor shear and condensate inundation. In both the experiments, the power input to the boiler was changed in six steps from 5 to 45 kW, which corresponded to the vapor velocity (based on the minimum free cross section) at the tube bundle inlet u_o of 3.3 to 18.4 m/s. For each step of the power input, experimental data at the condensation temperature difference ΔT of 1.1 to 25 K were obtained by changing the flow rate and temperature of the cooling water entering the test section.

The cooling water temperature could be changed between 280 and 323 K by recirculating a part of the cooling water flowing out of the test section. Hotter water from the test section and colder water from the cooling water tank were mixed in a circulation tank and fed to the test section (see Fig. 1). Each flow rate was controlled by changing the valve opening. Fine control of the cooling water temperature was achieved by changing the power input to the electric heater installed in the circulation tank. The variation of the cooling water temperature among the ten measurements was within 0.04 K. The uncertainty in the measured ΔT value was believed to be less than 0.08 K.

During the experiments, the superheater was switched off. Thus, the measured vapor temperatures upstream and downstream of the test section were assumed to be equal to the local saturation temperatures. The local saturation temperature in the tube bundle was determined by an interpolation procedure taking account of the static pressure drop. Following the previous study for the in-line tube bundle, the measured wall temperature was assumed to be equal to the average temperature of a superficial smooth tube obtained by cutting off the fins. Then the fin root temperature T_w was obtained from the measured value making a small correction (<0.15 K) for the radial wall conduction for one half of the tube thickness. The possible error in the T_w value was estimated to be within 0.08 K. Further discussion of the measured wall temperature is given in the previous paper (Honda et al., 1989a). The average heat transfer coefficient α and the average condensation number Nu for each tube row were, respectively, defined as

$$\alpha = (Q - Q_l)/k\pi dl\Delta T \tag{1}$$

$$\mathrm{Nu} = \alpha(\nu_l^2/g)^{1/3}/\lambda_l \tag{2}$$

where Q is the heat transfer rate calculated from the temperature rise and flow rate of the cooling water, Q_l is the heat loss to the environment, k is the number of active tubes in the tube row ($=2$ or 3), l is the effective length of the test tube ($=100$ mm), $\Delta T = T_s - T_{wm}$, and T_{wm} is the average wall temperature at the fin root for each tube row. The Q_l value was obtained from a calibration curve determined by preliminary experiments. It was found that $Q_l/Q < 0.04$. The procedure for determining the calibration curve for Q_l is described in detail by Honda et al. (1989a). The uncertainties in these measurements led to an uncertainty of 5 percent in the α value for $\Delta T \geq 3$ K. In the data reduction, the physical properties of the condensate were evaluated at the reference temperature $T_{wm} + 0.3\Delta T$.

Experimental Results and Discussion

Behavior of Condensate. Figure 4 compares the condensate flow patterns at the first and thirteenth rows of tube A for low and high values of u_o. The film Reynolds number Re (defined by Eq. (5)) for each condensate flow pattern is also shown in Fig. 4. The observed flow patterns are basically the same as those for the in-line tube bundle (Honda et al., 1989a). In Fig. 4(*a*) for $u_o = 4.0$ m/s, the condensate falls from the tube bottom in the forms of droplets and condensate columns at the first and thirteenth rows, respectively. The falling condensate impinges on the lower tube and flows down the tube through a number of grooves between adjacent fins. The other grooves between the impinging points are not affected by the falling condensate. For the latter portion, the flooding level (below which the interfin space is almost completely filled with condensate) agrees well with the theoretical prediction for stagnant vapor (Honda et al., 1983). In Fig. 4(*b*) for $u_o = 17.7$ m/s, the flooding level is not so obvious. A part of the falling

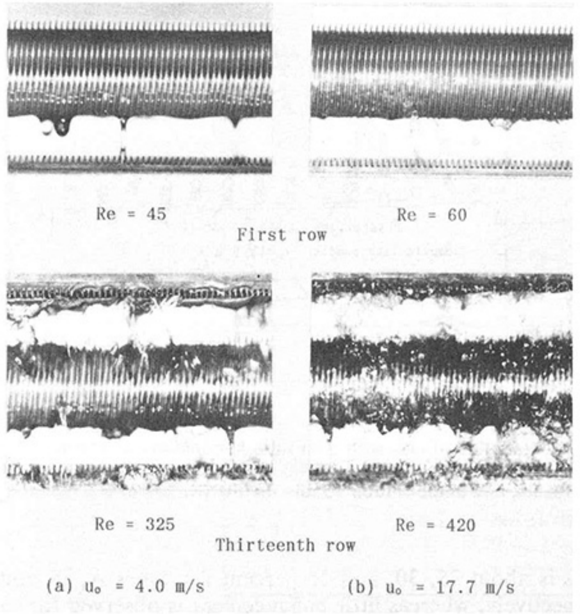

Fig. 4 Comparison of condensate flow patterns; tube A, $\Delta T \simeq 3$ K

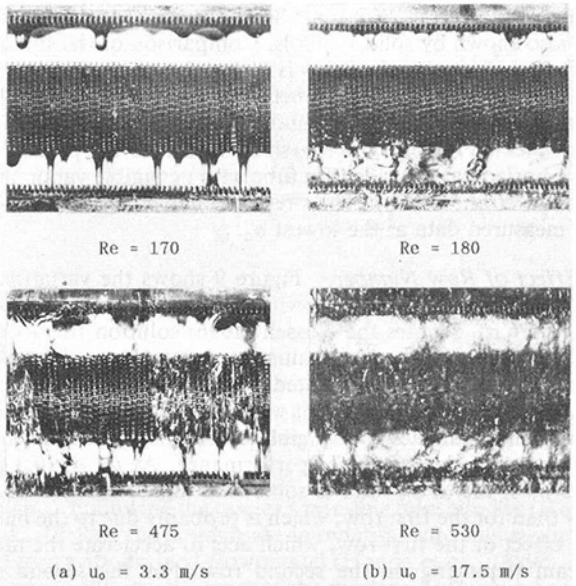

Fig. 5 Comparison of condensate flow patterns; tube D, $\Delta T \simeq 5$ K

condensate is disintegrated into small droplets by the vapor shear and impinges on the viewing window. However, the tube at the thirteenth row can be observed more clearly than the case of the in-line tube bundle (Honda et al., 1989a). This is due to the fact that some of the condensate falling on the viewing window is intercepted by the dummy half tubes at the twelfth row.

Figure 5 shows condensate flow patterns corresponding to the combination of low and high values of u_o and Re for tube D. Comparison with Fig. 4 reveals that the observed flow patterns are basically the same for tubes A and D. However, for the latter with three-dimensional fins, the flooding level is not clearly observed at low u_o and the generation of entrainment is more pronounced at high u_o.

It is relevant to note here that for tubes C–F with three-dimensional fins, the observed condensate flow pattern was the column mode for $u_o \leq 4$ m/s and Re $\geq$ 500. This is in contrast to the case of the in-line tube bundles (Honda et al., 1989a) where the observed flow pattern was the sheet mode for the same ranges of u_o and Re. This may be ascribed to a large difference in the vertical tube spacing between the two tube bundles (6.2 and 28.2 mm for the in-line and staggered tube bundles, respectively).

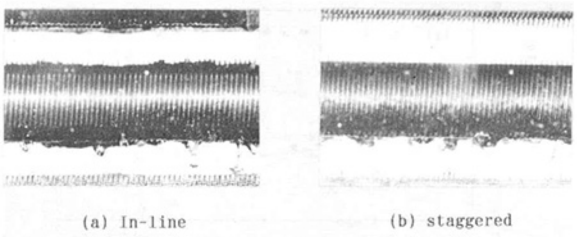

Fig. 6 Condensate flow patterns without condensate inundation; tube A, u_o = 17.7 m/s, $\Delta T \simeq 5$ K

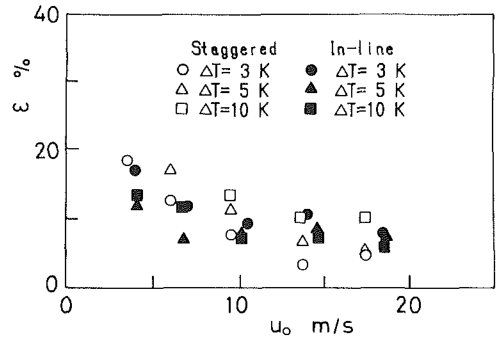

Fig. 7 Variation of ϵ with u_o; comparison of staggered and in-line (Honda et al., 1989a) tube bundles

Figure 6 compares the condensate flow patterns at a high vapor velocity between the in-line and staggered bundles of tube A without condensate inundation from the upper tubes. In Fig. 6(*a*) for the in-line tube bundle, the interfin space near the tube top is partially filled with condensate. In Fig. 6(*b*) for the staggered tube bundle, on the other hand, no condensate retention is observed near the tube top. This difference is related to the difference in the mainstream distribution between the two tube bundles. For the in-line tube bundle, the impact of the mainstream on the tube surface occurs at about 0.7 rad from the tube top, whereas it occurs at the tube top for the staggered tube bundle (Zukauskas, 1972). Thus, for the in-line tube bundle at high u_o, the condensate is retained near the tube top due to the positive pressure gradient and negative interfacial shear stress produced by the recirculating vapor flow downstream of the upper row.

Figure 7 shows the ratio of condensate falling on the duct wall to the total condensate flow rate, ϵ, for tube A plotted as a function of u_o with ΔT as a parameter. The ϵ value decreases gradually with increasing u_o. A relatively high ϵ value at low u_o was caused by the longitudinal flow of condensate hanging on the tube bottom toward the duct wall. Also shown in Fig. 7 are the previous results for the in-line bundle of tube A (Honda et al., 1989a). The two results are in fair agreement except that the staggered tube bundle shows a somewhat higher ϵ value at low u_o.

Heat Transfer Results

Effect of Vapor Velocity. Figure 8 shows the heat transfer results for the thirteenth row without condensate inundation from the upper tubes. In Figs. 8(*a–f*), experimental data for tubes A–F are plotted on the coordinates of α versus ΔT with u_o as a parameter, respectively. In each figure, the previous results for the in-line bundle of the same test tube (Honda et al., 1989a) are also shown by dash-dot lines. Generally, the

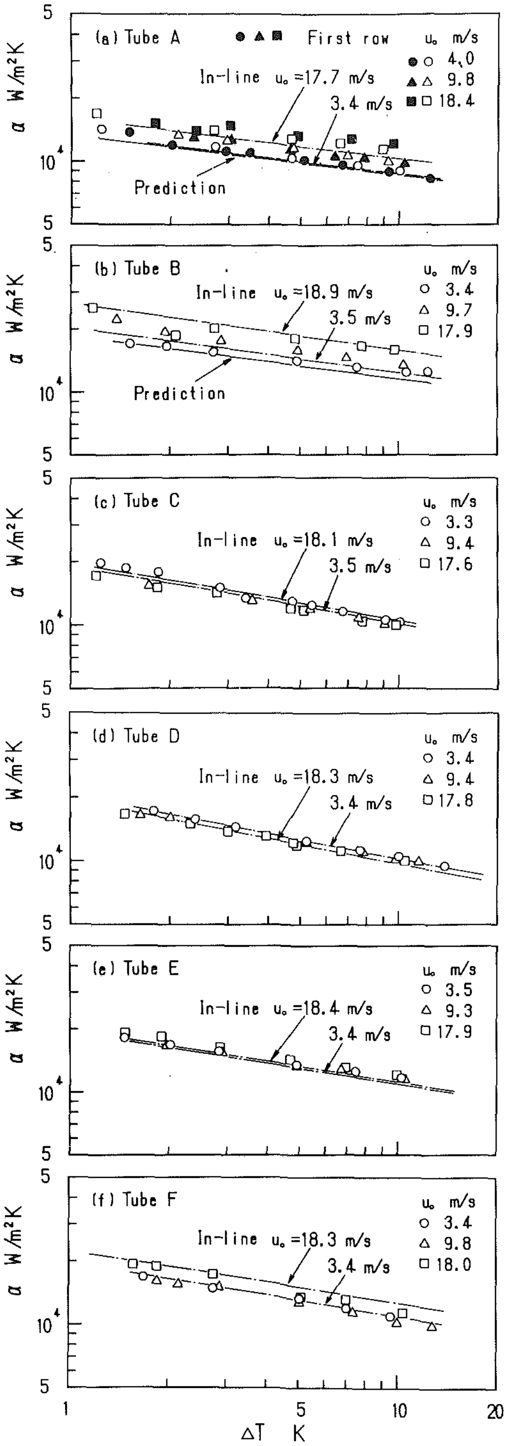

Fig. 8 Variation of α with ΔT for lower row without condensate inundation from upper tubes; comparison with in-line tube bundle results (Honda et al., 1989a) and theoretical predictions (Honda et al., 1989b).

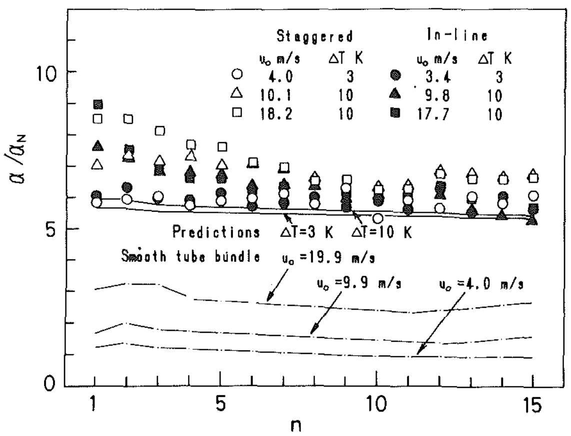

Fig. 9 Variation of α/α_N with n for tube A; comparison with in-line tube bundle results (Honda et al., 1989a), theoretical predictions (Honda et al., 1989b), and smooth tube bundle results (Honda et al., 1989c)

results for the staggered and in-line tube bundles are in fair agreement. This indicates that the difference in the condensate retention mode between the two tube bundles observed at high u_o (see Fig. 6) has a negligible effect on the average heat transfer performance.

Comparison of the results for tubes A–F reveals that the heat transfer coefficients for tubes B–F are almost the same at low ΔT and u_o. Tube A shows the lowest heat transfer coefficient at low u_o. Tube B shows the highest heat transfer coefficient at higher ΔT and u_o. The enhancement of heat transfer due to the increase of u_o from about 3.3 m/s to 18 m/s is about 25, 30, and 15 percent for tubes A, B, and F, respectively, whereas little enhancement is observed for tubes C–E. The foregoing results for tubes A and B are in accord with the previous results for refrigerants condensation on single flat-sided fin tubes (Gogonin and Dorokhov, 1977; Michael et al., 1989). In Fig. 8(*a*) for tube A, the data for the first row are also shown by solid symbols. Comparison of the first and thirteenth rows reveals that α is higher for the former at high u_o. However, the difference between the two is smaller than the case of the in-line tube bundle (Honda et al., 1989a). The solid lines in Figs. 8(*a*) and 8(*b*) show the theoretical predictions for a horizontal flat-sided fin tube with negligible vapor shear (Honda et al., 1989b). The predicted values agree well with the measured data at the lowest u_o.

Effect of Row Number. Figure 9 shows the variation of the enhancement ratio α/α_N with the row number n for tube A, where α_N denotes the Nusselt (1916) solution for a single smooth tube with the same values of d and ΔT as tube A. The experimental data are presented for three values of u_o. At u_o = 4.0 m/s, the α/α_N ratio is virtually constant for all tube rows. This indicates a negligible effect of condensate inundation on the heat transfer performance. At u_o = 10.1 and 18.2 m/s, the α/α_N ratio is somewhat higher for the second row than for the first row, which is probably due to the blockage effect of the first row, which acts to accelerate the mainstream impinging on the second row. For the second and subsequent rows, α/α_N decreases gradually with increasing n and takes almost a constant value for $n \geq 8$. The increase in the α/α_N ratio due to the increase of u_o from 4.0 to 18.2 m/s is about 44 percent for the first row and within 12 percent for the eighth and subsequent rows. It is relevant to note here that the vapor velocity at the tube bundle exit decreased to 1.5, 3.5, and 10.3 m/s for u_o = 4.0, 10.1, and 18.2 m/s, respectively. This indicates that the heat transfer performance is relatively insensitive to the vapor velocity at higher values of condensate inundation rate. Also shown in Fig. 9 are the experimental data for R-113 condensation on the in-line bundle of tube A (Honda et al., 1989a) and the staggered bundle of smooth tubes (Honda et al., 1989c), and theoretical predictions for a staggered bundle of horizontal flat-sided fin tubes with negligible vapor shear (Honda et al., 1989b). Comparison of the staggered and in-line tube bundles reveals that the α/α_N ratio is almost unchanged between the two at the lowest u_o. At higher values of u_o, the α/α_N ratio is somewhat higher for the staggered tube bundle at the second and subsequent rows. Comparison with the smooth tube bundle reveals that the heat transfer enhancement due to vapor shear is much smaller for tube A. It is also seen that the theoretical predictions are

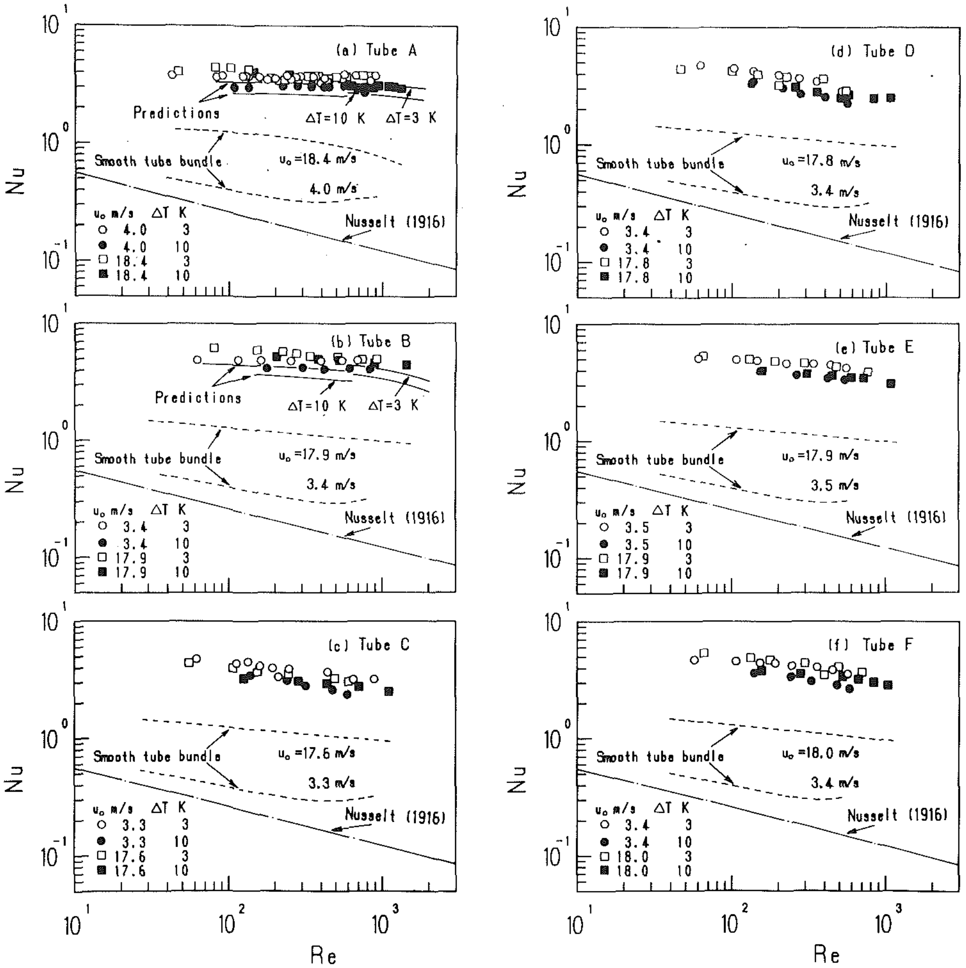

Fig. 10 Variation of Nu with Re; comparison with theoretical predictions (Honda et al., 1989b), smooth tube bundle correlation (Honda et al., 1989c), and Nusselt (1916) equation for single tube

generally smaller than the measurements. However, the deviation is within about 10 percent for $u_o = 4.0$ m/s.

Combined Effects of Vapor Shear and Condensate Inundation. Following the case of the in-line tube bundles (Honda et al., 1989a), the condensate inundation rate was evaluated by the gravity drained flow model (Honda et al., 1989c). According to this model, most of the condensate leaving the tube bottom falls vertically downward and impinges on the lower tube, whereas a small fraction γ of the condensate flows longitudinally toward the tube ends and falls down the duct wall. Thus, the flow rate of condensate leaving the nth row, W_n, is related to that at the $(n-2)$th row, W_{n-2}, and the heat transfer rate at the nth row, $(Q - Q_l)_n$, as follows:

$$W_n = (1-\gamma)W_{n-2} + (Q-Q_l)_n/h_{fg} \tag{3}$$

When γ is assumed to be constant for all rows, γ is related to ϵ, W_n, and $(Q - Q_l)_n$ as follows:

$$\epsilon = \gamma \sum_{n=1}^{15} W_n \Big/ \sum_{n=1}^{15} \{(Q-Q_l)_n/h_{fg}\} \tag{4}$$

The film Reynolds number for the nth row Re_n is defined as

$$\mathrm{Re}_n = 2W_n/k\mu_l l \tag{5}$$

The values of γ and W_n were obtained by substituting the measured values of $(Q - Q_l)_n$ and ϵ into Eqs. (3) and (4), and solving the resulting simultaneous equations iteratively. Then Re_n was obtained from Eq. (5). As can be seen from Figs. 4 and 5, the actual condensate flow pattern deviates from the gravity drained flow model as u_o increases. Comparison of the calculated Re_n values between this model and the uniformly dispersed flow model (Honda et al., 1989c), which is considered to be another extreme, revealed that the latter was larger than the former by about 60 percent for the second row, and 10 to 40 percent for the third and subsequent rows.

Figure 10 shows the heat transfer results for all tubes under combined effects of vapor shear and condensate inundation, where Nu is plotted as a function of Re with u_o and ΔT as parameters. The value of α at nominal ΔT was estimated from the measured data using the interpolation procedure adopted for the in-line tube bundle (Honda et al., 1989a). Generally, the Nu value is higher for higher u_o and smaller ΔT. Comparison of tubes A–F reveals that the Nu versus Re distribution is somewhat different in trend between tubes A and B with flat-sided annular fins and tubes C–F with three-dimensional fins. For tubes A and B, Nu decreases very slowly with increasing Re, and the effects of u_o and ΔT are less significant for larger Re. For tubes C–F, Nu decreases more sharply with increasing Re, and the effect of ΔT is more significant for larger Re. This indicates that the decrease of effective surface area (i.e., surface area covered with a thin condensate film) due to the increase of condensate inundation rate is more significant for the three-dimensional fin tube. This may be ascribed to the presence of longitudinal grooves between the three-dimensional fins, which act to equalize the condensate flow rate along the tube length and to retain some of the condensate within them.

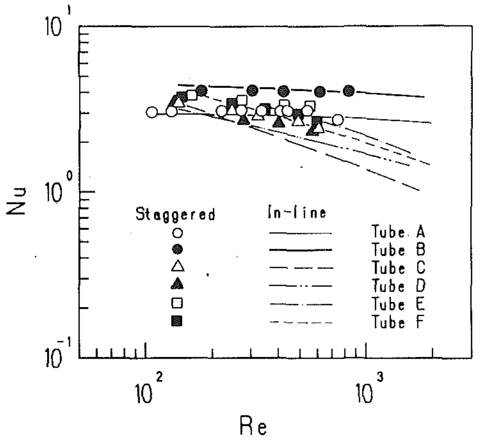

(a) $u_o \simeq 3.5$ m/s

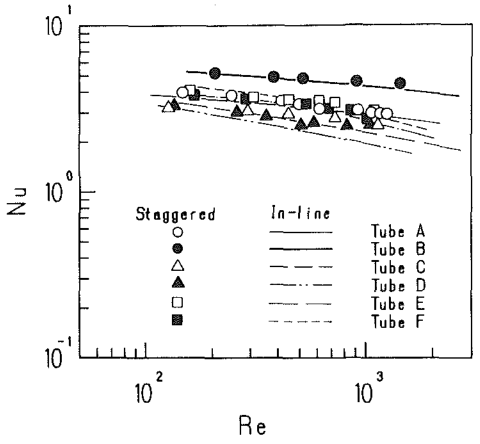

(b) $u_o \simeq 18$ m/s

Fig. 11 Variation of Nu with Re; comparison of staggered and in-line (Honda et al., 1989a) tube bundles, $\Delta T \simeq 10$ K

The solid, dotted, and dash-dot lines in Fig. 10 show the theoretical prediction for a staggered bundle of flat-sided fin tubes with negligible vapor shear (Honda et al., 1989b), the empirical equation for a staggered bundle of horizontal smooth tubes (Honda et al., 1989c), and the Nusselt (1916) equation for a horizontal smooth tube, respectively. It is seen that the predicted values of Nu for tubes A and B are 5 to 20 percent lower than the measured values for $u_o = 3.4 \sim 4.0$ m/s. The deviation is most significant at the transition point of the assumed condensate flow patterns between the column and sheet modes, where the predicted Nu value shows a stepwise change. Comparison of the smooth and finned tube bundles reveals that the heat transfer enhancement due to vapor shear is much smaller for the latter, which indicates the predominant effect of surface tension in enhancing film condensation on the fined tube.

Figure 11 shows a comparison of the present results for the staggered tube bundles with the previous results for the in-line tube bundles (Honda et al., 1989a) using the same test tubes. In Figs. 11(*a*) and 11(*b*), comparisons are made for low and high values of u_o, respectively. For tubes A and B with flat-sided annular fins, the heat transfer characteristics of the two tube bundles are virtually the same at low u_o, but the staggered tube bundle shows a slightly higher Nu value at high u_o. For tubes C–E with three-dimensional fins, the staggered tube bundle shows a higher Nu value than the in-line tube bundle irrespective of u_o, with the difference increasing with Re. For tube F with three-dimensional fins, on the other hand, the heat transfer characteristics of the two tube bundles are virtually the same. Comparison of all the data reveals that the highest heat transfer performance is provided by the staggered bundle of tube B with fin dimensions close to the theoretically determined optimum values. This indicates that the previously proposed method for optimizing the fin dimensions (Honda et al., 1990) can be an effective means for improving the design of shell and tube condensers. However, it should be noted that the theoretical model tends to underpredict the heat transfer coefficient at high values of u_o and Re (see Figs. 8–10). This is mainly due to the fact that the effects of vapor shear and the momentum of falling condensate were neglected in the theoretical model. The theory needs to be extended to include the effects of these factors to get a better agreement with the measured data.

Conclusions

Film condensation of downward flowing R-113 vapor on staggered bundles of horizontal finned tubes was experimentally investigated using six test tubes with different fin geometries. The results were compared with the previous results for in-line bundles of the same test tubes and a staggered bundle of smooth tubes. The conclusions are as follows:

1 For the flat-sided fin tubes, the falling modes of condensate were basically the same for the staggered and in-line tube bundles. For the three-dimensional fin tubes, different falling modes (i.e., column mode for the staggered tube bundle and sheet mode for the in-line tube bundle) were observed for the two tube bundles at a low vapor velocity and a high condensate inundation rate.

2 The flooding level of condensate for the flat-sided fin tubes agreed well with the theoretical prediction except for the region near the falling point of condensate. At a high vapor velocity, condensate retention was also observed near the top of the tube for the second and subsequent rows of the in-line tube bundle, whereas it was not observed for the staggered tube bundle.

3 The flat-sided fin tubes showed a very slow decrease in the heat transfer coefficient with increasing condensate inundation rate. The heat transfer performances of the in-line and staggered tube bundles were virtually the same at a low vapor velocity, but the latter showed a higher performance at a high vapor velocity.

4 The three-dimensional fin tubes showed a faster decrease in the heat transfer coefficient with increasing condensate inundation rate. The decrease was more marked for the in-line tube bundle and for a lower vapor velocity.

5 The measured heat transfer coefficient for the flat-sided fin tubes agreed well with the theoretical prediction at low values of the vapor velocity and condensate inundation rate. However, the former deviated toward a higher value with increasing the vapor velocity and condensate inundation rate.

6 Among the in-line and staggered bundles of the six finned tubes tested, the highest heat transfer performance was provided by the staggered bundle of the flat-sided fin tube with fin dimensions close to the theoretically determined optimum values.

References

Gogonin, I. I., and Dorokhov, A. R., 1977, "Heat Transfer in Condensation of Flowing R-21 Vapor on Horizontal Finned Tubes," *Khim. Neft. Mashinostr.*, No. 8, pp. 17–18.

Gogonin, I. I., Kabov, D. A., and Sosunov, V. I., 1983, "Heat Transfer in Condensation of R-12 Vapor on Bundles of Finned Tubes," *Kholodil'naya Tekhnika*, No. 1, pp. 26–29.

Honda, H., Nozu, S., and Mitsumori, K., 1983, "Augmentation of Condensation on Horizontal Finned Tubes by Attaching a Porous Drainage Plate," *Proceedings, ASME-JSME Thermal Engineering Joint Conference*, Vol. 3, pp. 289-295.

Honda, H., Uchima, B., Nozu, S., Nakata, H., and Torigoe, E., 1989a, "Film Condensation of Downward Flowing R-113 Vapor on In-Line Bundles of Horizontal Finned Tubes," ASME HTD-Vol. 108, pp. 117-125; also ASME JOURNAL OF HEAT TRANSFER, Vol. 113, No. 2, 1991, pp. 479-486.

Honda, H., Nozu, S., and Takeda, Y., 1989b, "A Theoretical Model of Film Condensation in a Bundle of Horizontal Low Finned Tubes," ASME JOURNAL OF HEAT TRANSFER, Vol. 111, No. 2, pp. 525-532.

Honda, H., Uchima, B., Nozu, S., Nakata, H., and Fujii, T., 1989c, "Condensation of Downward Flowing R-113 Vapor on Bundles of Horizontal Smooth Tubes," *Heat Transfer—Japanese Research*, Vol. 18, No. 6, pp. 31-52.

Honda, H., and Nozu, S., 1990, "Effects of Bundle Depth and Working Fluid on the Optimized Fin Geometry of a Horizontal Low Finned Condenser Tube," *Proceedings, 2nd Int. Symp. Condensers and Condensation*, HTFS, pp. 407-416.

Ishihara, K., and Palen, J. W., 1983, "Condensation of Pure Fluids on Horizontal Finned Tube Bundles," *Inst. Chem. Engrs. Symp. Ser.*, No. 75, pp. 429-446.

Katz, D. L., and Geist, J. M., 1948, "Condensation on Six Finned Tubes in a Vertical Row," *Trans. ASME*, Vol. 70, pp. 907-914.

Marto, P. J., 1988, "An Evaluation of Film Condensation on Horizontal Integral Fin Tubes," ASME JOURNAL OF HEAT TRANSFER, Vol. 110, No. 4(B), pp. 1287-1305.

McNaught, J. M., and Cotchin, C. D., 1989, "Heat Transfer and Pressure Drop in a Shell-and-Tube Condenser With Plain and Low-Fin Tube Bundles," *Chem. Eng. Res. Des.*, Vol. 67, pp. 127-133.

Michael, A. G., Marto, J. P., Wanniarachchi, A. S., and Rose, J. W., 1989, "Effect of Vapor Velocity During Condensation on Horizontal Smooth and Finned Tubes," ASME HTD-Vol. 114, pp. 1-10.

Mills, A. F., Hubbard, G. L., James, R. K., and Tan, C., 1975, "Experimental Study of Film Condensation on Horizontal Grooved Tubes," *Desalination*, Vol. 16, pp. 121-133.

Murata, K., Abe, N., and Hashizume, K., 1990, "Condensation Heat Transfer in a Bundle of Horizontal Integral-Fin Tubes," *Proc. 9th Int. Heat Transfer Conf.*, Vol. 4, pp. 259-264.

Nosetani, T., Hotta, Y., Sato, S., Onda, K., Nakamura, T., and Kato, Y., 1989, "In-Situ Evaluation of Enhanced Heat Transfer Tubes for Surface Condenser (SC Tubes)," ASME HTD-Vol. 108, pp. 97-104.

Nusselt, W., 1916, "Die Oberflächenkondensation des Wasserdampfes," *Zeit. Ver. Deut. Ing.*, Vol. 60, pp. 541-546, 569-575.

Pearson, J. F., and Withers, J. G., 1969, "New Finned Tube Configuration Improves Refrigerant Condensing," *ASHRAE Journal*, Vol. 11, pp. 77-82.

Smirnov, G. F., and Lukanov, I. I., 1972, "Study of Heat Transfer From Freon-11 Condensing on a Bundle of Finned Tubes," *Heat Transfer—Soviet Research*, Vol. 4, No. 3, pp. 51-56.

Sukhatme, S. P., 1990, "Condensation on Enhanced Surface Horizontal Tubes," *Proc. 9th Int. Heat Transfer Conf.*, Vol. 1, pp. 305-328.

Webb, R. L., 1988, "Enhancement of Film Condensation," *Int. Comm. Heat Mass Transfer*, Vol. 15, pp. 475-507.

Webb, R. L., and Murawski, C. G., 1990, "Row Effect for R-11 Condensation on Enhanced Tubes," ASME JOURNAL OF HEAT TRANSFER, Vol. 112, No. 3, pp. 768-776.

Zukauskas, A., 1972, "Heat Transfer From Tubes in Crossflow," *Advances in Heat Transfer*, T. F. Irvine, Jr., and J. P. Hartnett, eds., Academic Press, New York, Vol. 8, pp. 93-160.

Exciplex Fluorescence Thermometry of Falling Hexadecane Droplets

T. R. Hanlon

L. A. Melton

Department of Chemistry,
The University of Texas at Dallas,
Richardson, TX 75083

Exciplex fluorescence thermometry has been used to measure the temperature of 283 micron hexadecane droplets falling through a quiescent, oxygen-free, approximately 500°C ambient. After a period of negligible change, the derived droplet temperatures exhibit a sharp rise of about 100°C followed by a gentle increase to approximately 200°C. The derived temperatures, although averaged over most of the volume of the droplet, still provide some evidence of internal processes in the droplet due to the partially selective optical sampling of the droplet volume, in which fluorescence from the region between 0.50 and 0.75 of the droplet radius contributes disproportionately. At longer times, the droplet is presumed to be approximately homogeneous, and the exciplex fluorescence thermometry measurements provide accurate, interpretable temperatures for the freely falling droplets.

I Introduction

Attempts to model vaporizing fuel sprays depend strongly on the models of individual droplet heating and vaporization processes. To date where have been numerous theoretical (Dwyer and Sanders, 1988; Williams, 1985; Aggarwal et al., 1984) and experimental (Puri and Libby, 1989; Ray et al., 1988; Neal and Baganoff, 1985; Wang et al., 1984; Knight and Williams, 1980) studies. Several excellent reviews are available in the literature (Sirignano, 1983; Faeth, 1983; Law, 1982). Studies of the heat and mass transfer processes affecting individual droplets should lead to improved understanding, which can then be incorporated into the study of the complex dynamics of fuel sprays.

Currently, the literature contains little experimental data covering the temperature of droplets heating in a hot gas. The majority of the studies measuring this parameter are limited in the sense that the measurement itself was generally a perturbing factor. A typical measurement of droplet temperature involves insertion of a microthermocouple into a droplet suspended from a small wire (Trommelen and Crosby, 1970; Abdul-Rahman, 1969). Both the thermocouple and the suspension apparatus may interfere with the measurement and make interpretation difficult.

Recently, Wells and Melton (1990) published data covering temperature measurements of decane droplets falling through heated nitrogen. The technique of exciplex fluorescene thermometry (Murray and Melton, 1985), used by Wells and Melton (1990) to measure the temperature of droplets being heated in a hot gas, is a real-time, minimally perturbing, optical technique. In particular, this paper describes the use of low concentrations (approximately 50 ppm (w/w)) of the fluorescent dopant so that there is minimal perturbation of the droplet evaporation process.

Exciplex fluorescence thermometry can be both accurate and spatially precise, as has been demonstrated by Stufflebeam (1989) in his measurements of bulk fuel temperatures. One of the limitations of exciplex fluorescene thermometry (EFT) is that it requires that quenchers of the fluorescent dopants, in particular, oxygen, be excluded from both the liquid and gas phases of the system under investigation.

Seaver and Peele (1990) have reported a related, but different, noncontact fluorescent thermometry technique. They were able to measure temperatures between 0°C and 70°C in water drops by relying on the intensity changes in the fluorescence excitation spectrum of $[\mathrm{Eu(EDTA)(H_2O)}_x]^{-1}$. In that work, where the drops were acoustically levitated, exclusion of oxygen was not required since quenching does not affect excitation spectra, but $[\mathrm{Eu(EDTA)(H_2O)}_x]^{-1}$ is restricted to aqueous systems and, because spectral scans of the dye laser are required, the $[\mathrm{Eu(EDTA)(H_2O)}_x]^{-1}$ system cannot be used for real-time measurements.

In this work, we report the EFT-derived temperatures of 283 μm hexadecane droplets falling through hot nitrogen. EFT uses the temperature-dependent intensity ratio of spectrally separated emissions from a fluorescent dopant to derive the temperature of the hexadecane droplets as they heat up from room temperature. The highest measured droplet temperatures after 115 ms in an approximately 500°C ambient are near 200°C (the normal boiling point of hexadecane is 287°C). However, the temperature rise is not smooth; the inferred temperatures rise slowly, jump sharply, and finally increase slowly. It is possible that the sharp rise in the inferred temperature is due to partially selective optical sampling, perhaps of the core region of a vortex that arises due to internal circulation in the droplet. Images taken with a video microscopy system show that no significant evaporation occurs under the highest temperature conditions used.

In the study of droplet heating and vaporization, the internal spatially resolved temperature is of great importance. Such results are not yet available. Wells and Melton used high optical densities to restrict the absorption of light, and subsequent fluorescence, to a "near-surface" region. They cautiously interpreted results as near-surface temperatures. In these experiments with low optical densities, the distribution of excited molecules within the droplet and the subsequent collection of the fluorescence is not affected by the bulk absorptance of the molecules, but rather by refraction at the droplet/gas interface. Nonetheless, certain regions of the droplet (the volume between 0.5–0.75 of the radius) contribute most of the fluorescence and thus constitute the bulk of the "volume-averaged" temperature. Even in the absence of complete spatial information, these bulk experiments can still contribute to the understanding of droplet heating and evaporation, as for example the finding, cited in the previous paragraph that the droplet temperature is still some 80–90°C below the fluid boiling temperature after 120 ms in the heated ambient gas.

Because the excimer and monomer bands are quenched by oxygen at different rates, atmospheric oxygen will cause errors in inferred temperatures. Thus, exciplex fluorescence ther-

---

Contributed by the Heat Transfer Division for publication in the JOURNAL OF HEAT TRANSFER. Manuscript received by the Heat Transfer Division April 1991; revision received November 1991. Keywords: Combustion, Instrumentation, Sprays/Droplets.

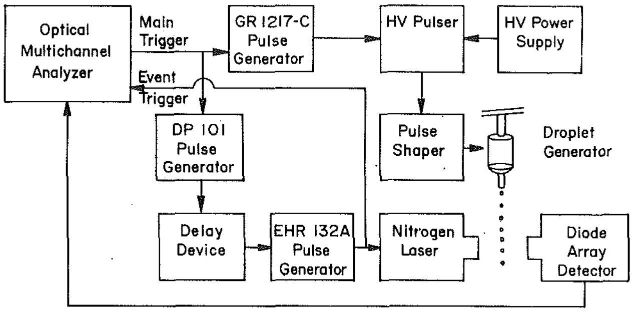

Fig. 1 Block diagram of experimental apparatus

mometry is not recommended for use in realistic combustion environments.

II Experimental

(A) Chemicals and Solutions. Hexadecane (anhydrous, 99+ percent purity) was obtained from Aldrich Chemical Company, Inc. Fluorescence from impurities in the hexadecane was still measurable after it had been chromatographed over activated Al_2O_3, but the residual fluorescence intensity was sufficiently low that it was negligible in comparison to the dopant fluorescence. 1, 3-Bis (1'-pyrenyl) propane (PYPYP) was obtained from Molecular Probes, Inc. and was used as received. A 0.1 mM solution of PYPYP in hexadecane was prepared and used for both droplet production and calibration work. Helium and nitrogen gases (99.99+ percent purity) were purchased from Big Three Inc. and used as received. In all experiments the PYPYP solution was purged with helium gas to remove dissolved oxygen.

(B) Experimental Apparatus and Procedures. The experimental design now being used is essentially the same as that used by Wells and Melton (1990). The purpose of that work was to use EFT to measure the temperature of hydrocarbon droplets as they fell through a heated environment. The purpose and overall experimental design of this work are very similar. The paragraphs below describe the details of the current experimental design and procedures, and, in particular, the changes from the Wells and Melton (1990) experiment in the apparatus, the fluorescent dopant system, and the procedures.

Droplets of a 0.1 mM solution of PYPYP in hexadecane were produced using a piezoelectric droplet generator of a design described generally by Shield et al. (1987). The generator is the same one used by Wells and Melton (1990). As before, steps were taken to insure that droplets were produced from oxygen-free liquid. In this case, helium was used as the purge gas for the fuel.

A block diagram of the system electronics is shown in Fig. 1. An optical mutlichannel analyzer (EG&G PARC OMA III Model 1460-V) with an intensified photodiode array detector (EG&G Model M-1420) coupled to a monochromator (Jarrell-Ash Model Monospec 27; 150 g/mm ruling, dispersion 24 nm/mm, f/3.8) was used to collect and process fluorescence data. A TTL output pulse (5 V, 16 μs) from the OMA acted as the trigger pulse for the experiment. This pulse was used to trigger the droplet generator and, after a variable delay, to trigger a light source, which was either a nitrogen laser or a strobe light. Since a high-voltage pulse (~900 V) is required to drive the piezoelectric droplet generator, the square-wave TTL pulse was used to trigger a pulse generator (General Radio Model 1217-C) whose output (25 V, 0.8 ms) was then sent to a custom-built high voltage pulser powered by a high-voltage power supply (Tennelec Model TC952). The output of the custom-built high-voltage pulser (840 V, 0.8 ms) was then used to drive the droplet generator. The OMA TTL pulse was also used to drive a second pulse generator (Datapulse Model 101) whose output (5 V, 2 ms) was then delayed (0–600 ms) by a custom-built signal delay device. The delayed pulse triggered a third pulse generator (EH Research Model 132A) whose output (40 V, 2 ms) was used to trigger the pulsed excimer laser (Lumonics Model TE861S), which was operated on N_2 at 337 nm (8 ns FWHM). This last pulse (attenuated 10×) was also used to signal the OMA to begin readout of its detector.

An important difference between this apparatus and that of Wells and Melton (1990) is the insertion of a pulse shaping circuit between the high-voltage pulser and the droplet generator. The pulse shaping circuit consisted of a 1000 V diode inserted along the high voltage lead followed by a 56 kX resistor and then a 2000 V, 0.01 1F capacitor, both of which were inserted in parallel between the high-voltage and ground leads. Previously, a 900 V, 2 ms square-wave pulse was used to drive the droplet generator. The inserted circuit altered this pulse to be approximately a "reverse sawtooth" pulse, which has a sharp rising edge and an exponentially decaying falling edge. Use of this pulse shape results in substantially improved producibility in the vertical position of the droplet in the fall tube (Winter, 1990). While lateral instability was minimal, ±1 droplet diameter, vertical instability of the droplet position with a square-wave pulse driving the droplet generator was as great as 1 cm, about 35 droplet diameters. The shaped pulse reduced vertical instability to approximately ±4 droplet diameters.

The cause of the vertical instability was determined by use of a video microscopy system (described below), which monitored the droplets at or near the nozzle of the droplet generator. The pictures obtained by the imaging system revealed that at the rising (leading) edge of the square-wave, high-voltage pulse, a reproducible volume of liquid, at a reproducible velocity, is forced out of the nozzle. At the falling edge of the high-voltage pulse a secondary, high-velocity jet of liquid (of a substantially smaller volume than the droplet) is ejected from the nozzle. Depending on the trigger pulse width, the "jet" either catches up to the primary droplet, or forms one or more satellite droplets, which trail after the primary droplet. The size of the main droplet was about 285 1m and the satellite droplets ranged in size from 20 1m to 50 1m. When the primary droplet is hit by the jet, it undergoes oscillations accompanied by fragmentation and/or changes in its velocity and/or its trajectory, which in turn leads to substantial vertical instability downstream from the nozzle. When the jet forms satellite droplets, the stability of the main droplet is not affected, but satellite droplets themselves interfere with the measurement. The reverse sawtooth pulse apparently allows the piezoceramic crystal to relax sufficiently slowly so that no secondary jet is produced. The height and width of the pulse were reduced to 840 V and 0.8 ms, respectively, before being sent through the shaping circuit.

The energy incident on the droplets was approximately 2.4 1J per pulse (337 nm) at a repetition rate of 0.3–1 Hz. The overall energy from the nitrogen laser was about 1.2 mJ per pulse.

The fall tube was significantly different from that used by Wells and Melton (1990). In that work, doped droplets were injected downward into a heated zone within a hollowed-out, brass block against counterflowing, heated nitrogen gas. Their droplets fell through the counterflowing gas stream and could be interrogated at only two points during their fall, just before entry into the heated zone and 9.5 cm into the heated zone. This work used a square, double-walled tube of optical quartz (Fig. 2), which had nearly unobstructed optical access to the droplet's fall. The droplets fall through the center tube, which was constructed by stacking three standard 1 cm × 1 cm × 4.5 cm quartz fluorescence cuvets and fusing them top to bottom (the bottoms of the two lower cuvets were removed and the uppermost cuvet was inverted with a small hole made

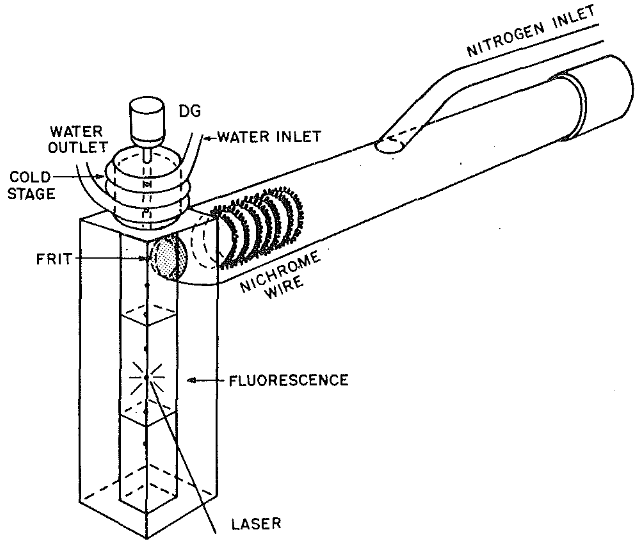

Fig. 2 Droplet heating /fall tube with cold stage

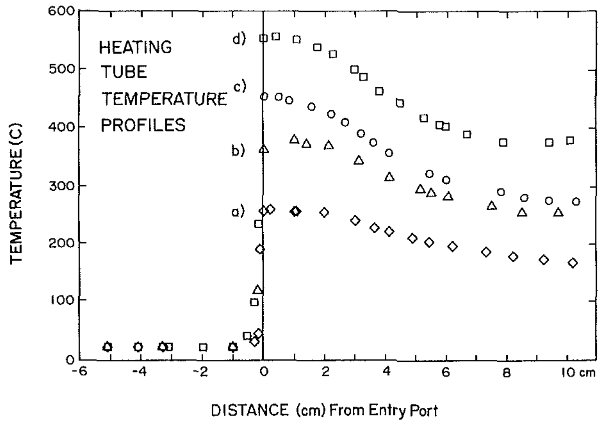

Fig. 3 Temperature profile in droplet fall tube at four different heater settings

for droplet entry). The fusion zones between the cuvets resulted in two 1-2 mm zones of optical distortion; no fluorescence studies were attempted in these zones. Optical access to the droplet in the last 30 mm of the fall tube was not possible due to a fiberglass plug, which partially blocked the gas flowing out of the heating tube. This plug was inserted to adjust the purging rate of the fall tube.

The current design introduces the flow gas at the top of the fall zone. A small quartz frit separates the inner quartz tube (the fall tube, 1 cm × 1 cm × 12.5 cm with a 2 mm hole at top center for droplet entry) from the potentially turbulent, substantially larger gas flow in the outer tube (the heating tube, 3.9 cm × 3.9 cm × 15 cm). The glass frit allows enough gas to go into and down the inner tube to purge its volume every 2 to 3 seconds. Electrical connections and gas enter the far end of the thermally insulated horizontal tube. Nitrogen gas passes over a resistively heated, bare nichrome wire element in the horizontal tube, which results in gas temperatures in the fall tube up to 560°C. Attempts to reach temperatures near 700°C resulted in failure of the heater elements.

A water-cooled, cylindrical brass cold stage (4 cm × 4 cm, shown in Fig. 2) was positioned above the droplet entry port of the droplet heating/fall tube and was separated from the all quartz apparatus by a 3-5 mm layer of ceramic insulation (Kaowool). A small box fan circulated room air over the droplet generator and the fuel reservoir in order to prevent the hot gas rising from the fall tube apparatus from heating them. The temperature profiles measured in the center of droplet fall tube at different gas flow rates/heater powers are shown in Fig. 3. Temperatures were measured using a type J Omega iron-constantan thermocouple read by an Omega HH-70JC meter (±1°C).

The current apparatus has three advantages over that previously used by Wells and Melton (1990): (1) Optical access to the droplets is possible over nearly all of their trajectory through the heated zone, (2) higher gas flow (purging) rates are possible since the gas flow is concurrent with the droplet's trajectory, and (3) higher temperature environments are obtainable. These changes make it possible to: (1) monitor drop temperature versus time (fall distance), (2) avoid problems of turbulence in the droplet fall zone and/or droplet levitation at the higher gas flow rates (both were troublesome in the previous droplet experiments), and (3) study droplet heating/vaporization under higher temperature conditions.

Additional modifications, although not fundamental to the experiment, make the apparatus easier to operate. The piezoelectric droplet generator is now mounted on a gimbaled positioner. The height of the fuel reservoir head relative to the droplet generator nozzle, which is critical for proper droplet production, can be adjusted, set, and then the generator and fuel reservoir can be moved as a single unit. The generator/reservoir unit is moved vertically on a pole, which is itself mounted to an x-y positioner. Thus, the droplet generator apparatus can be moved freely in a controlled manner in all directions (x, y, z, H, and u) needed to align the droplet generator nozzle properly with the 3-mm-dia hole in the center of the cold stage. The cold stage is aligned so that droplet emerging from its bottom fall through the 2-mm-dia droplet entry port at the top center of the fall tube.

The quartz heating/fall tube was mounted on an adjustable machinist's table, while the optical portions of the apparatus (laser beam, lenses, and OMA detector) were mounted on a fixed table. Thus, the laser beam and the detector apparatus remained at a set height. Irradiation of a droplet at any point along its trajectory down the inner quartz tube was accomplished by changing the height of the fall tube and droplet generator apparatus and then selecting the proper delay time for the light source trigger. This arrangement alleviated the need to realign the laser, detection apparatus, and associated optics when changing the droplet fall distance to be studied.

By adjusting the laser/strobe trigger pulse delay to account for the approximately 0.8 m/s velocity of the droplets, it was possible to image the droplet at almost any point (1-95 mm) below the entry port of the fall tube. Within the narrow range of gas flow rates used in the fall tube (3.5-5 cm^3/s, corrected for thermal expansion), the droplet velocity was independent of the gas flow rate (and temperature). The measured velocity corresponds to a Reynolds number of 10 at 400°C (Chigier, 1981). The calculated terminal velocity of a droplet at 400°C, using Stokes law, is 1.0 m/s.

(C) Optics. Fluorescence emission was collected at a right angle to the excitation beam. The 5-cm-dia collection lens (f/3.5) was aligned at a position 14.5 cm from the center of the fall tube and an equal distance from the detector slit. An aqueous solution of DDDC (2,7-dimethyl-3,6-diazocyclohepta-1,6-diene perchlorate) prevented any scattered 337 nm laser light from reaching the detector.

The fluorescence intensity of the PYPYP excimer peak from droplets at room temperature was sufficient to saturate the detector. For droplet measurements, the optics and laser intensity were adjusted to keep fluorescence intensity at less than 50 percent of the detector saturation level. The overall intensity of the dopant fluorescence decreases with increasing temperature, but since the thermometer is based on relative, not absolute intensities of excimer (I_E) and monomer (I_M), the decrease does not affect the determination of temperature, so

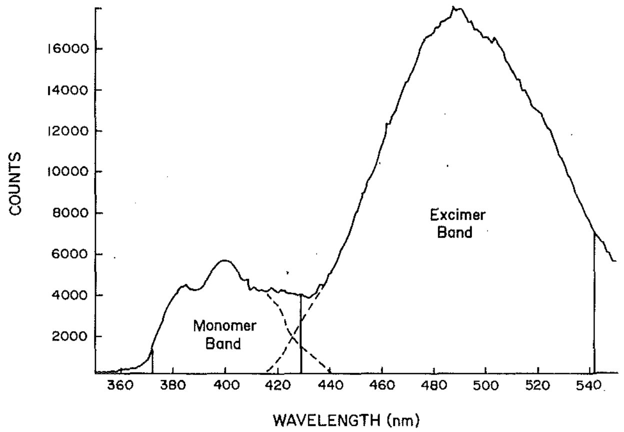

Fig. 4 Monomer and excimer integrals in a PYPYP/C$_{16}$ droplet spectrum

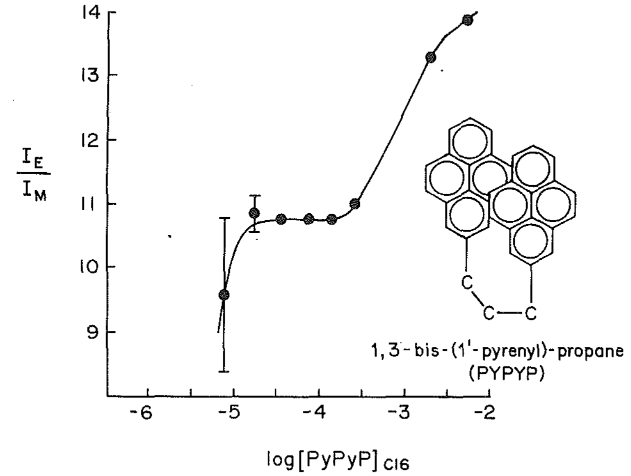

Fig. 5 PYPYP/C$_{16}$ excimer to monomer intensity ratio versus concentration at room temperature

long as an adequately intense signal is obtained. In most cases an adequate spectrum could be obtained from a single droplet, although in typical cases the spectra from 4-5 droplets were accumulated.

Background spectra, taken before each of the droplet measurements, were obtained without droplets in the laser beam pulse (accomplished by changing the laser trigger pulse delay) and were routinely subtracted from the droplet emission spectra. The background-corrected spectra were digitized and stored on disk for later processing by the OMA system. Wavelength calibration of the spectrometer was performed using a low-pressure Hg vapor pencil lamp (Hamamatsu Model C-940-001).

The integrated intensities, I_E and i_M, were obtained using the drop-line integration method from integrals of the spectral bands such as those shown in Fig. 4. The drop-line wavelength used in this study was 429 nm. I_M is the integral from 372-429 nm and I_E is the integral from 429-541 nm.

The possibility of droplet heating due to laser light was investigated. The I_E/I_M ratio was measured as a function of laser power by inserting filters in the incident laser beam. No significant effect was seen at any temperature in either droplet or calibration experiments.

Calibration of the 0.1 mM PYPYP in hexadecane (PYPYP/C$_{16}$) exciplex fluorescence thermometer was accomplished by recording emission spectra of bulk solution in degassed, sealed, 4 mm i.d. × 6 mm o.d. quartz tubes at known temperatures. The same detection system was used for both calibration and droplet work. Droplet solution or pure solvent was vacuum sealed in tubes after three freeze-pump-thaw cycles with a final freeze-pump before flame sealing the tubes.

The calibration tubes were checked for both thermal degradation and photodegradation by comparing their initial room temperature spectra with spectra taken after extended calibration runs. No thermal degradation was detected and, at the 337 nm laser wavelength used for all the reported temperature sensing experiments in this work, no evidence of photodegradation was detected. However, extended periods of exposure to 266 nm Nd:YAG laser (frequency quadrupled, Q-switched, Quantel International Model 671C-10, 2.5 mJ/pulse, 10 ns FWHM, 10 Hz) radiation did alter the room temperature fluorescence spectra of the calibration tubes.

For the imaging/sizing studies, the droplets were backlit with an externally triggered strobe light (Alpha-M Model 161, 2-3 microsecond pulse). A black and white CCD video camera (Sony Corporation of America Model XC-77RR) was mounted to a microscope (Bausch and Lomb Model Stereozoom 7) and coupled to a S-VHS VCR (Panasonic Model AG-1960). The droplet images captured on VCR tape were digitized using an IBM PC-AT compatible framegrabber board (Data Translation, Inc., Model DT2853). The imaging system was calibrated by imaging 1 mm spaced rulings at a set magnification. At the magnification used for this work (124×), each pixel of the digitized images was equal to 7.35 μm. No streaking was observed in the images, and measurements transverse and parallel to the fall direction gave the same results. Since droplet diameters could be measured to about ±1 pixel, the relative statistical error in the diameter of the 283 μm droplets was approximately ±2.5 percent. Greater magnification was possible using this same system, but the relative error in the diameters was not significantly improved.

III Results and Discussion

(A) Thermometry. The choice of an appropriate EFT Dopant depends on several factors. Differential evaporation of thermometry dopant(s) and fuel can lead to concentration-dependent as well as temperature-dependent calibration, and hence evaporation of the droplets can result in derived temperatures that are incorrect. The absorptance across the droplet determines whether "surface" or "volume-averaged" temperatures are determined. Different dopant systems have different temperature ranges for accurate thermometry. The following paragraphs describe why PYPYP was chosen as the EFT dopant for this work.

Wells and Melton (1990) found it necessary to argue that their pryrene-doped decane droplets were undergoing minimal evaporation. The problem they sought to avoid was a change in the dopant concentration due to droplet evaporation. With pyrene as the dopant, the equilibrium in Eq. (1) is affected by both temperature and

$$M^* + M \langle\text{----}\rangle E^* \qquad (1)$$

concentration. This means that as the droplet evaporates, the dopant concentration will change and the calibration curve, determined at a fixed concentration, will no longer be appropriate. The resulting derived temperatures for the Wells and Melton (1990) experiment would be systematically low.

The difficulty in calibration that would result from an unequal dopant/fuel evaporation ratio can be removed by using PYPYP as the dopant instead of pyrene. PYPYP is two pyrene moieties joined by a three-unit methylene chain. The pyrene moieties form an excimer whose properties are highly similar to those of the excimer formed by separate pyrene molecules, but, since the pyrene moieties are tethered to each other, it is possible to eliminate the concentration dependence of the excimer to monomer fluorescence ratio. Figure 5, which is a plot of the PYPYP I_E/I_M ratio versus concentration at room temperature (measured on a spectrofluorometer, Spex Fluorolog Model DM1B) demonstrates this effect. It shows that below

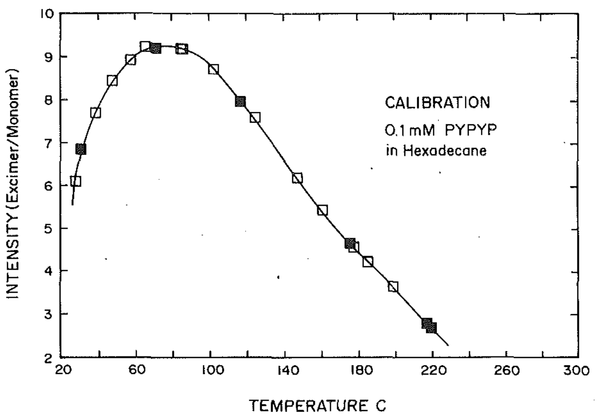

Fig. 6 Calibration curve: I_E/I_M versus temperature

a concentration of about 5×10^{-4} M PYPYP, the excimer-to-monomer fluorescence ratio is constant. As Gossage and Melton (1987) pointed out, the upper limit of dopant concentration for which I_E/I_M is independent of concentration is set by the point where significant intermolecular excimer formation, that is, interaction between pyrene moieties on different PYPYP molecules, begins to occur. For the PYPYP in hexadecane thermometer, this limit is about 5×10^{-4} M. In order to allow for changing concentrations, due primarily to the evaporation of the fuel/solvent and other effects, the starting dopant concentration was set a factor of five below this limit (1×10^{-4} M was used in this work). Then, even if 80 percent of the fuel evaporates and none of the relatively involatile PYPYP (B.P. >350°C) evaporates, the PYPYP concentration should remain at levels for which only the intramolecular excimer contributes significantly to the overall fluorescence signal; thus the I_E/I_M ratio is concentration independent and the calibration remains valid.

The PYPYP/C_{16} thermometer is most useful for temperatures greater than 100°C. If greater resolution of the temperatures below 100°C is needed, the intermolecular excimer thermometer based on pyrene, which Wells and Melton (1990) described, could be used. Since no evaporation of the hexadecane droplets was detected, the inherent concentration dependence of the pyrene-based thermometer should not interfere in the 25–110°C range over which it is effective. The PYPYP/C_{16} intramolecular thermometer is most effective in the 100–400°C range (Gossage and Melton, 1987), and thus, it is complementary to the pyrene intermolecular thermometer. While pyrene makes a better high-sensitivity, limited-ranged thermometer, PYPYP is a more useful wide-range, high-temperature thermometer (Gossage and Melton, 1987).

In EFT, the optical density of the droplet solution determines the region of the droplet from which the fluorescence, and hence the temperature reading, will originate. The molar extinction coefficient of PYPYP in hexadecane at 337 nm (e_{337}) as measured on a UV/Vis spectrofluorometer (Hewlett Packard Model 8450) is about 2.2×10^4 liter/mole-cm and thus, for the 0.1 mM PYPYP/C_{16} solutions used in these experiments, the droplet optical density (*ecd*, where *d* is the droplet diameter) was 0.06. Hence, fluorescence originated from dopant molecules in almost all regions of the droplet and the temperature readings from the PYPYP/C_{16} thermometer used for this work are to be interpreted as volume-averaged temperatures of the droplets. It should be noted that the light falling on the droplet is refracted. This results in the nonuniform illumination of the droplet volume and in nonuniform collection of the resulting fluorescence. These refraction effects are important and will be discussed in Section III (D).

Wells and Melton (1990) argued that the droplet optical density of their pyrene based EFT system was sufficiently high (*ecd* = 4) that the region of excitation was restricted to the near-surface region. Clearly, the surface temperature of a droplet is of significant interest, and, in the early stages of this work, attempts were made to design a variable optical density dopant system that would use naphthalenes as dopants for control of the droplet optical density and PYPYP (at concentrations levels within its concentration-independent range) as the temperature sensing dopant. Unfortunately, the naphthalenes fluoresce at wavelengths that coincide with PYPYP absorption and thus excite fluorescence from PYPYP molecules at depths well beyond that calculated on the basis of naphthalenes optical density. Consequently, no surface restriction of PYPYP excitation was achieved.

(B) Temperature Calibration. PYPYP/C_{16} emission spectra from the calibration samples were taken at temperatures ranging from 23°C to near 220°C. The resulting calibration curve, shown in Fig. 6, is a plot of intensity ratio (I_E/I_M) versus solution temperature. The solid data points of the plot were measured as the temperature of the calibration sample was being increased, while the open symbols denote data points taken as temperature was being decreased. Droplet temperatures are determined by comparing the I_E/I_M ratio obtained from droplet emission spectra to this curve. The uncertainty in the intensity ratio at each point is smaller than could be indicated on the plot and is less than ±1.5°C for the most uncertain readings.

The room temperature spectra from calibration tubes and droplets were indistinguishable. Therefore, it is believed that (1) no distoring refraction effects were altering the spectral intensities or shapes and (2) diffusion of atmospheric oxygen into the droplet fall tube was negligible; thus, the calibration procedures used for this work are valid.

The calibration curve in Fig. 6 shows three distinct sections: a rise from room temperature to ~65°C, a plateau section between ~65°C and ~85°C, and finally a steady decrease above ~100°C. It is apparent that, in hexadecane, PYPYP excimer formation is most favored around 75°C. Below this temperature, kinetic factors, namely the diffusion of the two pyrene moieties toward each other during the monomer excited state lifetime, dominate (Zachariasse, 1978). As the temperature increases, the viscosity of hexadecane decreases, and excimer formation increases. As temperature increases above 75°C, thermodynamic factors dominate and the monomer/excimer equilibrium in Eq. (1) shifts increasingly toward the monomer side.

The double-valued nature of the calibration curve creates some ambiguity in the interpretation of certain intensity ratios. For instance, an I_E/I_M of 8 could be interpreted as a temperature of 43°C or 116°C. However, since the experimental design allows droplets to be interrogated at almost any position/time during their fall, the double-valued nature of the calibration curve did not present a difficult problem. For example, if after some amount of time in a heating environment the droplets give an I_E/I_M of 8, and at slightly longer time a higher ratio, then droplet temperature is increasing from about 45°C. If, on the other hand, the ratio decreases from 8, then droplet temperature is increasing from about 115°C. From 55°C to about 105°C, the change in I_E/I_M is relatively small and, as a thermometer, the PYPYP/C_{16} system is neither accurate nor easy to interpret in this range. Above about 105°C the I_E/I_M ratio falls smoothly as temperature increases and interpretation is straightforward. The upper temperature sensing limit for the PYPYP/C_{16} system has been estimated to be around 400°C (Gossage and Melton, 1987). The calibration curve in Fig. 6 was not extended beyond 220°C since the highest derived droplet temperatures from these experiments did not exceed 220°C.

(C) Droplet Measurements. Figure 7 shows droplet temperature versus time and distance at the four different heating tube settings shown in Fig. 3. The I_E/I_M ratios were extrapolated to zero laser power before comparison with the cali-

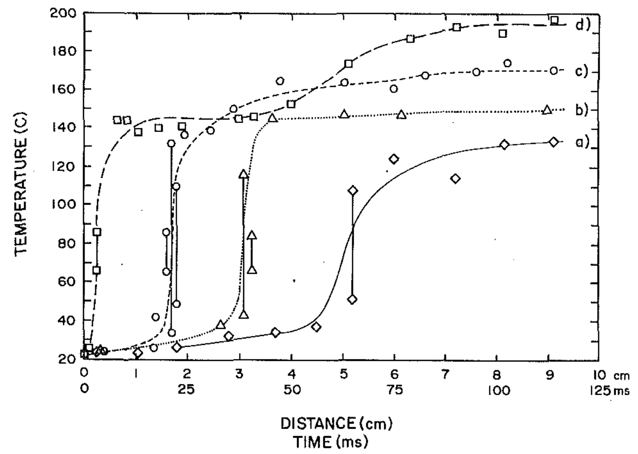

Fig. 7 Droplet temperature versus time and distance at four different heater settings (see Fig. 3)

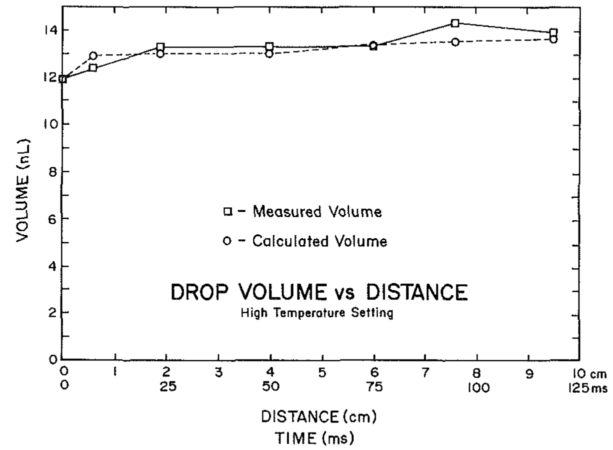

Fig. 8 Droplet volume versus time and distance at highest heater setting

bration curve, thus the reported temperatures reflect only the effects of the heated gas on the droplets. It should be noted that the vertical bars connecting pairs of data points in Fig. 7 are not standard error bars, but a reminder of the double-valued nature of the calibration curve. The true derived temperature for these paris of points is actually one end point or the other, within the error limits of the measurement (±7°C). The spatial resolution of the measurements is estimated to be ±1.5 mm. When obtaining droplet measurements at a single height the reproducibility of the measurement is as good as ±2°C, but changing the height increases this uncertainty to ±7°C.

The results shown in Fig. 7 are striking. The curves drawn in Fig. 7 are there to guide the reader and show generally the nature of the inferred droplet temperature rise. It is supposed that the droplets are at the temperature of the cold stage (23-26°C) as they enter the heated zone. After a lag period, during which the inferred temperatures remain close to room temperature, the duration of which varies depending on the heater setting, the inferred temperatures exhibit a steep rise. After this steep rise, the inferred temperature continues to increase, but at a much lower rate. At the highest heater setting, the sharp temperature rise is over within the first 10 ms of the droplet's fall in the heated zone. As the gas temperature is reduced the sharp rise occurs at successively longer times and the slope of the subsequent portion of the temperature versus time plot becomes smaller. The final temperature readings at around 115 ms were significantly lower than the boiling point of hexadecane (287°C).

The derived hexadecane droplet temperatures are consistent with those reported by Wells and Melton (1990), who worked with decane droplets in a lower temperature gas. Their apparatus could image the droplets at only two points, 5 mm and 95 mm into the heated zone, which prevented detection of the sharp temperature rise seen in this experimental work. The highest temperatures they reported were significantly below the boiling point of decane.

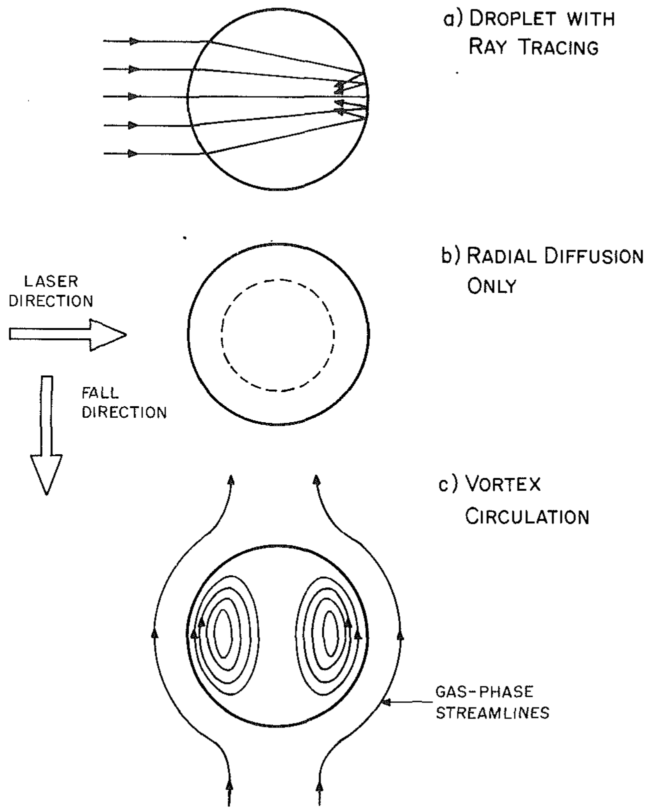

Fig. 9 Droplet with: (*a*) ray tracing, (*b*) radial diffusion only, (*c*) internal circulation

Figure 8 shows droplet volume (as determined by the imaging/sizing system) versus time and distance at the highest ambient temperature used. Also included in Fig. 8 is a curve showing the change in droplet volume using the assumption that a droplet whose size is determined at room temperature undergoes thermal expansion with no evaporation, as calculated by the procedure given by Wells and Melton (1990). Thermal expansion coefficients were taken from Doss (1943). Room temperature droplet diameters were 283 μm, which corresponds to a droplet volume of 11.9 nl; thermal expansion increases this volume by about 14 percent at 200°C. The imaging system has an estimated relative error of about ±8 percent for droplet volumes. As can be seen, the experimental and calculated curves in Fig. 8 are not significantly different. The implication is that the only significant change in droplet size/volume is due to thermal expansion and that no detectable amount (< 10-15 percent) of the hexadecane droplet has vaporized after about 120 ms in the gas at the highest temperature setting.

(D) Interpretation of Derived Droplet Temperatures. To interpret Fig. 7, which shows a sharp, steeped rise in droplet temperature, it is useful to examine these results in the context of (1) the potentially selective nature of excitation/fluorescence of the droplets, and (2) possible mechanisms for droplet heating.

Refractive (lensing) effects at the liquid-gas interface have been shown to result in zones of high intensity "hot-spots" within the droplets (Benincasa et al., 1987; Kwok et al., 1990).

Table 1 Fractional fluorescence from radial quartile sections of a spherical droplet

Radius range (r/r_o)	Fractional volume	Fraction of fluorescence
0.0–0.25	0.016	0.04
0.25–0.5	0.109	0.26
0.5–0.75	0.297	0.58
0.75–1.0	0.578	0.12

Droplet optical density, *ecd* = 0.06; Index or refraction, $n = 1.4$; f/3.5

Figure 9(*a*) schematically shows, via ray tracing, these lensing effects in a droplet irradiated as in this experiment. The convergence of the rays creates regions of high illumination on the back side and within the interior of the droplet, away from the light source. Analogous refraction effects lead to substantially greater probability of capture of isotropically emitted fluorescence from the side of the droplet away from the detector lens. Table 1 lists the calculated (Melton, 1991) fractions of light absorbed by, and detected from, successive radial quartile sections of the droplet. The third quartile section, which is less than 30 percent of the total droplet volume, is responsible for nearly 58 percent of the total detected fluorescence. This is what is meant by "partially selective optical sampling" of the droplet. The outer quartile section of the droplet, nearly 58 percent of droplet volume, produces less than 12 percent of the detected fluorescence, while the two inner sections, half of the droplet radius (12.5 percent of its volume), produce about 30 percent of the detected light.

Interpretation of the "volume-averaged" temperature requires consideration of these refraction effects and the temperature dependence of the fluorescence quantum yield. As shown in Table 1, 84 percent of the fluorescence detected from the PYPYP-doped hexadecane droplets originates from the second and third quartile sections (about 41 percent of the total droplet volume), and thus the derived volume-averaged temperature is significantly weighted toward the temperature of the liquid in this volume. Additionally, since lower-temperature PYPYP/C_{16} gives more intense fluorescence, the "volume-averaged" fluorescence would be biased even further toward low-temperature fluid in the selectively sampled zone. Thus, for a temperature step to be observed, the cool liquid in this selectively sampled zone must be heated significantly, i.e., 50–100°C.

The data in Table 1 are based on an index of refraction of 1.4. The index of refraction for hexadecane (n_D) at 20°C is 1.4345 (CRC, 1984), but the calculations that generated the data that are presented in Table 1 are not sensitive to small changes in the index of refraction; thus, while the percentages of detected fluorescence in Table 1 may change, the selective sampling effects will remain.

Temperature gradients within the heating droplets could distort the calculations given above due to the temperature dependence of the index of refraction. These "mirage" type effects may alter, but should not remove the selective sampling effects tabulated in Table 1.

If the droplet is considered to be a solid sphere (i.e., internal motion not present), then the only mechanism available for heating the interior of the droplet would be radial thermal diffusion. Figure 9(*b*) shows how a radially diffusing thermal wave would propagate into a droplet. The thermal wave would need to propagate to somewhere near a depth of (r/2) before observance of a temperature step, as seen in Fig. 7, would occur. A characteristic time for thermal diffusion to reach this depth has been estimated to be 6 ms ($t = r^2/a$, where r is droplet radius and a is thermal diffusivity of hexadecane), using equations from Prakash and Sirignano (1977).

A second mechanism for droplet heating is (shear-induced) internal circulation. A generalized depiction of this is shown in Fig. 9(*c*). The mechanism involves transport of hot surface liquid into the droplet interior with the result that the droplet interior regions heat more rapidly than they would with just radial diffusion (Law and Sirignano, 1977). Support for the existence of a circulating core region can be found in theoretical calculations (Dwyer and Sanders, 1984; Sirignano, 1983) and Winter and Melton (1990) were able to show experimental evidence of internal circulation (possibly shear-induced) within 300–500 μm decane droplets produced in a fashion similar to that used here. By comparing Figs. 9(*a*) and 9(*c*), it appears that the interior hot spot may coincide with part of the vortices caused by internal circulation. The sharp rise in derived temperature may actually signal the collapse of the core region of the internal vortex, as this would be the last volume of the droplet with which the hot surface liquid mixes. The time for circulation around a vortex is similarly estimated to be 3.5 ms (Prakash and Sirignano, 1977).

For both mechanisms, the droplet would continue to heat at later times, but the temperature would be virtually homogeneous. With lower gas temperatures, propagation of the thermal wave or the heating of the vortex center would require longer times, as the behavior shown in Fig. 7 indicates.

Since the estimated times for diffusion and internal circulation are so close to one another, the present treatment does not distinguish between the two mechanisms.

It should be noted that these refraction effects are always present in droplets that are illuminated by a source larger than the droplet diameter. The discussion given above has indicated that the partially selective optical sampling induced by the droplet refraction can be exploited to give selective information about the temperature in an internal shell of the droplet, even if it does not give full spatial profiles.

(E) Interpretation of Volume Measurements. Figure 8 shows that room temperature hexadecane droplets, not experiencing any loss of mass due to evaporation, would increase in volume due to thermal expansion by about 14 percent when heated to near 200°C. Thus, within the resolution of the this work, the measured volumes of the heated hexadecane droplets do not differ significantly from the calculated volumes. This indicates that the hexadecane droplets are not experiencing significant (>10–15 percent) evaporation.

(F) Extensions of Measurements. Attempts to extend PYPYP EFT to lower alkanes, in particular dodecane, were unsuccessful. Figure 5 shows that with hexadecane there is a usable range of concentrations where the intensity ratio is constant, but attempts to make a similar demonstration with PYPYP in dodecane revealed no such concentration-independent range above the concentration at which the overall intensity falls below a useful level. The PYPYP moelcules diffuse faster in the less viscous dodecane, and thus intermolecular excimer formation increases.

Methanol is known to form exciplexes (Bai, 1991). Thus it may be possible to develop EFT dopants for investigations of the heating/vaporization of methanol droplets.

IV Conclusion

The time-dependent temperature increase of hexadecane droplets exposed to a hot, relatively quiescent, oxygen-free environment has been measured using exciplex fluorescence thermometry. The derived droplet temperatures exhibit a gentle rise followed by a sharp jump and then a final gentle increase up to near 200°C. No droplet evaporation was detected after 120 ms in an approximately 500°C ambient. It has been postulated that the sharp jump in temperature results from the partially selective optical sampling of the droplet volume. It was not possible to determine whether internal circulation or radial diffusion is the dominant heat transfer mechanism in the droplet.

Acknowledgments

Funding for this work was provided by the Army Research Office through contract No. DAAL03-87-K-0120. We also gratefully acknowledge receipt of the University Research Instrumentation Program grant No. DAAL03-86-G-0115. Thanks to Oscar Arce for the dodecane measurements and special thanks to Dr. Tuqiang Ni for his assistance and helpful advice.

Endnote

As a clarification, it should be noted that exciplex and excimer refer to different chemical entities. Exciplex refers to an **excited** state **complex**, where the two species of the complex differ. On the other hand, excimer refers to an **excit**ed state **dimer**, where the two species of the complex are the same type of molecule. A particularly well-studied example of an excimer is the excited state species formed by two pyrene molecules, whereas an excited state complex of naphthalene and TMPD (N, N, N′, N′-tetramethyl-p-phenylene diamine) is an example of an exciplex (Murray and Melton, 1985). The first use of the technique known as exciplex fluorescence thermometry, as described in a patent issued to Melton in 1986 (U.S. Patent 4,613,237), used an exciplex as the fluorescent dopant and, even though excimer type dopants have been used in later developments of the technique, it is still generally referred to as **exciplex** fluorescence thermometry. In addition, it should be noted that both **intra**molecular and **inter**molecular excimers and exciplexes can be formed. Intramolecular describes a complex from separate moieties/pieces within a single molecule, and intermolecular describes one formed from two separate molecules.

References

Abdul-Rahman, Y. A. K., 1969, "Drying Droplets Containing Dissolved and Dispersed Gases," M. S. Thesis, University of Wisconsin, Madison, WI.

Aggarwal, S. K., Tong, A. Y., and Sirignano, W. A., 1984, "A Comparison of Vaporization Models in Spray Calculations," *Amer. Inst. of Aeronautics J.*, Vol. 22(10), p. 1448.

Bai, F., personal communication, 1991.

Benincasa, D. S., Chang, R. K., Barber, P. W., Zhang, J.-Z., and Hsieh, W.-F., 1987, "Spatial Distribution of the Internal and Near-Field Intensities of Large Cylindrical and Spherical Scatterers," *Appl. Optics*, Vol. 26, p. 1348.

CRC Handbook of Chemistry and Physics, 1984, CRC Press, Inc., Boca Raton, FL, 64th ed., pp. F-40-F-41.

Chigier, N., 1981, *Energy, Combustion, and Environment*, McGraw-Hill, New York, p. 273.

Doss, M. P., 1943, *Physical Constants of the Principal Hydrocarbons*, Technology and Research Division of The Texas Company, New York City, NY, 4th ed., p. 12.

Dwyer, H. A., and Sanders, B. R., 1983, "Comparative Study of Droplet Heating and Vaporization at High Reynolds and Peclet Numbers," presented at the 9th ICODERS, Poitiers, France, July 3-8, pp. 464-483.

Dwyer, H. A., and Sanders, B. R., 1984, "Detailed Computation of Unsteady Droplet Dynamics," *20th Symposium (Int.) on Combustion*, Combustion Institute, Pittsburgh, PA, pp. 1743-1749.

Dwyer, H. A., and Sanders, B. R., 1988, "Unsteady Influences of Droplet Dynamics and Combustion," *Combust. Sci. and Technol.*, Vol. 58, p. 253.

Faeth, G. M., 1983, "Evaporation and Combustion of Sprays," *Prog. Energy Combust. Sci.*, Vol. 9, p. 1.

Gossage, H. E., and Melton, L. A., 1987, "Fluorescence Thermometers Using Intramolecular Exciplexes," *Appl. Optics*, Vol. 26, p. 2256.

Knight, B., and Williams, F. A., 1980, "Observations on the Burning of Droplets in the Absence of Buoyancy," *Comb. Flame*, Vol. 38, p. 111.

Kwok, A. S., Chang, R. K., and Wood, C. F., 1990, "Fluorescence Imaging of CO_2 Laser-Heated Droplets," *Optics Lett.*, Vol. 15, p. 664.

Law, C. K., and Sirignano, W. A., 1977, "Unsteady Droplet Combustion With Droplet Heating—II: Conduction Limit," *Comb. Flame*, Vol. 28, p. 175.

Law, C. K., 1982, "Recent Advances in Droplet Vaporization and Combustion," *Prog. Energy Comb. Sci.*, Vol. 8, p. 171.

Melton, L. A., 1986, "Method for Determining the Temperature of a Fluid," U. S. Patent 4,613,237, awarded Sept. 23, assigned to United Technologies Corporation.

Melton, L. A., 1991, "Efficiency of Capture of Fluorescence From Droplets," unpublished results, University of Texas at Dallas, Richardson, TX.

Murray, A. M., and Melton, L. A., 1985, "Fluorescence Methods for Determination of Temperature in Fuel Sprays," *Appl. Optics*, Vol. 24, p. 2783.

Neal, D. R., and Baganoff, D., 1985, "Laser-Induced Fluorescence Measurement of Vapor Concentration Surrounding Evaporating Droplets," presented at the Southwest Conference on Optics, SPIE Vol. 540, p. 347.

Prakash, S., and Sirignano, W. A., 1977, "Liquid Fuel Droplet Heating With Internal Circulation," *Int. J. Heat Mass Transfer*, Vol. 21, p. 885.

Puri, I. K., and Libby, P. A., 1989, "Droplet Behavior in Counterflowing Streams," *Combust Sci. and Tech.*, Vol. 66, p. 267.

Ray, A. K., Lee, J., and Tilley, H. L., 1988, "Direct Measurements of Evaporation Rates of Single Droplets at Large Knudsen Numbers," *Langmuir*, Vol. 4, p. 631.

Seaver, M., and Peele, J. R. 1990, "Noncontact Fluorescence Thermometry of Acoustically Levitated Waterdrops," *Appl. Optics*, Vol. 29, p. 4956.

Shield, T. W., Bogy, D. B., and Talke, F. E., 1987, "Drop Formation by DOD Ink-Jet Nozzles: A Comparison of Experiment and Numerical Simulation," *IBM J. Res. Develop.*, Vol. 31, p. 96.

Sirignano, W. A., 1983, "Fuel Droplet Vaporization and Spray Combustion Theory," *Prog. Energy Combust. Sci.*, Vol. 9, p. 291.

Stufflebeam, J. H., 1989, "Exciplex Fluorescence Thermometry of Liquid Fuel," *Appl. Spectrosc.*, Vol. 43, p. 274.

Trommelen, A. M., and Crosby, E. J., 1970, "Evaporation and Drying of Drops in Superheated Vapors," *AIChE Journal*, Vol. 16, p. 857.

Wang, C. H., Liu, X. Q., and Law, C. K., 1984, "Combustion and Microexplosion of Freely Falling Multicomponent Droplets," *Comb. Flame*, Vol. 56, p. 175.

Wells, M. R., and Melton, L. A., 1990, "Temperature Measurements of Falling Droplets," ASME JOURNAL OF HEAT TRANSFER, Vol. 112, p. 1008.

Williams, F. A., 1985, "Ignition and Burning of Single Liquid Droplets," *Acta Astronautica*, Vol. 12, p. 547.

Winter, M., 1990, personal communication.

Winter, M., and Melton, L. A., 1990, "Measurement of Internal Circulation in Droplets Using Laser-Induced Fluorescence," *Appl. Optics*, Vol. 29, p. 4574.

Zachariasse, K. A., 1978, "Intramolecular Excimer Formation With Diarylalkanes as a Microfluidity Probe for Sodium Dodecyl Sulphate Micelles," *Chem. Phys. Lett.*, Vol. 57, p. 429.

J. R. Markham

P. E. Best[1]

P. R. Solomon

Z. Z. Yu

Advanced Fuel Research, Inc.,
East Hartford, CT 06108

Measurement of Radiative Properties of Ash and Slag by FT-IR Emission and Reflection Spectroscopy

This article presents laboratory measurements of the radiative properties of ash and slag deposits that have been extracted from combustion devices. The measurements were made by a technique employing a sample heating device that is coupled to a Fourier Transform Infrared (FT-IR) spectrometer to measure the sample's emission and directional-hemispherical reflection. By this technique, the temperature at the measurement point and the spectral emittance of the surface are both obtained. These measurements are then related to the physical and chemical properties of the surface to determine what controls the radiative properties. The measurements have shown that the physical state of a deposit (i.e., fused, sintered, or packed particles) greatly influenced the measured spectral emittance. The results were in agreement with mathematical models that account for the physical properties.

Introduction

Thermal radiation plays a key role in the operation and efficiency of combustion systems, accounting for over 90 percent of the heat transfer (Raask, 1985). The radiative heat transfer in coal-fired boilers is dominated by the properties of inorganic deposits on surfaces, and of entrained particulates, which are present in the system. The properties governing the emission, absorption, and attenuation of the radiative energy by deposits and entrained particulates are a key element in accurately predicting the radiative heat transfer. They are also necessary for in-situ determination of current deposit condition (composition, temperature) from optical measurements. As the need increases for higher efficiency and better pollution control, more complete knowledge of the boiler operating conditions is necessary. Thus, there is an increased need to know the radiative properties (emissivity and reflectivity) of deposits and particulates in coal-fired combustion systems.

In this paper, we report on the measurement in a laboratory apparatus of radiative properties at high temperature of samples extracted from furnaces. There are two basic methods for measuring the spectral emittance of a surface at an elevated temperature (Eckert and Goldstein, 1976): (*i*) measurement of the radiation emitted from the surface at a known temperature (spectral emittance), and (*ii*) measurement of radiation reflected from, and transmitted through the material (1 − spectral emittance). If the sample is heated in a furnace, the emission method suffers from problems associated with distinguishing emitted radiation from furnace radiation reflected from the surface.

In the reflection method, external radiation is reflected from the surface. It is modulated to distinguish it from the emitted or reflected furnace radiation. The reflected radiation must be measured over all angles of reflection, and this limits the degree to which the sample can be surrounded by the furnace. Precise knowledge of the sample temperature must be sacrificed to gain optical access.

The measurement technique recently described by Markham et al. (1990) overcame many of the problems of measuring emittance and temperature by using both the radiance and reflectance methods simultaneously in a geometry that eliminates any reflected furnace radiation. The reflectance measurement is used to determine the sample emittance but at an imprecisely known temperature. The emittance is then used in conjunction with the measurement of emitted radiation to determine the temperature. Therefore, both the emittance and temperature are determined. The measurements were performed using an apparatus consisting of a heating device, optics, and a Fourier Transform Infrared (FT-IR) spectrometer. The technique was validated by making spectral emittance measurements in the mid-IR, 1.6 to 20 μm, at moderate sample temperatures for a number of calibration samples.

This apparatus was employed on ash and slag samples of various chemical and physical conditions collected from several sources. In addition to applying the technique to measure radiative properties of ash and slag at elevated temperatures, the complex index of refraction was determined by absorption techniques employing fine particles of the materials suspended in KBr and CsI matrices. Spectral emittance was then calculated by semi-empirical models to compare with the observed emittances. The measurements and model results were employed to gain an understanding of how the chemical and physical states of the sample affect the emittance.

Experimental

Ash and Slag Samples. Fused and sintered slag deposits from the firing of Illinois No. 6 bituminous coal were supplied by the Babcock & Wilcox Company, and Brigham Young University. A powdery fly ash from the firing of a Texas lignite was supplied by Stanford University. Table 1 lists the ash and slag deposits measured for radiative properties. Sample #3 was also fractured to measure the radiative properties of internal surfaces. Table 2 lists the inorganic oxide composition of each sample (except for sample #5) as measured by elemental x-ray analysis.

Apparatus. The apparatus has previously been described in detail (Markham et al., 1990). It consists of an FT-IR spectrometer coupled with an optical attachment that allows for

---

[1] Present address: University of Connecticut, Institute of Materials Science, Storrs, CT 06268.

Contributed by the Heat Transfer Division for publication in the JOURNAL OF HEAT TRANSFER. Manuscript received by the Heat Transfer Division April 1991; revision received January 1992. Keywords: Furnaces and Combustors, Heat Exchangers, Radiation Interactions.

Table 1 Slag and ash samples

SAMPLE NO.	SLAG OR ASH DESCRIPTOR	ACQUIRED FROM	COAL	FIRED AT	PHYSICAL DESCRIPTION
1	Slag from refractory back wall of BCTU*	B&W	Illinois No. 6 (Bituminous)	B&W	Sintered Deposit
2	Slag from top of slagging panel in BCTU	B&W	Illinois No. 6 (Bituminous)	B&W	Fused Deposit
3	One-time molten pool of slag from inside BCTU	B&W	Illinois No. 6 (Bituminous)	B&W	Fused Deposit
4	San Miguel Ash	Sanford University	San Miguel (Texas Lignite)	San Miguel Station San Miguel, TX	Powdery Ash
5	BYU Slag	BYU	Illinois No. 6 (Bituminous)	BYU	Fused Deposit

* BCTU: Basic Combustion Test Unit at B & W

Table 2 Compositional x-ray analysis for ash and slag deposit samples

Inorganic Component	Sample #1 Sintered Deposit (Ill No. 6, Bit. Coal)	Sample #2 Fused Deposit (Ill No. 6, Bit. Coal)	Sample #3 Fused Deposit (Ill No. 6, Bit. Coal)	Sample #4 Powdery Ash (Texas Lignite)
Na_2O	0	0.05	2.76	2.11
MgO	0	0	1.47	0
Al_2O_3	10.96	11.12	18.16	17.11
SiO_2	52.17	59.28	56.21	70.63
K_2O	2.23	2.04	1.47	1.55
CaO	7.22	4.96	4.13	4.32
TiO_2	1.08	1.04	1.01	1.05
SO_3	2.56	0.09	0.12	0.94
Fe_2O_3	23.71	20.97	14.68	2.53

measuring infrared directional reflectance (specular and diffuse), directional transmittance, and near-normal angle radiance from a heated surface. For reflectance and transmittance measurements, the FT-IR spectrometer's source radiation is modulated by the interferometer prior to impingement with the hot sample. Since the detector that receives the reflected or transmitted IR radiation is sensitive only to modulated radiation, the radiance of the sample does not interfere with the measurement. The measurement of the hot sample's emitted radiation was achieved in a geometry that prevented any reflected furnace radiation from entering the collection optics. Samples were heated from the back or front with either a propane or oxy/acetylene torch. Surface-bonded thermocouples indicated that torch heating can maintain the temperature of the sample to within ±10 K during the measurement time. A minimal interfering radiance was contributed to the measurement from the gaseous combustion products (H_2O and CO_2). However, these contributions were confined to narrow and well-defined spectral regions. Since the sample measurement results in a broad band continuum spectrum, the added contributions of H_2O and CO_2 can easily be identified in the appropriate spectral regions. Spectral corrections for H_2O and CO_2 contributions were not performed. The narrow band contributions of H_2O and CO_2 in the beam path can have a subtractive effect if the gases are cooled and absorb sample radiation, or they can have an additive effect if the gases are sufficiently hot.

Analysis

Measurement Technique. Our measurements of directional reflectance and transmittance over all angles about a circumference around a sample allow "integration" of the measurements to yield the required directional-hemispherical properties for isotropic scatterers (Siegel and Howell, 1981). Isotropic, in this sense, does not require the material to scatter diffusely, but it does require that directional scattering be independent of azimuthal angle. Directional scattering from surfaces with a directional surface grain pattern, for instance, will be dependent on azimuthal angle, and was discussed previously (Markham et al., 1990). The optics and the computational routine developed to obtain the radiation integrated over a hemisphere allow for measurements to be taken for polar angles at 5-deg (8.8×10^{-2} r) intervals. The data collection of all the angular measurements required ~15 min/sample. Measurement time could be reduced, of course, at the sacrifice of the signal-to-noise ratio. If the solid angle subtended by the detector is $\Delta\Omega$, then the contribution by all radiation scattered through the angle θ to the total is

$$\Delta I_\theta = I_\theta 2\pi \sin\theta(8.8\times10^{-2})/\Delta\Omega$$

where I_θ is the power measured at angle θ. The total integrated radiation about the hemisphere is obtained by taking the sum of the ΔI_θ components.

Conservation of energy, that is, that radiation incident on a slab of material is either reflected, absorbed, or transmitted, allows us to determine the absorptivity of a material by closure:

$$\rho_\nu + \alpha_\nu + \tau_\nu = 1 \tag{1}$$

where α_ν is the absorptivity, ρ_ν is the directional-hemispherical reflectance, τ_ν is the directional-hemispherical transmittance, and the subscript ν indicates a spectral quantity. By a Kirchhoff analysis it can be shown that the emissivity, ϵ, is equal to the absorptivity, α (Bohren and Huffman, 1983):

$$\epsilon_\nu = \alpha_\nu \tag{2}$$

Hence, the spectral emittance of a material at an imprecisely known temperature can be determined:

$$\epsilon_\nu = 1 - \rho_\nu - \tau_\nu \tag{3}$$

All the deposits used in this study were 3 mm or greater in thickness, and measured to be opaque in our spectral regime. For opaque slabs ($\tau_\nu = 0$) we have that

$$\epsilon_\nu = 1 - \rho_\nu \tag{4}$$

The spectral emittance can then be used with the measured radiance, R_ν, to determine the precise temperature at the measurement point by:

$$R_\nu^b(T) = R_\nu/\epsilon_\nu \tag{5}$$

where $R_\nu^b(T)$ is the theoretical black body radiance corresponding to the surface temperature.

Once the temperature is known, the spectral emittance can be recalculated from the radiance and compared to that obtained from the reflection and transmission measurements. An example of the measurement technique as applied to a fused slag deposit is shown in Fig. 1. Figure 1(*a*) presents the spectral emittance, ϵ_ν, determined from the reflectance measurements of the hot sample at an imprecisely known temperature. This relatively smooth inorganic slab exhibits essentially gray body characteristics over this spectral regime. Slight variations are observed below 1500 cm^{-1}, which is the characteristic region of infrared absorption for mineral species found in ash and slag. Figure 1(*b*) is of the radiance measurement, R_ν; and Figs. 1(*c*) and 1(*d*) present the surface temperature determination from Eq. (5).

Overlayed in Figs. 1(*c*) and 1(*d*) are theoretical black body radiance spectra to compare to the experimental data. A temperature of 1630 K appears to be the best "fit" to the data. Figure 1(*e*) recalculates the spectral emittance from the determined temperature and the radiance measurement, R_ν, and compares it to the "closure" determined emittance. Good agreement is demonstrated.

For many of our technique validation samples, such as quartz, sapphire, sintered alumina, silicon nitride (Markham et al., 1990), as well as for many of the deposited surfaces, there was observed a spectral region where $\rho_\nu = \tau_\nu = 0$. At this spectral region, $\epsilon_\nu = 1.0$. This spectral region of black body emittance is attributed to the Christiansen effect, which occurs when the real part (n) of the refractive index of a material is unity and matches that of air (Bohren and Huffman, 1983). Under these conditions almost no reflection or scattering will be observed ($\rho_\nu = 0$) if the imaginary part (k) is sufficiently low. Reflectance for opaque slabs can be described by

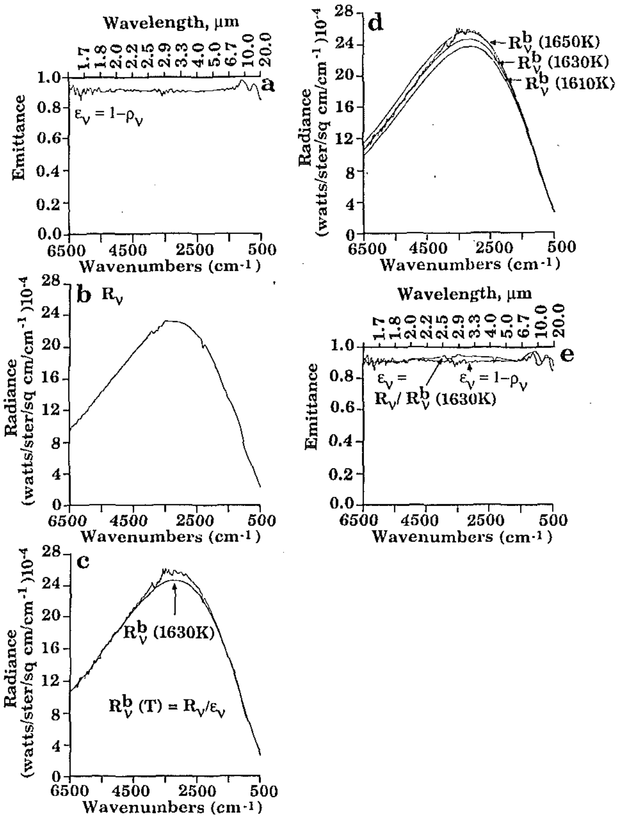

Fig. 1 **Spectral emittance and surface temperature from reflection and radiance measurements for slag from Babcock and Wilcox's basic combustion test unit, sample #3, top surface: (*a*) emittance = 1 – reflection, (*b*) radiance measurement, (*c*) calculated temperature spectrum (temperature = radiance/emittance) overlaid with best-fit theoretical blackbody temperature curve, (*d*) extent of deviation ±20 K from best-fit curve, and (e) comparison of spectral emittance determined from $\epsilon_\nu = 1 - \rho_\nu$ and $\epsilon_\nu = R_\nu/R_\nu^b$ (1630 K)**

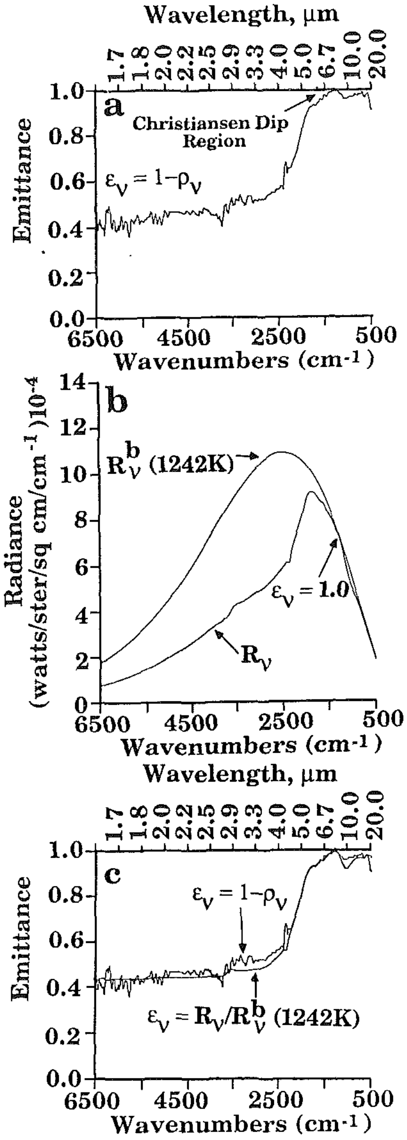

Fig. 2 **Spectral emittance and surface temperature from reflection and radiance measurements for a pressed wafer of San Miguel powdery ash (sample #4); a Christiansen dip is also observed: (*a*) emittance = 1 – reflection, (*b*) radiance measurement overlaid with a 1242 K theoretical black-body curve that matches intensity at the Christiansen frequency, and (c) emittance by closure versus emittance by Christiansen effect**

$$R = \frac{[(n-1)^2 + k^2]}{[(n+1)^2 + k^2]} \qquad (6)$$

When $n = 1$, Eq. (6) can be very small for small values of k. When $n = 1$ and k is as small as 0.1, $R = 0.002$ and $1 - R = \epsilon = 0.998$. The emittance deviates from 1.0 by only a fraction of a percent. For small values of k, one might think that the majority of the propagating wave would pass through the sample, but even small values of k produce substantial attenuation (absorption) by the medium. The attenuation of radiation is given by $I = I_0 e[-(4\pi k/\lambda)t]$, so for $k = 0.1$ at 10 µm wavelength, the incident radiation is attenuated by $1/e$ in a distance of 0.8×10^{-2} mm. For example, in coal, $k < 0.05$ over most regions of the infrared spectrum between 400 cm^{-1} to 4000 cm^{-1} (Brewster and Kunitomo, 1984; Huntjens and van Krevelan, 1954), but significant absorption occurs with a thickness on the order of 0.8×10^{-2} mm (Best et al., 1986).

For an IR opaque slab of material ($\tau_\nu = 0$), the Christiansen dip defines a spectral region where $\epsilon_\nu \approx 1.0$, thus allowing a fast (spectra have been collected every 0.11 s) and accurate (±5 K) method of determining the surface temperature and spectral emittance, since the temperature of the material can be determined by direct comparison of the radiance measurements at the Christiansen dip to the theoretical curves for $R_\nu^b(T)$.

The technique is demonstrated in Fig. 2 for a pressed wafer of fly ash that was heated with a torch flame. For this hot sample, the spectral emittance was determined by two methods: (1) by measuring the hemispherical reflectance and applying Eq. (4), and (2) by the Christiansen effect. Figure 2(*a*) displays the spectral emittance determined by the hemispherical reflectance measurement. In the reflectance measurement there was a Christiansen dip region where $\rho_\nu = 0$. This translates to $\epsilon_\nu = 1$ at ~1400 cm^{-1} in the emittance spectrum. Figure 2(*b*) overlays the radiance measurement, R_ν, with a theoretical black body spectrum calculated at 1242 K (R_ν^b(1242 K)), which coincides in amplitude at the Christiansen frequency. This determined temperature can now be used with R_ν to determine the spectral emittance (Eq. (5)). Figure 2(*c*) displays the excellent agreement in spectral emittance obtained by the two independent techniques.

It is not necessary to establish the complete hemispherical reflectance if a surface exhibits a Christiansen dip. Our hemispherical reflectance measurement system demonstrated that the observance of a Christiansen dip holds at all angles. Thus, a single angular reflectance measurement can be used to determine if a material exhibits a Christiansen dip, and if so allows for the temperature and spectral emittance to be determined from a radiance measurement.

The spectral frequency of the Christiansen dip is also indicative of the material's composition. The data of Table 2 indicates that sample #4 is primarily SiO_2. Previous measurements of SiO_2 have demonstrated black-body emittance at this spectral region (Markham et al., 1990; Myers et al., 1986).

Experimental Uncertainty. To make quantitative measurements, the FT-IR reflection experiments require normalizing the sample spectrum with a reference (or background) spectrum. A first surface gold mirror (totally reflecting) was placed at the sample position but mounted to rotate so that the specularly reflected beam can be focused onto the detector for all detector angles. This allows for a reference spectrum to be taken at each collection angle. Typically the deviation of detected intensity around the optical table was less than ±2 percent. Each angular measurement of reflected or transmitted radiation can then be normalized by a reference spectrum to indicate what percentage of the available incident radiation was detected in each angular direction.

The optical path and emission detector used for the radiance measurements were calibrated for energy losses and responsivity by placing a black-body cavity emitter at the sample location. The black body used for this calibration was a laboratory constructed cavity made of standard refractory materials and an electric heating coil. The accuracy of the calibration will be affected by the accuracy of the thermocouple system that indicates cavity temperature, and the quality of the cavity to behave as an ideal black body. The thermocouple system's accuracy would introduce an uncertainty of ±0.1 percent for the cavity at 1000 K. The black body quality of the cavity was estimated by comparing its response to a second laboratory emitter of similar but larger dimensions, and to a cavity formed by drilling a lateral hole in an electrically heated metallic tube that exhibited an outside surface emissivity of >0.5 (Ono et al., 1982). The consistent agreement in response indicated an apparent cavity emissivity of >0.98.

Spectral emittance determinations done by the closure method are dependent on the quality of the gold mirror reference, but independent of the black body calibration. Spectral emittance determinations done by the Christiansen effect method are dependent on the quality of the black body calibration, but independent of the gold mirror. For materials that allowed for determination by both independent methods, agreement to better than 0.05 emittance units was demonstrated (±5 percent). This seems to indicate that the majority of error comes from the numerous angular reflection measurements.

The accuracy of temperature determinations by closure appears to be within ±20 K based on: (1) the ability to distinguish visually the best agreement with theoretical radiance curves, (2) comparison to surface-bonded thermocouple measurements, and (3) comparison to the temperature determined at the Christiansen frequency for samples that demonstrated the Christiansen effect.

Results—Analysis of Measurements on Deposit Samples

Fused Deposits. Figure 3 compares the determined spectral emittance for all the fused slags acquired ranging in temperature from 300 K to 1630 K. All exhibit a high spectral emittance (≥ 0.9). The variations observed below $1500\ \text{cm}^{-1}$ indicate the sensitivity of the technique to discrete changes in chemical composition (mineral species) for the samples. Shaded in the figure are the interference regions of the combustion products (CO_2 and H_2O) of the flames used to heat the samples. A Christiansen dip where $\epsilon_\nu = 1.0$ is exhibited for all three measurements of the internal surface obtained by fracture of sample #3.

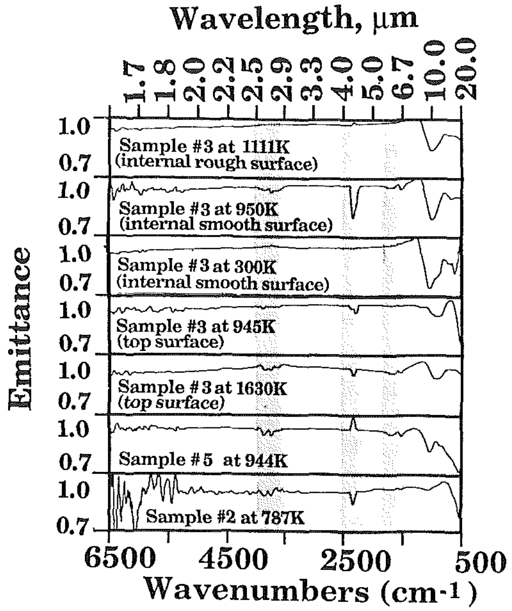

Fig. 3 Comparison of measured spectral emittance for several fused slag samples over a wide temperature range

Sintered or Powdery Deposits. As shown in Fig. 2, powdery ash deposits do not exhibit the near gray body spectral emittance of fused deposits. This is attributed to the differences in available scattering surfaces (texture) between the fused and powdery states. Powdery ash deposits and, to a lesser degree, sintered samples, consist of individual mineral particles that are weakly held together, whereas the fused deposits have solidified from a molten state to become more glassy in nature (Bohren and Huffman, 1983). The bed of particles of the powdery and sintered deposits increases the scattering efficiency of these materials by increasing the number of boundary surfaces available for scattering (reflecting) of the penetrating wave. This will cause a wavelength-dependent drop in emittance.

This is also demonstrated in Fig. 4, which compares the spectral emittance of the sintered deposit to the same material after grinding into individual particles (SEM photomicrographs indicated a broad distribution from submicron diameters to greater than 25 μm) and pressing into a wafer, and after melting the deposit into a fused slab. Fusing the sintered deposit results in a spectral emittance similar to those shown in Fig. 3. In the molten or liquid state, the spectral emittance is apparently only slightly higher than the fused state, but does exhibit a Christiansen dip. The occurrence of the Christiansen dip for this material in the molten state may be an indication of segregation of components in the melt, or of changes in the optical constants with temperature (Ebert and Self, 1989). These types of changes in a material's radiative properties emphasize that many parameters must be understood to extend laboratory measurements on extracted deposits to techniques for in-situ measurements. The hot CO_2 band at $\sim 4.5\ \mu$m is produced by the torch that is directly heating the measured spot. The melting point of the material was determined to be ~ 1400 K. The particle-like nature of the surface of the original sintered deposit increases the scattering efficiency of the material, which causes a wavelength-dependent drop in emittance. In the ground and pressed wafer the scattering efficiency is further increased resulting in a lower emittance. Figure 4(*b*) also demonstrates the change in spectral emittance for fine particulates of powdery ash (sample No. 4) after fusing the material. For this sample the Christiansen effect ($\sim 1400\ \text{cm}^{-1}$) was maintained for each surface morphology.

Of interest is that the fused surface exhibits a spectral emittance that is similar to the fused samples presented in Fig. 3, although this sample is considerably different in chemical com-

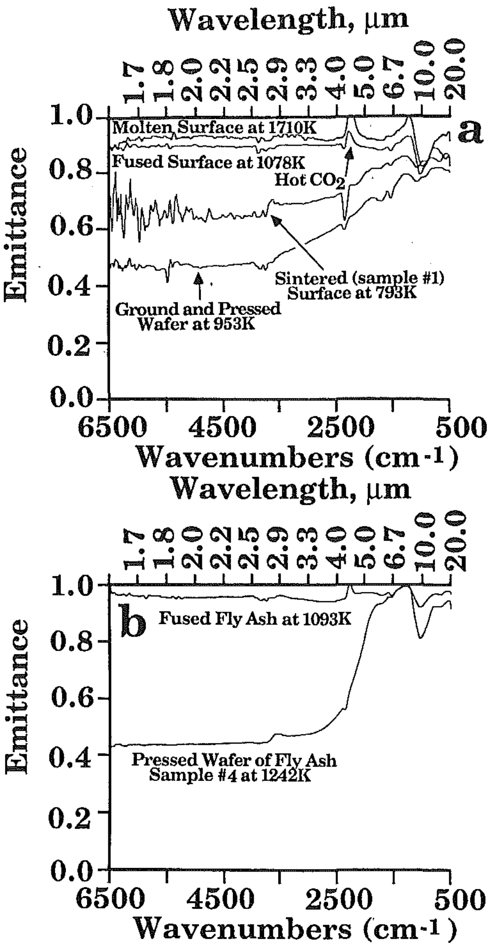

Fig. 4 Measured spectral emittance for (*a*) sintered slag deposit (sample #1) compared to the material after grinding and pressing into a wafer; and after thermally fusing the material, and (*b*) powdery ash (sample #4) compared to the emittance after thermally fusing the material

position (see Table 2). This indicates that the morphology of the deposit surface dominates the emittance characteristics.

Analysis of Growing Deposits. The influence that particle-like deposits will have on the emittance of a surface was readily demonstrated. The measurements technique was also applied to show the change in spectral emittance (and hence, in heat absorption rate) for a surface as the ash deposit thickness was increased. Measurements were performed on a heavily oxidized stainless steel surface after subjecting it to impaction with the particle and fume stream from the combustion of pulverized Illinois No. 6 bituminous coal. The steel surface temperature was measured with a 0.005-in.-dia thermocouple that was bonded to the surface. The temperature was held at 811 K ± 17 K (1000°F ± 30°F) during the ash deposition, and at 800 K ± 6 K (980°F ± 10°F) during the reflectivity measurements. These temperatures are in the range typical of a boiler wall or tube surface during operation.

Figure 5 demonstrates the change in the spectral emittance (emittance = 1 − reflectance) of the oxidized steel surface as it is increasingly coated with dusty ash deposit. Below 1500 cm^{-1}, where the strong absorption bands for coal ash are located, the emittance continually increases as more material is deposited. Above 1500 cm^{-1}, there is initially a slight rise in emittance and then a continual decrease in emittance as the ash coating thickens and increases the reflectivity in this spectral region. The thickness of the most heavy deposition was measured by SEM photomicrographs to be ~50 μm thick, but is already

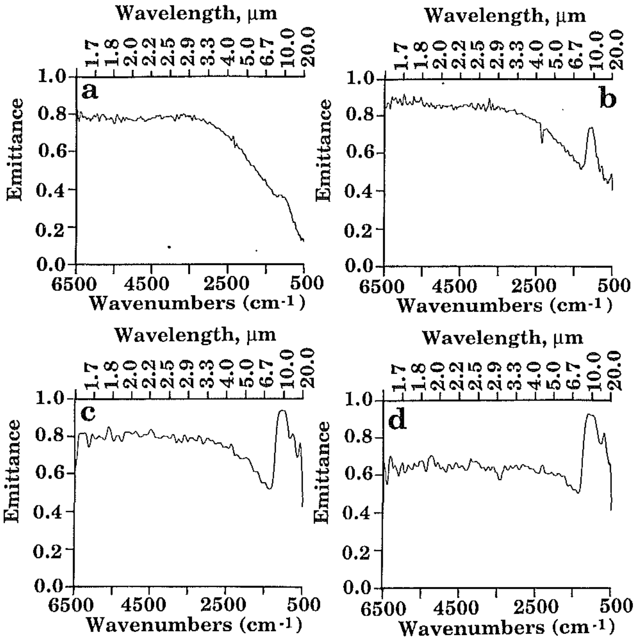

Fig. 5 Spectral emittance by measured hemispherical reflectance (emittance = 1 − reflectance) for (*a*) an oxidized stainless steel surface, and (*b*-*d*) the surface as increasingly more dusty ash is deposited on the surface; the surface temperature for ash deposition was held at 1000°F ± 30°F, and for measurements at 980°F ± 10°F

approaching the spectral shape for emittance of the much thicker pressed wafer of dusty fly ash shown in Fig. 4(*b*).

Model. The optical properties of a sample depend mainly on the optical constants, n and k, of the constituent material, and on its state of aggregation and surface condition. For example, from the emittance of the slag deposit in various states shown in Fig. 4, differences can clearly be observed between the homogeneous material in the liquid and fused states, the heterogeneous (i.e., containing voids) ground and pressed sample, and the heterogeneous sintered sample. The purpose of this effort was to incorporate the optical constants of the slag into various models, and to compare predictions of the models with the observed emittances. Two models have been considered, one for a homogeneous slab, and one for samples of particulate matter.

The optical constants, n_ν and k_ν, that were needed as input for each model were determined by a technique that uses absorption measurements, and thus eliminates the inaccuracies inherent in reflection techniques when applied to inhomogeneous materials such as ash or coal (Gerber and Hinderman, 1982; Solomon et al., 1986, 1987). The objective of the procedure as originally developed was to determine values of n_ν and k_ν that gave Mie theory predictions for spheres of the material in matrices of KBr and CsI, which were consistent with extinction measurements using KBr and CsI pellets (an extension of the method of Brewster and Kunitomo, 1984). The method can determine n and k except for a wavelength-independent constant addition to k. For dielectric samples this constant can usually be estimated by knowing that the material is reasonably transparent ($k \ll 1$) at short wavelengths. Figure 6 presents the measurements of the optical constants for the sintered sample #1. These are used as input for the model predictions of emissivity for ash and slag. The optical constants as a function of wavelengths as determined by this method compared well in regard to shape with measurements of Goodwin and Mitchner (1989), and Ebert and Self (1989). Goodwin and Mitchner observed that k is most affected for $\lambda < 4$ μm ($\lambda > 2500$ cm^{-1}) by the iron content, and at longer wavelengths (shorter wavenumbers) by the silica content. We observed a

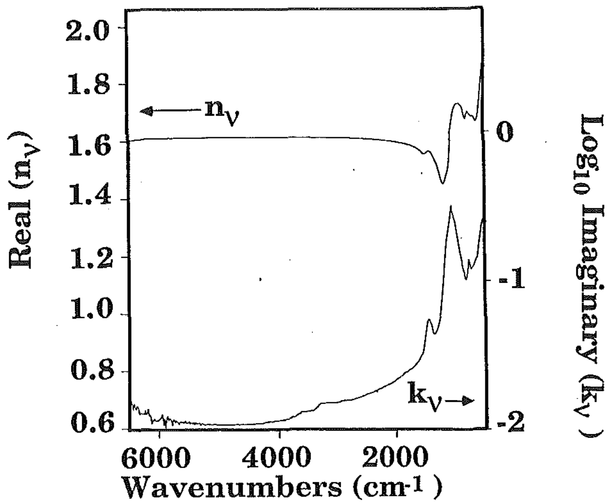

Fig. 6 Measured real and imaginary parts of the index of refraction, $N_\nu = n_\nu + ik_\nu$, for sample #1

higher amplitude than Goodwin and Mitchner in the iron-dependent region of our spectral regime between 1.6 and 4 μm (6500 to 2500 cm^{-1}), but this is consistent with Goodwin and Mitchner's trend of increasing k with increasing iron content. Our sample contained ~three times more iron than the synthetic slags of this reference. A substantial carbon (soot) content in the deposit would also elevate k (Foster and Howarth, 1968), but sample #1 was shown to contain negligible carbon residue by monitoring CO_2 evolution (FT-IR absorbance measurements) during oxidative heating in a thermogravimetric analyzer (Carangelo et al., 1990). The real part of the refractive index, n, does not exhibit a Christiansen frequency where $n = 1.0$, which is in agreement with the measured spectral emittance for this sample (Fig. 4*a*) in the solid state.

Homogeneous Slab Model. The emittance, ϵ_ν, of a smooth-surfaced, homogeneous slab at normal emergence is given by (Bohren and Huffman, 1983)

$$\epsilon_\nu = 1 - \frac{[(n_\nu - 1)^2 + k_\nu^2]}{[(n_\nu + 1)^2 + k_\nu^2]} \tag{7}$$

Predictions of this model give reasonable agreement with the measured emittance of the fused sample (compare ϵ_ν (closure) to ϵ_ν (optical constants) in Fig. 7).

There is another situation for which Eq. (6) applies. It is for a slab made by compressing or sintering very fine particles, so that over one wavelength the radiation samples many particles and voids (Bohren and Huffman, 1983). In this case an effective dielectric constant is estimated, and used to calculated n and k. The effective dielectric constant depends on the void fraction, and was calculated using the Maxwell-Garnett model (Bohren and Huffman, 1983). The emittance was calculated using this modified value of n and k for a number of void fractions. A calculation using a void fraction of about 0.15 is also presented in Fig. 7 and indicates a shift to better agreement with the data.

This suggests that fused surfaces are not optically smooth and require a minor component of void fraction for a more accurate prediction. It is possible but less likely that the discrepancy is due to the unknown constant added to the values of k. The emittance calculated from this model showed very poor agreement with the one measured for the ground and pressed sample of Fig. 4. From this comparison, it is concluded that the ground sample does not fulfill the requirement of the model, which is that the particle size be small compared to the wavelength. The next model we describe is more appropriate for this type of sample.

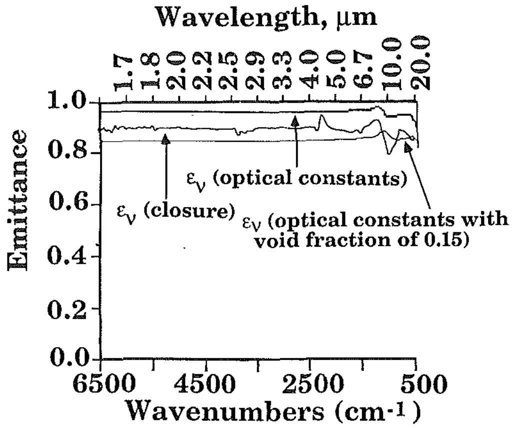

Fig. 7 Measured emittance for a fused surface of sample #1 compared to homogeneous slab prediction (ϵ_ν (optical constants)), and to prediction with a void fraction of 0.15; the predictions indicate that the fused surface is not optically smooth

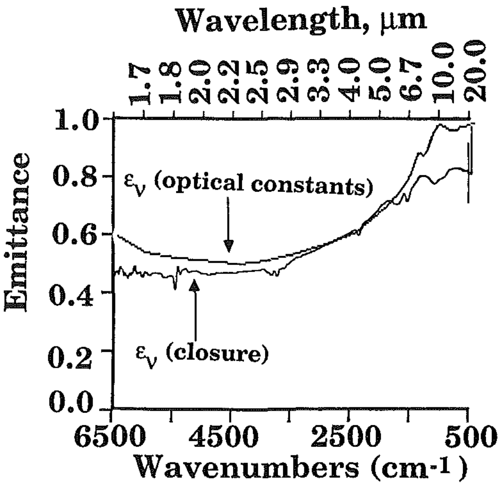

Fig. 8 Measured emittance compared to prediction for a ground sample of sample #1

Two-Stream Model. A simple, analytical model has been used to calculate the emissivity of an opaque sample consisting of a collection of spheres (Bohren, 1987). This approximate two stream model is much simpler to employ than exact three-dimensional models and is reasonably accurate. In this model the reflectivity of the sample is given by

$$\rho_\nu = \frac{(\sqrt{(1 - \omega_o g)} - \sqrt{(1 - \omega_o)})}{(\sqrt{(1 - \omega_o g)} + \sqrt{(1 - \omega_o)})} \tag{8}$$

where g is the asymmetry parameter, and

$$\omega_o = Q_{\text{sca}}/Q_{\text{ext}}. \tag{9}$$

The parameters Q_{sca} and Q_{ext} are the efficiency factors for scattering and extinction, respectively, and all quantities are spectral quantities. For the comparison in Fig. 8, we employed a constant value of $g (g = 0.6)$ as an empirical parameter. The agreement with experiment is satisfactory. Noticeably worse agreement was obtained when the mean particle radius was decreased by a factor of 2 or increased by a factor of 3. Likewise, for a mean particle radius of 1.0 μm, agreement with experiment was noticeably worse when the width of the particle size distribution was reduced by a factor of two. More sophisticated models for calculating the optical properties of dependent particle scattering are available (Kumar and Tien, 1990; Drolen and Tien, 1987; Cartigny et al., 1986).

Conclusions

This research has demonstrated that the radiative properties (i.e., emissivity and reflectivity) of extracted ash and slag combustion deposits at elevated temperature can routinely be measured in the laboratory. The technique combines spectroscopic measurements of radiance and reflectance in the mid-IR, between 1.6 and 20 μm, to determine the spectral emittance and the temperature at which the measurements were made.

Fused slag deposits, which exist as relatively smooth surfaced slabs, exhibited a high spectral emittance (≥ 0.9) over a wide temperature range (300 K to 1630 K). These measurements included the slag in both the solid and molten state.

Sintered slag deposits, due to their particle-like morphology, exhibited a wavelength-dependent emittance. In the long-wavelength spectral region where the chemical species of the slag were shown to absorb IR radiation, the emittance remained high. The scattering efficiency of the sintered morphology, however, increased toward shorter wavelength, and hence gave rise to lower emittance values. The degree of sintering, that is, to what extent the surface is particle-like and not glass-like controls the extent of emittance deviation from near blackbody character.

Fly ash deposits, which consist of finely packed particles, demonstrated the largest wavelength-dependent excursions (down to $\epsilon_\nu = 0.45$) due to the relatively high scattering efficiency of the deposits.

The results have shown that the radiative properties are highly dependent on the morphology of the combustion deposit and, in the wavelength region covered, appear to have only minimal dependence on chemical composition. Deposits of similar surface morphology showed little variation in integrated emittance with chemical composition up to 6500 cm^{-1}. Based on the results of this research it can be concluded that the rate of transfer of energy between surfaces and flames in a boiler or furnace environment will be greatly affected by the surface morphology of deposits. This morphology can change rapidly as a function of the surface temperature. The observations were compared to two morphology-dependent predictive models, which were shown to compare well with measured emissivities for both fused and sintered deposits.

Acknowledgements

This work was supported by the U.S. Department of Energy under Contract No. DE-AC22-87OC79901. The authors acknowledge the support of PETC Project Manager James Hickerson; and thank Sidney Self (Stanford University), Greg Clark (Babcock & Wilcox), and Geoffrey Germane (Brigham Young University) for supplying the ash and slag samples.

References

Best, P. E., Carangelo, R. M., Markham, J. R., and Solomon, P. R., 1986, "Tomographic Reconstruction of FT-IR Emission and Transmission Spectra in a Sooting Laminar Diffusion Flame: Species Concentrations and Temperatures," *Combustion and Flame*, Vol. 66, p. 47.

Bohren, C. F., and Huffman, D. R., 1983, *Absorption and Scattering of Light by Small Particles*, Wiley, New York.

Bohren, C. F., 1987, "Multiple Scattering of Light and Some of Its Observable Consequences," *Am. J. Phys.*, Vol. 55, p. 524.

Brewster, M. Q., and Kunitomo, T., 1984, "The Optical Constants of Coal, Char, and Limestone," ASME JOURNAL OF HEAT TRANSFER, Vol. 106, p. 678.

Carangelo, R. M., Solomon, P. R., Bassilakis, R., Gravel, D., Baillargeon, M., Baudais, F., and Vail, G., 1990, "Application of TG-FTIR in the Analytical Lab," *American Laboratory*, Apr., p. 51.

Cartigny, J. D., Yamada, Y., and Tien, C. L., 1986, "Radiative Transfer With Dependent Scattering by Particles: Part 1—Theoretical Investigation," ASME JOURNAL OF HEAT TRANSFER, Vol. 108, p. 608.

Drolen, B. L., and Tien, C. L., 1987, "Independent and Dependent Scattering in Packed-Sphere Systems," *J. Thermophysics and Heat Transfer*, Vol. 1, p. 63.

Ebert, J. L., and Self, S. A., 1989, "The Optical Properties of Molten Coal Slag," *National Heat Transfer Conference*, ASME HTD-Vol. 106, p. 123.

Eckert, E. R. G., and Goldstein, R. J., 1976, *Measurements in Heat Transfer*, 2nd ed., McGraw-Hill, New York.

Foster, P. J., and Howarth, C. R., 1968, "Optical Constants of Carbon and Coals in the Infrared," *Carbon*, Vol. 6, p. 719.

Gerber, H. E., and Hinderman, E. E., 1982, "Light Absorption by Aerosol Particles: First International Workshop," *Appl. Opt.*, Vol. 21, p. 370.

Goodwin, D. G., and Mitchner, M., 1989, "Infrared Optical Constants of Coal Slags: Dependence on Chemical Composition," *AIAA J. Thermophysics and Heat Transfer*, Vol. 3, p. 53.

Huntjens, F. J., and van Krevelan, D. W., 1954, "Chemical Structure and Properties of Coal. 2. Reflectance," *Fuel*, Vol. 33, p. 88.

Kumar, S., and Tien, C. L., 1990, "Dependent Absorption and Extinction of Radiation by Small Particles," ASME JOURNAL OF HEAT TRANSFER, Vol. 112, p. 178.

Markham, J. R., Solomon, P. R., and Best, P. E., 1990, "An FT-IR Based Instrument for Measuring Spectral Emittance of Material at High Temperature," *Review of Sci. Instr.*, Vol. 61, p. 3700.

Myers, V. H., Ono, A., and DeWitt, D. P., 1986, "A Method for Measuring Optical Properties of Semitransparent Materials at High Temperatures," *AIAA J.*, Vol. 24, p. 321.

Ono, A., Trusty, R. M., and DeWitt, D. P., 1982, "Experimental and Theoretical Study on the Quality of Reference Black Bodies Formed by Lateral Holes on a Metallic Tube," *Temperature, Its Measurement and Control in Science and Industry*, Am. Inst. Physics, New York, Vol. 5, part 1, p. 541.

Raask, E., 1985, *Mineral Impurities in Coal Combustion*, Hemisphere Publishing Corp., New York, p. 230.

Siegel, R., and Howell, J. R., 1981, *Thermal Radiation Heat Transfer*, 2nd ed., Hemisphere, Washington, DC.

Solomon, P. R., Carangelo, R. M., Best, P. E., Markham, J. R., and Hamblen, D. G., 1986, "The Spectral Emittance of Pulverized Coal and Char," *21st Symposium (Int.) on Combustion*, The Combustion Institute, Pittsburgh, PA, p. 437.

Solomon, P. R., Carangelo, R. M., Best, P. E., Markham, J. R., and Hamblen, D. G., 1987, "Analysis of Particle Emittance, Composition, Size and Temperature by FT-IR Emission/Transmission Spectroscopy," *Fuel*, Vol. 66, p. 897.

A. Sànchez
Research Assistant.

T. F. Smith
Professor.
Mem. ASME

Department of Mechanical Engineering,
The University of Iowa,
Iowa City, IA 52242

Surface Radiation Exchange for Two-Dimensional Rectangular Enclosures Using the Discrete-Ordinates Method

The purpose of this study is to develop a model based on the discrete-ordinates method for computing radiant exchange between surfaces separated by a transparent medium and to formulate the model so that arbitrary arrangements of the surfaces can be accommodated. Heat fluxes from the model are compared to those based on the radiosity/irradiation analysis. Three test geometries that include shadowing and irregular geometries are used to validate the model. Heat fluxes from the model are in good agreement with those from the radiosity/irradiation analysis. Effects of geometries, surface emittances, grid patterns, finite-difference weighting factor, and number of discrete angles are reported.

Introduction

Radiant exchange between surfaces separated by a radiatively nonparticipating medium occurs in numerous engineering applications including building interior thermal environments, electronic thermal control, solar energy usage, and spacecraft thermal control. In most applications, the components and enclosures are not simple geometries, and effects of shadowing, obstructing views, and irregularities must be taken into account. There exists, therefore, a need to develop methods that enable these and other factors to be included in a radiant exchange analysis. Several techniques are available for performing a radiant exchange analysis for surfaces separated by a transparent medium. Among them are the radiosity/irradiation method (RIM) (Sparrow and Cess, 1978; Siegel and Howell, 1981), the ray tracing technique (Greenberg, 1989; Baumeister, 1990), the Monte Carlo method (Siegel and Howell, 1981), and the stochastic method based on Markov chains (Naraghi and Chung, 1984, 1986; Billings et al., 1990). The ray tracing and Monte Carlo techniques have the capabilities of handling complex geometries but suffer from excessive computational times and uncertainties as to the number of rays needed to produce accurate results. View factors are fundamental to the RIM. Conceptually, view factors can be evaluated for complex geometries but difficulties arise when shadowing and obstructing effects are present. Recent computational advances have reduced the effort required to compute the view factors for complex enclosures (Walton, 1987; Greenberg, 1989; Rushmeier et al., 1990; Emery et al., 1991). Despite these techniques, there still exists a need for methods than can be applied conveniently to complex enclosures and that can be interfaced with models for other modes of heat transfer.

The discrete-ordinates method (DOM) (Fiveland, 1988; Sànchez et al., 1991) has undergone considerable development for analyzing radiant transfer in participating media, but has yet to be applied to radiant exchange for surfaces separated by a nonparticipating medium. For gaseous participating media, the spectral variation of the radiative properties is modeled as a series of absorbing bands separated by windows that are radiatively nonparticipating. Modest (1991) indicates that nongray effects for participating media can be accounted for in the general radiative transfer equation by using the weighted-sum-of-gray-gases model (WSGGM). Inherent within the WSGGM is the stipulation that an absorption coefficient is assigned a zero value to represent the transparent windows between absorbing bands. Hence, the accuracy of using the DOM to model radiant exchange within nonparticipating media needs to be established.

The objective of this study is to examine the feasibility of applying the DOM to the problem of computing the radiant exchange between surfaces separated by a transparent medium. The basic idea is to apply the general DOM to enclosures and to set some radiative properties in the DOM to some values in order to represent an opaque solid within the enclosure. Radiant exchange between surfaces forming the opaque solid and the other surfaces of the enclosure is then embedded within the DOM. The idea is based on the method used to solve flow and heat transfer problems in a domain containing both solid and fluid control volumes (conjugate heat transfer) (Patankar, 1990; House et al., 1990). In that method, the viscosity of a solid control volume is assigned a large value to force velocities to zero and the thermal conductivity of a solid control volume is assigned that of the solid.

Analysis

System Description. A generalized two-dimensional rectangular enclosure selected for study is shown in Fig. 1. The enclosure has a height H and width L. The walls are considered the boundary of the solution domain within which the radiant exchange is taking place. The enclosure may contain several protrusions mounted on the walls and obstructions, all of which contribute to the effects of multiple surfaces and shadowing. The protrusions and obstructions are opaque to radiation. Surfaces forming the enclosure, protrusions, and obstructions are diffusely emitting and reflecting, opaque, and gray and may have nonuniform radiative property and temperature distributions. The radiative properties are independent of temperature. Openings represented by pseudoblack surfaces could form a part of the enclosure walls. The intervening medium is radiatively transparent. As described later, three geometries of the generalized enclosure are configured to verify the accuracy of the DOM.

Radiative Transfer Equations. The governing radiative transfer equations for radiant exchange in a participating me-

---

Contributed by the Heat Transfer Division for publication in the JOURNAL OF HEAT TRANSFER. Manuscript received by the Heat Transfer Division April 10, 1991; revision received September 11, 1991. Keywords: Numerical Methods, Radiation, Radiation Interactions.

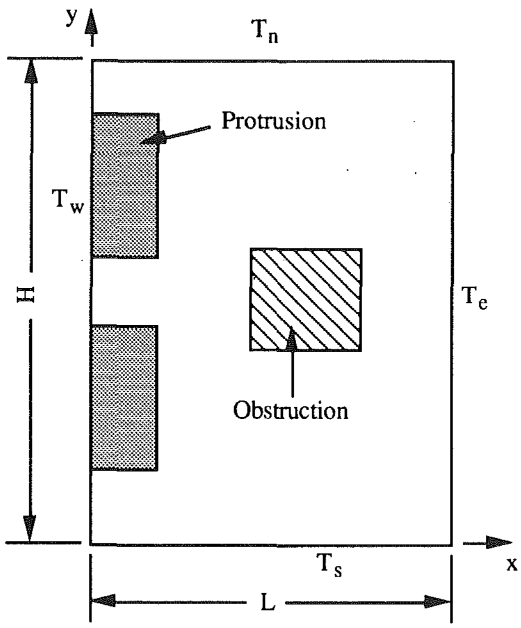

Fig. 1 Schematic diagram of typical enclosure

dium and the boundary conditions are presented to illustrate the nature of the problem that is being approximated. The radiative transport equation for the intensity for an absorbing and emitting medium is

$$\frac{\partial I}{\partial \xi} = -\kappa I + \kappa I_b \quad (1)$$

where ξ is the line-of-sight distance in the direction of propagation of the radiant intensity I, κ is the absorption coefficient of the medium, and I_b is the local blackbody intensity. Opaque and transparent media are represented by large and small values of the absorption coefficient, respectively. For a large value of the absorption coefficient, the intensity equals the blackbody intensity, and for an absorption coefficient of zero, the intensity remains unchanged. For a two-dimensional system, Eq. (1) is expressed as

$$\mu \frac{\partial I}{\partial x} + \eta \frac{\partial I}{\partial y} = -\kappa I + \kappa I_b \quad (2)$$

where $I = I(x, y; \mu, \eta)$, $I_b = I_b(x, y)$, and μ and η are direction cosines. At an opaque surface, the leaving intensity is composed of the emitted intensity and the reflected irradiation and is written as

$$I(x_a, y_a; \mu, \eta) = \epsilon I_b(x_a, y_a) + \frac{\rho}{\pi} \int_{2\pi} I'(x_a, y_a; \mu', \eta') \cos \phi' \, d\omega' \quad (3)$$

where the subscript a denotes a surface, ϵ is the surface emittance, and ρ is the surface reflectance $(=1-\epsilon)$. The prime denotes an incoming quantity, ϕ is the polar angle between the surface normal and the intensity, and ω is the solid angle. The integration in Eq. (3) is performed over the hemisphere above the surface. The net radiant energy leaving a surface is the difference between the radiosity and irradiation and is given by

$$q(x_a, y_a) = \int_{2\pi} I(x_a, y_a; \mu, \eta) \cos \phi \, d\omega - \int_{2\pi} I'(x_a, y_a; \mu', \eta') \cos \phi' \, d\omega' \quad (4)$$

Equations (1)–(4) apply on either a spectral or a gray basis. Equations (1)–(4) are the radiative transfer expressions being approximated.

Discrete-Ordinates Method. The development of the discretized form of the radiative transfer equations is initiated by subdividing the solution domain into a number of control volumes. Control volume P surrounded by control volumes E, S, W, and N is illustrated in Fig. 2(a). The interfaces between control volume P and the surrounding control volumes are designated by e, s, w, and n. In addition to the spatial discretization, the directions of propagation of the radiant intensity are discretized.

The intensity at point P in discrete direction i is I_i^P. For the positive x direction and for the ith direction, intensities entering and leaving control volume P are I_i^{wr}, I_i^{sr} and I_i^e, I_i^n. For the negative x direction, the corresponding intensities can be defined. The radiative properties of the w interface are denoted by ϵ_w, τ_w, and ρ_w for emittance, transmittance, and reflectance. Similarly, the radiant intensities and radiative properties of the other three interfaces can be introduced.

Application of Eq. (2) to discrete direction i yields

$$\mu_i \frac{\partial I_i}{\partial x} + \eta_i \frac{\partial I_i}{\partial y} = -\kappa_P I_i + \kappa_P I_b \quad (5)$$

where $I_i = I(x, y; \mu_i, \eta_i)$ and $i = 1$ to $4M$ with M denoting the number of discrete angles within a quadrant. The finite-dif-

Nomenclature

A = area, m^2
$e_{\max}$ = maximum error, percent
$e_{\rm rms}$ = root-mean-square error, percent
F_{i-j} = view factor between surfaces i and j
H = dimension of enclosure, m
I = radiant intensity, W/m^2-sr
K = surface location number
L = dimension of enclosure, m
N = number of surfaces exchanging radiant energy
M = number of discrete angles per quadrant
nx, ny = number of control volumes for x and y directions
q = net radiant energy leaving, W/m^2
T = temperature, K
V = volume, m^3
w = quadrature weighting factor
x = coordinate, m
y = coordinate, m
α = finite-difference weighting factor
ϵ = emittance
ζ = dimensionless distance
η = direction cosine
κ = absorption coefficient, m^{-1}
μ = direction cosine
ξ = distance along line-of-sight direction, m
ρ = reflectance
σ = Stefan–Boltzmann constant, 5.669×10^{-8} W/m^2-K^4
τ = transmittance
ϕ = polar angle
ω = solid angle, sr

Subscripts

a = surface area element
b = blackbody
e = east
n = north
s = south
w = west

Superscripts

e = east
n = north
r = entering
s = south
w = west
$'$ = incident quantity

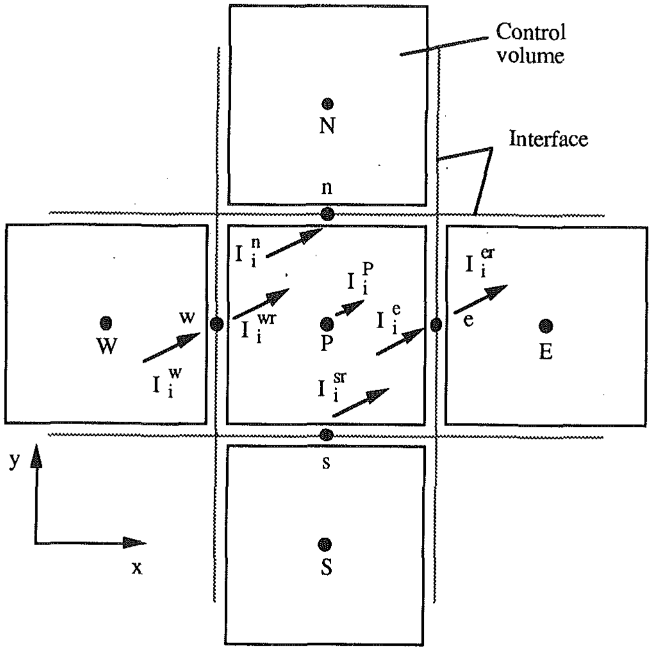

(a) Control volumes.

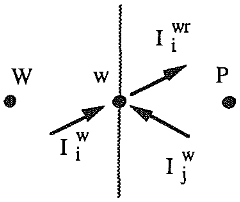

(b) Interface.

Fig. 2 Control volumes and interfaces

Table 1 Property relations

(a) Interior control volumes

Control volume*		Radiative properties for w-interface			Radiant intensity for w-interface
W	P	ε_w	τ_w	ρ_w	I_i^{wr}
T	T	0	1	0	I_i^w
S	S	0	0	1	$\frac{1}{\pi}\sum_{j=1}^{2M} w_j \mu_j I_j^w$
S	T	ε_w	0	$1-\varepsilon_w$	$\varepsilon_w I_{bw} + \frac{\rho_w}{\pi}\sum_{j=1}^{2M} w_j \mu_j I_j^w$
T	S	ε_w	0	$1-\varepsilon_w$	$\varepsilon_w I_{bw} + \frac{\rho_w}{\pi}\sum_{j=1}^{2M} w_j \mu_j I_j^w$

* S - solid; T - transparent

(b) Boundary control volume

- Control volume P is transparent: ε_w = given, $\rho_w = 1 - \varepsilon_w$
- Control volume P is solid: $\varepsilon_w = 0$, $\rho_w = 1$

ference form of Eq. (5) is derived by applying this expression to the control volume P, multiplying by $\Delta x \Delta y$, and integrating over the four faces of the control volume to yield

$$\mu_i A_x(I_i^e - I_i^{wr}) + \eta_i A_y(I_i^n - I_i^{sr}) + \Delta V_P \kappa_P I_i^P = \Delta V_P \kappa_P I_b^P \quad (6)$$

where $A_x = \Delta y$, $A_y = \Delta x$, and $\Delta V_P = \Delta x \Delta y$. The leaving intensities at the e and n interfaces are approximated by

$$I_i^e = \frac{1}{\alpha}\left[I_i^P - (1-\alpha) I_i^{wr}\right] \quad (7a)$$

$$I_i^n = \frac{1}{\alpha}\left[I_i^P - (1-\alpha) I_i^{sr}\right] \quad (7b)$$

α is the finite-difference weighting factor. Inserting Eqs. (7a) and (7b) into Eq. (6) and solving for I_i^P yield

$$I_i^P = \frac{|\mu_i| A_x I_i^{wr} + |\eta_i| A_y I_i^{sr} + \alpha \kappa_P I_b^P \Delta V_P}{|\mu_i| A_x + |\eta_i| A_y + \alpha \kappa_P \Delta V_P} \quad (8)$$

Application of Eq. (8) to the problem of radiative transfer for solid and transparent control volumes begins by first noting that, for a transparent control volume, $\kappa_P = 0\ \mathrm{m}^{-1}$ and, for a solid control volume, κ_P is assigned a very large value to simulate a highly attenuating medium (for example, $\kappa_P = 10^{20}\ \mathrm{m}^{-1}$). For these two situations, Eq. (8) reduces to:

Transparent Medium

$$I_i^P = \frac{|\mu_i| A_x I_i^{wr} + |\eta_i| A_y I_i^{sr}}{|\mu_i| A_x + |\eta_i| A_y} \quad (9a)$$

and

Solid Medium

$$I_i^P = I_b^P \quad (9b)$$

To verify Eq. (9a), consider radiation that propagates only in the x direction. Hence, $\eta_i = 0$ and Eq. (9a) reduces to

$$I_i^P = I_i^{wr} \quad (10)$$

This relation implies that, as expected, the intensity does not change in the direction of propagation as the radiation passes through a transparent medium.

The entering intensities must now be related to those leaving the control volumes. Consider interface w. The radiant intensities of interface w are shown in Fig. 2(b), where the leaving intensity for control volume P in the discrete direction j is I_j^w. For an interface, I_j^w may be transmitted through the interface or reflected by the interface into the ith direction. In terms of the radiative properties of the interfaces, the intensity entering control volume P from the w interface is evaluated by

$$I_i^{wr} = \tau_w I_i^w + \epsilon_w I_{bw} + \frac{\rho_w}{\pi} \sum_{j=1}^{2M} w_j \mu_j I_j^w \quad (11)$$

where I_{bw} is the blackbody intensity evaluated at the temperature of the w interface, and w_j are the angular quadrature weights for the j direction. The summation in Eq. (11) is over only those quadrants within a transparent control volume and only performed when the W control volume is opaque. A similar expression for the entering intensity I_i^{sr} for the s interface can be written.

The radiative properties of the interface between two control volumes are identified next. Specifically, for the w interface, the radiative properties of the interface are assigned the values stated in Table 1(a). The interface properties depend on the characteristics of the adjacent control volumes. For all cases, $\rho_w = 1 - \epsilon_w - \tau_w$. Hence, only two radiative properties of an interface, namely, ϵ_w and τ_w, need to be specified. Intensities I_i^{wr} derived from Eq. (11) for the various combinations are also stated.

Figure 3 applies for a control volume adjacent to a boundary of the enclosure; the interface w is considered to be a boundary node. The intensity leaving this face is

$$I_i^{wr} = \epsilon_w I_{bw} + \rho_w \sum_{j=1}^{2M} w_i \mu_j I_j^w \tag{12}$$

The conditions of the radiative properties are itemized in Table 1(*b*) for the two possible characteristics of control volume P, namely, opaque and transparent.

The net radiant energy leaving an interface is evaluated from the difference between the radiosity and irradiation. The expression for the radiant heat flux for interface w is

$$q_w = \sum_{i=1}^{2M} w_i \mu_i I_i^{wr} - \sum_{i=1}^{2M} w_i \mu_i I_i^w \tag{13}$$

The summations in Eq. (13) are for the four quadrants forming the entire space around interface w and include only those quadrants where the medium is transparent. If all quadrants cover a solid or cover a transparent medium, the radiant flux is zero. For a boundary control volume, the summations are over the hemisphere on the inside of the enclosure.

An important aspect of the DOM is the selection of the weighting factors and direction cosines for approximation of the hemispherical integrations. For surface radiant exchange, only the half-range heat fluxes need to be considered. They can be approximated by

$$\pi = 2\int_0^1 \mu d\mu = 2\sum_{i=1}^{M} w_i \mu_i \tag{14}$$

After experimenting with several quadrature sets (Truelove, 1987; Fiveland, 1988), a set based on equal weights and an equal angular increment of the polar angle ϕ was generated. The discretized polar angles for $i=1$ to M are $\phi_i = \Delta\phi/2 + (i-1)\Delta\phi$, where $\Delta\phi = \pi/2M$, and the equal weights are

$$w = \pi/2\sum_{i=1}^{M} \cos\phi_i \tag{15}$$

Heat fluxes computed using these weights and direction cosines are found to be more accurate than those using the other quadrature sets. The current set, however, may not be the optimum set.

Another important consideration is the selection of the value for the finite-difference weighting factor. Initially, this factor was taken as a constant, for example, $\alpha = 0.5$ or 1.0. However, values of radiant intensities for some of the transparent control volumes (opaque control volumes are not of concern) were found outside the range of physically allowable values. Therefore, for each discrete direction and spatial location, a check is made that the control volume intensity computed from Eq. (8) is bounded by the incoming intensities, for example, the south and west intensities in Fig. 2(*a*). If the check fails, the control volume intensity is assigned either the minimum or maximum of the incoming intensities. The leaving intensities given by Eqs. (7*a*) and (7*b*) are computed and compared to the minimum and maximum intensities. If the comparison fails, the value of α is increased by $\Delta\alpha$, taken as 0.01, and new leaving intensities are computed. In most cases, only one increment of the initial value of α is required. This procedure is continued until a leaving intensity is within the bounds; the other leaving intensity is then computed from Eq. (6). The values of α reported later are the initial values.

The solution procedure for the radiant intensities is similar to that used by Sànchez et al. (1991). An iterative procedure with sweeps for each of the two spatial directions and the four quadrants is necessary to solve for the intensities. Convergence of the intensities occurs when the variation in the intensity between iterations is less than an error criterion, taken as 1.0×10^{-3} percent.

The accuracy of the DOM is verified in part by checking that the overall energy balance is zero. The overall energy balance is computed by summing the product of the radiant heat flux and surface area for each interface and for all boundary surfaces.

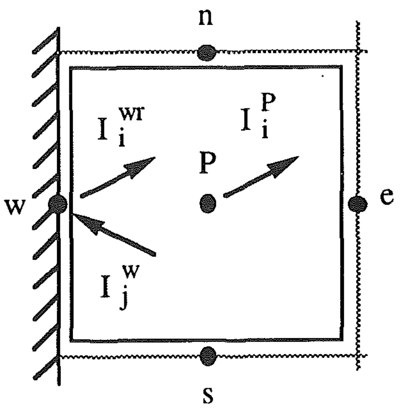

Fig. 3 Control volume at boundary

The DOM may be used to compute the view factors between any two opaque surfaces when all surfaces are black. If the view factor between surface i and surface j is sought, the blackbody emissive power of surface i is set equal to unity and that for all other surfaces is set equal to zero. The absolute value of the radiant flux for surface j is equal to the view factor F_{j-i}. Reciprocity gives the view factor F_{i-j}. Alternatively, the view factors could be evaluated from the set of equations given by

$$q_i = \sigma \sum_{j=1}^{N} F_{i-j}(T_i^4 - T_j^4) \tag{16}$$

which are solved simultaneously for F_{i-j}. In Eq. (16), N is the number of opaque surfaces within the enclosure and is determined by considering the interfaces between control volumes in Figs. 2 and 3. In view of the desire to compute radiant heat fluxes for general geometries as shown in Fig. 1, this study concentrates on the radiant heat fluxes.

Radiosity/Irradiation Method. Heat fluxes for the DOM are compared to those obtained from a radiant exchange analysis based on the RIM. For the RIM, the enclosure, including all protrusions and obstructions, is divided into N isothermal surfaces each with uniform irradiation, radiosity, and view factor. View factors are determined exactly using the cross-string method (Siegel and Howell, 1981), and all shadowing and occulting effects, when present, are taken into account. View factors computed using the cross-string method are interpreted as integrated values over a surface element. The reciprocity relation is used to reduce the number of view factors that must be found. For each surface, the enclosure relation is verified. Calculations from the RIM are checked to verify that the overall energy balance for the enclosure is zero.

Results and Discussion

The accuracy of the DOM is examined by configuring three test cases, namely, (1) a rectangular enclosure with no protrusions and obstructions, (2) a rectangular enclosure with a centered obstruction, and (3) a rectangular enclosure with two protrusions. Case 1 is used to examine in greater detail some of the characteristics of the DOM. Cases 2 and 3 exhibit shadowing and irregular geometry effects.

In addition to the radiative properties of the surfaces and the temperatures, solutions for the DOM depend on the selection of the finite-difference weighting factor, the number of discrete angles, and the grid spacing. Hence, one goal of the comparisons is to establish values of these parameters that yield accurate radiant heat fluxes. Heat fluxes for the DOM for all cases are computed using a single program, where only

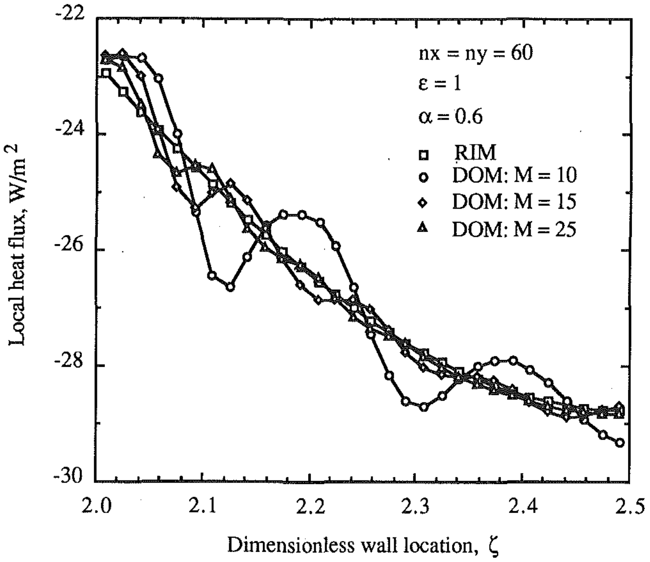

Fig. 4 Local heat fluxes for each wall for rectangular enclosure

Table 2 Overall heat fluxes

DOM M	Heat flux, W/m² north	 east
10	-18.844	-26.667
15	-18.834	-26.687
20	-18.824	-26.708
25	-18.820 (-18.876)*	-26.716 (-26.603)
50	-18.814 (-18.849)	-26.727 (-26.656)
RIM	-18.849	-26.657

*Numbers in parentheses are for α = 0.5.

the radiative properties of the interface and control volumes are adjusted to accommodate each geometry.

For the DOM, all enclosures are divided into *nx* and *ny* control volumes for the *x* and *y* directions, respectively. For the RIM, all horizontal and vertical walls of the enclosure are divided into *nx* and *ny* surfaces, respectively. The obstruction and protrusion surfaces are divided into elemental areas equal to those of the opposite enclosure walls.

Rectangular Enclosure. For the first test case, a square rectangular enclosure with $H=L=1.0$ m is examined. The walls of the enclosure are maintained at isothermal temperatures of $T_w=310$ K and $T_n=T_e=T_s=300$ K. All surfaces are black. The uniformity assumption of the wall temperature and emittance distributions may be relaxed because DOM and RIM are capable of handling arbitrary distributions. In addition, $\alpha=0.6$, $M=15$, and $nx=ny=60$. The number of surfaces for the indicated grid is $N=240$. The effects of these parameters are identified later. Unless otherwise noted, these conditions apply to the results. Because the west wall views an isothermal enclosure, heat fluxes are equal to a constant given by the difference of blackbody emissive powers evaluated at temperatures of 310 and 300 K. The other walls experience a negative heat flux that is a function of how well a surface element views the heated wall.

Heat fluxes from the DOM predict exactly those from the RIM for the west wall and are nearly indistinguishable from those of the RIM for the north and east walls. An indication of the agreement of the heat fluxes for the two methods is shown in Fig. 4, using expanded scales, where heat fluxes for the upper half of the east wall ($2.0\leq\zeta\leq2.5$) are shown. The dimensionless wall distance ζ has its origin at the lower-left-hand corner of the west wall in Fig. 1 and extends clockwise around the enclosure. In addition to heat fluxes for $M=15$, heat fluxes are shown for $M=10$ and 25. For $M=10$, significant oscillations of the heat fluxes for the DOM about those of the RIM are found. The maximum error between the RIM and DOM results for this wall section is -6.32 percent found at $\zeta=2.117$. The oscillations tend to be more noticeable for surface elements near a corner ($\zeta=2.0$). The oscillations and errors diminish, however, as the number of discrete angles increases. For example, for $M=25$, the maximum error is -0.84 percent occurring at $\zeta=2.067$.

Overall heat fluxes for a wall area may be predicted rather accurately by a low number of discrete angles. This is illustrated in Table 2, where heat fluxes for the DOM and RIM are presented for the north (same as south) and east walls. Heat fluxes for the DOM are provided for $\alpha=0.6$ and $M=10$, 15, 20, 25, and 50. The numbers in parentheses are discussed in the next paragraph. The error for the north and east walls is less than 0.04 percent for $M=10$ and deteriorates to near 0.2 percent for $M=25$. The error for larger values of M ($=50$) never exceeds 0.27 percent. A portion of these errors is attributed to the DOM computing the radiant exchange for a point on a surface element, whereas the view factors are integrated values.

As identified later, the accuracy of the DOM depends on, among other factors, the number of discrete angles and the finite-difference weighting factor. Overall heat fluxes shown in parentheses in Table 2 for $\alpha=0.5$ when $M=25$ and 50 illustrate the latter effect. For $\alpha=0.5$, the errors in the overall heat fluxes are less than 0.21 percent for $M=25$ and are nearly zero percent for $M=50$. Hence, through adjustment of the finite-difference weighting factor and the selection of the number of discrete angles, the DOM is capable of predicting accurate heat fluxes.

To identify further the error between local fluxes computed using the RIM and DOM and to examine the influence on the error of the emittance, finite-difference weighting factor, number of discrete angles, and grid, the root-mean-square (rms) error is computed using

$$e_{\rm rms}=\left[\frac{1}{N-1}\sum_{i=1}^{N}\left(\frac{q_{{\rm RIM},i}-q_{{\rm DOM},i}}{q_{{\rm RIM},i}}\right)^2\right]^{1/2} \tag{17}$$

where the subscripts RIM and DOM refer to heat fluxes computed using the RIM and DOM. The rms errors are displayed in Fig. 5 as a function of the finite-difference weighting factor for $nx=ny=20$ and 60 and for $\epsilon=1.0$, 0.5, and 0.1, where all walls have the same emittance. Heat fluxes for the DOM are for $M=25$. Consider first the rms errors for $\epsilon=1.0$. As α increases from 0.5, the rms error decreases, reaches a minimum, and then increases. The minimum rms errors occur near $\alpha=0.54$ and 0.62 for the coarser and finer grids, respectively, and are nearly identical at a value of 0.32 percent for the two grids. For $M=50$ and the finer grid (not shown), the minimum rms error is 0.13 percent found at $\alpha=0.54$, and at $\alpha=0.6$, it is 0.20 percent.

From Fig. 5, the rms errors diminish as the emittance is decreased. The minimum rms errors for $\epsilon=0.5$ and 0.1 are 0.18 and 0.035 percent, respectively. The value of α that yields a minimum rms error for a given grid is nearly independent of emittance. As an example, for the finer grid, the minimum rms errors occur near $\alpha=0.62$ for $\epsilon=1.0$, 0.5, and 0.1. The effect of the emittance on the local heat fluxes is examined further for Case 2.

The influence of the number of discrete angles on the local heat fluxes is presented in Fig. 6 for $\alpha=0.6$, $nx=ny=60$, and $\epsilon=1.0$. Heat flux results for the DOM and RIM are shown at spatial locations of $\zeta=1.0167$ (west end of the north wall), 1.4833 (center of north wall), 1.9833 (east end of north wall), 2.0167 (north end of east wall), and 2.4833 (center of east

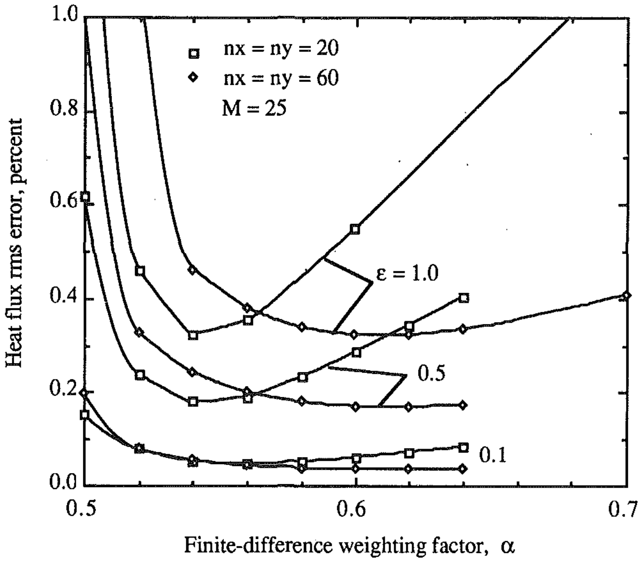

Fig. 5 The rms errors for rectangular enclosure

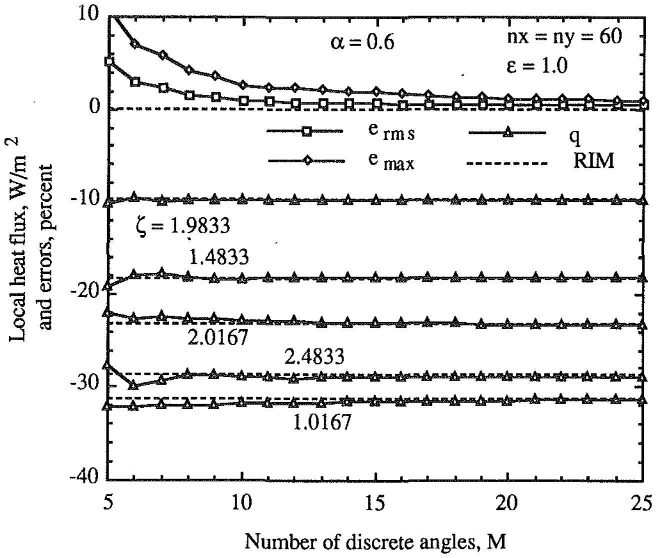

Fig. 6 Influence of number of discrete angles

wall). Also, the rms error and the absolute maximum error ($e_{\max}$) in local heat fluxes for the DOM are illustrated. The oscillatory behavior with decreasing amplitude of oscillation of some of the DOM heat fluxes as M increases is shown in the figure. For $M > 15$, local fluxes for the DOM are in good agreement with the RIM results for the indicated positions. The maximum error shows a decreasing trend as M increases. For $M > 14$, the maximum error is less than 2 percent and the rms error is less than 0.7 percent. For $M = 25$, the maximum error is less than 1.0 percent.

The control volumes used for the results in Figs. 4-6 are square. In some applications, it may not be desirable or possible to use square control volumes, and the effect of nonsquare control volumes needs to be examined. The rms errors for $L = 0.5$ m, $H = 1.0$ m, $ny = 60$, and $nx = 30$ and 60 were computed for various values of α. Control volumes are square for $nx = 30$ and are twice as high as wide for $nx = 60$. The results are similar to those in Fig. 5. The rms error does depend on the size of the control volume but the dependency is not significant. Minimum rms errors of 0.264 and 0.338 appear near $\alpha = 0.6$ and 0.7 for $nx = 30$ and 60, respectively. For $\alpha < 0.68$, rms errors for the square control volumes are smaller than those for the narrower control volumes. Selecting $\alpha = 0.6$ for both grids yields $e_{\mathrm{rms}} < 0.4$ percent.

The computations were performed on an Encore Multimax 320 computer system with a rating of 0.2 MFLOPS. The conditions for $nx = ny = 60$, black walls, and $\alpha = 0.6$ require central processor unit times of 166 and 279 s for $M = 15$ and 25, respectively. The corresponding times for $nx = ny = 20$ are 20 and 34 s. The computational times for the RIM for the finer and coarser grid patterns are 12.4 and 1.8 s. The higher times for the DOM should not penalize the attractiveness of this method because the setup times are significantly lower for this method than those for the RIM.

In the analysis, the equal angle quadrature set is noted to yield more accurate results than other sets. To illustrate this, the S8 quadrature set of Fiveland (1988) corresponding to 10 streams per quadrant is used to solve the rectangular enclosure case with black surfaces and $nx = ny = 60$. For this set, the minimum rms error of 13.4 percent is found at $\alpha = 1.0$. For the equal angle set with $M = 10$, the minimum rms error of 1.01 percent occurs near $\alpha = 0.90$. Hence, the equal angle set does yield more accurate heat fluxes. These findings imply that, for absorbing gases, a different discrete ordinate set should be used to evaluate radiant exchange in the transparent windows than that for the absorbing bands.

In summary, the results for the rectangular enclosure reveal that the DOM is capable of predicting accurate local and overall heat fluxes. As a compromise between computational effort and accuracy, the number of discrete angles could be as low as 15. Also, a value of $\alpha = 0.6$ would yield accurate results for the conditions examined.

Centered Obstruction. The second case involves a square enclosure with a square, centered obstruction. The enclosure has $H = L = 1.0$ m, $T_w = 320$ K, and $T_n = T_e = T_s = 300$ K. The obstruction has sides of length 0.5 m and a temperature of 300 K. All surfaces have the same emittance. Local radiant heat fluxes for the DOM and RIM are displayed in Fig. 7 for emittances of 0.5 and 1.0, $nx = ny = 40$, $\alpha = 0.6$, and $M = 15$. The dimensionless distance ζ has the same origin as in Fig. 4 and continues clockwise around the obstruction. Hence, the north surface of the obstruction lies within the range of $4.5 < \zeta < 5.0$. Because of blockage by the obstruction, the heat flux for $\epsilon = 1.0$ is zero for the east portion of the enclosure wall between $2.375 < \zeta < 2.625$ and for the east surface of the obstruction. Because of symmetry, heat fluxes for only the upper half of the enclosure and obstruction are plotted. There is good agreement between the DOM and RIM results.

Further evidence of the accuracy of the DOM was obtained by examining the heat flux rms error as a function of the finite-difference weighting factor. For these results, all surfaces have the same emittances of 1.0 and 0.5, and $M = 25$. As shown in Fig. 7, heat fluxes for some of the surface elements are zero. Thus, when computing the rms error, surface elements with a zero heat flux for the RIM are excluded from the summation in Eq. (17), and the value of N is reduced accordingly. Also, for the east surface of the enclosure wall, the heat flux is very small for the surface element just prior to the point where the obstruction blocks the view of the heated west wall. Specifically, at $\zeta = 2.3375$, heat fluxes for the RIM and DOM are $q_{\mathrm{RIM}} = -0.244$ W/m^2 and $q_{\mathrm{DOM}} = 1.548$ W/m^2, which convert to an error of 534 percent. Because the heat fluxes are small, this point and the corresponding point by symmetry are neglected in the summation of Eq. (17). The effect of α on e_{rms} is similar to that shown in Fig. 5. The optimum value of α occurs near 0.55 with rms errors of 1.28 and 0.92 percent for $\epsilon = 1.0$ and 0.5, respectively. These rms errors are larger than those for the rectangular enclosure without the obstruction because the surface elements with zero heat fluxes (for both the DOM and RIM, where there is exact agreement) are excluded from the summation.

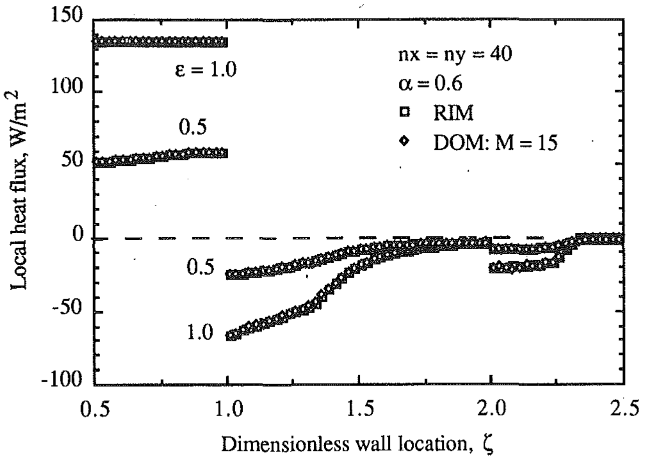

(a) Enclosure walls.

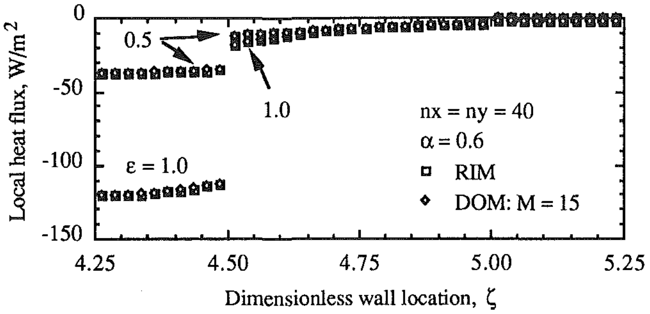

(b) Obstruction surfaces.

Fig. 7 Local heat fluxes for enclosure with obstruction

The influence of the number of discrete angles on the local heat fluxes, rms error, and absolute maximum error was also examined for black surfaces and $\alpha=0.6$. The effect of M is similar to that in Fig. 6. For $M=10$ and 25, $e_{\rm rms}=4.3$ and 1.7 percent, respectively.

Two Protrusions. The third test case was chosen as representative of an electronic chassis containing electronic components (protrusions) mounted on a printed circuit board (Smith et al., 1991). For this case, the rectangular enclosure in Fig. 1 has $H=50$ mm and $L=12$ mm. Two protrusions are centered on the west wall in Fig. 1. The protrusions have dimensions of 6 and 15 mm in the x and y directions, respectively, and are separated a distance of 10 mm. Hence, the west wall has exposed areas of 5 mm at the top and bottom and 10 mm at the center. The enclosure walls are assigned temperatures of $T_w=310$ K and $T_n=T_e=T_s=300$ K and emittances of $\epsilon_w=0.9$ and $\epsilon_n=\epsilon_e=\epsilon_s=0.5$. The protrusions have uniform temperatures of 320 K and emittances of 0.8. The higher temperature of the protrusions could be caused by internal heat generation within the protrusions. Numerical solutions for local radiant fluxes were obtained using $nx=12$ and $ny=50$. Local heat fluxes for the DOM and RIM are displayed in Fig. 8 for surface elements in the upper half of the system. Heat fluxes for the DOM are for $M=15$ and $\alpha=0.6$. The surface location number K represents the upper half of the west wall between the protrusions for $1\leq K\leq 5$, the upper protrusion for $6\leq K\leq 32$, the upper portion of the west wall for $33\leq K\leq 37$, the north wall for $38\leq K\leq 49$, and the upper half of the east wall for $50\leq K\leq 74$. There is good agreement between the heat fluxes based on the DOM and RIM.

The influence of the finite difference weighting factor on the heat flux rms error was examined. When computing the rms error, a large error was found at $K=35$, where $q_{\rm RIM}=0.00921$ W/m^2 and $q_{\rm DOM}=0.294$ W/m^2, which converts to an error of 3090 percent. From Fig. 8, the heat flux at this location is passing through zero. Hence, this location and the resultant error are not included in the summation of Eq. (17). The rms error has the same behavior as in Fig. 5, attaining a minimum of 0.741 percent near $\alpha=0.55$. For $\alpha=0.6$, the rms error is 1.56 percent.

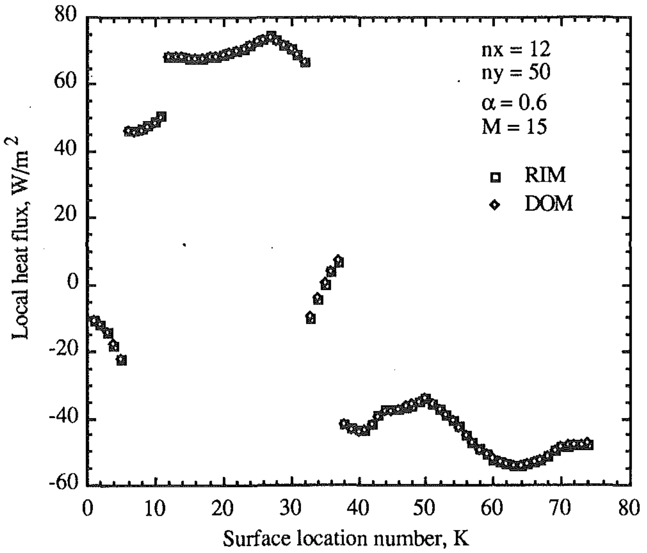

Fig. 8 Local heat fluxes for enclosure with protrusions

The effect of the number of discrete angles on the rms and maximum errors was examined for $\alpha=0.6$. The rms error is nearly independent of M with values of 1.558 and 1.556 percent for $M=15$ and 25. For $M>20$, the maximum error is less than 10 percent and is located at $K=34$, which is near the point where the heat flux passes through zero.

Conclusions

The discrete-ordinates method has been developed for evaluation of radiant exchange between surfaces separated by a transparent medium. The method uses the control volume approach to track the radiant intensity in discrete directions. The formulation is attractive in that arbitrary arrangements of solid objects separated by a transparent medium can be accommodated by appropriate selection of the radiative properties of the control volumes and of the interfaces between control volumes. Validation of the method was accomplished by comparing local heat fluxes to those computed from the radiosity/irradiation analysis. Three geometric configurations that include effects of shadowing and irregular boundaries are examined. In all comparisons, heat fluxes based on the discrete-ordinates method are in good agreement with those from the analysis. Effects of reflecting surfaces as well as nonsquare control volumes are presented. The comparisons also established that selecting a finite-difference weighting factor of 0.6 and the number of discrete angles of 15 yield accurate results. In the interest of improving and expanding the method, specification of the discrete angles could be re-examined, the method could be extended to surfaces with a bidirectional reflectance, three-dimensional geometries could be examined, and application of the method to radiant exchange when a participating medium separates the surfaces would be of interest.

Acknowledgments

The first author would like to acknowledge the financial support received from Universidad de los Andes and Fundación Gran Mariscal de Ayacucho, both of the Republic of Venezuela. The second author wishes to acknowledge support for this study by Rockwell International Corporation.

References

Baumeister, J. F., 1990, "Thermal Radiation Characteristics of Nonisothermal Cylindrical Enclosures Using a Numerical Ray Tracing Technique," *Radiation Heat Transfer: Fundamentals and Applications*, T. F. Smith, M. F. Modest, A. M. Smith, and S. T. Thynell, eds., ASME HTD-Vol. 137, pp. 73–79.

Billings, R. L., Barnes, J. W., Howell, J. R., and Slotboom, O. E., 1990, "Markov Analysis of Radiative Transfer in Specular Enclosures," *Radiation Heat Transfer: Fundamentals and Applications*, T. F. Smith, M. F. Modest, A. M. Smith, and S. T. Thynell, eds., ASME HTD-Vol. 137, pp. 89–94.

Emery, A. F., Johansson, O., Lobo, M., and Abrous, A., 1991, "A Comparative Study of Methods for Computing the Diffuse Radiation Viewfactors for Complex Structures," ASME JOURNAL OF HEAT TRANSFER, Vol. 101, pp. 413–422.

Fiveland, W. A., 1988, "Three-Dimensional Radiative Heat-Transfer Solutions by the Discrete-Ordinates Method," *Journal of Thermophysics and Heat Transfer*, Vol. 2, pp. 309–316.

Greenberg, D. P., 1989, "Light Reflection Models for Computer Graphics," *Science*, Vol. 244, pp. 166–173.

House, J. M., Beckermann, C., and Smith, T. F., 1990, "Effect of a Centered Conducting Body on Natural Convection Heat Transfer in an Enclosure," *Numerical Heat Transfer*, Part A, Vol. 18, pp. 213–225.

Modest, M. F., 1991, "The Weighted-Sum-of-Gray-Gases Model for Arbitrary Solution Methods in Radiative Transfer," *ASME/JSME Thermal Engineering Proceedings*, Vol. 4, pp. 3–10.

Naraghi, M. H. N., and Chung, B. T. F., 1984, "A Stochastic Approach for Radiative Exchange in Enclosures With Nonparticipating Medium," ASME JOURNAL OF HEAT TRANSFER, Vol. 106, pp. 690–698.

Naraghi, M. H. N., and Chung, B. T. F., 1986, "A Stochastic Approach for Radiative Exchange in Enclosures With Directional-Bidirectional Properties," ASME JOURNAL OF HEAT TRANSFER, Vol. 108, pp. 264–270.

Patankar, S. V., 1990, *Numerical Heat Transfer and Fluid Flow*, McGraw-Hill, New York.

Rushmeier, H. E., Baum, D. R., and Hall, D. E., 1990, "Accelerating the Hemi-Cube Algorithm for Calculating Radiation Form Factors," *Radiation Heat Transfer: Fundamentals and Applications*, T. F. Smith, M. F. Modest, A. M. Smith, and S. T. Thynell, eds., ASME HTD-Vol. 137, pp. 45–51.

Sànchez, A., Smith, T. F., and Krajewski, W. F., 1991, "Three-Dimensional Radiative Heat Transfer in a Polydispersion With Collimated Incident Source," accepted for the 1991 National Heat Transfer Conference.

Siegel, R., and Howell, J. R., 1981, *Thermal Radiation Heat Transfer*, Hemisphere Publishing, Washington, DC.

Smith, T. F., Beckermann, C., and Weber, S. W., 1991, "Combined Conduction, Natural Convection, and Radiation Heat Transfer in an Electronic Chassis," ASME *Journal of Electronic Packaging*, Vol. 113, pp. 382–391.

Sparrow, E. M., and Cess, R. D., 1978, *Radiation Heat Transfer*, Hemisphere Publishing, New York.

Truelove, J. S., 1987, "Discrete-Ordinate Solutions of the Radiation Transport Equation," ASME JOURNAL OF HEAT TRANSFER, Vol. 109, pp. 1048–1051.

Walton, G. N., 1987, "Algorithms for Calculating Radiation View Factors Between Plane Convex Polygons With Obstructions," *Fundamentals and Applications of Radiation Heat Transfer*, A. M. Smith and T. F. Smith, eds., ASME HTD-Vol. 72, pp. 45–52.

Effective Propagation Constant of Fibrous Media Containing Parallel Fibers in the Dependent Scattering Regime

Siu-Chun Lee
Vice President,
Applied Sciences Laboratory, Inc.,
Hacienda Heights, CA 91745

The radiative properties of a particulate medium are strongly influenced by the particle concentration and wavelength of the incident radiation. Independent scattering prevails at very low particle concentration, such that the spacing between the particles is much larger than the particle size and incident wavelength. As the particle spacing decreases, near-field multiple scattering and far-field interference of the scattered waves become increasingly pronounced. These dependent scattering effects cause the extinction efficiency and the phase velocity of electromagnetic waves, which are related to the effective propagation constant of the medium, to deviate from those in the independent scattering regime. This paper presents the theoretical formulation of the effective propagation constant of a nondissipative medium containing closely spaced parallel fibers. The dispersion relations for oblique incidence are derived for a transverse magnetic and a transverse electric mode incident wave. Numerical results for Rayleigh limit fibers are presented to illustrate the effect of fiber volume fraction on the propagation constant and extinction efficiency of the medium.

Introduction

Fibrous materials are commonly employed for thermal insulation in many engineering systems. The diameter of the individual fiber in these materials is usually comparable to the wavelength. Typically, fibrous materials for applications at moderate temperatures are of high porosity, whereas fabric blankets for high temperatures have very low porosity. Radiative energy transport through high-porosity fibrous materials can be analyzed by assuming independent scattering. Analytical models for the radiative properties and radiation heat transfer that account for the effect of fiber orientation have been developed by Lee (1986, 1988, 1989, 1990a).

High-density fabric materials for applications at elevated temperatures are generally manufactured by weaving fiber bundles into a matrix formation. Each fiber bundle contains a large number of tightly packed parallel fibers. The high packing densities of the fiber bundles and the matrix dictate that dependent scattering is dominant in the thermal radiation regime. An accurate analysis of the radiative properties of densely packed fibers, which properly accounts for the dependent scattering effects, is essential in the design of fabric materials to meet specific thermal performance requirements.

A rigorous treatment of dependent scattering requires consideration of both the near-field and far-field interactions of the scattered electromagnetic (EM) waves. In addition, the analysis for closely spaced fibers must account for the depolarization of the scattered waves at oblique incidence. Because of the complexity of including the near-field multiple scattering effects, the Rayleigh–Debye (also known as Rayleigh–Gans) theory, which considers only the far-field wave interference, is usually employed to evaluate the dependent scattering properties. This approach was employed by White and Kumar (1989) and Kumar and White (1990) to treat the case of normal incidence on parallel fibers. A recent study by Lee (1991a) showed that neglecting multiple scattering in the near field would lead to erroneous extinction and scattering coefficients if the Rayleigh–Debye conditions are not observed. In particular, the Rayleigh-Debye theory cannot correctly predict the extinction efficiency if the particles absorb radiation.

The dependent scattering formulations for the general case of an obliquely incident plane wave on an arbitrary configuration of homogeneous and radially stratified, parallel fibers have been developed by Lee (1990b, 1991b). Based on these formulations, the radiative properties of a collection of fibers can be evaluated by specifying the spatial location, size, and refractive index of each of the fibers. It is obvious that the numerical calculation becomes very cumbersome as the number of fibers increases. Since the constituent yarns in a high-density fabric contain a large number of parallel fibers, an analysis must be developed to evaluate the effective radiative properties of a high-density fiber matrix.

This paper presents the theoretical formulation for the effective propagation constant at oblique incidence for a medium of closely spaced, parallel fibers. The number of fibers and the volume of the medium are large, but their ratio, which is the number density, remains finite. The effective propagation constant yields the extinction efficiency and the phase velocity of wave propagation in the medium. In the following sections, a brief review of the dependent scattering formulation is first given. This is followed by the derivation of the dispersion relations that govern the effective propagation constant of a medium containing closely spaced, parallel fibers. Approximate expressions will be derived for Rayleigh limit fibers at normal and oblique incidence. Numerical results for Rayleigh limit fibers are shown to illustrate the effect of volume fraction on the propagation constant and extinction efficiency of the medium.

Dependent Scattering Formulation

The formal solution for dependent scattering is obtained by solving Maxwell's equations, as presented by Lee (1990b, 1991b). For the general case of oblique incidence, the polarization of the scattered waves is decomposed into the transverse magnetic (TM) and transverse electric (TE) modes. As a result, the total EM field in the vicinity of a fiber contains contri-

---

Contributed by the Heat Transfer Division for publication in the JOURNAL OF HEAT TRANSFER. Manuscript received by the Heat Transfer Division April 1991; revision received October 1991. Keywords: Porous Media, Radiation, Radiation Interactions.

butions from the external incident wave and the depolarized components of the scattered waves.

The depolarization effect results in a cross mode dependence of the coefficients of the scattered waves. For an incident wave of the TM mode, the following system of equations governing the scattered wave coefficients is obtained (Lee, 1990b):

$$\sum_{S=-\infty}^{\infty}\sum_{k=1}^{N}\{[\delta_{jk}\delta_{ns}+(1-\delta_{jk})G_{ks}^{jn}\,{}^{o}b_{jn}^{\mathrm{I}}]b_{ks}^{\mathrm{I}} + (1-\delta_{jk})G_{ks}^{jn}\,{}^{o}b_{jn}^{\mathrm{II}}a_{ks}^{\mathrm{I}}\} = \epsilon_j\,{}^{o}b_{jn}^{\mathrm{I}} \quad (1)$$

and

$$\sum_{S=-\infty}^{\infty}\sum_{k=1}^{N}\{[\delta_{jk}\delta_{ns}+(1-\delta_{jk})G_{ks}^{jn}\,{}^{o}a_{jn}^{\mathrm{I}}]a_{ks}^{\mathrm{I}} + (1-\delta_{jk})G_{ks}^{jn}\,{}^{o}a_{jn}^{\mathrm{II}}b_{ks}^{\mathrm{I}}\} = \epsilon_j\,{}^{o}a_{jn}^{\mathrm{I}} \quad (2)$$

where δ_{jk} and δ_{ns} are the Kronecker delta functions, the superscripts I and II denote the TM and TE modes, respectively, and the wave coefficients preceded by the superscript o refer to those for independent scattering. Expressions for the independent scattering wave coefficients can be found from Kerker (1969). The phase shift factor is given by

$$\epsilon_j(\mathbf{R}_j)=\exp(-ik_o\mathbf{R}_j\cdot\mathbf{e}^o) \quad (3)$$

where $\mathbf{R}_j$ is the radial vector pointing to fiber j, and $\mathbf{e}^o$ is the unit vector in the direction of the incident wave, as shown in Fig. 1. The pair-coupling function that relates the influence between a pair of fibers j and k is given by

$$G_{ks}^{jn}=(-i)^{s-n}H_{s-n}(l_oR_{kj})\exp[i(s-n)\gamma_{kj}] \quad (4)$$

where $l_o=k_o\cos\phi_i$, $R_{kj}=|\mathbf{R}_j-\mathbf{R}_k|$, and γ_{kj} is the polar angle that the line joining the centers of fibers j and k makes with the X axis. The corresponding equations for a TE mode incident wave can be obtained by replacing b_{jn}^{I}, a_{jn}^{I}, ${}^{o}b_{jn}^{\mathrm{I}}$, and ${}^{o}a_{jn}^{\mathrm{I}}$ by a_{jn}^{II}, b_{jn}^{II}, ${}^{o}a_{jn}^{\mathrm{II}}$ and ${}^{o}b_{jn}^{\mathrm{II}}$ in Eqs. (1) and (2).

Equations (1) and (2) can be solved for the dependent scattering wave coefficients by applying the independent scattering wave coefficients and by specifying the spatial location of each of the fibers. This system of equations becomes very large as the number of fibers increases. Therefore, it is necessary to develop analyses to evaluate the effective properties of a dense medium of fibers.

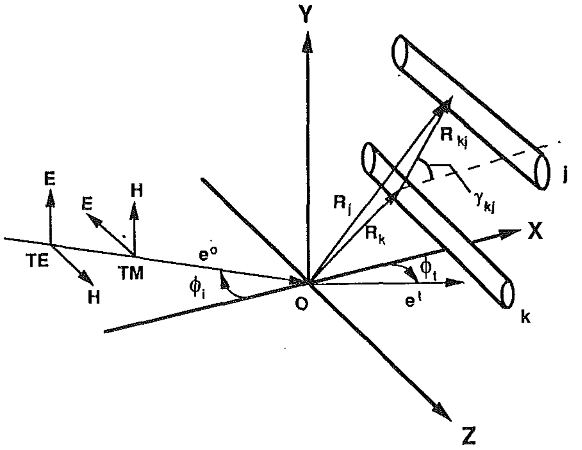

Fig. 1 A plane electromagnetic wave at oblique incidence on a medium of parallel fibers

Dependent Scattering in a Dense Medium

In this section the previous formulation for a finite configuration of fibers will be employed to derive the effective propagation constant of a dense medium of fibers as shown in Fig. 1. All the fibers are assumed to be located to the right of the coordinate origin. The volume V of the medium and the number of fibers N tend to infinity, but the number density $n_o=N/V$ is finite. The refractive index of the medium containing the fibers is unity. The unit vectors along the direction of the

Nomenclature

a_{jn} = coefficient of scattered wave, TE mode
A = coefficient in the pair correlation function
b_{jn} = coefficient of scattered wave, TM mode
$\mathbf{e}$ = unit vector
f = an arbitrary property of the fibers
f_v = volume fraction per unit length of fiber $=n_o\pi r_o^2L_o$
$F_{sn,1}$, $F_{sn,2}$, F_{sn}^o = functions defined by Eqs. (14), (15), and (18), respectively
$g(R)$ = pair correlation function
G_{ks}^{jn} = pair coupling function, defined by Eq. (4)
H_n = Hankel function of the second kind
i = $\sqrt{-1}$
J_n = integral order Bessel function
$\mathbf{k}$ = unit vector in the Z direction
k_o = wave number in vacuum $=2\pi/\lambda$
K = effective propagation constant of the medium $=K_R-iK_{\mathrm{I}}$
K_R, K_{I} = real part and imaginary parts of K, respectively
l_o = $k_o\cos\phi_i$
L = $K\cos\phi_t$
L_o = length of a fiber
$\mathbf{m}$ = refractive index of fiber
n = index, $-\infty<n<\infty$
n_o = number density of fibers $=N/V$
N = total number of fibers
$p(\mathbf{R}_1\ldots)$ = probability distribution function
Q_e = extinction efficiency of the medium
r_o = radius of fiber
$\mathbf{R}$ = radial vector
R_o = correlation length in the pair correlation function
s = index, $-\infty<s<\infty$
$S(\ )$ = surface
V = volume of medium
X, Y, Z = coordinate axes
X_n, Y_n = amplitudes of the average waves
$\langle\ \rangle$ = denotes the configurational average
α = size parameters $=2\pi r_o/\lambda$
γ = polar angle
δ_{jk}, δ_{ns} = Kronecker delta function
ϵ_j = phase shift of the incident wave at fiber j
ζ = distance between fiber centers divided by fiber diameter
λ = wavelength
ϕ_i, ϕ_t = azimuthal angles of the incident and transmitted waves, respectively
ψ = function defined by Eqs. (27) and (28)

Superscripts

max = maximum
o = incident wave, or independent scattering
s = scattered wave
t = transmitted wave
I, II = TM and TE modes, respectively

Subscripts

j, k, N = fiber j, k, N
Re = real part

incident and the transmitted waves are designated as $\mathbf{e}^o$ and $\mathbf{e}^t$, respectively. The effective propagation constant is derived by applying the concepts of average waves (Foldy, 1945) and configurational averages (Lax, 1951). The configurational average refers to the weighted property over a probability distribution function of the scatterers.

In general, the configurational average of an arbitrary property f by holding both the j and k particles fixed is given by

$$\langle f\rangle_{j,k}=\int fp(\mathbf{R}_1\mathbf{R}_2\ldots\mathbf{R}_N).dV_1\ldots dV_n\ldots dV_N, \qquad n\neq j,\ k \quad (5)$$

where p is the probability distribution function. For a medium of identical fibers of radius r_o, the joint probability distribution function is given by

$$p(\mathbf{R}_j,\mathbf{R}_k)=\begin{cases} g(\mathbf{R}_j,\mathbf{R}_k/V & |\mathbf{R}_j-\mathbf{R}_k|>2r_o\zeta \\ 0 & |\mathbf{R}_j-\mathbf{R}_k|\leq 2r_o\zeta \end{cases} \quad (6)$$

where $\zeta\geq 1$ is the interfiber spacing parameter, $g(\mathbf{R}_j,\mathbf{R}_k)$ is the pair correlation function, and $2r_o\zeta$ is the minimum center-to-center spacing between fibers j and k. The condition that the minimum separation must be greater than the fiber diameter $2r_o$ ($\zeta=1$) means that the fibers are nonpenetrating.

For a TM mode incident wave, the configurational averages of Eqs. (1) and (2) become

$$\langle b^{\rm I}_{jn}\rangle_j=\epsilon^o_j b^{\rm I}_{jn}-\frac{\rm I}{V}\sum_{\substack{k=1\\k\neq j}}^{N}\left\{{}^o b^{\rm I}_{jn}\sum_{S=-\infty}^{\infty}\int_{V'}\langle b^{\rm I}_{ks}\rangle_{kj}\right.$$
$$\left.\times G^{jn}_{ks}dV_k+{}^o b^{\rm II}_{jn}\sum_{S=-\infty}^{\infty}\int_{V'}\langle a^{\rm I}_{ks}\rangle_{kj}G^{jn}_{ks}dV_k\right\} \quad (7)$$

and

$$\langle a^{\rm I}_{jn}\rangle_j=\epsilon^o_j a^{\rm I}_{jn}-\frac{\rm I}{V}\sum_{\substack{k=1\\k\neq j}}^{N}\left\{{}^o a^{\rm I}_{jn}\sum_{S=-\infty}^{\infty}\int_{V'}\langle b^{\rm I}_{ks}\rangle_{kj}\right.$$
$$\left.\times G^{jn}_{ks}dV_k+{}^o a^{\rm II}_{jn}\sum_{S=-\infty}^{\infty}\int_{V'}\langle a^{\rm I}_{ks}\rangle_{kj}G^{jn}_{ks}dV_k\right\} \quad (8)$$

where the subscripts on the brackets $\langle\ \rangle$ denote the configurational average by holding the fiber corresponding to the subscript fixed. This set of equation involves an iteration of a hierarchy of successively higher order averages, which is very difficult to solve.

Equations (7)-(8) can be simplified by employing the quasi-crystalline approximation introduced by Lax (1952). This approximation states that

$$\langle b_{jn}\rangle_{jk}=\langle b_{jn}\rangle_j \text{ and } \langle a_{jn}\rangle_{jk}=\langle a_{jn}\rangle_j \quad (9)$$

which imply that there is no correlation between the j and k scatterers. In addition, the average wave is assumed to traverse the medium with a complex effective propagation constant K ($=K_R-iK_{\rm I}$). The effective refractive index of the medium is given by K_R/k_o, which is equal to the speed of light divided by the phase velocity of the average wave. The imaginary part $K_{\rm I}$ is proportional to the coherent extinction efficiency (Twersky, 1979). The average waves take the form of (Foldy, 1945):

$$\langle b^{\rm I}_{jn}\rangle=X_n\exp(-iK\mathbf{R}_j\cdot\mathbf{e}^t) \text{ and }$$
$$\langle a^{\rm I}_{jn}\rangle=Y_n\exp(-iK\mathbf{R}_j\cdot\mathbf{e}^t) \quad (10)$$

where X_n and Y_n are the amplitudes and the subscript j of the configurational averages has been omitted for brevity. Matching of the phases of the incident and the transmitted waves at the interface at $x=0$ ($k_o\mathbf{e}^o\cdot\mathbf{k}=K\mathbf{e}^t\cdot\mathbf{k}$) yields Snell's law as:

$$k_o\sin\phi_i=K\sin\phi_t \quad (11)$$

which specifies the direction of the transmitted wave. Substituting Eqs. (9) and (10) into Eqs. (7) and (8) yields

$$X_n=\epsilon_j{}^o b^{\rm I}_n\exp(iK\mathbf{R}_j\cdot\mathbf{e}^t)$$
$$-n_o\sum_{S=-\infty}^{\infty}({}^o b^{\rm I}_n X_s+{}^o b^{\rm II}_n Y_s)(F_{sn,\,1}+F_{sn,\,2}) \quad (12)$$

and

$$Y_n=\epsilon_j{}^o a^{\rm I}_n\exp(iK\mathbf{R}_j\cdot\mathbf{e}^t)$$
$$-n_o\sum_{S=-\infty}^{\infty}({}^o a^{\rm I}_n X_s+{}^o a^{\rm II}_n Y_s)(F_{sn,\,1}+F_{sn,\,2}), \quad (13)$$

where

$$F_{sn,\,1}=\int_V\exp[iK(\mathbf{R}_j-\mathbf{R}_k)\cdot\mathbf{e}^t]G^{jn}_{ks}dV_k \quad (14)$$

and

$$F_{sn,\,2}=\int_V\exp[iK(\mathbf{R}_j-\mathbf{R}_k)\cdot\mathbf{e}^t][(g\mathbf{R}_j,\mathbf{R}_k)-1]G^{jn}_{ks}dV_k. \quad (15)$$

The term $F_{sn,2}$ usually vanishes at a few diameters away from fiber k.

Since both $\exp[iK(\mathbf{R}_j-\mathbf{R}_k)\cdot\mathbf{e}^t]$ and G^{jn}_{ks} satisfy the Helmholtz equation, Eqs. (14) and (15) are first converted by means of the Helmholtz equation into the volume integral in Green's second identity, which is then transformed into a surface integral by applying Green's theorem as (Bose and Mal, 1973)

$$F_{sn,\,1}=\frac{(-i)^{s-n}}{(k_o^2-K^2)}\int_{S(\infty)-S(2r_o\zeta)}\left\{H_{s-n}(l_oR_{kj})\frac{\partial}{\partial R_{kj}}e^{iK(\mathbf{R}_j-\mathbf{R}_k)\cdot\mathbf{e}^t}\right.$$
$$\left.-e^{iK(\mathbf{R}_j-\mathbf{R}_k)\cdot\mathbf{e}^t}\frac{\partial}{\partial R_{kj}}H_{s-n}(l_oR_{kj})\right\}\mathbf{e}^{i(s-n)\gamma_{kj}}dS \quad (16)$$

where the surface $S(2r_o\zeta)$ defines the minimum fiber separation, and the surface at infinity $S(\infty)$ encloses all the fibers. By using the expansion

$$\exp[iK(\mathbf{R}_j-\mathbf{R}_k)\cdot\mathbf{e}^t]=\sum_{n=-\infty}^{\infty}i^nJ_n(LR_{kj})\exp(in\gamma_{kj}), \quad (17)$$

the surface integral of $F_{sn,1}$ at $2r_o\zeta$ becomes

$$F^o_{sn}=\frac{2\pi L_o}{k_o^2-K^2}\{2l_or_o\zeta J_{s-n}(2Lr_o\zeta)H'_{s-n}(2l_or_o\zeta)\}$$
$$-2Lr_o\zeta H_{s-n}(2l_or_o\zeta)J'_{s-n}(2Lr_o\zeta)\} \quad (18)$$

where L_o is the length of fibers, $L=K\cos\phi_t$, and the superscript prime denotes differentiation with respect to the argument.

In order to evaluate $F_{sn,2}$, a pair-correlation function must be assumed. For spherical particles the Percus-Yevick (1958) equation has been found to be the most accurate. However, to the best of the author's knowledge, a similarly accurate model for densely packed two-dimensional particles such as cylinders does not exist. A Monte Carlo analysis by Wood (1968) for a system of 12 disks yielded a pair correlation function that can be fitted by an exponentially decaying function. Hence, in the present study a general exponential function is assumed for the pair-correlation function:

$$g(R)=1+A\exp(-R/R_o) \quad (19)$$

where A is a coefficient and R_o is the correlation length (Bose and Mal, 1973), which approaches zero as the particle concentration tends to zero. Equation (15) then becomes

$$F_{sn,\,2}=2\pi AL_oR_o^2\int_{2r_o\zeta/R_o}^{\infty}J_{s-n}(LR_ox)H_{s-n}(l_oR_ox)e^{-x}xdx. \quad (20)$$

which can be evaluated numerically for general fiber sizes, or analytically for Rayleigh limit fibers (Bose and Mal, 1973). Specific values of A and R_o must be assumed in order to evaluate $F_{sn,2}$ numerically.

When Eqs. (16) and (20) are substituted into Eqs. (12) and (13), each of the resulting expressions contain terms that involve the incident field, the field at infinity, which is given by the surface integral at infinity, and the average waves. The incident field term cancels out the surface integral at infinity according to the extinction theorem (Lax, 1952). The remaining near-field terms form a system of homogeneous equations given by

$$X_n = -n_o \sum_{S=-\infty}^{\infty} ({}^o b_n^{\mathrm{I}} X_s + {}^o b_n^{\mathrm{II}} Y_s)(F_{sn}^o + F_{sn,\,2}) \tag{21}$$

and

$$Y_n = -n_o \sum_{S=-\infty}^{\infty} ({}^o a_n^{\mathrm{I}} X_s + {}^o a_n^{\mathrm{II}} Y_s)(F_{sn}^o + F_{sn,\,2}). \tag{22}$$

Dispersion Relations for the Effective Propagation Constant

Since the amplitudes X_s and Y_s of the average waves are nonzero, the determinant of the matrix of coefficient of Eqs. (21) and (22) must vanish. For a TM mode incident wave

$$\begin{vmatrix} \delta_{ns} + n_o {}^o b_n^{\mathrm{I}} F_{sn} & n_o {}^o b_n^{\mathrm{II}} F_{sn} \\ n_o {}^o a_n^{\mathrm{I}} F_{sn} & \delta_{ns} + n_o {}^o a_n^{\mathrm{II}} F_{sn} \end{vmatrix} = 0. \tag{23}$$

Similarly, for a TE mode incident wave the following expression results:

$$\begin{vmatrix} \delta_{ns} + n_o {}^o a_n^{\mathrm{II}} F_{sn} & n_o {}^o a_n^{\mathrm{I}} F_{sn} \\ n_o {}^o b_n^{\mathrm{II}} F_{sn} & \delta_{ns} + n_o {}^o b_n^{\mathrm{I}} F_{sn} \end{vmatrix} = 0. \tag{24}$$

where $F_{sn} = F_{sn}^o + F_{sn,\,2}$. These equations are known as the dispersion relations for the complex effective propagation constant at oblique incidence. The real and imaginary parts of each equation yield two expressions, which can be solved along with Snell's law given by Eq. (11) for the unknowns K_R and K_{I} for the TM and TE mode incident waves, respectively. These equations are usually solved numerically due to their complexity. Simplified expressions for fibers that are small compared to the wavelength are derived below.

Rayleigh Limit Solution

For fibers whose radii are much smaller than the wavelength, the average plane wave can be approximated by including only three terms corresponding to the amplitudes (X_{-1}, X_0, X_1) and Y_{-1}, Y_0, Y_1). In addition, Eq. (18) can be simplified to

$$F_{sn}^o = \frac{-4iL_o}{k_o^2 - K^2} \left\{ \left(\frac{L}{l_o}\right)^{s-n} - 2(l_o r_o \zeta)^2 \left[1 - \left(\frac{L}{l_o}\right)^2 \right] \ln(l_o r_o \zeta) \right\} \tag{25}$$

for $k_o r_o \ll 1$. At normal incidence $\phi_i = \phi_j = 0$ and Eq. (25) reduces to that obtained by other investigators (e.g., Bose and Mal, 1973; Varadan et al., 1978).

1 **Oblique Incidence.** By retaining only those terms corresponding to the amplitudes of order $n = -1, 0, 1$, two 6×6 determinants follow from Eqs. (23) and (24). A first-order approximation of the dispersion relations can be obtained by further neglecting the term of $O(\alpha^2)$ in Eq. (25). Further, the Rayleigh limit expressions will be derived within the context of the "hole correction" approximation, which is equivalent to neglecting the contribution of $F_{sn,\,2}$. The resulting expressions are then strictly valid for sparse concentrations.

Although the accuracy of the hole correction approximation is limited for higher concentrations, the simplicity of the resulting formulae justifies their application to obtain first-order estimates. By using the following properties of the independent scattering wave coefficients ${}^o a_n^{\mathrm{I}} = -{}^o b_n^{\mathrm{II}}$ and ${}^o a_o^{\mathrm{I}} = {}^o b_o^{\mathrm{II}} = 0$, the dispersion relation at oblique incidence becomes

$$\left(\frac{K}{k_o}\right)^2 = 1 - i\psi \tag{26}$$

where the function ψ is given by

$$\psi^{\mathrm{I}} = \frac{4f_v}{\pi\alpha^2} \{ {}^o b_o^{\mathrm{I}} + 2 {}^o b_1^{\mathrm{I}} \} \tag{27}$$

for the TM mode, and

$$\psi^{\mathrm{II}} = \frac{4f_v}{\pi\alpha^2} \{ {}^o a_o^{\mathrm{II}} + 2 {}^o a_1^{\mathrm{II}} \} \tag{28}$$

for the TE mode, where $f_v \{ = n_o \pi r_o^2 L_o \}$ is the volume fraction.

It must be reiterated that Eq. (26) is only a first-order approximation. Neglecting the $O(\alpha^2)$ term in Eq. (26) led to the disappearance of the terms involving the cross polarization modes ${}^o a_n^{\mathrm{I}}$ and ${}^o b_n^{\mathrm{II}}$. More accurate results at oblique incidence must be obtained by using Eqs. (23) and (24).

2 **Normal Incidence.** At normal incidence the independent scattering wave coefficients in the Rayleigh limit (Kerker, 1969) can be employed to derive very simple expressions for the dispersion relations:

$$\left(\frac{K}{k_o}\right)^2 = 1 - i f_v (\mathbf{m}^2 - 1) \left\{ \frac{\pi\alpha^2}{4} (\mathbf{m}^2 - 1) + i \right\} \tag{29}$$

for the TM mode, and

$$\left(\frac{K}{k_o}\right)^2 = 1 - i f_v \left(\frac{\mathbf{m}^2 - 1}{\mathbf{m}^2 + 1}\right) \left\{ \frac{\pi\alpha^2}{2} \frac{\mathbf{m}^2 - 1}{\mathbf{m}^2 + 1} + 2i \right\} \tag{30}$$

for the TE mode, where $\mathbf{m}$ is the complex refractive index of the fibers.

A first-order correction to Eq. (26) can be obtained by retaining the term of $O(\alpha^2)$ in Eq. (25). The resulting expression contains explicitly the interfiber separation parameter ζ as

$$\left(\frac{K}{k_o}\right)^2 = 1 - \frac{i\psi}{1 + i[2(\alpha\zeta)^2 \ln(\alpha\zeta)]\psi} \tag{31}$$

which reduces back to Eq. (26) if the term of $O(\alpha^2)$ in the denominator is neglected. The equation can be used to estimate the effect of minimum fiber separation on the effective propagation constant.

3 **Limit of $f_v \to 0$.** The limit of $f_v \to 0$ is, of course, the condition for independent scattering. It can be shown, after some manipulations, that Eq. (26) can be reduced to

$$\frac{K}{k_o} = \left[1 + \frac{1}{2} \mathrm{Re}(\psi) \right] - i \left[\frac{1}{2} \mathrm{Re}(\psi) \right] \tag{32}$$

where Re denotes the real part.

Extinction Efficiency of Medium

The extinction efficiency of the medium is related to the imaginary part K_{I} of the effective propagation constant by (Twersky, 1979)

$$Q_e = \frac{\pi\alpha}{f_v} \left(\frac{K_{\mathrm{I}}}{k_o}\right). \tag{33}$$

which is a function of the solid volume fraction f_v. The extinction efficiency in the independent scattering limit is obtained by substituting Eq. (32) into Eq. (33), as well as by using Eqs. (27) and (28):

$$\{ Q_e^{\mathrm{I}}, Q_e^{\mathrm{II}} \} = \frac{2}{\alpha} \mathrm{Re} \{ ({}^o b_o^{\mathrm{I}} + 2 {}^o b_1^{\mathrm{I}}), ({}^o a_o^{\mathrm{II}} + 2 {}^o a_1^{\mathrm{II}}) \} \tag{34}$$

which is independent of the volume fraction.

Equation (34) is identical to the efficiencies for the dominant modes (TM-TM and TE-TE), except for the absence of the higher-order terms, which contribute negligibly in the Rayleigh limit. Because the cross mode efficiencies vanish at normal

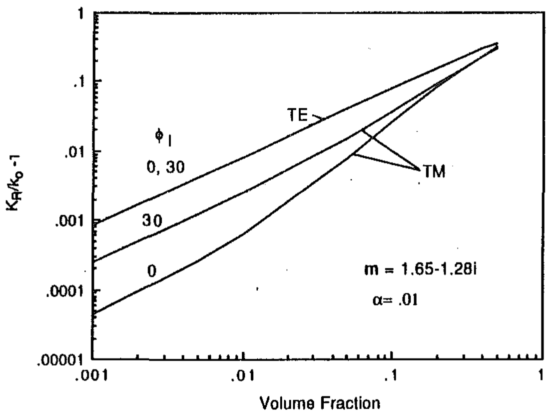

Fig. 2 Variation of the real effective propagation constant at normal and oblique incidence for absorbing fibers

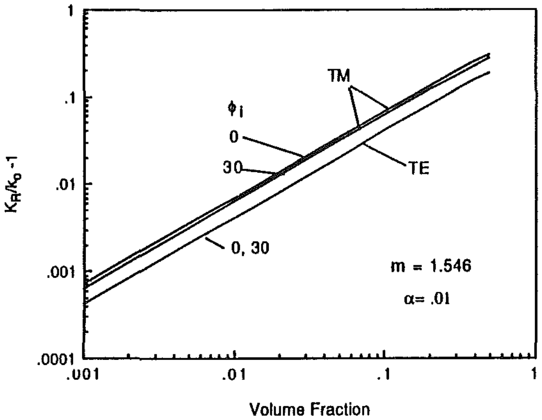

Fig. 3 Variation of the real effective propagation constant at normal and oblique incidence for nonabsorbing fibers

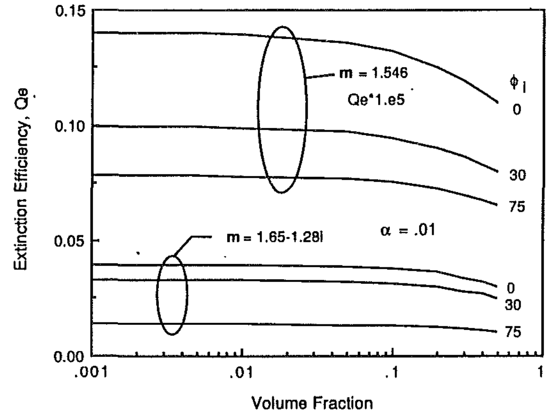

Fig. 4 Variation of the extinction efficiency with incident angle and volume fraction

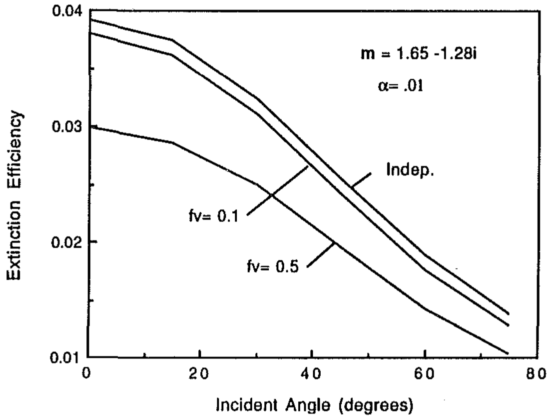

Fig. 5 Comparison of the extinction efficiencies for various volume fractions for absorbing fibers

incidence, Eq. (34) is accurate for normal incidence calculations. For oblique incidence, however, the cross polarization terms are absent as expected due to the approximation to Eq. (25) in the derivation of the dispersion relation. On the other hand, the cross mode extinction efficiencies cancel out each other for unpolarized radiation. Hence, it can be inferred that Eq. (26) should be accurate for oblique incidence calculations for unpolarized radiation.

Results and Discussion

This paper presented the theoretical formulation for the effective propagation constant K of a medium containing closely spaced, parallel fibers. The significance of the dependent scattering effects on K can be clearly illustrated by considering fibers in the Rayleigh limit. For the purpose of demonstration, the fiber size parameter α is chosen to be 0.01, and both absorbing ($\mathbf{m} = 1.65\text{-}1.28i$) and nonabsorbing ($\mathbf{m} = 1.546$) fibers are considered. The former corresponds to silica at 20.66 μm and the latter at 0.32 μm (Hsieh and Su, 1978).

It is reiterated that the Rayleigh limit expressions were derived by using the hole correction assumption, which is adequate for sparse concentrations. By including the contribution of $F_{sn,2}$ in the dispersion relations, expressions for the effective propagation constant that are accurate for large f_v can be obtained. Nevertheless, the approximate expressions are useful for obtaining estimates for the extinction efficiency and phase velocity in the dependent scattering regime.

It is evident from Eq. (26) that the effective propagation constant of a medium containing scatterers is always complex. The real part K_R is larger than k_o because the average waves propagate at a lower velocity due to scattering by the particles. A nonzero K_I reflects the conversion of coherent waves into incoherent waves by absorption and scattering (Karal and Keller, 1964). It must be emphasized that dependent scattering affects both the absorption and scattering of radiation.

Figures 2 and 3 show K_R/k_o as a function of fiber volume fraction for two incident angles. The TE mode K_R/k_o is relatively insensitive to the angle of incidence because of the approximations that were introduced in the derivation of Eq. (26). Since the phase velocity is inversely proportional to K_R/k_o, the increase in K_R/k_o with volume fraction indicates that the phase velocity is diminished due to more pronounced multiple scattering as the particle concentration increases. In the independent scattering limit f_v is very small and K_R/k_o deviates negligibly from unity. As f_v increases, K_R/k_o becomes considerably higher than unity, and the refraction of waves must be considered in the analysis of radiative energy transport.

Figure 4 shows the unpolarized extinction efficiency of the medium Q_e ($= \{Q_e^I + Q_e^{II}\}/2$) for several incident angles. In the case of $\mathbf{m} = 1.546$, the fibers are nonabsorbing and the extinction and scattering efficiencies are identical. The increase in multiple scattering with higher particle concentration reduces the extinction efficiency of the medium. In the opposite limit of very low volume fraction, Q_e converges to that for independent scattering.

The variation of the extinction efficiency with incident angle is shown in Figs. 5 and 6 for the two refractive indices. While the extinction efficiency is independent of volume fraction for independent scattering, it decreases with higher volume fraction due to the higher degree of multiple scattering when more fibers are packed into a given volume.

Finally, the effect of interfiber separation is shown in Fig. 7. A simple relationship exists between the maximum volume

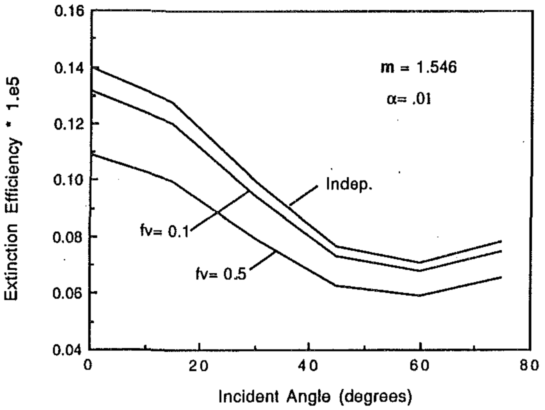

Fig. 6 Comparison of the extinction efficiencies for various volume fractions for nonabsorbing fibers

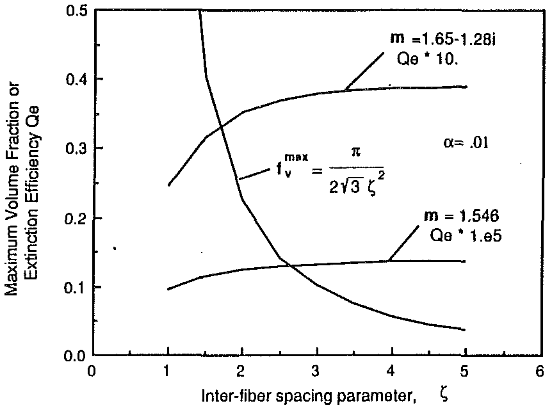

Fig. 7 Variation of the extinction efficiency with the minimum interfiber separation

fraction and the minimum fiber separation. Based on geometric consideration, a hexagonal arrangement of identical fibers corresponds to the maximum packing, for which the volume fraction f_v is equal to $\pi/(2\sqrt{3}\zeta^2)$. Figure 7 shows the extinction efficiencies at normal incidence for the maximum volume fraction corresponding to the interfiber spacing parameter ζ. Recall that $2r_o\zeta$ is the minimum distance between the centers of any pair of fibers. As the fiber separation increases, multiple scattering in the near field diminishes. For the given fiber size and refractive index, the extinction efficiency deviates less than 3 percent from the independent value when $\zeta = 3$ (maximum volume fraction $f_v^{\max} = 0.1$) for absorbing fibers and the deviation is about 5 percent for nonabsorbing fibers. The phase velocity at $f_v = 0.1$ is only slightly lower than its free space value, as shown in Fig. 2. This information can be used to evaluate the validity of the independent scattering assumption for specific fiber optical properties and volume fraction.

Summary

The analysis of radiative energy transport in a scattering medium requires detailed knowledge of the radiative properties of the medium. In the independent scattering regime the radiative properties of the medium are linearly proportional to those of the particles. However, if the scatterers are closely spaced, dependent scattering effects cause the effective refractive index and extinction efficiency of the medium to become significantly different from those for independent scattering.

In this paper a theoretical study was conducted on the complex effective propagation constant of a medium containing closely spaced, parallel fibers. The expressions that govern its functional dependence are known as the dispersion relations. The general dispersion relations for oblique incidence, as well as approximate expressions in the Rayleigh limit, have been derived in this paper.

The real part of the effective propagation constant K_R is inversely proportional to the phase velocity and the imaginary part K_I to the coherent extinction efficiency. The deviation of K_R/k_o from unity, which is a function of the fiber volume fraction, indicates that the phase velocity is reduced due to scattering by the fibers. At high particle concentrations when K_R/k_o is considerably different from unity, wave refraction governed by Snell's law must be considered in the analysis of radiative energy transport through the medium.

Although the present theoretical development focused on homogeneous fibers, all of the equations are equally applicable to radially stratified fibers, as long as the corresponding independent scattering wave coefficients for the nonhomogeneous fibers are used. This is because dependent scattering is an external effect, and all the information of the scatterer are contained in the independent scattering wave coefficients. This is easily realized by observing the similarities between the expressions for the dependent scattering wave coefficients for homogeneous cylinders (Lee, 1990b) and those for radially stratified cylinders (Lee, 1991b).

References

Bose, S. K., and Mal, A. K., 1973, "Longitudinal Shear Waves in a Fiber-Reinforced Composite," *Int. J. Solid Structures*, Vol. 9, pp. 1075-1085.

Foldy, L. L., 1945, "The Multiple Scattering of Waves. I. General Theory of Isotropic Scattering by Randomly Distributed Scatterers," *Physical Review*, Vol. 67, Nos. 3-4, pp. 107-119.

Hsieh, C. K., and Su, K. C., 1978, "Thermal Radiative Properties of Glass From 0.32 μm to 20.66 μm," *Solar Energy*, Vol. 22, pp. 37-43.

Karal, F. C., Jr., and Keller, J. B., 1964, "Elastic, Electromagnetic, and Other Waves in a Random Medium," *J. Math. Phys.*, Vol. 5, No. 4, pp. 537-547.

Kerker, M., 1969, *The Scattering of Light and Other Electromagnetic Radiation*, Academic Press, New York.

Kumar, S., and White, S., 1990, "Scattering Properties of Woven Fibrous Insulations: Effects of Interference for Normal Incidence," AIAA Paper No. 90-1674.

Lax, M., 1951, "Multiple Scattering of Waves," *Reviews of Modern Physics*, Vol. 23, No. 4, pp. 287-310.

Lax, M., 1952, "Multiple Scattering of Waves. II. The Effective Field in Dense Systems," *Physical Review*, Vol. 85, No. 4, pp. 621-629.

Lee, S. C., 1986, "Radiative Transfer Through a Fibrous Medium: Allowance for Fiber Orientation," *J. Quant. Spectrosc. Radiat. Transfer*, Vol. 36, No. 3, pp. 253-263.

Lee, S. C., 1988, "Radiative Heat Transfer Model for Fibers Oriented Parallel to Diffuse Boundaries," *J. Thermophysics Heat Transfer*, Vol. 2, No. 4, pp. 303-308.

Lee, S. C., 1989, "Effect of Fiber Orientation on Thermal Radiation in Fibrous Media," *Int. J. Heat and Mass Transfer*, Vol. 32, No. 2, pp. 311-319.

Lee, S. C., 1990a, "Scattering Phase Function for Fibrous Media," *Int. J. Heat and Mass Transfer*, Vol. 33, No. 10, pp. 2183-2190.

Lee, S. C., 1990b, "Dependent Scattering of an Obliquely Incident Plane Wave by a Collection of Parallel Cylinders," *J. Applied Physics*, Vol. 68, No. 10, pp. 4952-4957.

Lee, S. C., 1991a, "The Roles of Multiple Scattering and Wave Interference on Dependent Scattering by Parallel Fibers," AIAA Paper No. 91-1398.

Lee, S. C., 1991b, "Scattering of a Plane Wave at Oblique Incidence by a Collection of Radially Stratified Parallel Cylinders," submitted to *J. Quart. Spectrosc. Radiat. Transfer.*

Percus, J. K., and Yevick, G. J., 1958, "Analysis of Classical Statistical Mechanics by Means of Collective Coordinates," *Phys. Rev.*, No. 110, pp. 1-13.

Twersky, V., 1979, "Propagation in Pair-Correlated Distributions of Small-Spaced Lossy Scatterers," *J. Opt. Soc. Am.*, Vol. 69, No. 11, pp. 1567-1572.

Varadan, V. K., Varadan, V. V., and Pao, Y-H, 1978, "Multiple Scattering of Elastic Waves by Cylinders of Arbitrary Cross Sections, I. SH Waves," *J. Acoust. Soc. Am.*, Vol. 63, No. 5, pp. 1310-1319.

White, S., and Kumar, S., 1989, "Interference Effects on Scattering by Parallel Fibers," AIAA Paper No. 89-1717.

Wood, W. W., 1968, "Monte Carlo Calculations for Hard Disks in the Isothermal-Isobaric Ensemble," *J. Chem. Phys.*, Vol. 48, No. 1, pp. 415-434.

J. L. Lage
Assistant Professor,
Civil and Mechanical
Engineering Department,
Southern Methodist University,
Dallas, TX 75275-0335
Assoc. Mem. ASME

J. S. Lim

A. Bejan
J. A. Jones Professor of
Mechanical Engineering.
Fellow ASME

Department of Mechanical Engineering
and Materials Science,
Duke University,
Durham, NC 27706

Natural Convection With Radiation in a Cavity With Open Top End

The heat transfer by natural convection and radiation in a two-dimensional cavity with one side heated, one side and bottom insulated, and the top open was investigated numerically. The first part of the study focused on natural convection alone, and concluded with closed-form correlations for the heat transfer from each of the side walls. It was found that the fluid rises along both side walls in the boundary layer regime. In the second part of the study, the natural convection correlations were incorporated into a seven-equation model for combined convection and radiation. The procedure needed for calculating the floating temperature of the insulated wall was illustrated numerically. The individual effects of the dimensions of the cavity, the temperature of the heated wall, and the emissivities of the two side walls were also documented numerically.

1 Background

The fundamental heat transfer problem analyzed in this paper was recommended by an actual engineering problem encountered in the design of modern (low-emission) cogeneration plants. A plant of this type is being constructed on a neighboring campus (University of North Carolina, Chapel Hill) for the purpose of generating both steam and electric power. What distinguishes this plant is the fluidized bed combustion process, in which the fuel (crushed coal) is mixed with crushed limestone in order to reduce drastically the emission of SO_2 into the atmosphere.

A critical aspect in the design and operation of this plant is the voluminous stream of hot ash that must be removed, cooled, and shipped. The ash discharged from the bottom end of the fluidized bed combustor is held temporarily in a hopper sunk into the floor of the power plant (Fig. 1). Access space is provided between the hopper wall (T_1) and the pit wall (T_2). There are two points of concern in the design of the pit:

(*a*) the rate of heat transfer from the hopper wall to the ambient air, through the opening left at the top, and
(*b*) the equilibrium temperature of the pit wall.

Point (*b*) is an important safety consideration, because workers must have access to the bottom end of the hopper, while point (*a*) relates to the cooling that the ash experiences while in the hopper.

In section 3 we will see that the temperature of the pit wall is a "floating" parameter, i.e., a consequence of the interplay between convection and radiation in the open-ended air cavity. If we discount for a moment the effect of radiation and look only at natural convection, we are confronted with the problem of calculating the heat transfer through the cavity emphasized on the right side of Fig. 1. An often overlooked prerequisite for any convection heat transfer calculation is knowledge of the correct flow pattern. In Fig. 1 we see that if the pit temperature T_2 approaches the hopper temperature T_1, then heated air will rise along both walls, with cold ambient air falling back through the middle of the cavity. On the other hand, when the pit temperature resembles the ambient temperature T_∞, the heated air rises only along the hopper wall.

The objective of this study is to develop fundamental results that address issues (*a*) and (*b*) noted above. In the first part of the paper we specify the temperature of both walls and focus on the phenomenon of pure natural convection (e.g., the flow pattern, and the relation between T_2 and heat transfer). With this fundamental information in hand, in the second part of the paper we include the effect of radiation in order to pinpoint T_2 and the net rate of heat transfer out of the cavity.

It must be said that this two-part approach was chosen intentionally in order to give the present results more flexibility and generality. An alternative method that is well documented (e.g., Larson and Viskanta, 1976; Lauriat, 1980) consists of solving simultaneously the differential equations for natural convection and radiation, while the nonuniform temperature distribution of three refractory surfaces is one of the unknowns. Along that alternate route, the complete set of differential equations would have to be solved for each particular configuration represented by the geometric ratio L/H, the emissivities of all the participating surfaces, and the Rayleigh and Prandtl numbers.

The approach used in the present study consists of first solving the problem of pure natural convection, in order to develop simple and accurate correlations for the heat transfer rates from the two side walls as functions of the still unspecified temperature of the colder wall, T_2. This is the only stage in which we solve the differential equations for natural convec-

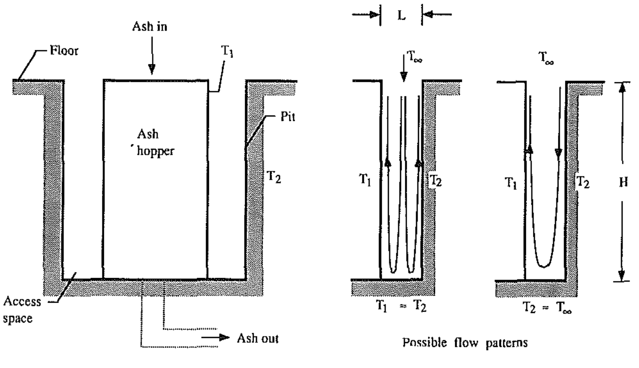

Fig. 1 Two-dimensional cavity with different side-wall temperatures, and open top end

---

Contributed by the Heat Transfer Division for publication in the JOURNAL OF HEAT TRANSFER. Manuscript received by the Heat Transfer Division January 1991; revision received January 1992. Keywords: Enclosure Flows, Natural Convection, Radiation.

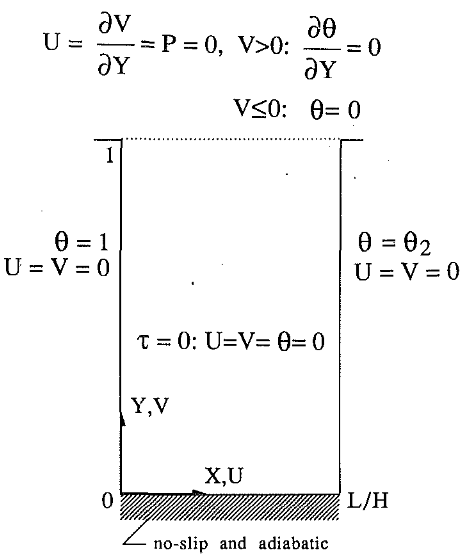

Fig. 2 The initial and boundary conditions for natural convection in the geometry of Fig. 1

tion; in fact, these equations have to be solved only for a few cases because the trends of natural convection heat transfer are relatively easy to correlate in closed form. In the second part of the study we incorporate this natural-convection information in a simple network model for radiation superimposed on natural convection. Only the algebraic system of equations associated with this network model has to be solved each time that the configuration of the cavity changes.

2 Natural Convection

Mathematical Formulation. The flow and heat transfer in the two-dimensional cavity are governed by the conservation of mass, momentum, and energy, according to the system of coordinates defined in Fig. 2:

$$\frac{\partial U}{\partial X}+\frac{\partial V}{\partial Y}=0 \tag{1}$$

$$\frac{DU}{D\tau}=-\frac{\partial P}{\partial X}+\nabla^2 U \tag{2}$$

$$\frac{DV}{D\tau}=-\frac{\partial P}{\partial Y}+\nabla^2 V+\frac{\text{Ra}}{\text{Pr}}\theta \tag{3}$$

$$\frac{D\theta}{D\tau}=\frac{1}{\text{Pr}}\nabla^2\theta \tag{4}$$

In these equations, $D/D\tau$ is shorthand for $\partial/\partial\tau+U\partial/\partial X+V\partial/\partial Y$, and

$$\text{Pr}=\frac{\nu}{\alpha}, \tag{5}$$

$$\text{Ra}=\frac{g\beta H^3(T_1-T_\infty)}{\alpha\nu} \tag{6}$$

The dimensionless variables employed in Eqs. (1)-(4) are defined by the relations

$$(X,\ Y)=\frac{(x,\ y)}{H}, \tag{7}$$

$$(U,\ V)=\frac{(u,\ v)}{\nu/H} \tag{8}$$

$$P=\frac{p+\rho g y}{\rho(\nu/H)^2}, \tag{9}$$

$$\tau=\frac{t\nu}{H^2} \tag{10}$$

$$\theta=\frac{T-T_\infty}{T_1-T_\infty} \tag{11}$$

for which the corresponding physical quantities (x, y, u, v, p, t, T) are defined in the Nomenclature.

The initial and boundary conditions are indicated directly on Fig. 2. The fluid (air, $\text{Pr}=0.72$) is initially motionless and at ambient temperature. The side walls and the bottom wall are impermeable and without slip. Noteworthy are the different temperatures of the side walls, $\theta=1$ on the left, and $\theta=\theta_2$ on the right, where

$$\theta_2=\frac{T_2-T_\infty}{T_1-T_\infty} \tag{12}$$

Of interest in this part of the study is the range $0<\theta_2<1$, i.e., pit temperatures that fall between the extremes represented by T_1 and T_∞. The bottom wall ($Y=0$) is modeled as adiabatic in order to allow for a smooth temperature transition from the hopper wall ($\theta=1$ at $X=0$) to the right side wall ($\theta=\theta_2$ at $X=L/H$). In section 3 we shall see that this adiabatic bottom model is consistent with the refractory surface model that will be adopted for the bottom wall.

Nomenclature

$C_{1,2}$ = dimensionless coefficients, Eq. (23)
F = geometric view factor
g = gravitational acceleration
H = height
J = radiosity
$\tilde{J}$ = dimensionless radiosity, Eq. (33)
k = fluid thermal conductivity
L = horizontal dimension of cavity
M = number of grid lines
N = radiation parameter, Eq. (36)
Nu_l = overall Nusselt number for the left side, Eq. (13)
Nu_{loc} = local Nusselt number for the right side, Eq. (17)
Nu_r = overall Nusselt number for the right side, Eq. (18)
Nu_t = total overall Nusselt number, Eq. (15)
p, P = pressure, Eq. (9)
Pr = Prandtl number = ν/α
q' = heat transfer rate per unit length
$\tilde{q}'$ = dimensionless heat transfer rate per unit length, Eq. (34)
q'' = local heat flux
Ra = Rayleigh number, Eq. (6)
Ra_∞ = constant, Eq. (37)
s_i = location of grid line i
t = time
T = temperature, K
T_1 = temperature of the left wall
T_2 = temperature of the right wall
T_∞ = ambient temperature
$\tilde{T}$ = dimensionless absolute temperature, Eq. (33)
u, U = horizontal velocity, Eq. (8)
v, V = vertical velocity, Eq. (8)
x, X = horizontal coordinate, Eq. (7)
y, Y = vertical coordinate, Eq. (7)
α = thermal diffusivity
α_s = grid stretching rate
β = coefficient of volumetric thermal expansion
γ = exponent, Eq. (23)
Δ = near-wall grid spacing
ϵ = emissivity
θ = dimensionless temperature, Eq. (11)
θ_2 = dimensionless right-side temperature, Eq. (12)
ν = kinematic viscosity
ρ = fluid density
σ = Stefan-Boltzmann constant
τ = dimensionless time, Eq. (10)
Ψ = dimensionless streamfunction
$(\;)_l$ = left side
$(\;)_r$ = right side
$(\;)_t$ = total, or top side
$\overline{(\;)}$ = average

Table 1 The effect of the $Y=1$ momentum boundary conditions on the accuracy and cost of the numerical solution: (I) $\partial U/\partial Y=0$ (Chan and Tien, 1985); (II) $\partial V/\partial Y=0$, Fig. 2

	Ra			
	10^5		10^9	
	I	II	I	II
Nu_l	9.13	9.04	99.17	99.11
CPU(s)	1,736	1,449	5,903	4,895

The top "boundary" is a plane that separates the cavity from the T_∞-air reservoir above it. The energy conditions imposed at $Y=1$ are the same as those used by Chan and Tien (1985). The fluid that enters the cavity ($V \le 0$) has the same temperature as the reservoir ($\theta=0$). The boundary regions through which the fluid leaves the cavity ($V>0$) satisfy the upwind condition $\partial\theta/\partial Y=0$. This condition is based on the assumption that in the boundary layer flow that crosses the $Y=1$ plane the contribution due to longitudinal convection is much greater than the contribution due to longitudinal conduction. It is valid at moderate and high Rayleigh numbers, that is in the flow region with distinct boundary layers. The momentum condition at $Y=1$ is discussed in the next subsection.

Numerical Method. The preceding problem was solved numerically by finite differences, using the control volume method described by Patankar (1980). The SIMPLEC algorithm of van Doormaal and Raithby (1983) was complemented with a power-law scheme for calculating the advection-diffusion terms. The resulting system of algebraic equations was solved by the Tri-Diagonal-Matrix-Algorithm. The integration in time was fully implicit, with the time derivatives being discretized over two time levels, resulting in a first-order truncation error in time.

With regard to a numerical domain that is restricted to the cavity fluid (e.g., Fig. 2), Chan and Tien (1985) have shown that when the cavity is square and the Rayleigh number moderate or high ($10^6 < Ra < 10^9$) there is no need to perform numerical calculations in the domain outside the cavity. Even the entrance effect that was noted by Chan and Tien in their Fig. 6 will be smaller in the present configuration because the cavity is slender ($L/H < 1$) and vertical.

The momentum boundary conditions for the top of the cavity (Fig. 2) were the same as those used by Behnia and de Vahl Davis (1990) for a similar problem. They were adopted by noting that in a power plant floor cavities are covered by grills in order to prevent the accidental fall of debris and personnel. The grill is effective in damping the external flow that may blow parallel to the floor of the power plant. The present model accounts for this by imposing $U=0$ at the top of the cavity, i.e., immediately below the grill. This assumption and Eq. (2) yield $\partial P/\partial X=0$, or $P=0$ (const) along the $Y=1$ boundary. The $P=0$ condition along the top boundary does not mean that there cannot be a counterflow through the $Y=1$ plane. The buoyancy effect changes as one moves horizontally across the top opening. The vertical pressure gradient in the region with inflow is different than the gradient in the region with outflow. The boundary conditions required by the outflow are $U=P=0$; however, the original SIMPLE algorithm does not allow for pressure boundary conditions to be specified. To get around this difficulty, we had two options: (*a*) change the algorithm in order to incorporate the pressure boundary condition [e.g., Lage and Souza Mendes (1987), pressure inlet conditions for chimney flow], or (*b*) use the continuity Eq. (1). The second option yields $\partial V/\partial Y=0$ for the entire top boundary. Both options lead to the same result (they are physically equivalent after all), but option (*b*) is much more suitable for the SIMPLE algorithm, and it is the one adopted in the present study.

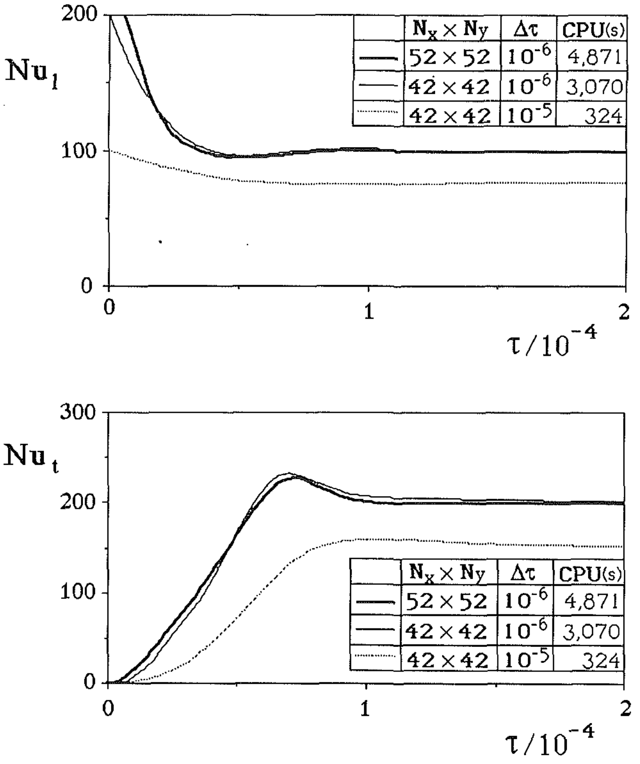

Fig. 3 The effect of the grid on the accuracy of the numerical solution ($Ra=10^9$, $Pr=0.72$, $L/H=1$, $\theta_2=1$)

Although the momentum condition $\partial V/\partial Y=0$ at $Y=1$ differs from the $\partial U/\partial Y=0$ condition used by Chan and Tien (1985), it was preferred because it speeds up the convergence (Table 1). The Chan and Tien (1985) condition is easier to justify on physical grounds; however, numerically it leads to nearly the same results as when the Behnia and de Vahl Davis (1990) condition was used. The numerical results reported in Table 1 were obtained using the IBM 3090-600G of the Cornell National Supercomputer Facility. The Nu_l values reported in the table refer to the height-averaged Nusselt number on the left side of the cavity:

$$Nu_l = \frac{\overline{q_l''} H}{k(T_1 - T_\infty)} = -\int_0^1 \left(\frac{\partial\theta}{\partial X}\right)_{X=0} dY \qquad (13)$$

The grid was distributed nonuniformly according to the rule

$$s_{i+1} = s_i + \alpha_s^i \Delta, \quad 0 \le i \le \frac{M}{2} \qquad (14)$$

where s_i is the location of grid line i, α_s is the stretching rate, Δ is the first (near wall) grid spacing, and M is the total number of grid lines. The index i increases away from each side wall; in other words, Eq. (14) applies to only half of the cavity in both directions.

The accuracy of the numerical results was established through the tests exhibited in Fig. 3, which correspond to the highest Rayleigh number ($Ra=10^9$) and the widest cavity ($L/H=1$). The lower graph shows the Nusselt number averaged over the top plane of the cavity,

$$Nu_t = \frac{\overline{q_t''} L}{k(T_1 - T_\infty)} = \int_0^{L/H} \left(Pr\, V\theta - \frac{\partial\theta}{\partial Y}\right)_{Y=1} dX \qquad (15)$$

Not plotted in Fig. 3 are the Nu_l and Nu_t curves that correspond to the 52×52 grid and $\Delta\tau = 10^{-7}$, because these curves fall on top of the curves drawn for 52×52 and $\Delta\tau = 10^{-6}$. It is worth noting that because of the range of time steps and grid sizes considered in Fig. 3, the time step shows a greater effect on the steady-state solution than the grid size. The trade-off between accuracy and cost recommended the use of 52×52 grid

Table 2 The conduction-referenced overall Nusselt number for natural convection heat transfer across a square cavity with differentially heated side walls (Pr = 0.72)

	Ra		
Reference	10^4	10^6	10^8
Marshall et al. (1978)	2.27	8.93	–
Roux et al. (1978)	2.23	–	–
Catton (1979, the Berkovsky-Polevikov correlations)	2.42	9.21	35.0
Lauriat (1980)	2.34	9.02	–
Henkes (1990)	–	8.82	30.2
Markatos and Pericleous (1984)	–	–	32.05
Abrams and Emery (1989)	–	–	35.63
Present study	2.24	8.89	30.1

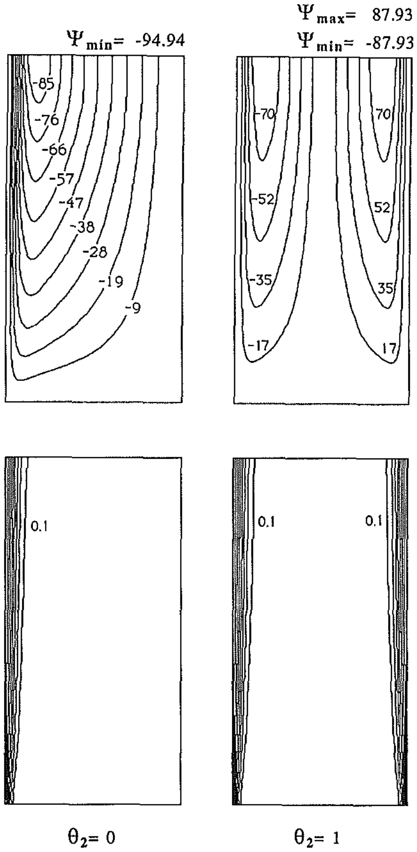

Fig. 4 The effect of the right-side temperature θ_2 on the flow pattern in the steady state (Pr = 0.72, Ra = 10^7, L/H = 0.5); top: streamlines; bottom: isotherms

lines with $\alpha = 1.1011$ and $\Delta = 0.005$, and $\Delta\tau = 10^{-6}$ for the solutions reported in this study. The convergence criterion was based on the relative change in the Nusselt number averaged over the top boundary,

$$\left|\frac{\mathrm{Nu}_t^{j+1} - \mathrm{Nu}_t^j}{\mathrm{Nu}_t^j}\right| \leq 10^{-6} \qquad (16)$$

where j denotes the number of iterations performed for a specific time τ.

The numerical code was tested further by simulating natural convection in a square cavity with differentially heated side walls, and comparing the overall heat transfer rate with calculations reported by others. This test is summarized in Table 2. The tabulated numbers represent the overall Nusselt number defined as the actual heat transfer rate divided by the heat transfer rate by pure conduction. The present calculations agree well with the older data even at Ra = 10^8, i.e., close to the end of the laminar regime (Bejan and Lage, 1990).

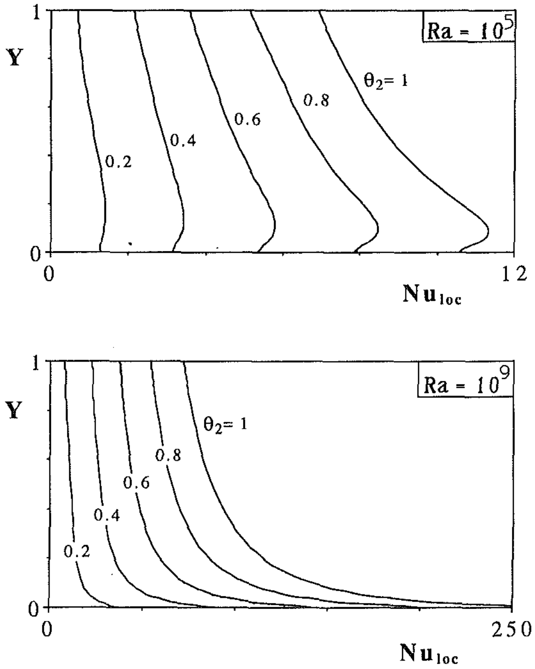

Fig. 5 The steady-state local heat flux distribution on the right side (Pr = 0.72, L/H = 1)

Results. Steady-state values for the heat transfer between air and cavity walls were obtained by following the time evolution of the flow that started at $\tau = 0$. Each case required the specification of four dimensionless parameters (Ra, Pr, L/H, θ_2), among which the Prandtl number was held fixed at Pr = 0.72 (air). The ranges covered by the remaining parameters were $10^5 \leq \mathrm{Ra} \leq 10^9$, $0.25 \leq L/H \leq 1$, and $0 \leq \theta_2 \leq 1$.

The right-wall temperature parameter θ_2 plays a decisive role with regard to the flow pattern that resides in the cavity in the steady state. The dimensionless streamfunction was defined by $\partial\Psi/\partial X = -V$, and $\partial\Psi/\partial Y = U$. Figure 4 shows that when $\theta_2 = 0$ the flow points upward only along the left wall, while at $\theta_2 = 1.0$ both side walls are swept by upflow. We found that the transition from one flow pattern to the other takes place at a critical value θ_2 that is much smaller than 1. This conclusion holds for the entire (Ra, L/H) range listed in the preceding paragraph.

For example, in the case where Ra = 10^8 and $L/H = 0.25$ the transition from the single-**U** pattern to the double-**U** pattern takes place when $\theta_2 \cong 0.05$. We determined the point of transition by calculating the H-averaged shear stress along the right side of the cavity. The flow pattern changes when the θ_2 value is such that the H-averaged shear stress changes sign. In this example then, the flow along the right wall is downward when $0 < \theta_2 < 0.05$, and upward when $\theta_2 > 0.05$.

We shall see that the numerical cases and applications described later in this paper represent flows with θ_2 values comparable with 1, in which the natural convection is in the regimes where the boundary layers are distinct (and upward) on both sides of the cavity. In conclusion, the calculation procedure that is constructed between this section and section 3 applies to the double-**U** flow pattern illustrated in the center of Fig. 1.

The effect of θ_2 is illustrated further in Fig. 5, which shows the local Nusselt number on the right side of the cavity,

$$\mathrm{Nu_{loc}} = \frac{q_r'' H}{k(T_1 - T_\infty)} = -\left(\frac{\partial\theta}{\partial X}\right)_{X=\frac{L}{H}} \qquad (17)$$

The local heat flux increases with both θ_2 and Ra. Its variation in the Y direction is similar to that associated with the classical natural convection boundary layer, provided θ_2 is greater than zero so that the fluid flows upward.

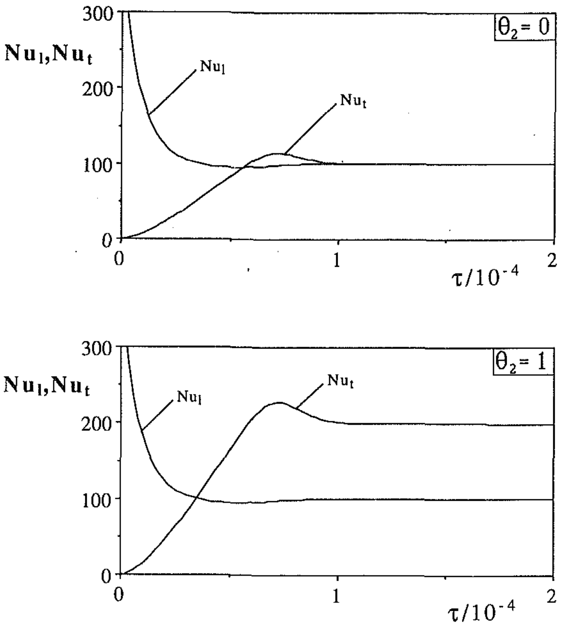

Fig. 6 The evolution of the average left-side and top-side Nusselt numbers (Pr = 0.72, Ra = 10^9, L/H = 1)

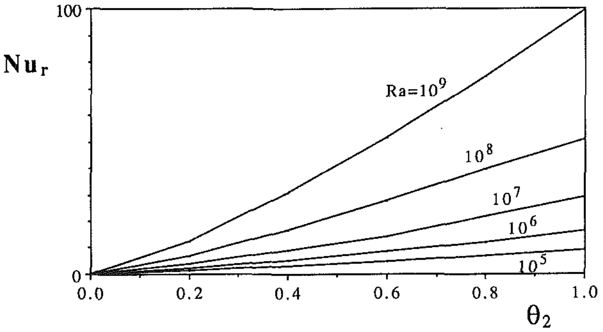

Fig. 7 The total heat transfer rate through the right side (Pr = 0.72, L/H = 1)

The evolution of the heat transfer rate to the steady state is presented in Fig. 6. This figure corresponds to the highest Rayleigh number considered in this study (Ra = 10^9). It shows that when $\theta_2 = 0$ the cold air that descends along the equally cold right wall does not experience any heat transfer with that wall, so that in the steady state the left-side heat transfer rate (Nu_l) matches the heat transfer rate through the top of the cavity (Nu_t). In the opposite extreme, when $\theta_2 = 1$, the flow pattern is symmetric about the vertical midplane, and the two side walls contribute equally to the total heat transfer rate Nu_t. This is why in the lower graph of Fig. 6 the asymptotic value of Nu_t is twice the asymptotic value of Nu_l.

The difference ($\mathrm{Nu}_t - \mathrm{Nu}_l$) is the average Nusselt number on the right side,

$$\mathrm{Nu}_r = \frac{\overline{q}_r'' H}{k(T_1 - T_\infty)} = -\int_0^1 \left(\frac{\partial \theta}{\partial X}\right)_{X=\frac{L}{H}} dY \tag{18}$$

i.e., the H-averaged value of the local Nusselt number defined in Eq. (17). The effect of θ_2 and Ra on the total heat transfer rate through the right wall is illustrated in Fig. 7.

Of primary interest in the second part of this study are the steady-state heat transfer rates. These have been calculated numerically and tabulated, as shown in Table 3 for the total (top) heat transfer rate. Even more useful are closed-form expressions that correlate these heat transfer results. One way to derive these expressions is by recognizing the scales of each vertical boundary layer (e.g., Bejan, 1984). The total heat transfer rates through the two side walls are roughly equal to

Table 3 The steady-state average Nusselt number for the top of the cavity, Nu_t, when Pr = 0.72

		θ_2					
L/H	Ra	0	0.2	0.4	0.6	0.8	1.0
1	10^5	9.04	10.40	11.94	13.72	15.76	18.12
	10^6	16.44	18.91	21.72	24.96	28.69	32.98
	10^7	29.93	34.40	39.53	45.44	52.22	60.04
	10^8	54.46	62.61	71.92	82.71	95.05	109.23
	10^9	99.11	113.91	130.93	150.48	172.96	198.79
0.5	10^7	28.29	32.52	37.35	42.95	49.35	56.70
	10^8	51.44	59.16	67.98	78.13	89.81	103.22
	10^9	93.66	107.60	123.70	142.19	163.42	187.82
0.25	10^7	27.76	31.87	36.66	42.13	48.43	55.68
	10^8	50.50	58.02	66.71	76.66	88.11	101.27
	10^9	91.89	105.60	121.39	139.50	160.33	184.31

$$q_l' \sim kH \frac{T_1 - T_\infty}{H\,\mathrm{Ra}^{-1/4}} = k(T_1 - T_\infty)\mathrm{Ra}^{1/4} \tag{19}$$

$$q_r' \sim kH \frac{T_2 - T_\infty}{H\,\mathrm{Ra}_2^{-1/4}} = k(T_1 - T_\infty)\mathrm{Ra}^{1/4}\theta_2^{5/4} \tag{20}$$

In Eq. (20) we made the observation that

$$\mathrm{Ra}_2 = \frac{g\beta H^3 (T_2 - T_\infty)}{\alpha\nu} = \mathrm{Ra}\cdot\theta_2 \tag{21}$$

The sum $(q_l' + q_r')$ is equal to the top-side heat transfer rate $\overline{q}_t'' L$ used in the definition of Nu_t, Eq. (15); therefore

$$\mathrm{Nu}_t = \frac{q_l' + q_r'}{k(T_1 - T_\infty)} \sim \mathrm{Ra}^{1/4}[1 + (\sim\theta_2^{5/4})] \tag{22}$$

The correlation recommended by this argument is

$$\mathrm{Nu}_t = C_1\,\mathrm{Ra}^{\gamma}(1 + C_2\theta_2^{5/4}) \tag{23}$$

in which C_1 and C_2 are dimensionless and of order 1, and γ is of order 1/4. Indeed, this formula reproduces all the Nu_t data of Table 2 within 4 percent when $C_1 = 0.44$, $C_2 = 1$, and $\gamma = 0.26$. The aspect ratio L/H does not appear in this correlation because in the present Ra and L/H range the boundary layers are thin when compared with L. Retracing the steps that led to Eq. (23), we discover the corresponding correlations for the individual side walls:

$$\mathrm{Nu}_l \cong 0.44\ \mathrm{Ra}^{0.26} \tag{24}$$

$$\mathrm{Nu}_r \cong 0.44\ \mathrm{Ra}^{0.26}\theta_2^{5/4} \tag{25}$$

In the case of $L/H = 0.25$, which is one of the numerical examples considered in the next section, Eq. (25) acquires an accuracy better than 0.6 percent if the 0.44 factor is replaced by 0.42.

The discovery that the boundary layers are sufficiently thin so that L/H does not appear in the correlations (23)–(25) suggests that these correlations will be approximated well by correlations known for the single vertical wall. A recommended correlation for laminar boundary layer natural convection over a single vertical wall (Incropera and De Witt, 1990, p. 543) is an expression developed for $0 < \mathrm{Ra} < 10^9$ by Churchill and Chu (1975). In the case of air (Pr = 0.72), the Churchill and Chu laminar correlation would replace Eq. (24) with

$$\mathrm{Nu}_l = 0.68 + 0.515\ \mathrm{Ra}^{0.25} \tag{26}$$

This alternative underpredicts the Nu_l value of Eq. (24) by 1.4 percent if Ra = 10^8, and by 4.2 percent if Ra = 10^9. This level of agreement is acceptable in natural convection in general, and, in particular, in view of the model (e.g., boundary conditions) chosen for the vertical cavity of Fig. 1. More important, however, is the implication that at Rayleigh numbers higher than 10^9 (turbulent flow), where, if used, Eqs. (23)–(25) would gradually become less accurate, the actual heat

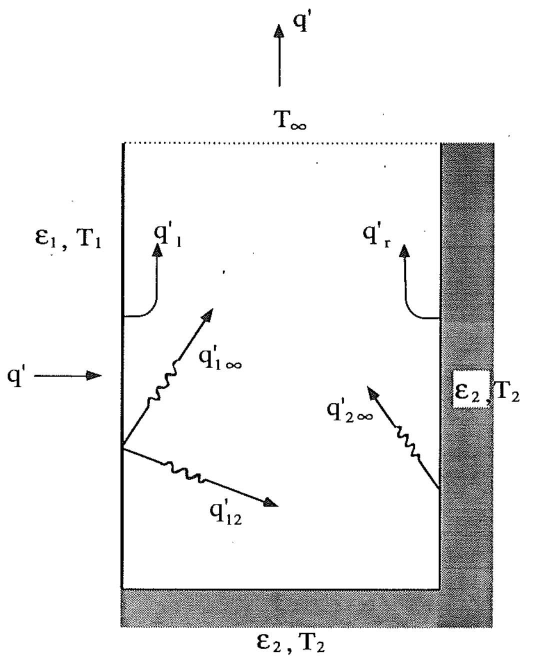

Fig. 8 Model for simultaneous natural convection and radiation in the open-ended cavity

transfer rate can be calculated confidently based on single-wall turbulent flow correlations that are available in the literature. Said another way, if, as we just saw, the boundary layers are thin enough in laminar flow so that Eq. (26) approximates well Eq. (24), then in the turbulent range ($Ra > 10^9$, for $Pr \sim 1$, Bejan and Lage, 1990) the boundary layers are even thinner so that Eqs. (24) and (25) can be "extended" by means of single-wall turbulent flow correlations. In the numerical application described at the end of the next section, for $Ra > 10^9$ we used the Churchill and Chu (1975) correlation for turbulent flow, which for air ($Pr = 0.72$) replaces Eq. (25) approximately with

$$Nu_r = (0.825 + 0.325\ Ra^{1/6})^2\, \theta_2^{5/4} \tag{27}$$

The large volume of experimental data that stands behind these natural convection correlations, for laminar and turbulent flow, is the reason why it is not necessary to subject the geometry of Fig. 1 to a small-scale laboratory simulation.

3 Natural Convection With Radiation

Radiation Model. One of the simplest models for the radiation heat transfer that is present in the open-ended cavity is the three-surface model presented in Fig. 8. The left wall is a diffuse-gray surface of emissivity ϵ_1 and absolute temperature T_1. The rest of the solid wall (side wall + bottom wall) is another diffuse-gray surface, with the emissivity ϵ_2 and absolute temperature T_2. This second surface is adiabatic on its back side; in other words, the net radiation heat transfer received by it is balanced by the heat transferred by natural convection to the air flow.

The third surface of the radiation enclosure model is the top opening ($Y = 1$), which is modeled as black and isothermal at the absolute temperature level T_∞. The isothermal surface model adopted for the right side and bottom walls is consistent with the natural convection model of Fig. 2. In that earlier model the right wall was isothermal, while the bottom wall acquired a temperature that varied from T_1 to T_2. It is a good approximation to assume now that the bottom wall temperature is represented well by T_2 in all the radiation heat transfer calculations because: (1) the bottom wall is less important than the right wall (smaller, $L/H < 1$, and farther from the top opening), and (2) the T_2 value that is revealed by the combined radiation and natural convection calculations is in fact of the same order of magnitude as T_1.

Seen from the outside, the total heat transfer rate q' originates from the back of the left surface, and is due to both natural convection and radiation:

$$q' = q'_1 + q'_{12} + q'_{1\infty} \tag{28}$$

The heat currents $q'_{12} + q'_{1\infty}$ are the net radiation heat transfer from surface 1 to surface 2, and the net radiation heat transfer from surface 1 to the top boundary. The statement that the back of surface 2 is adiabatic is

$$q'_{12} = q'_{2\infty} + q'_r \tag{29}$$

in which $q'_{2\infty}$ is the net radiation heat transfer from surface 2 to the top of the enclosure. The equations relating the radiation heat currents to the temperatures and radiosities of the three surfaces are (e.g., Incropera and DeWitt, 1990):

$$q'_{12} + q'_{1\infty} = \frac{\epsilon_1 H}{1 - \epsilon_1}(\sigma \mathrm{T}_1^4 - \mathrm{J}_1) \tag{30}$$

$$q'_{1\infty} = HF_{1\infty}(J_1 - \sigma T_\infty^4) \tag{31}$$

$$q'_{12} = HF_{12}(J_1 - J_2) \tag{32}$$

$$q'_{2\infty} = LF_{\infty 2}(J_2 - \sigma T_\infty^4) \tag{33}$$

$$q'_{12} - q'_{2\infty} = \frac{\epsilon_2 (L + H)}{1 - \epsilon_2}(J_2 - \sigma T_2^4) \tag{34}$$

Equations (29)–(34) and the natural convection correlation (25) [or Eq. (27) if $Ra > 10^9$] form a system of seven equations for the seven unknowns in this problem, namely

$$T_2,\ J_1,\ J_2,\ q'_r,\ q'_{12},\ q'_{1\infty},\ \text{and}\ q'_{2\infty}.$$

Results. The radiation contribution to the heat transfer mechanism adds also to the number of dimensionless groups that characterize each particular configuration. In order to see this, consider the following nondimensionalization of the variables that appear in the radiation model:

$$(\tilde{T}_1,\ \tilde{T}_2) = \frac{(T_1,\ T_2)}{T_\infty},\ (\tilde{J}_1,\ \tilde{J}_2) = \frac{(J_1,\ J_2)}{\sigma T_\infty^4} \tag{35}$$

$$(\tilde{q}'_r,\ \tilde{q}'_{12},\ \tilde{q}'_{1\infty},\ \tilde{q}'_{2\infty}) = \frac{1}{H\sigma T_\infty^4}(q'_r,\ q'_{12},\ q'_{1\infty},\ q'_{2\infty}) \tag{36}$$

The dimensionless version of Eqs. (29)–(34) is easy to write down, and will be omitted. The corresponding form of Eq. (25) is

$$\tilde{q}'_r \cong \frac{0.42}{N}(\tilde{T}_2 - 1)^{5/4}(\tilde{T}_1 - 1)^{0.01}\, Ra_\infty^{0.26} \tag{37}$$

in which N is the well-known radiation parameter (Larson and Viskanta, 1976)

$$N = \frac{H\sigma T_\infty^3}{k} \tag{38}$$

and Ra_∞ is a system constant proportional to H^3 and T_∞ (degrees Kelvin):

$$Ra_\infty = \frac{g\beta H^3 T_\infty}{\alpha\nu} \tag{39}$$

In conclusion, next to the dimensionless groups that played a role in the pure natural convection problem (section 2), the combined convection and radiation mechanism depends additionally on N, $\tilde{T}_1$, ϵ_1, and ϵ_2. In summary, the dimensionless parameters that can be specified in the present analysis are

$$\frac{L}{H},\ \tilde{T}_1,\ Ra_\infty,\ N,\ \epsilon_1,\ \epsilon_2$$

For example, in the case of $H = 1$ m and air with $T_\infty = 298$ K and properties evaluated at T_∞, two of these parameters are fixed, $N \cong 60$ and $Ra_\infty \cong 2.88 \times 10^{10}$.

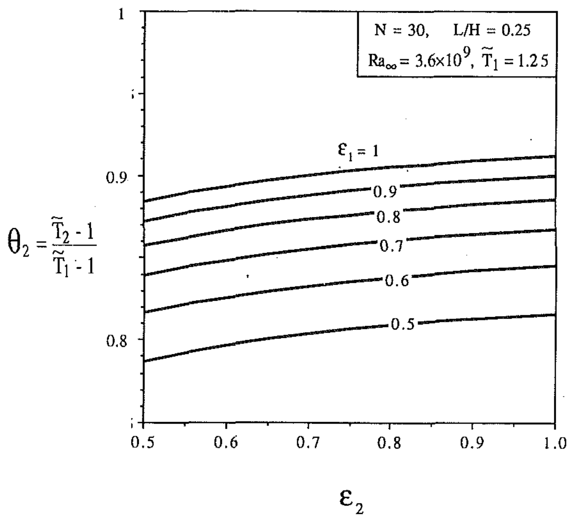

Fig. 9 The effect of the two emissivities on the temperature of the adiabatic surface

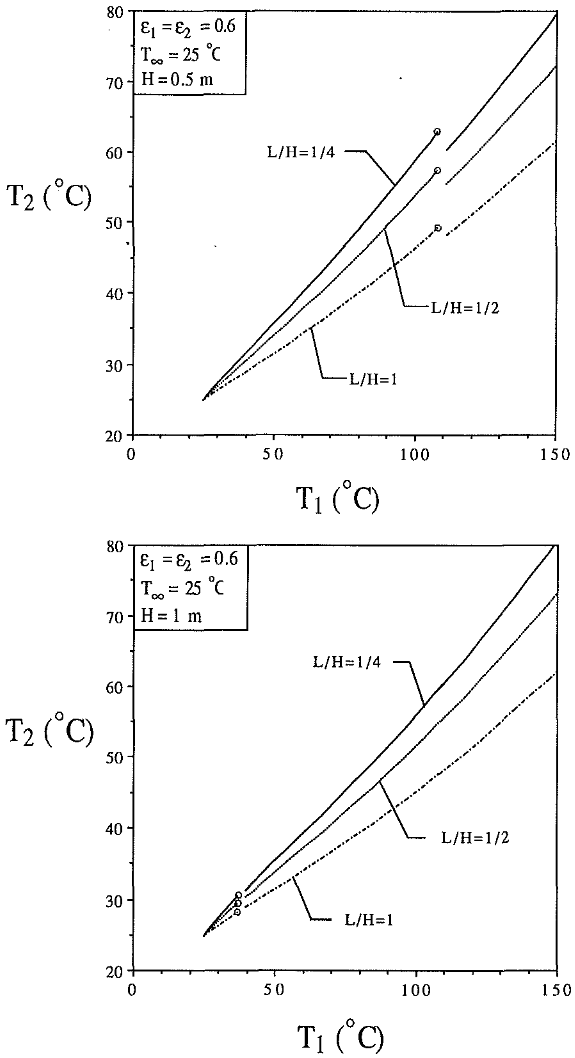

Fig. 10 The effect of cavity size (L, H) and hot wall temperature (T_1) on the temperature of the adiabatic surface (T_2)

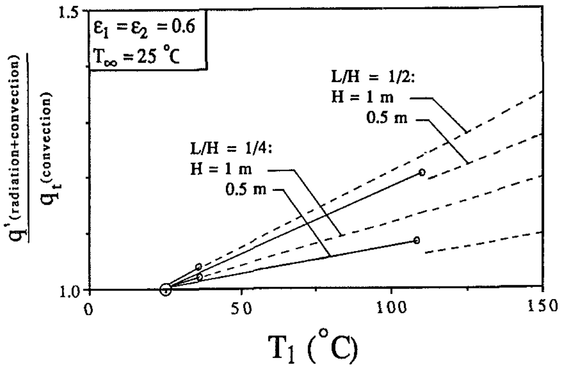

Fig. 11 The relative contribution of radiation to the overall rate of heat transfer through the cavity

The chief unknown in the system (25), (29)-(34) is the temperature T_2. Figure 9 shows a set of results that demonstrate the effect of the two emissivities when the other dimensionless parameters are fixed (or, physically, when T_1, T_∞, L, and H are fixed). The results for T_2 are presented in terms of the θ_2 parameter used in section 2, in order to show how close the right wall approaches the temperature of the heated wall. The T_2 value decreases as either ϵ_1 or ϵ_2 decreases; however, T_2 is considerably more sensitive to changes in ϵ_1.

In Fig. 10, the temperature of the adiabatic surface T_2 is presented in a more practical form, as a function of the actual temperature T_1 and the dimensions of the cavity. Each curve is interrupted by a circle, which corresponds to $Ra = 10^9$ as a landmark for the transition from laminar to turbulent flow along the vertical walls. The low-temperature portion of each curve corresponds to the laminar regime ($Ra < 10^9$), and is based on using Eq. (25) in conjunction with Eqs. (29)-(34). The high-temperature end of the curve was obtained using Eq. (27) instead of Eq. (25), and accounts for turbulent flow along the vertical surfaces. The small step change (break) between the two portions of the curve is due to the jump from the laminar correlation (25) to the turbulent correlation (27) across $Ra = 10^9$. The step change is such that T_2 drops below the "laminar" value, on account of the slightly more effective heat transfer provided by turbulent flow.

The two frames of Fig. 10 show that the adiabatic wall temperature T_2 decreases as the horizontal dimension L increases, i.e., as the top opening becomes a larger sink for radiation. The two graphs of Fig. 10 show that when the ratio L/H is fixed, the physical size of the cavity (namely, the height H) has a relatively insignificant effect on T_2. For any particular geometry (fixed H and L) the T_2 value increases almost linearly with the temperature of the heated wall, T_1.

The temperatures covered by Fig. 10 correspond to the range that is relevant to the safety issue (b) discussed in section 1. Temperatures of 100°C or less can be tolerated by properly equipped individuals who must work in the $H \times L$ space. The same range of temperatures is also consistent with the Boussinesq approximation on which the natural convection part of the calculations is based. That approximation is valid when $\beta(T_1 - T_\infty) < 1$, which, for air as an ideal gas at a temperature of order T_1, means $(T_1 - T_\infty)/T_1 < 1$.

The extent to which radiation contributes to the overall heat transfer rate from T_1 to T_∞ can be viewed in Fig. 11, where the total heat transfer rate q', Eq. (28), was divided by the total natural convection heat transfer rate q'_t. The latter was evaluated at the proper (equilibrium) value of θ_2 that was recommended by the present solution to the combined convection and radiation problem. The break in each curve is again due to the shift from the laminar correlation (25) to the turbulent correlation (27).

Figure 11 shows that the radiation effect gradually becomes important as the wall temperature level T_1 increases. Radiation plays a relatively greater role in a cavity whose top opening (L) is wider, or the aspect ratio L/H larger. In spite of this trend, in the temperature range considered in this example

(Figs. 9–11), the radiation contribution to the overall heat transfer rate is overshadowed by natural convection.

4 Concluding Remarks

In this paper we have analyzed the fundamentals of natural convection and radiation in a two-dimensional cavity with open top end. We first focused on pure natural convection, and developed closed-form heat transfer correlations that were later incorporated in a combined convection and radiation model. The main conclusions of this study are:

(*a*) The flow rises along both side walls when the Rayleigh number is high enough so that the boundary layers are distinct (thinner than L).

(*b*) The laminar natural convection correlations for the two vertical walls and the total heat transfer rate are given in Eqs. (23)–(25).

(*c*) The combined convection and radiation model consists of solving the system of Eqs. (27)–(32) and (25) [or (27)], and the solution depends on six dimensionless groups, L/H, $\tilde{T}_1$, Ra_∞, N, ϵ_1, ϵ_2.

(*d*) The individual effects of L, H, T_1, ϵ_1, and ϵ_2 are documented by the numerical example exhibited in Figs. 9–11.

One reviewer of the original manuscript questioned our neglect of the external turbulence (above the cavity) in the numerical modeling of the flow inside the cavity (section 2). The reason for this decision is that the natural convection velocity in the cavity is considerably greater than what might be due to forced convection along the floor of the power plant. For example, for $H \sim 1$ m and $\mathrm{Ra} \sim 10^9$, the velocity due to natural convection along the vertical walls is of the order of 1 m/s. The ventilation system in the hangar-size enclosure of the power plant would have to create enormously powerful jets in order to interfere with velocities of order 1 m/s in the slot discussed in this paper. The walls of the power plant (now, all glass) blow up long before the natural convection model of section 2 breaks down. Besides, the top of any floor cavity in the power plant is covered by a grill in order to prevent the fall of debris and personnel in the cavity. The grill is very effective in damping the flow that may be induced in the cavity by a draft that blows parallel to the floor of the power plant.

Another reviewer questioned the accuracy of the radiation network model of section 3 relative to the more general model (Larson and Viskanta, 1976) in which the temperature variation along the surfaces is taken into account. We explained our decision in the penultimate paragraph of section 1. Additionally, we must refer to Lauriat (1980) who answered numerically this very question. In the last table of his paper he showed that under conditions similar to the present ones the radiation network model reproduces very well (within less than 4 percent) the results of the more general model.

Acknowledgments

This work was supported by Duke University, the Electric Power Research Institute, and the State of North Carolina. The numerical work was conducted using: (1) the Cornell National Supercomputer Facility, a resource of the Center for Theory and Simulations in Science and Engineering (Cornell Theory Center), which receives major funding from the National Science Foundation and IBM Corporation, with additional support from New York State and members of the Corporate Research Institute, and (2) the North Carolina Supercomputer Center.

References

Abrams, A., and Emery, A. F., 1989, "Turbulent Free Convection in Square Cavities With Mixed Boundary Conditions," ASME HTD-Vol. 107, pp. 117–127.

Behnia, M., and de Vahl Davis, G., 1990, "Natural Convection Cooling of an Electronic Component in a Slot," *Proceedings of the Ninth International Heat Transfer Conference*, Vol. 2, pp. 343–348.

Bejan, A., 1984, *Convection Heat Transfer*, Wiley, New York, p. 120.

Bejan, A., and Lage, J. L., 1990, "The Prandtl Number Effect on the Transition in Natural Convection Along a Vertical Surface," ASME JOURNAL OF HEAT TRANSFER, Vol. 112, pp. 787–790.

Catton, I., 1979, "Natural Convection in Enclosures," *6th Int. Heat Transfer Conf. Toronto 1978*, Vol. 6, Hemisphere, Washington, DC, pp. 13–43.

Chan, Y. L., and Tien, C. L., 1985, "A Numerical Study of Two-Dimensional Laminar Natural Convection in Shallow Open Cavities," *Int. J. Heat Mass Transfer*, Vol. 28, pp. 603–612.

Churchill, S. W., and Chu, H. H. S., 1975, "Correlating Equations for Laminar and Turbulent Free Convection From a Vertical Plane," *International Journal of Heat and Mass Transfer*, Vol. 18, pp. 1323–1329.

Henkes, R. A. W. M., 1990, "Natural-Convection Boundary Layers," Ph.D. thesis, Technical University of Delft, The Netherlands.

Incropera, F. P., and DeWitt, D. P., 1990, *Fundamentals of Heat and Mass Transfer*, 3rd ed., Wiley, New York, Section 13.3.

Lage, J. L., and Souza Mendes, P. R., 1987, "Natural Convection in an Adiabatic Vertical Channel Due to an Attached Rectangular Isothermal Element," *Proceedings of the 11th Canadian Congress of Applied Mechanics*, Part C, pp. 18–19.

Larson, D. W., and Viskanta, R., 1976, "Transient Combined Laminar Free Convection and Radiation in a Rectangular Enclosure," *Journal of Fluid Mechanics*, Vol. 78, pp. 65–85.

Lauriat, G., 1980, "A Numerical Study of a Thermal Insulation Enclosure: Influence of the Radiative Heat Transfer," *Natural Convection in Enclosures*, ASME HTD-Vol. 8, pp. 63–71.

Markatos, N. C., and Pericleous, K. A., 1984, "Laminar and Turbulent Natural Convection in an Enclosed Cavity," *International Journal of Heat and Mass Transfer*, Vol. 27, pp. 755–772.

Marshall, R. S., Heinrich, J. C., and Zienkiewicz, O. C., 1978, "Natural Convection in a Square Enclosure by a Finite-Element Method Using Primitive Fluid Variables," *Numerical Heat Transfer*, Vol. 1, No. 3, pp. 315–330.

Patankar, S. W., 1980, *Numerical Heat Transfer and Fluid Flow*, Hemisphere, Washington, DC.

Roux, B., Grondin, J. C., Bontoux, P., and Gilly, B., 1978, "On a High-Order Accurate Method for the Numerical Study of Natural Convection in a Vertical Square Enclosure," *Numerical Heat Transfer*, Vol. 1, No. 3, pp. 331–350.

van Doormaal, J. P., and Raithby, G. D., 1983, "Enhancements of the Simple Method for Predicting Incompressible Fluid Flows," *Numerical Heat Transfer*, Vol. 7, pp. 147–163.

J. P. Gore

U.-S. Ip

Y. R. Sivathanu

School of Mechanical Engineering,
Purdue University,
West Lafayette, IN 47907

Coupled Structure and Radiation Analysis of Acetylene/Air Flames

A coupled radiation-structure analysis of turbulent, non-premixed, strongly radiating acetylene/air flames is described. The analysis extends the laminar flamelet concept to include the effects of local radiative heat loss/gain. A new method for the calculation of the radiative source term is presented. New measurements of mean and fluctuating emission temperatures and radiation intensities, and previous data concerning flame structure are used to evaluate the predictions. Results show good agreement between measurements and predictions of flame structure similar to past uncoupled calculations. The mean emission temperatures and the mean visible radiation intensities are substantially underpredicted by the uncoupled analysis. The coupled calculations provide reasonable estimates of both quantities.

Introduction

Several recent papers have addressed the structure and radiation properties of turbulent nonpremixed flames (Gore et al., 1987a, 1987b; Jeng and Faeth, 1984; Gore and Faeth, 1986, 1988). All these studies treated radiative heat losses from the flames as a perturbation of the temperature–mixture fraction state relationships. This was achieved by assuming that each location in the flame lost a fixed percentage of the energy release corresponding to local mixture fraction by radiation. Within this approximation, the conservation equation for total enthalpy was not solved. The structure analysis was thus decoupled from the radiation calculations. Heavily sooting acetylene/air flames radiate approximately 60 percent of their chemical energy release to the surroundings. Although the uncoupled analysis provided a reasonable first step for the prediction of these flames, it hampers our understanding of the interactions between the structure and radiation properties. The objective of the present study is to remove this deficiency by considering a coupled structure and radiation analysis.

Simplified coupled structure and radiation analyses have been reported in the literature. Sibulkin et al. (1981) considered a burning vertical fuel surface under laminar flame, optically thin and gray gas assumptions. Gosman and Lockwood (1973) used a flux model with the gray gas assumption for treating radiation calculations for a furnace. Negrelli et al. (1977) calculated the structure and radiation properties of laminar flames around porous cylinders. They used the exponential wide band model to show the limitations of the gray gas assumptions. James and Edwards (1977) added an exponential wide band model to the solution of planar jet diffusion flames burning methane. They assumed that the reaction proceeds to equilibrium composition and also used the mixing length model for turbulence calculation. Very few investigators have reported coupled calculations with radiation from soot. Tamanini (1979) considered a gray soot layer on the rich side in a turbulent boundary layer flame. The soot layer temperature was assumed constant (1400 K) and the entire flow was assumed optically thin.

Bhattacharjee and Grosshandler (1988) have reported coupled radiation and structure calculations for combustion chamber flows. A fast chemistry model with correlations for absorption coefficients in terms of fuel and product concentrations and temperature was used. The correlations for gas species were obtained from a model (Grosshandler, 1980) while the correlations for soot were obtained from a laminar flame model described by Grosshandler and Vantelon (1985). The effects of turbulence–radiation interactions were neglected. An effective angle method was used to estimate the radiative source term. Bhattacharjee and Grosshandler (1988) conclude that consideration of radiative heat loss is necessary in combustion chamber flows when a radiation–convection parameter is large. The authors state that lack of experimental confirmation is an inherent weakness of their study.

In the present study, coupled radiation–structure analysis is performed by solving the equation for conservation of energy in its mean total enthalpy form simultaneously with the structure properties. The radiative source term in this equation is estimated using a new method that accounts for the effects of turbulence radiation interactions. Nonpremixed acetylene air flames are selected for this extension due to their large radiative heat loss and relatively large energy absorption due to soot in the fuel lean regions. The predictions of the coupled and uncoupled calculations are compared with the measurements of: (1) flame structure (mixture fractions, soot volume fractions, mean and fluctuating emission temperatures), and (2) flame radiation (monochromatic intensity at 514 nm and 632 nm). The measurements of mixture fractions are taken from Gore and Faeth (1988) and the measurements of soot volume fractions are taken from Sivathanu et al. (1988). The measurements of mean and fluctuating emission temperatures and monochromatic intensity at 514 nm and 632 nm are completed in the present study.

For two-stream mixing and combustion problems, concentrations of major gaseous species are unique functions of the local instantaneous mixture fraction (defined as the fraction of mass that originated in the fuel stream) following the laminar flamelet concept of Bilger (1977) and Liew et al. (1981). The soot volume fractions are estimated using an extension of the laminar flamelet concept proposed by Gore and Faeth (1986, 1988). Local density and temperature are affected by radiation and are no longer universal functions of the mixture fraction. An equation for the conservation of total enthalpy is solved in order to treat the effects of radiation. The radiative sink/source term in this equation is obtained by integrating the equation of transfer over inhomogeneous paths through the flames.

The extension of the laminar flamelet concept to soot volume fractions may be questionable for some fuels when residence times are short (Sivathanu and Faeth, 1989, 1990). However, acetylene/air flames are unique in their heavy sooting tendency and measurements of Sivathanu and Faeth (1989, 1990) have shown that soot volume fractions for acetylene/air flames are independent of residence time over a broad range. Fortunately, effects of radiation are also important in approximately the same range. The characteristic residence times seen in the pres-

---

Contributed by the Heat Transfer Division for publication in the JOURNAL OF HEAT TRANSFER. Manuscript received by the Heat Transfer Division August 14, 1989; revision received October 2, 1991. Keywords: Fire/Flames, Radiation Interactions, Turbulence.

ent experiments are long enough from the point of view of the soot generation efficiencies (Sivathanu and Faeth, 1989, 1990). The laminar flamelet concept for soot volume fractions (Gore and Faeth, 1988) is used in the present study since few alternatives to this approach are presently available.

The size of the soot particles (in the flaming region of interest here) is relatively small compared to the wavelengths of interest. Typically, the Mie parameter $\pi d_s/\lambda$ is at least an order of magnitude smaller than unity. This validates the Rayleigh approximation for absorption cross section of soot (Tien and Lee, 1982). Within this approximation, refractive index of soot in the only property in addition to soot volume fractions needed for predicting radiation. The appropriate value of refractive index of soot in flames has been debated in the literature and several prescriptions are available (Dalzell and Sarofim, 1969; Lee and Tien, 1981; Charalampopoulos and Felske, 1987; Habib and Vervisch, 1988; Charalampopoulos and Chang, 1988). The refractive index of soot is also necessary in evaluating its volume fraction from absorption data. For consistent prescriptions during absorption and emission calculations, the data from Dalzell and Sarofim (1969) are used here. Other prescriptions may be tried as well, but are not expected to affect the present research issues.

In the following, theoretical methods used during earlier uncoupled analyses are reviewed before describing the coupling procedure. A new method for the calculation of the radiative source term including the effects of turbulence radiation interactions is then described. Following this, experimental data used for the evaluation of the analysis are briefly described. Existing measurements of mean structure properties are then used for evaluating the coupled and uncoupled analyses. New measurements of mean and fluctuating emission temperatures are then used to evaluate the two analyses. Finally, measurements of monochromatic intensities are compared with predictions of both analyses.

Theoretical Methods

Uncoupled Analysis. Before considering the coupled structure and radiation calculations, the uncoupled structure analysis is reviewed in the following. Jeng et al. (1982, 1984), and Jeng and Faeth (1984) have described the uncoupled analysis in detail. The methods developed by these authors were applied to soot containing flames by Gore and Faeth (1986, 1988). Major assumptions of the uncoupled analysis are as follows: low Mach number axisymmetric boundary layer flow with no swirl; equal exchange coefficients of all species and heat; buoyancy only affects the mean flow; and effect of radiation from the flame is the loss of a fixed (constant over the entire flame) fraction of chemical energy release. All the assumptions except for the last are justified by test conditions or by acceptable performance in the past (Jeng et al., 1982, 1984; Gore et al., 1987a, 1987b). For the heavily sooting flames with large radiative heat loss fractions, the assumption of a constant radiative heat loss fraction is questionable. The purpose of the coupled structure radiation calculations is to remove this deficiency.

In the uncoupled analysis, the flow properties are found by solving the governing partial differential equations for $\tilde{u}$, $\tilde{v}$, $\tilde{f}$, k, ϵ, and g. The enthalpy equation is not solved. Following Bilger (1977), all scalar properties in the turbulent flames are unique functions of the local mixture fraction. These unique functions have come to be called "state-relationships" (Faeth and Samuelsen, 1986). The state relationships for gaseous species and soot volume fractions are obtained using routine laminar flame measurements. The state relationships for temperature and density are found using the first law of thermodynamics, with measured species concentrations and thermochemical properties from Gordon and McBride (1971). Equation (1) shows the calculation for the temperature state relationship. The state relationship for density is obtained using the temperatures and the ideal gas law:

$$\left[\sum Y_i \int_{T_o}^{T} C_{pi}\,dT\right]_{\text{products}} = (1-X_R)\left[f h^o_{fF} - \left[\sum Y_i h^o_{fi}\right]_{\text{products}}\right] \qquad (1)$$

In the uncoupled analysis, the radiative heat loss fraction, X_R, is assumed to be a constant at all locations in the flame and is obtained from measurements of total radiative heat loss surrounding the test flames. The quantity in the parentheses on the right-hand side of Eq. (1) represents the chemical energy release corresponding to the local composition:

$$Q_{\text{CHEM}} = f h^o_{fF} - \left[\sum Y_i h^o_{fi}\right]_{\text{products}} \qquad (2)$$

Coupled Analysis. In the coupled analysis the radiative heat loss fraction is not prescribed externally. Instead, a governing equation for the conservation of the mean total enthalpy including the radiative heat loss/gain term is solved:

Nomenclature

a = gravitational acceleration
$a_{\lambda p}$ = Plank mean monochromatic absorption coefficient
$a_{\lambda i}$ = incident monochromatic absorption coefficient
C_{pi} = constant pressure specific heat of gas i
d = burner exit diameter
d_s = soot particle diameter
f = mixture fraction
f_v = soot volume fraction
g = square of mixture fraction fluctuations
H = total enthalpy (chemical + sensible)
H_r = total enthalpy at reference state
h^o_{fi} = heat of formation of species i
Δh_i = sensible energy of species i
I'_λ = spectral radiation intensity
$I'_{\lambda e}$ = emission intensity from individual segments
k = turbulent kinetic energy
m = burner mass flow rate
N = number of product species
Q_a = absorbed energy
Q_e = emitted energy
Q_{CHEM} = chemical energy release
r = radial distance
Re = burner exit Reynolds number
S_H = volumetric radiative source/sink term
T = temperature
u = streamwise velocity
V = volume
v = radial velocity
x = height above the burner
X_R = radiative heat loss fraction
Y_i = mass fraction of species i
ϵ = rate of dissipation of turbulence kinetic energy
θ = polar angle measured from a line parallel to flame axis
λ = wavelength
$\mu_{\text{eff},H}$ = effective viscosity
ρ = density
τ_λ = spectral transmittance
Φ = circumferential angle
Ω = solid angle

Subscripts

c = centerline quantity
o = burner exit quantity
p = product species

Superscripts

$(\bar{\ })$ = time-averaged quantity
$(\sim)$ = Favre-averaged quantity
$(\bar{\ })'$ = rms of a fluctuating quantity

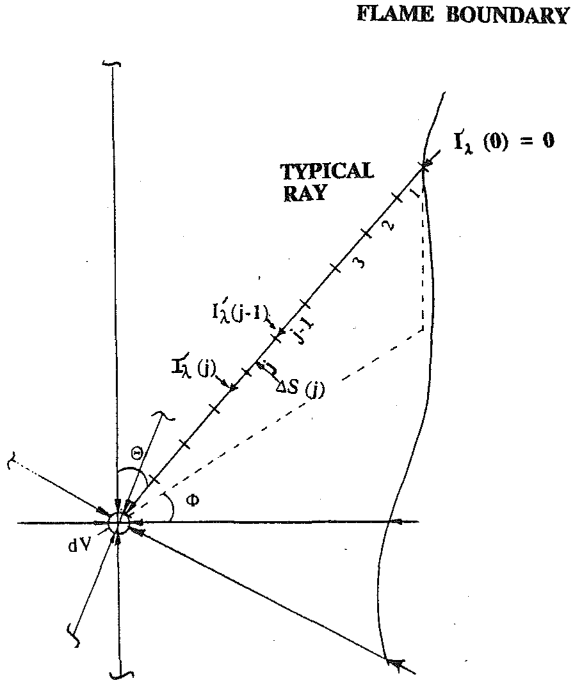

Fig. 1 Calculation of radiative source term for a small volume in the flame using a new multiray method

$$\frac{\partial}{\partial x}(\bar{\rho}\tilde{u}\tilde{H})+\frac{1}{r}\frac{\partial}{\partial r}(r\bar{\rho}\tilde{v}\tilde{H})=\frac{1}{r}\frac{\partial}{\partial r}\left(r\mu_{\mathrm{eff},H}\frac{\partial\tilde{H}}{\partial r}\right)-\overline{S_H} \quad (3)$$

The total enthalpy H is defined as:

$$\tilde{H}=\sum\tilde{Y}_p(h^o_{fp}+\widetilde{\Delta h}_p) \quad (4)$$

where the summation is over all product species denoted by the subscript p. The concentrations of species $\tilde{Y}_p$ have been observed to be independent of the radiative heat loss and are obtained from the laminar flamelet state relationships of Gore and Faeth (1988).

The radiative source term $\overline{S}_H$ in Eq. (3) is evaluated using a new method described in the following. The method accounts for the effects of turbulence–radiation interactions and of nonisotropic radiation field typical of practical flames.

Radiative Source Term. The time-averaged radiative source term $\overline{S}_H$ in Eq. (3) cannot be evaluated using time-averaged values of temperature and absorption coefficients due to the significant effects of turbulence–radiation interactions discovered in the past (Gore and Faeth, 1988). For the calculation of spectral radiation intensities leaving a single path at a few positions, Gore and Faeth (1988) used stochastic realizations of scalar properties along the ray to treat this effect. Application of the stochastic method to the evaluation of the radiative source term at all the grid points is computationally impossible. Therefore, a new method is developed to calculate the time-averaged $\overline{S}_H$ as described in the following.

The volumetric radiative source/sink term $\overline{S}_H$ in Eq. (3) is evaluated by considering a small volume of material within the flame as shown in Fig. 1. The net radiative heat loss (gain) by this material consists of energy emitted by the material to the surroundings minus the energy absorbed by the material from the incident radiation field:

$$\overline{S}_H=\overline{Q}_e-\overline{Q}_a \quad (5)$$

The energy emitted by the material depends on the local emission coefficient and temperature. While the energy absorbed by the material depends on the distribution of these quantities over the entire flame.

The treatment of turbulence radiation interactions in calculating the emission term is facilitated by the selection of dv as an optically infinitesimal volume. In this case, the emitted energy depends solely on the local properties and can be averaged by using the PDF approach as discussed later.

The energy absorbed by the volume dv depends on its absorption coefficient and the incident radiation intensity field. In order to include the effects of turbulence-radiation interactions on the incident radiation intensity field, it is necessary to decouple the field from the absorption coefficient within the small volume under consideration. A new numerical approximation to the equation of transfer resolved to the integral length scale must be selected in order to avoid the specification of multipoint joint probability density functions. These requirements imply that the calculations of the emitted and absorbed energy are resolved to two different scales. Therefore, these are completed separately and then the source term is calculated.

The absorption coefficients for soot particles are calculated using the Rayleigh approximation and the refractive index values discussed in the introduction. The absorption coefficients for the gaseous species are calculated using the narrow band model of Grosshandler (1980).

Emitted Energy. The instantaneous energy emitted by the infinitesimally small volume shown in Fig. 1 can be obtained by integrating the spectral emissive power over all wavelengths:

$$\text{Energy Emitted}=Q_e=4\int_0^\infty a_{\lambda P}e_{\lambda b}d\lambda \quad (6)$$

where $a_{\lambda P}$ is the Planck mean absorption coefficient corresponding to the local instantaneous properties and $e_{\lambda b}$ is the black body emissive power at the local instantaneous temperature. In order to calculate the average energy emitted by the volume dV, needed for evaluating S_H, the instantaneous Q_e given above must be averaged over time. Within the present combustion model, Q_e is a function of the local mixture fraction f and the local enthalpy H. Average value of $\overline{Q}_e$ can be obtained as:

$$\overline{Q}_e=\int_{H_r}^\infty\int_0^1 Q_e(f,H)P(f,H)dfdH \quad (7)$$

where $P(f, H)$ is the joint probability density function of mixture fraction and enthalpy. The additional information concerning H obtained from the coupled analysis allows the construction of $P(f, H)$ as:

$$P(f,H)=P(f)\delta(H(f,X_R)) \quad (8)$$

where $\delta(H(f, X_R))$ is a delta function centered at a value of enthalpy that is a function of the mixture fraction and the local radiative heat loss fraction. $P(f)$ is the probability density function of mixture fraction, which is assumed to be a clipped Gaussian function similar to the uncoupled analysis.

The approximation of the joint PDF given by Eq. (8) is a logical first step. In particular, this model treats the part of total enthalpy that is statistically dependent on the mixture fraction simultaneously with the part that depends on the history of radiative heat loss. This represents an improvement over models that assume statistical independence between mixture fraction and enthalpy and those that assume perfect statistical dependence between the two.

Absorbed Energy. The instantaneous energy absorbed within the small volume dv is calculated using Eq. (9).

$$\text{Energy Absorbed}=Q_a=\int_0^\infty\int_0^{2\pi}\int_0^\pi a_{\lambda i}I'_\lambda(s)\sin\theta d\theta d\phi d\lambda \quad (9)$$

Q_a is the sum of the absorbed portion of the intensity incident on the volume from all directions weighed by a factor depending on the direction. The weight factor is the fractional area on the surface of the spherical volume that is intercepted by an individual ray. $a_{\lambda i}$ in Eq. (9) is the incident monochromatic absorption coefficient, which is in general a function of local and global properties of the scalar and radiation field around the volume dv.

To evaluate the energy absorbed using Eq. (9) numerically, a finite number of rays such as those shown in Fig. 1 must be considered. Both the accuracy and the computer cost of the estimated Q_a improve with the number of rays. The number of rays required to calculate Q_a accurately is found to be 22, as discussed later.

In order to calculate the average energy absorbed by dv while accounting for turbulence–radiation interactions, joint multipoint probability density functions of scalar properties along individual radiation paths are needed. However, the current status of understanding of turbulent reacting flows precludes such an approach. For this reason, the term "$a_{\lambda i} I'_\lambda(s)$" in Eq. (9) must be approximated as the product of averages of $a_{\lambda i}$ and $I'_\lambda(s)$ over statistically independent realizations. Within this approximation, the $a_{\lambda i}$ of soot particles depends only on the local soot volume fraction. The $a_{\lambda i}$ of gaseous molecules depends on the concentrations of collision broadening species along individual rays. However, the absorption by gaseous species for the present flames is much smaller than that by soot particles and the collision broadening effects on $a_{\lambda i}$ can be neglected in the present calculations.

To calculate the average incident energy while accounting for the effects of turbulence–radiation interactions, the equation of transfer is numerically integrated using the following algorithm. Consider an incident ray on the volume dv as shown in Fig. 1. The ray is divided into N finite volumes of length $\Delta S(J)$. J designates a general volume along the radiation path. The average intensity leaving volume J is calculated as:

$$\overline{I'_\lambda}\ (J) = \overline{I'_\lambda (J-1)}\ \overline{\tau_\lambda}\ (J) + \overline{I'_{\lambda e}}\ (J) \qquad (10)$$

where $\overline{I'_\lambda (J-1)}$ is the intensity leaving volume $(J-1)$, $\overline{\tau_\lambda (J)}$ is the average transmittance of the path $\Delta S(J)$, and $I'_{\lambda e}$ is the average intensity emitted by the material in the path $\Delta S(J)$. The incident intensity $I'_\lambda(J-1)$ and the transmittance $\tau_\lambda(J)$ are uncorrelated within the present approximation. It is noted that this requirement can always be satisfied by selecting the $\Delta S(J)$ to be larger than the local integral length scale of turbulence (Kounalakis et al., 1988). The average intensity emitted by the material in the path $\Delta S(J)$ is given by:

$$\overline{I'_{\lambda e}}(J) = \int_{H_r}^{\infty}\int_0^1 (1-\tau_{\lambda J}(f, H)) I_{\lambda b}(f, H) P_J(f, H)\, df\, dH \qquad (11)$$

where $P_J(f, H)$ is the joint probability density function of mixture fraction and enthalpy for the volume J whose approximate form is given in Eq. (8).

Effective Number of Rays. The energy incident on the probe volume is calculated by numerically integrating Eq. (9) over all directions (θ, Φ). The accuracy of this procedure improves as the number of rays is increased. In the past the number of directions considered in such calculations have been limited to 2–6. In the present study, the effect of the number of rays on the calculated absorbed energy is studied at representative locations in the jet flame and an optimum number of rays is obtained.

Figure 2 shows a ratio of the absorbed energy divided by its estimate based on a two-ray calculation plotted as a function of number of rays for three radial positions in the flame at an axial location of $x/d = 50$. It is noted that the estimate based on a two-ray calculation is 40 percent lower than that based on the large-number-of-rays limit at the centerline. At $r/x = 0.1$, the estimate based on two rays is within 20 percent due to compensating errors. As the edge of the flame is approached, the estimate based on two rays is higher by 60 percent. For all three positions shown in Fig. 2 as well as for all other positions, the estimate of the energy absorption approaches its asymptotic large-ray limit at approximately 22 rays. Therefore, all calculations reported in the following are performed using 22 rays.

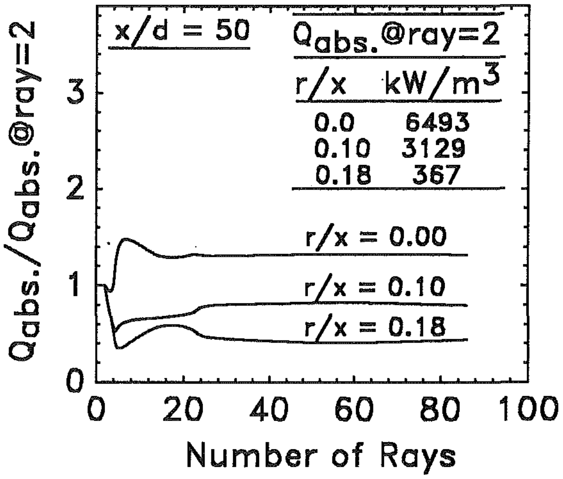

Fig. 2 Effect of number of rays considered in the calculation of the absorption part of the radiative source term

Computations. The initial conditions for all the unknown variables are prescribed at $x/d = 2$ following Gore and Faeth (1988). Initial conditions for the present tests are obtained from profiles for fully developed pipe flow (Hinze, 1975). Initial conditions for enthalpy are obtained by assuming an initial radiative heat loss fraction of zero as a first guess. The coupled calculations automatically correct this assumption by evaluating the radiative heat losses at the initial station. Integration of the governing equations for all the unknowns is carried out using the "GENMIX" algorithm of Spalding (1977).

The calculation of the energy absorption by a volume at a given axial location requires information concerning the scalar properties at downstream locations. Since the flow calculations utilize a marching procedure in the axial direction, absorption terms using 22 rays are calculated after completion of the marching solution based on an initial guess. The calculations are then repeated with the new absorption terms and convergence is obtained. The iterative process is initiated by a two-ray absorption term calculation, which can be completed simultaneously with the flow solution.

The uncertainties in the estimates of radiation source term due to the approximate integrations over wavelength, directions, and the radiation paths are estimated using multiple calculations at sample positions and found to be less than 15 percent.

The overall numerical uncertainties due to finite grid resolution in the flow code as well as the radiation absorption code are estimated by doubling the number of grid points and are estimated to be less than 20 percent.

Experimental Methods

Experimental data from earlier studies (Gore and Faeth, 1988; Sivathanu et al., 1988) for two acetylene/air flames are utilized for the evaluation of flame structure properties. In addition, a third acetylene/air flame is considered in the present work to study the effects of mean and fluctuating emission temperatures. The details of the apparatus used in earlier studies are described by the original authors. In the present study, acetylene is injected vertically upward from an uncooled tube (6.35 mm diameter, 250 mm long) and burned with room air. For the operating condition considered here, the flame attached

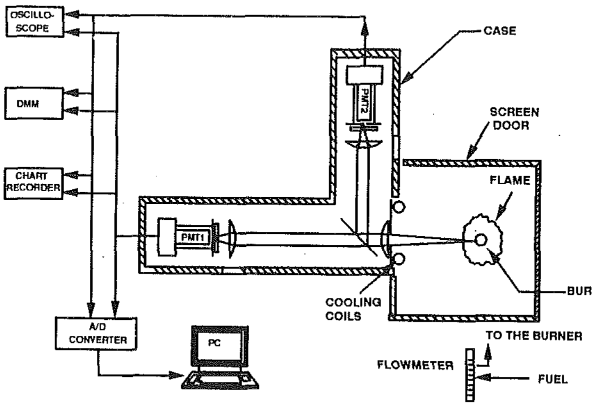

Fig. 3 A sketch of the two-wavelength emission instrument used for measuring path-integrated emission temperatures

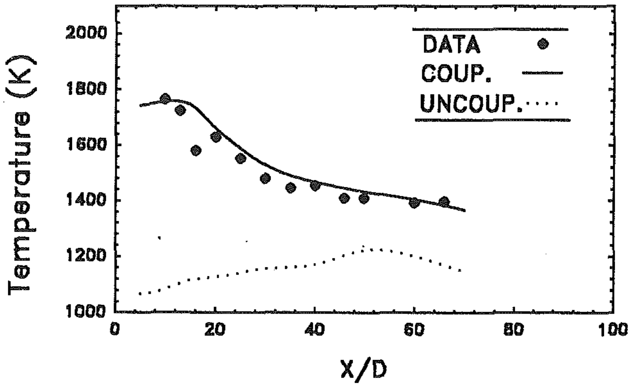

Fig. 4 Measurements and predictions of axial variation of mean emission temperatures for a C_2H_2/air diffusion flame, Re = 5300

naturally at the tube exit. The flame is protected from ambient disturbances by a 2.5-m-high, 1 m × 1 m square enclosure made out of wire screens. The burner could be traversed in the vertical direction with a positioning accuracy of 5 mm.

Instrumentation. The structure and radiation properties of the two earlier flames were measured by Gore and Faeth (1988) and Sivathanu et al. (1988). Measurements included mean and fluctuating velocities, mean mixture fractions, mean soot volume fractions, spectral radiation intensities, and total radiative heat fluxes. Since data for the evaluation of mean structure predictions are available from earlier studies, the present measurements concentrated on path integrated emission temperatures and monochromatic radiation intensities at $\lambda = 514$ nm and 632 nm.

Emission temperatures are estimated from simultaneous measurements of monochromatic (10 nm band width) radiation intensity at 514 nm and 632 nm following the methods described by Sivathanu and Faeth (1989, 1990), Cashdollar (1979), and Klingenberg (1985). Figure 3 shows a sketch of the experimental arrangement. A 10 mm field stop behind a water-cooled plate formed the front end of the instrument. Light leaving a 10 mm^2 area on the surface of the flame within a field angle of 2.4 deg is collected by a lens focused at the flame axis. The approximately collimated light beam passed through a 50/50 beam splitter before being focused on two photomultiplier tubes (Hamamatsu, model R268 with monochromatic filters, 514 ± 10 nm bandwidth and 632 ± 10 nm bandwidth and pinhole apertures). The photomultiplier tubes are equipped with current-to-voltage converters (Hamamatsu, C1053) for obtaining low noise amplification of the signal. The output voltage developed by the converters is sampled by an A/D converter and stored in a laboratory computer. The entire system is calibrated in terms of intensity by using a blackbody reference source (Infrared Industries, Model IR-463, maximum temperature 1000 ± 1°C). Calibration for the emission temperature is also checked by using a Pt-Pt-Rh 10 percent thermocouple (0.1 mm diameter) radiating from a nonluminous laminar diffusion flame burning methane and hydrogen. This allowed verification of the procedure for temperatures up to 2000 K.

The emission temperatures are inferred from monochromatic intensities, which in general depend on the entire radiation path. However, in the present problem, the radiation intensities at the relatively short wavelengths are dominated by one or two points along the radiation path that have the highest temperatures. Therefore, the measurements of emission temperatures can be approximately considered as the peak temperatures along the radiation path. The present theoretical calculations confirm this approximation to within ±50 K.

The experimental uncertainties in monochromatic radiation intensity measurements are less than 10 percent. The uncertainties in the emission temperatures are ca. 100 K. Measurements are repeatable within these limits.

Test Conditions. The test flames used by Gore and Faeth (1988) and Sivathanu et al. (1988) are utilized for the evaluation of velocity, mixture fractions, and soot volume fractions estimated by the analysis. A test flame burning at a Reynolds number of 5300 is considered in the present study. The present flame is stabilized over a long (length/diameter = 40) uncooled stainless steel tube with an inner diameter of 6 mm compared to the 5-mm-dia burner used earlier. The larger burner diameter and the identical Reynolds number lead to a Richardson number that is twice as high for the present flame compared to the Re = 5300 flame of Gore and Faeth (1988) enhancing the effects of buoyancy. The buoyancy-induced mixing is somewhat counteracted by the lower turbulence kinetic energy at the exit. Overall, the present flame is approximately 100 mm shorter than the Re = 5300 flame considered by Gore and Faeth (1988). The present test condition is selected based on the ease of operation and due to the fact that well-defined initial conditions are available in the literature.

Results and Discussion

Flame Structure. Predictions of mixture fractions and soot volume fractions based on the coupled and uncoupled analyses are compared with the experimental data. The agreement between these is very encouraging. Of particular interest is the fact that the effects of radiative coupling on the solution of the momentum and mixture fraction equations are minimal. These results concerning the coupled calculations of mixture fractions and soot volume fractions were reported by Gore (1988) and are not repeated here in the interest of brevity. The effects of coupling on the energy equations are substantial as discussed in the following using measurements and predictions of mean emission temperatures along the axis of the flames. Gore and Faeth (1988) have shown that radiation intensity is most sensitive to temperature. Unfortunately, local measurements of temperatures using fine wire thermocouples could not be obtained due to the problems of soot buildup (Gore and Faeth, 1988). Emission temperatures for narrow angle horizontal diametric paths at various distances from the injector exit are therefore considered.

Figure 4 shows the measurements and predictions of mean emission temperatures. Recall that these are obtained by simultaneous measurements and predictions of monochromatic intensities at two wavelengths. Predictions of the emission temperatures are obtained from the stochastic "data" generated using the coupled and the uncoupled calculations. The measurements show that the emission temperatures are high in the region near the injector exit and then decrease to reach almost a plateau of 1400 K at approximately $x/d = 50$. This

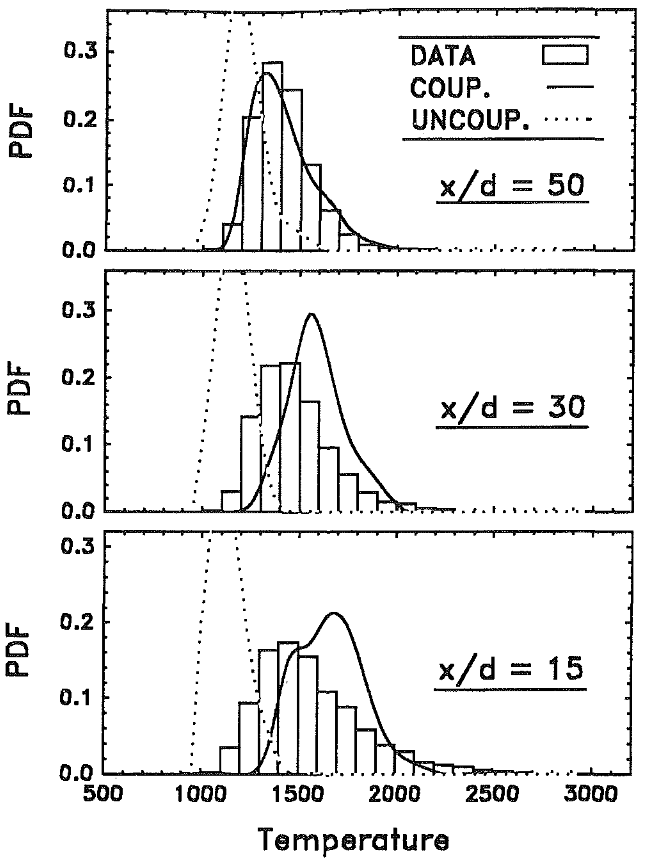

Fig. 5 Measurements and predictions of probability density function of emission temperatures at three axial positions for a C_2H_2/air diffusion flame, Re = 5300

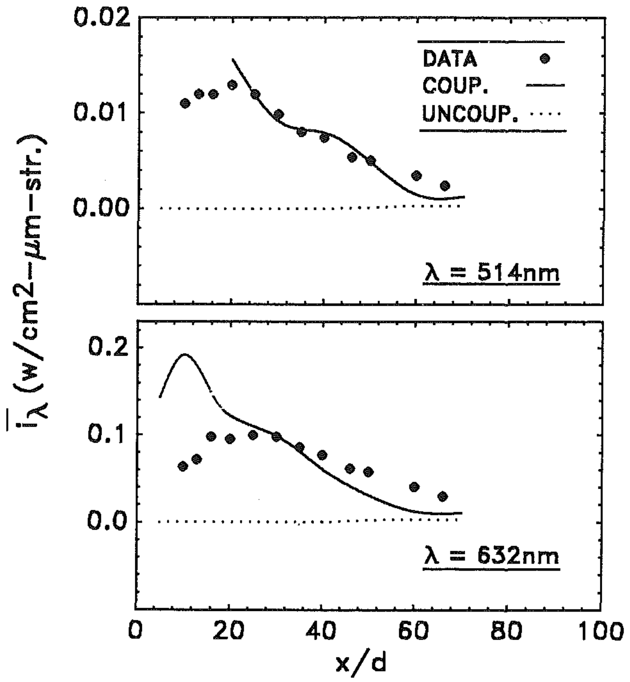

Fig. 6 Measurements and predictions of axial variation of mean visible monochromatic radiation intensities for C_2H_2/air flames, Re = 5300

value of the plateau of mean emission temperature has been observed by other investigators (Sivathanu and Faeth, 1989; Tamanini, 1979). As noted earlier, an examination of the predicted emission temperatures showed that these are within ± 25 K of the peak temperatures along the path.

The uncoupled analyses underpredict the emission temperatures by 200 to 700 K. The coupled calculations predict the trend and the magnitude of the emission temperatures reasonably well. The reason for the differences in the predictions of the two methods lies in the fact that the uncoupled calculations use relatively high radiative heat loss fractions in all regions of the flame. In reality the appropriate initial condition is $X_R = 0$; it then increases to its downstream value as the radiative heat loss progresses. The coupled calculations are designed to account for this fact.

Since radiation properties are nonlinear functions of the flame structure, an evaluation of the measurements and predictions of the fluctuating structure properties is necessary. Since temperatures have the strongest influence on radiation intensities (Gore and Faeth, 1988), fluctuations in emission temperatures are considered.

Figure 5 shows probability density of emission temperature for three positions for the present flames. The measurements show the fraction of data points (out of a total of 4000) that lie within a bin represented by half the difference between the neighboring points. The probability distribution functions of the coupled and the uncoupled predictions are calculated by generating 4000 stochastic realizations of the radiation paths involving integral scale sized eddies.

The measurements at $x/d = 15$ show that the instantaneous emission temperatures vary between 1100 K and 2900 K with the mean at approximately 1600 K. Maximum probability occurs at a temperature of 1500 K due to the long tail of the distribution at the high end. The uncoupled calculations predict a narrow probability distribution centered at 1200 K. Thus most of the high-temperature excursions are missed by this analysis. The coupled calculation predicts the mean temperature within 100 K and also predicts the width of the distribution reasonably well at the high-temperature end.

The behavior of the probability distributions at $x/d = 30$ is somewhat similar. The differences are as follows. The experimental data show a shorter tail on the high-temperature end, bringing the average and the most probable emission temperatures closer. This is a result of radiative cooling during the longer residence time available for the material reaching this position. The uncoupled calculations predict a narrow range of temperatures due to the limitations on the state relationships imposed by a constant radiative heat loss fraction. The coupled calculations again provide very encouraging predictions of the temperature distribution with the exception of the high measured probabilities between 1200–1300 K.

At $x/d = 50$, the high-temperature tail on the experimentally observed distribution function is considered shorter due to progressive radiative cooling. The uncoupled calculation predicts a lower mean and a narrower distribution of the temperatures. The coupled calculations estimate the temperature distribution remarkably well.

Flame Radiation. Figure 6 shows the measurements and predictions of monochromatic radiation intensity for a 10-mm-dia horizontal diametric path plotted as a function of distance from the injector. Measurements and predictions at 514 nm and 632 nm are shown. Predictions of monochromatic radiation intensities using both coupled and uncoupled methods are also shown in Fig. 6. Both predictions are based on the stochastic method to account for the effects of turbulence. In regions very near the injector, the experimentally observed radiation intensity increases and reaches a peak at approximately $x/d = 20$. The coupled analysis overestimates the intensity in region below approximately $x/d = 20$. This discrepancy is due to the gradient broadening errors in the measurements and the finite rate chemistry effects associated with the flame attachment region. In the region beyond $x/d = 20$, the coupled calculations provide a very good estimate of the radiation intensity at 514 nm, but underpredict the intensity at 632 nm by approximately 30 percent. The radiation intensities in the visible are very sensitive to temperatures. Therefore, this level of agreement is very encouraging.

The uncoupled calculations underpredict the radiation intensity by one to two orders of magnitude at the relatively short wavelength considered here. Gore and Faeth (1988) have shown that the uncoupled analysis generally underestimates the intensity in the infrared as well. These results highlight the importance of considering coupled radiation-structure analysis for strongly radiating flames.

Conclusions

1 The coupled calculations predict the experimentally observed trend of relatively high emission temperatures (greater than 1700 K) in the near injector region and the 1400 K plateau in the far field.

2 Coupled radiation-structure calculations also provide good estimates of radiation intensities in the visible. The differences between the measurements and predictions are higher for 632 nm than for 514 nm due to the compensating effects of temperature and soot volume fraction predictions.

3 The uncoupled calculations underpredict both the emission temperature and the visible radiation intensities substantially and are not recommended for strongly radiating flames.

Acknowledgments

This work was completed when the authors were members of the Mechanical Engineering Department at the University of Maryland. Financial support provided by the Center for Fire Research, National Institute of Standards and Technology under grant No. 60NANB8DO834 and the National Science Foundation, under Grant CTS-8914520, is acknowledged. The financial support and computer time provided by the General Research Board, the Physical Plant Department, the Computer Science Center, and the Engineering Research Center of the University of Maryland are also acknowledged.

References

Bhattacharjee, S., and Grosshandler, W. L., 1989, "Effects of Radiative Heat Transfer on Combustion Flows," *Comb. Flame*, Vol. 77, pp. 347-357.

Bilger, R. W., 1977, "Reaction Rates in Diffusion Flames," *Comb. Flame*, Vol. 30, pp. 277-284.

Cashdollar, K. L., 1979, "Three-Wavelength Pyrometer for Measuring Flame Temperatures," *Applied Optics*, Vol. 18, pp. 2595-2597.

Charalampopoulos, T. T., and Felske, J. D., 1987, "Refractive Indices of Soot Particles Deduced From In-Situ Laser Light Scattering Measurements," *Comb. Flame*, Vol. 68, pp. 283-294.

Charalampopoulos, T. T., and Chang, T., 1988, "In Situ Optical Properties of Soot Particles in Wavelength Range From 340 nm to 600 nm," *Combust. Sci. and Tech.*, Vol. 59, pp. 401-421.

Dalzell, W. H., and Sarofim, A. F., 1969, "Optical Constants of Soot and Their Application to Heat Flux Calculations," ASME Journal of Heat Transfer, Vol. 91, pp. 100-104.

Faeth, G. M., and Samuelsen, G. S., 1986, "Fast Reaction Non-premixed Combustion," *Prog. Energy Combust. Sci.*, Vol. 12, pp. 305-372.

Faeth, G. M., Gore, J. P., Chuech, S. G., and Jeng, S. M., 1989, "Radiation From Turbulent Diffusion Flames," *Ann. Rev. Numerical Fluid Mech. and Heat Trans.*, C. L. Tien and T. C. Chawla, eds., Hemisphere, New York, pp. 1-38.

Gordon, A. S., and McBride, B. J., 1971, "Computer Program for Calculation of Complex Chemical Equilibrium Compositions, Rocket Performance, Incident and Reflected Shocks and Chapman-Jouget Detonations," NASA SP273.

Gore, J. P., and Faeth, G. M., 1986, "Structure and Spectral Radiation Properties of Turbulent Ethylene/Air Diffusion Flames," *Twenty-First Symposium (International) on Combustion*, The Combustion Institute, Pittsburgh, PA, pp. 1521-1531.

Gore, J. P., Jeng, S. M., and Faeth, G. M., 1987a, "Spectral and Total Radiation Properties of Turbulent Carbon Monoxide/Air Diffusion Flames," *AIAA J.*, Vol. 25, No. 2, pp. 339-345.

Gore, J. P., Jeng, S. M., and Faeth, G. M., 1987b, "Spectral and Total Radiation Properties of Turbulent Hydrogen/Air Diffusion Flames," ASME Journal of Heat Transfer, Vol. 104, No. 1, pp. 165-171.

Gore, J. P., 1988, "Coupled Structure and Radiation Analysis of Turbulent Diffusion Flames," *Collected Papers in Heat Transfer 1988*, Vol. 2, K. T. Yang, ed., ASME, New York, pp. 77-86.

Gore, J. P., and Faeth, G. M., 1988, "Structure and Spectral Radiation Properties of Turbulent Acetylene/Air Diffusion Flames," ASME Journal of Heat Transfer, Vol. 110, No. 1, pp. 173-181.

Gosman, A. D., and Lockwood, F. C., 1973, "Incorporation of a Flux Model for Radiation Into a Finite Difference Procedure for Furnace Calculations," *Fourteenth Symposium (International) on Combustion*, The Combustion Institute, Pittsburgh, PA, pp. 661-671.

Grosshandler, W. L., 1980, "Radiative Heat Transfer in Nonhomogeneous Gases: A Simplified Approach," *Int. J. Heat Mass Trans.*, Vol. 23, pp. 1447-1459.

Grosshandler, W. L., and Vantelon, J. P., 1985, "Predicting Soot Radiation in Laminar Diffusion Flames," *Combust. Sci. and Tech.*, Vol. 44, pp. 125-141.

Habib, Z. G., and Vervisch, P., 1988, "On the Refractive Index of Soot at Flame Temperature," *Combust. Sci. and Tech.*, Vol. 59, pp. 261-274.

Hinze, J. O., 1975, *Turbulence*, McGraw-Hill, New York, pp. 724-742.

James, R. K., and Edwards, D. K., 1977, "Effects of Molecular Gas Radiation on a Planar, Two Dimensional, Turbulent Diffusion Flame," ASME Journal of Heat Transfer, Vol. 99, No. 1, pp. 221-226.

Jeng, S. M., Chen, L. D., and Faeth, G. M., 1982, "The Structure of Buoyant Methane and Propane Diffusion Flames," *Nineteenth Symposium (International) on Combustion*, The Combustion Institute, Pittsburgh, PA, pp. 349-358.

Jeng, S. M., and Faeth, G. M., 1984, "Radiative Heat Fluxes Near Turbulent Buoyant Methane Diffusion Flames," ASME Journal of Heat Transfer, Vol. 106, pp. 886-888.

Jeng, S. M., Lai, M. C., and Faeth, G. M., 1984, "Nonluminous Radiation in Turbulent Buoyant Axisymmetric Flames," *Comb. Sci. and Tech.*, Vol. 40, pp. 41-53.

Klingenberg, G., 1985, "Invasive Spectroscopic Technique for Measuring Temperature in Highly Pressurized Combustion Chambers," *Optical Engineering*, Vol. 24, p. 696.

Kounalakis, M. E., Gore, J. P., and Faeth, G. M., 1988, "Turbulence/Radiation Interactions in Nonpremixed Hydrogen/Air Flames," *Twenty-Second Symposium (International) on Combustion*, The Combustion Institute, Pittsburgh, PA, pp. 1281-1290.

Lee, S. C., and Tien, C. L., 1981, "Optical Constants of Soot in Hydrocarbon Flames," *Eighteenth Symposium (International) on Combustion*, The Combustion Institute, Pittsburgh, PA, pp. 1159-1166.

Liew, S. K., Bray, K. N. C., and Moss, J. B., 1981, "A Flamelet Model of Turbulent Non-premixed Combustion," *Comb. Sci. and Tech.*, Vol. 27, pp. 69-73.

Negrelli, D. E., Lloyd, J. R., and Novotny, J. L., 1977, "A Theoretical and Experimental Study of Radiation Convection Interaction in a Diffusion Flame," ASME Journal of Heat Transfer, Vol. 99, No. 1, pp. 212-220.

Sibulkin, M., Kulkarni, A. K., and Annamalai, K., 1981, "Effects of Radiation on the Burning of Vertical Fuel Surfaces," *Eighteenth Symposium (International) on Combustion*, The Combustion Institute, Pittsburgh, PA, pp. 611-617.

Siddal, R. G., and Selcuk, N., 1973, "Two-Flux Modelling of Two-Dimensional Transfer in Axi-symmetrical Furnaces," *J. Inst. Fuel*, Vol. 49, pp. 10-20.

Sivathanu, Y. R., Gore, J. P., and Faeth, G. M., 1988, "Scalar Properties in the Overfire Region of Sooting Turbulent Diffusion Flames," *Comb. Flame*, Vol. 73, pp. 315-329.

Sivathanu, Y. R., and Faeth, G. M., 1989, "Soot Properties in the Fuel Rich Region of Turbulent Diffusion Flames," presented at the 1989 Spring Technical Meeting, Central States Section of the Combustion Institute, Detroit, MI.

Sivathanu, Y. R., and Faeth, G. M., 1990, "Soot Volume Fractions in the Overfire Region of Turbulent Diffusion Flames," *Comb. Flame*, Vol. 81, pp. 133-149.

Spalding, D. B., 1977, *GENMIX: A General Computer Program for Two-Dimensional Parabolic Phenomena*, Pergamon Press, Oxford, United Kingdom.

Tamanini, F., 1979, "A Numerical Model for the Prediction of Radiation Controlled Turbulent Wall Fires," *Seventeenth Symposium (International) on Combustion*, The Combustion Institute, Pittsburgh, PA, pp. 1003-1013.

Tien, C. L., and Lee, S. C., 1982, "Flame Radiation," *Prog. Energy Combust. Sci.*, Vol. 8, pp. 41-59.

Heat and Mass Transport From Thermally Degrading Thin Cellulosic Materials in a Microgravity Environment[1]

G. Kushida[2]

H. R. Baum

T. Kashiwagi

Center for Fire Research,
National Institute of Standards and Technology,
Gaithersburg, MD 20899

C. di Blasi

Chemical Engineering Department,
University of Naples,
Naples, Italy

A theoretical model describing the behavior of a thermally thin cellulosic sheet heated by external thermal radiation in a quiescent microgravity environment is developed. This model describes thermal and oxidative degradation of the sheet and the heat and mass transfer of evolved degradation products from the heated cellulosic surface into the gas phase. At present, gas phase oxidation reactions are not included. Without buoyancy, the dominant vorticity creation mechanism in the bulk of the gas is absent except at the material surface by the requirement of the no-slip condition. The no-slip condition is relaxed, permitting the flow to be represented by a velocity potential. This approximation is permissible due to the combination of a microgravity environment and low Reynolds number associated with slow small-area heating by external radiation. Two calculations are carried out: heating without thermal degradation, and heating with thermal degradation of the sheet with endothermic pyrolysis, exothermic thermal oxidative degradation, and highly exothermic char oxidation. The results show that pyrolysis is the main degradation reaction. Moreover, self-sustained propagation of smoldering for cellulosic materials is very difficult due to the lack of sufficient oxygen supply in a quiescent environment.

Introduction

Ignition of solid fuels by external thermal radiation is a process that not only is of considerable scientific interest but that also has fire safety applications. This process is complicated by strong coupling between chemical reactions and transport processes not only in the gas phase but also in the condensed phase. Although the fundamental processes involved in radiative auto-ignition have been suggested by Akita (1978), Kashiwagi (1979, 1981), and Mutoh et al. (1978), there have been no definitive experimental or modeling studies due to the flow motion generated by buoyancy near the heated sample surface. It is extremely difficult to solve theoretical models accurately. One must solve the full Navier–Stokes equations over an extended region to represent accurately the highly unstable buoyant plume. In order to avoid the complicated nature of the starting plume problem under normal gravity, previous detailed radiative ignition models were assumed to be one-dimensional (Kashiwagi, 1974; Kindelan and Williams, 1977) or were applied at the stagnation point (Amos and Fernandez-Pello, 1988). The mismatch between experimental and calculated geometries means that theories cannot be compared directly with experimental results in normal gravity.

To overcome the above difficulty, a theoretical and experimental study for ignition and subsequent transition of flame spread in microgravity has been supported by NASA's Microgravity Science Program. The objective of this study is to be able to compare the theoretical results quantitatively to the experimental data and to obtain a more definitive understanding of the ignition mechanism by the use of a microgravity environment. In this paper the description of the theoretical model and the calculated results of heat and mass transport near the heated surface during a preheating period are described. The model has been developed by taking advantage of the microgravity environment as much as possible in the gas phase instead of modifying a conventional normal-gravity approach. Further extension including gas phase oxidation reactions to achieve ignition will be described in a future paper.

The theoretical model has been developed to be comparable to planned experiments in microgravity using NASA's two drop towers or the space shuttle. A thermally thin cellulosic sheet is considered as the sample fuel. Such a sample might ignite during test times available in the drop towers without requiring a pilot. This eliminates many complicating parameters such as pilot location, temperature, and size (Tzeng et al., 1990). The generation of high-temperature char at the sample surface acts as a self-induced pilot provided by highly exothermic char oxidation (Kashiwagi, 1981). The absorption of the external radiation by evolved degradation products in the gas phase (Amos and Fernandez-Pello, 1988; Kashiwagi, 1981) is not included in the model because a specific lamp, which emits the majority of its energy in near infrared, will be used to reduce the absorption as much as possible in the planned experiment. Although a slow flow along the sample surface, similar to a ventilation flow in a space craft, can have significant effects on the flame spread velocity (Olson et al., 1988), a quiescent environment is used first to develop the model.

2 Theory

2.1 Gas Phase Mathematical Model. The study of radiative ignition of solid fuels in a microgravity environment requires a description of time-dependent coupled processes in both the gas and condensed phases. The mathematical and computational complexity inherent in such a study suggests that the simplifications permitted by the microgravity environment and the small physical scale of the idealized experiment be built into the mathematical model. These simplifications principally affect the gas phase processes. The absence of gravity removes the buoyancy-induced vorticity generation mechanism. The small scale of the experiment, to-

---

[1] Contribution from the National Institute of Standards and Technology.

[2] Guest researcher from Nagoya University, Nagoya, Japan.

Contributed by the Heat Transfer Division and presented at the ASME/JSME Thermal Engineering Conference, Reno, Nevada, March 17–22, 1991. Manuscript received January 1991; revision received October 1991. Keywords: Mass Transfer, Microgravity Heat Transfer, Transient and Unsteady Heat Transfer.

gether with the absence of any significant externally imposed velocity, implies a low Reynolds number flow domain (characteristic length is about 1 cm, which is half the width of an external thermal radiation beam in this study). Classical analyses of low Reynolds number flows have demonstrated that using the Oseen approximation to the convective terms in the equations of motion "constitutes an ad-hoc uniformization" (Van Dyck, 1964) of the first approximation to the rigorous calculation of the flow past isolated bodies. The central point that emerges from these analyses is that diffusion dominates convection near the surface, so the fact that the Oseen flow *does not satisfy the no-slip boundary condition is irrelevant* at the lowest order in the theory. When surface pyrolysis or evaporation is present, the thermally induced surface blowing velocity must be taken into account, even at low Reynolds numbers. Both these concepts can be accommodated by assuming the velocity field to a potential flow. The uniform Oseen velocity is of course a trivial potential flow. The generalization to a flow past an arbitrarily shaped body with a prescribed surface blowing distribution can also be accommodated by a potential field, if vorticity generated in the interior of the flow can be ignored. Again, the only loss is the no-slip boundary condition. This approximation is adopted and is implicit in the analysis that follows.

The potential flow description of the velocity field greatly simplifies both the formulation and subsequent computation of a wide variety of low Reynolds number microgravity heat transfer and combustion problems. Accordingly, the formulation will be developed in a fairly general context and then specialized to the specific case of the radiative ignition of a thermally thin fuel. The starting point is the conservation of mass and energy in the gas. Under low Mach number combustion/heat transfer conditions, these equations can be written as:

$$
\begin{gathered}
D\rho/Dt+\rho\nabla\cdot\mathbf{v}=0\\
\rho C_P DT/Dt-\nabla\cdot(k\nabla T)=\dot{q}_R(\mathbf{r},\,t)
\end{gathered}
\tag{1}
$$

Here, $\dot{q}_R(\mathbf{r},\,t)$ is the net chemical and radiative heat release per unit volume into the gas of density ρ, temperature T, and velocity $\mathbf{v}$. The gas specific heat C_P and thermal conductivity k are in general functions of T. These equations are supplemented by an equation of state, taken in a form appropriate for low-Mach-number flows.

$$
\begin{gathered}
\rho h=\rho_\infty h_\infty\\
h=\int_0^T C_P(T)dT
\end{gathered}
\tag{2}
$$

The subscript ∞ refers to a suitable ambient or reference condition. This form allows C_P to vary with temperature without doing too much violence to the equation of state over temperature ranges appropriate to hydrocarbon combustion problems.

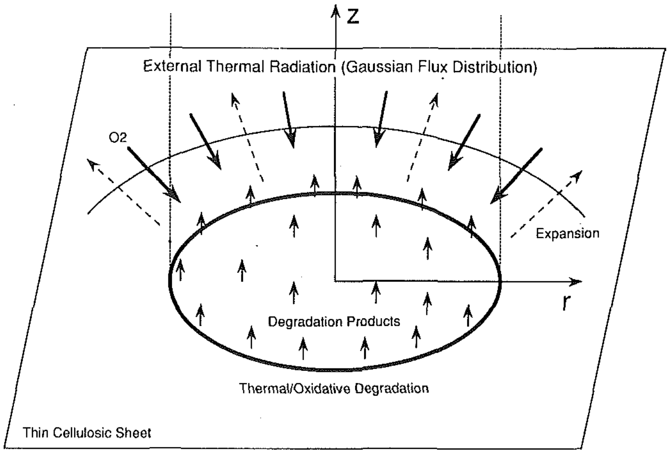

Fig. 1 Schematic radiative ignition process

Now multiply the first of Eqs. (1) by h and add it to the second. The result, after using Eq. (2), is:

$$
\rho_\infty h_\infty \nabla\cdot\mathbf{v}-\nabla\cdot(k\nabla T)=\dot{q}_R(\mathbf{r},\,t)
\tag{3}
$$

Equation (3) is the fundamental equation for determining the velocity field $\mathbf{v}$. Since $\mathbf{v}$ is a vector field, it can be decomposed into the gradient of a potential ϕ and a solenoidal field $\mathbf{u}$.

$$
\begin{gathered}
\mathbf{v}=\nabla\phi+\mathbf{u}\\
\nabla\cdot\mathbf{u}=0
\end{gathered}
\tag{4}
$$

Substitution of Eq. (4) into Eq. (3) yields:

$$
\begin{gathered}
\nabla^2\phi=(1/\rho_\infty h_\infty)(\dot{q}_R(\mathbf{r},\,t)+\nabla^2\psi)\\
\psi=\int_{T_\infty}^{T}k(T)dT
\end{gathered}
\tag{5}
$$

Note that the second term on the right-hand side of Eq. (5) can be eliminated by introducing a particular solution ϕ_P as:

$$
\phi_P=\psi/\rho_\infty h_\infty
\tag{6}
$$

Then, introducing a remainder potential $\Phi(\mathbf{r},\,t)$, ϕ may be expressed in the form:

$$
\begin{gathered}
\phi=\phi_P+\Phi(\mathbf{r},\,t)\\
\nabla^2\Phi=\dot{q}_R(\mathbf{r},\,t)/h_\infty\rho_\infty
\end{gathered}
\tag{7}
$$

Equations (6) and (7) relate the potential field to the temperature and species distributions in the gas phase. Since it is necessary to determine these latter quantities in any event,

Nomenclature

A = pre-exponential frequency factor
C, C_p = specific heat
D = mass diffusivity
E = activation energy
H = heat of reaction
h = enthalpy
K = complete elliptic integral of the first kind
k = thermal conductivity
$\dot{m}$ = mass flux of gas through condensed phase surface
Q = heat flux
$\dot{q}_R$ = net chemical and radiative heat release
R = universal gas constant
RR = reaction rate of solid species
T = temperature
t = time
r = radial coordinate
$\mathbf{u}$, $\mathbf{v}$ = velocity vectors
Y = mass fraction
z = axial coordinate
δ = thickness of paper
ϵ = emissivity
ν = stoichiometric coefficient
ρ = density
σ = Stefan-Boltzmann constant
Φ, ϕ = potential function

Subscripts

C = char
F = fuel
G = gas
OX = oxygen
rad = radiation
S = solid
0, ∞ = ambient or reference condition
1 = associated with reaction 1 (pyrolysis)
2 = associated with reaction 2 (thermal oxidative degradation)
3 = associated with reaction 3 (char oxidation)

solution of Eq. (7) represents the minimum additional work required to obtain a self-consistent velocity field. Implied in this statement is the assumption that the solenoidal velocity field **u** is not of interest in its own right. If **u** is of interest, then there is no alternative to solving the Navier–Stokes equations. However, a large portion of both the combustion and heat transfer literature consists of calculations in which the details of the velocity field are approximated, often crudely, in order to understand the thermophysical phenomenon of direct interest. In the present circumstances, the approximations have been justified in simple geometries by detailed analyses, and interest will be confined to species and temperature fields induced by radiative ignition.

Now consider the specific problem of a concentrated radiation source impinging on a thermally thin fuel slab. The geometry is shown in Fig. 1. Let r and z be radial and axial cylindrical coordinates as shown in the figure. Attention is focused on the preheating phase of the ignition process. The gas is assumed to be transparent to the radiation. Under these circumstances, the term $\dot{q}_R(r, z, t)$ in Eqs. (1) can be ignored. The gas phase energy and species conservation equations take the form:

$$\rho C_P(\partial T/\partial t + \nabla\phi\cdot\nabla T) = \nabla\cdot(k\nabla T)$$
$$\rho(\partial Y_i/\partial t + \nabla\phi\cdot\nabla Y_i) = \nabla\cdot(\rho D\nabla Y_i) \qquad (8)$$

Here, Y_i are the mass fractions of the oxygen $Y_{\rm OX}$, and the fuel species Y_F emitted by the pyrolyzing solid located at $z=0$. The diffusivity D, thermal conductivity k, specific heat C_p, and density ρ are assumed to be independent of the gas species but dependent on temperature. The values for air are used to represent these properties and the polynomial fitting of temperature for each property is used in the calculation. These equations are to be solved together with Eqs. (6) and (7), subject to boundary and initial conditions.

At time $t=0$, the entire system is assumed to be at rest at (cool) ambient temperature T_∞. Hence:

$$\phi(r, z, 0) = Y_F(r, z, 0) = 0$$
$$Y_{\rm OX}(r, z, 0) = Y_\infty$$
$$T(r, z, 0) = T_\infty \qquad (9)$$

Once the heating process has started, the solid fuel temperature $T_S(r, t)$ rises above ambient and at some later time a mass flux $\dot{m}(r, t)$ of gasified fuel is evolved from the fuel surface. The gas phase boundary conditions can be expressed in terms of these quantities as:

$$\partial\phi(r, 0, t)/\partial z = h(r, 0, t)\dot{m}(r, t)/\rho_\infty h_\infty$$
$$h(r, 0, t) = \int_0^{T_S} C_P dT$$
$$T(r, 0, t) = T_S(r, t)$$
$$\dot{m}(r, t) = \rho_\infty h_\infty\{\partial\phi(r, 0, t)/\partial z\}Y_F(r, 0, t)/h(r, 0, t)$$
$$-\rho_\infty h_\infty D(r, 0, t)\{\partial Y_F(r, 0, t)/\partial z\}/h(r, 0, t) \qquad (10)$$

Alternatively, the residual potential Φ is subject to the boundary condition:

$$\partial\Phi(r, 0, t)/\partial z = \{h(r, 0, t)\dot{m} - k\partial T(r, 0, t)/\partial z\}/\rho_\infty h_\infty \qquad (11)$$

Equation (11) replaces the first of Eqs. (10).

Table 1 Chemical properties of thermal degradation

	A	E [kJ/mol]	ν_C	ν_G	$\nu_{\rm OX}$	ν_A	ΔH [J/g]
(1)	1.4×10^{19} [min^{-1}]	220	0.27	0.73			+570
(2)	1.0×10^{17} [cm^3/g min]	170	0.27	0.83	0.10		−4,200
(3)	1.0×10^{13} [cm^3/g min]	160		2.00	1.00	0.00	−25,000

Far from the surface, ϕ, Y_i, and T must decay to their ambient initial values. Translating this into boundary conditions suitable for numerical computation, however, requires some care. Numerical boundary conditions are applied at the edge of a rectangular computational domain. Since Y_i and T decay exponentially to their ambient values, setting these quantities equal their values given in Eq. (9) is permissible until the first calculated nonambient contours of these quantities approach the computational boundary. However, the potential field decays slowly away from the heated region, i.e., $\phi \sim (r^2+z^2)^{-1}$. Thus, putting ϕ or its gradient equal to zero at the computational boundary would introduce unacceptable errors into the calculation. These errors can be avoided by using the solution to Eq. (7) (with $\dot{q}_R=0$) subject to the boundary condition given by Eq. (11).

$$\rho_\infty h_\infty\Phi = \int_0^\infty G(r, r_0, z)\partial\Phi(r_0, 0, t)/\partial z r_0 dr_0$$
$$G(r, r_0, z) = (2/\pi)K(k_b)/[(r+r_0)^2+z^2]^{1/2}$$
$$k_b^2 = 4rr_0/[(r+r_0)^2+z^2] \qquad (12)$$

Here K is the complete elliptic integral of the first kind. Now $\partial\Phi(r_0, 0, t)/\partial z$ is given by Eq. (11) at any instant of time, and the temperature is an exponentially decaying function of the radial integration variable in Eq. (12). Hence, use of Eq. (12) to evaluate Φ around the computational boundary provides a fast and highly accurate means of applying computational boundary conditions to Φ.

2.2 Condensed Phase Mathematical Model. In the present paper the condensed phase is initially a cellulosic sheet that changes gradually to char followed by ash, due to thermal degradation. The phase is assumed to be thermally thin and also depth-wise uniform in its composition. Although there are numerous studies on the thermal degradation of cellulose and wood (for example, Nakagawa and Shafizadeh, 1984), the expression of mass addition rates from a thermally degrading paper in air is needed in this study. Since detailed study of oxidation reactions of a paper and char is limited, a global approach of three reactions (Rogers and Ohlemiller, 1980) is used in this study.

(1) Endothermic Pyrolysis Reaction. The cellulosic material is endothermically degraded to a char.

$$\text{Fuel} \rightarrow \nu_{C1}\text{Char} + \nu_{G1}\text{Gases}$$

(2) Exothermic Thermal Oxidative Degradation Reaction. The cellulosic material is exothermically degraded to a char by oxidation. Generally, this reaction occurs in approximately the same temperature range as for the pyrolysis reaction.

$$\text{Fuel} + \nu_{OX2}\text{O}_2 \rightarrow \nu_{C2}\text{Char} + \nu_{G2}\text{Gases}$$

(3) Exothermic Char Oxidation Process. The char formed by the above reactions is exothermically reacted with oxygen to form gases and ash. Here, it is assumed that the reactivity of char formed from the above two reactions with oxygen is the same.

$$\text{Char} + \nu_{OX3}\text{O}_2 \rightarrow \nu_A\text{Ash} + \nu_{G3}\text{Gases}$$

In the above three reactions, the reaction rates RR_n are assumed to be given by the following expressions:

$$(1)\ RR_1 = A_1(\rho_S Y_F)\exp(-E_1/RT)$$
$$(2)\ RR_2 = A_2(\rho_G Y_{\rm OX})(\rho_S Y_F)\exp(-E_2/RT)$$
$$(3)\ RR_3 = A_3(\rho_G Y_{\rm OX})(\rho_S Y_C)\exp(-E_3/RT) \qquad (13)$$

Here, the pre-exponential frequency factor A, activation energy E for each reaction, stoichiometric coefficients (mass based) of species ν_C, ν_G, $\nu_{\rm OX}$, and ν_A must be specified. Although these reactions are assumed to be first order and second

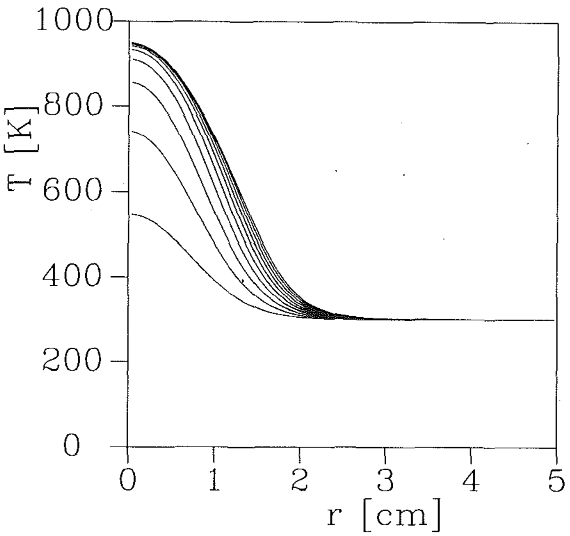

Fig. 2 Radial distribution of material surface temperature, at 1 s intervals

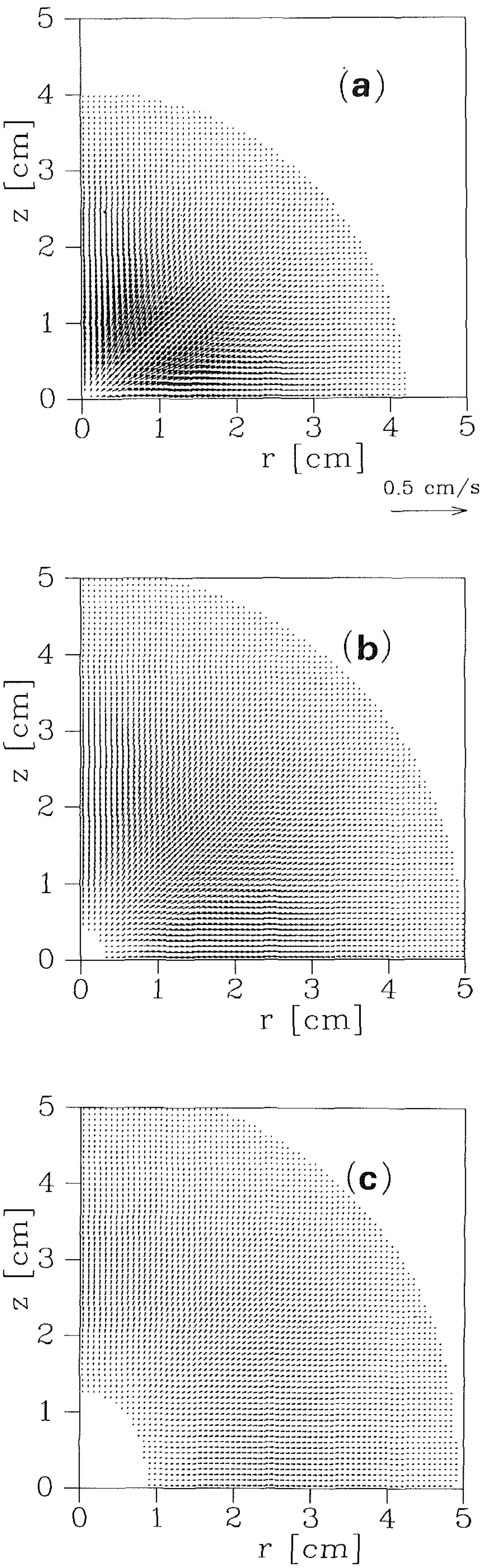

Fig. 3 Velocity vector distributions at (*a*) 1 s, (*b*) 3 s, and (*c*) 5 s (velocity vectors less than 1/40 of 0.5 cm/s are not plotted in the figure)

order, any other order of reaction can be used in the model. These parameters together with the heats of reaction ΔH are given in Table 1. The values for the pyrolysis reaction are measured by conducting a thermogravimetric analysis of a black paper that has been used for preliminary ignition experiments under normal gravity. The results of derivative thermogravimetry are analyzed by Kissinger's method (Kissinger, 1957). Although the measurement of kinetic constants for the above two oxidative reactions is in progress, the values listed for the two oxidative degradations are estimated from our preliminary results. A parametric study regarding values of kinetic constants for the two oxidative reactions has been conducted and the results are described in the final portion of this paper.

The equations for the condensed phase are given as follows:

Conservation of solid mass:

$$\partial \rho_S/\partial t = (\nu_{C1}-1)RR_1 + (\nu_{C2}-1)RR_2 + (\nu_A - 1)RR_3 \quad (14)$$

Conservation of cellulosic material:

$$\partial(\rho_S Y_F)/\partial t = -RR_1 - RR_2 \quad (15)$$

Conservation of char:

$$\partial(\rho_S Y_C)/\partial t = \nu_{C1}RR_1 + \nu_{C2}RR_2 - RR_3 \quad (16)$$

Conservation of energy:

$$(C_F\rho_S\delta)\partial T_s/\partial t = \{-\Delta H_1 RR_1 - \Delta H_2 RR_2 - \Delta H_3 RR_3\}\delta + (1-r)Q_{\text{rad}} - \epsilon\sigma(T_s^4 - T_0^4) + k\partial T/\partial z + \dot{m}\{h_s - h(r, 0, t)\} \quad (17)$$

where δ is the thickness of the paper and the heat flux distribution of the external radiation is assumed to be Gaussian. In the calculation reported here,

$$Q_{\text{rad}} = 50 \exp(-\alpha r^2) \quad [\text{kW/m}^2] \quad (18)$$

where $\alpha = 1.0 \times 10^4$ [m^{-2}]. The reflectivity, r, is assumed to be 0 and the emissivity, ϵ, is assumed to be 1.

The mass flux of gasified fuel through the sample surface is given by the following expression:

$$\dot{m} = [(1-\nu_{C1}RR_1 + (1-\nu_{C2})RR_2 + (1-\nu_A)RR_3] \times \delta \quad (19)$$

The cellulosic material used in the present study is a 0.25×10^3 m thick paper sheet. The properties are: C_S $(= C_F = C_C) = 1.255$ [kJ/(kgK)], $k_S = 6.0 \times 10^{-2}\rho_S/\rho_F$ [W/(mK)] (Nakagawa and Shafizadeh, 1984), $\rho_F = 0.6 \times 10^{-3}$ [kg/m^3].

2.3 Numerical Methods. The numerical calculation is performed by using a finite-difference method. The compu-

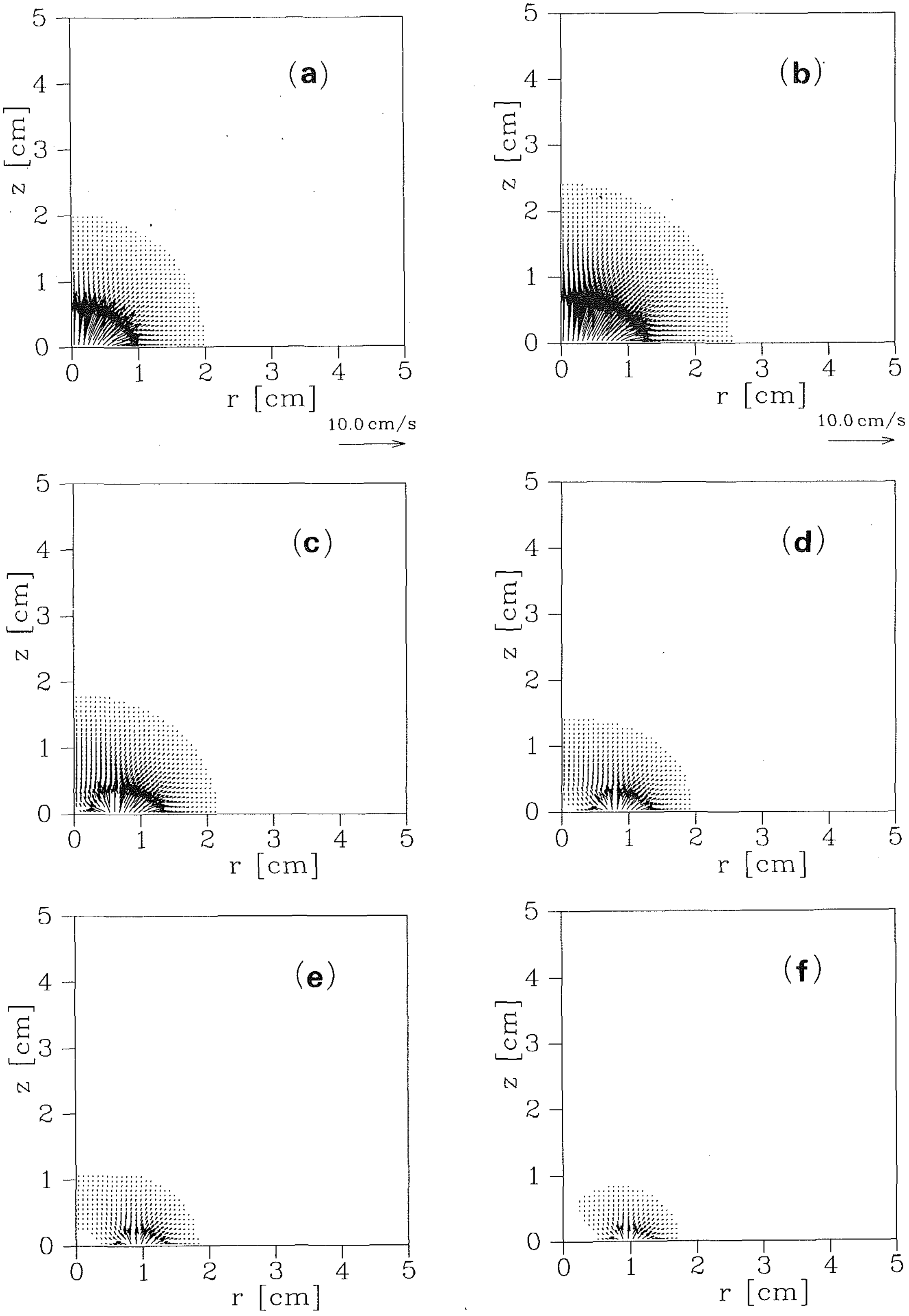

Fig. 4 Velocity vector distribution at (*a*) 2.0 s, (*b*) 3.5 s, (*c*) 5 s, (*d*) 6.5 s, (*e*) 8.0 s, (*f*) 9.5 s (velocity vectors less than 1/40 of 10 cm/s are not plotted in the figure)

tational domain is taken to be $r \leq 5.0$ cm and $z \leq 5.0$ cm. There are 71 and 72 grid cells in the r and z directions, respectively. The grid size was chosen after numerical experiments at half size together with Richardson extrapolation showed that the error is within 0.4 percent.

The equations to be solved for the gas phase are those for the potential function Φ, the temperature T, and the species Y_{OX}. For the condensed phase, the equations for the temperature T, the species Y_F and Y_C, and the solid density ρ_S also have to be solved. Since the condensed phase temperature

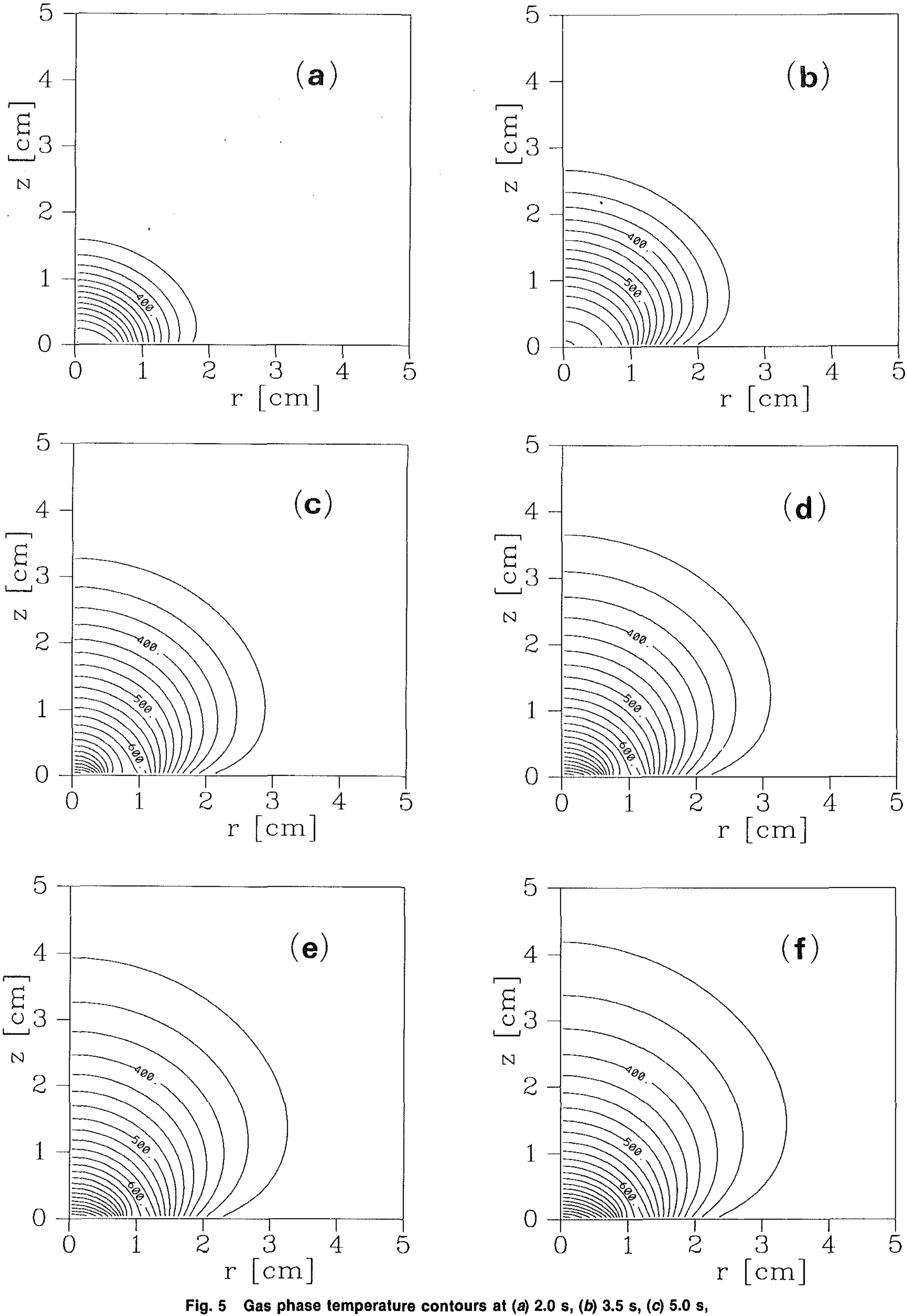

Fig. 5 Gas phase temperature contours at (*a*) 2.0 s, (*b*) 3.5 s, (*c*) 5.0 s, (*d*) 6.5 s, (*e*) 8.0 s, and (*f*) 9.5 s, at intervals of 25 K

equation is coupled with that for the gas phase, the two equations are solved simultaneously in the present analysis. The solution for Φ is computed by employing a direct solver of the Poisson equation in cylindrical coordinates using the standard five-point finite difference approximation on a staggered grid (FISHPAK). The equations for temperature and gas species employ a second-order difference scheme for both convection and diffusion terms. The boundary conditions for Φ are specified at the open boundaries by calculating Eq. (12). The derivative of the solution with respect to z is specified at $z=0$ by Eq. (11). As for the boundary conditions for temperature and species for the gas phase, the derivatives are taken to be zero at the open boundaries. The derivative of species with respect to z is also taken to be zero at $z=0$.

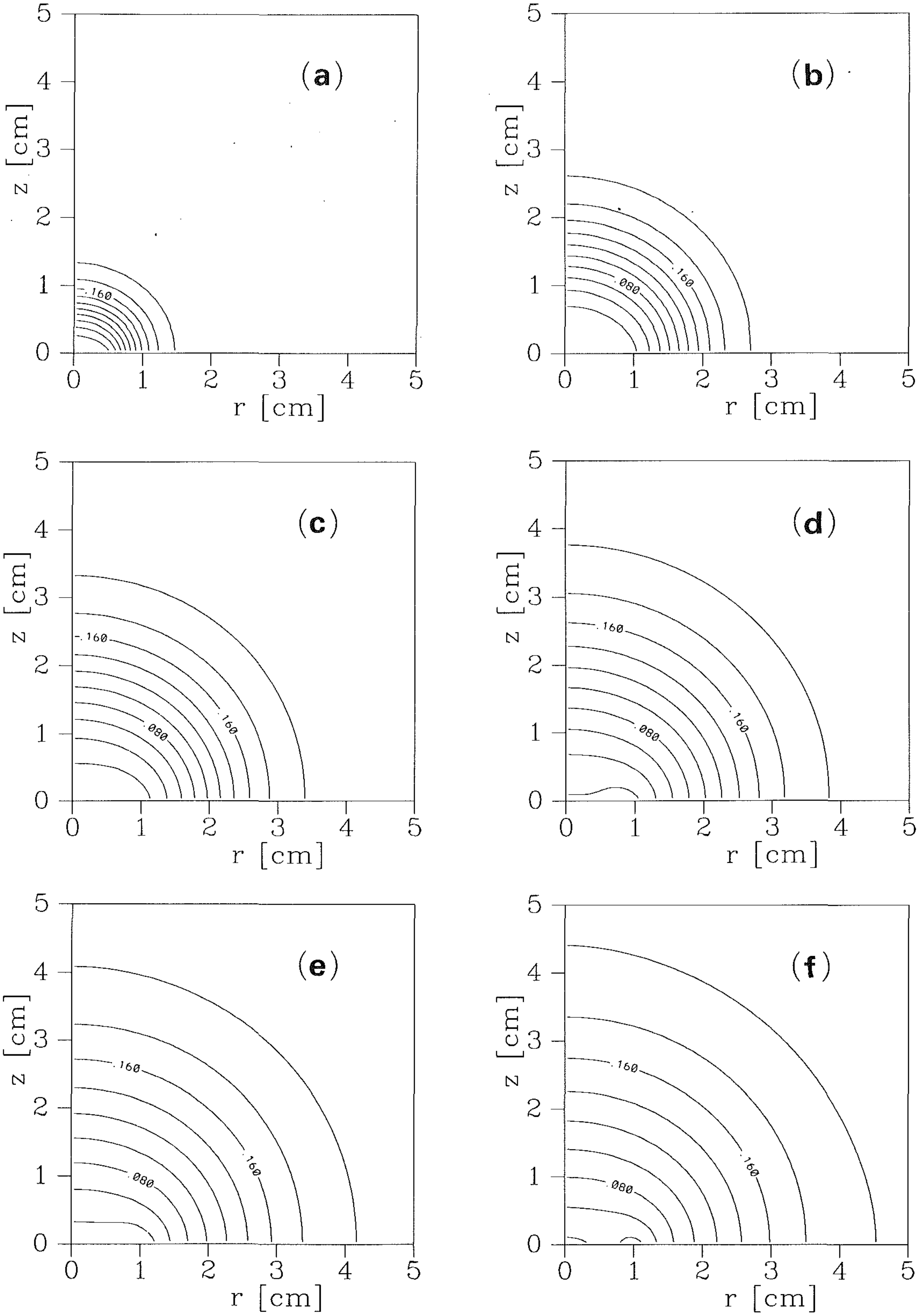

Fig. 6 Gas phase oxygen contour at (*a*) 2.0 s, (*b*) 3.5 s, (*c*) 5.0 s, (*d*) 6.5 s, (*e*) 8.0 s, and (*f*) 9.5 s at intervals of 0.02

The temperature variation with respect to the *z* direction in the condensed phase is ignored, because it is assumed to be thermally thin. The oxidation of the condensed phase is performed by consuming the oxygen in the control volume immediately above the sample surface. It is also assumed that the condensed phase does not become porous. Only the density of the solid material changes. The other equations ((14)–(17)) for the condensed phase are also solved using a finite difference approximation for a control volume of the same size as that in the gas phase. The time advance is made by using Euler's implicit method with an interval of 0.025 seconds, which satisfies the error estimate stated above.

3 Results and Discussion

3.1 Results Without Thermal Degradation. Figure 2 shows the change in the radial temperature distribution of the sample with time without the thermal degradation of the solid material. The temperature distribution corresponds to the Gaussian flux distribution of external radiation expressed by Eq. (18). The temperature increase slows down significantly at about 7 seconds because of the heat balance between external radiation and the reradiation loss from the high-temperature surface.

Figures 3 show the velocity vector distributions at 1, 3, and 5 seconds after irradiation, respectively. As shown in the figures, the gas phase is heated by heat conduction from the sample surface irradiated by external radiation, and the region of heated gas expands as time increases. The gas flow changes from the initial quiescent state into the outward flow motion from the region near the heated surface due to the expansion of the gas. The flow velocity gradually decreases after about 5 seconds and becomes almost zero everywhere in 10 seconds, although irradiation of the surface by the external radiation is still continued. In the absence of thermal degradation, the magnitude of the velocity is small for all times.

3.2 Results With Thermal Degradation. The results including the thermal degradation of the cellulosic sheet described in section 2.2 are shown in Figs. 4, 5, and 6, giving velocity vector distributions, temperature contours, and oxygen concentration contours up to 9.5 seconds, respectively. These show a rapid increase in flow velocity near the sample surface due to mass addition after the sample temperature becomes sufficiently high to cause thermal degradation. Blowing starts to become significant at about 1.5 seconds and continues to increase until about 3.5 seconds. Flow velocities normal to the sample surface with thermal degradation become as large as 50 times those without thermal degradation (shown in Fig. 3). Therefore, blowing significantly affects the flow motion in microgravity. (It should be noted, however, that local Reynolds numbers based on the velocity and distance from the axis of symmetry are still O(1).) Correspondingly, the high gas temperature region is expanded much further by the blowing due to thermal degradation. The mass addition of degradation gases rapidly dilutes the oxygen concentration near the heated sample surface. At about 2 seconds, the oxygen concentration at the center of the sample near the sample surface is nearly zero. This indicates that thermal degradation is mainly due to the pyrolysis reaction instead of the oxidative degradation reactions. After 4 seconds the location of maximum blowing velocity gradually moves from the center radially outward because the original cellulosic material is nearly consumed as the hard-to-degrade char is formed. In this way, the char region gradually expands from the center outward and the blowing nearly stops over the char region. The temperature contours indicate that near the axis heat flows from the hotter surface to the cooler gas phase. In the region where blowing is active, convection by degradation products from the surface to the gas phase is dominant. In the region outside of the pyrolyzing zone, the gas phase temperature near the surface is higher than that of surface, giving temperature contours that have a different shape from the oxygen concentration contours; the latter are nearly normal to the surface, indicating that there is little consumption by the oxidative reactions.

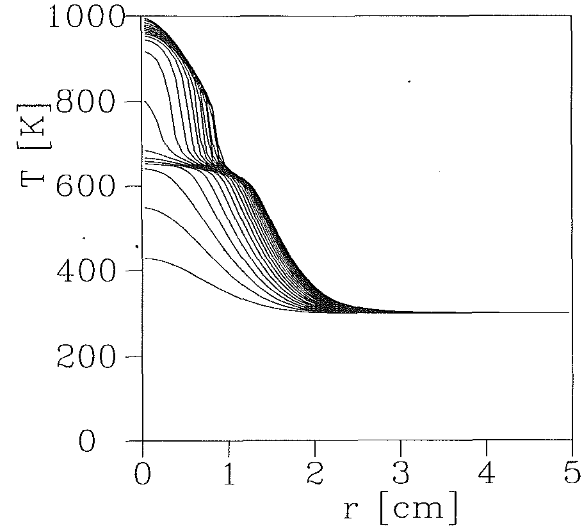

Fig. 7 Radial distribution of material temperature at intervals of 0.5 s

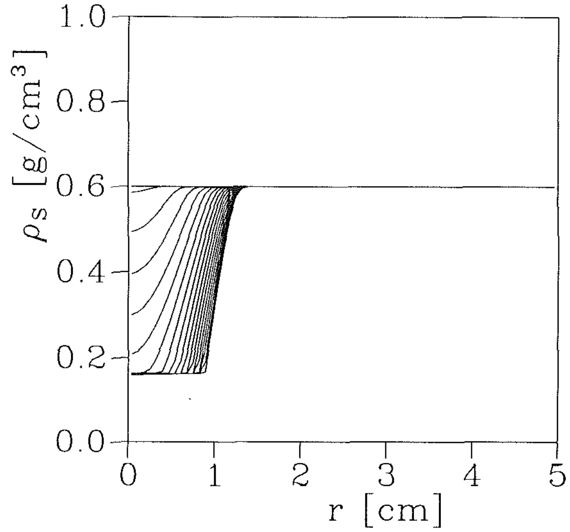

Fig. 8 Radial distribution of material density at intervals of 0.5 s

Changes in the radial temperature distribution of the cellulosic sheet with time are shown in Fig. 7. Similarly the radial density distribution of the sheet is shown in Fig. 8. As seen on the axis in Fig. 7, the temperature rapidly rises in the first few seconds, but the increase slows after the temperature reaches about 650 K. This slowdown is caused by the endothermic pyrolysis reaction, which becomes significant in this temperature range. After the temperature remains at about 650 K for few seconds, it rapidly rises close to 1000 K and then slows again at about 4 seconds. This rapid temperature increase is caused by the complete consumption of the original cellulosic material to form char, which reduces the endothermic pyrolysis reaction rate and also the mass of the sample (the density of cellulose is roughly four times larger than that of char (Nakagawa and Shafizadeh, 1984)) and furthermore decreases blowing convective cooling from the hot surface. Energy is balanced at the sample surface mainly between the external radiation and the reradiation loss from the high-temperature surface.

The density of the material rapidly decreases from the initial value of 0.6 g/cm^3 to about 0.16 g/cm^3, which is the value of the char density. After about 4 seconds the density of the material remains at about 0.16 g/cm^3, which indicates that the char oxidation reaction rate is not significant. The oxygen concentration contours show that oxygen concentration is extremely small at the sample surface in the region of active blowing, due mainly to dilution and poor oxygen supply by diffusion. Therefore, the oxidative degradation reaction and the char oxidative reaction do not participate significantly in the gasification process at an external radiant flux peak of 50 kW/m^2 in a quiescent environment. However, if there is a forced slow air flow along the sample surface such as a ventilation flow in a space craft, the oxidative degradation reactions might become important. Another possible scenario permitting char oxidation participation might occur if diffused oxygen leaks behind the outward moving blowing front generated by the pyrolysis reaction. A gradual increase in oxygen concentration near the axis by the sample surface can be observed from the oxygen concentration contours at 6.5 seconds. A slight dip in the contour of 2 percent oxygen concentration near the axis shows increased oxygen supply to this region by diffusion. This trend continues, and oxygen concentration reaches about 2.7 percent at 7 seconds. At this time the lowest oxygen concentration at the sample surface is in the region of active blowing at this time. However, this active blowing region gradually moves radially outward due to the consumption of the original cellulosic material. The level of blowing gradually decreases with increasing radius because the material temperature decreases with decrease in external flux. At 8 seconds the oxygen concentration near the axis reaches 3.5 percent. At 8.5 seconds the char oxidation reaction starts and the oxygen concentration near the surface decreases slightly. At 9 seconds within a 0.5 cm radius, the oxygen concentration near the surface decreases further due to the consumption of oxygen by the char oxidation reaction. The low oxygen concentration zone near the surface around 1 cm is due to dilution by degradation gases from the pyrolysis reaction. Since the temperature of the material is the highest at the axis, as shown in Fig. 7, due to Gaussian distribution of the external radiation, the char oxidation occurs only around the axis. However, the radial material density distribution, Fig. 8, indicates that a decrease in density by the consumption of char by oxidation is extremely small due to the lack of oxygen supply; the oxygen supply remains small due to dilution by degradation gases from the char oxidation reaction. Therefore, in a quiescent environment under microgravity the rate-controlling process for smoldering is the oxygen supply. The above results show that the two exothermic oxidative degradation reactions are severely limited even with continued external radiation. Therefore, self-supported smoldering (without external heat) of a cellulosic material is very difficult in a quiescent environment under microgravity.

3.3 Effect of Chemical Properties on Oxidation. These calculations were carried out using estimated values of the kinetic constants for the two oxidative degradations. Therefore, it might be premature to conclude that self-supported smoldering is severely limited in a quiescent environment under microgravity. A parametric study to examine effects of the kinetic constants for the two oxidation reactions on smoldering was conducted. Two types of calculations were performed; different kinetic constants for the oxidative degradation reactions were used in the above model, and a one-dimensional model ignoring gas phase phenomena was employed. The latter is basically a degradation kinetic model of the sheet with the specified initial oxygen concentration. Oxygen is consumed only by oxidation, and there is no oxygen supply or dilution by degradation gases. Although this model is limited to degradation of the sheet, the calculated results clearly show how the pyrolysis reaction and the two oxidative reactions compete to consume the cellulosic material and the oxygen. Since the calculation of the second model is much simpler, many cases were investigated using this model. The results indicate that smoldering tends to occur with lower values of ν_{OX2} and ν_{OX3}, higher values of ν_{C1} and ν_{C2}, and higher values of heat of oxidative degradations. The first reduces the consumption of oxygen, the second reduces the dilution by degradation gases, and the third increases energy heat release rates from the oxidative reactions. The effects of pre-exponential parameters and activation energies do not significantly affect the trend of self-supported smoldering and they mainly change the temperature at which each degradation reaction occurs. Therefore, in order to predict smoldering characteristics of a cellulosic material in a microgravity environment, the values of kinetic constants for the above three global degradation reactions must be determined.

4 Conclusion

The following conclusions are derived from the calculated results in a *quiescent* environment under microgravity.

1 The flow motion created by heat addition from the surface to the gas phase rapidly dies out even when heat is continuously added.

2 The mass addition of degradation products from the surface to the gas phase generates relatively large flow velocities near the surface up to 10 cm/s at an external radiant flux of 50 kW/m^2 and surface absorptivity of 1 (compared with the nonblowing case) and dominates the motion.

3 The degradation gases are mainly generated from the pyrolysis degradation reaction. The oxidative degradation reaction is severely limited due to the lack of oxygen supply caused by dilution by the degradation gases emitted from the pyrolysis reaction at external radiation of 50 kW/m^2 and surface absorptivity of 1.

4 Char oxidation could occur near the axis of symmetry as oxygen gradually diffuses back to the char surface after the pyrolysis process is completed.

5 Self-sustained smoldering is controlled and severely limited by the reduced oxygen supply.

Acknowledgments

This study is supported by the NASA Microgravity Science Program under the Inter-Agency Agreement No. C-32000-K.

References

Akita, K., 1978, "Ignition of Polymers and Flame Propagation on Polymer Surface," in: *Aspects of Degradation and Stabilization of Polymers*, H. H. G. Jellinek, ed., Elsevier Scientific, Chap. 10.

Amos, B., and Fernandez-Pello, A. C., 1988, "Model of the Ignition and Flame Development on a Vaporizing Combustible Surface in a Stagnation Point Flow: Ignition by Vapor Fuel Radiation Absorption," *Combustion Science Technology*, Vol. 62, pp. 331-343.

Kashiwagi, T., 1974, "A Radiative Ignition Model of a Solid Fuel," *Combustion Science Technology*, Vol. 8, pp. 225-236.

Kashiwagi, T., 1979, "Experimental Observation of Radiative Ignition Mechanisms," *Combustion Flame*, Vol. 34, pp. 231-244.

Kashiwagi, T., 1981, "Radiative Ignition Mechanism of Solid Fuels," *Fire Safety Journal*, Vol. 3, pp. 185-200.

Kindelan, M., and Williams, F., 1977, "Gas-Phase Ignition of a Solid With In-Depth Absorption of Radiation," *Combustion Science Technology*, Vol. 16, pp. 47-58.

Kissinger, H., 1957, "Reaction Kinetics in Differential Thermal Analysis," *Analytical Chem.*, Vol. 29, pp. 1702-1706.

Mutoh, N., Hirano, T., and Akita, K., 1978, "Experimental Study on Radiative Ignition of Polymethylmethacrylate," *Seventeenth Symposium (International) on Combustion*, The Combustion Institute, Pittsburgh, PA, pp. 1183-1190.

Nakagawa, S., and Shafizadeh, F., 1984, *Handbook of Physical and Mechanical Testing of Paper and Paperboard*, R. E. Mark, ed., Marcel Dekker, New York, Vol. 2, Chap. 23.

Olson, S. L., Ferkul, P. V., and Tien, J. S., 1988, "Near-Limit Flame Spread Over a Thin Solid Fuel in Microgravity," *Twenty Second Symposium (International) on Combustion*, The Combustion Institute, Pittsburgh, PA, pp. 1213-1222.

Rogers, F. E., and Ohlemiller, T. J., 1980, "Cellulosic Insulation Material I. Overall Degradation Kinetics and Reaction Heats," *Combustion and Science Technology*, Vol. 24, pp. 129-137.

Tzeng, L. S., Atreya, A., and Wichman, I. S., 1990, "A One-Dimensional Model of Piloted Ignition," *Combustion and Flame*, Vol. 80, pp. 94-107.

Van Dyck, M., 1964, *Perturbation Methods in Fluid Mechanics*, Academic Press, New York, pp. 149-158.

Journal of Heat Transfer

Technical Notes

This section contains shorter technical papers. These shorter papers will be subjected to the same review process as that for full papers.

An Analytical Solution of a One-Dimensional Thermal Contact Conductance Problem With One Heat Flux and One Insulated Boundary Condition

Y. M. Tsai[1] **and R. A. Crane**[1]

Nomenclature

A_n = subordinate coefficient appearing in solution
a, a_1, a_2 = arbitrary constants
Bi = Biot number
B_n = subordinate coefficient appearing in solution
C_{1n} = coefficient in solution associated with first eigenvalue
C_{2n} = coefficient in solution associated with second eigenvalue
d_i = constant of parabolic function
Fo = Fourier number
h_c = thermal contact conductance
k = thermal conductivity
q = heat flux
t = time variable
T = temperature
X = function of x
x = spatial variable
α = thermal diffusivity
Γ = function of t
λ = eigenvalue
φ = temperature subfunction of time variable
ϕ = temperature subfunction of spatial variable
ψ = temperature subfunction

Subscripts/Superscripts

1, 2 = refer to region 1, 2/refer to part 1, 2 of solution of ψ_{in}

Introduction

Heat transfer across surfaces in imperfect contact occurs in many practical situations. Since the thermal contact conductance problem has appeared in the literature, substantial efforts have been made to estimate the thermal conductance across the interface. Although the progress in predicting the thermal contact conductance based on geometric, mechanical, and thermophysical properties of the contacting surfaces has given us very important insight into thermal contact conductance problems, to a large extent, thermal contact conductance still has to be estimated according to individual application experimentally [1].

Some of the techniques recently developed of estimating thermal contact conductance are based on experimental temperature data at one or several interior positions of the contacting solids and the calculation of the temperature at these locations for known contact conductance [2–5]. Consequently, an accurate and efficient method for computing temperature distributions becomes quite important. FDM and FEM are most widely used. However, for most contact conductance computation methods, only the temperatures at the contacting regions and several other positions near the interface need to be determined, so the general FDM and FEM are not particularly efficient in solving this problem.

This paper presents an analytical temperature distribution solution to the one-dimensional symmetric system with heat flux on one outside surface and insulation on the other. This analysis provides a theoretical basis for transient measurement of thermal contact conductance. While it is common practice in steady-state measurements to use a water-cooled heat sink, it is possible to limit the transient solution to time interval prior to any detectable temperature increase at the cold end. This effectively eliminates the need for water cooling and permits the use of an insulated boundary. The analytical solution to the mentioned problem obtained shows that for a symmetric system the temperature distribution solution includes two sets of distinct eigenfunctions.

Formulation of the Problem

Two contacting, one-dimensional, cylindrical blocks of the same material and dimension are considered here. The thermal properties are assumed constant. The thermal contact conductance between the two contacting surfaces (at $x = 0$) is known as h_c and assumed time independent. At the left side surface ($x = -L$) a constant heat flux is applied, and the right side surface ($x = L$) is insulated. For simplicity the initial temperature is assumed uniformly zero. The governing heat conduction problem is defined as

$$\frac{\partial^2 T_1(x,t)}{\partial x^2}=\frac{1}{\alpha}\frac{\partial T_1}{\partial t} \qquad -L\le x\le 0 \tag{1a}$$

$$\frac{\partial^2 T_2(x,t)}{\partial x^2}=\frac{1}{\alpha}\frac{\partial T_2}{\partial t} \qquad 0\le x\le L \tag{1b}$$

$$-k\frac{\partial T_1}{\partial x}=q \qquad \text{at } x=-L \tag{1c}$$

$$k\frac{\partial T_1}{\partial x}=k\frac{\partial T_2}{\partial x} \qquad \text{at } x=0 \tag{1d}$$

$$-k\frac{\partial T_1}{\partial x}=h_c(T_1-T_2) \qquad \text{at } x=0 \tag{1e}$$

$$k\frac{\partial T_2}{\partial x}=0 \qquad \text{at } x=L \tag{1f}$$

$$T_1(x,t)=T_2(x,t)=0 \qquad \text{at } t=0 \tag{1g}$$

---

[1] Mechanical Engineering Department, University of South Florida, Tampa, FL 33620.

Contributed by the Heat Transfer Division of the AMERICAN SOCIETY OF MECHANICAL ENGINEERS. Manuscript received by the Heat Transfer Divsion March 1991; revsion October 1991. Keywords: Conduction.

Solution Using Superposition Method

The assumption of solution of the problem is made as follows:

$$T_i(x,t)=\psi_i(x,t)+\phi_i(x)+\varphi_i(t) \qquad i=1,2 \tag{2}$$

Now, in terms of Eq. (2) the formulation of the problem is composed of the following three subproblems:

1 Subproblem given as

$$\frac{d^2\phi_i}{dx^2}=a_i \qquad i=1,2 \tag{3}$$

subject to similar boundary conditions as defined by (1c)–(1f).

2 Subproblem given as

$$\frac{d\varphi_i}{dt}=a_i\alpha \qquad i=1,2 \tag{4}$$

subject to the condition $\varphi_1(t)=\varphi_2(t)$.

3 Subproblem given as

$$\frac{\partial^2\psi_i}{\partial x^2}=\frac{1}{\alpha}\frac{\partial\psi_i}{\partial t} \qquad i=1,2 \tag{5}$$

subject to similar boundary conditions as in subproblem (1) except at $x=L$, where $\partial\psi_1/\partial x=0$. From subproblem (2) it is seen that $a_1=a_2=a$. With this condition, and applying boundary conditions, subproblem (1) can be solved as follows:

$$\phi_i(x)=\frac{q}{4Lk}x^2-\frac{q}{2k}x+d_i, \qquad \text{where } d_1-d_2=\frac{q}{2h_c} \tag{6}$$

d_1 and d_2 will be determined later.

Subproblem 2 can be solved by direct integration:

$$\varphi_1(t)=\varphi_2(t)=\frac{\alpha q}{2Lk}t \tag{7}$$

Since the final solution of the problem is the summation of the solutions of the three subproblems, we need not give another constant to the solution of Eq. (7). The solution of subproblem (3) is in the form [6]:

$$\psi_1(x,t)=\sum_{n=1}^{\infty}C_n(\cos\lambda_{1n}x+B_{1n}\sin\lambda_{1n}x)e^{-\alpha\lambda_{1n}^2t} \tag{8a}$$

$$\psi_2(x,t)=\sum_{n=1}^{\infty}C_n(A_{2n}\cos\lambda_{2n}x+B_{2n}\sin\lambda_{2n}x)e^{-\alpha_{2n}^2t} \tag{8b}$$

Applying Eq. (1d) and the condition obtained after differentiating both sides of Eq. (1d) with respect to t, we have

$$\lambda_{1n}=\lambda_{2n}=\lambda_n \tag{8c}$$

When the left boundary conditions are applied, we end up with the following matrix:

$$\begin{pmatrix}\sin\lambda_nL & 0 & \cos\lambda_nL\\ 0 & -\sin\lambda_nL & \cos\lambda_nL\\ -h_c & h_c & -k\lambda_n\end{pmatrix}\begin{pmatrix}1\\ A_{2n}\\ B_{2n}\end{pmatrix}=\begin{pmatrix}0\\0\\0\end{pmatrix} \tag{8d}$$

$$B_{1n}=B_{2n} \tag{8e}$$

The eigenvalue can be determined by setting the determinant of the first matrix to zero, from which we obtain two distinct sets of eigenvalues; one is

$$\sin\lambda_nL=0,\ \lambda_n=\frac{n\pi}{L},\ n=0,1,2,\ldots \tag{8f}$$

and the other is defined by

$$\lambda_n\tan\lambda_nL=\frac{2h_c}{k} \tag{8g}$$

For each of the two sets of eigenvalues, there is one corresponding set of coefficients A_{2n} and B_{2n}, and the corresponding A_{2n} and B_{2n} can be found from (8d). For λ_n defined by $\lambda_n\tan\lambda_nL=2h_c/k$, we have

$$A_{2n}=-1, \qquad B_{2n}=B_{1n}=-\tan\lambda_nL \tag{8h}$$

$$\psi_{1n}^1=C_{1n}(\cos\lambda_nx-\tan\lambda_nL\sin\lambda_nx)e^{-\alpha\lambda_n^2t}$$

$$\psi_{2n}^1=C_{1n}(-\cos\lambda_nx-\tan\lambda_nL\sin\lambda_nx)e^{-\alpha\lambda_n^2t}$$

For $\lambda_n=n\pi/L$, $n=0,1,2,\ldots$

$$A_{2n}=1, \qquad B_{2n}=B_{1n}=0 \tag{8i}$$

$$\psi_{1n}^2=\psi_{2n}^2=C_{2n}\cos\frac{n\pi}{L}xe^{-\alpha(\frac{n\pi}{L})^2t}$$

The Determination of the Coefficients C_{1n} and C_{2n}

The problem has been solved except for the coefficients C_{1n} and C_{2n}, and they can be obtained through the initial condition. Since C_{2n} depends on d_1 and d_2, we can arbitrarily set d_1 and d_2 to any value as long as they satisfy the condition $d_1-d_2=q/2h_c$. For simplicity, here we choose $d_1=0$, $d_2=-q/2h_c$. Since $T_1(x,0)=T_2(x,0)=0$,

$$\sum_{n=1}^{\infty}C_{1n}(\cos\lambda_nx-\tan\lambda_nL\sin\lambda_nx)+\sum_{n=0}^{\infty}C_{2n}\cos\frac{n\pi}{L}x=-\frac{q}{4Lk}x^2+\frac{q}{2k}x \qquad \text{for } -L\le x\le 0 \tag{9a}$$

$$\sum_{n=1}^{\infty}C_{1n}(-\cos\lambda_nx-\tan\lambda_nL\sin\lambda_nx)+\sum_{n=0}^{\infty}C_{2n}\cos\frac{n\pi}{L}x=-\frac{q}{4Lk}x^2+\frac{q}{2k}x+\frac{q}{2h_c} \qquad \text{for } 0\le x\le L \tag{9b}$$

The eigenfunctions ψ^1 and ψ^2 that are both defined by Eq. (5) satisfy the following orthogonality relation (where $t=0$):

$$\int_{x=-L}^{0}\psi_{1n}\psi_{1m}dx+\int_0^L\psi_{2n}\psi_{2m}dx=\begin{cases}0 & \lambda_m\neq\lambda_n\\ \int_{-L}^{0}(\psi_{1n})^2dx+\int_0^L(\psi_{2n})^2dx & \lambda_m=\lambda_n\end{cases} \tag{9c}$$

Multiplying both sides of Eq. (9a) by $\psi_{1n}(x,0)$, Eq. (9b) by $\psi_{2n}(x,0)$ and summing up the resulting expression, the coefficients C_{1n} and C_{2n} can then be determined as follows:

$$C_{1n}=\frac{1}{\Delta_{1n}}\left[\int_{-L}^{0}\left(-\frac{q}{4Lk}x^2+\frac{q}{2k}x\right)(\cos\lambda_nx-\tan\lambda_nL\sin\lambda_nx)dx+\int_0^L\left(-\frac{q}{4Lk}x^2+\frac{q}{2k}x+\frac{q}{2h_c}\right)(-\cos\lambda_nx-\tan\lambda_nL\sin\lambda_nx)dx\right] \tag{9d}$$

$$\Delta_{1n}=\int_{-L}^{0}(\cos\lambda_nx-\tan\lambda_nL\sin\lambda_nx)^2dx+\int_0^L(-\cos\lambda_nx-\tan\lambda_nL\sin\lambda_nx)^2dx \tag{9e}$$

and

$$C_{20}=\frac{1}{2L}\left[\int_{-L}^{0}\left(-\frac{q}{4Lk}x^2+\frac{q}{2k}x\right)dx+\int_0^L\left(-\frac{q}{4Lk}x^2+\frac{q}{2k}x+\frac{q}{2h_c}\right)dx\right] \tag{9f}$$

$$C_{2n}=\frac{1}{\Delta_{2n}}\left[\int_{-L}^{0}\left(-\frac{q}{4Lk}x^2+\frac{q}{2k}x\right)\cos\frac{n\pi}{L}xdx\right.$$
$$\left.+\int_{0}^{L}\left(-\frac{q}{4Lk}x^2+\frac{q}{2k}x+\frac{q}{2h_c}\right)\cos\frac{n\pi}{L}xdx\right] \qquad (9g)$$

where

$$\Delta_{2n}=\int_{-L}^{L}\cos^2\frac{n\pi}{L}xdx \qquad (9h)$$

It is found that

$$C_{1n}=\frac{-q\cos\lambda_nL}{Lk\lambda_n^2+2h_c\cos^2\lambda_nL} \qquad (9i)$$

$$C_{20}=-\frac{qL}{12k}+\frac{q}{4h_c}, \qquad C_{2n}=-(-1)^n\frac{qL}{kn^2\pi^2} \qquad (9j)$$

Now the formal solution of this problem is complete, and with some trigonometric simplification it can be written as

$$T_1(x,\ t)=\sum_{n-1}^{\infty}C_{1n}\frac{\cos\lambda_n(L+x)e^{-\alpha\lambda_n^2t}}{\cos\lambda_nL}$$
$$+\sum_{n=1}^{\infty}C_{2n}\cos\frac{n\pi}{L}xe^{-\alpha(\frac{n\pi}{L})^2t}$$
$$+\frac{q}{h_c}\left[\frac{F_oB_i}{2}+B_i\left(\frac{x^2}{4L^2}-\frac{x}{2L}-\frac{1}{12}\right)+\frac{1}{4}\right] \quad -L\le x\le 0 \qquad (10a)$$

$$T_2(x,\ t)=\sum_{n=1}^{\infty}-C_{1n}\frac{\cos\lambda_n(L-x)e^{-\alpha\lambda_n^2t}}{\cos\lambda_nL}$$
$$+\sum_{n=1}^{\infty}C_{2n}\cos\frac{n\pi}{L}xe^{-\alpha(\frac{n\pi}{L})^2t}$$
$$+\frac{q}{h_c}\left[\frac{F_oB_i}{2}+B_i\left(\frac{x^2}{4L^2}-\frac{x}{2L}-\frac{1}{12}\right)-\frac{1}{4}\right] \quad 0\le x\le L \qquad (10b)$$

where λ_n is determined by

$$\lambda_nL\tan\lambda_nL=2B_i \qquad (10c)$$

and C_{1n} and C_{2n} are defined by Eqs. (9*i*) and (9*j*), respectively.

Sample of Test Cases

To show the results given by Eqs. (10*a*) and (10*b*), we give in Fig. 1 the temperature increases at $x = -0.01$ m and $x = 0.01$ m for different contact conductance values for the case of two contacting aluminum blocks; the thickness of each block is 0.025 m, and the heat flux equals 23.54 kW/m^2.

Conclusion

It is interesting that the temperature distribution solutions for the two regions, given by Eqs. (10*a*) and (10*b*), both involve the solution corresponding to the perfect contact situation, that is, when h_c goes to identify. It is easy to see that when $h_c\to\infty$, the temperature distributions for both regions are reduced to

$$T_1=T_2=\sum_{n=1}^{\infty}C_{2n}\cos\frac{n\pi}{L}xe^{-\alpha(\frac{n\pi}{L})^2t}$$
$$+\frac{\alpha q}{2Lk}t+\frac{q}{4Lk}x^2-\frac{q}{2K}x-\frac{qL}{12k}$$

which is exactly the solution to the corresponding continuous conduction problem.

The method to solve the temperature distribution in regions of either side of the contacting interface presented here is quite straightforward. It is found that the involvement of two distinct sets of eigenfunctions arises only in some special cases including the important one considered in this paper.

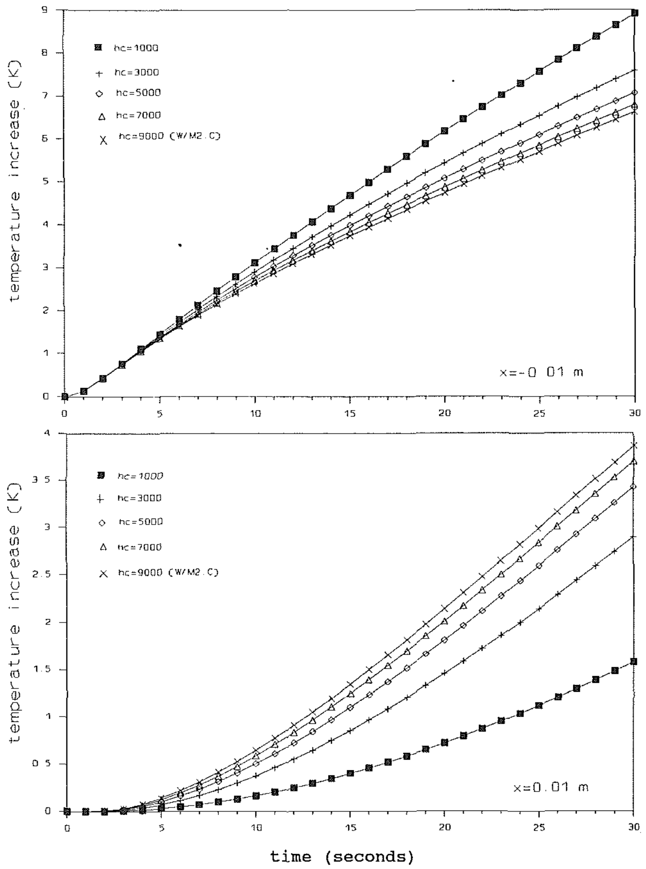

Fig. 1 Temperature increases (K) at $x = -0.01$ m and $x = 0.01$ m for different contact conductance

References

1 Fletcher, L. S., "Recent Developments in Contact Conductance Heat Transfer," ASME JOURNAL OF HEAT TRANSFER, Vol. 110, 1988, pp. 1059-1070.

2 Beck, J. V., "Transient Sensitivity Coefficients for the Thermal Contact Conductance," *Int. J. Heat Mass Transfer*, Vol. 10, 1967, pp. 1615-1617.

3 Beck, J. V., "Combined Parameter and Function Estimation in Heat Transfer With Application to Contact Conductance," ASME JOURNAL OF HEAT TRANSFER, Vol. 110, 1988, pp. 1046-1058.

4 Flach, G. P., and Özişik, M. N., "Inverse Heat Conduction Problem of Periodically Contacting Surfaces," ASME JOURNAL OF HEAT TRANSFER, Vol. 110, 1988, pp. 821-829.

5 Moore, C. J., Jr., "Heat Transfer Across Surfaces in Contact," Ph.D. Dissertation, Southern Methodist University, Dallas, TX, 1967.

6 Özişik, M. N., *Heat Conduction*, Wiley, New York.

A Model for Thermal Conductivity of Granular Porous Media

F. B. Nimick[1] **and J. R. Leith**[2]

Introduction

This note describes an improved model for estimating thermal conductivity of granular porous media, in which radiation and convection heat transfer effects can be considered negligible. Because the model proposed is semi-empirical in nature, only the thermal conductivities of solid and fluid phases and the

---

[1] Sandia National Laboratories, Albuquerque, NM 87185.

[2] Department of Mechanical Engineering, University of New Mexico, Albuquerque, NM 87131; Mem. ASME.

Contributed by the Heat Transfer Division of the AMERICAN SOCIETY OF MECHANICAL ENGINEERS. Manuscript received by the Heat Transfer Division October 5, 1990; revision received August 20, 1991. Keywords: Geophysical Heat Transfer, Porous Media, Thermophysical Properties.

$$C_{2n}=\frac{1}{\Delta_{2n}}\left[\int_{-L}^{0}\left(-\frac{q}{4Lk}x^2+\frac{q}{2k}x\right)\cos\frac{n\pi}{L}xdx\right.$$
$$\left.+\int_{0}^{L}\left(-\frac{q}{4Lk}x^2+\frac{q}{2k}x+\frac{q}{2h_c}\right)\cos\frac{n\pi}{L}xdx\right] \quad (9g)$$

where

$$\Delta_{2n}=\int_{-L}^{L}\cos^2\frac{n\pi}{L}xdx \quad (9h)$$

It is found that

$$C_{1n}=\frac{-q\cos\lambda_nL}{Lk\lambda_n^2+2h_c\cos^2\lambda_nL} \quad (9i)$$

$$C_{20}=-\frac{qL}{12k}+\frac{q}{4h_c}, \qquad C_{2n}=-(-1)^n\frac{qL}{kn^2\pi^2} \quad (9j)$$

Now the formal solution of this problem is complete, and with some trigonometric simplification it can be written as

$$T_1(x,t)=\sum_{n-1}^{\infty}C_{1n}\frac{\cos\lambda_n(L+x)e^{-\alpha\lambda_n^2t}}{\cos\lambda_nL}$$
$$+\sum_{n=1}^{\infty}C_{2n}\cos\frac{n\pi}{L}xe^{-\alpha(\frac{n\pi}{L})^2t}$$
$$+\frac{q}{h_c}\left[\frac{F_oB_i}{2}+B_i\left(\frac{x^2}{4L^2}-\frac{x}{2L}-\frac{1}{12}\right)+\frac{1}{4}\right] \quad -L\le x\le 0 \quad (10a)$$

$$T_2(x,t)=\sum_{n=1}^{\infty}-C_{1n}\frac{\cos\lambda_n(L-x)e^{-\alpha\lambda_n^2t}}{\cos\lambda_nL}$$
$$+\sum_{n=1}^{\infty}C_{2n}\cos\frac{n\pi}{L}xe^{-\alpha(\frac{n\pi}{L})^2t}$$
$$+\frac{q}{h_c}\left[\frac{F_oB_i}{2}+B_i\left(\frac{x^2}{4L^2}-\frac{x}{2L}-\frac{1}{12}\right)-\frac{1}{4}\right] \quad 0\le x\le L \quad (10b)$$

where λ_n is determined by

$$\lambda_nL\tan\lambda_nL=2B_i \quad (10c)$$

and C_{1n} and C_{2n} are defined by Eqs. (9*i*) and (9*j*), respectively.

Sample of Test Cases

To show the results given by Eqs. (10*a*) and (10*b*), we give in Fig. 1 the temperature increases at $x = -0.01$ m and $x = 0.01$ m for different contact conductance values for the case of two contacting aluminum blocks; the thickness of each block is 0.025 m, and the heat flux equals 23.54 kW/m^2.

Conclusion

It is interesting that the temperature distribution solutions for the two regions, given by Eqs. (10*a*) and (10*b*), both involve the solution corresponding to the perfect contact situation, that is, when h_c goes to identify. It is easy to see that when $h_c\rightarrow\infty$, the temperature distributions for both regions are reduced to

$$T_1=T_2=\sum_{n=1}^{\infty}C_{2n}\cos\frac{n\pi}{L}xe^{-\alpha(\frac{n\pi}{L})^2t}$$
$$+\frac{\alpha q}{2Lk}t+\frac{q}{4Lk}x^2-\frac{q}{2K}x-\frac{qL}{12k}$$

which is exactly the solution to the corresponding continuous conduction problem.

The method to solve the temperature distribution in regions of either side of the contacting interface presented here is quite straightforward. It is found that the involvement of two distinct sets of eigenfunctions arises only in some special cases including the important one considered in this paper.

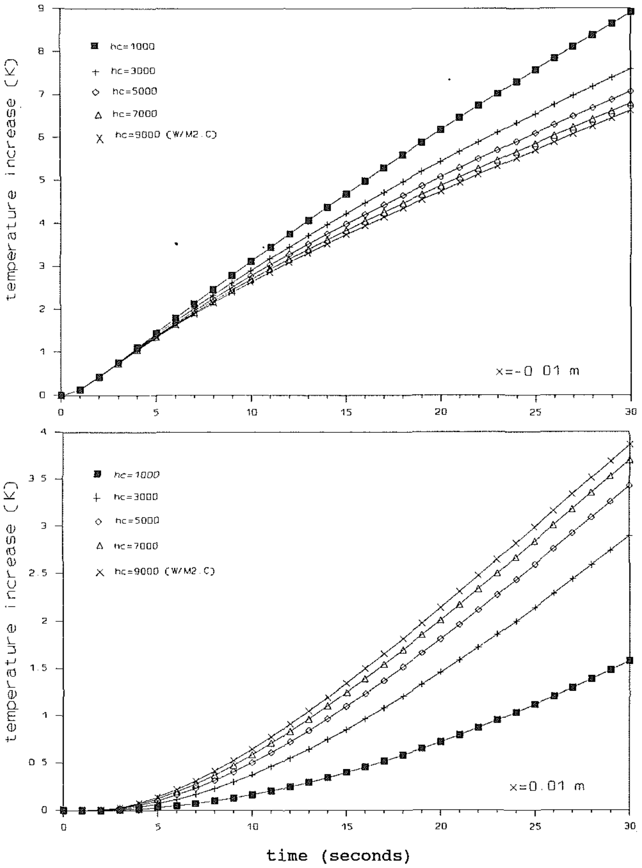

Fig. 1 Temperature increases (K) at $x = -0.01$ m and $x = 0.01$ m for different contact conductance

References

1 Fletcher, L. S., "Recent Developments in Contact Conductance Heat Transfer," ASME JOURNAL OF HEAT TRANSFER, Vol. 110, 1988, pp. 1059-1070.

2 Beck, J. V., "Transient Sensitivity Coefficients for the Thermal Contact Conductance," *Int. J. Heat Mass Transfer*, Vol. 10, 1967, pp. 1615-1617.

3 Beck, J. V., "Combined Parameter and Function Estimation in Heat Transfer With Application to Contact Conductance," ASME JOURNAL OF HEAT TRANSFER, Vol. 110, 1988, pp. 1046-1058.

4 Flach, G. P., and Özişik, M. N., "Inverse Heat Conduction Problem of Periodically Contacting Surfaces," ASME JOURNAL OF HEAT TRANSFER, Vol. 110, 1988, pp. 821-829.

5 Moore, C. J., Jr., "Heat Transfer Across Surfaces in Contact," Ph.D. Dissertation, Southern Methodist University, Dallas, TX, 1967.

6 Özişik, M. N., *Heat Conduction*, Wiley, New York.

A Model for Thermal Conductivity of Granular Porous Media

F. B. Nimick[1] and J. R. Leith[2]

Introduction

This note describes an improved model for estimating thermal conductivity of granular porous media, in which radiation and convection heat transfer effects can be considered negligible. Because the model proposed is semi-empirical in nature, only the thermal conductivities of solid and fluid phases and the

---

[1] Sandia National Laboratories, Albuquerque, NM 87185.

[2] Department of Mechanical Engineering, University of New Mexico, Albuquerque, NM 87131; Mem. ASME.

Contributed by the Heat Transfer Division of the AMERICAN SOCIETY OF MECHANICAL ENGINEERS. Manuscript received by the Heat Transfer Division October 5, 1990; revision received August 20, 1991. Keywords: Geophysical Heat Transfer, Porous Media, Thermophysical Properties.

porosity are required for estimation purposes. With the minimal property data required, inherent assumptions are that both fluid and solid phases are homogeneous and contact conductance is not a parameter. Use of the model gives thermal conductivity estimates that are between the bounding estimates discussed by Maxwell (1873) and Hashin and Shtrikman (1962). We illustrate here the utility of the model by comparing predictions with experimental data for a porous medium composed of fused silica powder and air.

Estimation of the thermal conductivities of granular mixtures has been studied extensively; the resulting publications are too numerous to summarize here. Several good reviews of the relevant literature have been made, including Woodside and Messmer (1961), Nozad et al. (1985), and Hadley (1986). The model presented here has been developed because none of the published models were found to be suitable for application to our experimental data. Most of the models predicted thermal conductivities higher than our measured data; the equation making the closest prediction (Eq. (10) below) underestimated the experimental values, as shown later.

The two equations originally derived by Maxwell (1873) were shown by Hashin and Shtrikman (1962) to be the most rigorous bounds for estimating the thermal conductivity of a mixture in the absence of geometric information. Both equations represent the physical model of noninteracting spheres of one material suspended in a matrix of a second material. The upper-bound equation represents low-conductivity (fluid) spheres in a high-conductivity (solid) matrix, and is expressed as follows:

$$k_m = k_s + \frac{\phi}{\dfrac{1}{k_f - k_s} + \dfrac{1-\phi}{3k_s}}, \tag{1}$$

where k_m is the thermal conductivity of mixture, k_s is the thermal conductivity of solid, k_f is the thermal conductivity of fluid, and ϕ is the porosity of the mixture, expressed as a volume fraction. The lower-bound equation, representing solid spheres suspended in a fluid matrix, is given by:

$$k_m = k_f + \frac{1-\phi}{\dfrac{1}{k_s - k_f} + \dfrac{\phi}{3k_f}}. \tag{2}$$

Although Eqs. (1) and (2) were derived rigorously by Hashin and Shtrikman (1962), the governing assumption that the spheres be noninteracting limits the applicability to values of ϕ close to either zero or one. Relatively few materials have porosities near these extreme values. Granular porous media, in particular, usually have porosities of 0.3 to 0.5, so that the two equations are not directly applicable for thermal-conductivity estimation for such materials.

Analysis

The deterministic model presented in this note is based on the assumption that any granular porous medium comprises regions of solid-continuous material and regions of fluid-continuous material. The proportions of the two types of regions vary depending on ϕ. Furthermore, the porosities are different in the two types of regions, with the porosity of the solid-continuous regions (ϕ_{sc}) less than ϕ and the porosity of the fluid-continuous regions (ϕ_{fc}) greater than ϕ. The functions selected to represent the two porosities are

$$\phi_{sc} = \phi - \phi^m \quad (m > 1) \tag{3}$$

and

$$\phi_{fc} = \phi^n \quad (0 < n < 1). \tag{4}$$

Let x_{fc} be the volume fraction of the fluid-continuous regions, where $x_{fc} + x_{sc} = 1$, so that

$$\phi = \phi_{sc}(1 - x_{fc}) + \phi_{fc}x_{fc}. \tag{5}$$

The thermal conductivities of the solid-continuous and fluid-continuous regions can be represented using Eqs. (1) and (2), respectively, with the appropriate choice of porosity. At very low values of ϕ, Eq. (1) should give an estimate for the thermal conductivity of the material. At large values of ϕ, Eq. (2) should give an estimate for the thermal conductivity.

To obtain the new deterministic equation, Eq. (1) is used, with the following substitutions: $\phi = x_{fc}$, $k_s = k_{sc}$, and $k_f = k_{fc}$. After rearrangement, the following equation is obtained:

$$k_m = k_{sc}\left[1 - \frac{3x_{fc}(1-A)}{2 + A + x_{fc}(1-A)}\right], \tag{6}$$

where

$$k_{sc} = k_s + \frac{\phi_{sc}}{\dfrac{1}{k_f - k_s} + \dfrac{1-\phi_{sc}}{3k_s}},$$

$$k_{fc} = k_f + \frac{1-\phi_{fc}}{\dfrac{1}{k_s - k_f} + \dfrac{\phi_{fc}}{3k_f}},$$

and

$$A = \frac{k_{fc}}{k_{sc}}.$$

The greatest potential drawback to the use of Eq. (6) is the presence of the two empirical constants m and n. To be of general use, the equation must not only provide a good fit to experimental results on one material, but also must then be directly applicable to other materials without derivation of new values for m and n.

Experiments

Thermal-conductivity measurements were obtained for mixtures of powdered solid with air using an adaptation of the needle-probe technique described by von Herzen and Maxwell (1959). The technique uses a thin heater with a relatively large length-to-diameter ratio to introduce a radial heat pulse into the powder. The temperature at the boundary between the heater and the powder is measured as a function of time, and, for values of $r^2/4\alpha t \ll 1$, is given approximately by

$$T - T_o = \frac{Q}{4\pi k}\left[-G + \ln t + \ln\left(\frac{4\alpha}{r^2}\right)\right], \tag{7}$$

where r is the radial distance from the center of the probe, α is the thermal diffusivity of the medium, T_o is the initial temperature of the medium, Q is the heat input per unit length of heater per unit time, and G is Euler's constant.

Thermal conductivity was measured by applying constant power to the thermal probe for approximately 90 seconds, recording the temperature change at the external surface of the heater as a function of time (t), then implementing a linear least-squares fit to the temperature data as a function of ln(t). The slope of the line thus obtained is used to calculate the thermal conductivity using the following equation:

$$k = \frac{E^2 \ln(t_2/t_1)}{4\pi RL(T_2 - T_1)}, \tag{8}$$

where E is the applied voltage, R is the resistance of the probe, L is the heated length of the probe, and $(T_2 - T_1)/\ln(t_2/t_1)$ is the slope obtained from the least-squares fit. Additional description of the technique is provided by Nimick (1990).

The container used to hold the powder is a graduated glass beaker, so that the volume (V) of material is known for each experiment. By determining the mass (M) of material as well, the dry bulk density (ρ_{db}) was calculated as $\rho_{db} = M/V$. This value then was combined with the known grain density (ρ_g) of the material to obtain the value of ϕ corresponding to each thermal-conductivity measurement:

$$\phi = 1 - \frac{\rho_{db}}{\rho_g}. \qquad (9)$$

Different values of ρ_{db}, and thus of ϕ, were obtained by variations in the amount of tapping and shaking to which the beaker was subjected after pouring in the granular material.

Fused silica was used as a thermal-conductivity standard for the primary set of measurements to derive values of m and n. Equation (6), with these empirical values, then was used to extrapolate thermal conductivities measured for plagioclase-feldspar powders to obtain zero-porosity thermal conductivities (k_s in Eqs. (7) and (8)) for the feldspars.

Results and Discussion

Figure 1 shows the fused-silica data together with Eqs. (1) and (2) and the version of Eq. (6) derived by a least-squares fit to the data. The fit produced values of $m = 2.127$ and $n = 0.929$, with a correlation coefficient of 0.9990. As illustrated in Fig. 1, the semi-empirical model defined by Eqs. (3)-(6)

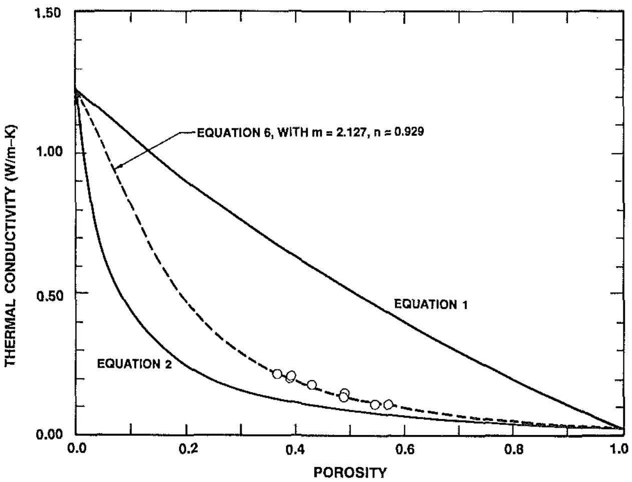

Fig. 1 Comparison of Eq. (6) with bounding estimates and experimental data for fused silica powder (Nimick, 1990). Each data point shown is taken as the average from three experiments at fixed probe position.

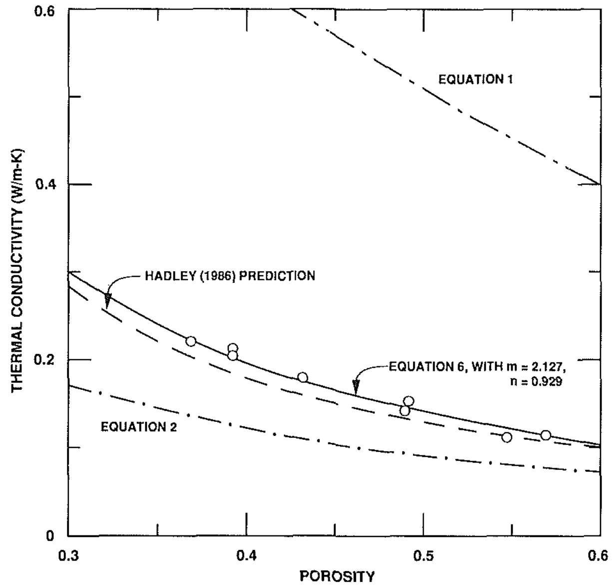

Fig. 2 Comparison of prediction of Hadley (1986) with experimental data, bounding estimates, and Eq. (6)

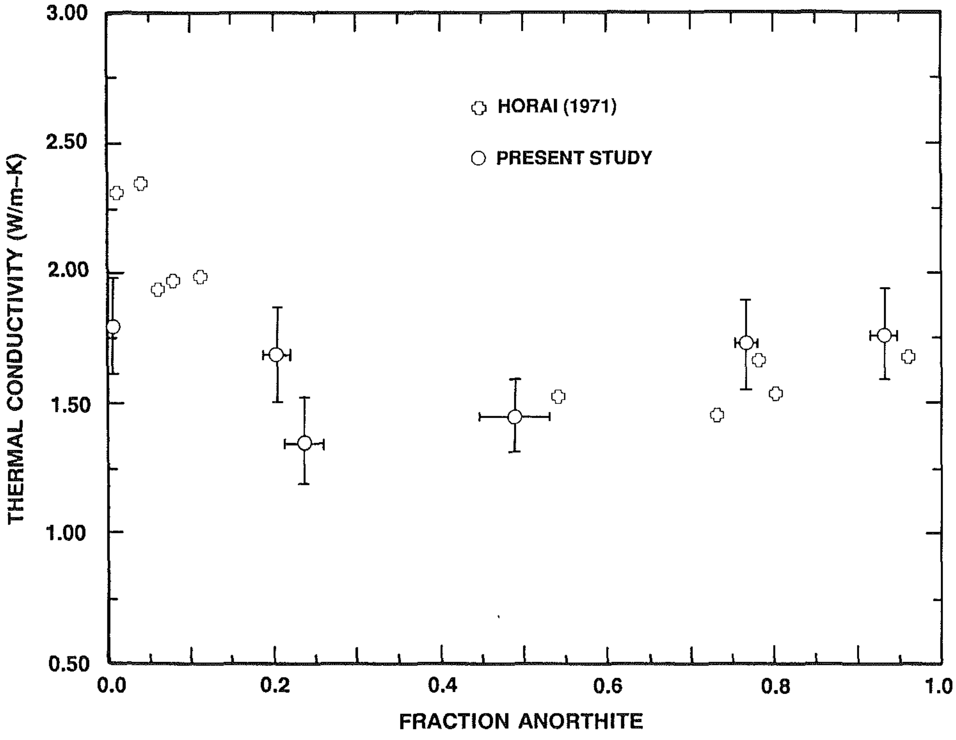

Fig. 3 Comparison of zero porosity thermal conductivity estimates with data from Horai (1971) for plagioclase feldspars. Error bars represent ±1 standard deviation in mean composition (based upon 350 experiments) and ± 10 percent estimated uncertainty in thermal conductivity. The zero porosity estimates are obtained by use of Eq. (6), with $m = 2.127$ and $n = 0.929$.

gives an excellent representation for the fused silica-air medium.

A comparison of the results in Fig. 1 with the model equation developed by Hadley (1986) is illustrated in Fig. 2. Hadley's model utilizes the Maxwell upper bound expression (Eq. (1)) as the mixture contribution and the results of a volume-averaging theory as a contact contribution, so that the thermal conductivity is expressed as

$$k=(1-a)\,\frac{\phi f_o k_f+(1-\phi f_o)k_s}{1-\phi(1-f_o)+\phi(1-f_o)k_s/k_f}+a\,\frac{2(1-\phi)k_s^2/k_f+(1+2\phi)k_s}{(2+\phi)k_s/k_f+1-\phi} \qquad (10)$$

in which a is a "consolidation parameter" and f_o is a weak function of the matrix porosity. The curve in Fig. 2 labeled as Hadley's prediction is based upon Eq. (10), with $f_o=0.8$ and $a=a(\phi)$ assumed from Fig. 6 in Hadley (1986). As noted in Fig. 2, Eq. (10) underpredicts our least-squares-based fit of fused silica-air measurements by 3-8 percent. An alternate interpretation is that the model we have proposed here yields comparable results to the mixture theory developed by Hadley (1986), and yet the present model does not require a judgment as to the relative influence of mixture conductivity and contact contribution.

Using the values of m and n noted above with Eq. (6) and calculating k_s from measured thermal conductivities for six different plagioclase-feldspar powders yields the data shown in Fig. 3. Previously published data for plagioclase-feldspar (Horai, 1971) are shown for comparison. After allowing for the ±15 percent uncertainty in the earlier data from Horai (1971), the agreement between the two data sets is quite good. This result supports the conclusion that Eq. (6) is of more general applicability than many empirical equations for estimation of thermal conductivity for granular porous media.

As pointed out earlier, empirical equations suffer from the inability to extrapolate constants to other materials. However, the new model equation has an advantage in this respect. Because no assumptions have been made about geometric characteristics (e.g., grain size and shape), the values of m and n should be applicable for any powder that is approximately similar to the fused silica powder. Figure 3 demonstrates that Eq. (6), with the values of m and n derived for fused silica, can be applied successfully to data for feldspar powders. Other materials for which successful application might be expected are powders of other silica-rich glasses as well as many anhydrous silicate minerals. In addition, different values of m and n could be derived for a powder from some different class of material (e.g., refractories), then applied to the other materials in that class. In view of the close proximity of our least-squares-based correlation to the Hadley model results (Fig. 2), however, we would expect accurate correlation of experimental results for granular media with large k_f/k_s for m and n in the range $1.9<m<2.3$ and $0.88<n<0.98$.

Acknowledgments

This work was supported by Sandia National Laboratories (under Contract #DE-AC04-76DP00789 with the U.S. Department of Energy).

References

Hadley, G. R., 1986, "Thermal Conductivity of Packed Metal Powders," *International Journal of Heat and Mass Transfer*, Vol. 29, pp. 909-920.

Hashin, Z., and Shtrikman, S., 1962, "A Variational Approach to the Theory of the Effective Magnetic Permeability of Multiphase Materials," *Journal of Applied Physics*, Vol. 33, No. 10, pp. 3125-3131.

Horai, K., 1971, "Thermal Conductivity of Rock-Forming Minerals," *Journal of Geophysical Research*, Vol. 76, No. 5, pp. 1278-1308.

Maxwell, J. C., 1873, *Electricity and Magnetism*, Clarendon Press, London, United Kingdom.

Nimick, F. B., 1990, "The Thermal Conductivity of Solid-Solution Minerals: Plagioclase Feldspars," M. S. Thesis, The University of New Mexico.

Nozad, I., Carbonell, R. G., and Whitaker, S., 1985, "Heat Conduction in Multiphase Systems. I. Theory and Experiment for Two-Phase Systems," *Chemical Engineering Science*, Vol. 40, pp. 843-856.

von Herzen, R., and Maxwell, A. E., 1959, "The Measurement of Thermal Conductivity of Deep-Sea Sediments by a Needle-Probe Method," *Journal of Geophysical Research*, Vol. 64, No. 10, pp. 1557-1563.

Woodside, W., and Messmer, J. H., 1961, "Thermal Conductivity of Porous Media. I. Unconsolidated Sands," *Journal of Applied Physics*, Vol. 32, pp. 1688-1699.

Optimum Placement of Heat Sources in Forced Convection

C. Y. Wang[1]

Introduction

In many practical instances of heat transfer, such as furnaces, a certain minimum temperature must be attained on a given region. Usually the region is heated by forced convection with isolated heat sources upstream. The present note studies the placement of these heat sources such that the minimum temperature requirement is satisfied with the least amount of total thermal energy input.

Figure 1(*a*) shows the situation considered. A circular region of radius R' is to be heated to at least temperature T_0. There are N discrete heat sources forced by a uniform flow of velocity U. The question is, how can we place these sources such that the least amount of energy is required? Since the thermal wake of a source is nonuniform, the answer is not obvious.

The Single Source

The governing equation for forced convection is

$$UT'_{z'}=a(T'_{x'x'}+T'_{y'y'}+T'_{z'z'}) \qquad (1)$$

where T' is the temperature and a is the thermal diffusivity. We normalize all lengths by $2a/U$, and the temperature by T_0, and drop primes. Equation (1) becomes

$$T_z=\frac{1}{2}\,(T_{xx}+T_{yy}+T_{zz}) \qquad (2)$$

Rosenthal (1946) originally solved Eq. (2) for a moving heat source on the surface of a conducting material. His solution can also be used in the forced convection of a fixed point source at the origin, viz.,

$$T=\left(\frac{qU}{8\pi akT_0}\right)(x^2+y^2+z^2)^{-1/2}\exp\left[z-\sqrt{x^2+y^2+z^2}\right] \qquad (3)$$

where q is the heat input and k is the thermal conductivity. It is evident the minimum temperature occurs on the boundary of the region, $z = H$, $r = R$ where we set $T = 1$. Thus

$$1=C(R^2+H^2)^{-1/2}\exp\left[H-\sqrt{R^2+H^2}\right] \qquad (4)$$

Here C is the normalized thermal energy $qU/8\pi akT_0$. In order to minimize C for fixed R, we set the derivative $C(H)$ to zero. The result is the algebraic relation

$$H\sqrt{H^2+R^2}+H-H^2-R^2=0 \qquad (5)$$

---

[1] Michigan State University, East Lansing, MI 48824; Mem. ASME.

Contributed by the Heat Transfer Division of the AMERICAN SOCIETY OF MECHANICAL ENGINEERS. Manuscript received by the Heat Transfer Division December 1990; revision received July 31, 1991. Keywords: Forced Convection, Wakes.

gives an excellent representation for the fused silica-air medium.

A comparison of the results in Fig. 1 with the model equation developed by Hadley (1986) is illustrated in Fig. 2. Hadley's model utilizes the Maxwell upper bound expression (Eq. (1)) as the mixture contribution and the results of a volume-averaging theory as a contact contribution, so that the thermal conductivity is expressed as

$$k=(1-a)\,\frac{\phi f_o k_f+(1-\phi f_o)k_s}{1-\phi(1-f_o)+\phi(1-f_o)k_s/k_f}+a\,\frac{2(1-\phi)k_s^2/k_f+(1+2\phi)k_s}{(2+\phi)k_s/k_f+1-\phi} \qquad (10)$$

in which a is a "consolidation parameter" and f_o is a weak function of the matrix porosity. The curve in Fig. 2 labeled as Hadley's prediction is based upon Eq. (10), with $f_o=0.8$ and $a=a(\phi)$ assumed from Fig. 6 in Hadley (1986). As noted in Fig. 2, Eq. (10) underpredicts our least-squares-based fit of fused silica-air measurements by 3-8 percent. An alternate interpretation is that the model we have proposed here yields comparable results to the mixture theory developed by Hadley (1986), and yet the present model does not require a judgment as to the relative influence of mixture conductivity and contact contribution.

Using the values of m and n noted above with Eq. (6) and calculating k_s from measured thermal conductivities for six different plagioclase-feldspar powders yields the data shown in Fig. 3. Previously published data for plagioclase-feldspar (Horai, 1971) are shown for comparison. After allowing for the ±15 percent uncertainty in the earlier data from Horai (1971), the agreement between the two data sets is quite good. This result supports the conclusion that Eq. (6) is of more general applicability than many empirical equations for estimation of thermal conductivity for granular porous media.

As pointed out earlier, empirical equations suffer from the inability to extrapolate constants to other materials. However, the new model equation has an advantage in this respect. Because no assumptions have been made about geometric characteristics (e.g., grain size and shape), the values of m and n should be applicable for any powder that is approximately similar to the fused silica powder. Figure 3 demonstrates that Eq. (6), with the values of m and n derived for fused silica, can be applied successfully to data for feldspar powders. Other materials for which successful application might be expected are powders of other silica-rich glasses as well as many anhydrous silicate minerals. In addition, different values of m and n could be derived for a powder from some different class of material (e.g., refractories), then applied to the other materials in that class. In view of the close proximity of our least-squares-based correlation to the Hadley model results (Fig. 2), however, we would expect accurate correlation of experimental results for granular media with large k_f/k_s for m and n in the range $1.9<m<2.3$ and $0.88<n<0.98$.

Acknowledgments

This work was supported by Sandia National Laboratories (under Contract #DE-AC04-76DP00789 with the U.S. Department of Energy).

References

Hadley, G. R., 1986, "Thermal Conductivity of Packed Metal Powders," *International Journal of Heat and Mass Transfer*, Vol. 29, pp. 909-920.

Hashin, Z., and Shtrikman, S., 1962, "A Variational Approach to the Theory of the Effective Magnetic Permeability of Multiphase Materials," *Journal of Applied Physics*, Vol. 33, No. 10, pp. 3125-3131.

Horai, K., 1971, "Thermal Conductivity of Rock-Forming Minerals," *Journal of Geophysical Research*, Vol. 76, No. 5, pp. 1278-1308.

Maxwell, J. C., 1873, *Electricity and Magnetism*, Clarendon Press, London, United Kingdom.

Nimick, F. B., 1990, "The Thermal Conductivity of Solid-Solution Minerals: Plagioclase Feldspars," M. S. Thesis, The University of New Mexico.

Nozad, I., Carbonell, R. G., and Whitaker, S., 1985, "Heat Conduction in Multiphase Systems. I. Theory and Experiment for Two-Phase Systems," *Chemical Engineering Science*, Vol. 40, pp. 843-856.

von Herzen, R., and Maxwell, A. E., 1959, "The Measurement of Thermal Conductivity of Deep-Sea Sediments by a Needle-Probe Method," *Journal of Geophysical Research*, Vol. 64, No. 10, pp. 1557-1563.

Woodside, W., and Messmer, J. H., 1961, "Thermal Conductivity of Porous Media. I. Unconsolidated Sands," *Journal of Applied Physics*, Vol. 32, pp. 1688-1699.

Optimum Placement of Heat Sources in Forced Convection

C. Y. Wang[1]

Introduction

In many practical instances of heat transfer, such as furnaces, a certain minimum temperature must be attained on a given region. Usually the region is heated by forced convection with isolated heat sources upstream. The present note studies the placement of these heat sources such that the minimum temperature requirement is satisfied with the least amount of total thermal energy input.

Figure 1(*a*) shows the situation considered. A circular region of radius R' is to be heated to at least temperature T_0. There are N discrete heat sources forced by a uniform flow of velocity U. The question is, how can we place these sources such that the least amount of energy is required? Since the thermal wake of a source is nonuniform, the answer is not obvious.

The Single Source

The governing equation for forced convection is

$$UT'_{z'}=a(T'_{x'x'}+T'_{y'y'}+T'_{z'z'}) \qquad (1)$$

where T' is the temperature and a is the thermal diffusivity. We normalize all lengths by $2a/U$, and the temperature by T_0, and drop primes. Equation (1) becomes

$$T_z=\frac{1}{2}\,(T_{xx}+T_{yy}+T_{zz}) \qquad (2)$$

Rosenthal (1946) originally solved Eq. (2) for a moving heat source on the surface of a conducting material. His solution can also be used in the forced convection of a fixed point source at the origin, viz.,

$$T=\left(\frac{qU}{8\pi akT_0}\right)(x^2+y^2+z^2)^{-1/2}\exp\left[z-\sqrt{x^2+y^2+z^2}\right] \qquad (3)$$

where q is the heat input and k is the thermal conductivity. It is evident the minimum temperature occurs on the boundary of the region, $z = H$, $r = R$ where we set $T = 1$. Thus

$$1=C(R^2+H^2)^{-1/2}\exp\left[H-\sqrt{R^2+H^2}\right] \qquad (4)$$

Here C is the normalized thermal energy $qU/8\pi akT_0$. In order to minimize C for fixed R, we set the derivative $C(H)$ to zero. The result is the algebraic relation

$$H\sqrt{H^2+R^2}+H-H^2-R^2=0 \qquad (5)$$

---

[1] Michigan State University, East Lansing, MI 48824; Mem. ASME.

Contributed by the Heat Transfer Division of the AMERICAN SOCIETY OF MECHANICAL ENGINEERS. Manuscript received by the Heat Transfer Division December 1990; revision received July 31, 1991. Keywords: Forced Convection, Wakes.

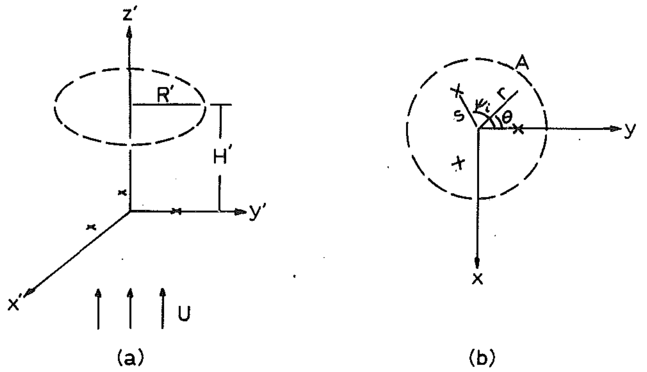

Fig. 1 (*a*) Heat sources are on $z' = 0$ plane. A circular region (within dashed lines) on $z' = H'$ plane is to be heated. (*b*) Top view. Crosses denote heat sources.

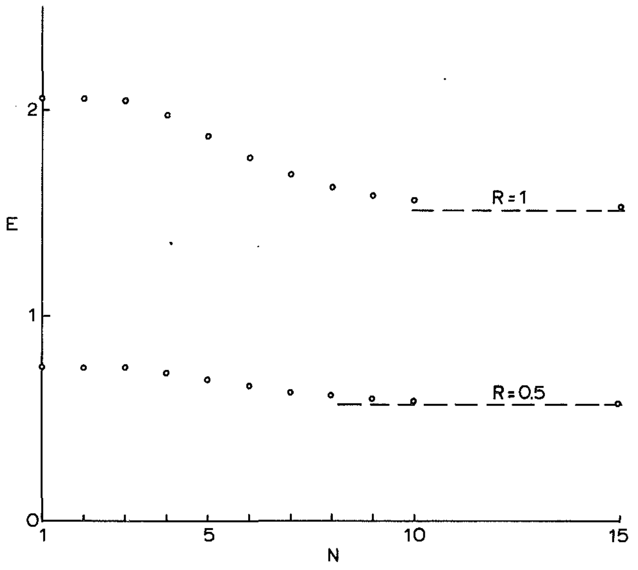

Fig. 2 Minimum total energy *E* for heating a given region as the number of sources *N* is varied; dashed line is the symptote for ring source ($N = \infty$)

Notice that H and R are not linearly related. For small R we find $H = O(R^2)$. A regular perturbation yields

$$H=R^2-R^3+2R^4+0(R^5) \tag{6}$$

However, since the energy required E or C increases exponentially with R, a single source may not be as efficient as multiple sources for large areas to be heated.

Multiple Sources

We consider N sources of equal strength, evenly spaced, on a circle of radius S at a distance H from the region to be heated. The locations of the sources in cylindrical coordinates are $r = S$, $\theta = \psi_i \equiv 2\pi(i-1)/N$, $i = 1, 2, \ldots, N$, $z = 0$ (Fig. 1*b*). Using superposition of the single source solution, the temperature at any point is

$$T=\sum_{i=1}^{N}\frac{C}{\sqrt{l_i}}\exp(z-\sqrt{l_i}) \tag{7}$$

$$l_i\equiv r^2+z^2+S^2-2rS\cos(\psi_i-\theta) \tag{8}$$

The total heat input is Nq or in normalized form, $E = NC$. Symmetry conditions show that the minimum temperature occurs either at the center or on the edge between adjacent sources (point A in Fig. 1*b*). At the center

$$T_C=\frac{NC}{\sqrt{H^2+S^2}}\exp\left[H-\sqrt{H^2+S^2}\right] \tag{9}$$

At point A,

$$T_A=C\sum_{i=1}^{N}\frac{1}{\sqrt{h_i}}\exp\left[H-\sqrt{h_i}\right] \tag{10}$$

$$h_i\equiv R^2+H^2+S^2-2RS\cos\left(\psi_i-\frac{\pi}{N}\right) \tag{11}$$

We require

$$T_C\geq 1, \quad T_A=1 \tag{12}$$

The problem is as follows. For given R, N we choose H, S such that NC is minimized, subjected to the conditions in Eq. (12).

Since an analytic relation is not possible, a numerical method is used to search for the minimum of the surface $NC(H, S)$. This can be achieved by a variety of optimization methods (e.g., Hamming, 1973). The grid method was used to achieve five-digit accuracy. We find for N less than about 6, T_C is always larger than 1, while for larger N, the heat input needs to be adjusted to keep T_C above unity.

The Ring Source

We have considered N discrete sources arranged in a circle. In the limit $N \to \infty$ while keeping total strength finite, a ring source is obtained. Let q' be the heat input per length of a ring with radius S'. The temperature at any point (r, θ, z) is the integral

$$T=\int_0^{2\pi}D\frac{1}{\sqrt{k_i}}\exp\left[z-\sqrt{k_i}\right]d\psi \tag{13}$$

where

$$k_i\equiv r^2+z^2+S^2-2rS\cos(\psi-\theta) \tag{14}$$

$$D\equiv q'S'U/8\pi akT_0 \tag{15}$$

Due to radial symmetry, we can set $\theta = 0$ without loss. The total normalized heat input $2\pi D$ is to be minimized, subject to the conditions

$$T\Big|_{\substack{r=R\\z=H}}=\int_0^{2\pi}D\frac{1}{\sqrt{p_i}}\exp\left[H-\sqrt{p_i}\right]d\psi=1 \tag{16}$$

$$p_i\equiv R^2+S^2+H^2-2RS\cos\psi \tag{17}$$

and

$$T\Big|_{\substack{r=0\\z=H}}=2\pi D\frac{1}{\sqrt{S^2+H^2}}\exp\left[H-\sqrt{S^2+H^2}\right]\geq 1 \tag{18}$$

The total energy is then

$$E=2\pi D=\frac{\pi}{Je^H} \tag{19}$$

where

$$J=\sum_0^{\pi}(p_i)^{-1/2}\exp(-p_i^{1/2})d\psi \tag{20}$$

For given R, we choose S, H to minimize E subject to Eq. (18). We find that the integrand of Eq. (20) is too stiff to be efficiently evaluated numerically by simple quadrature such as Simpson's rule. A variable-step Newton–Cotes algorithm was used to obtain five-digit accuracy.

Results and Discussion

Figure 2 shows the total minimum energy E for given region size R. In general, the energy E decreases as the number of sources is increased, due to a smaller mean deviation from the minimum temperature. The exception is $N = 2$, which has an optimum location at the center ($S = 0$), and thus has the same energy as the single source $N = 1$. Therefore, there is no

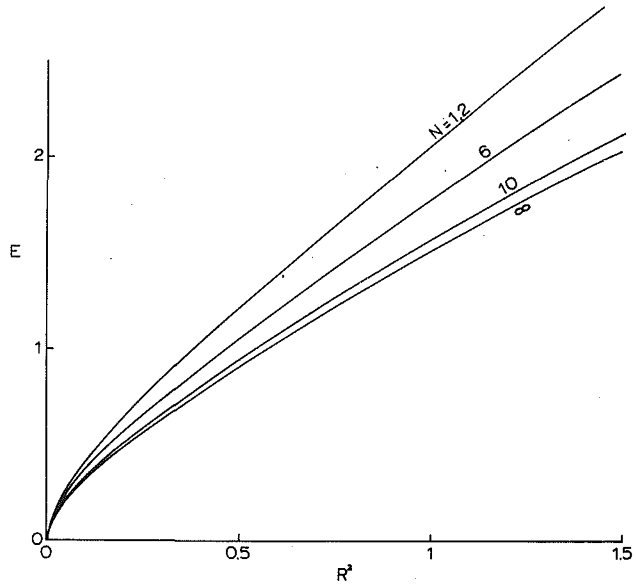

Fig. 3 Minimum total energy E as function of area

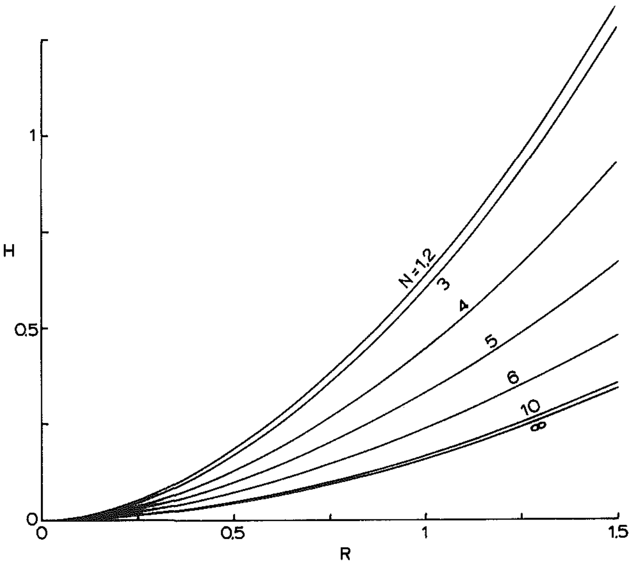

Fig. 4 Optimum distance H

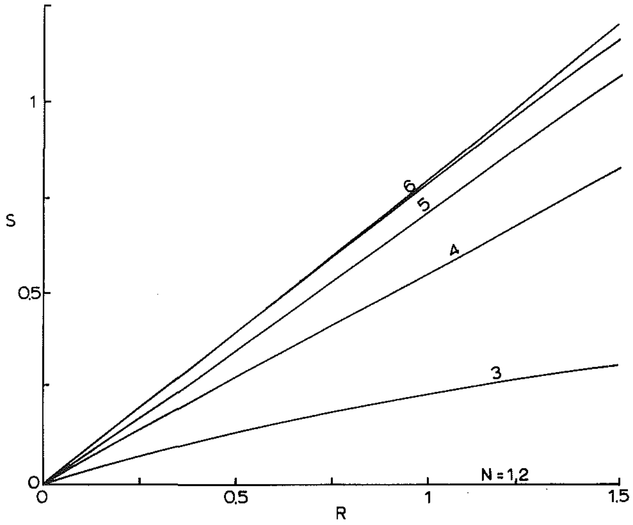

Fig. 5 Optimum location S

advantage to having two heating sources. The energy decrease is also very small for $N = 3$. Appreciable energy savings is obtained for $N = 4$ to $N = 7$ and the returns diminish again when $N \geq 8$. Comparing the energy for multiple sources and that for a single source, we find the savings can be as much as 25 percent. Figure 3 shows the minimum energy as a function of area R^2. Since the relation is concave down, it is more efficient to heat single larger areas than several smaller ones.

If the radius of region R is given and the number of sources N is chosen, the location of the sources to achieve minimum energy is unique. Figure 4 shows the computed proper distance H from the region and Fig. 5 shows the distance S from the center line. These figures are important for the design of the heating system.

We have considered N discrete sources arranged in a circle. There are other possible forms of arrangement notably an extra added source at the center. For the range of R considered, the extra source at the center is not necessary for $N \leq 6$, since R_C is larger than one. The extra source may be advantageous for larger N, but this situation has not been fully investigated. Also for large N and large R ($R' \gg 2a/U$), the optimum arrangement may be a distribution on several concentric circles.

Our results can also be applied to other similar transport processes, such as spraying, painting, and atomization of fuel for combustion.

References

Hamming, R. W., 1973, *Numerical Methods for Scientists and Engineers*, 2nd ed., McGraw-Hill, New York, pp. 657–676.

Rosenthal, D., 1946, "The Theory of Moving Sources of Heat and Its Application to Metal Treatments," *Trans. ASME*, Vol. 68, pp. 849–866.

Transient Response of Parallel and Counterflow Heat Exchangers

W. Roetzel[1] **and Y. Xuan**[1]

Nomenclature

A = heat transfer surface area, m^2
C = thermal flow rate of fluids, W/K
$\tilde{C}$ = heat capacity, J/K
h = heat transfer coefficient, W/(m^{2}K)
Ntu = number of transfer units
t = dimensionless temperature
T = dimensionless temperature corresponding to the Laplace transform
x = dimensionless distance
τ = time, s
τ_d = dwell time of fluids in the heat exchanger, s

Subscripts

1, 2 = fluids 1 and 2
w = core wall of the heat exchanger

Theoretical Analysis

The analysis of the transient behavior of shell and tube heat exchangers has been carried out by many researchers (Tan and Spinner, 1978; Romie, 1984, 1985). Making some assumptions, Romie (1984) has derived governing equations to describe the

---

[1] Institut für Thermodynamik, Universität der Bundeswehr Hamburg, Hamburg, Federal Republic of Germany.

Contributed by the Heat Transfer division of the American Society of Mechanical Engineers. Manuscript received by the Heat Transfer Division April 1, 1991; revision received August 21, 1991. Keywords: Heat Exchangers, Numerical Methods, Transient and Unsteady Heat Transfer.

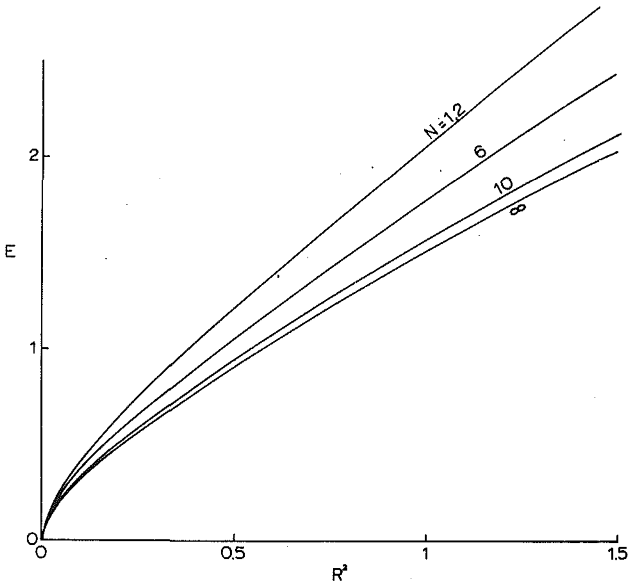

Fig. 3 Minimum total energy E as function of area

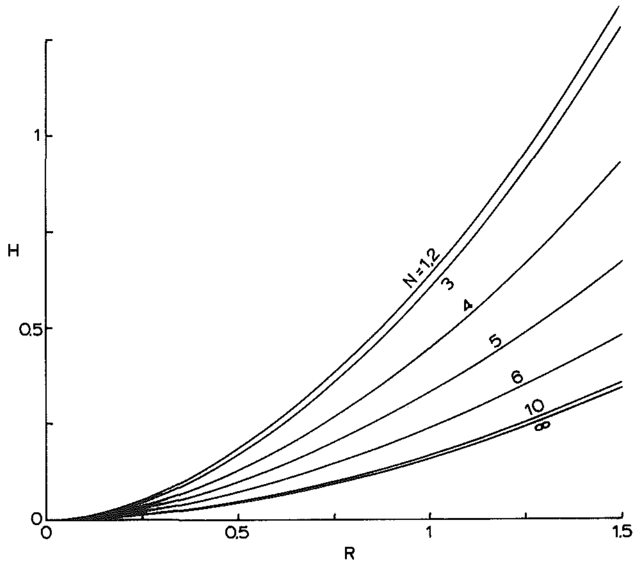

Fig. 4 Optimum distance H

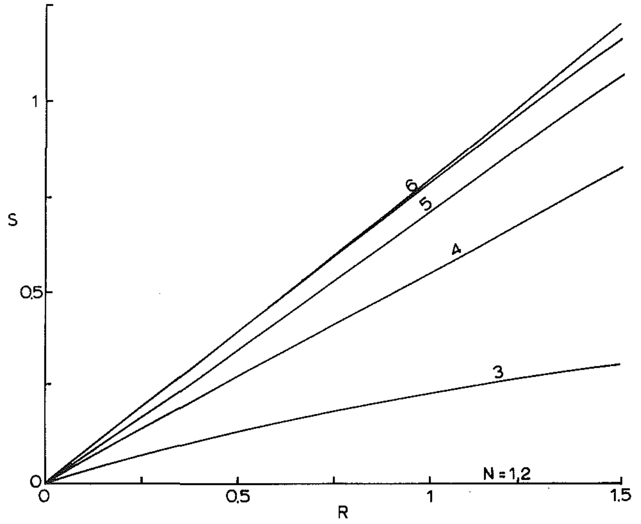

Fig. 5 Optimum location S

advantage to having two heating sources. The energy decrease is also very small for $N = 3$. Appreciable energy savings is obtained for $N = 4$ to $N = 7$ and the returns diminish again when $N \geq 8$. Comparing the energy for multiple sources and that for a single source, we find the savings can be as much as 25 percent. Figure 3 shows the minimum energy as a function of area R^2. Since the relation is concave down, it is more efficient to heat single larger areas than several smaller ones.

If the radius of region R is given and the number of sources N is chosen, the location of the sources to achieve minimum energy is unique. Figure 4 shows the computed proper distance H from the region and Fig. 5 shows the distance S from the center line. These figures are important for the design of the heating system.

We have considered N discrete sources arranged in a circle. There are other possible forms of arrangement notably an extra added source at the center. For the range of R considered, the extra source at the center is not necessary for $N \leq 6$, since R_C is larger than one. The extra source may be advantageous for larger N, but this situation has not been fully investigated. Also for large N and large R ($R' \gg 2a/U$), the optimum arrangement may be a distribution on several concentric circles.

Our results can also be applied to other similar transport processes, such as spraying, painting, and atomization of fuel for combustion.

References

Hamming, R. W., 1973, *Numerical Methods for Scientists and Engineers*, 2nd ed., McGraw-Hill, New York, pp. 657–676.

Rosenthal, D., 1946, "The Theory of Moving Sources of Heat and Its Application to Metal Treatments," *Trans. ASME*, Vol. 68, pp. 849–866.

Transient Response of Parallel and Counterflow Heat Exchangers

W. Roetzel[1] **and Y. Xuan**[1]

Nomenclature

A = heat transfer surface area, m^2
C = thermal flow rate of fluids, W/K
$\tilde{C}$ = heat capacity, J/K
h = heat transfer coefficient, W/(m^{2}K)
Ntu = number of transfer units
t = dimensionless temperature
T = dimensionless temperature corresponding to the Laplace transform
x = dimensionless distance
τ = time, s
τ_d = dwell time of fluids in the heat exchanger, s

Subscripts

1, 2 = fluids 1 and 2
w = core wall of the heat exchanger

Theoretical Analysis

The analysis of the transient behavior of shell and tube heat exchangers has been carried out by many researchers (Tan and Spinner, 1978; Romie, 1984, 1985). Making some assumptions, Romie (1984) has derived governing equations to describe the

---

[1] Institut für Thermodynamik, Universität der Bundeswehr Hamburg, Hamburg, Federal Republic of Germany.

Contributed by the Heat Transfer division of the American Society of Mechanical Engineers. Manuscript received by the Heat Transfer Division April 1, 1991; revision received August 21, 1991. Keywords: Heat Exchangers, Numerical Methods, Transient and Unsteady Heat Transfer.

transient operation in the heat exchanger. Using s as the Laplace transform variable with respect to $z = \tau/\tau_{d1}$, one can readily find the temperature profiles of both fluids and the wall in the image-domain of the Laplace transform subject to the uniform initial conditions: $t_1(x, 0) = t_2(x, 0) = t_w(x, 0) = 0$:

$$T_1(x, s) = B_1 \frac{a_{12}}{\lambda_1 - a_{11}} \exp(\lambda_1 x) + B_2 \frac{a_{12}}{\lambda_2 - a_{11}} \exp(\lambda_2 x) \tag{1}$$

$$T_2(x, s) = B_1 \exp(\lambda_1 x) + B_2 \exp(\lambda_2 x) \tag{2}$$

$$T_w = \frac{\alpha_1 T_1 + \alpha_2 T_2}{\alpha_1 + \alpha_2 + R_w s} \tag{3}$$

where B_1 and B_2 are two unknown constants to be determined according to the inlet boundary conditions. The eigenvalues λ_1 and λ_2 are as follows:

$$\lambda_{1,2} = \frac{(a_{11} + a_{22}) \pm \sqrt{(a_{11} - a_{22})^2 + 4a_{12}a_{21}}}{2}$$

$$a_{11} = \frac{\alpha_1 N_1}{\alpha_1 + \alpha_2 + R_w s} - s - N_1, \quad a_{12} = \frac{\alpha_2 N_1}{\alpha_1 + \alpha_2 + R_w s}$$

$$a_{21} = \frac{\text{sign } \alpha_1 N_2}{\alpha_1 + \alpha_2 + R_w s}, \quad a_{22} = \text{sign}\left(\frac{\alpha_2 N_2}{\alpha_1 + \alpha_2 + R_w s} - N_2 - R_\tau s \right)$$

The other parameters existing in the above expressions are defined as follows:

$$N_1 = \frac{(hA)_1}{C_1}, \quad N_2 = \frac{(hA)_2}{C_2}, \quad R_1 = \frac{C_1}{C_2} = \frac{1}{R_2}, \quad R_\tau = \frac{\tau_{d2}}{\tau_{d1}}$$

$$\text{Ntu}_1 = \left[\frac{1}{(hA)_1} + \frac{1}{(hA)_2} \right]^{-1} / C_1 = \frac{N_1 N_2 R_2}{N_1 + N_2 R_2}, \quad \text{sign} = \pm$$

$$R_{c1} = \frac{\tilde{C}_1}{\tilde{C}_2} = \frac{1}{R_{c2}}, \quad R_w = \frac{\tilde{C}_w}{\tilde{C}_1 + \tilde{C}_2},$$

$$\alpha_1 = \frac{N_1}{1 + R_{c2}}, \quad \alpha_2 = \frac{N_2}{R_\tau(1 + R_{c1})}$$

The positive sign (+) and negative sign (−) of sign (±) are valid for parallel and countercurrent flow, respectively. The shellside boundary condition is arbitrarily given: $t_1(0, z) = f_1(z)$; the tubeside condition: $t_2(0, z) = 0$ for parallel flow and $t_2(1, z) = 0$ for countercurrent flow. Therefore, for parallel flow, $T_1(x, s)$ and $T_2(x, s)$ are derived:

$$T_1(x, s) = \frac{F_1(s)}{\lambda_2 - \lambda_1} [(\lambda_2 - a_{11})\exp(\lambda_1 x) - (\lambda_1 - a_{11})\exp(\lambda_2 x)] \tag{4}$$

$$T_2(x, s) = \frac{(\lambda_1 - a_{11})(\lambda_2 - a_{11})}{a_{12}(\lambda_2 - \lambda_1)} F_1(s)(\exp(\lambda_1 x) - \exp(\lambda_2 x)) \tag{5}$$

For countercurrent flow:

$$T_1(x, s) = \frac{F_1(s)}{G(s)} [(\lambda_2 - a_{11})\exp(\lambda_1 x) - (\lambda_1 - a_{11})\exp(\lambda_1 - \lambda_2 - \lambda_2 x)] \tag{6}$$

$$T_2(x, s) = \frac{(\lambda_1 - a_{11})(\lambda_2 - a_{11})F_1(s)}{a_{12}G(s)} [\exp(\lambda_1 x) - \exp(\lambda_1 - \lambda_2 - \lambda_2 x)] \tag{7}$$

where $G(s) = [(\lambda_2 - a_{11}) - (\lambda_1 - a_{11}) \exp(\lambda_1 - \lambda_2)]$ and $F_1(s)$ is the transformed form of $f_1(z)$ in the image domain.

Inverse Laplace Transform

The inverse Laplace transform must be implemented from the above equations in the Laplace image domain to obtain the solutions to the original problem in the time domain. To obtain transient responses to an arbitrary inlet temperature change in a shell and tube heat exchanger, a numerical inversion method of the Laplace transform is used. This method originates from Gaver (1966) and was further developed by Stehfest (1970). The algorithm is described as follows:

$$f(z) = \frac{\ln 2}{z} \sum_{m=1}^{M} K_m F\left(m \frac{\ln 2}{z} \right)$$

$$K_m = (-1)^{m+M/2} \sum_{k=(m+1)/2}^{\min(m,\ M/2)} \frac{k^{M/2}(2k)!}{(M/2 - k)!k!(k-1)!(m-k)!(2k-m)!} \tag{8}$$

where M must be even. The word "min" means that the number of summed series terms will take the lower of m and $M/2$. The inverse Laplace transform is an ill-posed problem in the sense that a small change in the image function may give rise to a large change in the original function. Obviously, the accuracy of the inverse calculation depends on z and M besides the abovementioned dimensionless parameters. Theoretically, $f(z)$ becomes more accurate with greater M. Practically, however, a greater M may result in a false answer because of the rounding error. In fact, the absolute value of K_m increases with M without limit, which reflects the unboundedness of the inverse Laplace operator (Stehfest, 1970). For a given form $f_1(z)$ and z, one should select the optimum value of M so that the following condition is satisfied for any $\epsilon > 0$:

$$|f_{M1}(z) - f_{M2}(z)| < \epsilon \tag{9}$$

where ϵ is the required accuracy. $f_{M1}(z)$ is the value of $f(z)$ pertinent to the number M_1 and $f_{M2}(z)$ pertinent to M_2. There exists no optimum value of M that is fit for calculating temperatures at any time z and any position x. In fact, this value varies with z and x as well as some parameters such as Ntu_1, R_1, R_w, and R_τ. Normally, the maximum value of M is limited to 24; otherwise the truncation error may be too great and the optimum value of M lies in a small range $8 \le M \le 20$. The double precision arithmetic is recommended.

With this algorithm, one can expect to obtain the responses to a given arbitrary inlet temperature change, which has no discontinuities or rapid oscillation. There may exist various forms of inlet temperature changes and the common inlet changes may adhere to step, ramp, exponential, and periodic types. To examine the method developed here, some examples have been calculated under the following chosen parameters: $R_w = R_\tau = R_1 = 1.0$, $N_1 = N_2 = 2\ \text{Ntu}_1$. Two of these examples are illustrated in Figs. 1 and 2. Meanwhile, the results have shown that the energy balance between both fluids is precisely satisfied in the steady state, which demonstrates that the algorithm for numerically inverse Laplace transform can be applied to predicting transient response to an arbitrary inlet temperature change. One needs to pay attention to the computed results referring to small dimensionless times $z < 1.0$. The reason is the fact that there occur greater roundoff errors if $z < 1.0$. In fact, $z < 1.0$ means that the time τ of temperature propagation is smaller than the dwell time τ_{d1} of fluid 1 in the heat exchanger. The propagation front of the inlet temperature change has not reached both exits of the apparatus with parallel flow if $R_\tau \ge 1.0$ or the exit of fluid 1 for countercurrent flow, due to the simplification that the heat conduction along the axial direction is neglected. According to such characteristics of the transient process, one can easily distinguish and eliminate these errors.

Compared with the finite-difference procedure (Romie, 1984), the method presented in this note can be used to calculate directly the transient responses at arbitrary values of z and x, without performing many-step calculations pertinent to the selected time and space steps. Being different from other an-

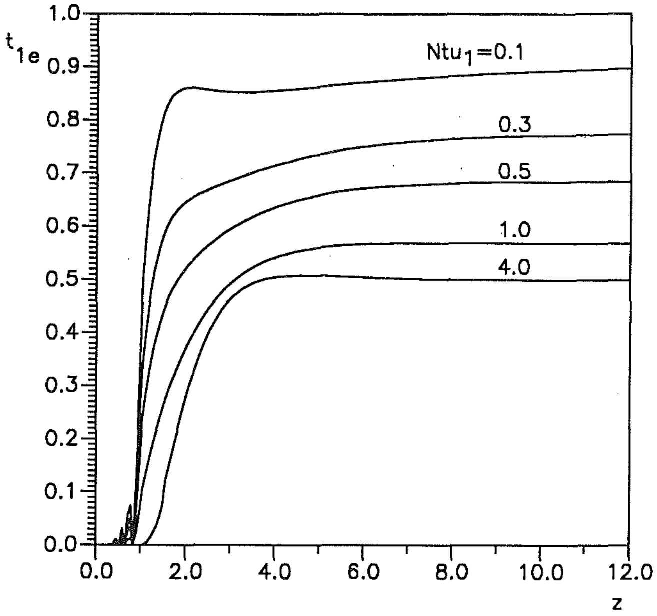

Fig. 1 Shellside exit temperature response t_{1e} to a step inlet temperature change in the parallel flow heat exchanger

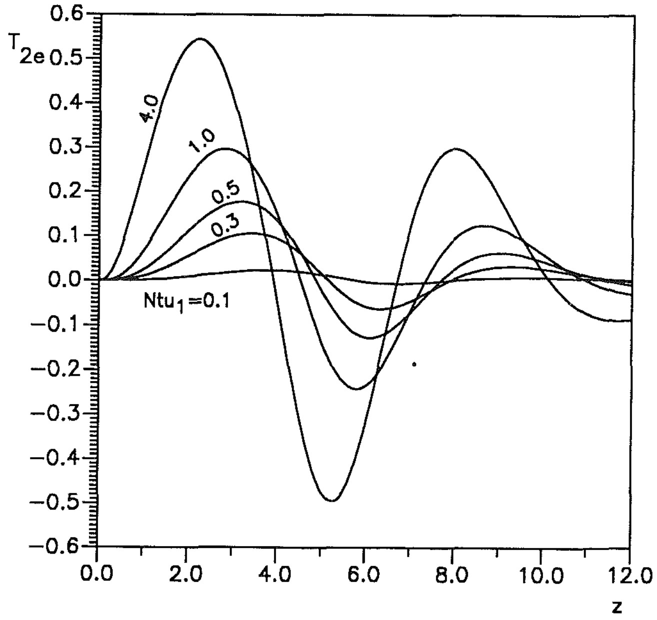

Fig. 2 Tubeside exit temperature response t_{2e} to a sinusoidal inlet temperature change $t_1(0, z)$ = sin z in the counterflow heat exchanger

alytical procedures (Romie, 1985; Tan and Spinner, 1978) that can only deal with the transient responses to a step input change, the abovementioned semi-analytical method can be applied to predicting the transient behavior subject to arbitrary inlet temperatures in shell and tube heat exchangers with parallel or countercurrent flow. In fact, the input temperature perturbation often takes a complicated form rather than a simple step change.

References

Gaver, D. P., 1966, "Observing Stochastic Process, and Approximate Transform Inversion," *Operations Research*, Vol. 14, pp. 444–459.

Romie, F. E., 1984, "Transient Response of the Counterflow Heat Exchanger," ASME JOURNAL OF HEAT TRANSFER, Vol. 106, pp. 620–626.

Romie, F. E., 1985, "Transient Response of the Parallel-Flow Heat Exchanger," ASME JOURNAL OF HEAT TRANSFER, Vol. 107, pp. 727–730.

Stehfest, H., 1970, "Numerical Inversion of Laplace Transforms," *Communications of the ACM*, Vol. 13, pp. 47–49.

Tan, K. S., and Spinner, I. H., 1978, "Dynamics of a Shell-and-Tube Heat Exchanger With Finite Tube-Wall Heat Capacity and Finite Shell-Side Resistance," *Ind. Eng. Chem. Fundam.*, Vol. 17, pp. 353–358.

Effect of Unbalanced Passes on Performance of Split-Flow Exchangers

N. Y. Vaidya[1] and V. Subramanian[1]

Nomenclature

a = external surface area per unit length of tube pass, m^2/m
A = total heat transfer surface area of the heat exchanger, m^2
c = specific heat of tube side fluid, J/(kg K)
C = specific heat of shell side fluid, J/(kg K)
F = LMTD correction factor
J = parameter of Eq. (6)
K = ratio of heat transfer coefficient times surface area of even and odd passes
L = total length of the heat exchanger, m
m_1, m_2 = parameters of Eqs. (2) and (3), respectively
P = thermal effectiveness = $(t_2-t_1)/(T_1-t_1)$
R = $(wc)/(WC)$ = $(T_1-T_2)/(t_2-t_1)$
t_1 = tube inlet temperature, K
t_2 = tube outlet temperature, K
T_1 = shell inlet temperature, K
T_2 = shell outlet temperature, K
T_3, T_4 = shell side outlet temperature in left and right end of the exchanger, K
U = overall heat transfer coefficient, $W/(m^2\ K)$
w = mass rate of flow of tube side fluid, kg/s
W = mass rate of flow of shell side fluid, kg/s
X = parameter of Eq. (7)
λ = parameter of Eq. (5)

Introduction

In conventional exchangers some tube passes are in parallel flow and others in countercurrent flow with respect to the shell fluid. This leads to a reduction in the mean temperature difference compared to the ideal value, which is the logarithmic mean temperature difference. In order to bring these two temperature differences closer, unbalanced tube passes are employed in a multipass heat exchanger. When the shell fluid enters at the midpoint of the exchanger and splits equally on either side, the pressure drop is lowered to about 1/8 of the normal value. This is an advantage when process conditions have pressure drop constraints. For the split-flow exchanger, when the tube passes are unbalanced, the equation for thermal effectiveness is still not available. The aim in the present study is to determine the benefits in making the tube passes unbalanced for the split-flow exchanger having four tube passes.

Design

Figure 1 shows a schematic diagram of a split-flow exchanger having four tube passes. The temperature distribution is also shown. When all four tube passes have the same value for *Ua*, which is the product of the overall heat transfer coefficient and external surface area per unit length of tube pass, then

---

[1] Bombay, India.

Contributed by the Heat Transfer Division of the AMERICAN SOCIETY OF MECHANICAL ENGINEERS. Manuscript received by the Heat Transfer Division April 1991; revision received October 1991. Keywords: Heat Exchangers, Materials Processing and Manufacturing Processes, Modeling and Scaling.

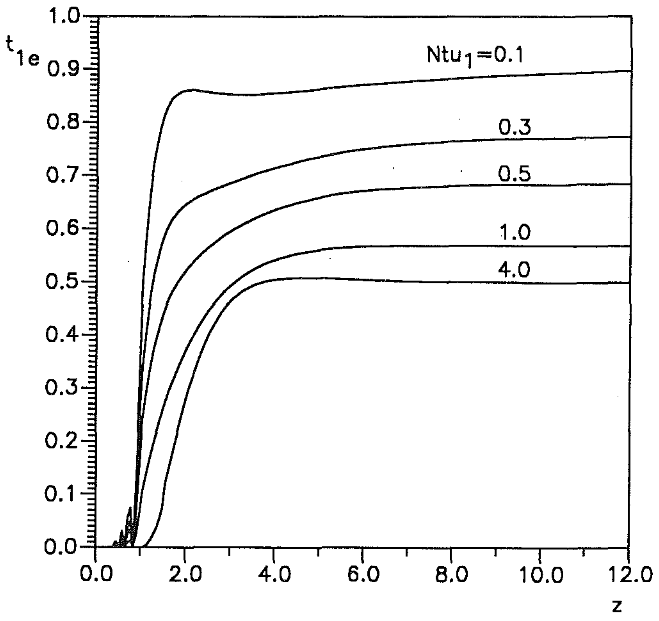

Fig. 1 Shellside exit temperature response t_{1e} to a step inlet temperature change in the parallel flow heat exchanger

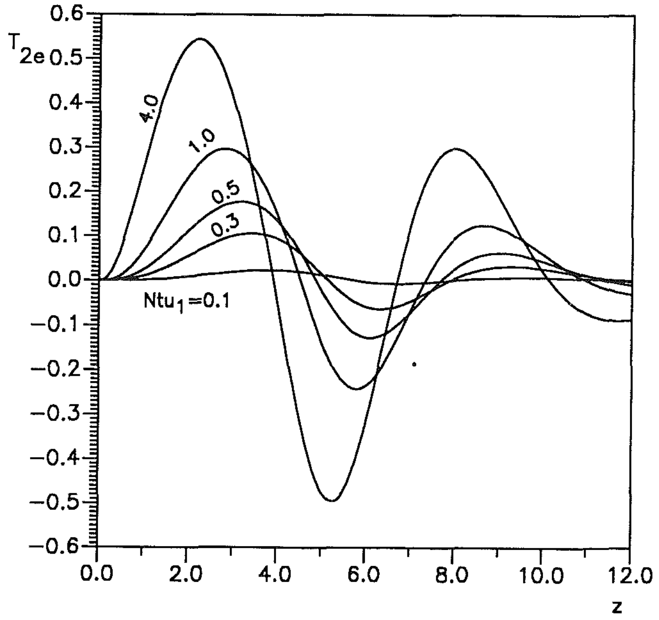

Fig. 2 Tubeside exit temperature response t_{2e} to a sinusoidal inlet temperature change $f_1(0, z)$ = sin z in the counterflow heat exchanger

alytical procedures (Romie, 1985; Tan and Spinner, 1978) that can only deal with the transient responses to a step input change, the abovementioned semi-analytical method can be applied to predicting the transient behavior subject to arbitrary inlet temperatures in shell and tube heat exchangers with parallel or countercurrent flow. In fact, the input temperature perturbation often takes a complicated form rather than a simple step change.

References

Gaver, D. P., 1966, "Observing Stochastic Process, and Approximate Transform Inversion," *Operations Research*, Vol. 14, pp. 444–459.

Romie, F. E., 1984, "Transient Response of the Counterflow Heat Exchanger," ASME Journal of Heat Transfer, Vol. 106, pp. 620–626.

Romie, F. E., 1985, "Transient Response of the Parallel-Flow Heat Exchanger," ASME Journal of Heat Transfer, Vol. 107, pp. 727–730.

Stehfest, H., 1970, "Numerical Inversion of Laplace Transforms," *Communications of the ACM*, Vol. 13, pp. 47–49.

Tan, K. S., and Spinner, I. H., 1978, "Dynamics of a Shell-and-Tube Heat Exchanger With Finite Tube-Wall Heat Capacity and Finite Shell-Side Resistance," *Ind. Eng. Chem. Fundam.*, Vol. 17, pp. 353–358.

Effect of Unbalanced Passes on Performance of Split-Flow Exchangers

N. Y. Vaidya[1] **and V. Subramanian**[1]

Nomenclature

a = external surface area per unit length of tube pass, m^2/m
A = total heat transfer surface area of the heat exchanger, m^2
c = specific heat of tube side fluid, J/(kg K)
C = specific heat of shell side fluid, J/(kg K)
F = LMTD correction factor
J = parameter of Eq. (6)
K = ratio of heat transfer coefficient times surface area of even and odd passes
L = total length of the heat exchanger, m
m_1, m_2 = parameters of Eqs. (2) and (3), respectively
P = thermal effectiveness = $(t_2-t_1)/(T_1-t_1)$
R = $(wc)/(WC)$ = $(T_1-T_2)/(t_2-t_1)$
t_1 = tube inlet temperature, K
t_2 = tube outlet temperature, K
T_1 = shell inlet temperature, K
T_2 = shell outlet temperature, K
T_3, T_4 = shell side outlet temperature in left and right end of the exchanger, K
U = overall heat transfer coefficient, $W/(m^2\ K)$
w = mass rate of flow of tube side fluid, kg/s
W = mass rate of flow of shell side fluid, kg/s
X = parameter of Eq. (7)
λ = parameter of Eq. (5)

Introduction

In conventional exchangers some tube passes are in parallel flow and others in countercurrent flow with respect to the shell fluid. This leads to a reduction in the mean temperature difference compared to the ideal value, which is the logarithmic mean temperature difference. In order to bring these two temperature differences closer, unbalanced tube passes are employed in a multipass heat exchanger. When the shell fluid enters at the midpoint of the exchanger and splits equally on either side, the pressure drop is lowered to about 1/8 of the normal value. This is an advantage when process conditions have pressure drop constraints. For the split-flow exchanger, when the tube passes are unbalanced, the equation for thermal effectiveness is still not available. The aim in the present study is to determine the benefits in making the tube passes unbalanced for the split-flow exchanger having four tube passes.

Design

Figure 1 shows a schematic diagram of a split-flow exchanger having four tube passes. The temperature distribution is also shown. When all four tube passes have the same value for *Ua*, which is the product of the overall heat transfer coefficient and external surface area per unit length of tube pass, then

---

[1] Bombay, India.

Contributed by the Heat Transfer Division of the American Society of Mechanical Engineers. Manuscript received by the Heat Transfer Division April 1991; revision received October 1991. Keywords: Heat Exchangers, Materials Processing and Manufacturing Processes, Modeling and Scaling.

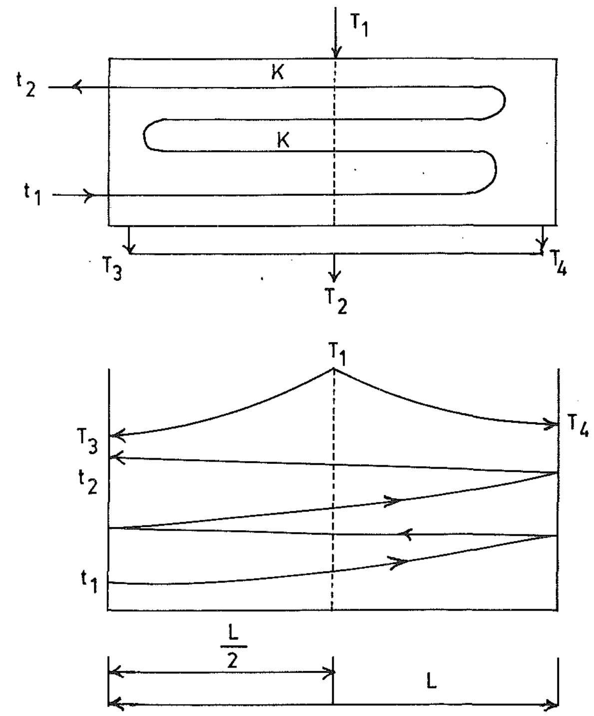

Fig. 1 Schematic diagram of a split-flow exchanger having four tube passes along with temperature distribution

the exchanger is balanced. In the present situation this product is equal to Ua for the first and third passes. For the second and fourth passes it equals KUa.

An expression for the thermal effectiveness of split-flow exchangers was derived by Jaw (1964). This expression holds when the exchanger is balanced. To obtain a similar expression when the tube passes are unbalanced, the approach is the same. The only alteration is by way of including K. Thermal effectiveness for an unbalanced split-flow exchanger having four tube passes is given by:

$$P=\frac{2\,(K+1)}{\dfrac{wc}{Ua}\left\{\dfrac{(m_1-m_2)\;(J-1)+m_1e^{(m_2L/2)}-m_2e^{(m_1L/2)}}{e^{(m_1L/2}-e^{(m_2L/2)}}\right\}+K+\;(K+1)(4RJ+X)}\tag{1}$$

where

$$m_1=\frac{Ua}{wc}\left\{2(K+1)R+\frac{K-1}{2}\right\}(1+\lambda)\tag{2}$$

$$m_2=\frac{Ua}{wc}\left\{2(K+1)R+\frac{K-1}{2}\right\}(1-\lambda)\tag{3}$$

$$R=\frac{wc}{WC}\tag{4}$$

$$\lambda=\frac{\sqrt{K+\left\{2(K+1)R+\dfrac{K-1}{2}\right\}^2}}{2(K+1)R+\dfrac{K-1}{2}}\tag{5}$$

$$J=\frac{1}{2}\left\{2-\frac{(m_1-m_2)\;(e^{(m_1L/2)}-e^{(m_2L/2)})}{m_1e^{(m_1-m_2)L/2}+m_2e^{(m_2-m_1)L/2}-\;(m_1+m_2)}\right\}\tag{6}$$

$$X=\frac{e^{(UA)/(2wc)}}{1+e^{(UA)/2(wc)}}\tag{7}$$

$$T_1-T_3=2\;RJ\;(t_2-t_1)\tag{8}$$

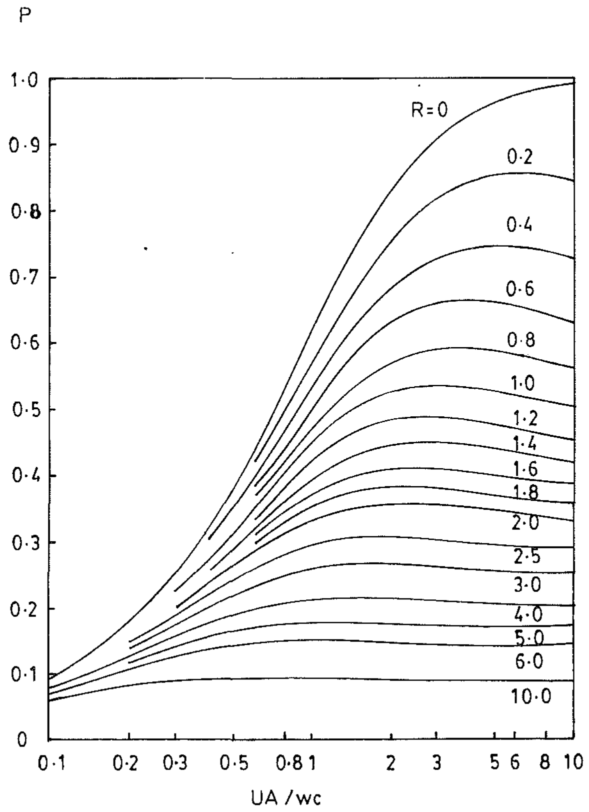

Fig. 2 Thermal effectiveness *P* versus number of transfer units *UA/wc* with *K* = 3 for different values of *R*

Using Eq. (1), the thermal effectiveness P is plotted as a function of number of transfer units UA/wc in Figs. 2, 3, 4, 5, and 6 with K = 3, 1, 0.75, 0.5, and 0.25, respectively. The values of R that are covered range between 0 and 10. In designing exchangers, the number of transfer units ranges from 0.2 to 3 (Rohsenow et al., 1985). Comparing the curves for an unbalanced pass split-flow exchanger with balanced pass exchanger, it is observed that when K = 3 the exchanger does not perform as well as a balanced exchanger. However, when K is 0.75, there is an improvement in effectiveness over the balanced exchanger. When K = 0.5 the performance improves further and still better values of effectiveness are obtained for K = 0.25. Thus there is a progressive enhancement in performance of the split-flow exchanger for lower values of K below unity. When the bias is in favor of first and third pass compared to second and fourth, a more efficient exchanger results. On the contrary, if the second and fourth pass are given higher weight, then the performance drops. In a four-pass parallel-counterflow exchanger better results are obtained when the second and fourth passes are characterized by KUa with the first and third passes having the value Ua, where K is greater than unity.

The correction factor F is related to thermal effectiveness as follows:

$$F=\frac{\ln\left\{\dfrac{1-P}{1-PR}\right\}}{\dfrac{UA}{wc}}\;(R-1)\tag{9}$$

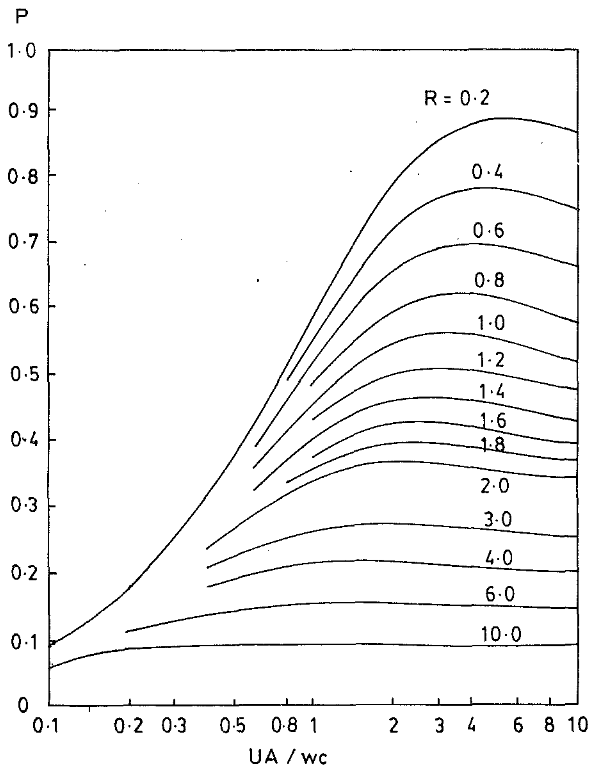

Fig. 3 Thermal effectiveness *P* versus number of transfer units *UA/wc* with *K* = 1 for different values of *R*

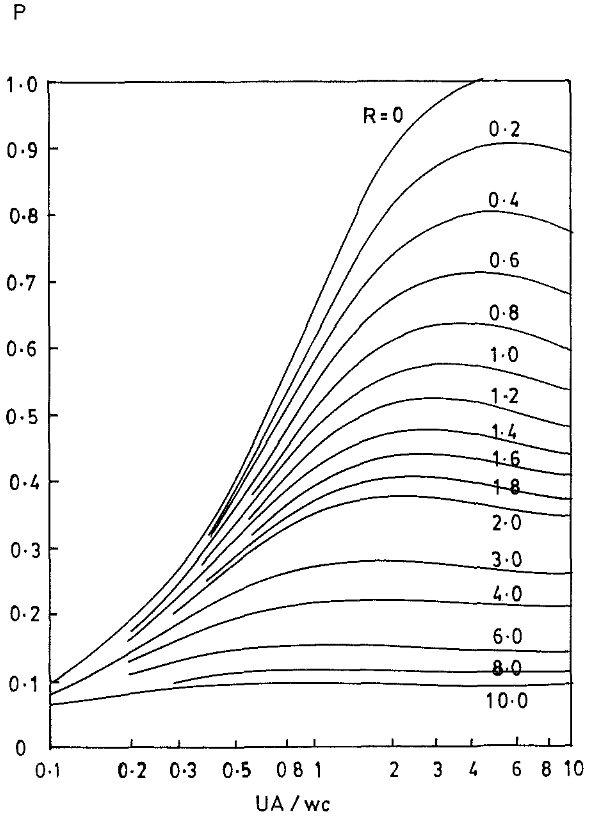

Fig. 4 Thermal effectiveness *P* versus number of transfer units *UA/wc* with *K* = 0.75 for different values of *R*

Let us now calculate the improvement in performance of the exchanger by setting $K = 0.25$. For $UA/wc = 2$, $R = 0.4$, P for the balanced pass exchanger with four tube passes (Fig. 3)

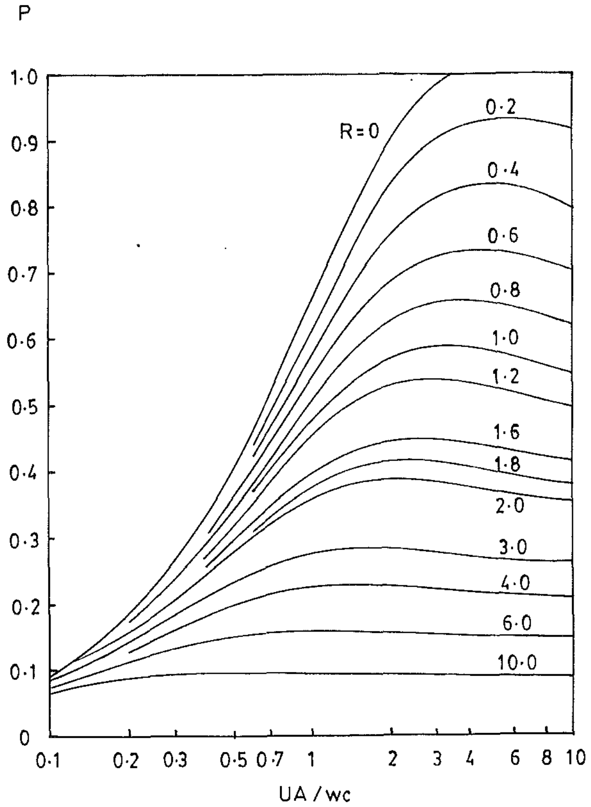

Fig. 5 Thermal effectiveness *P* versus number of transfer units *UA/wc* with *K* = 0.5 for different values of *R*

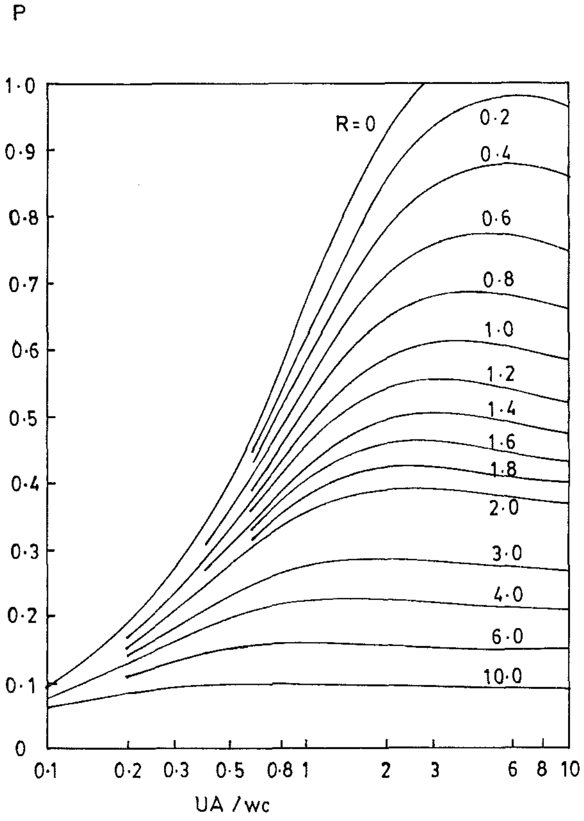

Fig. 6 Thermal effectiveness *P* versus number of transfer units *UA/wc* with *K* = 0.25 for different values of *R*

is 0.72. This gives $F = 0.78$. For $K = 0.25$, using Fig. 6, $P = 0.78$ and $F = 0.95$. This gives a 22 percent increase in the heat transfer. It is clear that arranging the passes as indicated will give favorable heat transfer characteristics.

Conclusion

The aim in the design of a multipass exchanger is to have proximity to countercurrent flow conditions to the maximum possible level. This requires arrangement of tube passes in a manner that makes the ratio of mean temperature difference to logarithmic mean temperature difference above about 0.7. In conventional exchangers better values of this ratio F are obtained when there is a bias in favor of countercurrent passes. The utility of having unbalanced passes in split-flow exchangers is thus the subject of this discussion. When K is greater than 1, a split-flow exchanger having four tube passes is less efficient in comparison with the balanced exchanger. But when K is less than 1, the unbalanced exchanger gives better performance.

References

Jaw, L., 1964, "Temperature Relations in Shell and Tube Exchangers Having One-Pass Split-Flow Shells," ASME JOURNAL OF HEAT TRANSFER, Vol. 86, pp. 408-416.

Rohsenow, W. M., Hartnett, J. P., and Ganic, E. N., 1985, *Handbook of Heat Transfer Applications*, 2nd ed., McGraw-Hill, New York, Chapter 4.

The Effect of Plate Spacing on Free Convection Between Heated Parallel Plates

N. K. Anand,[1,4] S. H. Kim,[2,4] and L. S. Fletcher[3,4]

Nomenclature

B = channel width
Gr = Grashof number
k = thermal conductivity
L = channel height
Nu = Nusselt number
p = dimensional pressure
P = nondimensional pressure of air $=(p-p_0)L^2/\rho\nu^2$
Pr = Prandtl number $=\mu c_p/K$
q = dimensional heat flux
q' = nondimensional heat flux
Q = nondimensional total surface heat rate
T = dimensional temperature
u = dimensional velocity in the axial direction
v = dimensional velocity in the transverse direction
U, V = nondimensional velocities: $U=uL/\nu$; $V=vL/\nu$
UWT = uniform wall temperature
UHF = uniform wall heat flux
x = axial coordinate
y = transverse coordinate
X, Y = nondimensional coordinates: $X=x/L$; $Y=y/L$
β = thermal expansion coefficient
γ = asymmetric heating parameter
θ = nondimensional temperature
μ = viscosity
ν = kinematic viscosity
ρ = density

Subscripts

a = air
B = refers to channel average
H = refers to uniform heat flux
l = refers to left plate
max = refers to maximum value
o = refers to channel inlet
opt = refers to optimum
r = refers to right plate
T = refers to uniform wall temperature
X = nondimensional axial coordinate

Superscript

$\bar{}$ = refers to average value

Introduction

In the past, considerable attention has been given to free convection between heated vertical parallel plates. This problem is of considerable interest to engineers because of its application to electronic equipment cooling and solar energy. Several investigators (Elenbaas, 1942; Sparrow and Bahrami, 1980; Wirtz and Stutzman, 1982; Azevedo and Sparrow, 1985; Sparrow and Azevedo, 1985; Webb and Hill, 1989) experimentally studied laminar free convection between parallel plates. Consideration was given to both symmetric and asymmetric heating. Also, other investigators (Aung et al., 1972; Aung, 1972; Bodoia and Osterle, 1962; Carpenter et al., 1976; Sparrow et al., 1984) studied this problem both experimentally and numerically.

Some attempts have been made to optimize the spacing between parallel plates in the past. Bodoia and Osterle (1962) analytically derived a criterion for an optimum plate spacing for which the heat dissipation is maximum. Levy (1971) obtained an optimum plate spacing by minimizing the temperature difference between the wall and inlet air temperature with respect to the plate spacing (B). The optimization function was obtained by making a global/lumped system type heat balance. The Nusselt number correlation developed by Bodoia and Osterle (1962) was used by Levy in his analysis and consideration was given to symmetrically heated channels subjected to a UWT condition.

Bar-Cohen and Rohsenow (1984) proposed a technique for determining the optimum plate spacing between an array of parallel plates. Consideration was given to channels subjected to both UWT and UHF conditions. Also, both symmetric and asymmetric heating conditions were considered. For free convection heat transfer in parallel plate channels, the heat transfer coefficient for fully developed flow between two plates was the lower bound, and the heat transfer coefficient for a single plate was the upper bound. Using the heat transfer relations for the lower and upper bounds, a composite expression was obtained that was valid for convective heat transfer between the fully developed limit and the single plate limit. An optimization function was then obtained by developing a lumped system energy balance, and the heat transfer coefficient was represented by composite relations for both the UWT and UHF cases. An optimum plate spacing for different thermal configurations was obtained by maximizing the heat dissipation. Although Bar-Cohen and Rohsenow (1984) considered an array of plates, the composite relations for the heat transfer coefficients actually were based on a single-channel analysis. Thermal coupling between two adjacent channels as result of wall conduction was not considered. Kim et al. (1991) numerically studied free convection in channels formed by a series

---

[1] Associate Professor, Assoc. Mem. ASME.

[2] Graduate Research Assistant.

[3] Thomas A. Dietz Professor, Fellow ASME.

[4] Department of Mechanical Engineering, Texas A&M University, College Station, Texas, 77843.

Contributed by the Heat Transfer Division and presented at the ASME Winter Annual Meeting, Dallas, Texas, November 25-30, 1990. Manuscript received by the Heat Transfer Division November 1990; revision received December 1991. Keywords: Electronic Equipment, Numerical Methods, Solar Energy.

is 0.72. This gives $F = 0.78$. For $K = 0.25$, using Fig. 6, $P = 0.78$ and $F = 0.95$. This gives a 22 percent increase in the heat transfer. It is clear that arranging the passes as indicated will give favorable heat transfer characteristics.

Conclusion

The aim in the design of a multipass exchanger is to have proximity to countercurrent flow conditions to the maximum possible level. This requires arrangement of tube passes in a manner that makes the ratio of mean temperature difference to logarithmic mean temperature difference above about 0.7. In conventional exchangers better values of this ratio F are obtained when there is a bias in favor of countercurrent passes. The utility of having unbalanced passes in split-flow exchangers is thus the subject of this discussion. When K is greater than 1, a split-flow exchanger having four tube passes is less efficient in comparison with the balanced exchanger. But when K is less than 1, the unbalanced exchanger gives better performance.

References

Jaw, L., 1964, "Temperature Relations in Shell and Tube Exchangers Having One-Pass Split-Flow Shells," ASME JOURNAL OF HEAT TRANSFER, Vol. 86, pp. 408–416.

Rohsenow, W. M., Hartnett, J. P., and Ganic, E. N., 1985, *Handbook of Heat Transfer Applications*, 2nd ed., McGraw-Hill, New York, Chapter 4.

The Effect of Plate Spacing on Free Convection Between Heated Parallel Plates

N. K. Anand,[1,4] S. H. Kim,[2,4] and L. S. Fletcher[3,4]

Nomenclature

B = channel width
Gr = Grashof number
k = thermal conductivity
L = channel height
Nu = Nusselt number
p = dimensional pressure
P = nondimensional pressure of air $=(p-p_0)L^2/\rho\nu^2$
Pr = Prandtl number $=\mu c_p/K$
q = dimensional heat flux
q' = nondimensional heat flux
Q = nondimensional total surface heat rate
T = dimensional temperature
u = dimensional velocity in the axial direction
v = dimensional velocity in the transverse direction
U, V = nondimensional velocities: $U=uL/\nu$; $V=vL/\nu$
UWT = uniform wall temperature
UHF = uniform wall heat flux
x = axial coordinate
y = transverse coordinate
X, Y = nondimensional coordinates: $X=x/L$; $Y=y/L$
β = thermal expansion coefficient
γ = asymmetric heating parameter
θ = nondimensional temperature
μ = viscosity
ν = kinematic viscosity
ρ = density

Subscripts

a = air
B = refers to channel average
H = refers to uniform heat flux
l = refers to left plate
max = refers to maximum value
o = refers to channel inlet
opt = refers to optimum
r = refers to right plate
T = refers to uniform wall temperature
X = nondimensional axial coordinate

Superscript

$\bar{\ }$ = refers to average value

Introduction

In the past, considerable attention has been given to free convection between heated vertical parallel plates. This problem is of considerable interest to engineers because of its application to electronic equipment cooling and solar energy. Several investigators (Elenbaas, 1942; Sparrow and Bahrami, 1980; Wirtz and Stutzman, 1982; Azevedo and Sparrow, 1985; Sparrow and Azevedo, 1985; Webb and Hill, 1989) experimentally studied laminar free convection between parallel plates. Consideration was given to both symmetric and asymmetric heating. Also, other investigators (Aung et al., 1972; Aung, 1972; Bodoia and Osterle, 1962; Carpenter et al., 1976; Sparrow et al., 1984) studied this problem both experimentally and numerically.

Some attempts have been made to optimize the spacing between parallel plates in the past. Bodoia and Osterle (1962) analytically derived a criterion for an optimum plate spacing for which the heat dissipation is maximum. Levy (1971) obtained an optimum plate spacing by minimizing the temperature difference between the wall and inlet air temperature with respect to the plate spacing (B). The optimization function was obtained by making a global/lumped system type heat balance. The Nusselt number correlation developed by Bodoia and Osterle (1962) was used by Levy in his analysis and consideration was given to symmetrically heated channels subjected to a UWT condition.

Bar-Cohen and Rohsenow (1984) proposed a technique for determining the optimum plate spacing between an array of parallel plates. Consideration was given to channels subjected to both UWT and UHF conditions. Also, both symmetric and asymmetric heating conditions were considered. For free convection heat transfer in parallel plate channels, the heat transfer coefficient for fully developed flow between two plates was the lower bound, and the heat transfer coefficient for a single plate was the upper bound. Using the heat transfer relations for the lower and upper bounds, a composite expression was obtained that was valid for convective heat transfer between the fully developed limit and the single plate limit. An optimization function was then obtained by developing a lumped system energy balance, and the heat transfer coefficient was represented by composite relations for both the UWT and UHF cases. An optimum plate spacing for different thermal configurations was obtained by maximizing the heat dissipation. Although Bar-Cohen and Rohsenow (1984) considered an array of plates, the composite relations for the heat transfer coefficients actually were based on a single-channel analysis. Thermal coupling between two adjacent channels as result of wall conduction was not considered. Kim et al. (1991) numerically studied free convection in channels formed by a series

---

[1] Associate Professor, Assoc. Mem. ASME.

[2] Graduate Research Assistant.

[3] Thomas A. Dietz Professor, Fellow ASME.

[4] Department of Mechanical Engineering, Texas A&M University, College Station, Texas, 77843.

Contributed by the Heat Transfer Division and presented at the ASME Winter Annual Meeting, Dallas, Texas, November 25–30, 1990. Manuscript received by the Heat Transfer Division November 1990; revision received December 1991. Keywords: Electronic Equipment, Numerical Methods, Solar Energy.

of parallel plates by taking into consideration the thermal coupling between two adjacent channels.

Bar-Cohen and Rohsenow (1984) declared the B/L value corresponding to the maximum channel average Nusselt number to be the maximum plate spacing for single channels. Composite expressions involving the single plate limit and the fully developed limit for single-channel Nusselt numbers were used, and the maximum B/L was determined by inspection. Most optimization studies reported in the literature used a lumped system type heat balance, and a heat transfer correlation known a priori was used to formulate the optimization functions. Also, the criteria used to determine the optimum plate spacing were not universal.

The objective of this paper is to predict the optimum plate spacing for single channels by using the governing equations for a continuous system model. No heat transfer coefficient known a priori will be used in these calculations, but will be calculated as part of the solution. The scope of this work includes both UWT and UHF heating conditions, and calculations are made for asymmetric heating parametric values (γ_T or γ_H) of 0., 0.1, 0.5, and 1. In this work, consideration will be given to a Grashof number range of 10 to 10^5.

Model Development and Solution Methodology

Laminar flow of air with constant thermophysical properties between vertical parallel plates is considered. The Boussinesq approximation is invoked to confine the variation of air density to the buoyancy term in the axial momentum equation. The two-dimensional flow equations for air are based on the boundary layer approximations. Based on the aforementioned simplifying assumptions, the model equations in nondimensional form can be written as

Continuity—Air

$$\partial U/\partial X + \partial V/\partial Y = 0 \qquad (1)$$

Axial Momentum—Air

$$U(\partial U/\partial X) + V(\partial U/\partial Y) = -(\partial P/\partial X) + (\partial^2 U/\partial Y^2) + \mathrm{Gr}\theta \qquad (2)$$

Energy—Air

$$U(\partial\theta/\partial X) + V(\partial\theta/\partial Y) = (\partial^2\theta/\partial Y^2)(1/\mathrm{Pr}) \qquad (3)$$

where

$$\mathrm{Gr}_T = g\beta(T_l - T_o)L^3/\nu^2, \quad \theta = (T - T_o)/(T_l - T_o) \quad \text{(UWT case)}$$

$$\mathrm{Gr}_H = g\beta q_l L^4/k\nu^2, \quad \theta = (T - T_o)/q_l L/k \quad \text{(UHF case)}$$

$$\gamma_T = \theta_r/\theta_l \text{ (UWT case) and } \gamma_H = q_r/q_l \text{ (UHF case)}$$

Basically, the model equations are the same as the ones employed by Aung et al. (1972). However, in this work the plate-spacing-to-channel-length ratio (B/L) has been made an independent parameter by defining a Grashof number based on channel length (L). Conditions at the channel inlet ($X=0$) include $P=0$, $U=U_o$, $V=0$, and $\theta=0$. At left ($Y=0$) and right ($Y=B/L$) walls the no-slip condition ($U=V=0$) was imposed. For the UWT case, $\theta_l=1$ at $Y=0$ and $\theta_r=\gamma_T$ at $Y=B/L$. For the UHF condition, $\partial\theta/\partial Y=1$ at $Y=0$ and $\partial\theta/\partial Y=\gamma_H$ at $Y=B/L$. The resulting three coupled partial differential equations were solved by an implicit finite difference method. The solution procedure used in this work is similar to the one used in an earlier investigation (Kim et al., 1991). Air velocity at the channel entrance was estimated and calculations were marched to the channel exit. If the calculated pressure at the channel exit was equal to the ambient pressure, then calculations were terminated. If not, the estimated value of the inlet velocity was altered until the solution converged within a tolerance limit of 5×10^{-6}. Grid independence was declared for each case when the maximum error in the heat balance was less than 2 percent for the UHF case. The grid size used for the UWT case was the same as that for the UHF case. Based on these studies, 195 nonuniform grid points with an expansion factor of 3 percent were used in the axial direction. In the transverse direction, a uniform grid spacing was adapted and varied from 51 to 151. In general, the number of grid points used in the transverse direction increased with increases in Gr and B/L.

As stated earlier, the channel inlet velocity u_o is not known and must be determined as part of the solution. The pressure at the channel exit is p_o and pressure at the channel inlet is assumed to be p_o. From potential flow theory it is known that the dimensional pressure at the channel inlet is less than p_o and is equal to $-\rho u_o^2/2$. However, the use of p_o at the channel inlet is a reasonable assumption based on the fact that the numerical prediction of Aung et al. (1972), using p_o at the channel inlet, compares within 5 percent of the experimental results of Webb and Hill (1989). The effect of inlet condition was studied in depth by Aihara (1973), and Chappidi and Eno (1990). It is clear from these two studies that inlet conditions affect the local Nusselt number and have insignificant impact on the average Nusselt number. It should be noted that the optimum plate spacing presented in this work is based on the channel average Nusselt number.

Results and Discussion

The impact of the presence of the opposing plate on the heat transfer at the left wall is studied by examining the variation of average Nusselt number for the left surface with B/L. The average Nusselt number for the left surface for both UWT and UHF cases is given by

$$\overline{\mathrm{Nu}}_{l,T} = \int_0^1 \frac{\partial\theta}{\partial Y}\bigg|_{Y=0} dX \text{ and } \overline{\mathrm{Nu}}_{l,H} = \int_0^1 \frac{1}{\theta}\bigg|_{Y=0} dX \qquad (4)$$

Figures 1(a) and 1(b) show the variation of average Nusselt

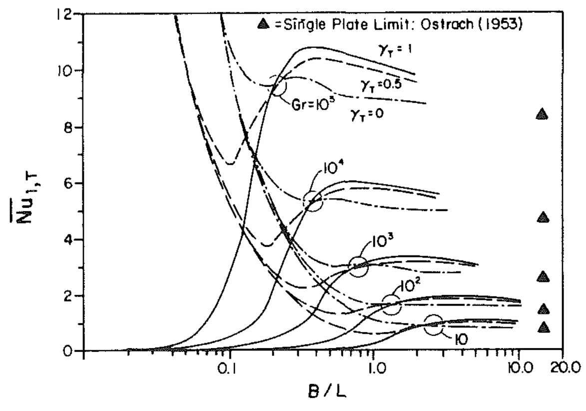

Figure 1a: UWT CASE

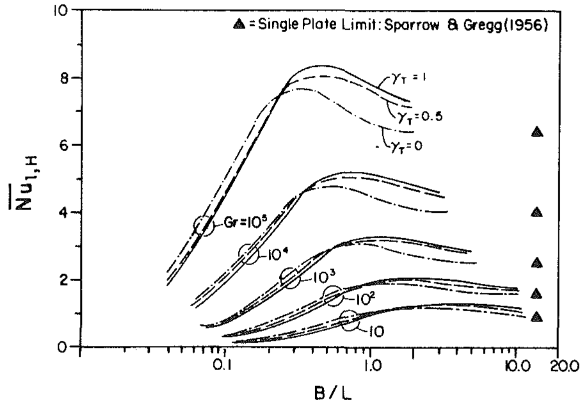

Figure 1b: UHF CASE

Fig. 1 Variation of average Nusselt number with plate spacing for the left plate

numbers for the UWT and UHF cases, respectively. Calculations are presented for different values of Grashof numbers (Gr_T and Gr_H) and asymmetric heating parameters (γ_T and γ_H). As expected, for large values of plate spacing (B/L) the average Nusselt numbers for the left plate approach that for the single plate for both the UWT and UHF cases. It is evident from Fig. 1 that as B/L decreases, the average Nusselt number increases up to a point, and this is due to the "chimney effect." The impact of the "chimney effect" is higher at higher values of Gr and asymmetric heating parameter, γ. However, at lower values of B/L, $\overline{\mathrm{Nu}}_l$ decreases with a decrease in B/L. As the spacing between the plates is reduced, the thermal boundary layers on these plates begin to meet, resulting in fully developed heat transfer. As B/L decreases further, the entry length decreases and the average $\overline{\mathrm{Nu}}_l$ approaches the fully developed limit. For the UWT case for $\gamma_T=1$, $\overline{\mathrm{Nu}}_{l,T}$ approaches zero. However, $\overline{\mathrm{Nu}}_{l,T}$ for $\gamma_T \leq 1$ approaches the corresponding fully developed limit, where the fully developed limit for $\gamma_T<1$ is a nonzero finite value.

For fixed values of Gr and B/L, $\overline{\mathrm{Nu}}_l$ increases with increase in γ. This is because as γ increases, the buoyancy force increases, resulting in an increased mass flow rate of air and heat transfer. However, at lower values of B/L, $\overline{\mathrm{Nu}}_l$ increases with a decrease in γ. The reason for the higher $\overline{\mathrm{Nu}}_l$ for $\gamma \leq 1$ is that the thermal entry length will be longer when compared to that for $\gamma=1$.

The plate spacing (B/L) is an optimum value when the average channel Nusselt number ($\overline{\mathrm{Nu}}_B$) based on the channel height is maximum. The average channel Nusselt numbers for the UWT and UHF cases are

$$\overline{\mathrm{Nu}}_{B,T}=\frac{(\overline{Q}_l+\overline{Q}_r)/2}{(\theta_l+\theta_r)/2} \text{ and } \overline{\mathrm{Nu}}_{B,H}=\frac{(Q_l+Q_r)}{(\overline{\theta}_l+\overline{\theta}_r)/2} \tag{5}$$

where

$$\overline{\theta}=\int_0^1 \theta_X dX \text{ and } \overline{Q}=\int_0^1 q_X' dX \tag{6}$$

Thus for the UWT case, the optimum plate spacing is declared when the total heat rate from the walls is a maximum. The plate spacing is said to be optimum for the UHF case when the average surface temperature of the channel walls is at a minimum. The variations of $\overline{\mathrm{Nu}}_B$ with B/L for the UWT and UHF cases for different values of Gr and γ are discussed in detail by Anand et al. (1990). The B/L value corresponding to the maximum value of $\overline{\mathrm{Nu}}_B$ is defined as the optimum plate spacing ($(B/L)_{\mathrm{opt}}$). To begin with, three points in the neighborhood of the $\overline{\mathrm{Nu}}_B$ peak were selected. If the relative difference between any two of these three points was less than 10^{-6}, then such a value of $\overline{\mathrm{Nu}}_B$ was determined to be maximum. If not, the region of three points was divided further until the aforementioned criterion was satisfied.

The variation of optimum plate spacing with Gr for the UWT and UHF cases is shown in Figs. 2 and 3, respectively. In Figs. 2 and 3, $(B/L)_{\mathrm{opt}}$ obtained in this study is compared with the maximum value of plate spacing obtained by Bar-Cohen and Rohsenow (1984). Both the $(B/L)_{\mathrm{opt}}$ and the maximum plate spacing (Bar-Cohen and Rohsenow, 1984) were based on the same criterion, i.e., the spacing corresponding to the maximum average channel Nusselt number. However, the difference between the two results is attributed to the difference in approach. The present work differs from the work of Bar-Cohen and Rohsenow (1984) in that $(B/L)_{\mathrm{opt}}$ in this work was obtained by solving discrete/continuous model equations. It should be noted that no heat transfer correlation known a priori was used in the present work; rather, the heat transfer coefficient was obtained as a part of the solution.

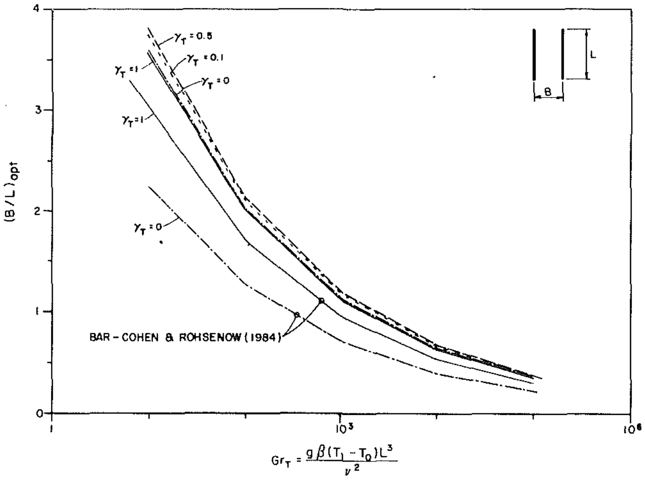

Fig. 2 Optimum plate spacing for UWT case

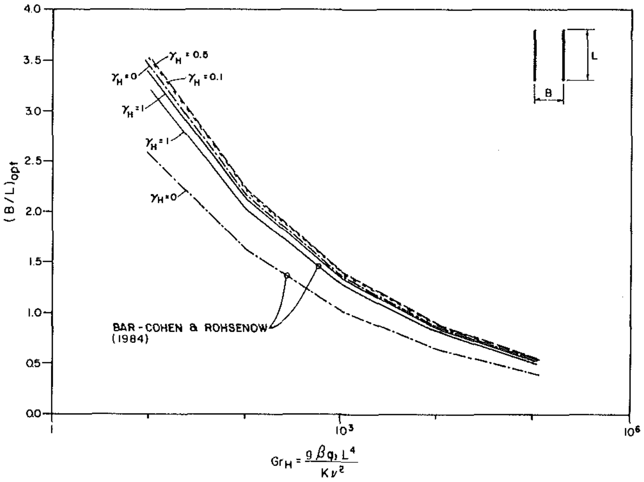

Fig. 3 Optimum plate spacing for UHF case

Figures 2 and 3 indicate that $(B/L)_{\mathrm{opt}}$ is a minimum for symmetric heating conditions ($\gamma=1$). As γ decreases to 0.5, the values for $(B/L)_{\mathrm{opt}}$ increase and then decrease as γ approaches 0. This behavior can be explained by examining the air inlet velocity U_o. Air inlet velocity for various parametric runs is presented elsewhere by the authors (Anand et al., 1990). Higher values of U_o reduce the thermal boundary layer thickness, resulting in smaller plate spacings. Also, highly asymmetric heating ($\gamma=0$) leads to smaller plate spacing since the thickness of the thermal boundary layer on the one wall is zero. The inlet velocity of air (U_o) for $\gamma=1$ and $\mathrm{Gr}=10^5$ is approximately twice that for $\gamma=0$, because U_o is proportional to the buoyancy force. The buoyancy force for $\gamma=1$ is much greater when compared to the value for $\gamma=0$. However, for values of $0 \leq \gamma \leq 1$, the thermal boundary layers develop on both surfaces, and the buoyancy force is lower when compared to the case of $\gamma=1$, thus leading to a greater value for $(B/L)_{\mathrm{opt}}$. From the design point of view, lower values of $(B/L)_{\mathrm{opt}}$ are better. Thus, the worst scenario from the present study occurs at $\gamma=0.5$. Finally, it can be concluded that the $(B/L)_{\mathrm{opt}}$ is a weak function of the asymmetric heating parameters. Calculations in this study are limited to $\mathrm{Gr} \leq 10^5$. The CPU resources required to achieve convergence for $\mathrm{Gr}>10^5$ were not available for this study. Nevertheless, from Figs. 2 and 3 it is clear that $(B/L)_{\mathrm{opt}}$ decreases with increase in Gr; hence, $(B/L)_{\mathrm{opt}}$ for $\mathrm{Gr}>10^5$ will be less than for $\mathrm{Gr}=10^5$. The $(B/L)_{\mathrm{opt}}$ values for $\mathrm{Gr}>10^5$ have not been determined, but $(B/L)_{\mathrm{opt}}$ for $\mathrm{Gr}=10^5$ may be considered the upper bound for all values of $\mathrm{Gr}>10^5$.

Acknowledgments

This work was supported in part by the Texas A&M Engineering Excellence fund. Computations on the Texas A&M

CRAY-YMP were made possible through a grant from the Texas A&M Supercomputer Center.

References

Aihara, T., 1973, "Effects of Inlet Boundary Conditions on Numerical Solutions of Free Convection Between Vertical Parallel Plates," Report of the Institute of High Speed Mechanics, Vol. 28, pp. 1-27.

Anand, N. K., Kim, S. H., and Fletcher, L. S., 1990, "The Effect of Plate Spacing on Free Convection Between Heated Parallel Plates," ASME HTD-Vol. 153, pp. 81-87.

Aung, W., Fletcher, L. S., and Sernas, V., 1972, "Developing Laminar Free Convection Between Vertical Plates With Asymmetric Heating," *International Journal of Heat and Mass Transfer*, Vol. 15, pp. 2293-2308.

Aung, W., 1972, "Fully Developed Laminar Free Convection Between Vertical Plates Heated Asymmetrically," *International Journal of Heat and Mass Transfer*, Vol. 15, pp. 1577-1580.

Azevedo, L. F., and Sparrow, E. M., 1985, "Natural Convection in Open-Ended Inclined Channels," ASME JOURNAL OF HEAT TRANSFER, Vol. 107, pp. 893-901.

Bar-Cohen, A., and Rohsenow, W. M., 1984, "Thermally Optimum Spacing of Vertical, Natural Convection Cooled, Parallel Plates," ASME JOURNAL OF HEAT TRANSFER, Vol. 106, pp. 116-123.

Bodoia, J. R., and Osterle, J. F., 1962, "The Development of Free Convection Between Heated Vertical Plates," ASME JOURNAL OF HEAT TRANSFER, Vol. 84, pp. 40-44.

Carpenter, J. R., Briggs, D. G., and Sernas, V., 1976, "Combined Radiation and Developing Laminar Free Convection Between Vertical Flat Plates With Asymmetric Heating," ASME JOURNAL OF HEAT TRANSFER, Vol. 98, pp. 95-100.

Chappidi, P. R., and Eno, B. E., 1990, "A Comparative Study of the Effect of Inlet Condition on a Free Convection Flow in Vertical Channel," ASME JOURNAL OF HEAT TRANSFER, Vol. 112, pp. 1082-1085.

Elenbaas, W., 1942, "Heat Dissipation of Parallel Plates by Free Convection," *Physica*, Vol. 9, pp. 1-23.

Kim, S. H., Anand, N. K., and Fletcher, L. S., 1991, "Free Convection Between Series of Vertical Parallel Plates With Embedded Line Heat Sources," ASME JOURNAL OF HEAT TRANSFER, Vol. 113, pp. 108-115.

Levy, E. K., 1971, "Optimum Plate Spacing for Laminar Natural Convection Heat Transfer From Parallel Vertical Isothermal Flat Plates," ASME JOURNAL OF HEAT TRANSFER, Vol. 93, pp. 463-465.

Ostrach, S., 1953, "An Analysis of Laminar Free Convection Heat Transfer About a Flat Plate Parallel to the Direction of the Generating Body Force," NACA Report 1111.

Sparrow, E. M., and Gregg, J. L., 1956, "Laminar Free Convection From a Vertical Plate," *Transactions of ASME*, Vol. 78, pp. 435-440.

Sparrow, E. M., and Bahrami, P. A., 1980, "Experiments on Natural Convection From Vertical Parallel Plates With Either Open or Closed Edges," ASME JOURNAL OF HEAT TRANSFER, Vol. 102, pp. 221-227.

Sparrow, E. M., Chrysler, G. M., and Azevedo, L. F., 1984, "Observed Flow Reversals and Measured-Predicted Nusselt Numbers for Natural Convection in a One-Sided Heated Vertical Channel," ASME JOURNAL OF HEAT TRANSFER, Vol. 106, pp. 325-332.

Sparrow, E. M., and Azevedo, L. F., 1985, "Vertical-Channel Natural Convection Spanning Between the Fully Developed Limit and the Single Plate Boundary-Layer Limit," *International Journal of Heat and Mass Transfer*, Vol. 28, pp. 1847-1857.

Webb, B. W., and Hill, D. P., 1989, "High Rayleigh Number Laminar Natural Convection in an Asymmetrically Heated Vertical Channel," ASME JOURNAL OF HEAT TRANSFER, Vol. 111, pp. 649-656.

Wirtz, R. A., and Stutzman, R. J., 1982, "Experiments on Free Convection Between Vertical Plates With Symmetric Heating," ASME JOURNAL OF HEAT TRANSFER, Vol. 104, pp. 501-507.

Induced Convective Enhancement of the Critical Heat Flux From Partially Heated Horizontal Flat Plates in Saturated Pool Boiling

T. S. Bockwoldt,[1,5] S. M. Jeter,[2,5] S. I. Abdel-Khalik,[3,5] and J. G. Hartley[4,5]

Introduction

Current developments in high-power electronics and other energy-intensive applications have accentuated the need for higher performance heat transfer. Nucleate boiling heat transfer is one of the most effective modes of heat transfer, with pool boiling being perhaps the simplest type of passive two-phase cooling. Unfortunately, the maximum heat flux attainable in nucleate pool boiling is limited by the relatively low critical heat flux at the onset of film boiling. Several methods have been suggested to enhance the critical heat flux. In particular, Costello et al. (1965) showed that the critical heat flux in saturated pool boiling could be enhanced by simply increasing the width of the pool while maintaining a fixed heater size. When the pool area is larger than the heater area, induced convective currents sweep over the heater, increasing the critical heat flux. Similar observations were reported by Lienhard and Keeling (1970). Additionally, the immersion depth of the heater has been seen to have a small effect on the critical heat flux as reported by Westwater (1986).

Elkassabgi and Lienhard (1987) examined the combined effects of immersion depth and pool size on the critical heat flux for a small-diameter horizontal cylinder in saturated pool boiling. In their apparatus, the heated cylinder was mounted horizontally in a methanol-filled cavity parallel to and midway between two parallel plates or sidewalls. The authors noted that for sufficiently wide sidewall separations there is no effect from immersion depth, or from further increase in the sidewall separation, on the critical heat flux. When the sidewalls are closer, both the immersion depth and the sidewall separation influence the critical heat flux, and these influences are interdependent. For a specific sidewall spacing, the critical heat flux increases with immersion depth and approaches a maximum value that depends on the particular sidewall spacing. The increase with immersion depth is greater when the sidewalls are closely spaced and tends to disappear for very wide spacing.

No similar study for flat plate heaters appears in the literature. While as noted above the effect of heater size and immersion depth have been studied independently, no systematic investigation of the combined effects has been conducted previously. This paper presents the results of such a study.

Experimental Apparatus and Procedure

This investigation was carried out at the Energy Systems Laboratory of the Georgia Institute of Technology using an experimental apparatus originally designed for spray cooling. The apparatus, illustrated in Fig. 1, consists of a heated copper bar with a cylindrical base 22.5 cm high and 10.2 cm in diameter. The top of the bar is machined into a truncated cone 4.3 cm high ending with a 1.5-cm-dia cylindrical tip 3.7 cm long. The 1.5-cm-dia tip is the heat transfer surface and is nickel plated to control corrosion or erosion. The copper cylinder is electrically heated with four resistance elements rated up to 2800 W in combination. The tip temperature is controlled by an electronic module, which, in this application, functions essentially as an overtemperature shut off.

The heated cylinder is surrounded by mineral fiber and enclosed in a box made of waterproof insulating board to minimize energy losses to the ambient. A PTFE splash shield seals the tip preventing water from leaking into the insulated box. The PTFE shield was fabricated to provide a snug fit by drilling an undersized hole, which was burnished before being pressed over the tip. The boiling pool is contained in a glass tube mounted on the splash shield.

The data acquisition system consists of a personal computer, a data acquisition and control board, a submultiplexer board that accepts thermocouple inputs, twelve fine-gage K-type thermocouples, and a customized data acquisition program. Pertinent thermocouple locations are shown in Fig. 2. The heat flux is calculated using the familiar conduction formula:

---

[1] Graduate Research Assistant, Nuclear Engineering Program.

[2] Associate Professor, Mechanical Engineering Program.

[3] Professor, Nuclear Engineering Program.

[4] Professor, Mechanical Engineering Program.

[5] The George W. Woodruff School of Mechanical Engineering, Georgia Institute of Technology, Atlanta, GA 30332.

Contributed by the Heat Transfer Division of the AMERICAN SOCIETY OF MECHANICAL ENGINEERS. Manuscript received by the Heat Transfer Division December 27, 1990; revision received August 27, 1991. Keywords: Augmentation and Enhancement, Boiling, Natural Convection.

CRAY-YMP were made possible through a grant from the Texas A&M Supercomputer Center.

References

Aihara, T., 1973, "Effects of Inlet Boundary Conditions on Numerical Solutions of Free Convection Between Vertical Parallel Plates," Report of the Institute of High Speed Mechanics, Vol. 28, pp. 1-27.

Anand, N. K., Kim, S. H., and Fletcher, L. S., 1990, "The Effect of Plate Spacing on Free Convection Between Heated Parallel Plates," ASME HTD-Vol. 153, pp. 81-87.

Aung, W., Fletcher, L. S., and Sernas, V., 1972, "Developing Laminar Free Convection Between Vertical Plates With Asymmetric Heating," *International Journal of Heat and Mass Transfer*, Vol. 15, pp. 2293-2308.

Aung, W., 1972, "Fully Developed Laminar Free Convection Between Vertical Plates Heated Asymmetrically," *International Journal of Heat and Mass Transfer*, Vol. 15, pp. 1577-1580.

Azevedo, L. F., and Sparrow, E. M., 1985, "Natural Convection in Open-Ended Inclined Channels," ASME Journal of Heat Transfer, Vol. 107, pp. 893-901.

Bar-Cohen, A., and Rohsenow, W. M., 1984, "Thermally Optimum Spacing of Vertical, Natural Convection Cooled, Parallel Plates," ASME Journal of Heat Transfer, Vol. 106, pp. 116-123.

Bodoia, J. R., and Osterle, J. F., 1962, "The Development of Free Convection Between Heated Vertical Plates," ASME Journal of Heat Transfer, Vol. 84, pp. 40-44.

Carpenter, J. R., Briggs, D. G., and Sernas, V., 1976, "Combined Radiation and Developing Laminar Free Convection Between Vertical Flat Plates With Asymmetric Heating," ASME Journal of Heat Transfer, Vol. 98, pp. 95-100.

Chappidi, P. R., and Eno, B. E., 1990, "A Comparative Study of the Effect of Inlet Condition on a Free Convection Flow in Vertical Channel," ASME Journal of Heat Transfer, Vol. 112, pp. 1082-1085.

Elenbaas, W., 1942, "Heat Dissipation of Parallel Plates by Free Convection," *Physica*, Vol. 9, pp. 1-23.

Kim, S. H., Anand, N. K., and Fletcher, L. S., 1991, "Free Convection Between Series of Vertical Parallel Plates With Embedded Line Heat Sources," ASME Journal of Heat Transfer, Vol. 113, pp. 108-115.

Levy, E. K., 1971, "Optimum Plate Spacing for Laminar Natural Convection Heat Transfer From Parallel Vertical Isothermal Flat Plates," ASME Journal of Heat Transfer, Vol. 93, pp. 463-465.

Ostrach, S., 1953, "An Analysis of Laminar Free Convection Heat Transfer About a Flat Plate Parallel to the Direction of the Generating Body Force," NACA Report 1111.

Sparrow, E. M., and Gregg, J. L., 1956, "Laminar Free Convection From a Vertical Plate," *Transactions of ASME*, Vol. 78, pp. 435-440.

Sparrow, E. M., and Bahrami, P. A., 1980, "Experiments on Natural Convection From Vertical Parallel Plates With Either Open or Closed Edges," ASME Journal of Heat Transfer, Vol. 102, pp. 221-227.

Sparrow, E. M., Chrysler, G. M., and Azevedo, L. F., 1984, "Observed Flow Reversals and Measured-Predicted Nusselt Numbers for Natural Convection in a One-Sided Heated Vertical Channel," ASME Journal of Heat Transfer, Vol. 106, pp. 325-332.

Sparrow, E. M., and Azevedo, L. F., 1985, "Vertical-Channel Natural Convection Spanning Between the Fully Developed Limit and the Single Plate Boundary-Layer Limit," *International Journal of Heat and Mass Transfer*, Vol. 28, pp. 1847-1857.

Webb, B. W., and Hill, D. P., 1989, "High Rayleigh Number Laminar Natural Convection in an Asymmetrically Heated Vertical Channel," ASME Journal of Heat Transfer, Vol. 111, pp. 649-656.

Wirtz, R. A., and Stutzman, R. J., 1982, "Experiments on Free Convection Between Vertical Plates With Symmetric Heating," ASME Journal of Heat Transfer, Vol. 104, pp. 501-507.

Induced Convective Enhancement of the Critical Heat Flux From Partially Heated Horizontal Flat Plates in Saturated Pool Boiling

T. S. Bockwoldt,[1,5] S. M. Jeter,[2,5] S. I. Abdel-Khalik,[3,5] and J. G. Hartley[4,5]

Introduction

Current developments in high-power electronics and other energy-intensive applications have accentuated the need for higher performance heat transfer. Nucleate boiling heat transfer is one of the most effective modes of heat transfer, with pool boiling being perhaps the simplest type of passive two-phase cooling. Unfortunately, the maximum heat flux attainable in nucleate pool boiling is limited by the relatively low critical heat flux at the onset of film boiling. Several methods have been suggested to enhance the critical heat flux. In particular, Costello et al. (1965) showed that the critical heat flux in saturated pool boiling could be enhanced by simply increasing the width of the pool while maintaining a fixed heater size. When the pool area is larger than the heater area, induced convective currents sweep over the heater, increasing the critical heat flux. Similar observations were reported by Lienhard and Keeling (1970). Additionally, the immersion depth of the heater has been seen to have a small effect on the critical heat flux as reported by Westwater (1986).

Elkassabgi and Lienhard (1987) examined the combined effects of immersion depth and pool size on the critical heat flux for a small-diameter horizontal cylinder in saturated pool boiling. In their apparatus, the heated cylinder was mounted horizontally in a methanol-filled cavity parallel to and midway between two parallel plates or sidewalls. The authors noted that for sufficiently wide sidewall separations there is no effect from immersion depth, or from further increase in the sidewall separation, on the critical heat flux. When the sidewalls are closer, both the immersion depth and the sidewall separation influence the critical heat flux, and these influences are interdependent. For a specific sidewall spacing, the critical heat flux increases with immersion depth and approaches a maximum value that depends on the particular sidewall spacing. The increase with immersion depth is greater when the sidewalls are closely spaced and tends to disappear for very wide spacing.

No similar study for flat plate heaters appears in the literature. While as noted above the effect of heater size and immersion depth have been studied independently, no systematic investigation of the combined effects has been conducted previously. This paper presents the results of such a study.

Experimental Apparatus and Procedure

This investigation was carried out at the Energy Systems Laboratory of the Georgia Institute of Technology using an experimental apparatus originally designed for spray cooling. The apparatus, illustrated in Fig. 1, consists of a heated copper bar with a cylindrical base 22.5 cm high and 10.2 cm in diameter. The top of the bar is machined into a truncated cone 4.3 cm high ending with a 1.5-cm-dia cylindrical tip 3.7 cm long. The 1.5-cm-dia tip is the heat transfer surface and is nickel plated to control corrosion or erosion. The copper cylinder is electrically heated with four resistance elements rated up to 2800 W in combination. The tip temperature is controlled by an electronic module, which, in this application, functions essentially as an overtemperature shut off.

The heated cylinder is surrounded by mineral fiber and enclosed in a box made of waterproof insulating board to minimize energy losses to the ambient. A PTFE splash shield seals the tip preventing water from leaking into the insulated box. The PTFE shield was fabricated to provide a snug fit by drilling an undersized hole, which was burnished before being pressed over the tip. The boiling pool is contained in a glass tube mounted on the splash shield.

The data acquisition system consists of a personal computer, a data acquisition and control board, a submultiplexer board that accepts thermocouple inputs, twelve fine-gage K-type thermocouples, and a customized data acquisition program. Pertinent thermocouple locations are shown in Fig. 2. The heat flux is calculated using the familiar conduction formula:

---

[1] Graduate Research Assistant, Nuclear Engineering Program.

[2] Associate Professor, Mechanical Engineering Program.

[3] Professor, Nuclear Engineering Program.

[4] Professor, Mechanical Engineering Program.

[5] The George W. Woodruff School of Mechanical Engineering, Georgia Institute of Technology, Atlanta, GA 30332.

Contributed by the Heat Transfer Division of the American Society of Mechanical Engineers. Manuscript received by the Heat Transfer Division December 27, 1990; revision received August 27, 1991. Keywords: Augmentation and Enhancement, Boiling, Natural Convection.

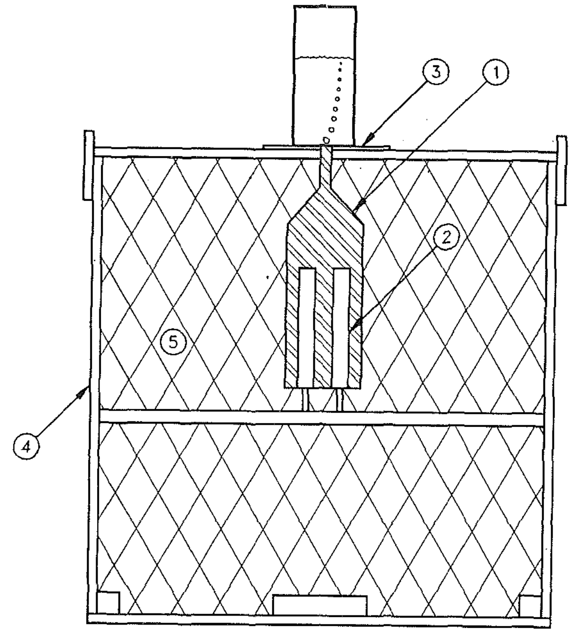

Fig. 1 Schematic of the high flux heat transfer apparatus with the following major components: (1) heated copper cylinder, (2) electric resistance heater, one of four, (3) splash shield, (4) water resistant enclosure, (5) bulk insulation

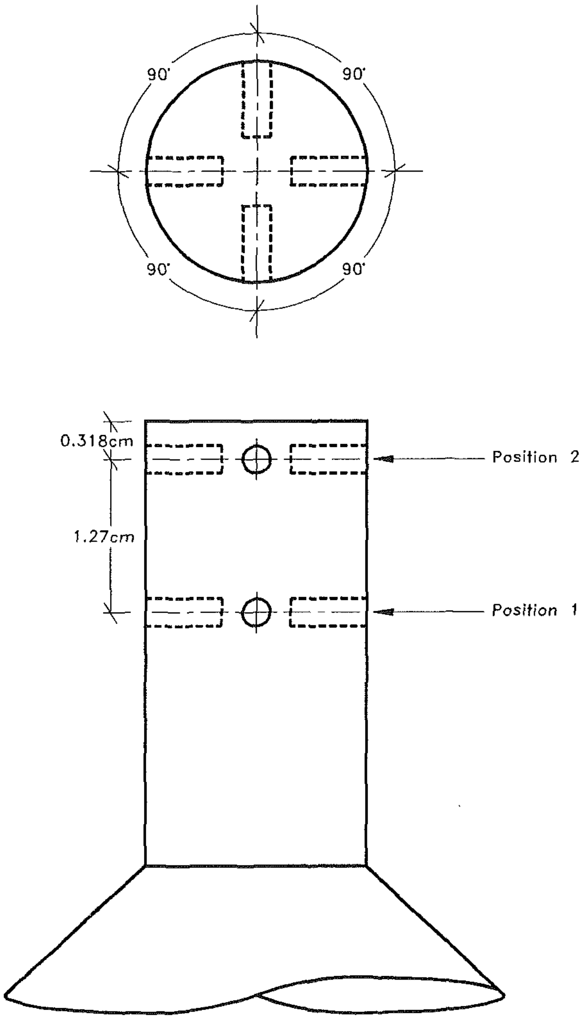

Fig. 2 Detail of the tip of the heated cylinder showing the two thermocouple positions used to determine the heat flux and to extrapolate the tip temperature

$$q'' = (\Delta T_{12} * k_{Cu})/L_{12} \tag{1}$$

where ΔT_{12} is the temperature difference between thermocouple positions one and two, k_{Cu} is the thermal conductivity of copper, and L_{12} is the distance between thermocouple positions one and two (1.27 cm). Position one is located 1.588 cm below the tip, while position two is located 0.318 cm below the tip. Each position has three thermocouples, and the three temperatures are averaged to give the temperature for that position. The tip temperature can be extrapolated from the measured temperatures, but this value was not an object of attention in the present investigation. The fourth hole at position one is occupied by a thermocouple used as the sensor by the electronic temperature controller. The estimated error in the heat flux calculation, from error propagation analysis, is 3.6 percent (Bockwoldt, 1990). This analysis was confirmed by two quasi-steady-state heat balance tests, which showed discrepancies of 0.5 and 4.8 percent between the energy input to the system and the energy output (including losses to the ambient). Therefore, both analysis and experiment indicate that the expected error in the heat flux measurements should be less than 5 percent.

Fifty-four experimental observations of the critical heat flux were made for five borosilicate glass tubes having inner diameters of 1.6, 3.0, 4.7, 7.5, and 14.4 cm. The outer edges of the glass tubes were sealed to the PTFE splash shield with silicone marine sealant and allowed to cure for 24 hours. Silicone rubber is stable in boiling water and served as a suitable sealant for this purpose. To begin an observation, the heated tip was immersed in a small amount of degassed and distilled water, and the surface was then heated to approximately 105°C to allow the water to reach saturation temperature. Once saturated conditions were reached, degassed and distilled water at saturation temperature was added to give the desired immersion depth for the experiment, and the temperature set point on the electronic controller was reprogrammed to 200°C. This value is well above the temperature expected at the critical heat flux, about 120°C to 130°C, but low enough to protect the apparatus. The autotransformer supplying the heaters was adjusted to deliver a moderate power of approximately 700 W so that the temperature of the cylinder would increase only slowly until burnout occurred. Since the cylinder heated up only gradually, nearly steady-state heat rates and temperatures prevail at any instant until the critical heat flux is reached. The cylinder tip heats up rapidly at the crisis, and the controller will respond almost immediately to the rapid rise in temperature by de-energizing the heaters. As the cylinder was heated, the immersion depth was maintained manually by adding saturated makeup water when needed. The immersion depths were measured only after burnout when vigorous boiling had subsided.

The heat transfer surface was not cleaned during this investigation because surface cleaning initially depresses the effectiveness of boiling. Performance returns gradually as the surface is used. Cleaning the surface between experimental runs also was not practicable because of the time required for the sealant to cure after the boiling tube was replaced. Our procedure was to clean the heated surface initially with acetone and commercial detergents and then allow it to age through nine repeated runs during which the critical heat flux increased by one-third before reaching a steady asymptotic value. The reported data were all taken in this aged condition. To preserve the heated surface, it was kept immersed in distilled water between experiments.

As verified by probing the fluid with a manually scanned thermocouple, the vigorous boiling at the tip was sufficient to keep the liquid well mixed and saturated in all the pools except the 14.4 cm tube. Between 3 and 6°C of subcooling was initially present in the largest tube. In order to overcome this subcooling problem, the 14.4 cm tube was wrapped in mineral fiber in-

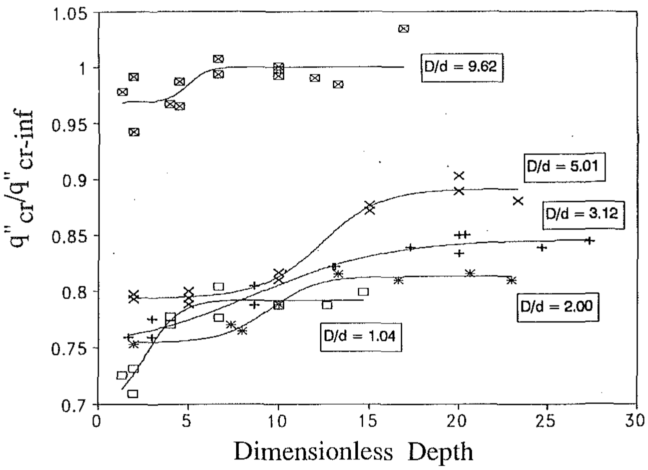

Fig. 3 The variation of the dimensionless critical heat flux (q''_{cr}/q''_{cr-inf}) with dimensionless immersion depth (*H/d*) for a series of water-filled tubes of indicated dimensionless diameter ratios (*D/d*) with data points identified as follows: $D/d = 1.04$ (□), $D/d = 2.00$ (*), $D/d = 3.12$ (+), $D/d = 5.01$ (×), and $D/d = 9.62$ (⊠)

sulation, and the experiments were repeated. Insulation alone was insufficient to overcome the subcooling entirely, but only 1 to 2°C of subcooling remained. Available data on burnout during subcooled boiling from Elkassabgi and Lienhard (1988) suggest that the critical heat flux is linearly dependent upon the degree of subcooling. Applying this principle to data for two different levels of subcooling allows us to extrapolate the critical heat flux to saturated conditions. This procedure yields an extrapolated asymptotic maximum critical heat flux of 2.27 MW/m^2 for the 14.4 cm tube. This maximum heat flux for the largest tube our experiment could accommodate is the best available estimate of the limiting value for an infinite pool.

Experimental Results

Three different flow regimes were observed for the vapor rising above the heater. In the smallest tube, 1.6 cm diameter, which was only slightly larger than the 1.5-cm-dia heated surface, the steam exhibited chugging or slug flow. The steam was in nearly constant contact with the tube wall in the form of vapor slugs competing for space with the water above the heater. The other two flow regimes may be characterized as "interactive" and "noninteractive." In the noninteractive regime, a steady train of bubbles rises from the heater to the surface without touching the tube wall. These bubbles drive a roughly toroidal flow in the liquid. The interactive flow regime occurs when the depth is large compared to the diameter. As the pool is made deeper, the almost symmetric toroidal flow becomes unstable, and portions of the flow grow in size and sweep entirely across the heater. This forces the relatively long train of bubbles or stream of vapor to attach to the tube wall, and the location of the attachments shifts unpredictably as different sectors of the circulation grow and decline. The largest tube exhibited noninteractive flows for all immersion depths, while the intermediate diameter tubes only experienced the noninteractive flow when the immersion depths were small.

Figure 3 shows the experimental data and the regression lines of the form:

$$q''_{cr}/q''_{cr-inf} = A_1/(A_2 \exp(A_3(A_4 - H/d)) + 1) + A_5 \qquad (2)$$

where *H/d* is the dimensionless immersion depth and q''_{cr-inf} is the postulated limiting heat flux into an infinite pool as estimated by the data for the 14.4 cm tube. Each of the five regression lines has rms deviations of less than 3 percent. The five A_i parameters were determined using a nonlinear least-squares fitting routine from Bevington (1969). The values for the parameters are available from Bockwoldt (1990). The data shown for the 14.4 cm tube have been adjusted to correct for the influence of subcooling during the test. The sigmoidal functional form was selected because it has the appropriate shape to represent the transition to a limiting asymptotic maximum, $q''_{cr,max}$, as the immersion depth increases for a fixed diameter. Each curve represents the dependence on immersion depth for an individual tube very accurately, and as a group, the curves closely reproduce the influence of pool diameter as well. Since there is no unified physical model to describe both influences, no attempt was made to generate a single surface that represents all diameters and depths together since it is not clear that such a surface would be more useful than the family of curves given here.

As a group, the curves show a monotonic increase in q''_{cr} with tube size with one exception. The curve for the smallest tube does cross over the lines for two of the larger tubes, but only at intermediate immersion depths. This is probably because of a fundamental difference in flow regimes. For the larger tubes, even though the details of the flow varied, the principal mode of enhancement always induced roughly toroidal recirculating flows from the sides. Such flows are never very important for the smallest tube, which is hardly larger than the heater. Instead, a slugging flow prevails in the smallest tube, and when the water is shallow, vapor bubbles can lift and hold the entire column of liquid, starving the surface and promoting burnout. When the liquid is deeper, the vapor bubble elongates to escape and the liquid column collapses, impacting the surface with strong induced currents. This complicated pattern that washes the surface forcefully increases abruptly as the dimensionless depth reaches about 5:1, but little further increase is seen since it is impossible for the toroidal recirculating flows to form in the small tube. Interestingly, in the intermediate range of immersion depths, the smallest tube actually outperforms tubes more than three times larger because of the strong agitation as elevated columns of liquid fall on the surface. The two regimes of flow, slugging flow probably dominated by surface tension effects at smaller pool diameters, and recirculating flow dominated by viscous effects at larger diameters, further discourage attempting a unified model. Despite these complications, the overall behavior for every tube is an increase in the critical heat flux from a minimum at shallow immersion to an asymptotic maximum at greater depth. Even the smallest tube follows this trend, albeit with a steeper initial increase. Of equal significance, the critical heat flux increases monotonically with increasing pool diameter except for that part of the immersion depth range of the smallest tube where the abrupt increase in critical flux with immersion depth during slugging flow is unique.

For all the tubes studied, the critical heat flux approaches an asymptotic maximum as the immersion depth increases. Over the size range in this investigation, the increase is linear with increasing pool diameter, as given by the following regression equation:

$$q''_{cr,max}/q''_{cr-inf} = 0.025(D/d) + 0.766 \qquad (3)$$
$$\text{for } 1.04 < D/d < 9.62$$

where *D* is the tube inner diameter and *d* is the heater diameter. Equation (3) accounts for more than 99 percent of the variation in the data set, which is conclusively supportive of the linear relationship at smaller diameters; however, the linear relation must give way to an asymptotic trend at very large diameters.

Discussion and Conclusions

The data from the current investigation follow the same general trends as Lienhard and Elkassabgi's data for similar experiments with small heated cylinders. Both sets of data show similar trends with respect to increasing immersion depth and pool size. Lienhard and Elkassabgi also found a linear relationship between the sidewall separation and the maximum critical heat flux. They examined sidewall separations from 2.46 to 14.76 times the diameter of their horizontal cylindrical heaters, while this investigation examined pool diameters from 1.04 to 9.60 times the diameter of the flat plate heater. Lienhard and Elkassabgi expressed doubt that the linear dependence of the critical heat flux would persist down to a sidewall separation equal to the heater diameter; however, in this experiment, the linear relationship between maximum critical flux and pool diameter at deep immersion depths prevails over the entire range of pool sizes examined.

Because our apparatus limits the largest experimental diameter ratio and because it was not possible to maintain our largest bath precisely saturated, we did not determine the "infinite pool" critical heat flux for this geometry directly. However, since the critical heat flux curve for the 14.4 cm tube is already nearly flat, it must be close to the limiting value for an infinite pool with this geometry, and the minimal extrapolation necessary to estimate saturation conditions should also be reliable.

The experimental data strongly suggest that immersion depth and pool diameter do affect the critical heat flux in circular flat plate geometries. Furthermore, one can significantly enhance the critical heat flux, by as much as 25 percent for just the smaller tubes in the current investigation, by simply increasing the diameter and depth of the pool and allowing induced convective currents to sweep over the heater. Slugging flow causes an abrupt increase in the critical heat flux with immersion depth when the pool diameter is nearly equal to the heater diameter, but when the pool is as little as twice the heater diameter, induced recirculating flows increase the critical heat flux smoothly as the depth of the liquid is increased. Also, when the tube diameter is much larger than the heater diameter, the immersion depth has little effect on the critical heat flux. For intermediate pool sizes, a pronounced and steady increase was observed as the immersion depth was increased, with up to 30 cm of water being required to reach the maximum critical heat flux for the midrange of tube sizes.

While little theoretical justification is available at present, the observational evidence is clear that increasing the pool diameter and/or the immersion depth can enhance the heat transfer within limits. The enhancement is accentuated when the pool diameter and/or immersion depth are initially so small that the induced convective cells are constricted. Then, increasing the immersion depth or pool diameter promotes more vigorous convection unimpeded by the confining effects of the walls and the free surface or by the viscous effects of the walls. It also appears that interactions between the escaping steam and the tube wall play a role in the immersion depth effects observed. In most cases critical heat flux increased most strongly with increasing immersion depth only after the steam column began to interact with the tube wall. This occurred when the immersion depth was a few times larger than the diameter of the tube. Once the surrounding liquid volume is large enough, the walls and free surface do not significantly confine the convective cells and there will be no further appreciable increase in the critical heat flux with continued extension of the free volume. This limiting, "infinite pool" condition has also been observed by Lienhard and Elkassabgi for the cylindrical geometry.

References

Bevington, P. R., 1969, *Data Reduction and Error Analysis for the Physical Sciences*, McGraw-Hill, New York.

Bockwoldt, T. S., 1990, "Induced Convective Enhancement of the Critical Heat Flux for Partially Heated Surfaces in Pool Boiling," Master's Thesis, Georgia Institute of Technology, Atlanta, GA.

Costello, C. P., Bock, C. O., and Nichols, C. C., 1965, "A Study of Induced Convective Effects on Saturated Pool Boiling Burnout," *CEP Symposium Series*, No. 59, Vol. 61, pp. 271–280.

Elkassabgi, Y., and Lienhard, J. H., 1987, "Sidewall and Immersion-Depth Effects on Pool Boiling Burnout for Horizontal Cylindrical Heaters," ASME JOURNAL OF HEAT TRANSFER, Vol. 109, pp. 1055–1057.

Elkassabgi, Y., and Lienhard, J. H., 1988, "Influences of Subcooling on Burnout of Horizontal Cylindrical Heaters," ASME JOURNAL OF HEAT TRANSFER, Vol. 110, pp. 479–486.

Lienhard, J. H., and Keeling, K. B., Jr., 1970, "An Induced-Convection Effect Upon the Peak-Boiling Heat Flux," ASME JOURNAL OF HEAT TRANSFER, Vol. 93, pp. 1–5.

Westwater, J. W., Hwalek, J. J., and Irving, M. E., 1986, "Suggested Standard Method for Obtaining Boiling Curves by Quenching," *Ind. Eng. Chem. Fund.*, Vol. 25, No. 4, pp. 685–692.

Melting of Metals Driven by Natural Convection in the Melt: Influence of Prandtl and Rayleigh Numbers

D. Gobin[1] **and C. Bénard**[1]

1 Introduction

The analysis of the melting process of a pure material from an isothermal vertical wall has motivated a significant number of experimental and numerical studies in the last ten years. When the only external field is gravity and if no capillary or solutal effects have to be taken into account, the melting process is controlled by thermally induced natural convection in the liquid phase (see the review by Viskanta, 1985).

Most of the available experimental and numerical results have been obtained for the melting of phase-change materials (PCMs) with a high Prandtl number liquid phase; experiments were performed with pure organic PCMs ($\Pr \approx 50$) that have well-known physical properties and allow precise measurements of the temperature field and interface position. Since the first attempt to solve numerically the complete set of equations by Sparrow et al. (1977), numerical simulations of a melting isothermal solid have been successfully compared to experimental data (Ho and Viskanta, 1984; Bénard et al., 1985). Recently a comprehensive scaling analysis of the problem has been presented by Jany and Bejan (1988).

Detailed experimental results concerning melting of PCMs with a low Prandtl number (metals) have appeared only recently and comparisons with numerical solutions (Webb and Viskanta, 1986; Lacroix, 1989; Bénard and Gobin, 1989) show qualitative agreement, but the influence of the governing parameters on the kinetics of the melting process has not been clearly analyzed. The purpose of this paper is to provide results on the heat transfer characteristics of the system over a wide range of Ra and Pr numbers in the low Pr domain.

2 Problem Definition and Solution Procedure

A two-dimensional rectangular enclosure (height H, width L) is filled with a pure metal initially in the solid phase at the fusion temperature $T_0 = T_F$. At time $t = 0$, the temperature of one vertical wall is raised at $T_1 > T_F$, while the opposite wall is maintained at T_0 (no heat conduction in the solid phase). When melting proceeds in the enclosure, natural convection develops in the melt, causing heat transfer at the interface to be nonuniform, and the melting front moves faster at the top of the cavity. The coupled problem to be solved is described by the set of equations governing natural convection in the nonrectangular liquid domain and by the local energy balance

---

[1] Fluides, Automatique et Systèmes Thermiques, Laboratoire de l'Université Pierre et Marie Curie, Orsay, France.

Contributed by the Heat Transfer Division of the AMERICAN SOCIETY OF MECHANICAL ENGINEERS. Manuscript received by the Heat Transfer Division July 1990; revision received July 1991. Keywords: Liquid Metals, Natural Convection, Phase-Change Phenomena.

tionship between the sidewall separation and the maximum critical heat flux. They examined sidewall separations from 2.46 to 14.76 times the diameter of their horizontal cylindrical heaters, while this investigation examined pool diameters from 1.04 to 9.60 times the diameter of the flat plate heater. Lienhard and Elkassabgi expressed doubt that the linear dependence of the critical heat flux would persist down to a sidewall separation equal to the heater diameter; however, in this experiment, the linear relationship between maximum critical flux and pool diameter at deep immersion depths prevails over the entire range of pool sizes examined.

Because our apparatus limits the largest experimental diameter ratio and because it was not possible to maintain our largest bath precisely saturated, we did not determine the "infinite pool" critical heat flux for this geometry directly. However, since the critical heat flux curve for the 14.4 cm tube is already nearly flat, it must be close to the limiting value for an infinite pool with this geometry, and the minimal extrapolation necessary to estimate saturation conditions should also be reliable.

The experimental data strongly suggest that immersion depth and pool diameter do affect the critical heat flux in circular flat plate geometries. Furthermore, one can significantly enhance the critical heat flux, by as much as 25 percent for just the smaller tubes in the current investigation, by simply increasing the diameter and depth of the pool and allowing induced convective currents to sweep over the heater. Slugging flow causes an abrupt increase in the critical heat flux with immersion depth when the pool diameter is nearly equal to the heater diameter, but when the pool is as little as twice the heater diameter, induced recirculating flows increase the critical heat flux smoothly as the depth of the liquid is increased. Also, when the tube diameter is much larger than the heater diameter, the immersion depth has little effect on the critical heat flux. For intermediate pool sizes, a pronounced and steady increase was observed as the immersion depth was increased, with up to 30 cm of water being required to reach the maximum critical heat flux for the midrange of tube sizes.

While little theoretical justification is available at present, the observational evidence is clear that increasing the pool diameter and/or the immersion depth can enhance the heat transfer within limits. The enhancement is accentuated when the pool diameter and/or immersion depth are initially so small that the induced convective cells are constricted. Then, increasing the immersion depth or pool diameter promotes more vigorous convection unimpeded by the confining effects of the walls and the free surface or by the viscous effects of the walls. It also appears that interactions between the escaping steam and the tube wall play a role in the immersion depth effects observed. In most cases critical heat flux increased most strongly with increasing immersion depth only after the steam column began to interact with the tube wall. This occurred when the immersion depth was a few times larger than the diameter of the tube. Once the surrounding liquid volume is large enough, the walls and free surface do not significantly confine the convective cells and there will be no further appreciable increase in the critical heat flux with continued extension of the free volume. This limiting, "infinite pool" condition has also been observed by Lienhard and Elkassabgi for the cylindrical geometry.

References

Bevington, P. R., 1969, *Data Reduction and Error Analysis for the Physical Sciences*, McGraw-Hill, New York.

Bockwoldt, T. S., 1990, "Induced Convective Enhancement of the Critical Heat Flux for Partially Heated Surfaces in Pool Boiling," Master's Thesis, Georgia Institute of Technology, Atlanta, GA.

Costello, C. P., Bock, C. O., and Nichols, C. C., 1965, "A Study of Induced Convective Effects on Saturated Pool Boiling Burnout," *CEP Symposium Series*, No. 59, Vol. 61, pp. 271–280.

Elkassabgi, Y., and Lienhard, J. H., 1987, "Sidewall and Immersion-Depth Effects on Pool Boiling Burnout for Horizontal Cylindrical Heaters," ASME JOURNAL OF HEAT TRANSFER, Vol. 109, pp. 1055–1057.

Elkassabgi, Y., and Lienhard, J. H., 1988, "Influences of Subcooling on Burnout of Horizontal Cylindrical Heaters," ASME JOURNAL OF HEAT TRANSFER, Vol. 110, pp. 479–486.

Lienhard, J. H., and Keeling, K. B., Jr., 1970, "An Induced-Convection Effect Upon the Peak-Boiling Heat Flux," ASME JOURNAL OF HEAT TRANSFER, Vol. 93, pp. 1–5.

Westwater, J. W., Hwalek, J. J., and Irving, M. E., 1986, "Suggested Standard Method for Obtaining Boiling Curves by Quenching," *Ind. Eng. Chem. Fund.*, Vol. 25, No. 4, pp. 685–692.

Melting of Metals Driven by Natural Convection in the Melt: Influence of Prandtl and Rayleigh Numbers

D. Gobin[1] **and C. Bénard**[1]

1 Introduction

The analysis of the melting process of a pure material from an isothermal vertical wall has motivated a significant number of experimental and numerical studies in the last ten years. When the only external field is gravity and if no capillary or solutal effects have to be taken into account, the melting process is controlled by thermally induced natural convection in the liquid phase (see the review by Viskanta, 1985).

Most of the available experimental and numerical results have been obtained for the melting of phase-change materials (PCMs) with a high Prandtl number liquid phase; experiments were performed with pure organic PCMs ($\mathrm{Pr} \approx 50$) that have well-known physical properties and allow precise measurements of the temperature field and interface position. Since the first attempt to solve numerically the complete set of equations by Sparrow et al. (1977), numerical simulations of a melting isothermal solid have been successfully compared to experimental data (Ho and Viskanta, 1984; Bénard et al., 1985). Recently a comprehensive scaling analysis of the problem has been presented by Jany and Bejan (1988).

Detailed experimental results concerning melting of PCMs with a low Prandtl number (metals) have appeared only recently and comparisons with numerical solutions (Webb and Viskanta, 1986; Lacroix, 1989; Bénard and Gobin, 1989) show qualitative agreement, but the influence of the governing parameters on the kinetics of the melting process has not been clearly analyzed. The purpose of this paper is to provide results on the heat transfer characteristics of the system over a wide range of Ra and Pr numbers in the low Pr domain.

2 Problem Definition and Solution Procedure

A two-dimensional rectangular enclosure (height H, width L) is filled with a pure metal initially in the solid phase at the fusion temperature $T_0 = T_F$. At time $t = 0$, the temperature of one vertical wall is raised at $T_1 > T_F$, while the opposite wall is maintained at T_0 (no heat conduction in the solid phase). When melting proceeds in the enclosure, natural convection develops in the melt, causing heat transfer at the interface to be nonuniform, and the melting front moves faster at the top of the cavity. The coupled problem to be solved is described by the set of equations governing natural convection in the nonrectangular liquid domain and by the local energy balance

---

[1] Fluides, Automatique et Systèmes Thermiques, Laboratoire de l'Université Pierre et Marie Curie, Orsay, France.

Contributed by the Heat Transfer Division of the AMERICAN SOCIETY OF MECHANICAL ENGINEERS. Manuscript received by the Heat Transfer Division July 1990; revision received July 1991. Keywords: Liquid Metals, Natural Convection, Phase-Change Phenomena.

equation at the moving interface. The fluid flow is supposed to be laminar and the classical assumptions of Newtonian, incompressible fluid with the Boussinesq approximation are used. The density variation upon melting is neglected, the solid-liquid interface is assumed to be a smooth surface, and melting occurs at a fixed temperature T_F.

The solution procedure uses a front tracking method based on the classical quasi-steady and quasi-stationary hypotheses, which allows us to immobilize the front to solve the fluid flow problem and the interface motion separately, and to look for a steady-state solution of the natural convection equations in the melt.

Under the assumptions mentioned above, the complete set of equations is then:

in the liquid cavity:

$$\nabla\bullet\mathbf{V}=0 \tag{1}$$

$$(\mathbf{V}\bullet\nabla)\mathbf{V}=\nabla^2\mathbf{V}-\nabla P+\mathrm{Gr}_H\theta\mathbf{k} \tag{2}$$

$$(\mathbf{V}\bullet\nabla)\theta=\frac{1}{\mathrm{Pr}}\,\nabla^2\theta \tag{3}$$

at the interface, the energy balance equation:

$$\nabla\theta\bullet\mathbf{n}=\rho^*\,\frac{\partial c}{\partial\tau}. \tag{4}$$

The variables are set in a dimensionless form using the height H of the enclosure and the kinematic viscosity ν. The parameters of the problem are $\mathrm{Ste}=C_P\Delta T/L_F$, $\mathrm{Pr}=\nu/\alpha$, and $\mathrm{Gr}_H=g\beta\Delta TH^3/\nu^2$. $\partial c/\partial\tau$ ($\tau=\mathrm{FoSte}$) is the local velocity of the melting front along $\mathbf{n}$, the normal vector to the interface. Dirichlet thermal boundary conditions are taken on the vertical wall and at the interface, and the horizontal walls are adiabatic. In the liquid cavity, zero velocity dynamic boundary conditions are considered at the four walls.

The system of nonlinear Eqs. (1)–(3) governing natural convection in the irregular liquid cavity is transformed using an algebraic transformation of coordinates (Faghri et al., 1984). This version of the numerical code is based on the method presented by Gadgil and Gobin (1984), including recent improvements of the coordinate transformation (Manseur, 1988). The transformed equations are discretized on a square computational domain, using the hybrid differencing scheme (Patankar, 1980). The SIMPLE algorithm is used to solve the pressure-velocity coupling and the solution of the discretized equations is obtained with an ADI procedure. The coordinate transformation introduces the spatial derivatives of the dimensionless interface position $C(z)$ up to the third order and cross terms in the calculation of the heat fluxes at the surface of the control volumes, leading to a nine-point formulation.

With the converged temperature and velocity fields in the fixed liquid domain, the local heat transfer is calculated at the interface. As the cold wall is considered to be at the fusion temperature, *the melting front velocity is known explicitly*. The melting rate is assumed to be constant during a given time step and a new position of the melting front is obtained, defining new coordinate transformation coefficients.

The calculation is initialized with a rectangular cavity of width δ and the corresponding time given by the Neumann solution of the one-dimensional Stefan problem. For a given Rayleigh number, this solution is relevant up to a maximum width δ of the liquid cavity. In the absence of a criterion to determine this limit, a number of numerical calculations is rectangular enclosures have been performed for different aspect ratios at a given Ra_H. It was found that the pure conduction solution was still accurate for an aspect ratio $H/\delta=8$ at $\mathrm{Ra}_H\approx10^5$, and $H/\delta=12.5$ at $\mathrm{Ra}_H\approx10^6$.

The grid defined on the square computational domain is irregularly spaced in order to provide better resolution of the velocity and temperature gradients at the solid walls. Numerical tests concerning the 23×23 irregular grid used in our computations and a successful comparison with the experimental data on the melting of tin (Wolff and Viskanta, 1987) are presented elsewhere (Bénard and Gobin, 1989).

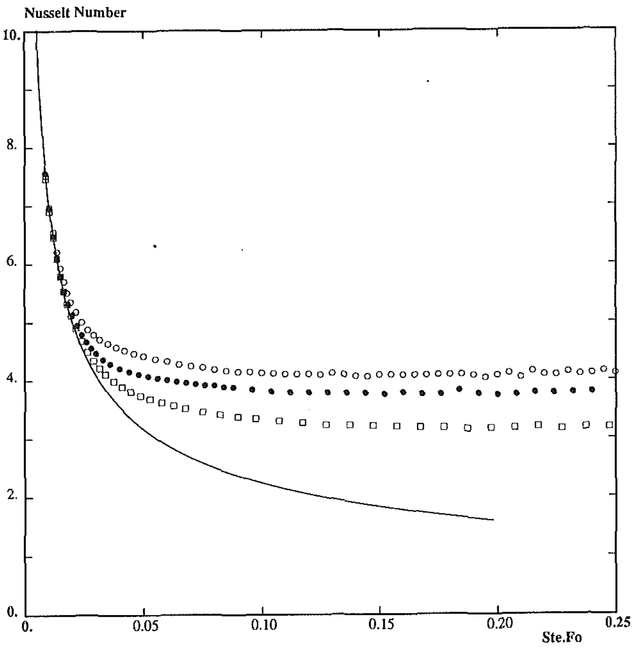

Fig. 1 Time evolution of the average Nusselt number at the interface; influence of the Rayleigh and Prandtl numbers; Ste = 0.01, *A* = 0.5:

— pure conduction
□ RaPr = 2000, Pr = 0.02, Ra = 10^5
○ RaPr = 5000, Pr = 0.02, Ra = 2.5×10^5
● RaPr = 5000, Pr = 0.05, Ra = 10^5

3 Heat Transfer Results and Discussion

The purpose of this section is to correlate the heat transfer at the interface to the dimensionless parameters of the problem. Recent numerical studies in the $\mathrm{Pr}\ll1$ domain (Webb and Viskanta, 1986; Lacroix, 1989) have considered the influence of the Rayleigh number on the Nusselt number at the melting front at Pr = 0.021. A correlation of the classical form

$$\overline{\mathrm{Nu}}=C\mathrm{Ra}_H^m \tag{5}$$

has been proposed for developed natural convection in the melt, with $C=0.157$ and $m=0.262$ (Lacroix) or 0.263 (Webb).

To the authors' knowledge, the influence of Pr is not documented in the previous studies on melting of metals; this is the motivation of this study. In order to reduce the number of simulations, some parameters are kept constant: Ste = 0.01 and $A=0.5$. The order of magnitude of Pr is typically $\mathrm{Pr}\approx10^{-2}$ and Ra_H is in the range 10^4–10^6. In a first set of simulations, Pr = 0.020 and $\mathrm{Ra}_H=2.5\times10^4$, 10^5, 2.5×10^5, and 10^6. In the second set of calculations, $\mathrm{Ra}_H=10^5$, and several values of Pr are considered (Pr = 0.01, 0.02, 0.05, and 0.10).

The time evolution of the average Nusselt number at the interface is displayed on Fig. 1 for selected values of Ra and Pr, and compared to the analytical Neumann solution of the Stefan problem (approximately $\overline{\mathrm{Nu}}=1/\sqrt{2\tau}$). It appears clearly on the figure that *the initialization of the process and the choice of the fusion time steps give a good description of the initial conductive regime*. Natural convection in the liquid phase progressively dominates the melting process and the $\overline{\mathrm{Nu}}$ curve separates from the Neumann solution. After a transition period, $\overline{\mathrm{Nu}}$ finally reaches a constant value. Figure 1 shows this evolution for three different sets of parameters:

1 As expected, at a given Pr number (Pr = 0.02), the departure from the pure conduction solution occurs at earlier

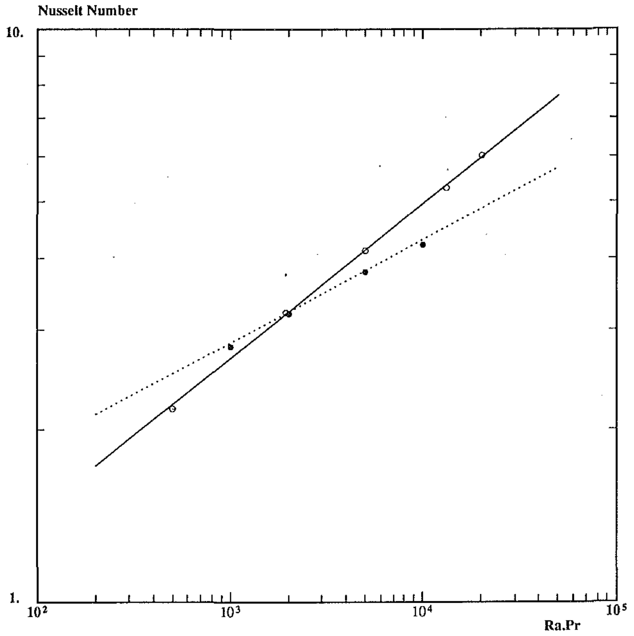

Fig. 2 Heat transfer correlations: $\overline{\mathrm{Nu}}$ versus (RaPr); separate influence of Ra and Pr (Eq. (6)):
—○— Pr = const (Pr = 0.02)
··· ● ··· Ra = const (Ra = 10^5)

times, and the melting rate is more important, for higher Ra numbers. This behavior has been shown and commented in previous studies.

2 At a given Rayleigh number ($\mathrm{Ra}_H = 10^5$), the calculations show a significant influence of the Pr number. Higher Prandtl numbers result in earlier onset of the convective regime and higher heat transfer. This influence is not taken into account in the correlations presented earlier, which considered the Ra number as the only independent parameter.

3 $\overline{\mathrm{Nu}}$ is more sensitive to the variations of Ra; as a consequence, the evolution is different for the same value of the dimensionless group RaPr (here, RaPr = 5000).

If we refer to the scaling theory presented by Bejan (1984) for natural convection in rectangular enclosures at low Pr, and applied to melting processes by Jany and Bejan (1988), the influence of Pr on the Nusselt number in the fully developed convection regime should appear through the parameter (RaPr) since the scale for $\overline{\mathrm{Nu}}$ is $(\mathrm{RaPr})^{1/4}$. The results of the two sets of simulations (constant Pr = 0.02, constant Ra = 10^5) are plotted on a logarithmic scale on Fig. 2 as a function of (RaPr) in the range 500 to 20,000. The results show that, in the domain of Ra and Pr numbers considered in this study, the behavior of $\overline{\mathrm{Nu}}$ cannot be described only by the parameter RaPr. Separate influence of Pr and Ra appears through different exponents in the following correlation:

$$\overline{\mathrm{Nu}} = 0.29\ \mathrm{Ra}^{0.27}\mathrm{Pr}^{0.18} \quad (6)$$

which fits our numerical results by less than 2 percent. For the particular case Pr = 0.02, the $\overline{\mathrm{Nu}}$-Ra_H correlation:

$$\overline{\mathrm{Nu}} = 0.14\mathrm{Ra}_H^{0.27} \quad (7)$$

is in very good agreement with the relation proposed by Webb or Lacroix (Eq. (5)) for a similar value of the Prandtl number (Pr = 0.021); the difference is less than 3 percent in the range $10^4 < \mathrm{Ra} < 10^6$.

However, the relevance of the (RaPr) group in the analysis of this problem has to be considered more carefully. A plot of the time evolution of $\overline{\mathrm{Nu}}$ normalized with the scale $\mathrm{Ra}^{0.27}$ $\mathrm{Pr}^{0.18}$ shows that the transition from the initial conduction regime to the final convection regime is a direct function of the parameter (RaPr). Moreover, different simultions corresponding to the same value of RaPr (for $\mathrm{Pr}_1 \neq \mathrm{Pr}_2$ and $\mathrm{Ra}_1 \neq \mathrm{Ra}_2$) present the same evolution. This is verified for RaPr = 2000 and RaPr = 5000. This result indicates that the transient evolution in the transition regime depends on a new scale based on the dimensionless group (RaPr). A fit based on our numerical simulations for different values of Ra and Pr leads to scale the dimensionless time using $\tau^{0.75}$ $(\mathrm{RaPr})^{0.36}$. The time evolution of $\overline{\mathrm{Nu}}$ using these scales is represented on Fig. 3 for RaPr ranging from 1000 to 10,000. It can be seen on the figure that the results cluster on a unique curve.

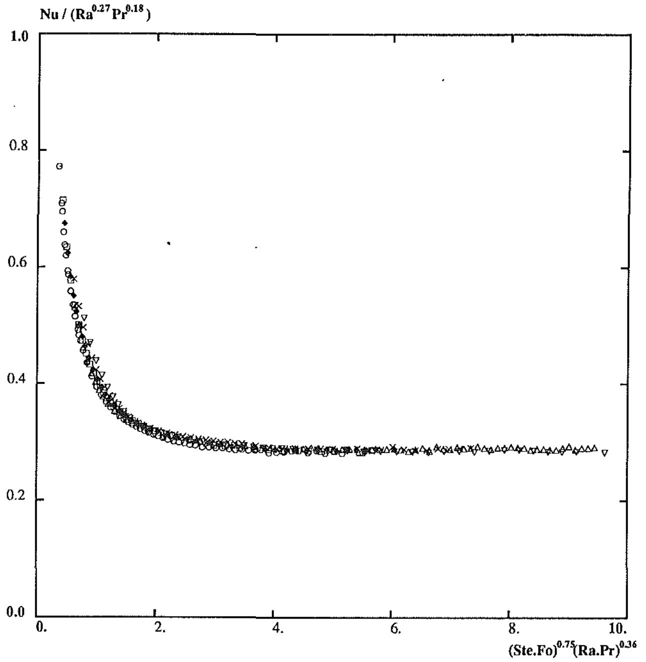

Fig. 3 Time evolution of the average Nusselt number at the interface: $\overline{\mathrm{Nu}}/\mathrm{Ra}^{0.27}$ $\mathrm{Pr}^{0.18}$ as a function of $\tau^{0.75}(\mathrm{Ra}\cdot\mathrm{Pr})^{0.36}$
○ RaPr = 1000, Pr = 0.01
□ RaPr = 1926, Pr = 0.0157
◆ RaPr = 2000, Pr = 0.02
△ RaPr = 5000, Pr = 0.02
× RaPr = 5000, Pr = 0.05
▽ RaPr = 10,000, Pr = 0.10

The time evolution of the heat transfer at the interface may be described as follows:

1 For small values of τ (pure conduction regime), the Nusselt number is given by $\overline{\mathrm{Nu}}_0 = 1/\sqrt{2\tau}$.

2 For high values of τ (convection regime) $\overline{\mathrm{Nu}}$ reaches the constant value $\overline{\mathrm{Nu}}_\infty$ (Eq. (6)) (we assume that there is no contact with the cold wall).

3 During the transition regime, the time scale of the $\overline{\mathrm{Nu}}$ evolution is a function of RaPr.

Those considerations may be used to propose a correlation for the $\overline{\mathrm{Nu}}$ versus τ evolution during the whole melting process, if the interface does not reach the cold wall. Use of the canonical expression recommended by Churchill (1983) (referenced by Jany and Bejan, 1988) leads to the general expression:

$$\overline{\mathrm{Nu}}(\tau) = \overline{\mathrm{Nu}}_\infty + \overline{\mathrm{Nu}}_0\left[1 - \left(1 + \frac{1}{(c_1(\mathrm{RaPr})^m\tau^n)^2}\right)^{-1/2}\right] \quad (8)$$

which verifies $\overline{\mathrm{Nu}} \rightarrow \overline{\mathrm{Nu}}_0$ if $\tau \rightarrow 0$ and $\overline{\mathrm{Nu}} \rightarrow \overline{\mathrm{Nu}}_\infty$ if $\tau \rightarrow \infty$, provided that $n > 0$.

The three constants c_1, m, and n have been determined from our numerical results using a classical multivariable conjugate gradient minimization method (routine ZXCGR of the IMSL library): $c_1 = 1$, $m = 0.36$, $n = 0.75$. The correlation resulting from Eq. (8) with these values is plotted on Fig. 4 and compared to the numerical results for different values of Ra and Pr. The excellent agreement shows the ability of relation (8) to represent

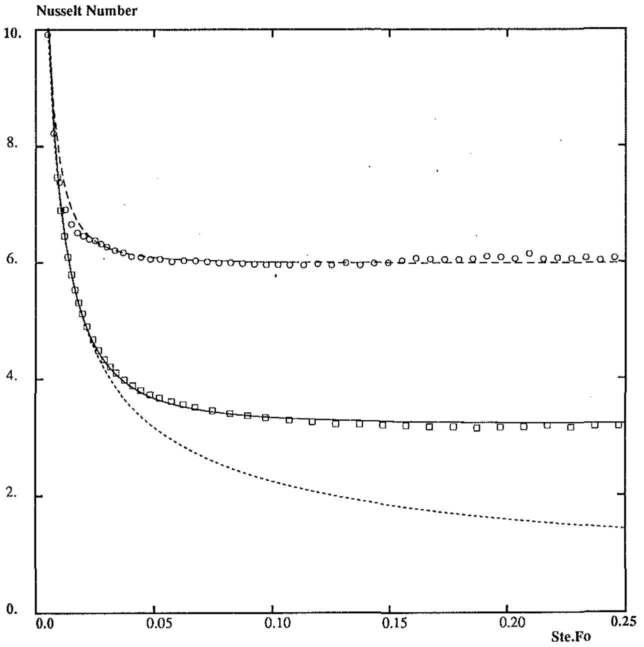

Fig. 4 Comparison of the numerical results with correlation (8):
····· pure conduction
— RaPr = 1000, Pr = 0.01 (correlation)
□ (simulation)
— — — · RaPr = 10,000, Pr = 0.1 (correlation)
o (simulation)

the time evolution of the average Nusselt at the interface for the range Ra and Pr numbers considered in this study.

4 Conclusion

The problem of melting of an isothermal metal from a vertical wall is studied numerically and results concerning the heat transfer rate in the convection regime are presented for a range of Ra and Pr numbers, indicating a significant influence of the Pr number. The relevance of the dimensionless group (RaPr) for heat transfer correlations is not verified in the fully developed convection regime, since the Prandtl and Rayleigh numbers appear with different exponents. It is shown, however, that a scaling law, based on RaPr, may be used to describe the transition from the initial conduction regime to the final convection limit of the melting process. Finally a global correlation is given for the time evolution of the average heat transfer at the melting front.

As a conclusion, the present study shows that further investigation is required to determine the scaling laws for the melting problem in the low-Pr domain. The stability of such flows in deforming cavities is not clearly understood; studies concerning the onset of oscillatory convection due to three-dimensional effects should be made possible by the development of vectorial computers (e.g., Chuan and Schreiber, 1990).

References

Beckermann, C., and Viskanta, R., 1989, "Effect of Solid Subcooling on Natural Convection Melting of a Pure Metal," ASME JOURNAL OF HEAT TRANSFER, Vol. 111, pp. 416–424.

Bejan, A., 1984, *Convection Heat Transfer*, Wiley, New York.

Bénard, C., Gobin, D., and Martinez, F., 1985, "Melting in Rectangular Enclosures: Experiments and Numerical Simulations," ASME JOURNAL OF HEAT TRANSFER, Vol. 107, pp. 794–803.

Bénard, C., and Gobin, D., 1989, "Numerical Simulation of Melting Processes for Metals," *Multiphase Flow, Heat and Mass Transfer*, ASME HTD-Vol. 109, pp. 55–60.

Chuan, C. H., and Schreiber, W. C., 1990; "The Development of a Vectorized Computer Code for Solving Three-Dimensional Transient Heat Convection Problems," *Proc. Heat Transfer Conf.*, Portsmouth, United Kingdom, pp. 147–158.

Faghri, M., Sparrow, E. M., and Prata, A. T., 1984, "Finite-Difference Solutions of Convection-Diffusion Problems in Irregular Domains, Using a Nonorthogonal Coordinate Transformation," *Num. Heat Transfer*, Vol. 7, pp. 183–209.

Gadgil, A., and Gobin, D., 1984, "Analysis of Two-Dimensional Melting in Rectangular Enclosures in Presence of Convection," ASME JOURNAL OF HEAT TRANSFER, Vol. 106, pp. 20–26.

Ho, C. J., and Viskanta, R., 1984, "Heat Transfer During Melting From an Isothermal Vertical Wall," ASME JOURNAL OF HEAT TRANSFER, Vol. 106, pp. 12–19.

Jany, P., and Bejan, A., 1988, "Scaling Theory of Melting With Natural Convection in an Enclosure," *Int. J. Heat Mass Transfer*, Vol. 31, pp. 1221–1235.

Lacroix, M., 1989, "Computation of Heat Transfer During Melting of a Pure Substance From an Isothermal Wall," *Num. Heat Transfer*, Vol. 15-B, pp. 191–210.

Manseur, A., 1988, "Etude numérique de la convection naturelle dans des domaines irréguliers confinés," Thèse de l'Université Paris VI, France.

Patankar, S. V., 1980, *Numerical Heat Transfer and Fluid Flow*, Hemisphere Corp., New York.

Sparrow, E. M., Patankar, S. V., and Ramadhyami, S., 1977, "Analysis of Melting in the Presence of Natural Convection in the Melt Region," ASME JOURNAL OF HEAT TRANSFER, Vol. 99, pp. 520–526.

Viskanta, R., 1985, "Natural Convection in Melting and Solidification," in: *Natural Convection: Fundamentals and Applications*, S. Kakaç et al., eds., Hemisphere Corp., New York.

Webb, B. W., and Viskanta, R., 1986, "Analysis of Heat Transfer During Melting of a Pure Metal From an Isothermal Vertical Wall," *Num. Heat Transfer*, Vol. 9, pp. 539–558.

Wolff, F., and Viskanta, R., 1987, "Melting of a Pure Metal From a Vertical Wall," *Experimental Heat Transfer*, Vol. 1, pp. 17–30.

Solution of One- and Two-Phase Melting and Solidification Problems Imposed With Constant or Time-Variant Temperature and Flux Boundary Conditions

C. K. Hsieh[1] and Chang-Yong Choi[1]

Introduction

The solution of Stefan problems has been a subject of intense interest for years. Yet, there is still a lack of accurate methods for the solution of problems imposed with time-variant conditions. In fact, there has been an unsettled issue on the functional dependency of the interface position with time. It is thus the purpose of this paper to address this issue. In addition, the paper is offered to develop a unified approach for the solution of one- and two-phase melting or solidification problems in a semi-infinite domain imposed with constant or time-variant temperature or flux conditions.

Analysis

A semi-infinite medium with equal phase properties is taken for analysis. In the absence of convection, the solution is divided into two stages. In the premelt stage, sensible heat is added to the surface in order to raise its temperature to the phase-change temperature. Then the medium starts to melt and the melting stage begins, when the phase change starts at the surface and the interface position moves inward with time. For generality, a source and sink method is devised for the solution of this problem. This method is an extension of the Lightfoot method, which was originally developed for the so-

---

[1] Mechanical Engineering Department, University of Florida, Gainesville, FL 32611.

Contributed by the Heat Transfer Division of the AMERICAN SOCIETY OF MECHANICAL ENGINEERS. Manuscript received by the Heat Transfer Division November 30, 1990; revision received August 20, 1991. Keywords: Conduction, Moving Boundaries, Phase-Change Phenomena.

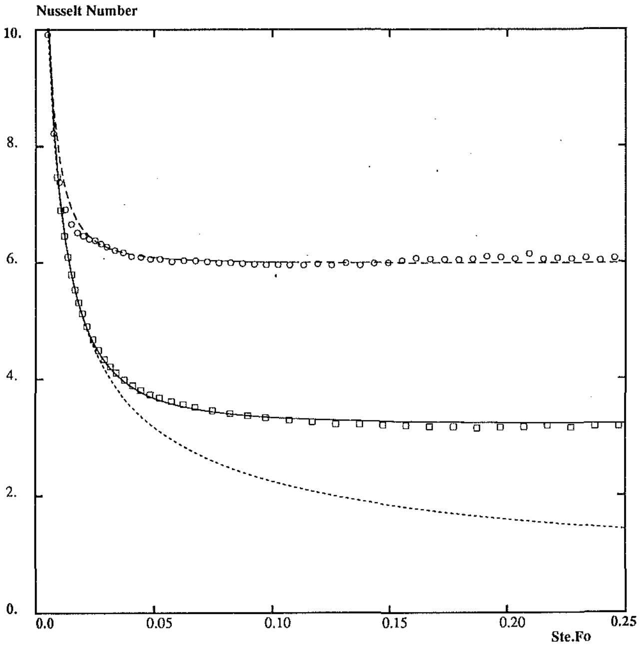

Fig. 4 Comparison of the numerical results with correlation (8):
····· pure conduction
— RaPr = 1000, Pr = 0.01 (correlation)
□ (simulation)
— — —· RaPr = 10,000, Pr = 0.1 (correlation)
○ (simulation)

the time evolution of the average Nusselt at the interface for the range Ra and Pr numbers considered in this study.

4 Conclusion

The problem of melting of an isothermal metal from a vertical wall is studied numerically and results concerning the heat transfer rate in the convection regime are presented for a range of Ra and Pr numbers, indicating a significant influence of the Pr number. The relevance of the dimensionless group (RaPr) for heat transfer correlations is not verified in the fully developed convection regime, since the Prandtl and Rayleigh numbers appear with different exponents. It is shown, however, that a scaling law, based on RaPr, may be used to describe the transition from the initial conduction regime to the final convection limit of the melting process. Finally a global correlation is given for the time evolution of the average heat transfer at the melting front.

As a conclusion, the present study shows that further investigation is required to determine the scaling laws for the melting problem in the low-Pr domain. The stability of such flows in deforming cavities is not clearly understood; studies concerning the onset of oscillatory convection due to three-dimensional effects should be made possible by the development of vectorial computers (e.g., Chuan and Schreiber, 1990).

References

Beckermann, C., and Viskanta, R., 1989, "Effect of Solid Subcooling on Natural Convection Melting of a Pure Metal," ASME JOURNAL OF HEAT TRANSFER, Vol. 111, pp. 416–424.

Bejan, A., 1984, *Convection Heat Transfer*, Wiley, New York.

Bénard, C., Gobin, D., and Martinez, F., 1985, "Melting in Rectangular Enclosures: Experiments and Numerical Simulations," ASME JOURNAL OF HEAT TRANSFER, Vol. 107, pp. 794–803.

Bénard, C., and Gobin, D., 1989, "Numerical Simulation of Melting Processes for Metals," *Multiphase Flow, Heat and Mass Transfer*, ASME HTD-Vol. 109, pp. 55–60.

Chuan, C. H., and Schreiber, W. C., 1990; "The Development of a Vectorized Computer Code for Solving Three-Dimensional Transient Heat Convection Problems," *Proc. Heat Transfer Conf.*, Portsmouth, United Kingdom, pp. 147–158.

Faghri, M., Sparrow, E. M., and Prata, A. T., 1984, "Finite-Difference Solutions of Convection-Diffusion Problems in Irregular Domains, Using a Nonorthogonal Coordinate Transformation," *Num. Heat Transfer*, Vol. 7, pp. 183–209.

Gadgil, A., and Gobin, D., 1984, "Analysis of Two-Dimensional Melting in Rectangular Enclosures in Presence of Convection," ASME JOURNAL OF HEAT TRANSFER, Vol. 106, pp. 20–26.

Ho, C. J., and Viskanta, R., 1984, "Heat Transfer During Melting From an Isothermal Vertical Wall," ASME JOURNAL OF HEAT TRANSFER, Vol. 106, pp. 12–19.

Jany, P., and Bejan, A., 1988, "Scaling Theory of Melting With Natural Convection in an Enclosure," *Int. J. Heat Mass Transfer*, Vol. 31, pp. 1221–1235.

Lacroix, M., 1989, "Computation of Heat Transfer During Melting of a Pure Substance From an Isothermal Wall," *Num. Heat Transfer*, Vol. 15-B, pp. 191–210.

Manseur, A., 1988, "Etude numérique de la convection naturelle dans des domaines irréguliers confinés," Thèse de l'Université Paris VI, France.

Patankar, S. V., 1980, *Numerical Heat Transfer and Fluid Flow*, Hemisphere Corp., New York.

Sparrow, E. M., Patankar, S. V., and Ramadhyami, S., 1977, "Analysis of Melting in the Presence of Natural Convection in the Melt Region," ASME JOURNAL OF HEAT TRANSFER, Vol. 99, pp. 520–526.

Viskanta, R., 1985, "Natural Convection in Melting and Solidification," in: *Natural Convection: Fundamentals and Applications*, S. Kakaç et al., eds., Hemisphere Corp., New York.

Webb, B. W., and Viskanta, R., 1986, "Analysis of Heat Transfer During Melting of a Pure Metal From an Isothermal Vertical Wall," *Num. Heat Transfer*, Vol. 9, pp. 539–558.

Wolff, F., and Viskanta, R., 1987, "Melting of a Pure Metal From a Vertical Wall," *Experimental Heat Transfer*, Vol. 1, pp. 17–30.

Solution of One- and Two-Phase Melting and Solidification Problems Imposed With Constant or Time-Variant Temperature and Flux Boundary Conditions

C. K. Hsieh[1] and Chang-Yong Choi[1]

Introduction

The solution of Stefan problems has been a subject of intense interest for years. Yet, there is still a lack of accurate methods for the solution of problems imposed with time-variant conditions. In fact, there has been an unsettled issue on the functional dependency of the interface position with time. It is thus the purpose of this paper to address this issue. In addition, the paper is offered to develop a unified approach for the solution of one- and two-phase melting or solidification problems in a semi-infinite domain imposed with constant or time-variant temperature or flux conditions.

Analysis

A semi-infinite medium with equal phase properties is taken for analysis. In the absence of convection, the solution is divided into two stages. In the premelt stage, sensible heat is added to the surface in order to raise its temperature to the phase-change temperature. Then the medium starts to melt and the melting stage begins, when the phase change starts at the surface and the interface position moves inward with time. For generality, a source and sink method is devised for the solution of this problem. This method is an extension of the Lightfoot method, which was originally developed for the so-

---

[1] Mechanical Engineering Department, University of Florida, Gainesville, FL 32611.

Contributed by the Heat Transfer Division of the AMERICAN SOCIETY OF MECHANICAL ENGINEERS. Manuscript received by the Heat Transfer Division November 30, 1990; revision received August 20, 1991. Keywords: Conduction, Moving Boundaries, Phase-Change Phenomena.

lution of solidification problems imposed with constant temperature conditions (Lightfoot, 1929). In this paper, a heat sink is postulated in association with a melting front while a heat source is with a freezing front. Then, as in the Lightfoot method, the original problems in two regions can be consolidated into a single problem in one big domain, which is divided into two by the moving source or sink front. One temperature will then be derived, and whether it is in the solid or liquid region depends on the value of the position that is assigned in the temperature equation. Any boundary condition can be imposed, and the equivalent problem in the melting stage becomes:

Governing Equation:

$$\frac{\partial T}{\partial t}=\alpha\frac{\partial^2 T}{\partial x^2}\pm\frac{\alpha}{k}\rho L\frac{dR(t)}{dt}\,\delta[x-R(t)],\ T(x,\,t),\ 0<x<\infty\qquad t_0<t \tag{1}$$

Initial Condition:

$$T(x,\,t_0)=T_0(x,\,t_0) \tag{2}$$

Boundary Conditions:

$$T(0,\,t)=F(t) \tag{3a}$$

or

$$-k\,\frac{\partial T(0,\,t)}{\partial x}=G(t) \tag{3b}$$

$$T(\infty,\,t)=0 \tag{4}$$

Interface Conditions:

$$T(R(t),\,t)=T_m, \tag{5a}$$

$$R(t_0)=0 \tag{5b}$$

where all notations have their usual meanings and $\delta[x-R(t)]$ denotes the Dirac delta function. The signs preceding this function are used for freezing (+) and melting(−).

In the premelt stage the temperature can be derived as

$$T_0(x,\,t)=\sqrt{\frac{\alpha}{\pi}}\int_{s=0}^{t}\frac{E(s)}{(t-s)^{1/2}}\exp\left[-\frac{x^2}{4\alpha(t-s)}\right]ds,\ 0\le t\le t_0 \tag{6}$$

where

$$E(s)=\begin{cases}\dfrac{x}{2\alpha}\,\dfrac{F(s)}{t-s} & (7a)\\[2ex] \dfrac{1}{k}\,G(s) & (7b)\end{cases}$$

for $F(s)$ or $G(s)$ imposed at the boundary. As defined, the upper time limit (t_0) for this stage can be determined by solving the following two equations:

$$F(t_0)=T_m \tag{8}$$

when the temperature is imposed at the surface, and

$$\frac{1}{k}\sqrt{\frac{\alpha}{\pi}}\int_{s=0}^{t_0}\frac{G(s)}{(t_0-s)^{1/2}}\,ds=T_m \tag{9}$$

when the heat flux is imposed at the surface.

Two special cases are worthy of note. When $F(0)\ge T_m\ne 0$ for a melting problem or $F(0)\le T_m\ne 0$ for a freezing problem, the phase changes immediately upon imposition of the boundary conditions. Then the premelt stage does not exist; however, there are still two phases in the medium. Another case arises when $T_0(x,0)=T_m=0$, corresponding to a medium without superheating or subcooling. For this case, the phase changes immediately irrespective of the conditions imposed. Again the premelt stage does not exist; the problem, however, reduces to a one-phase problem.

The equivalent problem can be solved by using Green's function

$$G(x,\,t|x',\,\tau)=\frac{1}{\sqrt{2\pi\alpha(t-\tau)}}\left[\exp\left(-\frac{(x-x')^2}{4\alpha(t-\tau)}\right)\pm\exp\left(-\frac{(x+x')^2}{4\alpha(t-\tau)}\right)\right] \tag{10}$$

where the plus and minus signs are to be used when the flux and temperature conditions are imposed at the boundary, respectively. The temperature can be derived as

$$T(x,\,t)=T_0(x,\,t-t_0)+\int_{x'=0}^{\infty}T_0(x',\,t_0)G(x,\,t-t_0|x',\,0)\,dx'$$
$$\pm\frac{L}{c}\int_{\tau=0}^{t-t_0}\frac{dR(\tau+t_0)}{d\tau}\,G(x,\,t-t_0|R(\tau+t_0),\,\tau)\,d\tau,\ t_0\le t \tag{11}$$

where the signs preceding the last term are to be taken such that freezing, relating to a heat source for front, is positive, and melting, relating to a heat sink, is negative. The first term on the right-hand side can be obtained by referring to Eq. (6) in which t is changed to $t-t_0$, and $F(s)$ and $G(s)$ are changed to $F(s+t_0)$ and $G(s+t_0)$, respectively; the other s in this equation remain unchanged.

Equation (11) can be used to derive a general solution as (Choi, 1991)

$$\frac{T(x,\,t)}{T_m}=\frac{T_0(x,\,t)}{T_m}\pm\frac{\hat{H}(t-t_0)}{\text{Ste}}\int_{\tau=0}^{t-t_0}\frac{dR(\tau+t_0)}{d\tau}\times G(x,\,t-t_0|R(\tau+t_0),\,\tau)d\tau \tag{12}$$

where

$$\hat{H}(t-t_0)=\begin{cases}1 & \text{for } t>t_0\\ 0 & \phantom{\text{for }} t\le t_0\end{cases} \tag{13}$$

$$\text{Ste}=\frac{cT_m}{L} \tag{14}$$

Here, with the use of the circumflexed Heaviside function given by Eq. (13), Eq. (12) holds for all time and for both one- and two-phase problems.

Equation (12) can be used to determine the interface position by setting x to $R(t)$ and $T(R(t),\,t)$ to T_m as

$$\pm\left[1-\frac{T_0(R(t),\,t)}{T_m}\right]=\frac{\hat{H}(t-t_0)}{\text{Ste}}\int_{\tau=0}^{t-t_0}\frac{dR(\tau+t_0)}{d\tau}\,G(R(t),\,t-t_0|R(\tau+t_0),\,\tau)\,d\tau \tag{15}$$

where the plus and minus signs on the left-hand side are to be used for freezing and melting, respectively.

Exact Solutions

Nothing is compromised in the derivation above; the interface position given implicitly in Eq. (15) is exact but expressed in an integro-differential form. This equation can be used for tests for boundary conditions that might lead to an exact solution of the problem. Such tests are important because, in coordinate transformation, one often uses a square root relationship of time for the interface location in scaling the position coordinate if the medium is imposed with a temperature condition; on the other hand, a linear relationship of time is used if the medium is imposed with a flux condition. It is informative to test whether such relations exist exactly.

The structure of the present solution turns out to be well suited for such tests. Since the boundary-condition effect has been confined to the left-hand side of Eq. (15) while the interface-position effect has been confined to the right-hand side of this same equation, one can use a variety of polynomials of t for the F, G, and R functions and introduce them into

Eq. (15) to relate the coefficients in the polynomials. As expected, the exact solutions are impossible, other than a constant temperature condition imposed on the medium with uniform initial temperature; see Choi (1991). For other boundary conditions, the linear or square-root interface positions only exist approximately as shown numerically later.

Numerical Solutions

It is expected that, for a monotonic condition imposed at the boundary, (*i*) the interface position must be zero at time equal to t_0; i.e., Eq. (5*b*); and (*ii*) the interface position curve is monotonic and is a gradual function of time. Then if the entire time range is divided into small time intervals Δt, the $dR(t)/dt$ in Eq. (15) can be treated as constant and removed from the integral in a local linearization process as

$$\pm\left[1-\frac{T_0(R(t_N),\, t_N)}{T_m}\right] = \frac{\hat{H}(t-t_0)}{\text{Ste}}\sum_{n=1}^{N}\left[\frac{dR(t_n^-)}{dt}\int_{\tau=t_{n-1}-t_0}^{t_n-t_0}\frac{1}{2\sqrt{\pi\alpha(t_N-t_0-\tau)}}\left\{\exp\left[-\frac{(R(t_N)-R(\tau+t_0))^2}{4\alpha(t_N-t_0-\tau)}\right] \pm\exp\left[-\frac{(R(t_N)+R(\tau+t_0))^2}{4\alpha(t_N-t_0-\tau)}\right]\right\}d\tau\right] \tag{16}$$

The interface position can be evaluated iteratively.

For the Stefan problems, this local linearization will introduce errors at small time, which can certainly be reduced by taking small time intervals. At large time, since the interface position varies almost linearly with time for all Stefan problems, the accurate terms in the summation in Eq. (16) rapidly outnumber the inaccurate terms to the extent that the present solution is always accurate at large time. Numerical results indicate that the interface positions calculated by this method are unique, convergent, accurate, and stable (Choi, 1991). As for the interface position at small time, one can estimate it by setting N in Eq. (16) to unity as

$$\pm\left[1-\frac{T_0(R(t_1),\, t_1)}{T_m}\right] = \frac{1}{\text{Ste}}\left\{\text{erf}\left(\frac{1}{2\sqrt{\text{Fo}_1}}\right)\pm\frac{1}{2}\left[1-\text{erf}\left(\frac{1}{2\sqrt{\text{Fo}_1}}\right) - \exp\left(\frac{2}{\text{Fo}_1}\right)\text{erfc}\left(\frac{3}{2\sqrt{\text{Fo}_1}}\right)\right]\right\} = \frac{1}{\text{Ste}}\begin{pmatrix}\text{SSG}\\ \text{SSF}\end{pmatrix} \tag{17}$$

where Fo_1 represents the Fourier modulus for the first time interval, $\text{Fo}_1 = \alpha\,(\Delta t)_1/R^2(t_1)$, and SSF and SSG represent the braced expression when the temperature and flux conditions are imposed on the boundary, respectively. Charts for these functions for graphic determination of $R(t)$ are given in Fig. 1.

Results and Discussion

Trends of Interface Position Curves. Aluminum has been used for all tests. Nine cases were tested for temperature conditions. For the results that follow, a small time interval of $\Delta t = 0.05$ s has been used; error is estimated to be less than 0.1 percent. The conditions for these tests are summarized in Table 1, and the results are plotted in dimensionless form in Fig. 2, where length, L, is taken to be 0.025 m. The following conclusions may be drawn:

1 By examining curves 1, 2, 3, and 5, it may be said that a step change of the surface temperature beyond the melting point results in a curvature of the interface-position curves at small time. At large time, the slope of the curves changes, which is related to how fast the surface temperature rises with time.

2 A gradual rise of the surface temperature diminishes the curvature at small time; see curves 4 and 6. Such a trend holds for both one- and two-phase problems. It is also expected that a sensible heating prior to melting delays the phase change; see curves 7–9. However, the trends of these curves remain unchanged. More important, the interface positions for curves 4 and 6–9 vary almost linearly with time, which suggests that an indiscriminate use of the square root relationship for the

Table 1 Nine cases tested for temperature boundary conditions and seven cases tested for flux boundary conditions

	Curve No.	Boundary Condition	Phase-change T in K	Number of Phases	Initial T in K and State	Remarks
TEMPERATURE BOUNDARY CONDITIONS	1	$F(t) = 1000$ (K)	932	1	932 (solid at phase-change temperature)	Step change of surface temperature at $t = 0$
	2	$F(t) = 1000 + 5t$				Same as 1 followed by a linear temperature rise with time
	3	$F(t) = 1000 + 5t^2$				Same as 1 followed by a quadratic temperature rise with time
	4	$F(t) = 932 + 40t$				Surface temperature rises gradually and linearly with time.
	5	$F(t) = 1500$		2	300 (subcooled solid)	Step change of surface temperature at $t = 0$
	6	$F(t) = 932 + 40t$				Step change of surface temperature to melting point and followed by a linear temperature rise with time
	7	$F(t) = 732 + 40t$				Same as 6 except step change of temperature to a lower value
	8	$F(t) = 732 + 8t^2$				Same as 7 except a quadratic temperature rise with time
	9	$F(t) = 300 + 79t$				Surface temperature rises gradually and linearly with time.
FLUX BOUNDARY CONDITIONS	10	$G(t) = 3\times10^6$ (W/m^2)	932	1	932 (solid at phase-change temperature)	Step input of heat at $t = 0$
	11	$G(t) = 3\times10^6 + 5\times10^4 t$				Same as 1 followed by a linear flux rise with time
	12	$G(t) = 3\times10^6 + 5\times10^4 t^2$				Same as 1 followed by a quadratic flux rise with time
	13	$G(t) = 6.39\times10^6$				Same as 1 except a large step heat input
	14	$G(t) = 6.39\times10^6$		2	300 (subcooled solid)	Same as 4 except the solid is subcooled, $t_0 = 5$ sec
	15	$G(t) = 6.39\times10^6 + 2.83\times10^5 t$				Same as 5 followed by a linear flux rise with time, $t_0 = 4$ sec
	16	$G(t) = 6.39\times10^6 + 3.87\times10^5 t^2$				Same as 5 followed by a quadratic flux rise with time, $t_0 = 3$ sec

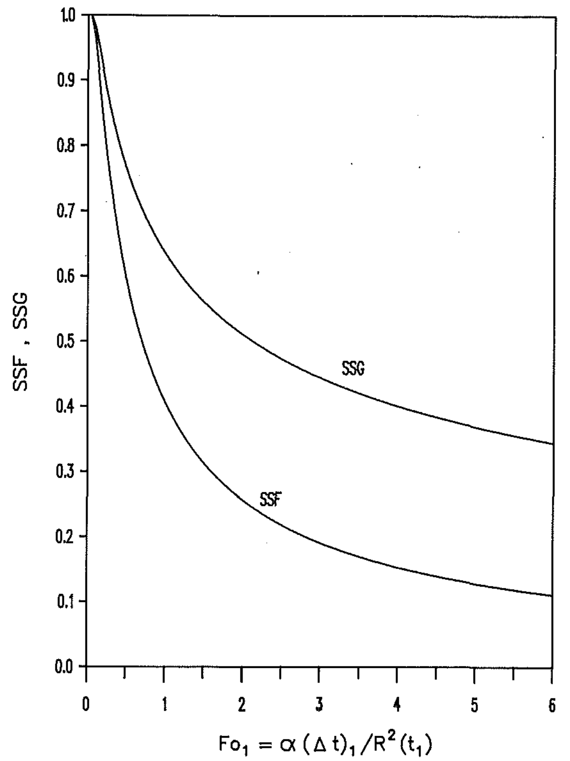

Fig. 1 SSF and SSG curves for determination of interface position of Stefan problems imposed with any temperature and flux conditions

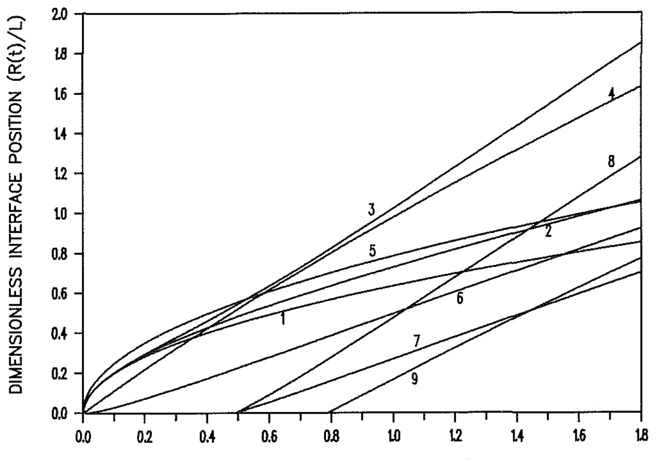

Fig. 2 Trends of interface position of Stefan problems imposed with constant or time-variant temperature conditions

interface position in scaling may be subject to error in coordinate transformation.

Discussion of the trends due to temperature conditions is now complete; attention is now directed to the tests of heat flux conditions. Seven tests are made as listed in the same table; their results are plotted in Fig. 3. Trends of these curves are summarized as follows:

1 By examining curves 10–12, it may be said that the flux conditions imposed at the boundary for time greater than zero have an effect of changing the slope of the position curves at large time. These curves may be considered as the counterparts of the curves 1 through 3 earlier. However, a large step input of heat at the boundary at time equal to zero tends to deflect

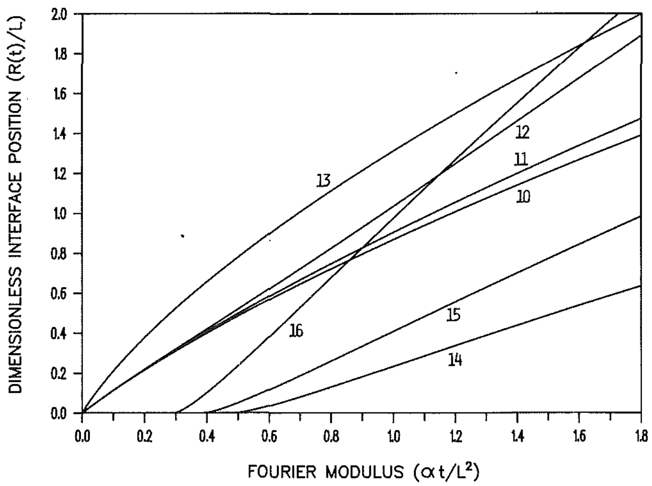

Fig. 3 Trends of interface position of Stefan problems imposed with constant or time-variant heat flux conditions

the curve to the extent that a curvature is now found in curve 13 over a wide range of time (compare it with curve 10).

2 A sensible heating prior to melting delays the onset of phase change; see curves 14–16. Again the slopes of these curves are consistent with the rate of heat input at the surface. It is noted that the $G(t)$ functions chosen for these tests are designed so that the onset of melting occurs sequentially at 3, 4, and 5 seconds. As shown in the figure, the trends of these curves are independent of the onset time. On the other hand, curves 13 and 14 are for the same flux imposed on a medium with and without subcooling. There is a curvature in curve 13 while curve 14 stays almost linear over a wide range of time. This suggests that the subcooling has an effect on the interface position. In general, the tests suggest that, for a moderate heat flux imposed on the boundary, the interface positions vary almost linearly with time. Using linear interface relations to scale the positions in the coordinate transformation is thus justified.

A characteristic is found, however, in some position curves, namely, curves 6 and 8 in Fig. 2 and curves 14–16 in Fig. 3. They have small upward curvature at small time. This may be used to explain why there are different functional dependencies of the position curves at small time in the literature (Evans et al., 1950; Tao, 1979; Yao and Prusa, 1989).

Comparison With Other Analytical Solutions in the Literature. Use is made of the present method to test the accuracy of four analytical solutions developed in the literature. Curve 1 in Table 1 is used to check the analytical solutions developed by Goodman (1964) (integral method (IM)) and Menning and Ozisik (1985) (coupled integral equations (CIE)). It is found that using a cubic temperature profile in IM yields an interface position that is as accurate as the CIE; errors are within 1 percent. Next curve 2 in Table 1 is used for comparison of the Ozisik's CIE method; again the CIE results are good. For this case the largest deviation of the interface position is found at small time, where the error is 1.5 percent. It is noted that curves 1 and 2 have been shown earlier in Fig. 2. Since the errors in these methods are small, they are not replotted here.

When the surface temperature changes rapidly with time (see curve 3 in Table 1), the accuracy of the CIE deteriorates rapidly. As shown in Fig. 4, there is good agreement between the present method and the CIE at small time. However at large time of 20 s, the interface position of the CIE is in error by as much as 20 percent, and such error is expected to grow further with time. This completes the tests of the temperature conditions; attention is now directed toward the heat flux conditions as follows.

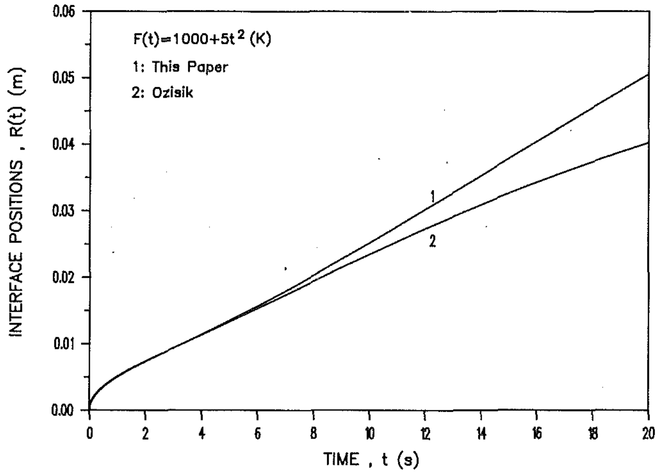

Fig. 4 Comparison of the present method with the method developed in the literature for the solution of Stefan problems imposed with rapidly varying temperature condition

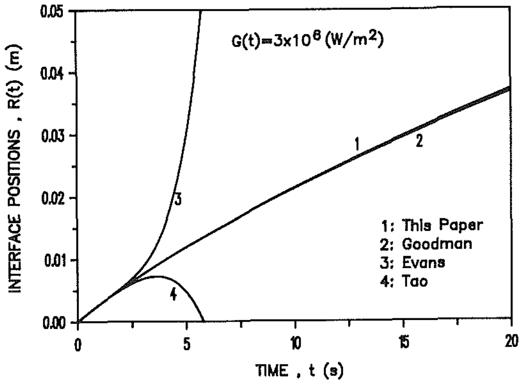

Fig. 5 Comparison of the present method with the methods developed in the literature for the solution of Stefan problems imposed with constant flux condition

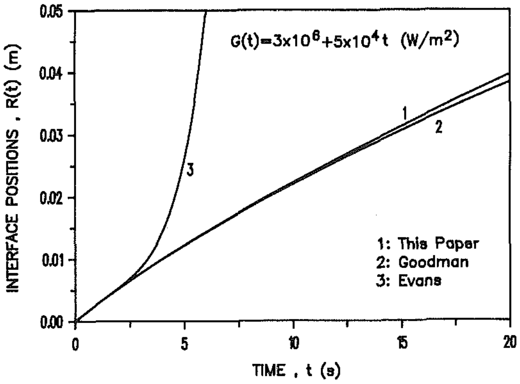

Fig. 6 Comparison of the present method with the methods developed in the literature for the solution of Stefan problems imposed with linear heat flux condition

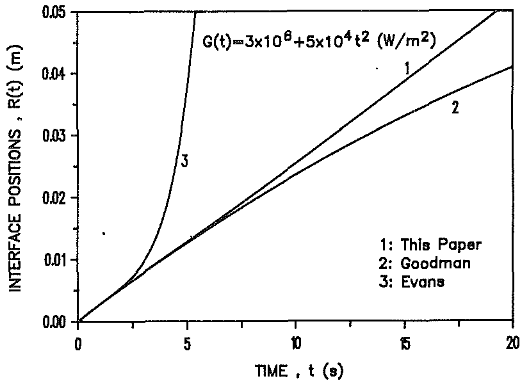

Fig. 7 Comparison of the present method with the methods developed in the literature for the solution of Stefan problems imposed with quadratic heat flux condition

Use is made of curve 10 to test the Stefan problems imposed with a constant heat flux. As shown in Fig. 5, both the methods developed by Evans (1950) (power series (PS)) and Tao (1979) (complimentary error functions (CEF)) are accurate over a small time period of 1 s; however, at a slightly larger time of 2 s, their accuracy starts to deteriorate. Nevertheless, Goodman's IM (1964) is still accurate over a wide range of time; the maximum error is only 1.3 percent at a large time of 20 s.

The same is true for a linear flux condition imposed at the boundary; see curve 11 and Fig. 6. Again Evan's PS method (1950) yields results that are as accurate as the present solution method at small time. It again fails at large time. However, Goodman's IM (1964) is still useful; the largest error is 3 percent at a large time of 20 s.

A different state of affairs is found, however, for a heat flux condition that varies rapidly with time. Using curve 12 in Table 1, it can be shown in Fig. 7 that, this time, even Goodman's IM (1964) fails to predict the interface position. Since the strength of the present method is its accuracy at large time, the observations made above that are related to the failure of those methods imposed with rapidly varying boundary conditions are general and applicable to materials of similar Stefan numbers.

Concluding Remarks

Some remarks are made to close this paper. It is a common notion that the source and sink method suffers from the constraint that the properties of different phases must be equal. It has been reported in Yao and Prusa (1989) that the effect due to density change is small for the Stefan problems. In fact, one can still account for the property changes, if necessary, by using double layers of sources and sinks as did Kolodner (1956). The property changes can thus be accommodated.

References

Choi, C. Y., 1991, "Application of Source-and-Sink Method and Boundary Element Method to the Solution of Stefan Problems Imposed With Constant or Time-Variant Temperature and Flux Conditions," Ph.D. Thesis, University of Florida, Gainesville, FL.

Evans, G.W., Isaacson E., and MacDonald, J. K. L., 1950, "Stefan-Like Problems," *Q. Appl. Math.*, Vol. 8, pp. 312-319.

Goodman, T. R., 1964, "Application of Integral Methods to Transient Nonlinear Heat Transfer," *Adv. Heat Transfer*, Vol.1, pp. 71-79.

Kolodner, I. I., 1956, "Free Boundary Problem for the Heat Equation With Applications to Problems of Change of Phase," *Comm. Pure Appl. Maths.*, Vol. 9, pp. 1-31.

Lightfoot, N. M. H., 1929, "Solidification of Molten Steel," *Proc. Lond. Math. Soc.*, Ser. 2., Vol. 31, pp. 97-116.

Menning, J., and Ozisik, M. N., 1985, "Coupled Integral Equation Approach for Solving Melting or Solidification," *Int. J. Heat Mass Transfer*, Vol. 28, pp. 1481-1485.

Tao, L. N., 1979, "On Free Boundary Problems With Arbitrary Initial and Flux Conditions," *J. Appl. Math. Phys.* (*ZAMP*), Vol. 30, pp. 416-426.

Yao, L. S., and Prusa, J., 1989, "Melting and Freezing," *Adv. Heat Transfer*, Vol. 19, pp. 1-95.

The Pressure Melting of Ice Under a Body With Flat Base

A. Bejan[1] and P. A. Tyvand[2]

Nomenclature

A = physical constant, Eq. (6)
B = parameter, Eq. (9)
F' = force per unit length
F'' = average excess pressure = F'/L
h = thickness of liquid film, Fig. 1
h_{sf} = latent heat of melting
k_2 = thermal conductivity of water (liquid)
L = width of flat object, Fig. 1
P = pressure
P_0 = atmospheric pressure
Pe = Peclet number
r = radial position on disk-shaped contact area
R = radius of disk-shaped contact area
Re = Reynolds number
Q = water volumetric flow rate
Q_0 = value of Q at $x=0$, Fig. 1
s_{sf} = change in specific entropy during melting = $s_f - s_s$
T = temperature
T_m = melting point
T_0 = ice point = 0°C
v_{sf} = change in specific volume during melting = $v_f - v_s < 0$
V = speed of penetration into the ice block
x, y = Cartesian coordinates, Fig. 1
ΔT = constant temperature difference
μ = viscosity of water
ξ = dimensionless position = x/L, Fig. 1
ρ = density of ice
$(\ )_s$ = solid
$(\ )_f$ = liquid

1 Introduction

One of the anomalous thermodynamic properties of water is that the melting point of ice decreases as the pressure increases. This behavior was discovered independently by Kirchhoff (1858) and Thomson (1873). It inspired Reynolds (1901) to speculate that the "pressure-melting" of ice and snow might be responsible for the low coefficient of friction experienced during skating and skiing. According to him, the pressure applied by the skate on the ice surface would cause superficial melting, which in turn would lubricate the relative motion between skate and ice.

Although the pressure-melting phenomenon received some attention from early tribologists, this interest decreased after Bowden and Hughes' (1939) work, which showed that the superficial melting under the skate is due to friction (viscous dissipation) in the water film. The research that followed focused on the frictional melting and lubrication characteristics of ice (e.g., Evans et al., 1976; Tusima, 1977, Oksanen and Keinonen, 1982; Bejan, 1989), i.e., on the *relative* motion between a solid and the ice surface.

In this first note we consider a different fundamental aspect of the pressure-melting of ice, namely the indentation caused by a flat solid that is pressed against a block of ice. Unlike in the work referenced above, there is no lateral motion between the solid body and the ice block. The only motion that occurs is the normal progress that the solid body makes into the ice. This motion is made possible by the melting of the ice situated in front of the body. In this way, the pressure melting process is related to the contact melting process that occurs when a temperature difference (ΔT) is maintained between the solid body and the phase-change material (e.g., Moore and Bayazitoglu, 1982; Bareiss and Beer, 1984; Moallemi et al., 1986; Webb et al., 1987; Roy and Sengupta, 1987; Bejan, 1989). The fundamental differences between the pressure melting of ice and the ΔT-driven melting of a normal phase-change material are discussed further in section 5.

2 Flat Two-Dimensional Body

Consider first the incipient sinking motion experienced by a two-dimensional body of width L, which rests on the flat surface of a block of ice (Fig. 1). The body and the ice block are at the ambient temperature T_0. For simplicity, we take this temperature to be equal to the ice point, $T_0 = 0$°C, which is nearly the same as the triple-point temperature. The pressure that builds under the body places the water in the liquid domain, as shown by the P-T diagram in Fig. 2. In this way, the body is supported by a film of water, the temperature of which decreases in the vertical direction, from T_0 at the bottom of the body, to $T_m(P)$ at the melting front.

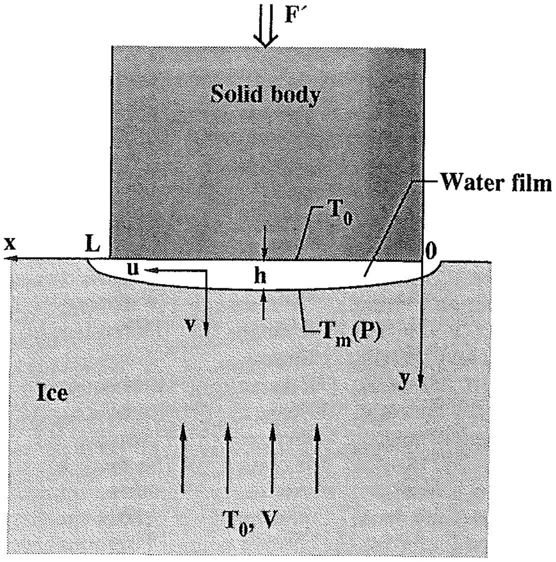

Fig. 1 Two-dimensional body pressing against a block of ice

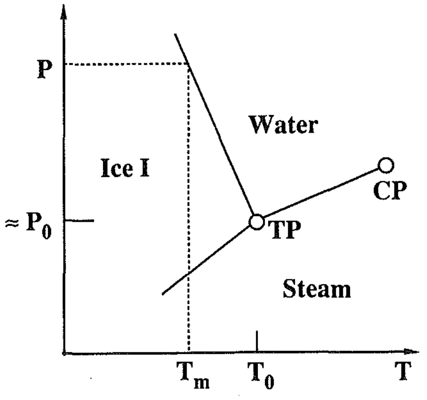

Fig. 2 The *P-T* diagram for water

---

[1] J. A. Jones Professor of Mechanical Engineering, Department of Mechanical Engineering and Materials Science, Duke University, Durham, NC 27706; Fellow ASME.

[2] Department of Agricultural Engineering, Agricultural University of Norway, 1432 Ås-NLH, Norway.

Contributed by the Heat Transfer Division of the AMERICAN SOCIETY OF MECHANICAL ENGINEERS. Manuscript received by the Heat Transfer Division March 11, 1991; revision received August 11, 1991. Keywords: Environmental Heat Transfer, Geophysical Heat Transfer, Phase-Change Phenomena.

The objective of the following analysis is to determine the relationship between the force (weight) applied by the body and its sinking rate V. In the frame (x, y) attached to the bottom of the body, V is the velocity with which T_0-ice flows upward in order to maintain the melting process, i.e., to replace the water liquid that squirts to the sides. Subject to the classical assumptions of film lubrication theory (e.g., Batchelor, 1967), the flow of the water film is governed by the Reynolds equation

$$\frac{dP}{dx}=\mu\frac{\partial^2 u}{\partial y^2} \tag{1}$$

subject to the no-slip conditions $u=0$ at $y=0$, h. The film thickness $h(x)$ is one of the unknowns in this problem. Integrating Eq. (1) twice we obtain

$$u(x, y)=\frac{1}{2\mu}\frac{dP}{dx}(y^2-hy) \tag{2}$$

and, after one more integration,

$$Q(x)=\int_0^h u\,dy=\frac{h^3}{12\mu}\left(-\frac{dP}{dx}\right) \tag{3}$$

The function $Q(x)$ represents the volumetric flow rate in the x direction, expressed per unit length in the direction perpendicular to the plane (x, y). By integrating the mass conservation equation $\partial u/\partial x+\partial v/\partial y=0$ across the liquid film (from $y=0$ to $y=h$), and by using the definition (3), we obtain

$$\frac{dQ}{dx}=V \tag{4}$$

Equations (3) and (4) contain three unknown functions of x, namely P, Q, and h. The third and final equation is the statement that the energy is conserved as ice turns into water across the melting front,

$$\frac{k_2}{h}[T_0-T_m(P)]=\rho V h_{sf} \tag{5}$$

Several assumptions have been made in writing this equation. It was assumed that the liquid film is sufficiently slender ($h \ll L$) and that the water flow is sufficiently slow so that the heat transfer in the liquid space is dominated by conduction in the vertical direction. This thermal assumption is compatible with the hydraulic characteristics assumed in writing the Reynolds Eq. (1) (Bejan, 1989). It means that the temperature distribution across the film is linear.

On the left side of Eq. (5), k_2 is the thermal conductivity of the liquid. On the right side, ρ is the density of ice, and h_{sf} is the latent heat of melting associated with T_0 (or P_0). It is worth noting that Eq. (5) does not clash with the fact that the ice temperature actually varies in the y direction, immediately under the melting front. Equation (5) is simply the first law of thermodynamics for the control volume contained between the planes $y=0$ and $y=\infty$.

With reference to Fig. 2 and the Clausius-Clapeyron relation

$$\frac{dP}{dT_m}=-A \tag{6}$$

in which $A=-s_{sf}/v_{sf}=-h_{sf}/(T_0 v_{sf})$, the relationship between T_m and P in the vicinity of T_0 is approximately linear:

$$T_m=T_0-\frac{P-P_0}{A} \tag{7}$$

The value of the A constant is 13.6 MPa/K, while the "Ice I" domain on the P-T diagram of Fig. 2 extends up to pressures of about 2000 atm (Bejan, 1988, p. 266). By eliminating T_m between Eqs. (5) and (7) we conclude that

$$\frac{k_2}{Ah}(P-P_0)=\rho V h_{sf} \tag{8}$$

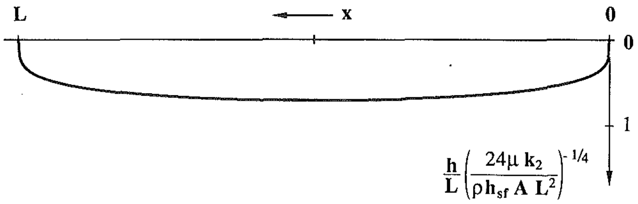

Fig. 3 The shape of the liquid film region maintained under the two-dimensional body of Fig. 1

Equations (3), (4), and (8) can be solved analytically by working with the excess pressure $(P-P_0)$ as an unknown (instead of P), and by using the notation

$$B=\frac{k_2}{\rho h_{sf} A V} \tag{9}$$

First, we integrate Eq. (4)

$$Q=xV+Q_0 \tag{10}$$

and eliminate Q and h between Eqs. (3), (8), and (10):

$$-\frac{d}{dx}[(P-P_0)^4]=\frac{48\mu}{B^3}(xV+Q_0) \tag{11}$$

Next, we integrate this equation in x, and recognize that $P=P_0$ at both ends of the liquid film ($x=0$, L). These two end conditions yield $Q_0=-VL/2$ and, after setting $\xi=x/L$,

$$P-P_0=\left(\frac{24\mu VL^2}{B^3}\right)^{1/4}(\xi-\xi^2)^{1/4} \tag{12}$$

The total normal force per unit depth F' [N/m] exerted by body on the block of ice is then

$$F'=\int_0^L (P-P_0)dx=\left(\frac{24\mu VL^6}{B^3}\right)^{1/4}\int_0^1(\xi-\xi^2)^{1/4}d\xi \tag{13}$$

in which the definite integral on the right side has the value 0.618. Alternatively, we can report this result in terms of the average excess pressure F'' [N/m^2] exerted by the body,

$$F''=\frac{F'}{L}=1.368\,VL^{1/2}\left(\frac{\mu^{1/3}\rho h_{sf}A}{k_2}\right)^{3/4} \tag{14}$$

This form shows that the melting speed (V) is proportional to the applied pressure (F''), and inversely proportional to the square root of the body width (L).

The thickness of the liquid film can be found by combining Eqs. (8), (9), and (12)

$$\frac{h}{L}=\left(\frac{24\mu k_2}{\rho h_{sf}AL^2}\right)^{1/4}(\xi-\xi^2)^{1/4} \tag{15}$$

The film thickness increases as $x^{1/4}$ away from the right corner, and is nearly constant over most of the width L. The shape of the liquid film region is presented in Fig. 3.

3 The Film Slenderness and Small-(Re, Pe) Constraints

Equation (15) shows that the slenderness of the liquid film ($h \ll L$) is assured if the property group on the right side of the equation is small,

$$\left(\frac{\mu k_2}{\rho h_{sf}AL^2}\right)^{1/4} \ll 1 \tag{16}$$

Recall that the film slenderness assumption was invoked before writing the Reynolds Eq. (1) and the energy continuity Eq. (5). Now if we substitute in the inequality (16) the properties of 0°C-water ($\mu=0.0179$ g/cm·s, $k_2=0.56$ W/m·K), the density of ice ($\rho=917$ kg/m^3), $h_{sf}=333.4$ kJ/kg, and $A=13.6$ MPa/K, we find that the film slenderness assumption is valid when

$$L \gg 5\times10^{-10}\ \mathrm{m} \tag{17}$$

The Reynolds Eq. (1) rests also on the assumption that the Reynolds number $\mathrm{Re} = uh/\nu$ is small. We can evaluate Re by noting that $uh \sim VL$, for which the V scale is furnished by Eq. (14) with the physical properties listed above. In this way the inequality $\mathrm{Re} < 1$ translates into

$$\frac{F''}{1\ \mathrm{atm}}\left(\frac{L}{1\ \mathrm{m}}\right)^{1/2} \lesssim 3 \tag{18}$$

The assumption that longitudinal convection can be neglected in the energy equation for the liquid film region requires that the Peclet number $\mathrm{Pe} \doteq uh/\alpha$ be small. This assumption is responsible for the linear temperature distribution across the film, and for the left side of Eq. (5). In the same way as in the preceding paragraph, we find that the constraint $\mathrm{Pe} < 1$ is equivalent to

$$\frac{F''}{1\ \mathrm{atm}}\left(\frac{L}{1\ \mathrm{m}}\right)^{1/2} \lesssim 0.2 \tag{19}$$

The low Peclet number condition (19) is somewhat more restrictive than the low Reynolds number criterion (18). They both place an upper limit on the applied pressure, or on the width of the solid body. Taken together, the inequalities (17) and (19) limit the range of body widths L for which the preceding theory is valid.

4 Body With Disk-Shaped Base

An analysis that is analogous to what we presented in section 2 can be constructed for the case where the base of the solid body (i.e., the body-ice contact area) is a disk of radius R. To save space, we omit the analytical steps and report only the key results, in which r is the radial position measured away from the center of the disk:

$$P - P_0 = \left(\frac{12\mu V R^2}{B^3}\right)^{1/4}\left[1 - \left(\frac{r}{R}\right)^2\right]^{1/4} \tag{20}$$

$$F = \frac{4\pi}{5}(12)^{1/4} V R^{5/2}\left(\frac{\mu^{1/3}\rho h_{sf} A}{k_2}\right)^{3/4} \tag{21}$$

$$\frac{h}{R} = \left(\frac{12\mu k_2}{\rho h_{sf} A R^2}\right)^{1/4}\left[1 - \left(\frac{r}{R}\right)^2\right]^{1/4} \tag{22}$$

The analogy between these results and those obtained for the two-dimensional contact surface becomes clearer as we calculate the average excess pressure that corresponds to the total normal force F:

$$F'' = \frac{F}{\pi R^2} = 1.489 V R^{1/2}\left(\frac{\mu^{1/3}\rho h_{sf} A}{k_2}\right)^{3/4} \tag{23}$$

This expression has the same appearance as Eq. (14).

5 Comparison With the Contact Melting Due to a Temperature Difference

The contact melting phenomenon analyzed in this note is due to the pressure that is maintained over the contact area. The solid body and the ice block (sufficiently far from the contact area) are at the same temperature, T_0. Because of this thermal equilibrium, no melting occurs if the body and the ice block are not pressed against each other, hence the name "pressure melting."

One of the reviewers of this note observed that because of the Clausius-Clapeyron relation (7), the interfacial pressure is equivalent to maintaining a temperature difference across the water film. This led to the question of whether the present pressure-melting results could have been deduced from the results reported for contact melting due to an imposed temperature difference. The answer turns out to be no.

The ΔT-driven contact melting process for the geometry of Fig. 1 was one of the problems analyzed by Bejan (1989). If ΔT is the x-independent temperature difference maintained between the solid body (hot) and the phase-change material (cold), the melting rate is

$$V = \left(\frac{k_2 \Delta T}{\rho h_{sf} L}\right)^{3/4}\left(\frac{F'}{\mu}\right)^{1/4} \tag{24}$$

In this expression F' is the total force per unit length, or $F''L$, where F'' is the average pressure between the block and the phase-change material. The other symbols are defined in the Nomenclature.

It is true that the Clausius-Clapeyron relation (7) can be used to define an "equivalent" temperature difference based on the average pressure F'',

$$\overline{T_0 - T_m} = \frac{F''}{A} \tag{25}$$

It is easy to see, however, that if this temperature difference is substituted in place of ΔT in Eq. (24), the resulting expression for V does not reproduce all the features of Eq. (14). A perfect match is obtained only if ΔT is replaced with $0.658\ F''/A$, in other words, if the equivalent temperature difference of Eq. (25) is defined (by convention) as being equal to $0.658\ F''/A$.

This mismatch stresses the basic differences that exist between the pressure melting and ΔT-melting problems. In the latter, the temperature difference ΔT and film thickness are x independent (Bejan, 1989). When pressure is the cause of melting, the temperature difference $T_0 - T_m(P)$ and the film thickness h are both functions of x.

Acknowledgments

The work reported in this paper was supported by Duke University and the Norwegian research council NLVF. Dr. A. Morega's help is greatly appreciated.

References

Bareiss, M., and Beer, H., 1984, "An Analytical Solution of the Heat Transfer Process During Melting of an Unfixed Solid Phase Change Material Inside a Horizontal Tube," *International Journal of Heat and Mass Transfer*, Vol. 27, pp. 739-746.

Batchelor, G. K., 1967, *An Introduction to Fluid Dynamics*, Cambridge University Press, Cambridge, United Kingdom, pp. 219-222.

Bejan, A., 1988, *Advanced Engineering Thermodynamics*, Wiley, New York, pp. 334-340.

Bejan, A., 1989, "The Fundamentals of Sliding Contact Melting and Friction," ASME JOURNAL OF HEAT TRANSFER, Vol. 111, pp 13-20.

Bowden, F. P., and Hughes, T. P., 1939, "The Mechanism of Sliding on Ice and Snow," *Proc. Roy. Soc. London*, Vol. A172, pp. 280-298.

Evans, D. C. B., Nye, J. F., and Cheeseman, K. J., 1976, "The Kinetic Friction of Ice," *Proc. Roy. Soc. London*, Vol. A347, pp. 493-512.

Kirchhoff, G., 1858, "Bemerkung über die Spannung des Wasserdampfes bei Temperaturen, die dem Eispunkte nahe sind," *Pogg. Ann.*, Vol. 103, pp. 206-209.

Moallemi, M. K., Webb, B. W., and Viskanta, R., 1986, "An Experimental and Analytical Study of Close-Contact Melting," ASME JOURNAL OF HEAT TRANSFER, Vol. 108, pp. 894-899.

Moore, F. E., and Bayazitoglu, Y., 1982, "Melting Within a Spherical Enclosure," ASME JOURNAL OF HEAT TRANSFER, Vol. 104, pp. 19-23.

Oksanen, P., and Keinonen, J., 1982, "The Mechanism of Friction of Ice," *Wear*, Vol. 78, pp. 315-324.

Reynolds, O., 1901, *Papers on Mechanical and Physical Subjects*, Vol. 2, Cambridge University Press, United Kingdom, pp. 734-738.

Roy, S. K., and Sengupta, S., 1987, "The Melting Process Within Spherical Enclosures," ASME JOURNAL OF HEAT TRANSFER, Vol. 109, pp. 460-462.

Thomson, J., 1873, "A Quantitative Investigation of Certain Relations Between the Gaseous, the Liquid, and the Solid States of Water-Substance," *Proc. Roy. Soc.*, Vol. 22, pp. 27-36.

Tusima, K., 1977, "Friction of a Steel Ball on a Single Crystal of Ice," *J. Glaciology*, Vol. 19, pp 225-235.

Webb, B. W., Moallemi, M. K., and Viskanta, R., 1987, "Experiments on Melting of Unfixed Ice in a Horizontal Cylindrical Capsule," ASME JOURNAL OF HEAT TRANSFER, Vol. 109, pp. 454-459.

The Pressure Melting of Ice Due to an Embedded Cylinder

P. A. Tyvand[1] **and A. Bejan**[2]

Nomenclature

A = physical constant = 13.6 MPa/K
D = diameter
f = function of $\hat{y}$, Eq. (15)
F' = force per unit length
G = negative of the pressure gradient, Eq. (16)
h_{sf} = latent heat of melting
$k_{1,2,3}$ = thermal conductivity of ice, water, and solid cylinder
K = cable tension
P = pressure
P_0 = atmospheric pressure
Pe = Peclet number
r = radial position, Fig. 1
R = cylinder radius, Fig. 1
S = width of ice block, Fig. 2
T = temperature
T_m = melting point
T_0 = ice point, 0°C
u, v = velocity components in (x, y) system
$\hat{u}$, $\hat{v}$ = velocity components in $(\hat{x}, \hat{y})$ system
$\mathbf{v}$ = velocity vector in region (2), Fig. 1
V = speed of penetration into the ice block
x, y = Cartesian coordinates, Fig. 1
$\hat{x}$, $\hat{y}$ = local curvilinear coordinates, Eq. (9)
z = lateral coordinate, Fig. 2
$\alpha_{1,2,3}$ = thermal diffusivity of ice, water, and solid cylinder
η = thickness of liquid film, Fig. 1
$\bar{\eta}$ = average film thickness
θ = angular position, Fig. 1
μ = viscosity of water
ρ = density of ice
φ = angle, Eq. (9)

1 Mathematical Formulation

In this second part of the pressure melting study begun in the preceding note (Bejan and Tyvand, 1992) we consider the motion of a cylinder through a block of ice. The cylinder is pushed laterally through the ice block. The ice melts over the leading portion of the cylinder, the water films acts as lubricant (flows around the cylinder), and refreezes over the trailing portion of the cylinder. Figure 1 shows a cross section through the embedded cylinder.

The same problem was solved first by Nye (1967), who proceeded from the assumption that the thickness of the water film is constant. Our objective in this note is to present a general and formal treatment, in which the film thickness is allowed to vary around the cylinder. In this way we arrive not only at Nye's constant-thickness results but also at the limiting conditions under which those results are valid. We then extend the analysis to a cylinder with an elliptical cross section, and report also the shape of the cylindrical cable that moves through a block of ice.

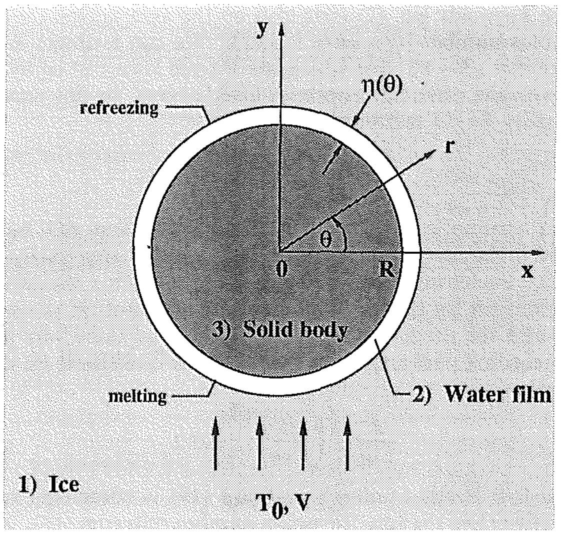

Fig. 1 Melting and refreezing around a cylinder pushed sideways into a block of ice

The present pressure-melting phenomenon is related to the melting caused by a heat source that sinks through a block of phase-change material (Emerman and Turcotte, 1983; Moallemi and Viskanta, 1985a, 1985b). In the latter the melting is due to the temperature difference ΔT maintained between the buried heat source and the phase-change material. The fundamental differences between pressure-melting and ΔT-melting are discussed at the end of section 2.

We introduce the Cartesian system (x, y), with the origin in the center of the cylinder of radius R. The y axis points in the direction of the uniform flow of ice $V\mathbf{j}$. The unit vectors in the x and y directions are denoted by $\mathbf{i}$ and $\mathbf{j}$, and the polar coordinates are given by

$$r = (x^2+y^2)^{1/2}, \quad \theta = \tan^{-1}\left(\frac{y}{x}\right) \tag{1}$$

The pressure-melting and refreezing sustains a water film of radial thickness $\eta(\theta)$. Assuming that the film Reynolds number is small, the momentum equation is the same as for creeping flow,

$$\nabla P = \mu \nabla^2 \mathbf{v} \tag{2}$$

In this equation $\mathbf{v}$ is the water velocity vector, while the buoyancy effect was assumed negligible. The mass continuity equation is $\nabla \cdot \mathbf{v} = 0$. The hydrodynamic lubrication problem statement ends with the boundary conditions

$$\mathbf{v} = 0 \quad \text{at} \quad r = R \tag{3}$$

$$\mathbf{v} = V\mathbf{j} \quad \text{at} \quad r = R + \eta(\theta) \tag{4}$$

In setting up the heat transfer part of the problem it is helpful to use the index (1) for the ice domain, (2) for the water film, and for (3) the solid cylinder (Fig. 1). The thermal conductivities and thermal diffusivities for each domain are k_i and α_i (i = 1, 2, 3). The are constant in each domain. We further assume that convection is negligible relative to conduction in domains (1) and (2), in other words that the characteristic Peclet numbers are small, $\mathrm{Pe}_1 = VR/\alpha_1 < 1$, and $\mathrm{Pe}_2 = V_2\bar{\eta}/\alpha_2 < 1$. In the second of these conditions, we have used V_2 as the velocity scale for the liquid film; this scale will be determined later, as VR/η in Eq. (22). We assume also that the dissipation of mechanical energy in the fluid film is negligible.

The energy equation that is valid under these conditions in domains (1), (2), and (3) is $\nabla^2 T = 0$. As in Bejan and Tyvand (1992), we assume that the ice is at the normal melting point sufficiently far from the cylinder, $T \rightarrow T_0$ as $r \rightarrow \infty$. Along the water-ice interface the temperature and pressure are related

---

[1] Department of Agricultural Engineering, Agricultural University of Norway, 1432 Ås-NLH, Norway.

[2] J. A. Jones Professor of Mechanical Engineering, Department of Mechanical Engineering and Materials Science, Duke University, Durham, NC 27706, USA; Fellow ASME.

Contributed by the Heat Transfer Division of the AMERICAN SOCIETY OF MECHANICAL ENGINEERS. Manuscript received by the Heat Transfer Division March 11, 1991; revision received August 11, 1991. Keywords: Environmental Heat Transfer, Geophysical Heat Transfer, Phase-Change Phenomena.

through the Clausius-Clapeyron equation, which can be integrated by treating A as a constant,

$$P=P_0-A(T_m-T_0), \quad \text{at} \quad r=R+\eta(\theta) \tag{5}$$

The conservation of energy at the water-ice interface requires that

$$k_2\left(\frac{\partial T}{\partial n}\right)_2-k_1\left(\frac{\partial T}{\partial n}\right)_1=\rho h_{sf}V\mathbf{j}\cdot\mathbf{n}, \quad \text{at} \quad r=R+\eta(\theta) \tag{6}$$

for which ρ and h_{sf} are defined in the Nomenclature. We have introduced $\mathbf{n}$ as the outward unit vector at the interface between domains (1) and (2). This unit vector can be expressed in terms of the function $\eta(\theta)$, in order to rewrite the condition (6) as

$$k_2\left(\frac{\partial T}{\partial n}\right)_2-k_1\left(\frac{\partial T}{\partial n}\right)_1=\rho h_{sf}V\frac{\sin\theta-\dfrac{1}{r}\dfrac{d\eta}{d\theta}\cos\theta}{\left[1+\dfrac{1}{r^2}\left(\dfrac{d\eta}{d\theta}\right)^2\right]^{1/2}} \tag{7}$$

Finally, the conservation of energy at the interface between the solid cylinder and the water layer is governed by

$$k_2\left(\frac{\partial T}{\partial r}\right)_2=k_3\left(\frac{\partial T}{\partial r}\right)_3, \quad \text{at} \quad r=R \tag{8}$$

Furthermore, the temperature must vary continuously across the interface, $T_2 = T_3$, at $r = R$.

2 Thin Water Film Around the Cylinder

The full nonlinear thermomechanical free-boundary problem constructed in the preceding section is quite formidable, but it could be solved numerically by iteration techniques. In this section we develop an analytical solution expanded in powers of $\bar{\eta}/R$, where $\bar{\eta}$ is the average film thickness. Consider the local curvilinear coordinate system $(\hat{x}, \hat{y})$ along the cylinder,

$$\hat{x}=r-R, \quad \text{and} \quad \hat{y}=R(\theta-\varphi) \tag{9}$$

In this new system $\hat{x}$ is the radial coordinate and $\hat{y}$ is measured along the cylindrical surface, while the angle φ is fixed, but arbitrary. The Jacobian of the transformation (9) is

$$\frac{\partial(x,y)}{\partial(\hat{x},\hat{y})}=1+\frac{\hat{x}}{R}=1+O\left(\frac{\bar{\eta}}{R}\right) \tag{10}$$

which is valid in the flow domain (2) where $0<\hat{x}<\eta$. This result shows that the curvature and stretching in the local coordinate system $(\hat{x}, \hat{y})$ can only be disregarded to the leading order in the thin-film expansion. From this point on we set $\varphi = 0$.

We now state an important hypothesis, which will be justified *a posteriori*:

$$\eta=\text{constant to the leading order in the thin-film expansion} \tag{11}$$

This hypothesis enables us to decouple the thermomechanical problem, and to solve the hydrodynamic part separately. The latter begins with Eq. (2), which reduces to

$$\nabla P=\mu\frac{\partial^2\mathbf{v}}{\partial\hat{x}^2} \tag{12}$$

This momentum equation is valid to the leading order of $\bar{\eta}/R$. Let $\hat{u}$ and $\hat{v}$ represent the velocity components along the $\hat{x}$ and $\hat{y}$ axes, so that the boundary conditions (3) and (4) are rewritten as

$$\hat{u}=\hat{v}=0, \quad \text{at} \quad \hat{x}=0 \tag{13}$$

$$(\hat{u},\hat{v})=V\left(\sin\frac{\hat{y}}{R}, \cos\frac{\hat{y}}{R}\right), \quad \text{at} \quad \hat{x}=\eta \tag{14}$$

Integrating up the $\hat{x}$ component of Eq. (12), and inserting into the $\hat{y}$ component, we find:

$$\frac{\partial P}{\partial\hat{y}}=\frac{df}{d\hat{y}}=\mu\frac{\partial^2\hat{v}}{\partial\hat{x}^2} \tag{15}$$

In conclusion, the leading order flow is of the Poiseuille type, and it is driven by the pressure gradient around the circumference

$$G(\hat{y})=-\frac{\partial P}{\partial\hat{y}} \tag{16}$$

The radial flow component $\hat{u}$ is negligible relative to $\hat{v}$, although it is of order $(\bar{\eta}/R)^0$. It is negligible because the circumferential flow $\hat{v}$ arises as a singular perturbation, of order $(\bar{\eta}/R)^{-1}$. To the leading order $(\bar{\eta}/R)^{-1}$ then, we have the following homogeneous boundary conditions for the local Poiseuille flow,

$$\hat{v}=0 \quad \text{at} \quad \hat{x}=0 \quad \text{and} \quad \hat{x}=\eta \tag{17}$$

These show that the tangential component of the external (ice) flow does not influence the lubricating flow of the water film. By integrating Eq. (15) and applying the boundary conditions (17) we obtain

$$\hat{v}(\hat{x},\hat{y})=\frac{G(\hat{y})}{2\mu}(\eta-\hat{x})\hat{x} \tag{18}$$

Although $\hat{u}$ is negligible relative to $\hat{v}$, the gradient $\partial\hat{y}/\partial\hat{x}$ is not negligible,

$$\frac{\partial\hat{u}}{\partial\hat{x}}=-\frac{\partial\hat{v}}{\partial\hat{y}}=-\frac{1}{2\mu}\frac{dG}{d\hat{y}}(\eta-\hat{x})\hat{x} \tag{19}$$

Integration of $\hat{u}$ determines the pressure gradient

$$G(\hat{y})=\frac{12\mu VR}{\eta^3}\cos\frac{\hat{y}}{R} \tag{20}$$

and the leading order expressions for the velocity components

$$\hat{u}=V\left(3-2\frac{\hat{x}}{\eta}\right)\left(\frac{\hat{x}}{\eta}\right)^2\sin\frac{\hat{y}}{R} \tag{21}$$

$$\hat{v}=6V\frac{R}{\eta}\left(1-\frac{\hat{x}}{\eta}\right)\frac{\hat{x}}{\eta}\cos\frac{\hat{y}}{R} \tag{22}$$

The entire leading-order velocity field can be summarized as

$$\mathbf{v}=6V\mathbf{i}_\theta\frac{R}{\eta^3}(R+\eta-r)(r-R)\cos\theta \tag{23}$$

valid to $O(\bar{\eta}/R)^{-1}$. In Eq. (23), $\mathbf{i}_\theta$ is the circumferential unit vector $\mathbf{i}_\theta = -\mathbf{i}\sin\theta + \mathbf{j}\cos\theta$.

Turning our attention to the heat transfer part of the problem, it is necessary to remember that the buried cylinder of Fig. 1 first entered the block of ice by pressing against its exposed surface. This means that when the liquid space was first sealed around the cylinder, the top of the liquid film was at atmospheric pressure, $P(x=0, y=R)=P_0$. By integrating Eq. (16) and using this top pressure condition, we obtain the pressure distribution in the liquid film,

$$P=P_0+\frac{12\mu VR^2}{\eta^3}(1-\sin\theta) \tag{24}$$

which is valid to the leading order. It is easy to show that the leading-order viscous shear stress $\mu\partial\hat{v}/\partial\hat{x}$ is one order of magnitude smaller than the pressure amplitude (the pressure difference between the bottom and the top of the cylinder). It can also be shown that the dissipation of mechanical energy can be neglected in the energy equation for the liquid film. In conclusion, the net force per unit length $\mathbf{F}'$, exerted by the water film on the cylinder, is due solely to the integrated effect of the pressure in the liquid,

$$\mathbf{F}'=F'\mathbf{j}=12\pi\mu V\left(\frac{R}{\eta}\right)^3\mathbf{j} \tag{25}$$

The temperature distribution along the water–ice interface is obtained by combining Eqs. (5) and (24),

$$T_m = T_0 + \frac{12\mu V R^2}{\eta^3 A}(\sin\theta - 1), \quad \text{at} \quad r = R + \eta \tag{26}$$

The solution to Laplace's equation $\nabla^2 T = 0$ in the solid domain (3) is $T = a_3 y + b_3$. The ice thermal conductivity k_1 is of the same order of magnitude as the thermal conductivity of water. In order to work consistently to the leading order, we must neglect the external heat transfer through the ice domain (1), although that small contribution can be deduced easily from the external 'dipole'' temperature field. The energy continuity condition (7) assumes the simpler form

$$k_2\left(\frac{\partial T}{\partial r}\right)_2 = \rho h_{sf} V \sin\theta, \text{ at } r = R \tag{27}$$

which shows that the leading-order temperature gradient across the film is independent of r:

$$\frac{\partial T}{\partial r} = \frac{\rho h_{sf} V}{k_2}\sin\theta, \quad R < r < R + \eta \tag{28}$$

This and Eq. (8) yield

$$\left(\frac{\partial T}{\partial r}\right)_3 = \frac{\rho h_{sf} V}{k_3}\sin\theta, \; r = R \tag{29}$$

which confirms $T = a_3 y + b_3$ as the temperature distribution in the solid cylinder,

$$T = \frac{\rho h_{sf} V}{k_3} y + T^* \tag{30}$$

with $T^* = T_0 - 12\mu V R^2/\eta^3 A$.

We now invoke $T_2 = T_3$ at $r = R$, combine Eqs. (26) and (28), and arrive at the equation for the film thickness

$$\frac{\eta^4}{k_2} + \frac{R\,\eta^3}{k_3} = \frac{12\mu R^2}{\rho h_{sf} A} \tag{31}$$

This equation is valid to the leading order in the thin-film expansion, and justifies the hypothesis that η is constant, Eq. (11). It was obtained earlier by Nye (1967). Two limiting cases are of special interest:

I The case $k_3/R >> k_2/\eta$, when the solid cylinder is effectively at constant temperature, and all the temperature difference is bridged by the liquid film. In this case Eq. (31) yields

$$\eta = \left(\frac{12\mu k_2}{\rho h_{sf} A}\right)^{1/4} R^{1/2} \tag{32}$$

and the total force (25) becomes

$$F' = (12\mu)^{1/4}\pi V R^{3/2}\left(\frac{\rho h_{sf} A}{k_2}\right)^{3/4} \tag{33}$$

II The case $k_3/R << k_2/\eta$, when all the temperature difference is spanned by the solid cylinder. Equations (31) and (25) yield in this case

$$\eta = \left(\frac{12\mu k_3 R}{\rho h_{sf} A}\right)^{1/3} \tag{34}$$

$$F' = \pi R^2 V \frac{\rho h_{sf} A}{k_3} \tag{35}$$

In summary, the movement of the cylinder causes melting over the lower half of the liquid–solid interface, and solidification over the upper half. These two processes are driven by the vertical heat transfer through the cylindrical body, as the average temperature of the cylinder matches the far-field ice temperature. In the ΔT-driven melting studies reviewed in section 1, the heat transfer is from the body (heat source) to the surrounding medium.

Another important distinction between pressure-melting and ΔT-driven melting is that in the latter the thickness of the liquid film varies appreciably around the body circumference. In the notation of Fig. 1, the theoretical film thickness around a buried cylindrical heat source varies as $1/\cos(\theta + \pi/2)$, meaning that it should be infinite at $\theta = 0, \pi$ (Moallemi and Viskanta, 1985a). The same behavior is exhibited by the theoretical film thickness around a buried spherical heat source (Emerman and Turcotte, 1983).

3 Cylinder With Elliptical Cross Section

A similar analysis can be performed for the case where the cylinder cross section is slightly elliptical,

$$R(\theta) = \overline{R}(1 + \epsilon\cos 2\theta), \quad (|\epsilon| << 1) \tag{36}$$

In the thin water film limit, the resulting film thickness and net force per unit length are

$$\eta(\theta) = \overline{\eta}(1 + \delta\cos 2\theta), \quad (|\delta| << 1) \tag{37}$$

$$\mathbf{F}' = 12\pi\mu V\left(\frac{\overline{R}}{\overline{\eta}}\right)^3\left(1 + \frac{3}{2}\epsilon + \frac{3}{2}\delta\right)\mathbf{j} + O(\epsilon^2, \delta^2) \tag{38}$$

with the $\overline{\eta}$ and δ values obtained by solving the system

$$\frac{\overline{\eta}^4}{k_2} = \frac{12\mu\overline{R}^2}{\rho h_{sf} A}(1 + 2\delta) - \frac{\overline{R}\,\overline{\eta}^3}{k_3}\left(1 - \frac{3}{2}\epsilon + \frac{\delta}{2}\right) \tag{39}$$

$$\left(\epsilon + \frac{\delta}{2}\right)\frac{\overline{\eta}^4}{k_2} = \frac{2\mu\overline{R}^2}{\rho h_{sf} A}(\delta - 2\epsilon) - \frac{\overline{R}\,\overline{\eta}^3}{k_3}\frac{\epsilon}{2} \tag{40}$$

In the two limits discussed in the preceding section the results reduce to:

I) $k_3/\overline{R} >> k_2/\overline{\eta}$,

$$\delta = -4\epsilon, \quad \overline{\eta} = \left[\frac{12\mu k_2 \overline{R}^2}{\rho h_{sf} A}(1 - 8\epsilon)\right]^{1/4} \tag{41}$$

$$F' \cong 12\pi\mu V\left(\frac{\overline{R}}{\overline{\eta}}\right)^3\left(1 - \frac{9}{2}\epsilon\right) \tag{42}$$

II) $k_3/\overline{R} << k_2/\overline{\eta}$,

$$\delta = -\epsilon, \; \overline{\eta} = \left(\frac{12\mu k_3 \overline{R}}{\rho h_{sf} A}\right)^{1/3} \tag{43}$$

$$F' \cong 12\pi\mu V\left(\frac{\overline{R}}{\overline{\eta}}\right)^3 \tag{44}$$

When the cylinder is a poor conductor (limit II), the departure from the circular shape (ϵ) has no effect on the relationship between force and speed of penetration. This is in agreement with Nye's (1967) general conclusion that the body shape has no effect on the melting speed when the body is a poor conductor.

4 The Shape of a Flexible Cable "Cutting" a Block of Ice

Let us assume that the circular cylinder of Fig. 1 behaves in three dimensions as a perfectly flexible cable. We will follow standard cable theory; see, e.g., Meriam and Kraige (1987). This theory generally assumes that the radius of curvature of the cable is everywhere large compared to the thickness (diameter) of the cable in the local plane through the deformed cable. This assumption coincides with the requirement for applying two-dimensional theory to the present pressure-melting process.

We introduce a z axis perpendicular to the x-y plane (Fig. 2). The cable shape is represented by the curve $y(z)$. To the leading order of our thin-film approximation, the tangential force acting on the cable is zero. By the tangential force balance, this immediately gives the result for the cable tension: K = const along the cable. Note the difference compared with the standard case of a strictly vertical, variable load distribution, where only the horizontal component of the tension

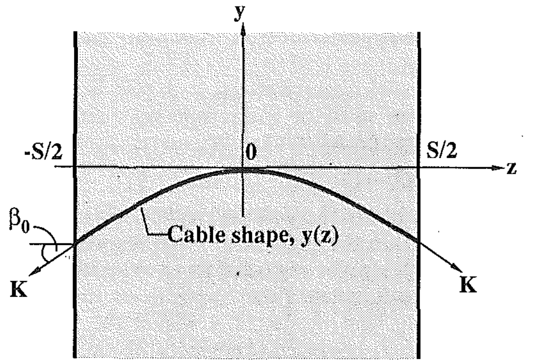

Fig. 2 The shape of a flexible cable moving downward through a block of ice

vector is constant along the cable. In the present case its absolute value is constant.

We assume that the cable is in uniform translation with velocity $-V\mathbf{j}$ relative to the ice block. The normal force of an arc length element of the cable will then be given by $F'dz$, where F' is the force per unit length, dictated by the total translational velocity V through Eqs. (33) and (35). From the normal force balance for an arc length element of the cable we find $F'dz = -K\,d\beta$, where β is the slope angle defined by $\tan\beta = dy/dz$. We immediately find:

$$dy = -\tan\left(\frac{F'z}{K}\right)dz \tag{45}$$

This equation is integrated to give the cable shape:

$$y(z) = \frac{K}{F'}\ln\left(\cos\frac{F'z}{K}\right) \tag{46}$$

As shown in Fig. 2, we have chosen the integration constant so that the origin is at the mount of the curve $y(z)$, in other words, $y(0) = 0$.

Let us now assume that the width of the ice block is constant, denoted by S, so that the ice domain is given by $-S/2 < z < S/2\,(S >> R)$. Let the angle between the cable and the outward vector at the side boundary of the ice block be denoted by β_0. From Eq. (45) we find

$$\beta_0 = \frac{F'S}{2K} \tag{47}$$

If S, K, and β_0 are chosen a priori, F' is determined by Eq. (47) and V by Eq. (33) or (35).

5 Concluding Remarks

In this and the preceding note we have shown how a solid body moves through a block of ice when a net force is maintained between the body and the ice. We constructed this analysis in two stages. In the first note (Bejan and Tyvand, 1992), we analyzed the earliest phase of the pressure melting process, when the solid is just beginning to penetrate the block of ice. In this second note, we reconsidered Nye's (1967) problem of describing the steady progress of the solid body when it is completely surrounded by ice.

The main results of this study is the predicted relationship between the applied force and the speed with which the body moves through the ice. This relationship is presented in Eqs. (14) and (23) of Bejan and Tyvand (1992), and (33) and (35) of this note. Although these equations refer to different stages in the pressure-melting process, it is important to note that the relationship between force and speed does not change appreciably from one stage to the next. In order to see this, review cases I and II at the end of section 2, and note that the case that corresponds to the model of Bejan and Tyvand (1992) is case I (there the solid was isothermal, and the entire temperature drop occurred across the liquid film). Furthermore, to the width L of Bejan and Tyvand (1992) corresponds the diameter $D = 2R$ in Fig. 1. Equation (33) can then be rewritten in terms of D,

$$\frac{F'}{D} = 2.067\,VD^{1/2}\left(\frac{\mu^{1/3}\rho h_{sf}A}{k_2}\right)^{3/4} \tag{48}$$

in order to show that the result for the buried cylinder is, in a scaling sense, the same as the result for the flat body pressing against the ice surface [Eq. (14) in the preceding note].

Acknowledgments

The work reported in this paper was supported by Duke University and the Norwegian research council NLVF.

References

Bejan, A., and Tyvand, P. A, 1992, "The Pressure Melting of Ice Under a Body With Flat Base," ASME JOURNAL OF HEAT TRANSFER, Vol. 114, this issue, pp. 529–531.

Emerman, S. H, and Turcotte, D. L., 1983, "Stokes's Problem With Melting," *International Journal of Heat and Mass Transfer*, Vol. 26, pp. 1625–1630.

Meriam, J. L., and Kraige, L. G., 1987, *Engineering Mechanics, Vol. 1, Statics*, Wiley, New York.

Moallemi, M. K., and Viskanta, R., 1985a, "Melting Around a Migrating Heat Source," ASME JOURNAL OF HEAT TRANSFER, Vol. 107, pp. 451–458.

Moallemi, M. K., and Viskanta, R., 1985b, "Experiments on Fluid Flow Induced by Melting Around a Migrating Heat Source," *Journal of Fluid Mechanics*, Vol. 157, pp. 35–51.

Nye, J. F., 1967, "Theory of Regelation," *Philosophical Magazine*, Vol. 16, pp. 1249–1266.

Maximum Air Flow Rate Into a Roof-Vented Enclosure Fire

M. Epstein[1]

Introduction

An important problem related to the storage of flammable chemicals and waste materials and to fires in buildings or ships involves the combustion of liquid (or sometimes solid) material in an enclosure (i.e., tank, compartment, hold, etc.) that is open to the atmosphere through a vent in the roof of the enclosure. Early in the life of a vented compartment fire, there is ample air in the compartment to support the fire. At a later stage, however, inadequate air is present in the room and the air must be supplied through the vent. Historically, the compartment fire has been treated by a steady-state analysis in which the compartment pressure is assumed constant in time and a countercurrent flow of outflowing hot combustion products and inflowing fresh air is established within the vent. Prahl and Emmons (1975), for example, have treated the steady-state compartment fire ventilated by countercurrent flow through a doorway or window (wall vent). Steady-state fire experiments in model and full-scale enclosures with wall vents have been successfully conducted by Gross and Robertson (1965), Tewarson (1972), Takeda and Akita (1981), and Steckler et al. (1982).

The objective of the analysis given in this note is to determine the maximum possible steady-state combustion rate within a roof-vented enclosure. This is accomplished by considering the

---

[1] Fauske & Associates, Inc., Burr Ridge, IL 60521.

Contributed by the Heat Transfer Division of the AMERICAN SOCIETY OF MECHANICAL ENGINEERS. Manuscript received by the Heat Transfer Division February 1991; revision received October 1991. Keywords: Enclosure Flows, Fire/Flames, Natural Convection.

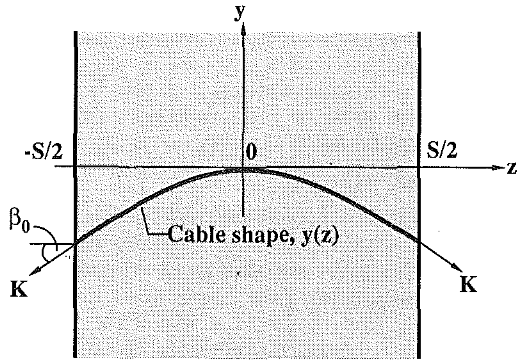

Fig. 2 The shape of a flexible cable moving downward through a block of ice

vector is constant along the cable. In the present case its absolute value is constant.

We assume that the cable is in uniform translation with velocity $-V\mathbf{j}$ relative to the ice block. The normal force of an arc length element of the cable will then be given by $F'dz$, where F' is the force per unit length, dictated by the total translational velocity V through Eqs. (33) and (35). From the normal force balance for an arc length element of the cable we find $F'dz = -K\,d\beta$, where β is the slope angle defined by $\tan\beta = dy/dz$. We immediately find:

$$dy = -\tan\left(\frac{F'z}{K}\right)dz \tag{45}$$

This equation is integrated to give the cable shape:

$$y(z) = \frac{K}{F'}\ln\left(\cos\frac{F'z}{K}\right) \tag{46}$$

As shown in Fig. 2, we have chosen the integration constant so that the origin is at the mount of the curve $y(z)$, in other words, $y(0) = 0$.

Let us now assume that the width of the ice block is constant, denoted by S, so that the ice domain is given by $-S/2 < z < S/2\,(S >> R)$. Let the angle between the cable and the outward vector at the side boundary of the ice block be denoted by β_0. From Eq. (45) we find

$$\beta_0 = \frac{F'S}{2K} \tag{47}$$

If S, K, and β_0 are chosen a priori, F' is determined by Eq. (47) and V by Eq. (33) or (35).

5 Concluding Remarks

In this and the preceding note we have shown how a solid body moves through a block of ice when a net force is maintained between the body and the ice. We constructed this analysis in two stages. In the first note (Bejan and Tyvand, 1992), we analyzed the earliest phase of the pressure melting process, when the solid is just beginning to penetrate the block of ice. In this second note, we reconsidered Nye's (1967) problem of describing the steady progress of the solid body when it is completely surrounded by ice.

The main results of this study is the predicted relationship between the applied force and the speed with which the body moves through the ice. This relationship is presented in Eqs. (14) and (23) of Bejan and Tyvand (1992), and (33) and (35) of this note. Although these equations refer to different stages in the pressure-melting process, it is important to note that the relationship between force and speed does not change appreciably from one stage to the next. In order to see this, review cases I and II at the end of section 2, and note that the case that corresponds to the model of Bejan and Tyvand (1992) is case I (there the solid was isothermal, and the entire temperature drop occurred across the liquid film). Furthermore, to the width L of Bejan and Tyvand (1992) corresponds the diameter $D = 2R$ in Fig. 1. Equation (33) can then be rewritten in terms of D,

$$\frac{F'}{D} = 2.067\ VD^{1/2}\left(\frac{\mu^{1/3}\rho h_{sf}A}{k_2}\right)^{3/4} \tag{48}$$

in order to show that the result for the buried cylinder is, in a scaling sense, the same as the result for the flat body pressing against the ice surface [Eq. (14) in the preceding note].

Acknowledgments

The work reported in this paper was supported by Duke University and the Norwegian research council NLVF.

References

Bejan, A., and Tyvand, P. A, 1992, "The Pressure Melting of Ice Under a Body With Flat Base," ASME Journal of Heat Transfer, Vol. 114, this issue, pp. 529–531.

Emerman, S. H, and Turcotte, D. L., 1983, "Stokes's Problem With Melting," *International Journal of Heat and Mass Transfer*, Vol. 26, pp. 1625–1630.

Meriam, J. L., and Kraige, L. G., 1987, *Engineering Mechanics, Vol. 1, Statics*, Wiley, New York.

Moallemi, M. K., and Viskanta, R., 1985a, "Melting Around a Migrating Heat Source," ASME Journal of Heat Transfer, Vol. 107, pp. 451–458.

Moallemi, M. K., and Viskanta, R., 1985b, "Experiments on Fluid Flow Induced by Melting Around a Migrating Heat Source," *Journal of Fluid Mechanics*, Vol. 157, pp. 35–51.

Nye, J. F., 1967, "Theory of Regelation," *Philosophical Magazine*, Vol. 16, pp. 1249–1266.

Maximum Air Flow Rate Into a Roof-Vented Enclosure Fire

M. Epstein[1]

Introduction

An important problem related to the storage of flammable chemicals and waste materials and to fires in buildings or ships involves the combustion of liquid (or sometimes solid) material in an enclosure (i.e., tank, compartment, hold, etc.) that is open to the atmosphere through a vent in the roof of the enclosure. Early in the life of a vented compartment fire, there is ample air in the compartment to support the fire. At a later stage, however, inadequate air is present in the room and the air must be supplied through the vent. Historically, the compartment fire has been treated by a steady-state analysis in which the compartment pressure is assumed constant in time and a countercurrent flow of outflowing hot combustion products and inflowing fresh air is established within the vent. Prahl and Emmons (1975), for example, have treated the steady-state compartment fire ventilated by countercurrent flow through a doorway or window (wall vent). Steady-state fire experiments in model and full-scale enclosures with wall vents have been successfully conducted by Gross and Robertson (1965), Tewarson (1972), Takeda and Akita (1981), and Steckler et al. (1982).

The objective of the analysis given in this note is to determine the maximum possible steady-state combustion rate within a roof-vented enclosure. This is accomplished by considering the

---

[1] Fauske & Associates, Inc., Burr Ridge, IL 60521.

Contributed by the Heat Transfer Division of the American Society of Mechanical Engineers. Manuscript received by the Heat Transfer Division February 1991; revision received October 1991. Keywords: Enclosure Flows, Fire/Flames, Natural Convection.

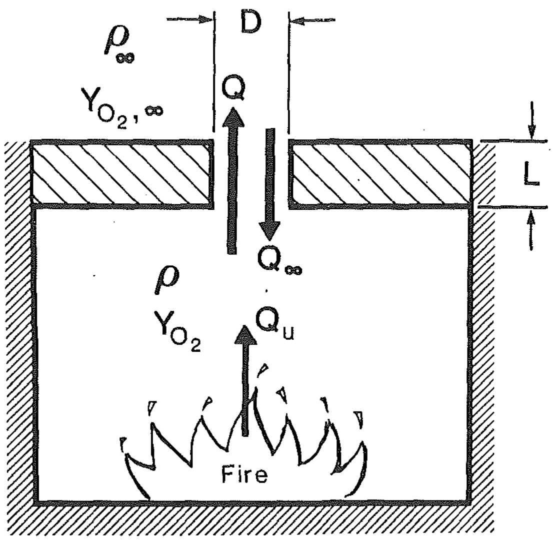

Fig. 1 Schematic representation of a roof-vented enclosure subjected to internal heating by fire

case in which the burning rate is controlled by the rate at which air (oxygen) from the ambient enters the enclosure through the vent. An expression for the maximum possible steady-state rate-of-burning in a roof-vented enclosure has been derived by Cooper (1989). His analysis is based on the assumption that the air flow rate into the tank is a linear function of the pressure drop across the vent. In the present study, available empirical correlations (Epstein, 1988; Epstein and Kenton, 1989) on combined natural convection and forced flow through openings in horizontal partitions provide the necessary information concerning the rate of air flow into the enclosure.

Physical Model and Analysis

The physical system under consideration is illustrated in Fig. 1. Because of combustion heating, the density ρ of the gas inside the enclosure is less than the density ρ_∞ of the outside atmosphere. This density difference induces a buoyancy-driven downflow of the heavier ambient air through the vent at a volumetric rate Q_∞ (in units of, say, $m^3\ s^{-1}$). Combustion heating is also responsible for an oppositely directed upflow Q of the lighter gas from the enclosure through the vent to the ambient. This upflow is a consequence of the gas volume "generated" by heating. Except for the combustion zone, the properties of the gas within the tank are assumed to be spatially uniform and constant in time so that a statistically steady countercurrent flow process occurs at the vent.

By virtue of steady-state mass continuity, the volumetric flows of gas Q_∞ and Q, into and out of the enclosure, respectively, are related by the expression

$$\rho_\infty Q_\infty = \rho Q \tag{1}$$

The temperature difference between the enclosure and the surrounding ambient air creates a pressure difference ΔP across the vent. At this point the appropriate theoretical approach would appear to be the application of Bernoulli's equation along with the assumption of smooth, "noninteracting" streamlines to obtain the relationships between the volumetric flow components within the vent and ΔP, namely $Q_\infty(\Delta P)$ and $Q(\Delta P)$. By eliminating ΔP between these relations and using Eq. (1), the desired relation between Q_∞ and the density ratio ρ_∞/ρ can be obtained (see below). This procedure has proved successful for the stably stratified flow through a wall vent (see, e.g., Steckler et al., 1982). Unfortunately, owing to the chaotic flow pattern that exists within the roof vent when countercurrent flow prevails (Epstein, 1988; Epstein and Kenton, 1989) expressions for $Q_\infty(\Delta P)$ and $Q(\Delta P)$ cannot be obtained from hydraulic theory. Here we present a semi-empirical model of the fire-driven countercurrent flow through a roof vent.

It follows from the inequality $\rho_\infty > \rho$ and Eq. (1) that $Q > Q_\infty$. Thus there must be a net upward volumetric flow through the vent given by

$$Q_u = Q - Q_\infty = Q_\infty(\rho_\infty/\rho - 1) \tag{2}$$

The term Q_u represents the volumetric flow produced by the heating of gas within the enclosure. With respect to the flow within the vent, Q_u may be regarded as an externally imposed, upward, forced volumetric flow opposite to the downward buoyant flow Q_∞. That is, the flow within the vent may be viewed as combined, countercurrent natural and forced convection flow (Q_∞ and Q_u, respectively). This is the flow pattern that was studied experimentally by Epstein and Kenton (1989). They measured the downward buoyancy-driven component Q_∞ in the presence of an imposed upward flow Q_u within an opening in a horizontal partition that separates two unstably stratified fluids. They found that Q_∞ can be correlated by the following formula:

$$Q_\infty = Q_{cc}(1 - Q_u/q)^{2.3} \tag{3}$$

The quantity Q_{cc} is the buoyantly driven volumetric countercurrent flow through the vent in the absence of both the vent pressure drop and the imposed flow (i.e., when $Q_u = 0$ but the same unstable density gradient exists across the vent as when the imposed flow is present). The quantity q in Eq. (3) is the value of the imposed flow necessary to prevent the downward buoyant flow through the vent. The functional form of Eq. (3), including the representation of the fluid transport rates in terms of volumetric flows, is suggested by the application of hydraulic theory to wall vents. As such Eq. (3) may be regarded as a momentum balance applied to the vent, which implicitly accounts for the effect of the pressure rise due to the supply flow (fire draft) Q_u. The reader is referred to Epstein and Kenton (1989) for further details regarding the development of Eq. (3).

Note that the limit of pure countercurrent flow $Q_u = 0$ or, equivalently, $Q_\infty = Q_{cc}$ [see Eq. (3)] cannot be achieved during steady-state combustion as the presence of the fire demands that $Q_u > 0$. The condition $Q_\infty = Q_{cc}$ is a transient one that begins after the fire dies out ($Q_u = 0$) and continues so long as the density difference $\rho_\infty - \rho$ exists. Note also that under this transient compartment cooling condition Eq. (1) and the second equality in Eq. (2) are no longer valid. Similarly, the purging limit $Q_u = q$, therefore $Q_\infty = 0$ in Eq. (3), cannot be achieved during a compartment fire. It is inconceivable that the strength of the fire, which is regulated by the incoming air, can increase sufficiently to cause the outside air to stop flowing into the compartment. Thus during steady-state combustion the incoming ambient air flow must fall between the limits $Q_\infty = 0$ and $Q_\infty = Q_{cc}$.

Epstein (1988) has provided an empirical correlation for the purely buoyantly driven, countercurrent exchange flow rate Q_{cc} in the form of a Froude number versus the aspect ratio of the opening (vent). His result is

$$Q_{cc} = F_{cc}(L/D)\left[2\left(\frac{\rho_\infty/\rho - 1}{\rho_\infty/\rho + 1}\right)gD^5\right]^{1/2} \tag{4}$$

where D is the diameter of the vent, g is the gravitational constant, and F_{cc} (L/d) is a vent shape factor, which depends on the length-to-diameter ratio (aspect ratio) of the vent (see Fig. 1):

$$F_{cc}(L/D) = \frac{0.055[1+400(L/D)^3]^{1/6}}{\{1+0.00527[1+400(L/D)^3]^{1/2}[(L/D)^6+117(L/D)^2]^{3/4}\}^{1/3}} \tag{5}$$

The magnitude of the forced flow q required to purge the opening of the oppositely directed buoyant flow Q_∞ was measured by Epstein and Kenton (1989) and, again, correlated in the form of a Froude number versus L/D:

$$q=F_p(L/D)\left[2\left(\frac{\rho_\infty/\rho-1}{\rho_\infty/\rho+1}\right)gD^5\right]^{1/2} \tag{6}$$

where F_p (L/D) is the vent shape factor for the purging condition; namely,

$$F_p(L/D) = \frac{0.19[1+4\times 10^3(L/D)^3]^{1/9}}{\{1+5.091\times 10^{-2}(L/D)^{16/7}[1+4\times 10^3(L/D)^3]^{4/9}\}^{1/4}} \tag{7}$$

A major result of the above-referenced experimental investigations is that both Q_{cc} and q increase with increasing L/D until $L/D \approx 0.7$. Beyond this value the flow rates decrease with increasing L/D. This behavior is quantified by Eqs. (5) and (7).

It should be mentioned at this juncture that the density ratio range covered in the experiments reported by Epstein (1988) and Epstein and Kenton (1989) was such that $\rho_\infty/\rho < 1.2$. Here we will assume that Eqs. (3) through (7) are valid for values of ρ_∞/ρ of at least 2.0. There is evidence to suggest that these empirical correlations are valid for values of ρ_∞/ρ greater than 1.2. Gardner's (1977) theoretical treatment of the countercurrent exchange flow of stratified fluids within a short, horizontal transfer pipe connecting two closed compartments shows that the flow rate is to first order only a function of the Froude number. The influence of the density ratio over its entire physical range $1 < \rho_\infty/\rho < \infty$ is a variation in the Froude number of only about 30 percent. Moreover, the present author used hydraulic theory to solve the problem of the wall-vented enclosure fire with and without the near-unity density ratio assumption. The numerical results obtained by extrapolating the equation for Q_∞ based on ρ_∞/ρ near unity differed no more than 15 percent from the expression derived for arbitrary ρ_∞/ρ over the range $1.0 \leq \rho_\infty/\rho \leq 3.0$. (This treatment will be presented elsewhere.) Thus correlations (3)–(7) may presumably be trusted to predict approximately the magnitude of the vent flows for the large density ratios encountered in enclosure fire problems. While the above correlations are based mainly on data with round openings, the experimental evidence suggests that Eqs. (3)–(7) can be applied with reasonable accuracy to square openings of length of a side S by making the identification $D = 1.1\ S$.

Substituting Eqs. (2), (4), and (6) into Eq. (3) and rearranging terms gives the following implicit expression for the buoyant flow rate of air Q_∞ into the enclosure as a function of the density ratio ρ_∞/ρ:

$$\frac{Q_\infty}{(2gD^5)^{1/2}}=F_{cc}(L/D)\bullet\left(\frac{\rho_\infty/\rho-1}{\rho_\infty/\rho+1}\right)^{1/2} \times\left\{1-\frac{1}{F_p(L/D)}[(\rho_\infty/\rho)^2-1]^{1/2}\frac{Q_\infty}{(2gD^5)^{1/2}}\right\}^{2/3} \tag{8}$$

Results

The dimensionless inflow of air is plotted against ρ_∞/ρ in Fig. 2 for selected values of L/D. The nonmonotonic arrangement of the curves as a function of L/D is due to the fact that both F_{cc} and F_p exhibit maximum values at $L/D \approx 0.7$. We note that for all the cases shown Q_∞ reaches a maximum value at $\rho_\infty/\rho \approx 2.0$. Obviously, as the ratio ρ_∞/ρ increases the buoyant force at the vent and, therefore, Q_∞ increase. However, as can be seen from Eq. (2), the upward volumetric flow rate Q_u, which opposes Q_∞, also increases with increasing ρ_∞/ρ. For low values of ρ_∞/ρ the buoyant force wins out over Q_u and the curve rises. But, when ρ_∞/ρ is large, the buoyant force begins to lose to the purging effect of increasing Q_u and the curve exhibits a peak value. If we assume that the gaseous environment in the enclosure is a perfect gas similar to the outside air, the temperature T within the enclosure can be related to the outside air temperature by

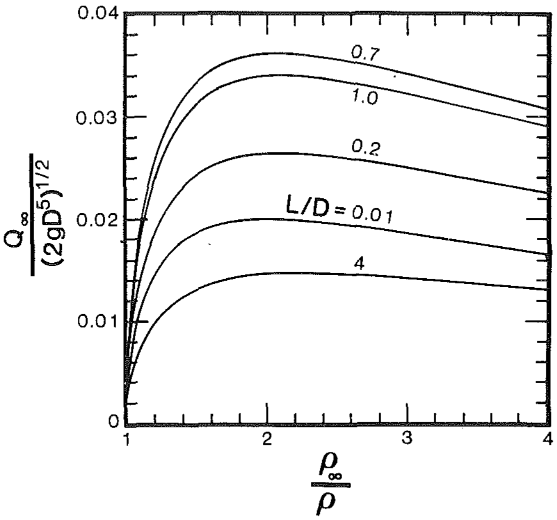

Fig. 2 Dimensionless volumetric air flow rate into enclosure as a function of atmosphere-to-enclosure environment density ratio; effect of vent aspect ratio

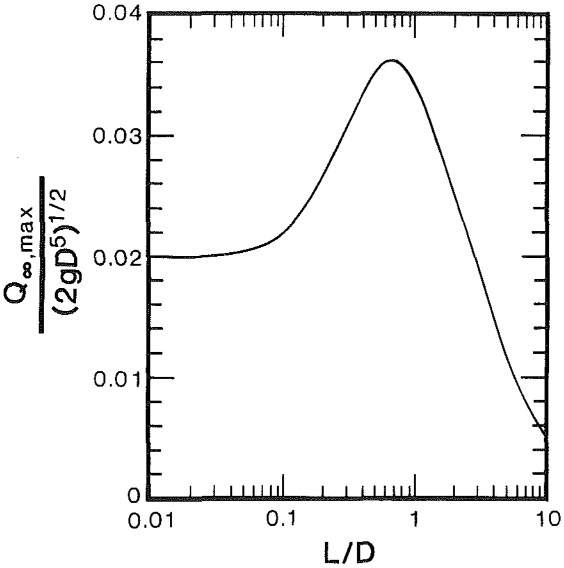

Fig. 3 Maximum dimensionless volumetric air flow rate into enclosure as a function of roof vent aspect ratio

$$\frac{T}{T_\infty}\approx\frac{\rho_\infty}{\rho} \tag{9}$$

Thus Q_∞ reaches a maximum value $Q_{\infty,\max}$ when $T \approx 2T_\infty = 600$ K. Figure 2 graphically demonstrates that Q_∞ is relatively insensitive to ρ_∞/ρ once ρ_∞/ρ exceeds 2.0. Thus the choice of $Q_{\infty,\max}$ will not lead to intolerable overestimates of the air ingression rate for most situations of practical interest. The maximum dimensionless Q_∞ is plotted in Fig. 3 versus L/D. As should be expected, the shape of the curve is similar to the measured F_{cc} and F_p shape factors versus L/D trends correlated by Eqs. (5) and (7).

Maximum Combustion Rate

The net O_2 mass flow rate $\dot{m}_{O_2}$ into the enclosure is

$$\dot{m}_{O_2}=Y_{O_2,\infty}\rho_\infty Q_\infty-Y_{O_2}\rho Q \tag{10}$$

where $Y_{O_2,\infty}$ and Y_{O_2} are the oxygen mass fractions of the flows entering and leaving the enclosure, respectively (see Fig. 1). The maximum net O_2 supply rate is [see Eq. (1)]

$$\dot{m}_{O_2,\max} = \rho_\infty Q_{\infty,\max}(Y_{O_2,\infty} - Y_{O_2}) \qquad (11)$$

It follows from Eq. (11) and the stoichiometry of the reaction in oxygen that the maximum mass rate of burning of fuel $\dot{m}_{F,\max}$ is

$$\dot{m}_{F,\max} = \frac{M_F \rho_\infty Q_{\infty,\max}}{M_{O_2} n}(Y_{O_2,\infty} - Y_{O_2}) \qquad (12)$$

where M_F and M_{O_2} are the molecular weights of fuel and oxygen, respectively, and n is the number of moles of oxygen consumed per mole of fuel burned.

As an illustration of the use of Eq. (12), consider the combustion of methane for which $n = 2$, $M_F = 16$, and $M_{O_2} = 32$. If the aspect ratio of the vent is small ($L/D \rightarrow 0$) we have, from Fig. 3,

$$Q_\infty = 0.02(2gD^5)^{1/2},\ L/D \rightarrow 0 \qquad (13)$$

Cooper's (1989) theory, which is based on the presumption that the air ingression rate is a linear function of the pressure drop across the vent, yields a similar functional form for Q_∞. However, the numerical coefficient in his expression exceeds that of Eq. (13) by about a factor of 2.6. Clearly, from Eq. (12), the maximum rate of fuel consumption is achieved when diffusion-controlled combustion occurs within the enclosure and results in products of combustion with negligible or zero oxygen mass fraction, $Y_{O_2} = 0$. The ambient oxygen mass fraction $Y_{O_2,\infty} = 0.23$. Introducing these quantities into Eq. (12) leads to the result

$$\dot{m}_{CH_4,\max} = 1.62 \times 10^{-3} \rho_\infty (gD^5)^{1/2},\ L/D \rightarrow 0 \qquad (14)$$

for the maximum steady-state rate of combustion of methane in an enclosure with an orifice-type roof vent of diameter D.

To the best of the author's knowledge, no experimental data have been reported in the open literature on steady-state roof-vented enclosure fires. It is hoped that the present treatment will encourage future laboratory studies of this important fire problem.

References

Cooper, L. Y., 1989, "Calculation of the Flow Through a Horizontal Ceiling/Floor Vent," NISTIR 89-4052, National Institute of Standards and Technology, Gaithersburg, MD.

Epstein, M., 1988, "Buoyancy-Driven Exchange Flow Through Small Openings in Horizontal Partitions," ASME JOURNAL OF HEAT TRANSFER, Vol. 110, pp. 885-893.

Epstein, M., and Kenton, M. A., 1989, "Combined Natural Convection and Forced Flow Through Small Openings in a Horizontal Partition, With Special Reference to Flows in Multicompartment Enclosures," ASME JOURNAL OF HEAT TRANSFER, Vol. 111, pp. 980-987.

Gardner, G. C., 1977, "Motion of Miscible and Immiscible Fluids in Closed Horizontal and Vertical Ducts," *Int. J. Multiphase Flow*, Vol. 3, pp. 305-318.

Gross, D., and Robertson, A. F., 1965, "Experimental Fires in Enclosures," *10th Symposium (Int.) on Combustion*, The Combustion Institute, Pittsburgh, PA, pp. 931-942.

Prahl, J., and Emmons, H. W., 1975, "Fire Induced Flow Through an Opening," *Combustion and Flame*, Vol. 25, pp. 369-385.

Steckler, K. D., Quintiere, J. G., and Rinkinen, W. J., 1982, "Flow Induced by Fire in a Compartment," *19th Symposium (Int.) on Combustion*, The Combustion Institute, Pittsburgh, PA, pp. 913-920.

Steckler, K. D., Baum, H. R., and Quintiere, J. G., 1984, "Fire Induced Flows Through Room Openings—Flow Coefficients," *20th Symposium (Int.) on Combustion*, The Combustion Institute, Pittsburgh, PA, pp. 1591-1600.

Takeda, H., and Akita, K., 1981, "Critical Phenomenon in Compartment Fires With Liquid Fuels," *18th Symposium (Int.) on Combustion*, The Combustion Institute, Pittsburgh, PA, pp. 519-529.

Tewarson, A., 1972, "Some Observations on Experimental Fires in Enclosures, Part II—Ethyl Alcohol and Paraffin Oil," *Combustion and Flame*, Vol. 19, pp. 363-371.

Heat and Mass Transfer in a Paper Sheet During Drying

J. Seyed-Yagoobi,[1] D. O. Bell,[1] and M. C. Asensio[1]

Nomenclature

c = specific heat, J/kg-K
h = heat transfer coefficient, W/m^2-K
H = enthalpy, J/kg
J = mass flux, kg/m^2-s
k = thermal conductivity, W/m-K
M = mass of water in sheet, kg/m^3
MC = moisture content, dry basis = weight of water/weight of dry fibers
q'' = heat flux, W/m^2
s = saturation = volume liquid/volume voids
t = time, s
T = temperature, K
W = basis weight = weight of bone-dry sheet/sheet area, kg/m^2
z = paper thickness direction (from cylinder surface to air), m
Z = paper thickness or gap thickness between dryer surface and paper, m
Δ = step size in z direction, m
ϵ = porosity
ρ = density, kg/m^3

Subscripts

a = air
c = contact
f = fiber
final = sheet exiting dryer section
sh = sheet
su = surface
v = vapor
v,i = vapor from interior
v,o = vapor to exterior
w = water

Introduction

Paper and fiber board are dried by threading a continuous wet web around each of a series of 50 to 70 dryer drums. The cylinders are internally heated by condensing steam. Part of a conventional multicylinder dryer section is shown in Fig. 1. The dryer felt is a highly porous material whose main purpose is to hold the paper sheet in close contact with the dryer shell to increase the heat transfer between the paper and dryer and to help prevent shrinkage and deformation of the paper sheet. The sheet moisture content entering the drying section is 150 to 200 percent (dry basis) and the final moisture content varies from 2 to 9 percent.

Many attempts have been made to analyze the paper drying process both theoretically and experimentally. Most theoretical models contain critical assumptions that considerably simplify the heat and mass transport phenomena within the sheet during drying. Kirk (1984) and Iida (1985) provide a review of existing paper drying simulation models. Most of the existing models assume variables such as temperature, moisture content, or thermal conductivity remain uniform through the sheet thickness, and that water fluxes are negligible. Furthermore, a ma-

---

[1] Department of Mechanical Engineering, Texas A&M University, College Station, TX 77843-3123.

Contributed by the Heat Transfer Division and presented at the National Heat Transfer Conference, Minneapolis, Minnesota, July 28-31, 1991. Manuscript received by the Heat Transfer Division April 24, 1991; revision received September 16, 1991. Keywords: Mass Transfer, Materials Processing and Manufacturing Processes, Porous Media.

where $Y_{O_2,\infty}$ and Y_{O_2} are the oxygen mass fractions of the flows entering and leaving the enclosure, respectively (see Fig. 1). The maximum net O_2 supply rate is [see Eq. (1)]

$$\dot{m}_{O_2,\max} = \rho_\infty Q_{\infty,\max}(Y_{O_2,\infty} - Y_{O_2}) \tag{11}$$

It follows from Eq. (11) and the stoichiometry of the reaction in oxygen that the maximum mass rate of burning of fuel $\dot{m}_{F,\max}$ is

$$\dot{m}_{F,\max} = \frac{M_F \rho_\infty Q_{\infty,\max}}{M_{O_2} n}(Y_{O_2,\infty} - Y_{O_2}) \tag{12}$$

where M_F and M_{O_2} are the molecular weights of fuel and oxygen, respectively, and n is the number of moles of oxygen consumed per mole of fuel burned.

As an illustration of the use of Eq. (12), consider the combustion of methane for which $n = 2$, $M_F = 16$, and $M_{O_2} = 32$. If the aspect ratio of the vent is small ($L/D \rightarrow 0$) we have, from Fig. 3,

$$Q_\infty = 0.02(2gD^5)^{1/2},\ L/D \rightarrow 0 \tag{13}$$

Cooper's (1989) theory, which is based on the presumption that the air ingression rate is a linear function of the pressure drop across the vent, yields a similar functional form for Q_∞. However, the numerical coefficient in his expression exceeds that of Eq. (13) by about a factor of 2.6. Clearly, from Eq. (12), the maximum rate of fuel consumption is achieved when diffusion-controlled combustion occurs within the enclosure and results in products of combustion with negligible or zero oxygen mass fraction, $Y_{O_2} = 0$. The ambient oxygen mass fraction $Y_{O_2,\infty} = 0.23$. Introducing these quantities into Eq. (12) leads to the result

$$\dot{m}_{CH_4,\max} = 1.62 \times 10^{-3} \rho_\infty (gD^5)^{1/2},\ L/D \rightarrow 0 \tag{14}$$

for the maximum steady-state rate of combustion of methane in an enclosure with an orifice-type roof vent of diameter D.

To the best of the author's knowledge, no experimental data have been reported in the open literature on steady-state roof-vented enclosure fires. It is hoped that the present treatment will encourage future laboratory studies of this important fire problem.

References

Cooper, L. Y., 1989, "Calculation of the Flow Through a Horizontal Ceiling/Floor Vent," NISTIR 89-4052, National Institute of Standards and Technology, Gaithersburg, MD.

Epstein, M., 1988, "Buoyancy-Driven Exchange Flow Through Small Openings in Horizontal Partitions," ASME JOURNAL OF HEAT TRANSFER, Vol. 110, pp. 885–893.

Epstein, M., and Kenton, M. A., 1989, "Combined Natural Convection and Forced Flow Through Small Openings in a Horizontal Partition, With Special Reference to Flows in Multicompartment Enclosures," ASME JOURNAL OF HEAT TRANSFER, Vol. 111, pp. 980–987.

Gardner, G. C., 1977, "Motion of Miscible and Immiscible Fluids in Closed Horizontal and Vertical Ducts," *Int. J. Multiphase Flow*, Vol. 3, pp. 305–318.

Gross, D., and Robertson, A. F., 1965, "Experimental Fires in Enclosures," *10th Symposium (Int.) on Combustion*, The Combustion Institute, Pittsburgh, PA, pp. 931–942.

Prahl, J., and Emmons, H. W., 1975, "Fire Induced Flow Through an Opening," *Combustion and Flame*, Vol. 25, pp. 369–385.

Steckler, K. D., Quintiere, J. G., and Rinkinen, W. J., 1982, "Flow Induced by Fire in a Compartment," *19th Symposium (Int.) on Combustion*, The Combustion Institute, Pittsburgh, PA, pp. 913–920.

Steckler, K. D., Baum, H. R., and Quintiere, J. G., 1984, "Fire Induced Flows Through Room Openings—Flow Coefficients," *20th Symposium (Int.) on Combustion*, The Combustion Institute, Pittsburgh, PA, pp. 1591–1600.

Takeda, H., and Akita, K., 1981, "Critical Phenomenon in Compartment Fires With Liquid Fuels," *18th Symposium (Int.) on Combustion*, The Combustion Institute, Pittsburgh, PA, pp. 519–529.

Tewarson, A., 1972, "Some Observations on Experimental Fires in Enclosures, Part II—Ethyl Alcohol and Paraffin Oil," *Combustion and Flame*, Vol. 19, pp. 363–371.

Heat and Mass Transfer in a Paper Sheet During Drying

J. Seyed-Yagoobi,[1] D. O. Bell,[1] and M. C. Asensio[1]

Nomenclature

c = specific heat, J/kg-K
h = heat transfer coefficient, W/m^2-K
H = enthalpy, J/kg
J = mass flux, kg/m^2-s
k = thermal conductivity, W/m-K
M = mass of water in sheet, kg/m^3
MC = moisture content, dry basis = weight of water/weight of dry fibers
q'' = heat flux, W/m^2
s = saturation = volume liquid/volume voids
t = time, s
T = temperature, K
W = basis weight = weight of bone-dry sheet/sheet area, kg/m^2
z = paper thickness direction (from cylinder surface to air), m
Z = paper thickness or gap thickness between dryer surface and paper, m
Δ = step size in z direction, m
ϵ = porosity
ρ = density, kg/m^3

Subscripts

a = air
c = contact
f = fiber
final = sheet exiting dryer section
sh = sheet
su = surface
v = vapor
v,i = vapor from interior
v,o = vapor to exterior
w = water

Introduction

Paper and fiber board are dried by threading a continuous wet web around each of a series of 50 to 70 dryer drums. The cylinders are internally heated by condensing steam. Part of a conventional multicylinder dryer section is shown in Fig. 1. The dryer felt is a highly porous material whose main purpose is to hold the paper sheet in close contact with the dryer shell to increase the heat transfer between the paper and dryer and to help prevent shrinkage and deformation of the paper sheet. The sheet moisture content entering the drying section is 150 to 200 percent (dry basis) and the final moisture content varies from 2 to 9 percent.

Many attempts have been made to analyze the paper drying process both theoretically and experimentally. Most theoretical models contain critical assumptions that considerably simplify the heat and mass transport phenomena within the sheet during drying. Kirk (1984) and Iida (1985) provide a review of existing paper drying simulation models. Most of the existing models assume variables such as temperature, moisture content, or thermal conductivity remain uniform through the sheet thickness, and that water fluxes are negligible. Furthermore, a ma-

---

[1] Department of Mechanical Engineering, Texas A&M University, College Station, TX 77843-3123.

Contributed by the Heat Transfer Division and presented at the National Heat Transfer Conference, Minneapolis, Minnesota, July 28–31, 1991. Manuscript received by the Heat Transfer Division April 24, 1991; revision received September 16, 1991. Keywords: Mass Transfer, Materials Processing and Manufacturing Processes, Porous Media.

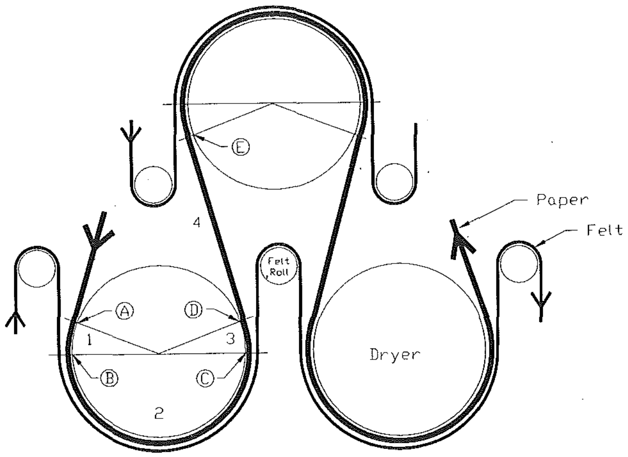

Fig. 1 Nomenclature for the four phases of felt-covered cylinder drying

jority of the models have been developed for corporate use and the details of the models have remained proprietary. A better understanding of the transport phenomena in the paper sheet is needed to model the heat and mass flow through the paper accurately. A flexible model for the entire drying system could aid in the design and maintenance of dryer systems, overall system efficiency, and improved product quality.

Theoretical Analysis

Han (1970) complied the work of several researchers to develop a model for cylinder dryers based on partial differential equations representing the heat and mass transfer in the paper sheet. Han suggested that the partial differential equations could be solved for the moisture and temperature distributions, but gave no solution method or results based on his analysis. The theoretical analysis presented here is partially based on Han's model where the governing differential equations have been improved and a set of realistic boundary conditions have been derived. Details of the model analysis and numerical techniques are given by Bell (1990). A macroscopic approach is used for the theoretical analysis since the thickness of a paper sheet is at least an order of magnitude higher than the diameter of a single wood fiber.

The mass balance is used to calculate the moisture distribution in the paper sheet. The conservation of mass reduces to:

$$\frac{\partial M}{\partial t} = -\frac{\partial J_w}{\partial z} - \frac{\partial J_v}{\partial z} \tag{1}$$

The energy equation includes both the liquid and vapor migration and variations in sheet properties through the sheet thickness:

$$[c_w\rho_w s\epsilon + c_f\rho_f(1-\epsilon)]\frac{\partial T}{\partial t} = -\frac{\partial q''}{\partial z} - \frac{\partial[J_wH_w + J_vH_v]}{\partial z} \tag{2}$$

Fourier's Law, Darcy's Law, and Fick's Law were used to determine q'', J_w, anmd J_v, respectively. The porosity, ϵ, was calculated from the density of a bone-dry sheet, W/Z, as $1-(W/Z)/\rho_f$. Assuming the sheet thickness to be composed of layers of fiber, air, and water, the sheet caliper at any point in the drying process was calculated based on the local moisture content as follows:

$$Z = Z_{\text{final}}\left(1 + \frac{MC\rho_{sh-\text{final}}}{\rho_w}\right) \tag{3}$$

Boundary Equations

In order to solve the equations for all the nodes (interior and surface) explicitly in time, realistic boundary equations with a time-dependent term were derived. True boundary nodes would be simply planes of no mass, resulting in coupled nonlinear mass and energy equations to be solved simultaneously. To avoid this difficulty, the surface nodes in this model were assumed to be located slightly (one-half step size in the z direction) inside the paper sheet, and not exactly on the surfaces. This approximation simplifies the numerical solution technique and is acceptable for very small step sizes in the z direction.

The model used the four phases developed by Nissan and Kaye (1955) as shown in Fig. 1. The dryer section is divided into cycles of these four phases:

Phase 1: The sheet is in contact with the outer surface of the cylinder and is not covered with the felt.

Phase 2: The sheet remains in contact with the cylinder and is covered on its outer surface by the felt.

Phase 3: The sheet remains in contact with the cylinder but is no longer covered with the felt (similar to Phase 1).

Phase 4: The sheet is no longer in contact with the dryer cylinder and moisture is free to evaporate from both sides.

For Phases 1, 2, and 3, the boundary conditions at the surface in contact with the heated cylinder ($z=0$) are:

$$\frac{\partial M}{\partial t} = \frac{1}{\Delta z}(-J_w - J_v) \tag{4}$$

$$[c_w\rho_w s\epsilon + c_f\rho_f(1-\epsilon)]\frac{\partial T}{\partial t} = \frac{1}{\Delta z}\left(\frac{k_c}{Z_c}(T_{su}-T) + k\frac{\partial T}{\partial z} - J_wH_w - J_vH_v\right) \tag{5}$$

The contact conductance in the above equation, k_c/Z_c, is calculated assuming the heat is transferred across a stagnant air gap where k_c is a function of the interface temperature.

For Phases 1 and 3, the boundary conditions at the surface in contact with the moving air ($z=Z$) are:

$$\frac{\partial M}{\partial t} = \frac{1}{\Delta z}(J_w + J_{v,i} - J_{v,o}) \tag{6}$$

$$[c_w\rho_w s\epsilon + c_f\rho_f(1-\epsilon)]\frac{\partial T}{\partial t} = \frac{1}{\Delta z}\left(-k\frac{\partial T}{\partial z} + J_{v,i}H_v + J_wH_w - J_{v,o}H_v - h(T-T_a)\right) \tag{7}$$

Although Phase 2 is similar to Phases 1 and 3, the surface in contact with the moving air ($z=Z$) must be treated differently in Phase 2 because of the presence of felt. The $z=Z$ moisture boundary condition remains essentially the same as in Phases 1 and 3, but with a reduction in the evaporation because of the felt. Evaporation still takes place, but at a reduced rate compared to the other phases. The evaporation calculated without the effect of the felt is multiplied by 80 percent to account for the reduced rate (Pulkowski, 1990). The moisture boundary condition with reduced evaporation is as follows:

$$\frac{\partial M}{\partial t} = \frac{1}{\Delta z}(J_w + J_{v,i} - 0.8\,J_{v,o}) \tag{8}$$

At $z=Z$, the energy equation given for Phases 1 and 3 is not valid for Phase 2 since the presence of the felt blocks the removal of heat by convection. Therefore, the energy equation does not include the convection term and does include the 80 percent reduction in evaporation. Thus, the energy boundary condition for Phase 2 is:

$$[c_w \rho_w s \epsilon + c_f \rho_f (1-\epsilon)] \frac{\partial T}{\partial t}$$
$$= \frac{1}{\Delta z}\left(-k\frac{\partial T}{\partial z} + J_{v,i}H_v + J_w H_w - 0.8 J_{v,o} H_v\right) \quad (9)$$

In Phase 4, the mass and energy boundary conditions for the paper side continually exposed to the moving air ($z = Z$) are the same as those given for Phases 1 and 3, Eqs. (6) and (7). At the $z = 0$ boundary, the paper sheet is no longer in contact with a heated cylinder but is instead exposed to the outside air. The boundary conditions become:

$$\frac{\partial M}{\partial t} = \frac{1}{\Delta z}(-J_w - J_{v,i} - J_{v,o}) \quad (10)$$

$$[c_w \rho_w s \epsilon + c_f \rho_f (1-\epsilon)] \frac{\partial T}{\partial t}$$
$$= \frac{1}{\Delta z}\left(k\frac{\partial T}{\partial z} - J_{v,i}H_v - J_w H_w - J_{v,o} H_v - h(T - T_a)\right) \quad (11)$$

The convection coefficient is calculated by assuming flow over a cylinder in Phases 1, 2, and 3. The Nusselt number is found from an experimental correlation proposed by Churchill and Bernstein (1977), which is recommended for all $\mathrm{Re}_d\mathrm{Pr} > 0.2$. The convection coefficient in Phase 4 is predicted using a Nusselt number correlation for turbulent flow over a flat plate.

Table 1 Test operating conditions for the simulation model

Paper	Basis weight	0.3 kg/m^2 (61.4 lb/1000 ft^2)
	Initial moisture content	1.5 kg H_2O/kg fiber, 150%
	Initial sheet temperature	43.3°C (110°F)
	Final moisture content	0.06 kg H_2O/kg fiber, 6%
	Final thickness	0.5x10^{-3} m (1.64x10^{-3} ft)
	Apparent density	600.0 kg/m^3 (37.5 lb/ft^3)
	Cellulose density	1500.0 kg/m^3 (93.6 lb/ft^3)
	Specific heat	1340.0 J/kg°C (0.32 Btu/lb°F)
Air	Temperature	49.9°C (121.7°F)
	Relative humidity	50%
Machine	Sheet speed	4.63 m/s (911 ft/min)
	Cylinder diameter	1.52 m (5.0 ft)
	Cylinder surface temperature	100°C (212°F)
	Length	
	- Phase 1	0.32 m (1.04 ft)
	- Phase 2	2.39 m (7.85 ft)
	- Phase 3	0.32 m (1.04 ft)
	- Phase 4	0.94 m (3.10 ft)
	Air gap thickness between cylinder and paper	2.54x10^{-5} m (8.33x10^{-5} ft)

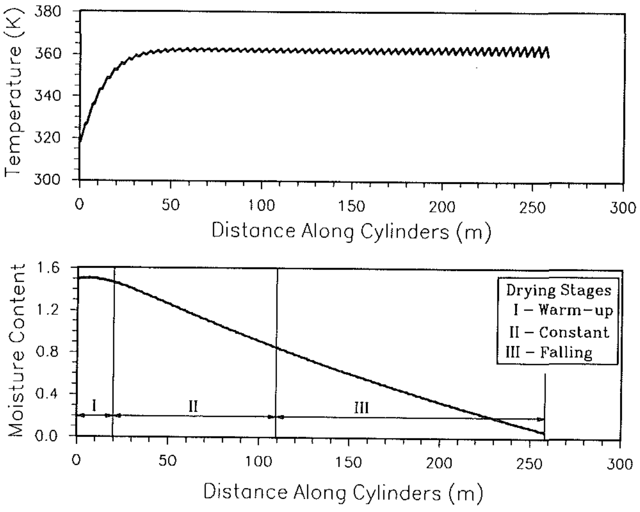

Fig. 2 Average sheet temperature and moisture content during drying

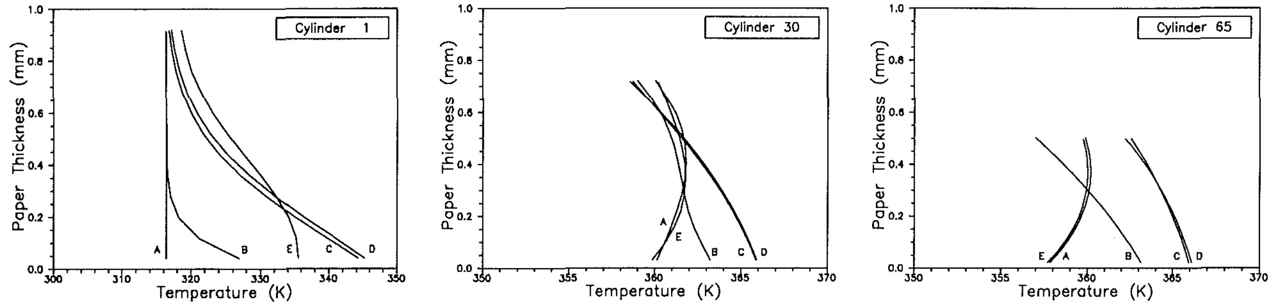

Fig. 3 Temperature profiles within the sheet at cylinders 1, 30, and 65

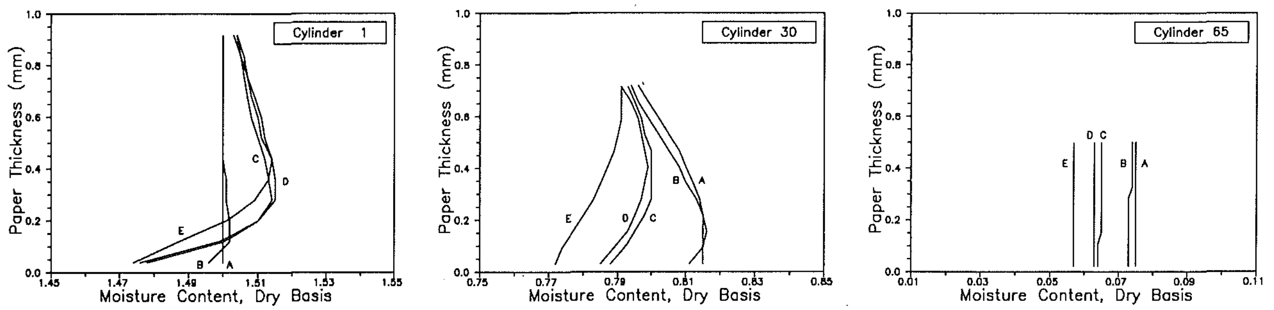

Fig. 4 Moisture content profiles within the sheet at cylinders 1, 30, and 65

These convection coefficients are also used to calculate the mass transfer coefficients from the Chilton-Colburn (1933) analogy to determine the evaporation rate at the paper–air interface, J_{vo}.

Numerical Results

Test operating conditions used in this study are listed in Table 1. The average sheet temperature and moisture content for the test conditions are shown in Fig. 2. The simulation predicted that 65 cylinders were required for drying before the sheet moisture content reached 6 percent. The three distinct stages of drying, i.e., an initial warm-up period followed by a constant rate period and a falling rate period, are denoted in Fig. 2 by I, II, and III, respectively. Use of a variable contact conductance at the cylinder drum/paper interface would lengthen the falling rate period as the heat input into the sheet would be reduced as the sheet dried.

The temperature and moisture content profiles through the paper thickness for cylinders 1, 30, and 65 are shown in Figs. 3 and 4, respectively. The letters on the figures (A–E) correspond to the end of each phase as marked on the cylinder in Fig. 1. The temperature profile in Fig. 3 shows the paper sheet entering cylinder 1 at a constant temperature (A). At the end of Phases 1–3 (B, C, and D), the temperature of the paper nearest the cylinder increases due to the heat conduction from the dryer while the temperature at the air side is the lowest due to the heat being removed by evaporation and convection. With the exception of the initial cylinder, the temperature is higher within the sheet than on the edges by the end of Phase 4 (E). By the end of the dryer section, the temperature profile is similar for the start of each cylinder, i.e., A and E are approximately identical.

As shown in Fig. 4, the inlet moisture distribution is assumed to be constant. By the end of Phase 1 on the first cylinder, the moisture begins to move from the heated side of the paper sheet to the middle of the sheet. Following the warm-up period, the moisture content at the paper–air interface drops during drying due to the evaporation. By the end of Phases 2 and 3, the moisture content at the paper–cylinder interface decreases sharply. For cylinder 30, the sheet that enters with the highest moisture content is found near the edge of the sheet that comes into contact with the heated drum. Toward the end of the dryer section (cylinder 65), the moisture content profile within the sheet is almost uniform.

The model presented above is more flexible than most models previously reported since the internal dynamics of the drying process can be studied and variations in sheet properties throughout the dryer section can be characterized. Changes in sheet caliper and porosity during drying are included in the model and contribute to the manifestation of three distinct drying stages. This results in a definite falling-rate period without artificially decreasing the drying rate as previous studies required. Furthermore, parametric studies can be performed to study the effects of various operating conditions, such as multiple drying stages, on the drying process.

Acknowledgment

This project was funded in part by the Texas Drying Research Consortium, funded by the Energy Research Applications Program of the Texas Higher Education Coordinating Board. Additional support was provided by an Award for Creativity in Engineering from the Division for Engineering Infrastructure Development, National Science Foundation.

References

Bell, D. O., 1990, "Theoretical and Numerical Analysis of Heat and Mass Transfer in a Paper Sheet During Drying," M.S. Thesis, Department of Mechanical Engineering, Texas A&M University, Dec.

Churchill, S. W., and Bernstein, M., 1977, "A Correlating Equation for Forced Convection from Gases and Liquids to a Cylinder in Crossflow," ASME JOURNAL OF HEAT TRANSFER, Vol. 99, pp. 300–306.

Colburn, A. P., 1933, "A Method of Correlating Forced Convection Heat Transfer Data and a Comparison With Fluid Friction," *Transactions of the American Institute of Chemical Engineers*, Vol. 29, pp. 174–210.

Han, S. T., 1970, "Drying of Paper," *TAPPI Journal*, Vol. 53, No. 6, pp. 1034–1046.

Iida, K., 1985, "The Computer Simulation of Web Drying in a Paper Machine Drying Section," presented at the Pulp and Paper Technology Conference, Tokyo, Japan.

Kirk, L. A., 1984, "A Literature Review of Computer Simulation and Paper Drying," *Advances in Drying*, A. Mujumdar, ed., Hemisphere Publishing Corp., Washington, DC, Vol. 3, pp. 1–37.

Nissan, A. H., and Kaye, W. G., 1955, "An Analytical Approach to the Problem of Drying of Thin Fibrous Sheets on Multicylinder Machines," *TAPPI Journal*, Vol. 38, No. 7, pp. 385–398.

Pulkowski, J. H., 1990, Beloit Corporation, Rockton, IL, Private Communication.

Journal of Heat Transfer

Discussion

Similarity Solution of Combined Convection Heat Transfer From a Rotating Cone or Disk to Non-Newtonian Fluids[1]

P. Mitschka.[2] The problem considered belongs to the class of three-dimensional rotational boundary layer flows of the generalized Newtonian fluids (GNF) of the power-law type. The correct order-of-magnitude analysis of the full equations of motion (see Mitschka et al., 1987, 1989) leads to the conclusion that viscous terms in the transformed Eqs. (12) and (13) of the discussed paper must be formulated as

$$[(F''^2+\underline{G'^2})^{(n-1)/2}F''] \text{ and } [(\underline{F''^2}+G'^2)^{(n-1)/2}G']$$

In this two-gradient (2G) formulation, both dominant velocity gradients, F'' and G', appear in the *invariant* viscosity function $(F''^2+G'^2)^{(n-1)/2}$. This satisfies the rules for correct formulation of GNF models for nonviscometric flows (Bird et al., 1960; Schowalter, 1980).

In the paper discussed, however, the expressions for the viscous terms are given as

$$(|F''|^{(n-1)}F'') \text{ and } (|G'|^{(n-1)}G')$$

i.e., in a form that results from an arbitrary omitting of the underlined terms of the 2G formulation. These expressions (one-gradient (1G) formulation) do not satisfy the requirement of invariant viscosity function and are, thus, from the point of view of contemporary non-Newtonian fluid mechanics incorrect.

The influence of 1G and 2G viscosity functions will be demonstrated on the heat transfer data given by Wang and Kleinstreuer in their Fig. 13, for the uniform surface temperature case.

In Fig. 1, results for this heat transfer problem without ($\lambda_T=0$) and with assisting ($Z=1$, $\lambda_T=2$) buoyancy effects are compared for $\Pr=100$ in the form of dependences of temperature gradients at the wall, $-\theta'(0)$, on the power-law flow index n. As expected, differences in the velocities fields due to the 1G or 2G form of the viscous terms in the boundary layer momentum equations are reflected in the heat transfer characteristics resulting from the solution of coupled energy equation. These differences increase with the increasing pseudoplasticity of the power-law fluid (i.e., with decreasing n) and cannot be, in general, neglected.

Thus, in analyses of this class of rheodynamic and heat/mass transfer problems of GNF, only the correct invariant 2G version of the three-dimensional rotational boundary layer equations should be used.

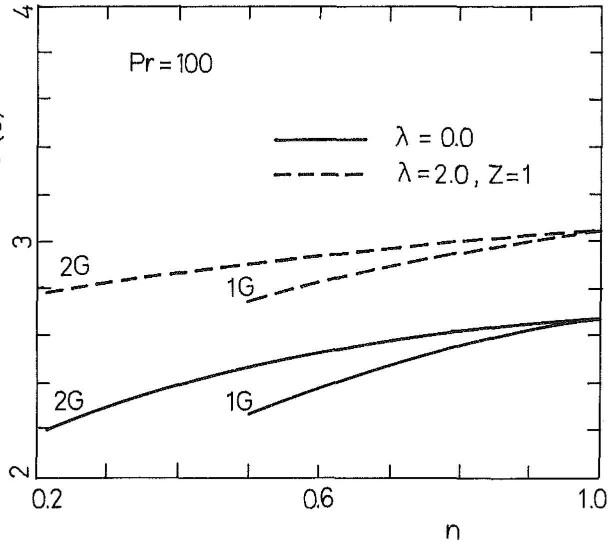

Fig. 1 Comparison of wall temperature gradients in heat transfer from cones and disks rotating in pseudoplastic power-law fluid for 1G and 2G viscous terms

References

Bird, R. B., Stewart, W. E., and Lightfoot, E. N., 1960, *Transport Phenomena*, Wiley, New York.

Mitschka, P., Wein, O., and Wichterle, K., 1987, "Rotational Flows of Non-Newtonian Fluids," in: *Advances in Transport Processes, Vol. V: Transport Phenomena in Polymeric Systems—1*, R. A. Mashelkar, A. S. Mujumdar, and R. Kamal, eds., Wiley Eastern Ltd., New Delhi, pp. 37-116; reedited by Ellis Horwood Ltd., Chichester, United Kingdom, 1989.

Schowalter, W. R., 1960, "The Application of Boundary-Layer Theory to Power-Law Pseudoplastic Fluids: Similar Solutions," *AIChE Journal*, Vol. 6, pp. 24-28.

Authors' Closure

As stated in the Analysis section of the paper by Wang and Kleinstreuer (p. 939), "the velocity and temperature fields are function of x and y only, and transverse curvature effects can be neglected since $\delta/r \ll 1$." Thus our two-dimensional "viscometric" boundary-layer flow equations based on the premise are correct (cf. pp. 102 and 103 plus associated tables from Bird et al. (1960)). A generalization to three-dimensional, "nonviscometric" boundary-layer flow, as discussed above, constitutes a different problem, which, of course, has a (somewhat) different solution.

---

[1] By T.-Y. Wang and C. Kleinstreuer, published in the November 1990 issue of the ASME JOURNAL OF HEAT TRANSFER, Vol. 112, No. 4, pp. 939-944.

[2] Institute of Chemical Process Fundamentals, Czechoslovak Academy of Sciences, 165 02 Praha 6—Suchdol, Czechoslovakia.